Aalborg Universitet

AALBORG UNIVERSITY

Simulated increase in monoarticular hip muscle strength reduces the first peak of knee compression forces during walking

Jolas, Elisa; Simonsen, Morten Bilde; Andersen, Michael Skipper

Published in:
Computer Methods in Biomechanics and Biomedical Engineering

DOI (link to publication from Publisher):
10.1080/10255842.2023.2246304

Creative Commons License
CC BY 4.0

Publication date:
2023

Document Version
Publisher's PDF, also known as Version of record

Link to publication from Aalborg University

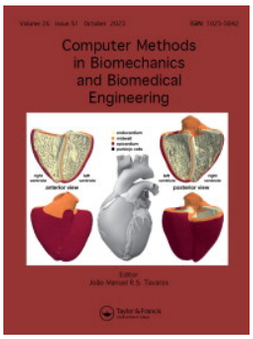
Citation for published version (APA):
Jolas, E., Simonsen, M. B., & Andersen, M. S. (2023). Simulated increase in monoarticular hip muscle strength reduces the first peak of knee compression forces during walking. *Computer Methods in Biomechanics and Biomedical Engineering*, 183-185. https://doi.org/10.1080/10255842.2023.2246304

General rights
Copyright and moral rights for the publications made accessible in the public portal are retained by the authors and/or other copyright owners and it is a condition of accessing publications that users recognise and abide by the legal requirements associated with these rights.

- Users may download and print one copy of any publication from the public portal for the purpose of private study or research.
- You may not further distribute the material or use it for any profit-making activity or commercial gain
- You may freely distribute the URL identifying the publication in the public portal -

Take down policy
If you believe that this document breaches copyright please contact us at vbn@aub.aau.dk providing details, and we will remove access to the work immediately and investigate your claim.

Downloaded from vbn.aau.dk on: May 02, 2026



Taylor & Francis
Taylor & Francis Group

Computer Methods in Biomechanics and Biomedical Engineering

ISSN: (Print) (Online) Journal homepage: www.tandfonline.com/journals/gcmb20

ABSTRACTS 48th Congress of the Society of Biomechanics

Yohan Payan & Lucie Bailly

To cite this article: Yohan Payan & Lucie Bailly (2023) ABSTRACTS 48th Congress of the Society of Biomechanics, Computer Methods in Biomechanics and Biomedical Engineering, 26:sup1, S1-S341, DOI: 10.1080/10255842.2023.2246304

To link to this article: https://doi.org/10.1080/10255842.2023.2246304

© 2023 The Author(s). Published by Informa UK Limited, trading as Taylor & Francis Group.

Published online: 24 Oct 2023.

Submit your article to this journal

Article views: 743

View related articles

View Crossmark data

Full Terms & Conditions of access and use can be found at
https://www.tandfonline.com/action/journalInformation?journalCode=gcmb20

COMPUTER METHODS IN BIOMECHANICS AND BIOMEDICAL ENGINEERING
2023, VOL. 26, NO. S1, S1–S338
https://doi.org/10.1080/10255842.2023.2246304

Taylor & Francis
Taylor & Francis Group

OPEN ACCESS Check for updates

ABSTRACTS 48th Congress of the Society of Biomechanics

Yohan Payan and Lucie Bailly

Chairs of the SB2023 Congress

Edito

The Biomechanics Society was founded in 1976 with the aim of sharing and disseminating up-to-date knowledge in the field of the mechanics of living matter to the international French-speaking community. At the interface of several disciplines such as mechanics, physics, biology, physiology, neurophysiology, medicine, engineering, computer science, robotics and imaging, research in biomechanics ranges from the molecular scale to that of complete living organisms. It includes experimental, theoretical, and computational developments, combining *in vivo*, *in vitro* and in silico approaches, while responding to major societal challenges in the fields of health, sports, transport, ergonomics and industrial design.

This year, the 48th annual congress of the Biomechanics Society holds on the University Grenoble Alpes campus (https://sb2023-grenoble.sciencesconf.org/) from 25th to 27th October 2023 and brings together nearly 200 researchers, clinicians and industrial partners from 15 countries: France, Switzerland, Belgium, Spain, the Netherlands, Danemark, UK, Germany, Ireland, Tunisia, Iran, USA, Canada, Japan, Australia. Following a review process involving at least two reviewers per article, the Scientific Committee of the congress has selected 124 abstracts for publication in this Special Issue of the Computer Methods in Biomechanics and Biomedical Engineering (CMBBE) journal. In addition to the research topics discussed in every annual congress of the Biomechanics Society, this issue highlights two scientific themes specific to Grenoble and the Auvergne-Rhônes-Alpes region, namely 'Biomechanics and mountains' and 'Large-scale facilities for small-scale imaging in biomechanics'. Eleven themes are then covered this year:

- Biomechanics and mountains (page S3)
- Large-scale facilities for small-scale imaging in biomechanics (page S23)
- Cellular and tissue biomechanics (page S38)
- Cardiovascular and respiratory biomechanics (page S102)
- Motion analysis and simulation (page S152)
- Biomechanics of human-system interaction, ergonomics and robotics (page S195)
- Handicap and rehabilitation biomechanics (page S232)
- Sport biomechanics (page S259)
- Musculoskeletal biomechanics (page S284)
- Injury biomechanics and traumatology (page S309)
- Tissue engineering and material by design (page S327)

This 48th edition also hosts three outstanding keynote speakers. Two are related to our special sessions. Nicolas Coulmy is head of the Sports and Scientific Department of the French Ski Federation. Aurélien Gourrier is a CNRS researcher using synchrotron radiation methods to study the biomechanical impact of the nanoscale structure of bony structures. A third keynote speaker, Estefanía Peña, professor at the University of Zaragoza (Spain), develops models and numerical simulations to study the behavior of biological soft tissues.

This edito provides us the opportunity to express our sincere gratitude to all the members of the Organizing and the Scientific Committees, to the trustees of the Biomechanics Society, to the hosting institutions (CNRS, Univ. Grenoble Alpes, Grenoble INP, Univ. Savoie Mont-Blanc) and laboratories (TIMC, 3SR, GIPSA-lab, LIPHY, LIBM, IAB, LRP), the ANR, the MACI, the METRO and Auvergne-Rhônes-Alpes region, the industrial partners (Biometrics France, Bruker, Trinoma) as well as the research networks (Fed3G, Labex CAMI, Labex Tec21, SBCF, SFGBM, GDR MECABIO SANTE, GDR IMABIO, GDR Sport et Activité Physique) that kindly endorsed and sponsored this 48th edition.

© 2023 The Author(s). Published by Informa UK Limited, trading as Taylor & Francis Group.
This is an Open Access article distributed under the terms of the Creative Commons Attribution License (http://creativecommons.org/licenses/by/4.0/), which permits unrestricted use, distribution, and reproduction in any medium, provided the original work is properly cited. The terms on which this article has been published allow the posting of the Accepted Manuscript in a repository by the author(s) or with their consent.

Organizing committee

- Yohan Payan, PhD (Chair) – CNRS, TIMC Lab
- Lucie Bailly, PhD (Chair) – CNRS, 3SR Lab
- Bruno Watier, PhD (Co-Chair) – President of the French Biomechanics Society
- Noémie Briot, PhD – Univ. Grenoble Alpes, TIMC Lab
- Violaine Cahouet, PhD – Univ. Grenoble Alpes, GIPSA-lab
- Grégory Chagnon, PhD – Univ. Grenoble Alpes, TIMC Lab
- Mickaël Chollet, PhD student – Univ. Savoie Mont-Blanc, LIBM
- Clément de Loubens, PhD – CNRS, LRP
- Frédérique Hintzy, PhD – Univ. Savoie Mont-Blanc, LIBM
- Xavier Hugues, PhD student – Univ. Grenoble Alpes, GIPSA-lab
- Dácil Idaira Yánez Martín, PhD student – Univ. Grenoble Alpes, LRP
- Jacques Ohayon, PhD – Univ. Savoie Mont-Blanc, TIMC Lab
- Emmanuelle Planus, PhD – Univ. Grenoble Alpes, IAB
- Franck Quaine, PhD – Univ. Grenoble Alpes, GIPSA-lab
- Claude Verdier, PhD – CNRS, LIPHY

Scientific committee

- Nasser Rezzoug (Chair) – Vice-President of the French Biomechanics Society
- Clément de Loubens (Chair)
- Lucie Bailly
- Xavier Hugues
- Yohan Payan
- Jacques Ohayon
- **Coordinators of thematic sessions**: Michel Behr, Yoann Blache, Matthieu Chabanas, Emilie de Brosses, Valérie Deplano, Xavier Gidrol, Laurent Héliot, Frédérique Hintzy, Christophe Marquette, Simon Mendez, Françoise Peyrin, Hélène Pillet, Charles Pontonnier, Thomas Robert, Baptiste Sandoz, Isabelle Tardieux, Alexandre Terrier
- **Reviewers of the abstracts**: J.-M. Allain, P. Alvarez, K. Anselme, Y. Aoustin, J.-P. Arnoux, P. Assemat, S. Avril, C. Azevedo Coste, M. Babel, N. Bahlouli, L. Bailly, N. Bailly, A. Baldit, C. Baron, J. Bascou, T. Bege, M. Begon, M. Behr, A. Bel-Brunon, S. Bensamoun, E. Bergamini, G. Bidaux, Y. Blache, O. Boiron, V. Bonnet, X. Bonnet, C. Bruna-Rosso, K. Bruyère, V. Cahouet, C. Cavinato, P. Canadas, M. Chabanas, P. Chabrand, G. Chagnon, C. Chappard, M. Charbonneau, A. Chauvière, L. Cheze, T. M. Chikhaoui, J. Clément, N. Coulmy, N. Crevier-Denoix, E. Cutri, C. de Loubens, P. Decq, V. Deplano, A. Dieterlen, M. Dorsemaine, R. Dumas, G. Dumont, S. Duprey, M. Dupuis, C. Duraffourg, M. Evin, H. Follet, L. Fradet, E. Franceschini, F. Quaine, F. Bailly, F. Prince, F. Bertrand, J. Fullana, D. Garcia, R. Gauthier, M. Genet, A. Germaneau, M. Giandolini, Q. Grimal, E. Groult, C. Guivier-Curien, N. Hagemeister, C. Hautier, C. Hayot, L. Héliot, F. Hintzy, T. Hoc, X. Hugues, J. Husson, N. Jarrassé, Y. Lafon, J.-D. Laporte, S. Laporte, C. Laurent, S. Le Floch', C. Le Mouel, P. Legreneur, T. Lemaire, P. Levitz, D. Marchat, F. Marin, C. Masson, P. Maurice, S. Mendez, D. Mitton, F. Moissenet, K. Monier, S. Monneret, T. Monnet, B. Morel, C. Morin, G. Mornieux, A. Müller, A. Naaim, C. Nicol, F. Noe, A. Nordez, J. Ohayon, M. Ottenio, F. Peyrin, H. Pillet, A. Pinzano, C. Pontonnier, P. Pudlo, G. Rao, G. Recher, T. Rezgui, N. Rezzoug, T. Robert, I. Rogowski, A. Salles, P. Samozino, B. Sandoz, E. Simoneau, P. Swider, I. Tardieux, C. Terryn, R. Tisserand, R. Trama, Y. Usson, C. Verdier, L. Vico, L. Vigouroux, B. Watier.

Session biomechanics and mountains

Biomechanics of snowboarding with an above-knee prosthesis, page S4.
Combining video analysis and multibody simulation to study spinal fractures mechanism during a snowboarding crash, page S6.
Comparison of the propulsive force production capacities between flat acceleration sprinting and uphill running at constant velocity, page S9.
Evolution of the torque applied to the alpine ski binding as a function of speed, page S11.
Fatigue induced by trail-running impairs ankle eversion control with no inter-limb differences, page S13.
Kinematic and kinetic comparisons of Jump pull ups used in rock-climbing evaluations, page S15.
Mechanical work during ski mountaineering: the effects of climbing slopes, page S18.
Numerical investigation of head injury risks during ski collisions against obstacles, page S21.

Biomechanics of snowboarding with an above-knee prosthesis

X. Bonnet[a], S. Loubet[b] and P. Baratero[b]

[a]Institut de Biomecanique Humaine Georges Charpak, Ecole Nationale Superieure d'Arts et Métiers, Paris, France; [b]ANICES, Association Nicoise d'Initiatives Culturelles et Sportives, Nice, France

1. Introduction

Snowboarding is a relatively new winter sport that was introduced at the Olympic Games in 1998 and the Paralympic Games in 2014. Today, amputee athletes can compete in one of three categories: LL1 for above knee amputation, LL2 for below knee amputation and UL for upper limb amputation.

To ride a snowboard, the snowboarder must control his toe and heel edges. This involves flexing the ankles and knees, among other movements necessary for snowboarding. Different prosthesis exists for people with lower limb amputations. The movements of the knee and ankle joints are passively controlled by hydrau-pneumatic shock absorbers. For LL1 riders, it is essential to align their prosthesis (socket, knee, ankle) with their body and the board. From there, snowboarders need to know how to shift their weight to get the right edges.

Different studies have proposed protocols to measure the kinematics of the body during snowboarding activities from calibrated optical environments (Back et al. 2013) or embedded magnetic systems (McAlpine 1994). More recently, quantified motion analysis protocols have also been proposed based on inertial motion units (IMU) allowing the kinematic analysis without limiting the measurement area (Krüger and Edelmann-Nusser 2009). The kinematics of the lower limb is reported in the literature for able-bodied snowboarders and for snowboarders with below knee amputations (Minnoye and Plettenburg 2009), but not for snowboarders with above knee amputations who must also ride their prosthetic knees.

The objective of this study is to quantify the kinematics of the prosthetic knee and ankle for an above-knee amputee rider during a slalom of 15 heel and toe turns and to compare this kinematics to a non lower limb amputee rider. This study could lead to a better understanding of the capabilities and limitations of the prosthetic components, help athletes and coaches to use their prosthesis and eventually help to design devices more adapted to the practice of each individual.

2. Methods

One LL1 and one UL athletes participated in this study. LL1 snowboarder included in this study used her prosthesis for the front leg. The prosthesis was composed of the Procarve foot and knee joint. Measurements were performed on a typical slalom composed with 15 front and 15 back turns.

Riders were equipped with 8 IMUS (Xsens) on the trunk, the pelvis, both tight, both leg and both feet. Measurements were performed using the Awinda station at 100 Hz, synchronized with a webcam on a portable computer. Kinematic analysis was computed using Xsens MVN 2023. Dynamic calibration was performed without the board before each slope descent. Trunk kinematic and video clips were used to identify the beginning of each back side turn. The kinematic of the knee and the ankle were then normalized according % of cycle (one cycle represents one back turn followed by one front turn).

The ground reaction force was not measured, but its point of application and orientation was estimated using the method proposed by (Staniszewski 2019) to understand knee kinematics for subject LL1 during turns.

3. Results and discussion

Figure 1 presents the evolution of the knee flexion during a cycle of back and front turn for the rider

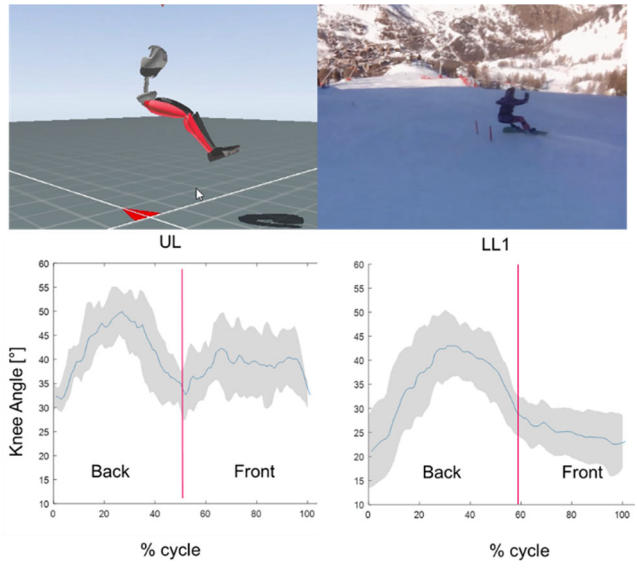


Figure 1. (Upper) Lower limbs plus sternum kinematic measurement with 8 IMUs. (Lower) Knee kinematics for UL and LL1 rider.



Figure 2. Ground reaction force estimated during a back and a front turn.

without lower limb amputation (UL) and the rider with above knee amputation (LL1).

Knee flexion was close to 30° during the turn transition, reached 50° during the backside turn and 40° during the frontside turn for the UL rider. Prosthetic knee flexion was near 20° of flexion during the transition turn, increased to 40° during the back side turn but presented no more flexion during the front side turn for the LL1 subject.

The ankle range of motion was similar for both subjects with no motion during the back side turn (due to the spoiler) and close to 20° of dorsiflexion during the front side turn.

Ground reaction forces were not recorded during the experiment, but they can be estimated using the slope angle, the direction angle, and the centrifugal force which is a function the snowboarder's velocity and the turn radius (Vaverka et al. 2012). Balance during snowboarding is maintained by keeping the center of mass aligned with the ground reaction force (Staniszewski 2019). Limb flexion is needed during turn to damp this force and extension is needed during the transition to unload the board and switch the edge in contact with the snow.

During a carved back turn (Figure 2 left), the ground reaction force goes from the heel edge of the board to the body center of mass. It results an external knee flexion moment, which allows the prosthetic knee to flex against the resistance of the shock absorber. Ankle plantarflexion is well limited by the spoiler of the board.

During a carved front turn, the ground reaction force goes from the toe edge of the board to the body center of mass. It results an external dorsiflexion moment at the ankle allowing the ankle to flex, but if this ankle motion is limited, an external extension moment is applied on the knee joint restricting prosthetic knee flexion.

4. Conclusions

Riding a snowboard with a prosthetic ankle and knee is a challenge. The alignment of the joints of the prosthesis with the snowboard and the rider is critical in order to ensure proper functioning of the prosthesis and to allow for carved turns on both the back side and the front side. The resistance of the shock absorbers must be correctly adjusted to allow for an adapted range of motion and the requirements are strong to maintain both balance in turns and contact with the snow. Further work will be conducted in order to characterize the behavior of the prosthetic foot and knee as a function of their alignment, the adjustment of the pneumatic systems and perhaps identify new technological solutions to allow better prosthetic functioning.

Acknowledgements

The authors would like to thank the ANICES association for having allowed the realization of these experiments and Trinoma for the loan of the Xsens license.

References

Back J, Son W, Lee J, Jo S, Yi J, Panday SB. 2013. Kinematical analysis of the turn transition phase of the snowboarders' carving turn. IJBSBT. 5(6):43–54. doi:10.14257/ijbsbt.2013.5.6.05.

Krüger A, Edelmann-Nusser J. 2009. Biomechanical analysis in freestyle snowboarding: application of a full-body inertial measurement system and a bilateral insole measurement system. Leis Loisir. 2(1–2):17–23. doi:10.1080/19346182.2009.9648494.

McAlpine P. 1994. Biomechanical analysis of snowboard jump landings : a focus on the ankle joint complex. Thesis [Internet]. p. 0–268. http://researchspace.auckland.ac.nz.

Minnoye SLM, Plettenburg DH. 2009. Design, fabrication, and preliminary results of a novel below-knee prosthesis for snowboarding: a case report. Prosthet Orthot Int. 33(3):272–283. doi:10.1080/03093640903089576.

Staniszewski M. 2019. Biomechanical conditions of maintaining balance in snowboarding. J Sports Med Phys Fitness. 59(11):1870–1877. doi:10.23736/S0022-4707.19.09747-0.

Vaverka F, Vodickova S, Elfmark M. 2012. Kinetic analysis of ski turns based on measured ground reaction forces. J Appl Biomech. 28(1):41–47. doi:10.1123/jab.28.1.41.

KEYWORDS Snowboard; kinematic; IMU; above knee amputee; prosthetics

Xavier.bonnet@ensam.eu

Combining video analysis and multibody simulation to study spinal fractures mechanism during a snowboarding crash

N. Bailly[a,b], L. Fouda[a], S. Bonte[c], A. Thouze[c] and W. Wei[a]

[a]Aix Marseille Univ, Univ Gustave Eiffel, LBA, Marseille, France; [b]iLab-Spine: International Laboratory on Spine Imaging and Biomechanics; [c]Decathlon SportsLab, Villeneuve d'Ascq, France

1. Introduction

Spinal injury is one of the two most common injuries leading to severe or life-threatening traumatic injuries in snowboarding (Yamakawa et al. 2001). To design effective protection against those injuries, it is critical to understand the injury mechanism. Yet, very little is known about these mechanisms in snowboarding, and snowboarding back protectors are currently evaluated based on the standard test of motorcycling back protectors (EN1621.2).

The traditional approach to obtaining impact conditions and injury mechanisms in traffic accidents is to experimentally or numerically reproduce accidents (Wei et al. 2023). However, these methods neglect active muscle and protective reflexes that are likely to modify the kinematics of the accident and its consequences. This is especially problematic in the case of crashes related to snowboarding jump in which the aerial maneuvers have a large influence on the impact conditions. Recently, the increase in the quality of videos obtained by 'consumer' cameras opened the opportunity to analyze impact conditions directly on crash videos (Steenstrup et al. 2018).

The objective of this work is to study the injury mechanism (impact speed, impact force, and spinal loading) in a case of a jump-related snowboarding crash leading to multiple vertebral fractures. This will be performed by a novel approach combining video analysis and multibody simulation of the crash.

2. Methods

2.1. Presentation of the case

The crash occurred in a terrain park. A 22-year-old snowboarder went too fast on a big jump, missed the landing zone, and landed on his back on a flat hard snow surface. He suffered L2-L5 lumbar fractures, a C5 fracture plus torn cervical ligaments as well as a femoral fracture. The crash was filmed by a friend (30 fps) and shared on the YouTube platform.

2.2. Video analysis

The normal (V_n) and tangential (V_t) impact velocity and the impact angle of the back (α) relative to the ground were measured using the software Kinovea according to the method described by Shishov et al. (2021). The known size of legs (1.02 m) of the snowboarder was used to calibrate the dimension of the picture and the displacement of the buttocks was tracked until the impact. To account for the high measurement uncertainties due to the limited video quality and the displacement of the camera, the dimension of the legs in the calibration stage was first overestimated and then underestimated to obtain respectively the lower and upper bound of the impact speeds and impact angle.

2.3. Multibody reconstruction of the impact

The human facet model, previously used to reconstruct typical snowboarding backward falls was used to reproduce the impact condition on the back measured in the model (Wei et al. 2019). In thise model, each functional spinal unit is detailed. The multibody model had been calibrated against the spinal segment range of motions, and validated against the body dynamic responses in the vehicle-pedestrian collision and snowboarding backward fall conditions. The hard snow surface had been calibrated against experimental drop tests on snow in a previous study (Bailly et al. 2017). The Multibody model was positioned a few centimeters above the snow ground in the same posture as in the video, with an angle of impact (α) and with an axial rotation (β). The model was then projected on the ground with a normal and tangential velocity (V_n and V_t). A three level full factorial design of experiments was used to vary α, β, Vn, Vt within the range measured in the video (Figure 1b). We evaluated the effect of those parameters on the impact force on the back, measured as the contact forces between the snow surface and the back surface. Additionally, we examined the force and moment sustained by each vertebra and the range of motion of each functional spinal unit, measured at its kinematic joint. The vertebral force and moment as well as the range of motion were compared to published injury thresholds to evaluate the risk of injury (Yoganandan et al. 1988; Stemper et al. 2018; Wei et al. 2019).

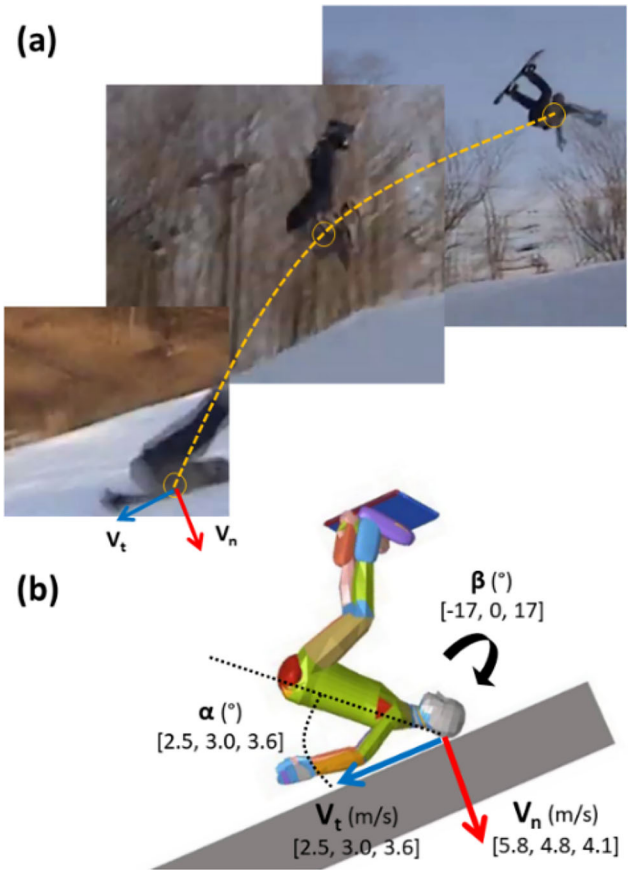


Figure 1. Video analysis (a) and design of experiment of the multibody study (b) of a snowboarding crash.

3. Results and discussion

The range of normal and tangential impact velocities were measured as [5.8, 4.1] m/s and [2.5, 3.6] m/s with the impact angle [24.6, 59]° and the axial rotation [−17, 17]°. A total of 81 multibody simulations were performed. The mean impact force on the back was 11,9 ± 5,3 kN. This force was mainly affected by the angle of impact (α) and the normal impact velocity (Figure 2).

On average, the force threshold for vertebral fracture was only exceeded for the two lumbar vertebras L4 and L5. On average, the bending moment threshold for injury was exceeded in the lumbar spine in L4-L5 and L5-Sacrum as well as in the lower cervical spine in the C7-T1 junction. Thus, the multibody model predicted injuries in both the lower lumbar spine and the lower cervical spine which is consistent with the injuries sustained by the snowboarder. The model suggests that the fractures are due to excessive moment in the cervical spine and a combination of excessive force and moment in the lumbar spine which is consistent with compression fractures caused by a hyperflexion.

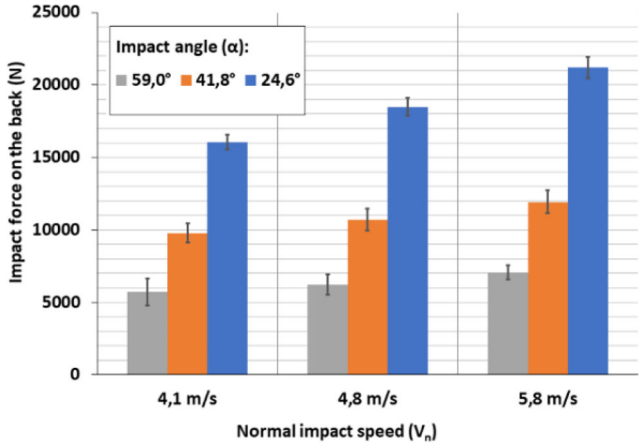


Figure 2. Effect of normal impact speed and impact angle on the average maximal impact force in the back during the snowboarding crash.

On average, injury threshold on the range of motion of each functional spinal unit was also exceeded in lower cervical spine (C7-T1), lumbar spine (L2-L3 and L4-L5) but also on the dorsal spine (T5-T7), which was not observed in the snowboarder.

The normal impact speed of the back of the snowboarder [5.8, 4.1] m/s was similar to the impact speed used to evaluate current back protectors (EN1621.2). However, the mean impact force (11.9 ± 5.3 kN) was lower than the pass/fail force threshold of the standard test (≤18 kN in EN1621.2, level 1).

4. Conclusions

In this work, the novel approach of combining video analysis and numerical simulation was successfully used to investigate the back impact condition and injury mechanism in a case of a snowboarding crash leading to multiple vertebral fractures. The combined analysis did predict the two main spinal zones in which the fracture occurred and the impact speed and impact force on the back were compared to the current standard evaluation of back protectors. This work was only performed on one case: further crash analysis is thus needed to properly evaluate current protection and its standard evaluation.

References

Bailly N, Llari M, Donnadieu T, Masson C, Arnoux P-J. 2017. Head impact in a snowboarding accident. Scand J Med Sci Sports. 27(9):964–974. doi:10.1111/sms.12699.

Shishov N, Elabd K, Komisar V, Chong H, Robinovitch SN. 2021. Accuracy of Kinovea software in estimating body segment movements during falls captured on standard video: effects of fall direction, camera perspective and

video calibration technique. PLoS One. 16(10):e0258923. doi:10.1371/journal.pone.0258923.

Steenstrup SE, Mok K-M, McIntosh AS, Bahr R, Krosshaug T. 2018. Head impact velocities in FIS World Cup snowboarders and freestyle skiers: do real-life impacts exceed helmet testing standards? Br J Sports Med. 52(1):32–40. doi:10.1136/bjsports-2016-097086.

Stemper BD, Chirvi S, Doan N, Baisden JL, Maiman DJ, Curry WH, Yoganandan N, Pintar FA, Paskoff G, Shender BS. 2018. Biomechanical tolerance of whole lumbar spines in straightened posture subjected to axial acceleration. J Orthop Res. 36(6):1747–1756. doi:10.1002/jor.23826.

Wei W, Evin M, Bailly N, Arnoux P-J. 2023. Biomechanical evaluation of Back injuries during typical snowboarding backward falls. Scand J Med Sci Sports. 33(3):224–234. doi:10.1111/sms.14254.

Wei W, Evin M, Bailly N, Llari M, Laporte J, Arnoux P. 2019. Spinal injury analysis for typical snowboarding backward falls. Scand J Med Sci Sports. 29(3):450–459.

Yamakawa H, Murase S, Sakai H, Iwama T, Katada M, Niikawa S, Sumi Y, Nishimura Y, Sakai N. 2001. Spinal injuries in snowboarders: risk of jumping as an integral part of snowboarding. J Trauma. 50(6):1101–1105. doi:10.1097/00005373-200106000-00020.

Yoganandan N, Pintar F, Sances A, Jr, Maiman D, Myklebust J, Harris G, Ray G. 1988. Biomechanical investigations of the human thoracolumbar spine. SAE Trans. 97(5):676–684.

KEYWORDS Snowboard; spinal injury; back protector

Nicolas.bailly@univ-eiffel.fr

Comparison of the propulsive force production capacities between flat acceleration sprinting and uphill running at constant velocity

M. Vonderscher[a], B. Morel[a], J. B. Morin[b], M. Bowen[a] and P. Samozino[a]

[a]Interuniversity Laboratory of Human Movement Sciences, Univ Savoie Mont Blanc, Chambéry, France; [b]Interuniversity Laboratory of Human Movement Sciences, Univ Lyon, UJM-Saint-Etienne, Saint-Etienne, France

1. Introduction

Runner's velocity during uphill running (e.g. trail) is closely tied to runner's capacity to generate propulsive (i.e. tangential to the ground) force. Propulsive force capacities in running have been well described through the linear Force-Velocity (FV) relationship. The latter is characterized by the theoretical maximal force that can be produced at a null velocity (F_0), the theoretical maximal velocity above which no force can be produced (V_0) and the maximal power (P_{max}). Typically, FV relationship can be determined during a single sprint acceleration on flat ground. In this case, the inertia to overcome during the acceleration induces velocity changes (from 0 to maximal velocity) along the sprint and thus, various force production (Rabita et al. 2015, Samozino et al. 2016). FV relationship can also be determined during several resisted sprints on flat ground while focusing on force produced at maximal (constant) velocity. Under these conditions, the additional resistances (i.e. towed sled) across different trials limit the maximal velocity the runner can reach, which corresponds to various points along the FV curve (Cross et al. 2018). The equivalence in FV relationships reported between these two methods (Cross et al. 2018) supports the fact that, on flat ground, the FV relationship during running can be interpreted either as the decrease in the maximal propulsive force when velocity increases or as the decrease of the maximal velocity when the propulsive force to produce increases. Since in the initial phase of sprint running, the overall acceleration acting on the runner's body is similar to the acceleration acting when running at constant velocity up an 'equivalent slope', di Prampero et al. (2005) suggested that uphill running at constant velocity is mechanically analogue to acceleration phases during flat ground sprinting. Delaney et al. (2022) showed that variables of the FV relationship obtained from an acceleration on flat ground are correlated to maximal velocity reached over different slopes. However, this study only covered a narrow range of slopes and velocity conditions and did not make any direct comparison between force production capacities on flat and uphill terrains. Di Prampero et al.'s (2005) analogy was also indirectly explored in lizard suggesting a decrease in maximal velocity when required force production increases due to increasing slope (Huey and Hertz 1982). Thus, it remains unclear whether propulsive force production capacities in running are similar during acceleration conditions on flat ground and at steady velocity conditions in uphill sections. This study aimed to test the di Prampero et al.'s mechanical analogy between sprint acceleration phases and uphill running at a constant velocity through the comparison of propulsive force capacities produced at the same velocity during uphill/flat and steady state/accelerated running. It was assumed that, regarding the mechanical analogy suggested by di Prampero et al. (2005), force production capacities at any given velocity conditions are equivalent whatever the mechanical conditions, be they imposed by hill gradients or inertia.

2. Methods

Twenty participants (14 men and 6 women; 23.3 ± 2.8 years old; 67.0 ± 8.8 kg; 1.75 ± 0.09m), free of any recent injury, volunteered to participate in two sessions for flat ground and uphill sprint measurements, respectively. Each session started with a standardized warmup including 10 min moderate velocity running, athletic drills, and progressive sprints. Then, for the flat ground session, each participant performed 3 sprints at maximal intensity. A radar device (ATS Pro II, Stalker, Texas, USA) measured runner's instantaneous velocity during each sprint (46.875 Hz). The velocity-time relationships were fitted with an exponential function to determine, from an inverse dynamics approach applied to the center of mass, the running propulsive (horizontal) FV relationship for each sprint (Samozino et al. 2016). The 3 FV curves were then pooled and the highest forces in each velocity were fitted with a linear function to compute each subject's 'best' FV relationship. The same radar device measured runner's velocity during sprints of the uphill session. This second session comprised five 30-m sprints in slopes of 4, 8, 15, 20 and 28%. Propulsive (i.e. tangential) force production capacities were estimated at maximal (steady) velocity, from the fundamental dynamic principle as $F_P = m \cdot g \cdot \sin(\alpha) + F_{air}$ with m the participant's mass (in kg), g the gravitational constant (9.81 m s^{-2}), α the gradient (rad) and F_{air} the estimated aerodynamical force (Samozino et al. 2016). Propulsive forces at maximal velocity (mean of the last 2s of the sprint) during uphill conditions were compared to propulsive force production capacities at the same velocity obtained from FV

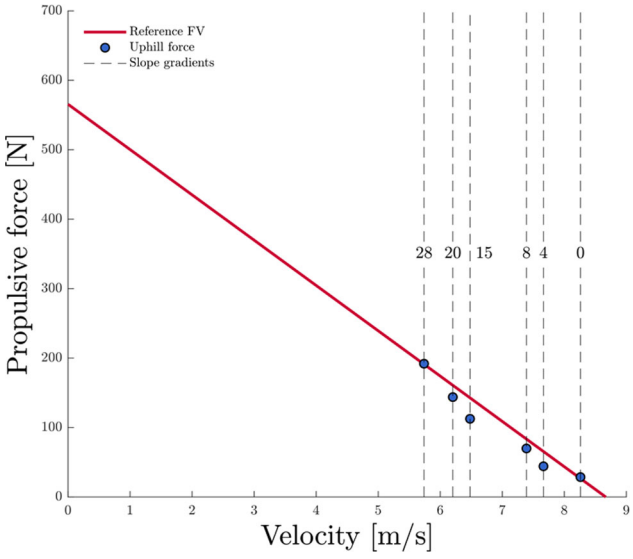


Figure 1. Typical data obtained for flat ground running FV relationship (red line) and force production capacities at maximal velocity reached during uphill running (blue dots).

relationship determined during flat acceleration sprinting, through systematic and random errors and correlation analyses. Results were expressed as mean ± SD.

3. Results and discussion

Mean FV relationship parameters were $F_0 = 511 \pm 98.1$ N, $V_0 = 7.71 \pm 0.80$ m s^{-1}, and $P_{max} = 997 \pm 257$ W. FV relationship and force production capacities from uphill sprints are presented in Figure 1 for a typical subject. For all subjects, systematic and random differences between propulsive force capacities predicted from FV relationship (red line) and estimated during uphill sprints (blue dots) were quite low with −16.4 N (17.0%) and 21.2 N (24.4%), respectively, for force values ranging between 15.5 and 224 N. The correlation between the predicted force capacities from the flat ground FV relationship and estimated in uphill running was very high ($r = 0.95$, regression curve: $y = -0.91x - 6.46$). These results evidenced that propulsive force production capacities are equivalent when compared at the same running velocity between flat sprinting acceleration and constant velocity uphill running (i.e. be they imposed by inertia on flat ground or slope during uphill running). The slight lower force capacities observed for uphill sprints (17.0%) may be explained by a potential small fatigue effect due to the repeated bouts or by potential differences in running biomechanics between the two running conditions. A similar shift was reported for the comparison between unique sprint and multiple sled towing sprints FV relationships (Cross et al. 2018). Associated to previous findings (Cross et al. 2018), present results support that propulsive force production capacities during running are very similar whatever the running mechanical conditions (inertia, resistance, hill gradients), provided they are compared at the same velocity. This offers new insights in trail runners' evaluation since the force capacities evaluated on a flat track appear to be representative of those encountered for equivalent slopes. The FV relationship obtained during a single 30-m flat accelerated sprint can thus also describe the maximal velocity a trail runner can reach in various slopes (with slope = asin(F/(mg)), in °).

4. Conclusions

This study showed the similarity in propulsive force production capacities between acceleration phases on flat ground and constant velocity running uphill, supporting di Prampero et al.'s (2005) analogy. This finding offers a new perspective on assessing force production capacities in trail runners, as flat ground results can be extended to uphill mountain terrains, as long as the mechanical conditions are equivalent.

Acknowledgements

This work was supported by French National Research Agency (ANR-22-CE14-0073]).

References

Cross MR, Samozino P, Brown SR, Morin JB. 2018. A comparison between the force–velocity relationships of unloaded and sled-resisted sprinting: single vs. multiple trial methods. Eur J Appl Physiol. 118(3):563–571. doi:10.1007/s00421-017-3796-5.

Delaney JA, McKay BA, Radcliffe J, Benton DT, Samozino P, Morin JB, Duthie GM. 2022. Uphill sprinting load– and force–velocity profiling: assessment and potential applications. J Sports Sci. 40(3):281–287. doi:10.1080/02640414.2021.1992868.

Di Prampero PE, Fusi S, Sepulcri L, Morin JB, Belli A, Antonutto G. 2005. Sprint running: a new energetic approach. J Exp Biol. 208(14):2809–2816. doi:10.1242/jeb.01700.

Huey RB, Hertz PE. 1982. Effects of body size and slope on sprint speed of a lizard (Stellio (Agama) Stellio). J Exp Biol. 97(1):401–409. doi:10.1242/jeb.97.1.401.

Rabita G, Dorel S, Slawinski J, Sàez-de-Villarreal E, Couturier A, Samozino P, Morin JB. 2015. Sprint mechanics in world-class athletes: a new insight into the limits of human locomotion. Scand J Med Sci Sports. 25(5):583–594. doi:10.1111/sms.12389.

Samozino P, Rabita G, Dorel S, Slawinski J, Peyrot N, Saez de Villarreal E, Morin JB. 2016. A simple method for measuring power, force, velocity properties, and mechanical effectiveness in sprint running. Scand J Med Sci Sports. 26(6):648–658. doi:10.1111/sms.12490.

KEYWORDS Sprint; force; velocity; uphill; trail

mylene.vonderscher@etu.univ-smb.fr

Evolution of the torque applied to the alpine ski binding as a function of speed

A. Node, M. Chollet and F. Hintzy

LIBM, Bourget-du-Lac, France

1. Introduction

The main purposes of the ski binding were to hold the ski to the ski boot and also to release the boot when too much mechanical stress was exerted on the system. To achieve this, the binding consists of a metal spring tensioned, this tension varying according to the mechanical stress it should receive. The mechanical stress corresponds to the torque (M) and are related to the forces by the formula,

$$M_{x,\,y,\,z} = F_{x,\,y,\,z}.\ L$$

with L the lever arm between the point of application of the force and the pivot point, with F the force on one of the 3 axes ($_{x,y,z}$). The torque around the z-axis, i.e. the torque that generates a lateral rotation around the longitudinal axis of the skier, allowed the release of the front stop. The torque of the y-axis, which generates an antero-posterior rotation in the skier's frame of reference and allows the release of the heel pad. But do we know the torque applied to the binding on these two axes? What factors influence them? A DIN 11 088 standard was created in 2006 and presents the evolution of the torque as a function of the mass of the skier, the torque increasing with the mass. But other factors could also influence the torque? The skier displacement's was subjected to several forces (aerodynamic, friction, weight, radial). The sum of these forces varied during turning due to the appearance of the radial force (F_{rad}) directed towards the inside of the turn. The radial force is located at the ski-snow interface and is calculated according to the fundamental principle of dynamics:

$$F_{rad} = v^2.mr$$

with v the speed, m the mass and r the radius. Knowing the radial force is related to speed, the higher the speed, the higher the radial force. Moreover, skiing motion is the result of the conversion of the potential energy into either kinetic energy or dissipation *via* ski − snow and aerodynamic friction (Lind and Sanders 2004). Therefore, potential energy and speed varied during skiing. Delhaye (2021) showed also that better skiers (highest speeds) exhibit greater positive and negative rate of force development, as well as higher positive My. Consequently, the speed of the skier should influence the moment applied to the bindings. And yet, the standard DIN 11 088 do not take this into account. Only one recommendation proposes to choose a torque higher than that proposed by the standard DIN, if the skier is very good, therefore surely very fast. The aim of our study was therefore to test the effect of speed on the torque applied to ski bindings. This would make it possible to modify the standards and thus possibly reduce knee pathologies in alpine skiing. In effect, 76% of serious knee injuries are caused by bindings that do not release (Bouter et al. 1989).

2. Methods

Fourteen alpine skiers were equipped with ski-mounted force plates and a positional device (Real-Time-Kinematic) to measure respectively $M_{z,y}$ (200 Hz) and instantaneous speed (10 Hz). They ran a 2-giant slalom turns section starting from different race starts placed at 8 heights on the slope. Two starting height conditions were kept for analysis for each skier: the one with the lowest entrance velocity (V_{min}) and the second one with the maximal entrance velocity (V_{max}). The data was then analyzed only in the first turn. The turn was interpolated over a period of 1000 points in order to be compare between skiers. Then the average evolutions of M_y and M_z torques in the conditions at V_{max} and V_{min} were plotted. In order to evaluate the effect of speed on torque, the individual torque was averaged over the entire turn at both V_{max} and V_{min}. As the evolution of the torque varies positively (y: anterior displacement; z: lateral displacement) and negatively (y: posterior displacement; z: medial displacement), it was done in absolute values. Moreover, it was normalized to the mass. Normal distribution and sphericity were checked. A Wilcoxon test was performed to identify differences in M_y and M_z between V_{max} and V_{min} conditions.

3. Results and discussion

The proposed setup allowed to significantly vary the entry speed into the turn: V_{min} and V_{max} being respectively 38.1 ± 3.2 and 74.5 ± 5.7 km h^{-1}.

Figures 1 and 2 presented the evolution of both M_y and M_z during the turn. High standard deviations can be observed visually in both M_y and M_z. The average M_y (0.074 ± 0.027 Nm/BW at V_{max} and 0.059 ± 0.022 Nm/BW at V_{min}) and M_z (0.013 ± 0.007 Nm/BW at

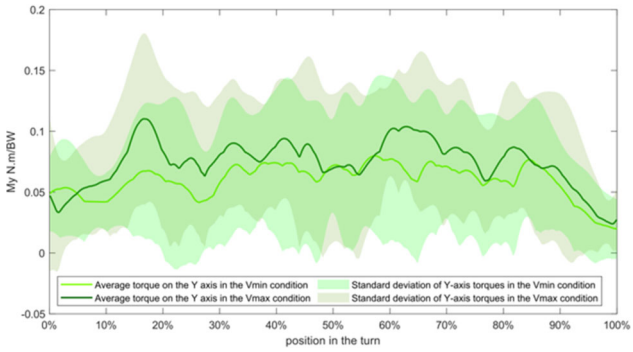


Figure 1. Evolution of the *y*-axis torque with both the maximum and minimum speed corner entry condition.

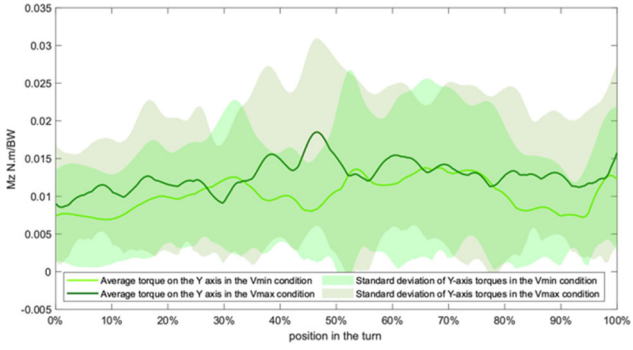


Figure 2. Evolution of the z-axis torque of both the maximum and minimum speed corner entry condition.

V_{max} and 0.01 ± 0.005 Nm/BW at V_{min}) torque during the entire turn were significantly higher when skiers entered at V_{max} vs. V_{min} ($p = 0.034$ for M_y and $p = 0.039$ for M_z). The results are therefore in line with our hypotheses: the speed of the skier influences the torque applied to the binding during a turn. These results are related to those of (Cross et al. 2021) who showed that the maximum isometric forces experienced by the skier were negatively correlated with performance time, so these maximum isometric forces are positively correlated with speed and those of Delhaye (2021) who showed that better skiers (highest speeds) exhibit greater positive and negative rate of force development, as well as higher positive *My*.

4. Conclusions

The results of the study show that there is an effect of alpine skiing speed on the torque applied to the binding. The tightening DIN 11 088 standard should therefore take the speed parameter into account to better adjust the tightening of the bindings. However, it will be difficult to calculate the optimal torque value, given the large differences between skiers, as shown by the present high standard deviations.

References

Bouter LM, Knipschild PG, Volovics A. 1989. Binding function in relation to injury risk in downhill skiing. Am J Sports Med. 17(2):226–233. doi:10.1177/036354658901700213.

Cross MR, Delhaye C, Morin JB, Bowen M, Coulmy N, Hintzy F, Samozino P. 2021. Force output in giant-slalom skiing: a practical model of force application effectiveness. PLoS One. 16(1):e0244698. doi:10.1371/JOURNAL.PONE.0244698.

Delhaye C. 2021. Relation entre la performance et la cinétique de l'appui, au cours d'un virage en ski alpin. Thèse de doctorat Université Savoie Mont-Blanc.

Lind D, Sanders SP. 2004. Physics of Skiing – Skiing at triple point. 2nd ed. Cham: Springer Science.

KEYWORDS Ski binding; torques; forces; speed

antoine.node@gmail.com

Fatigue induced by trail-running impairs ankle eversion control with no inter-limb differences

G. Ravier and J. Dury

Sport and Performance Department, University of Franche Comte, Laboratory of C3S (UR 4660), Besançon, France

1. Introduction

In recent decades, trail running has become very popular. However, research on injury incidence remains limited. A recent study reported that toenails (24.8%), ankle (14.5%) and knee (17.5%) joints being the most frequently locations of injury. Specifically, with under 20 trail runners, lateral ankle sprain (LAS) accounted for 50% of injuries (Sanchez-Garcia et al. 2022). Before designing preventive programs, the development of a comprehensive model for injury causation is needed. It consists of analyzing complex interactions between internal (predisposing the athlete) and external (sport's characteristics) risk factors (Delahunt and Remus 2019). Among internal risk factors associated with LAS, deficits in evertor muscle strength have been reported. To date, there is a lack of data on risk factors for LAS associated with trail running. Trail running is characterized by hilly running on uneven terrain. In response to prolonged running course, marked neuromuscular alterations of quadriceps and calf have been reported (Giandolini et al. 2016). Neuromuscular fatigue and biomechanical constraints associated with trail running could induce alterations on the mechanisms implicated in ankle stability, such as neuromuscular activity of evertors and inversion control. To date, little is known about ankle joint constraints in the frontal plane and subtalar Henke's axis (inversion/eversion), and peroneus muscles fatigue associated with trail running. This study investigated the exercise-induced effects on the ankle control, and inter-limb differences.

2. Methods

Seventeen (20.2 ± 1.5 years) healthy recreational trail runners (5 females and 12 males) performed a circuit consisting of 16 km with 400 m of positive elevation. The protocol (CERSTAPS n° IRB 00012476-2021-21-06-118) comprised a medical examination (echography of ankle lateral collateral ligament and laxity of ankle, and the Cumberland Ankle Instability Test), a familiarization session, and a testing session. Before and immediately after the trail running course, three 4s maximal isometric contractions (MVC) of ankle eversion (1-min rest) were performed on preferred (P) and non-preferred (NP) legs (Figure 1). The force output was measured (100 Hz) with strain gauge sensor (Force sensor 500 kg, Ergotest, Norway). MVCs (N) were determined by applying a moving mean window of 500 ms. Rate of force development (RFD, N s^{-1}) was measured as the amount of force that was generated in the first 200 ms of the MVC. Electromyographic activity (EMG) was recorded from the peroneus (longus + brevis) muscles according to the SENIAM group guidelines. The electrode positions were marked on the skin to be replaced after the running circuit. EMG signals (2 kHz) were amplified with a bandwidth frequency (0.3–2 kHz, PowerLab System, Bioamp, AD Instrument, Sydney, Australia), and analyzed with LabChart 7 software. EMG (mV) was determined from raw signals by applying a moving root-mean-square window of 500 ms, and the peak value was retained. For all parameters, the best repetition was retained for further analysis.

The functional assessment of the ankle joint was assessed from a weight bearing inversion test using an ankle-destabilization device (Myolux Medik II; ICC Physio, Le Bourget du Lac, France) (Figure 1). Test consisted of completing 20 inversion movements (P and NP legs) standing on the one leg with 30° range of inversion as slowly as possible. Kinematic parameters were derived from two inertial measurement units (IMU) located on the footwear. A performance score (INVscore, %) was automatically generated from IMU of the manufacturer (51 Hz, Shimmer3, Dublin, Ireland). It corresponds to the sum of repetitions below

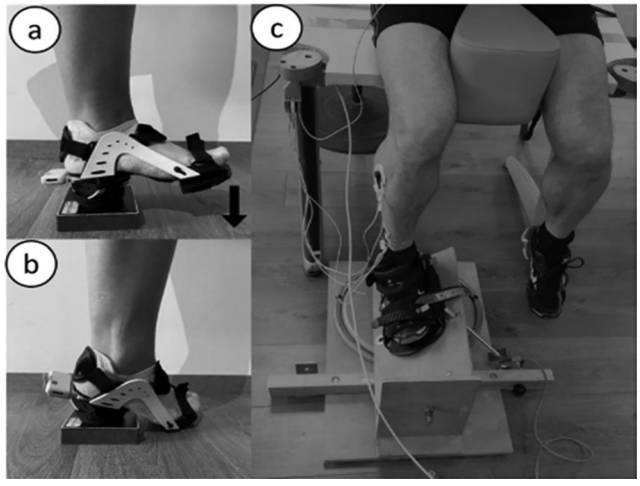


Figure 1. Ankle-destabilisation device for weight-bearing inversions (a,b) and pedal equipped with dynamometer for MVC (c).

a selected angular velocity threshold (fixed at 60° s^{-1}). Moreover, by adding an IMU (148 Hz, Delsys trignoTM, Delsys Inc., Natick, USA), instantaneous angular velocity (tri-axial gyroscope) was calculated throughout repetitions as the composite angular velocity (ω) around the sagittal (x), frontal (y) and transverse (z) planes with the following equation: $\omega = \sqrt{\omega x^2 + \omega y^2 + \omega z^2}$. The highest ω obtained for each repetition was retained, then mean (INVmean, ° s^{-1}) of the 20 repetitions were calculated.

Data are reported as mean ± standard deviation (SD). Analysis of variance was used to determine the significant mean effects for changes over time (pre- to post-trail running) and interaction effects between P and NP legs. A paired t-test was applied to reveal differences between P and NP legs for pre values, and between pre- to post-running for P/NP ratio. Level of significance was p value ≤ 0.05.

3. Results and discussion

Inter-limb asymmetry has been commonly investigated by using isometric and isokinetic strength tests. Data are expressed in percentage of differences, ratio or calculated from mean values. In the present study, healthy trail runners showed inter-limb asymmetry of 15% for MVC, 14% for RFD and 7% for ωINV. To date, a higher 15% inter-limb asymmetry in eccentric isokinetic ankle strength has been associated with greater risk of sport injury (Fousekis et al. 2012). When considering P/NP ratio, pre-running values ranged between 1.1 and 1.2 for all variables. Finally, comparison between P and NP values (Table 1) revealed significant differences only for MVC and RFD. Nevertheless, the most important finding of the study was that inter-limb asymmetry was not improved in response to trail running (Table 1). Because of the specific context of running, comprising variation in gradients, uneven terrain with stones and tree roots, adoption of a preferential limb for push-off and landing could have had resulted in unequal strength loss. The present results not revealed inter-limb differences in fatigability.

The second important result was that trail running altered neuromuscular function of evertors as demonstrated by reduction in MVC, RFD and EMG activity of peroneus (Table 1). Previous studies (Giandolini et al. 2016) have already reported a decrease of 15–20% in the MVC of both knee extensors and plantar flexors in response to short distance format, whereas alterations in evertors have never been analysed. Because weakness in evertor muscles is one of the most important internal risk factors for LAS, the present results seem important for prevention strategies with trail-runners.

Table 1. Preferred (P) and non-preferred (NP) lower limb response to trail-running.

	Pre-run	Post-run	Time legs T × L	CV
MVC_P	219 ± 87*	187 ± 87	**<0.0001**	−16
MVC_{NP}	185 ± 66	170 ± 72	>0.05	−9
			> 0.05	
RFD_P	807 ± 323*	671 ± 317	**= 0.001**	−17
RFD_{NP}	692 ± 255	630 ± 276	>0.05	−9
			> 0.05	
EMG_P	0.89 ± 0.33	0.80 ± 0.27	**<0.0001**	−9
EMG_{NP}	0.77 ± 0.25	0.65 ± 0.20	>0.05	−15
			> 0.05	
ωINV_P	58 ± 17	67 ± 19	**= 0.012**	+19
ωINV_{NP}	54 ± 12	61 ± 18	>0.05	+13
			> 0.05	
$Score_P$	94 ± 11	89 ± 15	>0.05	−5
$Score_{NP}$	91 ± 14	89 ± 14	> 0.05	−2
			> 0.05	

Mean ± SD for preferred (P) and nonpreferred (NP) legs; ANOVA (time, legs, interactions effects). *: revealed significant difference (P *vs.* NP) for pre-running. Variations (CV, %) between pre- to post-running are specified.

Finally, trail-running induced functional impairment in biomechanics during weight bearing inversion test (Table 1). Angular velocity increased in post- compared to pre-running similarly for both P (+19%) and NP (+13%) lower limbs. This result suggests neuromuscular alteration in eccentric regimen. The ωINV is a relevant variable for revealing exercise-induced fatigue.

4. Conclusions

This study demonstrated neuromuscular alterations of evertors and ability in braking inversion in response to trail running. Fatigue does not affect inter-limb asymmetry in trail running. Basing on these results, eccentric reinforcement could be proposed as part of prevention program.

References

Delahunt E, Remus A. 2019. Risk factors for lateral ankle sprains and chronic ankle instability. J Athl Train. 54(6): 611–616. doi:10.4085/1062-6050-44-18.

Fousekis K, Tsepis E, Vagenas G. 2012. Intrinsic risk factors of noncontact ankle sprains in soccer: a prospective study on 100 professional players. Am J Sports Med. 40(8): 1842–1850. doi:10.1177/0363546512449602.

Giandolini M, Vernillo G, Samozino P, Horvais N, Edwards WB, Morin J-B, Millet GY. 2016. Fatigue associated with prolonged graded running. Eur J Appl Physiol. 116(10): 1859–1873. doi:10.1007/s00421-016-3437-4.

Sanchez-Garcia LF, Penichet-Tomas A, Pueo B, Jimenez-Olmedo JM. 2022. Injury incidence and pattern in elite young male and female trail runners. Appl Sci. 12(3): 1155. doi:10.3390/app12031155.

KEYWORDS Inter-limb; neuromuscular; kinematics; eccentric; ankle inversion

gilles.ravier@univ-fcomte.fr

Kinematic and kinetic comparisons of jump pull ups used in rock-climbing evaluations

X. Hugues, V. Cahouet, R. Rogue and F. Quaine

Univ. Grenoble Alpes, CNRS, Grenoble INP, GIPSA-lab, Grenoble, France

1. Introduction

Arm power estimation tests are a gold standard to access the climber strength (MCT Details | ircra). They are performed with variation normal pull-up (PU), one hand slap test and arm jump test using both hands (Laffaye et al. 2014) to reach as high as possible (Draper et al. 2011). Rock climbing is a sport involving vertical quadruped motricity with static and dynamic movements. More recently the bouldering, route and speed climbing are more and more dynamically oriented. Speed climbing is pushing the limit in term of speed, force and coordination. The countermovement (CM) and concentric (Con) jump pull-up (JPU) could represent two different types of muscle contraction that could be directly applicable in rock climbing. This abstract aims to compare the two different forms of jump pull-up with kinematic and kinetic approaches.

2. Methods

2.1. Participants

Seventeen skilled climbers over 7c French route grade performed 4 jump pull-ups (JPU) in two different modalities: concentric (Con) JPU and countermovement (CM) JPU with stretch shortening cycle.

2.2. Protocol

Climbers were asked to jump in order to reach as high as possible with both hands simultaneously. In both modalities, each climber was asked to stabilize before starting the movement, with engaged shoulder and slightly bent arm (around 120°) for the Con JPU and at first 90° elbow inclination, before going down to 120° and up in an explosive way. Natural velocity was required

2.3. Material and data analysis

Each participant was equipped with an adapted Qualisys markers set to measure upper-limbs and body displacement. The jump height was measured using Qualisys marker at the hand. Each articular angle was measured in the upper-limb segments plane for shoulder θ_e, elbow θ_c and wrist θ_p joints as presented in Figure 1. These were obtained from marker positions and were derived (finite centered differences) to get corresponding angular velocity. The maximal velocity apparition time of each joint was estimated and then normalized with respect to the ascending pull-up time. Two three-axis force sensors (225 Hz) were used to measure each hand reaction force during the JPU (Figure 1). Each force component was normalized to body weight. Both movement and force measured data were filtered with a fourth order low pass Butterworth filter with a cut off frequency of 10 Hz. For the height and the forces, a linear mixed model was used to compare modalities to account for inter-individual variability, followed by a comparison test between the 2 modalities. For peak joint velocities, a beta regression of y-value]0;1[was used to account for interindividual variability, followed by a comparison test.

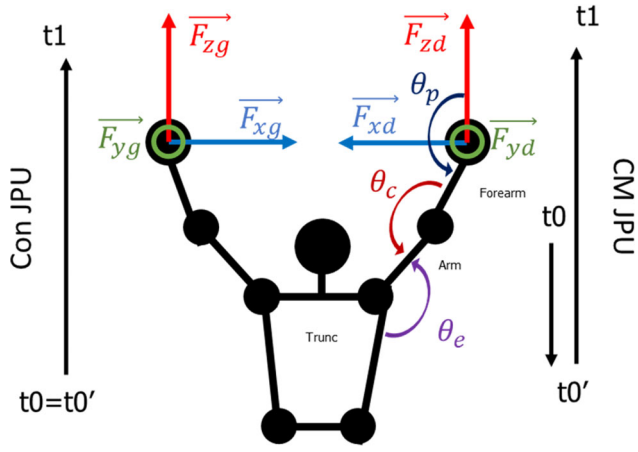


Figure 1. Schematic representation of the upper body with forces, angles of interest and vector of the CM and Con JPU (t0 = start of the movement, t0′ = ascending phase, t1 = take-off phase).

3. Results and discussion

3.1. Jump height

There is a significant difference between the measured mean jump height between the CM and Con JPU conditions, respectively 604.0 ± 24.8 mm and 584.9 ± 24.4 mm, ($Z = -3.36$; $p < 0.001$, $R^2 = 0.94$). The height estimated in the countermovement condition is 19 mm higher than the one estimated in concentric. The CM JPU is providing better result, certainly due the uptake of the slack muscle length (Van Hooren and Bosch 2016).

3.2. Angular velocity peak

Figure 2 displays a typical angular velocity-time evolution for the shoulder, elbow and wrist joints in the

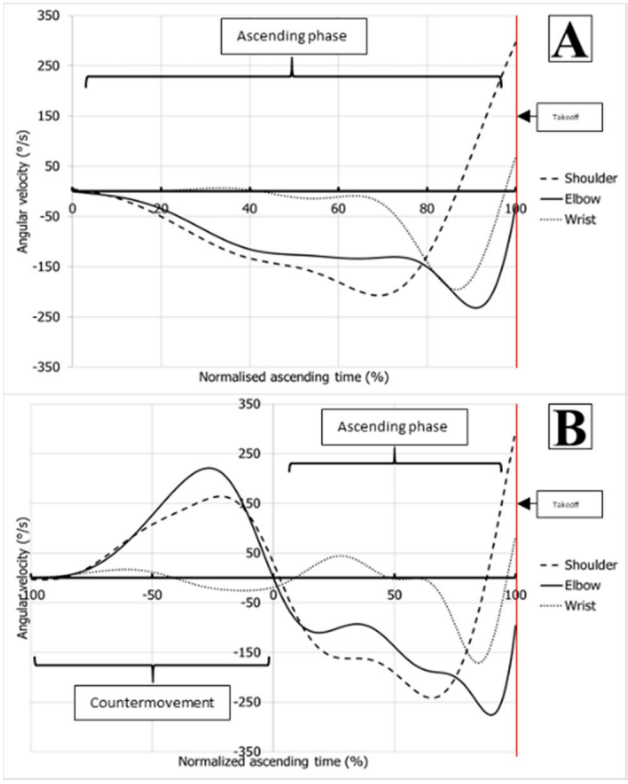


Figure 2. Typical example of angular velocity-time curves in Con JPU **A** and in CM JPU **B**.

two studied modalities. Excluding the CM phase, angular velocities evolve in a similar way for both JPU. All joints are flexing during the whole movement with negative angular velocities in sagittal plane, excepted at the end of the pull-up where the shoulder and the wrist joints switch to extension in the frontal plane. At the moment of takeoff, shoulder joint exhibits especially height extension velocity in comparison with elbow and wrist joints. There is then a composition of the angular closure of the elbow and an angular opening of the shoulder that allows the upward movement to be prolonged. Time delay between the maximal 3 joints velocities does not depend on the modality (chisq (2) = 2.86; $p = 0.239$). The maximal angular velocity at shoulder joint appears significantly earlier than at the elbow ($Z = -14.35$; $p < 0.0001$) and the wrist ($Z = 12.82$; $p < 0.0001$). On the other hand, no significant time delay is obtained between the maximal angular velocity at wrist and elbow joints ($Z = -1.9$; $p > 0.136$). The shoulder seems to act mostly in the first part of the pull-up, while the elbow has a higher angular velocity near the end of the pull-up. Joint motion pattern exhibit a proximal-to-distal sequence for the first two joints as it has been generally observed in upper-limb throwing (Putnam 1993) or vertical jumping (Bobbert and van Ingen Schenau 1988). However, no significant trend can be established for the wrist. One explanation could be the lack of force production around this joint for a large angle amplitude.

Table 1. Maximal absolute forces at the hands during the JPU movement in both modalities.

Modality	Fx	Fy	Fz
CM JPU	22.5%	40.0%	154.6%
Con JPU	21.7%	37.0%	152.4%

3.3. Forces at the hands

Table 1 shows the maximal values reached by the sum of each axial absolute force during the concentric ascending phase, related to the participant's weight. The differences in maximal forces measured, between the CM and Con JPU are not significant (Fx: $p = 0.4$; Fy: $p = 0.07$; Fz: $p = 0.84$), although we can identify a tendency for antero-posterior force to be higher during CM JPU than Con JPU. The increased performance of the CM JPU does not come with higher maximal forces. In addition, the maximal measured efforts in frontal and sagittal planes are not neglectable (from 22% to 40% of the weight). This suggests that these efforts should be taken into account, even if they do not directly contribute to performance.

4. Conclusions

The CM JPU performance has a significantly superior height compared to the Con JPU.

Both JPU are sequenced in a proximal-to-distal pattern for shoulder and elbow joints and generate a maximal hand reaction force of similar amplitude. CM JPU does not imply producing greater efforts in the ascent phase to provide higher jump.

This study allows us to highlight the non-vertical stabilization forces present during the pull-up movement which represent a significant part of the effort. produced.

References

Bobbert MF, van Ingen Schenau GJ. 1988. Coordination in vertical jumping. J Biomech. 21(3):249–262. doi:10.1016/0021-9290(88)90175-3.

Draper N, Dickson T, Blackwell G, Priestley S, Fryer S, Marshall H, Shearman J, Hamlin M, Winter D, Ellis G. 2011. Sport-specific power assessment for rock climbing. J Sports Med Phys Fitness. 51(3):417–425. https://europepmc.org/article/med/21904280.

Laffaye G, Collin JM, Levernier G, Padulo J. 2014. Upper-limb power test in rock-climbing. Int J Sports Med. 35(8):670–675. doi:10.1055/S-0033-1358473.

MCT Details | ircra. [accessed 2023 Apr 4]. https://www.ircra.rocks/mct.

Putnam CA. 1993. Sequential motions of body segments in striking and throwing skills: descriptions and explanations. J Biomech. 26(Suppl. 1):125–135. doi:10.1016/0021-9290(93)90084-R.

Van Hooren B, Bosch F. 2016. Influence of muscle slack on high-intensity sport performance: a review. Strength Cond J. 38(5):75–87. doi:10.1519/SSC.0000000000000251.

KEYWORDS Arm power; Jump pull-up; movement analysis; Biomechanical coordination; rock climbing

Xavier.hugues@grenoble-inp.fr

Mechanical work during ski mountaineering: the effect of climbing slopes

F. Hintzy, S. Bellabouvier and P. Samozino

Laboratoire LIBM, Université Savoie Mont Blanc, France

1. Introduction

Ski mountaineering (SkiMo) is a winter sport that involves alternately climbing and descending slopes on a snow-covered support. The climbing section being highly strenuous and energy demanding, numerous research has been done on the physiological determinants of performance. However, few studies has focused on the biomechanical aspects of this locomotion while it is also very stressful and interesting from this point of view. The climbing section involved the generation of propulsive force by upper- and lower-body muscles to overcome gravity (i.e. increase potential energy). Power output is limited by equipment, such as the restriction of ankle flexion-extension by the ski boots or the deformation of the skis. In addition, high slopes can be climbed, thanks to the high friction generated by the skins under the ski sole and the snow. The propulsive phase can be followed by a gliding phase, which is also limited by the high friction produced by the skins reducing the gliding length. Therefore, the climb in SkiMo requires an important mechanical work production. To our knowledge, only 2 studies have measured power output in SkiMo using multisensor inertial measurement unit attached to a ski with specific algorithm proposed by Gellaerts et al. (2018). Praz et al. (2016) investigated the evolution of the mechanical efficiency (mechanical work divided by metabolic work) at different speeds and slope gradients. But no power data is presented or discussed. Recently, Kayser and Mariani (2022) present the performance analysis of the uphill sections of a long-distance SkiMo team competition. Power values from 237 to 321 W are just presented but not discussed. It therefore seems relevant to study the mechanical work developed during skiing. The external mechanical work (Wext) corresponds to the sum of the positive increments of the total mechanical energy of the center of mass (CoM), the latter being the sum at each instant of the gravitational potential (PE) and kinetic (KE) energies (Cavagna et al. 1963). The fluctuation of these mechanical energies come from either an energy supply linked to a muscular contraction or a transfer between potential and kinetic energies, requiring no muscular contraction (Cavagna et al. 1963). A small part of PE is not transferred and used to overcome friction during the gliding phase (if any). The percentage of alternate transfer between PE and KE (R%) depends on locomotion and external factors such as speed and slope (Minetti et al. 2002). When walking, R% is the result of a swinging inverted pendulum trajectory of the CoM (Margaria and Cavagna 1965) and can reach 65%. It varied according to the slope, mechanical energy transfer was less effective when the slope rose (Gottschall and Kram 2006). In contrast, during running, there is no transfer between KE and PE. So what about SkiMo? The aim of this study was to determine the mechanical external work in SkiMo using the Cavagna et al.'s method, to quantify the power output, energy transfer and to study the possible effect of the slope.

2. Methods

Seventeen male ski-mountaineers (22 ± 4 yr; 179.4 ± 5.3; 68.6 ± 6.0 kg; minimum 5 years of practice) performed a field ski-mountaineering ascending test on a groomed alpine skiing track. All used the same equipment (pair of skis, bindings, skins, ski boots; Salomon, Annecy, France). After a standardized warm up route, they tested successively two slope gradients (20 and 38%) over a distance of 400 m. The velocity was self-selected so as to be sub-maximal. A single camera (GoPro Hero 7 Black, 60 Hz) fixed perpendicularly to the movement of the skier was used to acquire the coordinates of markers. The parallax error was corrected, and a moving average window over 6 frames was applied. Biomechanical parameters (frequency in cycle min^{1}, velocity in km h^{-1}) were calculated thank to a lateral malleolus marker. The vertical and horizontal CoM displacement was estimated from the position of the greater trochanter to calculate respectively the fluctuation of PE and KE per cycle. R% was determined as $((W_{PE} + W_{KE} - W_{EXT})/(W_{KE} + W_{PE})) \times 100$, with W_{PE}: potential work, W_{KE}: kinetic work and W_{EXT}: external work, expressed in J min^{-1}. Five to seven cycles per slope were measured and averaged. After checking for normal distribution, Student's *t*-test were performed to compare variables between slope conditions. Pearson correlation was also conducted to assess associations of tested variables.

3. Results and discussion

With increasing slope gradient, self-selected velocity and frequency decreased significantly ($p < 0.001$;

Table 1. Biomechanical parameters in both slopes.

	Slope 20%	Slope 38%
Frequency (c min^{-1})	111.8 ± 9.1	62.7 ± 8.8
Velocity (km h^{-1})	6.35 ± 0.95	2.92 ± 0.99
R% (%)	25.0 ± 3.8	14.3 ± 5.7

Table 1). It is relevant to take an interest in kinematic parameters since they are influenced by snow conditions, slope and speed during SkiMo (Praz et al. 2016). Authors showed that higher speed on moderate uphill slope is achieved by increasing both stride length and frequency, with a shortened propulsive phase, but no significant variation in its relative duration. Moreover, velocity uphill during skiMo is achieved primarily by more frequent (rather than longer) strides due primarily to high resistive forces.

The major finding was the climbing SkiMo locomotion allows the transfer of energy between PE and KE during the propulsive cycle. During the first half of the single propulsive period, KE of the CoM decreases and is converted into PE. Conversely, during the second half of the single propulsive period, PE of the CoM decreases and is converted into KE. This energy transfer is ∼24% for a slope of 20%. This value is much lower than the R% measured during walking, but this is mainly explained by the SkiMo equipment (heavy weight at the extremity of the lower limb, degradation of the ankle kinematics, .) and by the specific SkiMo locomotion (gliding phase, friction force, .)

Moreover, R% decreases significantly with the slope ($0 < 0.001$; Table 1), being only 14% for the 38% slope. When the slope is slight, it is easy to compensate the PE thanks to the KE. However, when climbing, the PE needs are greater, so the compensations by the KE become more complicated. Especially since, in our present study, the self-selected velocity has significantly decreased with the increase in the slope. Consequently, increasing the slope during SkiMo requires an increase in PE but leads to a decrease in KE. The degradation of R% with slope has already been shown during walking (Gottschall and Kram 2006).

Finally, R% was influenced by the velocity, as shown by the positive linear relationship between R% and velocity for both slopes mixed ($r = 0{,}85$ $p < 0.01$; Figure 1) and for each slope ($r = 0{,}74$ $p < 0.01$ at 20%, $r = 0{,}83$ $p < 0.01$ at 38%). Higher speed is associated to higher KE during the CoM displacement, which allows a greater transfer of energy between KE and PE, PE being required to pass the CoM above the foot and to overcome gravity during a climb. However, the results should be viewed with caution, as slope effect on R% can also be the consequence of the difference in velocity between the two slopes.

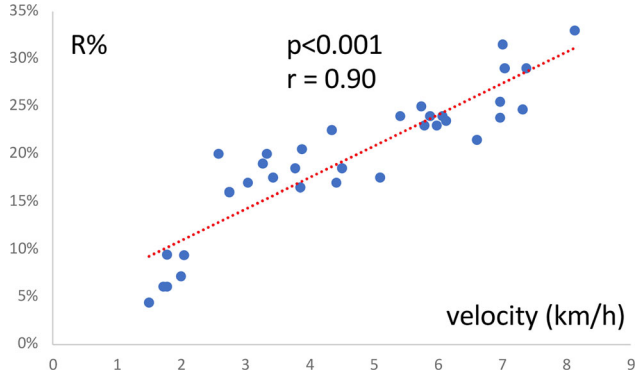


Figure 1. Evolution of percentage of energy transfer (R%) with the velocity.

4. Conclusions

The climb in SkiMo requires a consequent mechanical work production, even if a part of the CoM mechanical energy comes from a transfer between the gravitational potential and kinetic energies during the propulsive phase. This transfer is degraded with the increase in the slope.

It is therefore important to take this transfer into account when determining the mechanical work or power output during SkiMo to avoid any overestimations. Yet, further development is required to obtain a reliable estimate of the mechanical work, also considering the lost frictional force.

Moreover, when the aim is to associate mechanical and metabolic work, the determination of the internal work can be important. Indeed, the masses at the extremities of the lower limb being high, the inertia must be taken into account and therefore the internal work necessary to accelerate these segments.

Acknowledgements

Thanks to Salomon SA for the equipment and to the skiers for the mechanical work produced.

References

Cavagna GA, Saibene FP, Margaria R. 1963. External work in walking. J Appl Physiol. 18:1–9. doi:10.1152/jappl.1963.18.1.1.

Gellaerts J, Bogdanov E, Dadashi F, Mariani B. 2018. In-field validation of an inertial sensor-based system for movement analysis and classification in ski mountaineering. Sensors. 18(3):885. doi:10.3390/s18030885.

Gottschall JS, Kram R. 2006. Mechanical energy fluctuations during hill walking: the effects of slope on inverted pendulum exchange. J Exp Biol. 209(Pt 24):4895–4900. doi:10.1242/jeb.02584.

Kayser B, Mariani B. 2022. Exceptional performance in competitive ski mountaineering: an inertial sensor case

study. Front Sports Act Living. 4:854614. doi:10.3389/fspor.2022.854614.
Margaria R, Cavagna GA. 1965. The mechanics of walking. J Physiol. 57:655–656.
Minetti AE, Moia C, Roi GS, Susta D, Ferretti G. 2002. Energy cost of walking and running at extreme uphill and downhill slopes. J Appl Physiol. 93(3):1039–1046. doi:10.1152/japplphysiol.01177.2001.
Praz C, Fasel B, Vuistiner P, Aminian K, Kayser B. 2016. Optimal slopes and speeds in uphill ski mountaineering: a field study. Eur J Appl Physiol. 116(10):2017–2024. doi:10.1007/s00421-016-3455-2.

KEYWORDS Center of mass; transfert; velocity; kinetic; potential

frederique.hintzy@univ-smb.fr

Numerical investigation of head injury risks during ski collisions with obstacles

M. Dorsemaine[a,b,c], C. Masson[a], S. Riveill[b] and P.-J. Arnoux[a,c]

[a]Aix Marseille Univ, Univ Gustave Eiffel, LBA, Marseille, France; [b]Domaines Skiables de France, Francin, France; [c]iLab-Spine: International Laboratory on Spine Imaging and Biomechanics

1. Introduction

Various obstacles can be found on or close to ski slopes: trees, rocks, lifts, snowmaking equipment, etc. Collisions with these obstacles (CWO) while skiing or snowboarding are rare (<3% (Dorsemaine et al. 2023)) but constitute a major cause of severe traumatic brain injury or death on ski areas (Ruedl et al. 2011; Bailly et al. 2017).

The performances of safety padding used on obstacles to protect skiers has been experimentally evaluated using isolated head impactors (Dorsemaine et al. 2021) or partial Anthropomorphic Testing Device (Scher et al. 2021). These studies investigated the parameters influencing padding performances and assessed the injury risks for given testing conditions. However, padding performances regarding the diversity of accident conditions and impact conditions remain unknown.

To investigate this point, numerical simulations are complementary tools that have been used to characterize impact conditions during unprotected CWO (Dorsemaine, Llari, et al. 2023). Therefore, the aim of this study is to evaluate the protection brought by padding regarding head injuries in multiple scenarios of CWO.

2. Methods

To investigate multiple scenarios of CWO while skiing, a skier model (Bailly et al. 2018) previously used to define impact conditions in CWO was used on Madymo 7.5.

2.1. Padding calibration and validation

A 15-cm thick padding was first modelled and calibrated using experimental drop tests where a 6 kg metallic head impactor fell from 2 m and 3 m on a padding sample on the floor (Dorsemaine et al. 2023). The tests were numerically modelled on Madymo to calibrate the padding mechanical behavior. The impactor was modelled rigid and the padding behavior was a combination of an elastic force, a velocity-dependent damping force and a friction force.

Additional experimental drop tests were conducted with a 7.1 kg head impactor for drop heights up to 5 m to assess the model validity for higher impact energies.

2.2. CWO modelling

The padding and skier models were then used to investigate CWO injury risks using a full design of experiments (DOE). The input parameters were: the skier morphology (5th, 50th, 95th percentile), his initial speed (30, 45, 60 km/h), his orientation towards the slope (0°, 45°), the slope difficulty (green, blue, red, dark), the obstacle shape (tree, lift pole, wall), its protection (none, padding). Collision occurred either after a fall caused by a snow mound (2 possible positions) with the 2 obstacle distances (5 m, 10 m); or without previous fall leading to a direct collision of the skier with the obstacle. Among the 2160 simulations done, 1846 induced a CWO (Figure 1). Head injury risks were assessed using maximal linear head accelerations with 2 thresholds: 78 g for mild injuries and 180 g for severe injuries (Newman et al. 2000; Mertz et al. 2003). The analysis focused on the impact with the obstacle. Post-processing was performed on Matlab 2020 and R, with Wilcoxon and Kruskal-Wallis tests.

3. Results and discussion

Numerical acceleration curves and maximal acceleration values were close to experimental tests for the calibration process (<11% of variation) and for the validation at higher drop heights.

The padding significantly reduced maximal head accelerations ($p < 0.05$): 368 ± 275 g without padding versus 215 ± 241 g with padding. Without padding,

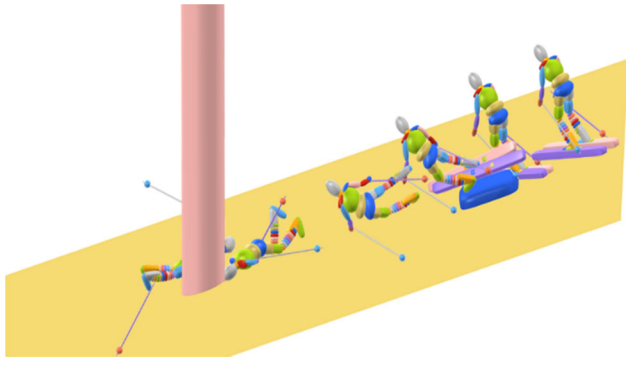


Figure 1. Example of a collision after a fall against a tree protected by a padding.

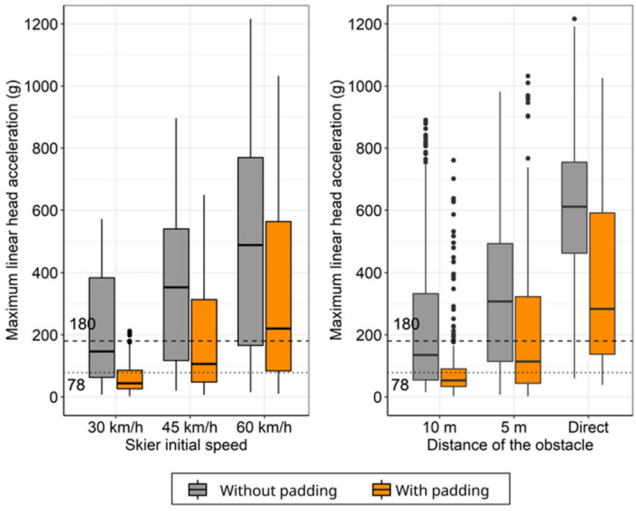


Figure 2. Influence of initial speed and obstacle distance on head maximal acceleration according to obstacle protection.

most accident conditions were at risk of mild or severe injuries (Figure 2). Maximal head accelerations were significantly influenced by skier initial speed, obstacle shape and obstacle distance ($p < 0.05$, Figure 2). In particular, the risk of severe head injury was moderate for initial speed up to 45 km/h and for collision after a fall (distance of 5 m or 10 m). These conditions were still likely to induce mild head injuries. However, direct collisions or collisions with an initial speed of 60 km/h were most of the times at risk of severe head injury.

The influences of skier initial speed and obstacle distance on injury risks were expected. However, it still brought useful information on padding performances and on the conditions where the padding reduced the injury risks compared to the cases without padding. For some conditions, the risk of injury remained important even with padding. For these cases, complementary prevention and protection measures should be considered to dissipate energy prior to the impact.

4. Conclusions

This work brought the first evaluation of padding performances to protect from head injury risks in various accident conditions. It also brought a first identification of padding limits to protect from injuries. These results are useful information for padding manufacturers to improve the performances of their products but also for ski areas to guide them on the prevention of CWO, especially on high speed areas. Future studies could focus on investigating critical scenarios using anthropomorphic dummies in full-scale tests to create experimental data for simulation validation and extend this analysis to other protection device used on ski slopes.

Acknowledgements

We would like to thank Maxime Llari for his help on the calibration process of the padding.

References

Bailly N, Afquir S, Laporte J-D, Melot A, Savary D, Seigneuret E, Delay J-B, Donnadieu T, Masson C, Arnoux P-J. 2017. Analysis of injury mechanisms in head injuries in skiers and snowboarders. Med Sci Sports Exerc. 49(1):1–10. doi:10.1249/MSS.0000000000001078.

Bailly N, Llari M, Donnadieu T, Masson C, Arnoux P-J. 2018. Numerical reconstruction of traumatic brain injury in skiing and snowboarding. Med Sci Sports Exerc. 50(11):2322–2329. doi:10.1249/MSS.0000000000001701.

Dorsemaine M, Bailly N, Riveill S, Faucheur T, Perretier C, Masson C, Arnoux P-J. 2021. About some factors influencing safety mattress performances in head impact collisions: a pilot study. J Sci Med Sport. 24(10):1067–1072. doi:10.1016/j.jsams.2021.02.015.

Dorsemaine M, Llari M, Riveill S, Laporte J-D, Jacot C, Masson C, Arnoux P-J. 2023. Collisions against obstacles while skiing: typology of victims and impact conditions. Sci Sports. doi:10.1016/j.scispo.2022.07.010.

Dorsemaine M, Masson C, Laporte J-D, Jacot C, Martin J-L, Riveill S, Arnoux P-J. 2023. Collisions against obstacles in winter sport ski areas. Wilderness Enviro Med. 34(1):7–14. doi:10.1016/j.wem.2022.09.002.

Dorsemaine M, Masson C, Riveill S, Arnoux P-J. 2023. Padding performance according to impact conditions and cycle of use in ski areas. J Sci Med Sport Plus. 2: 100038. https://doi.org/10.1016/j.jsampl.2023.100038

Mertz H, Irwin A, Prasad P. 2003. Biomechanical and scaling bases for frontal and side impact injury assessment reference values. Stapp Car Crash J. 47:155–188.

Newman J, Barr C, Beusenberg M, Fournier E, Shewchenko N, Welbourne E, Withnall C. 2000. A new biomechanical assessment of mild traumatic brain injury. Part 2: results and conclusions. IR CO BI Conference -Montpellier (France), September 2000.

Ruedl G, Bilek H, Ebner H, Gabl K, Kopp M, Burtscher M. 2011. Fatalities on Austrian ski slopes during a 5-year period. Wilderness Environ Med. 22(4):326–328. doi:10.1016/j.wem.2011.06.008.

Scher IS, Stepan L, Shealy JE, Hoover RW. 2021. Examining ski area padding for head and neck injury mitigation. J Sci Med Sport. 24(10):1010–1014. doi:10.1016/j.jsams.2020.04.019.

KEYWORDS Mattress; injury risk; multibody; ski; head

marine.dorsemaine@univ-eiffel.fr

Large-scale facilities for small-scale imaging in biomechanics

Comparison of healthy and dentino-genesis imperfecta-affected dentin: ultrastructure and mechanics, page S24.
Deep Learning for bone segmentation: towards automating failure load simulations, page S27.
Exploring damaged elastic arteries by Synchrotron X-ray Micro-CT, page S30.
High-resolution imaging of the Osteocyte Lacuno-Canalicuar Network of peri-implant newly formed bone, page S33.
Human femoral lacuno-canalicular network by X-ray nano-CT, page S36.

Comparison of healthy and dentinogenesis imperfecta-affected dentin: ultrastructure and mechanics

M. Riou[a,b,c], M. Leclercq[d], M. Vallet[d,e], S. Touraivane[d], T. Reiss[d], P. Haghi[d], N. Roubier[d], C. Acevedo[f], B. Fournier[a,b,c], M. de la Dure-Molla[a,b,g] and E. Vennat[d]

[a]Dental Faculty, Paris, France; [b]Odontology Department, APHP, Reference Center of Oral and Dental Rare Diseases. Hôpital Rothschild, Paris, France; [c]Centre de Recherche des Cordeliers, Universite de Paris, Sorbonne Universite, INSERM UMRS 1138, Paris, France; [d]Université Paris-Saclay, CentraleSupélec, ENS Paris-Saclay, CNRS, LMPS, Gif-sur-Yvette, France; [e]Laboratoire SPMS, CentraleSupélec, CNRS UMR 8580, Université Paris-Saclay, Gif-sur-Yvette, France; [f]Department of Mechanical Engineering, University of UT, Salt Lake City, UT, USA; [g]Reference center for Skeletal Dysplasia, INSERM UMR1163, Institut Imagine, Necker Hospital, Paris, France

1. Introduction

The tooth is the hardest organ in the human body, composed mainly of dentin, which lies between enamel and pulp. Dentin is a mineralized collagen framework comprising 70% carbonated hydroxyapatite, 20% organic matrix (mainly type I collagen), and 10% water. The tooth's remarkable ability to withstand mechanical forces without fracturing comes from its complex micro- and nano-structural organizations. Dentinogenesis Imperfecta (DI) is a rare genetic disease that causes severe dentin hypomineralization and damage to its structure (de la Dure-Molla 2015). In some cases, DI is caused by a type I collagen mutation (Yamaguti 2023), which leads to the modification of dentinal tissue organization at the nanoscale and microscale. Clinically, DI results in the accelerated attrition of the dentin tissue, ultimately culminating in tooth loss, likely as a consequence of decreased mechanical properties. In this study, we present an original analysis of the ultrastructure and nanostructure of healthy dentin compared to dentin affected by DI. The collagen fibrils and hydroxyapatite entanglement in both samples is observed by Scanning Electron Microscopy (SEM) and Transmission Electron Microscopy (TEM). In future work, we will be to assess the local mechanical properties using nano-indentation.

2. Methods

2.1. Sample preparation

One deciduous tooth with no visible pathological signs was prepared for the control sample. In contrast, a deciduous molar was chosen for pathological dentin from a patient diagnosed with DI exhibiting damage to type I collagen. All samples were sectioned from the crown to the root and mechanically polished using abrasive Si-C paper with decreasing grain size. The samples were then dehydrated progressively through a series of increasing ethanol concentrations. A thin layer of carbon, a few nanometers thick, was deposited on the samples to limit charging effects.

2.2. Scanning electron microscopy

The sample was observed under SEM (Helios660, FEI) in backscattered electron (BSE) mode (voltage 15 kV, current 0.8 nA).

2.3. Focused-Ion beam

Thin slices for transmission electron microscopy were prepared in the different samples using a focused ion beam–scanning electron microscope (Helios660, FEI). The chosen area were extracted perpendicular to the dentino-enamel junction, in middle dentin, and away from the 'comet-like' structures.

2.4. Transmission electron microscopy

The obtained sections were observed with a transmission electron microscope (TITAN3 G280-300 S/TEM, FEI). We used both high-angle annular dark-field scanning transmission electron microscopy (HAADF STEM) mode at 300 keV for imaging the sections. The samples were analyzed by Energy dispersive X-ray spectroscopy (EDS) to determine the atomic percent (at%) of carbon (C), oxygen (O), Magnesium (Mg), Calcium (Ca), and Phosphorus (P). The Ca/P ratio was therefore calculated.

2.5. Image analysis

The TEM image analysis was done using the ImageJ Fiji software. Due to FIB-SEM for TEM slice preparation, the curtaining effect was reduced by the software's BandPassFilter tool. Collagen fibrils and mineral lamellae of hydroxyapatite crystals dimensions were quantified using ImageJ plot profile tool.

3. Results and discussion

Using SEM on the healthy samples, we observed dentin structure characterized by tubules embedded in a mineralized organic matrix. In contrast, the tooth affected by DI presented fewer tubules, and the peritubular dentin was thinner. Parallel to the enamel-dentin junction and concentric around the pulp

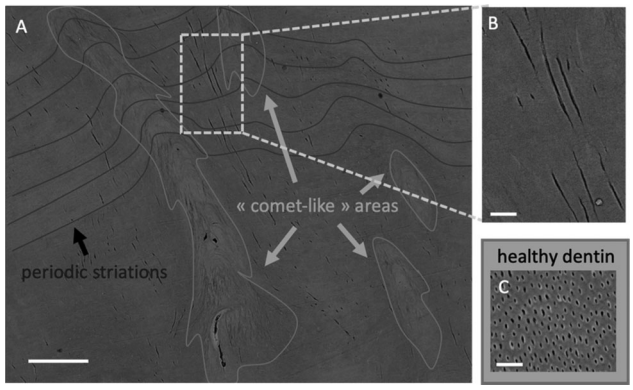


Figure 1. *SEM image of the tooth affected by DI (A and B) compared to healthy dentin (C). Scale bars: 100 μm (A) and 20 μm (B and C).*

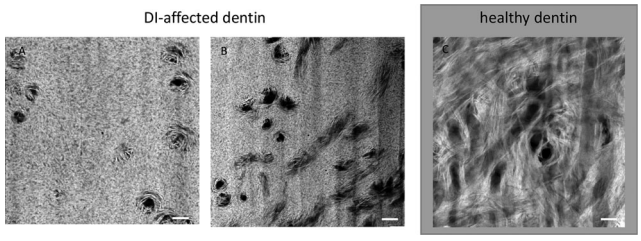


Figure 2. TEM images DI-affected (A and B) and healthy dentin (C) samples. High angle annular dark filed detector – Scanning TEM. Scale bar: 50 nm.

chamber, we observed striations indicating an alternation of areas with mineral density variations and comet-like structures that seem to constitute mineralization defects around some tubules (Figure 1).

We also found the interlocking of collagen fibrils and hydroxyapatite crystals using transmission electron microscopy. In the healthy samples, we visualized collagen fibrils all lying in the same plane, recognizable by their characteristic periodic contrast. These fibrils were mineralized with carbonated hydroxyapatite crystals. In the DI samples, the collagen fibrils appeared to have a different organization, with varying orientation planes of these fibrils. Some areas were afibrillar, with a higher electronic density (Figure 2).

The mineral part occupies more than 90% of the surface in A and B areas (Figure 2). It is more difficult to assess this ratio in healthy dentin, but a mineral content of 55% in volume has been evaluated by Vennat et al. 2009. Therefore, a drastic decrease in organic content is present locally in DI-affected dentin.

We can infer that the modifications in the mineral/organic organization and ratios in DI teeth will play an essential role in the mechanical properties of the affected tissue. The areas with a high mineral content will tend to be harder, stiffer, and more brittle. It is supported by the fact that we observed cracks initiating inside the highly mineralized 'comet-like' areas (white arrows in Figure 1). We also observed cracks passing through the interface between two periodic striations.

Looking at the crystals' size, we did not observe any statistical difference between healthy dentin and dentin affected by DI. Using the EDS analysis, we found Ca/P ratios approximatively at 1.67 (ideal hypothetical value in hydroxyapatite crystals), with a tendency to lower values in dentin affected by dentinogenesis.

4. Conclusions

Cutting-edge imaging techniques enabled us to better describe and characterize dentin tissue's nano- and microstructure. Healthy and DI-affected dentins highlight very different micro- and nano-structures.

At the microscale, the DI-affected tissue exhibited periodic striations, and 'comet-like' structures together with a very low tubule density.

At the nanoscale, the difference is also striking with a mineral content that seems to be globally more present and distributed abnormally in DI affected dentin.

This work paves the way to a better understanding of the mechanical properties of the affected tissue in relation to its abnormal micro- and nano-structure.

Nano-indentation on the affected tissue will be performed to assess the local mechanical properties and we plan to build a finite element model of the tissue based on experimental results to probe the impact of the modified micro- and nano- structure on the resulting effective properties.

Acknowledgements

We acknowledge the 'Filière Tête-Cou' for its financial support (Ultradents project).

References

de La Dure-Molla M, Philippe Fournier B, Berdal A. 2015. Isolated dentinogenesis imperfecta and dentin dysplasia: revision of the classification. Eur J Hum Genet. 23(4): 445–451. doi:10.1038/ejhg.2014.159.

Vennat E, Bogicevic C, Fleureau J-M, Degrange M. 2009. Demineralized dentin 3D porosity and pore size

distribution using mercury porosimetry. Dent Mater. 25(6):729–735. doi:10.1016/j.dental.2008.12.002.

Yamaguti PM, de La Dure-Molla M, Monnot S, Cardozo-Amaya YJ, Baujat G, Michot C, Fournier BPJ, Riou MC, Caldas Rosa ECC, Soares de Lima Y, et al. 2023. Unequal Impact of COL1A1 and COL1A2 Variants on Dentinogenesis Imperfecta. J Dent Res. 102(6):616–625. doi:10.1177/00220345231154569.

KEYWORDS Dentin; dentinogenesis imperfecta; ultrastructure; electronic microscopy

margot.riou@aphp.fr

Deep learning for bone segmentation: towards automating failure load simulations

E. Saillard[a], M. Gardegaront[a,c], F. Bermond[c], D. Mitton[c], J.-B. Pialat[b,d], C. Confavreux[d], H. Follet[a] and T. Grenier[b]

[a]INSERM, LYOS UMR 1033, Univ Lyon, Lyon, France; [b]INSA-Lyon, CREATIS, UMR5220, Univ Lyon, Villeurbanne, France; [c]Univ Eiffel, LBMC UMRT9406, Univ Lyon, Lyon, France; [d]Hospices Civils de Lyon, France

1. Introduction

Bone segmentation is an important step in performing biomechanical simulations on in-vivo CT data as it is a mandatory step to obtain meshes needed for numerical simulations. Segmentation can be a tedious task when done manually, and expert segmentations are subject to intra-operator and inter-operator variability.

Nowadays, deep learning approaches can perform this image segmentation task automatically (Aljabri and AlGhamdi 2022). These approaches must be trained on many images to guarantee a minimum of generalization to new images. However, it is not always possible to have many images with their manual segmentations. It is then necessary to use training techniques to make the best use of the available data.

In this paper, we propose a dedicated pipeline of pre-processing, deep learning-based segmentation and post-processing for human femurs and vertebras segmentation of CT-scans volumes.

For both tasks, we experimented with three U-Net architectures and showed that out-of-the-box models enable automatic and high-quality volume segmentation, if carefully trained.

2. Methods

In this section, we first detail the database used for the two segmentation tasks, then the preprocessing developed to ensure the deep learning networks trains correctly (architectures used presented in section 2.3).

2.1. Datasets

For the femur segmentation task, we used our in-house MEKANOS dataset that consists of eleven CT-scans of hips, where both femurs are present. Those scans were acquired in clinical routine following a standard procedure (axial slice 512×512 pixels, slice thickness 0.7 mm) and with different manufacturer acquisition systems. Some femurs have metastatic osteolytic lesions which complicate the segmentation task. For this database, 11 3D manual segmentations are available, corresponding to 18 femurs. 12 femurs were used for training, 4 for validation and 2 for testing.

For the vertebra segmentation task, we used two publicly available datasets: VerSe2019 and VerSe2020 (Sekuboyina 2021). Those datasets contain 374 CT-scans of various sizes all with manual segmentation. The number of vertebras on each scan ranges from 3 to 25, with all types of vertebras present in the dataset. In this study we retained 368 patients who do not have additional transitional T13 scanned. 246 scans were used for training, 62 for validation and 60 for testing.

2.2. Pre-processing pipeline

For femur segmentation, we propose a fully automated pre-processing pipeline to facilitate the deep learning training. This consists in transforming the scans with two femurs into separate femur volumes with the same orientation, and then obtain the resolution and intensity range for all volumes. This preprocessing task is done in several steps (Figure 1). It allows to increase the size of the dataset: all femurs

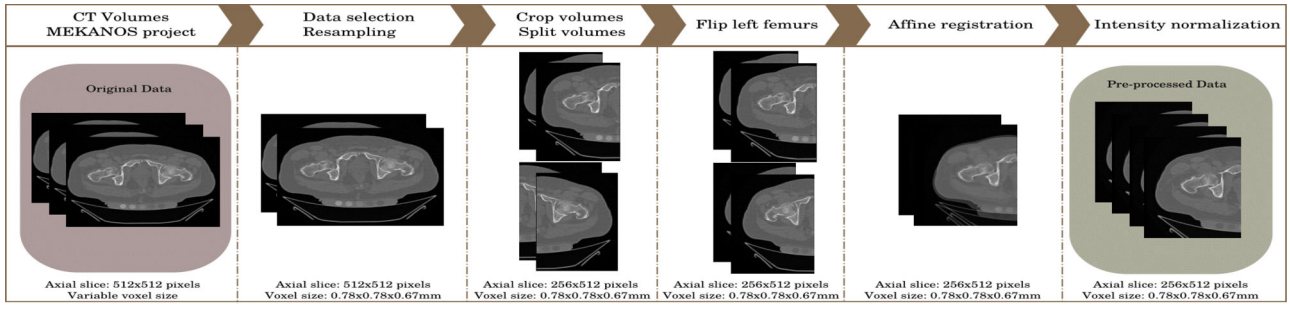


Figure 1. Pre-processing pipeline proposed for femur segmentation.

are seen as right femur. Then, the intensity values of these volumes are clipped and normalized from 0 to 1.

2.3. Neural networks

We used several convolutional neural networks all based on the U-Net architecture (Aljabri and AlGhamdi 2022). We implemented a 2D multi-planar U-Net, as well as a 3D U-Net. We compared the results with nnUNet, the state-of-the-art convolutional neural network for medical image segmentation (Isensee 2021).

Three 2D-Unet were trained on axial, coronal and sagittal slices. The 3 resulting segmentations were then fused using majority voting. The 3D-UNet model was trained using random patches of size $64 \times 64 \times 64$. 2D and 3D UNets were trained using Adam optimizer ($\beta 1 = 0.9$, $\beta 2 = 0.999$) and a DICE loss, for 250 and 500 epochs respectively, with a learning rate $\alpha = 2 \times 10^{-4}$, a batch size of 16 and 34.5 M parameters total for 2D-UNet, $\alpha = 3 \times 10^{-5}$, a batch size of 4 and 12 M parameters for 3D-UNet. Data augmentation, such as random rotations, translations, shearing and scaling was used to prevent overfitting. We also added morphological post-processing operations to remove small unwanted islands. The nnUNet architecture used is the '3d-fullres', with patch sizes automatically selected and default parameters. The optimizer used is SGD with an initial learning rate of 0.01. The batch size was set to 2 for both trainings, with a total number of parameters of 30.8 M for femur segmentation and 31.2 M for vertebrae segmentation.

3. Results and discussion

To quantify the results, we used the Sørensen-Dice score (noted DSC) to evaluate the similarity between the ground-truth and the automatic segmentations ([0;1] where 1 is the best), as well as the Hausdorff distance (noted HD) to evaluate the maximum errors of the automatic segmentations (in mm, smaller the better). All metrics are computed on 3D volumes. We used a 5-fold cross-validation to quantify more accurately the results.

As shown in Table 1, the DSC obtained for both tasks exceed 0.9 which are good segmentation performance when our pre-processing is used. The results also show that U-Net 3D and nnUNet outperform the multi-axial 2D-UNet for the femur segmentation task. U-Net 3D and nnUNet perform very similarly on this task, with only a slight improvement of HD for U-Net 3D. Our femur segmentation pipeline shows results comparable to state-of-the-arts methods (Liang 2021), and our vertebras segmentation method shows results similar to the best methods using the VerSe datasets (Isensee 2021).

Table 1. Segmentation results obtained with our different models.

Task/Dataset	Algorithm	DSC	HD (mm)
Femur segmentation MEKANOS database	U-Net 2D multi axial No pre-processing	0.74 ± 0.085	49.86 ± 12.57
	U-Net 2D multi axial	0.93 ± 0.011	2.3 ± 0.82
	U-Net 3D	0.96 ± 0.008	**2.2 ± 0.71**
	nnUNet 3d_fullres	**0.96 ± 0.006**	2.4 ± 0.84
Vertebras segmentation VerSe database	nnUNet 3d_fullres	**0.88 ± 0.016**	**19.74 ± 9.45**

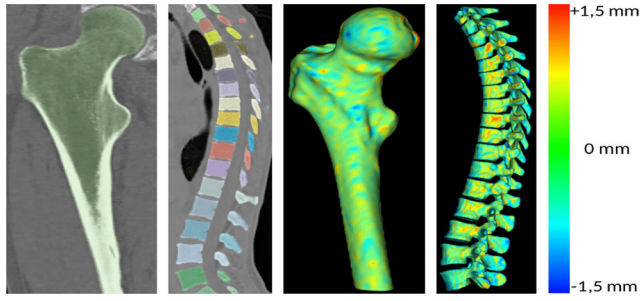


Figure 2. Automatic segmentations obtained with nnUNet(left), pixels distance to the ground-truth(right).

For vertebras segmentation, nnUNet proved very efficient, but the HD is much higher, due to small mislabelling of some vertebras. Figure 2 shows results obtained with our approach and the errors made when comparing to experts. The proximal part of the femur is more prone to segmentation errors than the distal part, but inaccuracies remain minimal. For vertebra segmentation, the vertebral body and pedicle are less likely to be mislabelled or mis-segmented than the spinous or transverse process, where the delimitation between 2 vertebras is more difficult to assess.

The total training time is 12 h for 2D-UNet per axis, 16 h for 3D-UNet and 48 h for nnUNet on the femur dataset. This substantial difference is also present during inference, where nnUNet takes 30 min for a prediction when standard models only take 3 min.

4. Conclusions

In this paper, we proposed a dedicated pre-processing pipeline for femur segmentation as well as deep learning based segmentation methods for femurs and vertebras segmentation. From our experiments, we showed that it is primordial to use pre-processing in order to improve the segmentation results. U-Net architectures are efficient and can serve as primary tools to perform automated bone segmentations. The

results obtained allow us to envision the use of this approach in a broader pipeline in biomechanical simulations on patients with metastatic lesions.

Acknowledgements

This work was partly funded by LabEx Primes, France (ANR-11-LABX-0063) and MSDAVENIR Research Grant. The images were selected and acquired in clinical routine thanks to the MEKANOS clinical research assistants.

References

Aljabri M, AlGhamdi M. 2022. A review on the use of deep learning for medical images segmentation. Neurocomputing. 506:311–335. doi:10.1016/j.neucom.2022.07.070.

Isensee F, Jaeger PF, Kohl SAA, Petersen J, Maier-Hein KH.,. 2021. nnU-Net: a self-configuring method for deep learning-based biomedical image segmentation. Nat Methods. 18(2):203–211. doi:10.1038/s41592-020-01008-z.

Liang K, Fu H, Zhou H, Jiang L, Yin X, Zhang M, Peng X. 2021. Accurate and Dautomatic 3D segmentation of femur and pelvis from CT images of the hip based on deep learning. JIST. 65(3):030411-1–030411-6. doi:10.2352/J.ImagingSci.Technol.2021.65.3.030411.

Sekuboyina A, Husseini ME, Bayat A, Löffler M, Liebl H, Li H, Tetteh G, Kukačka J, Payer C, Štern D, et al. 2021. VerSe: a vertebrae labelling and segmentation benchmark for multi-detector CT images. Med Image Anal. 73:102166. doi:10.1016/j.media.2021.102166.

KEYWORDS Deep learning; bone segmentation; CT-scan; spine; femur

thomas.grenier@creatis.insa-lyon.fr

Exploring damaged elastic arteries by synchrotron X-ray micro-CT

Xiaowen Liang[a,b], Aïcha Ben Zemzem[a], Laetitia Vanalderwiert[a], Béatrice Romier-Crouzet[a], Sébastien Blaise[a], Timm Weitkamp[c], Manuel Dauchez[a], Stéphanie Baud[a], Laurent Debelle[a], Nicolas Passat[b] and Sébastien Almagro[a]

[a]UMR MEDyC, CNRS 7369, Université de Reims Champagne Ardenne, SFR CAP SANTE, Reims, France; [b]CReSTIC, Université de Reims Champagne Ardenne, Reims, France; [c]Synchrotron SOLEIL, Gif-sur-Yvette, France

1. Introduction

Diabetes is a chronic pathology affecting about 10% of the world population. It accelerates arterial stiffness and increases the probability of cardiovascular diseases. The effect of diabetes on the stiffness of the vascular system has been broadly estimated to correspond to 6–15 years of chronological aging (Vatner et al. 2021). This pathology is mainly characterized by an important level of blood glucose leading to the formation of cross-links within elastin fibers and collagens, resulting in a decrease of arterial wall distensibility.

Large arteries such as the aorta contain, in their extracellular matrix, an amorphous elastic hydrophobic polymer named elastin, which is the major component of elastic fibers. Its entropic elasticity and its concentric lamellar organization within the aortic wall allow the aorta to remain in a reversible deformation domain during the cardiac cycle, which alternate phases of overpressure and contraction. Alterations to elastin due to a pathological situation or aging permanently affect the arterial mechanics.

Synchrotron X-ray microtomography (µ-CT) enables imaging of large sample volumes with sub-micrometric resolution associated to millimeter size field (Weitkamp et al. 2020; Ben Zemzem et al. 2021). We have developed a protocol to harvest mice aorta, with a limited collapse, for µ-CT imaging.

2. Methods

2.1. Animals and sample preparation

Mouse procedures were authorized and realized in accordance with local laws (agreement D-51-454-2). The mice, 6-month-old C57BL6J (control, $n = 4$) and 6-month-old *db/db* (diabetic, $n = 6$), were purchased from C. River and share the same genetic background.

Aortas were collected after euthanasia and heparin injection, the heart and aorta were then flushed with phosphate buffered saline to remove residual blood. The aorta was further prefixed by injecting 4% formalin then filled of 1% low melting agarose to keep the aorta opened and to prevent collapse during dehydration and inclusion steps. Gel solidification in the lumen exerts a counterpressure to avoid collapse. The heart and aorta were collected with surrounding tissues. Finally, the samples were fixed in 4% formalin, dehydrated, and embedded in paraffin. The final samples were about 4-cm-long paraffin rods containing the heart and aorta.

2.2. Imaging procedures

Synchrotron X-ray µ-CT was performed on the ANATOMIX beamline (SOLEIL synchrotron, Gif-sur-Yvette, France) with an effective pixel size of 0.65 µm at the sample level. Tomographic reconstruction was performed using the standard processing pipeline at the beamline. The reconstructed volume stacks for each scan contained $2048 \times 2048 \times 2048$ voxels of size $(0.65\ \mu m)^3$, giving a 32 GB file per stack.

2.3. Arterial structure segmentation

Arterial structures were segmented automatically from reconstructed stacks with bespoke Matlab scripts as previously described (Ben Zemzem et al. 2021). The result of this segmentation for each tomography volume scan is a 2048-image 3D stack containing 8-bit voxels of the arterial wall.

2.4. Reserve length of elastic lamellae

Elastic lamellae are first 'fragmented' using thresholding. Typically, about 15–30 fragments are kept per image, leading to about 2,000–30,000 fragments per stack. 10 images stacks were retained for control mice, 11 for diabetic mice.

3. Results and discussion

Figure 1a shows a typical reconstructed raw 2D image plane extracted from a synchrotron X-ray µ-CT acquisition (2048^3 voxels) at 0.65 µm/voxel for an aortic segment of a 6-month control mouse. The sample was not sectioned and not stained.

The phase-contrast image exhibits the different structures of the aortic environment from the thoracic region. Figure 1b shows an automatic segmentation of elastic structures by our program.

Elastic lamellae are altered in diabetic mice (Figure 2 upper row versus lower row). The control presents

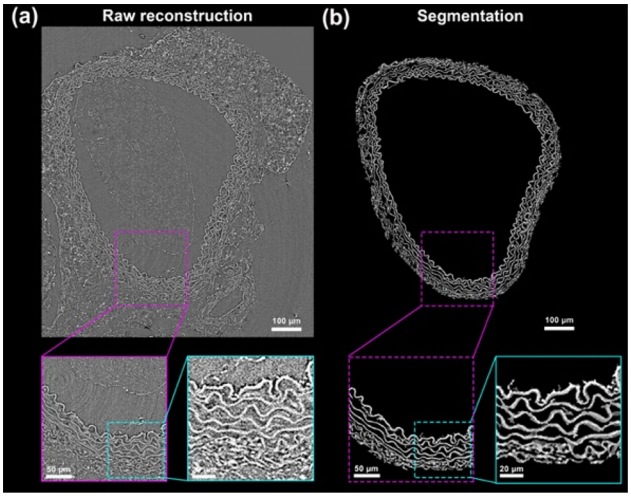


Figure 1. 2D-plane reconstruction from synchrotron acquisition and its automatic segmentation.

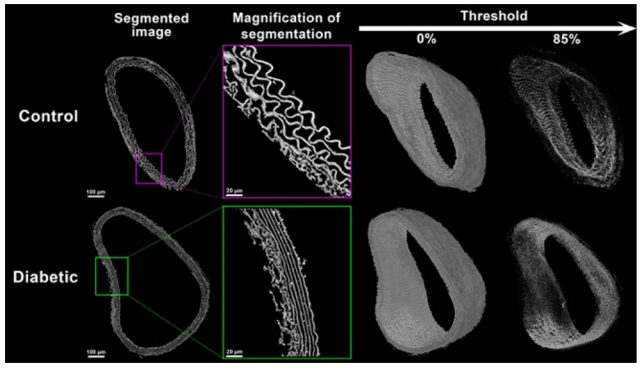


Figure 2. Comparison of control (upper row) and diabetic (lower row) elastic structures in one 2D plane (left) versus 3D perspective of 800 planes (right).

a wavy aspect indicating a reserve length. This reserve length allows a spring to be stretched above its apparent length, i.e. its end-to-end distance. If a spring is stretched too much or altered, it loses its reserve and its ability to be reversibly deformed when overstretched. To assess the reserve length of these lamellae, we compute, for a given segment, the ratio (r) between its Euclidean (i.e. end-to-end) and geodesic lengths (i.e. its real length). 127,180 measurements were made on control mice ($r = 0.823$, $\sigma = 0.047$), 159,485 on diabetic mice ($r = 0.889$, $\sigma = 0.026$) to have an exhaustive view over the length, for each elastic lamella and in each orientation. Our analysis shows that diabetic mice have lost a significant part ($p < 0.004$) of their reserve length (59.5% less) as compared to the control group (Ben Zemzem et al. 2022).

We have previously shown (Ben Zemzem et al. 2021) that an inner lattice-like network (Figure 2, upper right image) is present inside the elastic structure, to which it seems to confer flexibility and resistance. 6-month-old diabetic mice exhibit a drastic destruction of this network (Figure 2, lower right image) in comparison of normal mice of the same age, suggesting a structural role for this lattice-like network.

To go further in our study, we have developed an approach combining standard image analysis and deep learning approaches to segment and separate finely the elastic lamellae to study them one by one, associated with the capabilities of the ROMEO supercomputer (Reims), allows us to extract parameters such as local geometry (thickness, density, local curvature) and the geometry of arteriola branching.

4. Conclusions

In-line phase-contrast synchrotron X-ray microtomography of the arterial wall with label-free tissues grants access to fine details of elastic structures. The strength of this method lies in its large field, its excellent resolution, and a good contrast for intramural elastic structures. Coupled to an automatic image analysis program, this technique provides information that cannot be obtained using other imaging methods. Moreover, for each sample, it allows the computation of thousands of measurements for a given feature, such as the ratio between Euclidean and geodesic distances of a segment of an elastic lamella.

Our results show that the reserve length of elastic lamellae is reduced in diabetic mice together with the loss of filaments that support the wall. This suggests that elasticity is correlated to the existence of this lattice-like network that has disappeared at 6 months of diabetes.

The challenge is to extract measurements that allow us to accurately estimate the physiological age of the artery. We plan to develop a pressurization system to image and measure the deformation of arterial wall structures under X-ray beam, so as to decipher the link between small scale alterations and their biomechanical incidence. Further, as the methods we use allow us to make contiguous tomographic scans, we can merged them into a global view of the murine arterial network. This aorta envelope will be used to model the blood flow inside this deformable network.

Acknowledgements

The chair MAgICS, the University of Reims Champagne-Ardenne and DRRT of Champagne-Ardenne funded this work. The authors acknowledge Synchrotron SOLEIL to have provided beamtime for this study under project 20191028. ANATOMIX is funded by the Investments for

the Future program of the French National Research Agency, project NanoimagesX (ANR-11-EQPX-0031). Fundings from the 'Grand-Est' Region (OMAGE & FHU program), ERRDF and CNRS are acknowledged.

References

Ben Zemzem A, Genevaux A, Wahart A, Bodey AJ, Blaise S, Romier-Crouzet B, Jonquet J, Bour C, Cogranne R, Beauseroy P, et al. 2021. X-ray microtomography reveals a lattice-like network within aortic elastic lamellae. FASEB J. 35(10):e21844.

Ben Zemzem A, Liang X, Vanalderwiert L, Bour C, Romier-Crouzet B, Blaise S, Sherratt MJ, Weitkamp T, et al. 2022. Early alterations of intra-mural elastic lamellae revealed by synchrotron X-ray micro-CT exploration of diabetic aortas. Int J Mol Sci. 23(6):3250.

Vatner SF, Zhang J, Vyzas C, Mishra K, Graham RM, Vatner DE. 2021. Vascular stiffness in aging and disease. Front Physiol. 12:762437. doi:10.3389/fphys.2021.762437.

Weitkamp T, Scheel M, Perrin J, Daniel G, King A, Le Roux V, Giorgetta J-L, Carcy A, et al. 2020. Microtomography on the ANATOMIX beamline at Synchrotron SOLEIL. 2380.

KEYWORDS Synchrotron X-ray; extracellular matrix; microCT; cardiovascular diseases; diabetes

sebastien.almagro@univ-reims.fr

High-resolution imaging of the osteocyte lacuno-canalicuar network of peri-implant newly formed bone

Khaoula Abouzaid[a], Thomas Reiss[b], Guillaume Haïat[a], Hugues Albini-Lomami[a], Elsa Vennat[b] and Sophie Le Cann[a]

[a]CNRS, MSME UMR 8208, France; [b]CentraleSupélec, ENS Paris-Saclay, CNRS, LMPS, Université Paris-Saclay, France

1. Introduction

Bone implants are widely used in orthopedic and dental surgery to restore bone function and structure. However, the interface between the implant and the bone can be a site of complications such as implant loosening, bone resorption, and inflammation.

The bone tissue is highly hierarchical. At the submicron scale, the osteocyte lacuno-canalicular network (OLCN) is a complex system of channels that interconnects the osteocytes and allows for the exchange of nutrients, waste products, and signaling molecules. During bone modelling and remodelling, this network plays a crucial role in maintaining bone health and responding to mechanical loading. Understanding the formation and maintenance of the OLCN at the implant interface is essential for developing new strategies to enhance osseointegration and prevent implant failure (Haridy et al. 2021; Shah et al. 2018).

To access the level of resolution needed to investigate the OLCN, high-resolution imaging techniques can be used, such as scanning electron microscopy (SEM) (Schneider et al. 2010) which can be combined with Focused Ion Beam (FIB-SEM) to extend from 2D to 3D information, or nano-computed tomography (nano-CT) (Peyrin et al. 2014). Such high-resolution techniques are only usable with adapted image processing and analysis methods, to quantify the structural properties of the OLCN, such as the degree of porosity, the dimensions of osteocyte lacunae and canaliculi, and the connectivity of the network. Applied to the bone tissue, such approaches have provided valuable information on the morphology and organization of the OLCN (Hemmatian et al. 2021), revealing for instance the spatial heterogeneity of the network (Meijering et al. 2016) or that the geometrical properties of osteocyte lacunae are almost independent on age (Wittig et al. 2016). Work investigating the adaptation of the bone tissue to the presence of an implant is still scarce, data suggests for instance that collagen fibrils are oriented parallel with the implant surface.

Using a bone chamber implant model integrated into rabbit bone for several weeks, we propose to investigate the newly-formed bone tissue close to a metallic implant with FIB-SEM and image processing.

2. Methods

2.1. Sample

A standardized coin-shaped TiAl6V4 implant (Ø5mm, H3mm) with a bone chamber (Figure 1A) was osseointegrated for 7 weeks in rabbit cortical bone (tibia). After harvesting, the sample was embedded in PMMA and sliced to expose the newly-formed bone at the implant surface (Figure 1B).

2.2. Image acquisition

A $20 \times 30 \times 30$ μm^3 region close to the implant (roughly at a distance of 20 µm) was imaged using a FIB-SEM (FEI Helios NanoLab 660) in back-scattered electron (BSE) mode, and 'Slice and View' software (Figure 1C). The resulting 3D images stack consists of 1027 2D grayscale cross-sections (pixel size 16.8 nm) with a distance of 20 nm between each slice.

2.3. Image pre-processing

The acquired images were processed using Fiji to remove brightness and reduce noise and artifacts. First, a 3D Gaussian filter with a standard deviation of 3 was used to reduce noise. Then, a bandpass filter with a high spatial frequency of 150 pixels and a low spatial frequency of 3 pixels was applied to remove

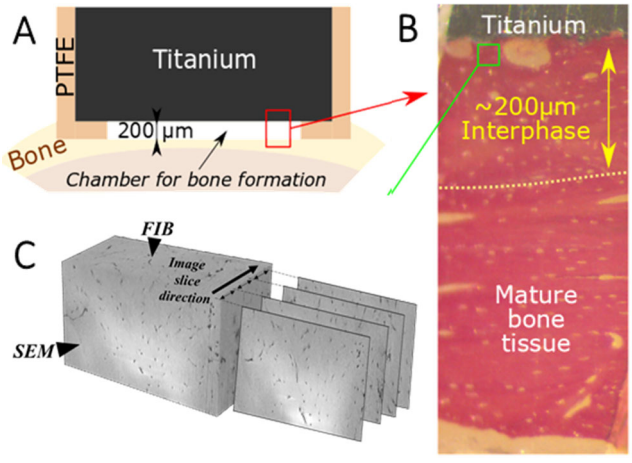


Figure 1. (A) Bone-chamber implant. (B) Sample with bone tissue stained in red (picrofushin), C. FIB-SEM 'slice and view'.

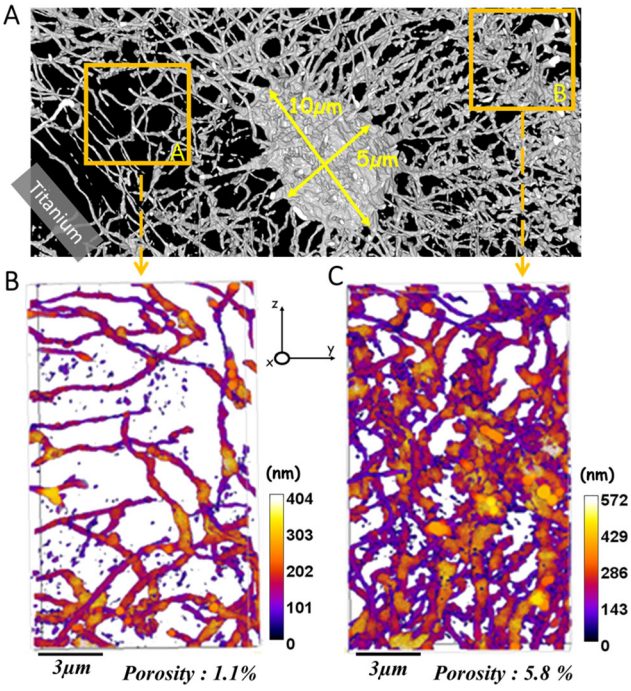


Figure 2. (A) OLCN network in the Immature bone tissue and the two subvolumes of interest. (B,C) Thickness distribution and average porosity of canaliculi connected to the same osteocyte.

localized brightness, mostly due to charging effects around cavities (e.g. osteocytes cavities). Finally, to eliminate the curtaining artifacts coming from the etching with the ion beam, Fast Fourier Transform (FFT) was applied to obtain the frequency spectrum. Periodic horizontal bands were observed and identified as the artifacts and subsequently removed.

2.4. Image analysis

Once cleaned, the images were threshold-segmented to isolate the OCLN network (low gray values) from the mineralized bone (high gray values). Two preferential subvolumes ($9 \times 9 \times 16$ µm) were identified around the osteocyte cavity, which displayed visual differences in porosity. Canaliculi thickness maps were extracted using the BoneJ plugin and analyzed using a MATLAB routine.

3. Results and discussion

After a healing period of 7 weeks, the analyzed peri-implant bone region presented a well-defined lacuno-canalicular network, with an osteocyte lacuna connected to a dense meshwork of canaliculi (Figure 2A).

The ellipsoidal lacuna was of approximate dimensions of 10 µm in the large axis and 5 µm in the small axis, and appeared visually aligned parallel with the direction of the implant surface. The two isolated subvolumes of the newly formed bone region presented different local porosity of 1.1% (Figure 2B) and 5.8% (Figure 2C) which is consistent with literature data on bone (Buenzli and Sims 2015). The relative maximum canaliculi thickness was observed to vary between the subvolumes, with the higher porosity subvolume exhibiting a denser and thicker network of canaliculi (average of 240 ± 80 nm) compared to the lower porosity one (average of 200 ± 60 nm).

The subvolume presenting lower porosity and thinner canaliculi being closer to the implant, this heterogeneity may be due to the adaptation of the tissue to the implant, which could influence the local bone formation process (Robling and Bonewald 2020).

4. Conclusions

The observed difference in local porosity and canaliculi thickness in the peri-implant newly formed bone tissue could be due to the heterogeneity of the newly formed bone. Such local variations highlight the importance of considering the local sub- microstructure when designing and evaluating bone implants. The ongoing analysis and perspectives of this work focus on the OLCN orientation and connectivity, to provide further insights into the bone 3D adaptation process near the implant. Moreover, data will be compared to mature bone regions of the same sample, to help understand the differences in the bone tissue's local micro and sub-nanostructure.

Acknowledgements

Funding by Paris Ile-de-France Region (DIM 'Respore'), the CNRS (MITI interdisciplinary program) and the EU H2020 research and innovation programme (the MSCA-IF Bomb project #797764). We thank EquipEx MATMECA for access to the FIB-SEM.

References

Buenzli PR, Sims NA. 2015. Quantifying the osteocyte network in the human skeleton. Bone. 75:144–150. doi:10.1016/j.bone.2015.02.016.

Haridy Y, Osenberg M, Hilger A, Manke I, Davesne D, Witzmann F. 2021. Bone metabolism and evolutionary origin of osteocytes: novel application of FIB-SEM tomography. Sci Adv. 7(14):eabb9113. doi:10.1126/sciadv.abb9113.

Hemmatian H, Bakker AD, Klein-Nulend J, van Lenthe GH.,. 2021. Alterations in osteocyte lacunar morphology affect local bone tissue strains. J Mech Behav Biomed Mater. 123:104730. doi:10.1016/j.jmbbm.2021.104730.

Meijering E, Carpenter AE, Peng H, Hamprecht FA, Olivo-Marin J-C. 2016. Imagining the future of bioimage

analysis. Nat Biotechnol. 34(12):1250–1255. doi:10.1038/nbt.3722.

Peyrin F, Dong P, Pacureanu A, Langer M. 2014. Micro- and nano-CT for the study of bone ultrastructure. Curr Osteoporos Rep. 12(4):465–474. doi:10.1007/s11914-014-0233-0.

Robling AG, Bonewald LF. 2020. The osteocyte: new insights. Annu Rev Physiol. 82:485–506. doi:10.1146/annurev-physiol-021119-034332.

Schneider P, Meier M, Wepf R, Müller R. 2010. Towards quantitative 3D imaging of the osteocyte lacuno-canalicular network. Bone. 47(5):848–858. doi:10.1016/j.bone.2010.07.026.

Shah FA, Thomsen P, Palmquist A. 2018. A Review of the Impact of Implant Biomaterials on Osteocytes. J Dent Res. 97(9):977–986. doi:10.1177/0022034518778033.

Wittig NK, Bach-Gansmo FL, Birkbak ME, Laugesen M, Brüel A, Thomsen JS, Birkedal H. 2016. Organ and tissue level properties are more sensitive to age than osteocyte lacunar characteristics in rat cortical bone. Bone Reports. 4:28–34. doi:10.1016/j.bonr.2015.11.003.

KEYWORDS Bone-implant interface; electron microscopy; osteocyte lacuno-canalicular network; porosity; thickness

khaoula.abouzaid@u-pec.fr

Human femoral lacuno-canalicular network by X-ray nano-CT

R. Gauthier[a], B. Yu[b], C. Olivier[c], J. Villanova[d], M. Langer[e], H. Follet[f], D. Mitton[g] and F. Peyrin[b,d]

[a]CNRS, INSA Lyon, Université Claude Bernard Lyon 1, MATEIS, UMR5510, Univ Lyon, Villeurbanne, France; [b]INSA Lyon, Université Claude Bernard Lyon 1, UJM-Saint Etienne, CNRS UMR 5220, Inserm U1206, CREATIS, Univ Lyon, Lyon, France; [c]Univ. Grenoble Alpes, Inserm, Strobe, Grenoble, France; [d]ESRF, The European Synchrotron, Grenoble, France; [e]Univ. Grenoble Alpes, CNRS, UMR 5525, VetAgro Sup, Grenoble INP, TIMC, Grenoble, France; [f]Univ Lyon, Université Claude Bernard Lyon 1, INSERM, LYOS UMR1033, Lyon, France; [g]Univ Lyon, Univ Gustave Eiffel, Univ Claude Bernard Lyon 1, LBMC UMR_T9406, Lyon, France

1. Introduction

Bone mechanobiology is involved in bone biomechanical integrity. Understanding how this mechanobiological remodeling operates *in vivo* is interesting in terms of potential future bone regenerative strategies development. But while both osteoclasts and osteoblasts, bone resorbing and forming cells, are mechanosensitive, the whole bone mechanobiological remodeling is regulated by the osteocytes. These cells are able to identified a damaged region before activating recruited osteoclasts and osteoblasts to resorb this region and form a new bone.

When dealing with bone mechanobiology, it is thus determinant to consider how the osteocytes are mechanically stimulated and how the signalling biomolecules are transported towards the osteoclasts and osteoblasts.

Within bone, osteocytes are trapped in micrometric lacunae all interconnected through submicrometric canaliculi crossing the whole matrix. This Lacuno-Canalicular Network (LCN) is filled with a physiological fluid transmitting the mechanical signals to the osteocytes, and acting as the carrying media for biomolecules. The LCN permeability, involved in both cells mechanosensation and molecular transport, is known to depend on its morphology (Lemaire 2012). But due to the submicrometric canalicular dimensions and the associated difficulty to characterize it, numerical models used to estimate bone LCN fluids flow are only based on simplified LCN morphologies. In the present study, synchrotron radiation nano-computed tomography (SR-μCT) has been used to develop a human LCN morphology database to be used in future for more realistic biomechanical models.

2. Materials and methods

The femoral diaphyses from 27 human donors (15 females and 12 males) aged from 50 to 95 years old were harvested. Parallelepiped cortical bone samples ($0.4 \times 0.4 \times 4\,mm^3$) were cut with the long axis along the haversian canal axis.

The 27 bone samples were imaged at the ESRF (Grenoble, France) on the beamline ID16B. Each sample was scanned at 4 different distances from the source, with 3400 projections recorded at each distance over 360°. The X-ray beam energy was set to 29.6 keV. Phase retrieval was performed using a multi distance Paganin method (Yu 2018). Finally, applying a standard filtered back projection algorithm provided volumes made of $2560 \times 2560 \times 2160$ voxels with a resulting isotropic voxel size of 100 nm.

Osteocytes lacunae were segmented by applying a hysteresis thresholding (Dong 2014). Canaliculi segmentation was performed using a more complex procedure, described in Yu (2018), including the enhancement of their visibility through a Sato's vesselness enhancement method before applying the hysteresis thresholding.

Finally, morphometric parameters, such as the canalicular and LCN (canaliculi + lacunae) total volume fraction (Ca.V/BV and LCN.V/BV in %, respectively) where BV is the bone volume, the canalicular diameter (Ca.D in μm), and the canalicular number in function of the distance to their closest lacuna (Ca.N) were quantified. This parameter was obtained by measuring the number of holes in a surface growing from the lacunar wall to a surface 12 μm away from it (Yu 2021).

3. Results and discussion

The proposed image processing protocol was applied to the 27 human femoral volumes corresponding to a physical field of view of $256 \times 256 \times 216\,\mu m^3$. The segmented lacunae and canaliculi are illustrated in Figure 1.

Canalicular volume accounted in average for 0.4% of the total bone volume. This value increased to 1.1 when considering the whole LCN. This means that

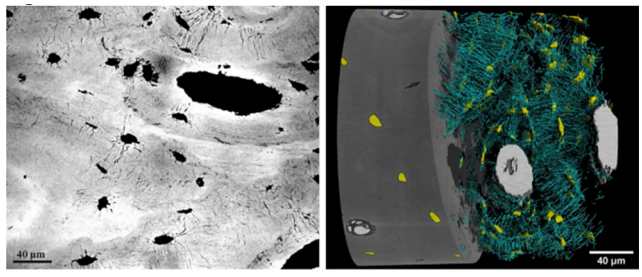


Figure 1. Slice from the VOI and 3D segmented volume with canaliculi and lacunae in blue and yellow.

Table 1. Averaged value and standard deviation (SD) for the LCN morphometric parameters.

	Ca.V/BV (%)	LCN.V/BV (%)	Ca.D (µm)
Averaged	0.4	1.1	0.36
SD	0.1	0.2	0.03

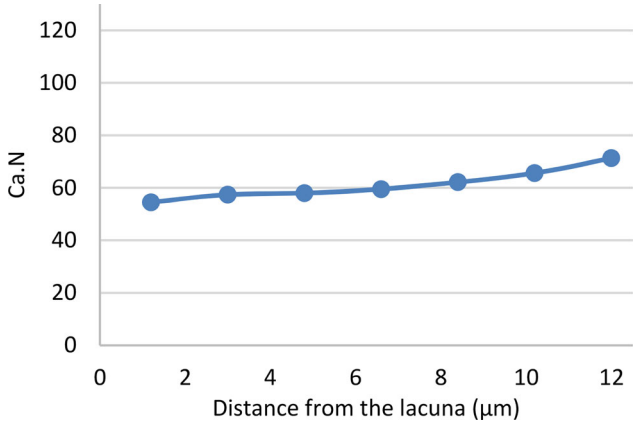


Figure 2. Distribution of the number of canaliculi with the distance to the lacunar wall.

the canaliculi volume represented 36% of the LCN, the remaining being occupied by the lacunae. The canalicular diameter was measured at 0.36 µm, with quite a low standard deviation (8% of the averaged value) over the investigated population (Table 1).

It was observed that the number of canaliculi increased slightly with the distance to the lacuna, from 54 canaliculi at the lacunar wall to 71 at 12 µm from it (Figure 2). This result suggests that the canalicular network branches out as it spreads from the lacuna. It is interesting to notice the high standard deviation obtained for these measurements.

To accurately predict fluid circulation, LCN morphological properties, such as tortuosity or local thickness, are needed (Lemaire 2012). Similarly, it is known that the canalicular ramification may play a role in maintaining the LCN permeability in the case of canaliculi interruption (Bortel 2022). The current results have shown that the number of canaliculi tends to increase with the distance to a lacuna, suggesting a ramification of the network (Figure 2).

Still, an important variation is observed on this parameter, highlighting the diversified investigated population. For example, the female population presented a trend toward a higher number of canaliculi per lacuna compared to the male population. Additionally, it was observed a high intra-individual variability, with an averaged standard deviation of 31 canaliculi per lacuna for an averaged number of 54 canaliculi per lacuna at 1 µm from it over the investigated population. This result suggests that the LCN morphology varies within bone matrix. This is in accordance with previous results showing lacunar parameters depending on their localization with bone microstructure (Gauthier 2019).

While in the current study, only global parameters are provided, the data set allows to locally investigate the LCN morphology. Such a local investigation is determinant to better understand the LCN permeability distribution depending on bone organization.

4. Conclusions

To the authors' knowledge, this database is unique and promising in terms of better understanding of the LCN and the further numerical modeling of human cortical bone load-induced fluid flow.

Acknowledgements

This work was done in the framework of LabEx PRIMES ANR-11-LABX-006 of Université de Lyon. We thank the ESRF for support through the Long-Term Proposal MD830 and for provision of beam time (experiment MD933) using the ID16B beamline.

References

Bortel E, Grover LM, Eisenstein N, Seim C, Suhonen H, Pacureanu A, Westenberger P, Raum K, Langer M, Peyrin F, et al. 2022. Interconnectivity Explains High Canalicular Network Robustness between Neighboring Osteocyte Lacunae in Human Bone. Adv NanoBiomed Res. 2(4):2100090. doi:10.1002/anbr.202100090.

Dong P, Haupert S, Hesse B, Langer M, Gouttenoire PJ, Bousson V, Peyrin F. 2014. 3D osteocyte lacunar morphometric properties and distributions in human femoral cortical bone using synchrotron radiation micro-CT images. Bone. 60:172–185. doi:10.1016/j.bone.2013.12.008.

Gauthier R, Follet H, Olivier C, Mitton D, Peyrin F. 2019. 3D analysis of the osteonal and interstitial tissue in human radii cortical bone. Bone. 127:526–536. doi:10.1016/j.bone.2019.07.028.

Lemaire T, Lemonnier S, Naili S. 2012. On the paradoxical determinations of the lacuno-canalicular permeability of bone. Biomech Model Mechanobiol. 11(7):933–946. doi:10.1007/s10237-011-0363-6.

Yu B, Pacureanu A, Olivier C, Cloetens P, Peyrin F. 2021. Quantification of the bone lacunocanalicular network from 3D X-ray phase nanotomography images. J Microsc. 282(1):30–44. doi:10.1111/jmi.12973.

Yu B, Weber L, Pacureanu A, Langer M, Olivier C, Cloetens P, Peyrin F. 2018. Evaluation of phase retrieval approaches in magnified X-ray phase nano computerized tomography applied to bone tissue. Opt Express. [26(9):11110–11124. accessed 2023 Jan 27] doi:10.1364/OE.26.011110.

KEYWORDS Bone lacunocanalicular network; synchrotron radiation tomography; bone permeability

remy.gauthier@cnrs.fr

Cellular and tissue biomechanics

Acoustic streaming in bone pericellular fluid under ultrasound stimulation, page S39.
Bending the disc: biomechanics of drosophila wing development, page S41.
Changes in endothelial cell microrheology in medium modified by cancer cells, page S43.
Corneal mechanics for the early detection of the keratoconus using patient-specific geometry and microstructural data, page S46.
Estimation of soft-tissue stiffness using ultrasound indentation for pressure ulcer prevention, page S48.
Experimental study of the different layers of the human oesophagus, page S51.
Friction when changing neighbours: adhesion dynamics and active stresses regulate cell intercalation behaviour in an active tissue, page S54.
Hematocrit profile relaxation after a t-shaped bifurcation, page S56.
Imaging small intestinal motility at macro and micro scales, page S58.
Investigating human defecation by coupling fluid mechanical modeling and x-ray video-defecography, page S60.
Mechanical analysis of tumor cell of glioblastoma by combining confocal microscopy, digital volume correlation, scanning ion confocal microscopy and finite element model, page S63.
Mechanical and microstructural characterization of the tunica albuginea, page S66.
Mechanical behavior of stomach tissue: a preliminary study, page S69.
Mechanical properties of spinal nerve roots along the cervical spine, page S72.
Modeling of bulge test of the fascia lata using the discrete element modeling method, page S74.
Modeling spheroids rheology, page S77.
Quantitative analysis of the fibrous microstructure of 3d collagen gels, page S80.
Quasi-static brain dura mater biaxial tensile testing: preliminary results, page S83.
Reproducibility of a finite element model of the human femur in torsional load, page S86.
Skin-to-bone interaction: destructive and non-invasive mechanical characterization and modeling of porcine scalp, page S89.
Spatial resolution and repeatability of the human brain magnetic resonance elastography, page S92.
Strain measurement by digital volume correlation applied to optical coherence, page S94.
The role of mechanical damage in abdominal wall incisional hernia: mechanical characterization and finite element modelling, page S96.
The soft tissues tension-compression asymmetry: challenges and solutions, page S99.

Acoustic streaming in bone pericellular fluid under ultrasound stimulation

C. Baron[a], E. Doveri[b], P. Jodlowski[a], P. Lasaygues[b] and C. Guivier-Curien[a]

[a]Aix Marseille Univ, CNRS, Centrale Méditerranée, IRPHE UMR 7342, Marseille, France; [b]Aix Marseille Univ, CNRS, Centrale Méditerranée, LMA UMR 7031, Marseille, France

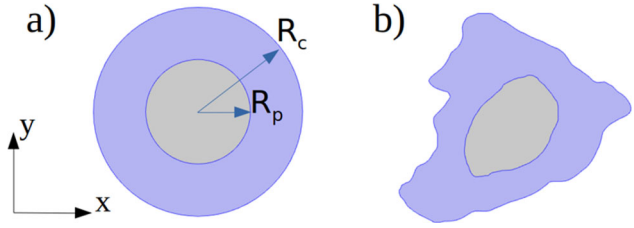


Figure 1. (a) Idealized I-model and (b) realistic R-model of PCF (in blue) and process (in gray). $R_c = 0.25\,\mu m$ is the canaliculus radius, $R_p = R_c/2$ is the process radius.

1. Introduction

The use of ultrasound (US) stimulation for bone healing is a therapeutic approach that dates back over half a century. Nevertheless, the therapeutic efficacy of US stimulation of bone remodelling remains an open question, as the underlying mechanisms involved are still poorly understood. Among the possible hypotheses, the propagation of ultrasonic waves in bone tissue could generate acoustic streaming (AS) resulting in fluid shear stress exerted on the wall of osteocytes known as the mechanosensitive conductors of bone remodeling. Osteocytes are dendritic cells surrounded by a viscous pericellular fluid (PCF), ubiquituous in the bone extra-cellular matrix (ECM) forming a complex micrometric 3D network called the lacuno-canalicular network (LCN). A first finite-element (FE) model is proposed to investigate the AS induced by a US stimulation inside the PCF considered as a viscous fluid. The resulting wall shear stress (WSS) applied on the osteocyte process is estimated for different shapes of PCF space and different viscosities of PCF.

The aim is to explore the relevance of two simplifying assumptions commonly used in the literature: a geometry of the space occupied by the PCF equivalent to an annular-section tube, and a PCF viscosity equal to the viscosity of water. Finally, its quantification is questioned in regard of stress levels that can trigger a biological response.

2. Methods

It has been clearly demonstrated that the most sensitive parts of the osteocyte are its processes. According to the ratio of the transverse dimensions of the canaliculus (~0.1 µm) to its length (~10 µm), a 2D FE model is implemented on Comsol Multiphysics (v. 6.0) representing a cross-section of an osteocyte process surrounded by a layer of viscous fluid representing the PCF bounded by a wall representing the ECM. The goal of this work is to estimate the influence of the shape of the canaliculi and process on the WSS (averaged WSSav and maximum value WSSmax along the contour of the process). An idealized (I-model) geometry of two concentric circles is compared to realistic (R-model) contour extracted from images published in (Kamioka et al. 2012) (Figure 1).

The acoustic properties of the cell process and of the PCF are similar to those of water, except that the viscosity of the PCF is supposed to vary between 0.65×10^{-3} Pa s (viscosity of water at 37 °C) and 0.05 Pa s (Lee et al. 1993). The ECM/PCF interface is considered as a wall.

To mimic the influence of US stimulation, we assume that the walls are oscillating in the x-direction. A first order oscillating velocity $\mathbf{U1}(f) = i2\pi f d0\mathbf{ex}$ parallel to the x-direction is imposed along the ECM/PCF interface to model a harmonic acoustic wave at frequency f of 1 MHz with an amplitude of displacement d0.

The Navier-Stokes equations are solved inside the PCF domain using the perturbation method in order to calculate the acoustic streaming velocity V2 (time average of the 2nd order term) and to deduce the resulting WSS applied at the PCF/process interface. In Comsol Multiphysics 6.0, the Thermoviscous Acoustics module (in frequency domain) is used in order to resolve the first order acoustic field. Then, the acoustic streaming is taken into account by using the Laminar Flow module and weak form formulations (Muller and Bruus 2014).

3. Results and discussion

The acoustic streaming velocity V2 is calculated inside the PCF space.

Considering the PCF as water at 37 °C ($\mu PCF = \mu water = 0.0065$ Pa s), and the amplitude of the oscillation $d0 = 0.4$ nm the I-model provides a $V2max = 0.09\,\mu m/s$ whereas the R-model gives $V2max = 0.11\,\mu m/s$ (Figure 2).

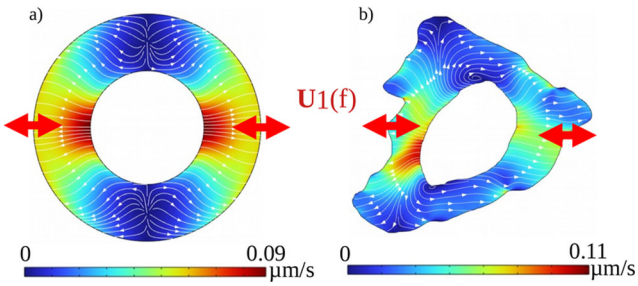


Figure 2. Acoustic streaming velocity V2 for (a) idealized and (b) realistic contours of PCF and process.

Table 1. Ratios of WSS between idealized (I-model) and realistic (R-model) contours for 3 values of PCF viscosity.

µPCF/µwater	1	3.85	7.7
WSSav(R-model)/WSSav(I-model)	2.5	3	3
WSSmax(R_model)/WSSmax(I-model)	16	19	19.5

The influence of the geometry is quite the same whatever the viscosity (Table 1). WSS_{max} is more dependent to the geometry of the contours as expected (Table 1). It is worth noting that the WSS_{av} values for the R-model is more than 2 times higher than WSS_{av} for the I-model and up to 20 times for WSS_{max} values (Table 1) showing that it is necessary to take into account a realistic geometry to relevantly investigate US stimulation effect on osteocytes.

Regarding the potential biological response of osteocytes under US stimulation, it is interesting to know that for viscosity higher than µref, a value of $d0 = 0.8$ nm is sufficient to induce WSSmax higher than 0.8 Pa which has been defined as the threshold to trigger osteocyte mechanotransduction (Weinbaum et al. 1994). The WSSav reaches this threshold for an oscillation amplitude $d0 = 2$ nm if µPCF = 0.025 Pa s and for $d0 = 1.8$ nm if µPCF = 0.05 Pa s. Note that WSSav along the process contour is proportional to $d0^2$ for the two geometries.

Although the model is 2D and has the limitations mentioned above, it tends to confirm that acoustic streaming can be induced by US stimulation in such a way that it can trigger biological response. Moreover, one of the strengths of this model is to easily investigate other contour shapes to test the WSS pattern associated with. One can notice that these realistic geometries can be further complicated including the tethering elements and ECM protrusions present inside the PCF space. In addition, the viscous fluid model of PCF and cell can be improved considering them as poroelastic medium and viscoelastic solid respectively. These considerations will affect the fluid velocity patterns obtained. Some further investigations are in progress to question the choice of mimicking US stimulation by an oscillating velocity. Moreover the low intensity ultrasound stimulation used in therapeutics is a pulsed stimulation, which needs to develop a model in time domain. This work can give new insights on stimulation of bone remodeling and could help to understand the underlying mechanisms in order to a better care for the patient.

Acknowledgements

The authors acknowledge the support of the French Agence Nationale de la Recherche (ANR), under grant ANR-22-CE51-0038-01 (project INVICT-US).

References

Kamioka H, Kameo Y, Imai Y, Bakker AD, Bacabac RG, Yamada N, Takaoka A, Yamashiro T, Adachi T, Klein-Nulend J. 2012. Microscale fluid flow analysis in a human osteocyte canaliculus using a realistic high-resolution image-based three-dimensional model. Integr Biol (Camb). 4(10):1198–1206. doi:10.1039/c2ib20092a.

Lee GM, Zhang F, Ishihara A, McNeil CL, Jacobson KA. 1993. Unconfined lateral diffusion and an estimate of pericellular matrix viscosity revealed by measuring the mobility of gold-tagged lipids. J Cell Biol. 120(1):25–35. doi:10.1083/jcb.120.1.25.

Muller PB, Bruus H. 2014. Numerical study of thermoviscous effects in ultrasound-induced acoustic streaming in microchannels. Phys Rev E Stat Nonlin Soft Matter Phys. 90(4):043016. doi:10.1103/PhysRevE.90.043016.

Weinbaum S, Cowin SC, Zeng Y. 1994. A model for the excitation of osteocytes by mechanical loading-induced bone fluid shear stresses. J Biomech. 27(3):339–360. doi:10.1016/0021-9290(94)90010-8.

KEYWORDS Acoustic streaming; osteocyte; mechanotransduction; FE model; fluid wall shear stress

cecile.baron@univ-amu.fr

Bending the disc: biomechanics of *Drosophila* wing development

Stefan Harmansa[a]*, Alexander Erlich[a,b,c]*, Christophe Eloy[b], Giuseppe Zurlo[d] and Thomas Lecuit[a,e]

[a]Aix-Marseille Université & CNRS, IBDM – UMR 7288 & Turing Center for Living Systems (CENTURI), Marseille, France; [b]Aix-Marseille Université, CNRS, Centrale Marseille, IRPHE, Turing Centre for Living Systems, Marseille, France; [c]Present address: Université Grenoble Alpes, CNRS, LIPHY, Grenoble, France; [d]School of Mathematical and Statistical Sciences, University of Galway, Galway, Ireland; [e]Collège de France, Paris, France

*These authors contributed equally: Stefan Harmansa, Alexander Erlich

1. Introduction

During animal development, mechanical forces play a crucial role in shaping tissues, including the processes of cell growth and proliferation. Differential growth, where tissues or regions of tissue grow at different rates, can lead to residual stress and geometric incompatibility, affecting the shaping of structures (Rodriguez et al. 1994, Goriely 2017). Differential growth can also be seen in multi-layered tissues, such as organs, where it can drive folding and morphogenesis (Tozluoğlu et al. 2019). The *Drosophila* wing imaginal disc is a multi-layered epithelial structure used to study the effects of growth and elastic deformation on tissue shaping. The extracellular matrix (ECM) has recently gained attention and has been shown to be important for controlling growth and shape in some morphogenetic and artificial tissues (Oltean et al. 2016; Dolega et al. 2021). The ECM can act as an actively growing dynamical constraint to the tissue layers, controlling organ morphogenesis. How the wing disc obtains its bent shape, how its mechanical stresses develop, and in particular the role of the ECM in this process is the subject of this presentation.

2. Results

The Drosophila wing imaginal disc is a multi-layered epithelial structure that is studied to explore how growth and elastic deformation of individual layers affect the typical domed shape of the wing disc. The disc is composed of two stacked epithelial mono-layers; the bottom pseudostratified disc proper epithelium (DP) and the overlying squamous peripodial epithelium (PPE). A layer of ECM covers both the basal as well as the apical surface of the disc. Through

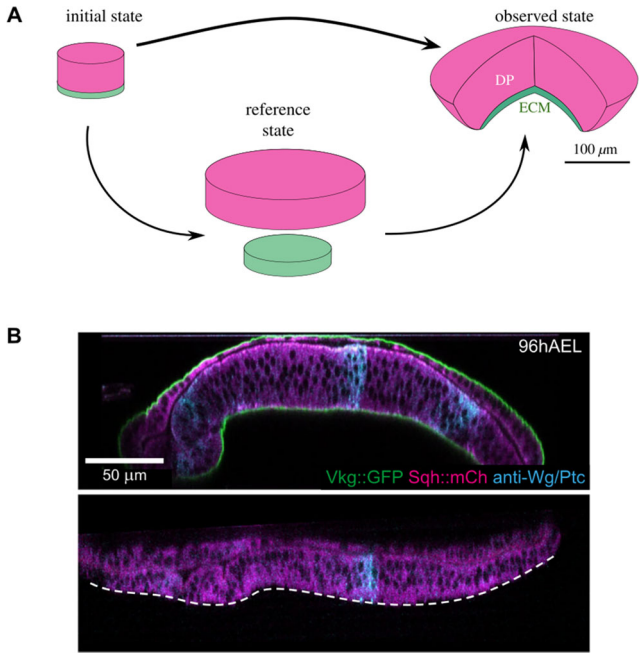


Figure 1. The wing disc as a growing bilayer. (A) Mechanical model, incorporating differential growth between the disc pouch (purple) and the ECM (green). (B) Destructive experiment in which the ECM, green, is chemically removed (collagenase), revealing the nearly flattened stress-free configuration of the disc pouch (purple).

destructive experiments such as the one shown in Figure 1B, we determine that the apical ECM, as well as the PPE layer, play no role in the mechanics and bending of the wing disc, reducing the four-layer structure to a bilayer between the DP tissue layer and ECM layer. A key destructive experiment, the acute removal of the ECM, reveals the stress-free configuration of the DP and leads to a flattening of the DP, demonstrating the essential role of the ECM in wing disc bending. The DP tissue layer grows in-plane, and outgrows the basal ECM layer, leading to a geometric incompatibility between the two layers, similarly to a bimetal thermostat. The basal ECM layer grows non-planarly. A quantification of the difference in growth anisotropy between the basal ECM and the DP contributes to additional curvature of the bilayer structure.

3. Discussion

The wing imaginal disc of *Drosophila* was studied to determine the impact of growth on the development of its shape. Tissue thickening and bending in a dome were seen to emerge due to differential growth between a bi-layer structure, which was associated with the build-up of elastic stress. The elastic energy created by differential growth was later released by destructive experiments that allowed the individual constituents of the bilayer in isolation. A model of

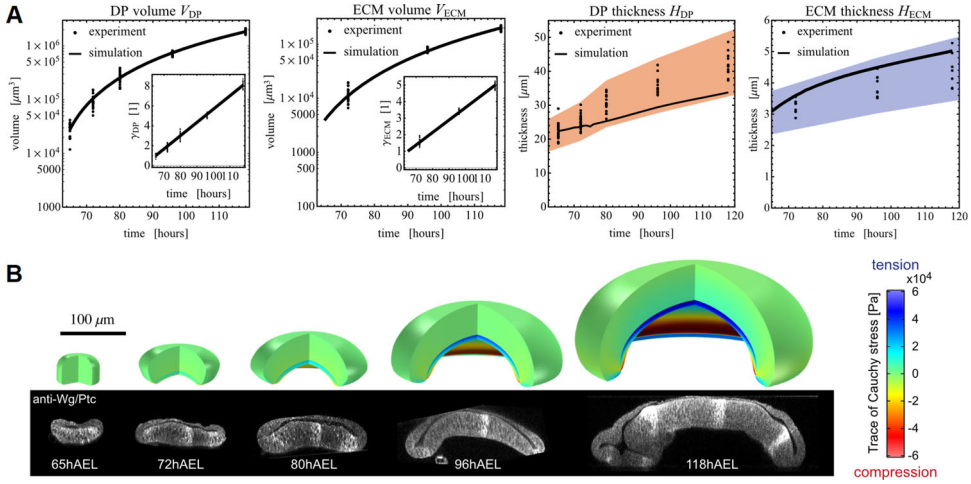


Figure 2. Experimental results captured by mechanical model of the wing disc. (A) The volumes of DP and ECM parametrise the model, which captures relevant geometric properties such as DP and ECM thicknesses. (B) The 3D morphology is captured by the model, showing a concentration of stresses at the interface between the layers.

the disc as a neo-Hookean growing solid captured 3rd instar wing disc development, but future models will need to incorporate the influence of actomyosin contractility. The observed difference in growth anisotropy between the disc pouch and the ECM, controlled by the matrix metalloproteinase MMP2 in the ECM, further fine-tunes the 3D shape of the disc, providing a possible universal mechanism for budding, invagination, and folding processes during animal development.

References

Dolega ME, Monnier A, Brunel, B, Joanny J-F, Recho P, Cappello G. 2021. Extracellular matrix in multicellular aggregates acts as a pressure sensor controlling cell proliferation and motility. eLife. 10:e63258. doi:10.7554/eLife.63258.

Goriely A. 2017. The mathematics and mechanics of biological growth. Interdisciplinary Applied Mathematics. Available from: 10.1007/978-0-387-87710-5.

Harmansa S, Erlich A, Eloy C, Zurlo G, Lecuit T. 2023. Growth anisotropy of the extracellular matrix shapes a developing organ. Nat Commun. 14(1):1220. doi:10.1038/s41467-023-36739-y.

Oltean A, Huang J, Beebe DC, Taber LA. 2016. Tissue growth constrained by extracellular matrix drives invagination during optic cup morphogenesis. Biomech Model Mechanobiol. 15(6):1405–1421. Available from: doi:10.1007/s10237-016-0771-8.

Rodriguez EK, Hoger A, McCulloch AD. 1994. Stress-dependent finite growth in soft elastic tissues. J Biomech. 27(4):455–467. doi:10.1016/0021-9290(94)90021-3.

Tozluoğlu M, Duda M, Kirkland NJ, Barrientos R, Burden JJ, Muñoz JJ, Mao Y. 2019. Planar Differential Growth Rates Initiate Precise Fold Positions in Complex Epithelia. Dev Cell. 51(3):299–312.e4. doi:10.1016/j.devcel.2019.09.009.

KEYWORDS Morphogenesis; finite elasticity; growth anisotropy

alexander.erlich@univ-grenoble-alpes.fr

Changes in endothelial cell microrheology in medium modified by cancer cells

G. M. Kefala[a,b], D. Tsvirkun[a], C. Verdier[a] and V. M. Laurent[a]

[a]CNRS, Laboratoire Interdisciplinaire Physique (LIPhy), Université Grenoble Alpes, Grenoble, France; [b]Leiden Institute of Physics (LION), Leiden Universiteit, Leiden, The Netherlands

1. Introduction

During the process of metastasis, cancer cells are detached from the primary tumour and may find their way into the blood system, from where they can migrate in a distant site. Endothelial cells line the vascular wall of all blood and lymphatic vessels and regulate its permeability for substances and migratory cells. Previous studies have focused on the properties of cancer cells (Abidine et al. 2018), as well as their interaction with endothelial cells (Sundar Rajan et al. 2017), as they attach to and transmigrate through the endothelium barrier. For many authors, the most widely accepted hypothesis was that transmigration is a characteristic of cancer cells, overlooking the possibility of endothelial cells actively participating in this process (Mierke 2012). In this paper, endothelial monolayers were studied with a previously developed AFM microrheology technique (Abidine et al. 2018) when cultured in cancer cell conditioned medium, at different dilutions. This medium is enriched with molecules secreted by the cancer cells, which may play a role during the cancer cells' migration and alter the endothelial cells' behaviour (Ritchie et al. 2021). We show the first results of the viscoelastic properties of endothelial cells under these experimental conditions.

2. Methods

2.1. Cell culture and preparation

Human Umbilical Vein Endothelial Cells (HUVECs) were cultured in supplemented Endothelial Cell Growth Medium (ECGM, PromoCell) at 37^oC, 5% CO_2, 95% humidity. Cells with passage numbers 4–6 were used. T24 cells (Human bladder carcinoma cells) were grown in RPMI 1640 medium (Gibco) supplemented with 10% Fetal Bovine Serum (Gibco) and 1% penicillin-streptomycin. For the AFM measurements, HUVECs were seeded in monolayer in Petri dishes with glass coverslips at the bottom, at least 72 h before the experiment. Less than 24 h before the measurements, the medium was exchanged with a mixture of ECGM and T24-conditioned ECGM (ECGM-T24) in ratio 2:3 (low dilution) and 1:10 (high dilution) correspondingly. ECGM-T24 was prepared by culturing T24 cells in ECGM for 2 days.

2.2. Microrheology

We used a novel AFM technique which allows for a microrheological study of cells, by applying an initial indentation δ_0 and superposing a small oscillatory displacement δ. The elastic modulus E can be calculated from the microrheology data during the initial approach, by using the Hertz formula $F_0 = \frac{3}{4}\frac{E\delta_0^2 tan\theta}{1-\nu^2} g[\chi(\delta_0, h)]$ (1), where $F_0 = kd$ is the initial force, k is the cantilever stiffness and d its vertical displacement. ν is the cell's Poisson's ratio (∼0.5), $\theta = 19^o$ the half angle of the pyramid cantilever tip, and $g[\chi(\delta_0, h)]$ a correction factor for the hard substrate effect, dependent on the parameter $\chi = \frac{\delta_0}{h} tan\theta$, with h the height of the cell (Abidine et al. 2018). The elastic modulus G' and viscous modulus G'' can be calculated as a function of frequency using the linearized form of (1) (Alcaraz et al. 2003). Cantilevers with a pyramidal tip and with stiffness approximately 0.016 N/m were chosen. An approach set point of 0.5 nN and a displacement of $\delta/\delta_0 = 0.1$ were used for the measurements. A range of oscillatory frequencies between 1 Hz and 160 Hz was used. The indentation was always performed on the top of the nucleus. The statistical significance was tested with unpaired *t*-test and Wilcoxon's test. The results are displayed as Mean ± SEM (Standard Error of the Mean).

3. Results and discussion

AFM measurements were performed on single cells in endothelial monolayers. The indentations on the cells were in the range of 0.4–1.2 μm. Measurements were taken on endothelial cells cultured in conventional ECGM, serving as the controls ($n = 8$, $n = 20$), on endothelial cells cultured in T24-conditioned ECGM in low ($n = 26$) and high dilution ($n = 20$). Height measurements on HUVECs cultured in T24 medium (low: 2.6±0.2 μm, high: 2.4±0.2 μm) did not show significant differences from the controls (low: 2.7±0.3 μm, high: 2.5±0.3 μm). In Figure 1, the Young's modulus E as calculated using Equation (1), is displayed. For both dilutions, the endothelial cells cultured in ECGM-T24 showed lower E values (low: 4.4±0.9 kPa, high: 1.5±0.3 kPa) compared to their controls (low: 6.9±2.3 kPa, high: 2.4±0.4 kPa). This indicates that T24 secreted molecules in the medium

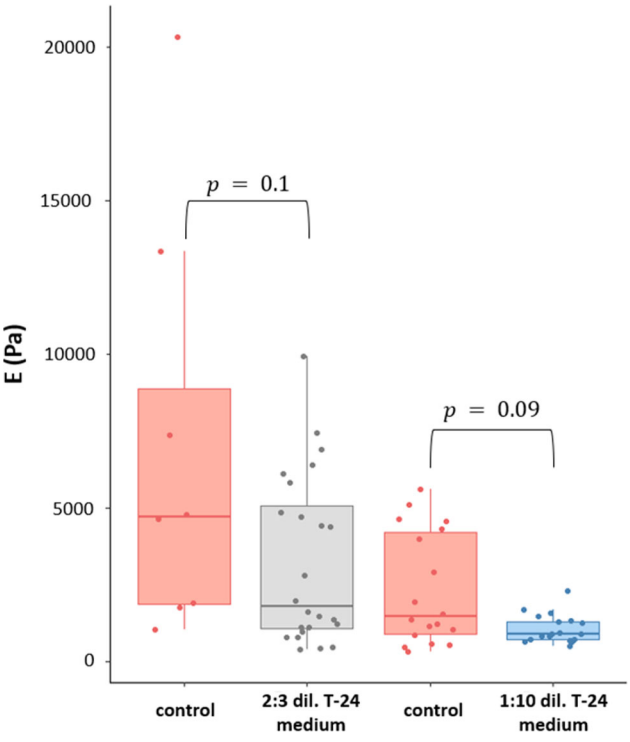


Figure 1. Young's modulus E of controls (red, $n = 8$ and $n = 20$), HUVECs in 2:3 (Grey, $n = 26$) and 1:10 (blue, $n = 20$) diluted ECGM-T24.

influenced the HUVECs, by decreasing their stiffness. The p values were bigger than 0.05, denoting the need of a larger amount of data to reach significance.

Figure 2 shows the shear moduli G' and G'', as a function of frequency. The moduli of the 2:3 and 1:10 dilution experiments are displayed in black and blue, respectively. In orange and red, the curves of the corresponding controls are shown. The fitting was performed following the model of Alcaraz et al. (2003), where $G' = af^b$ and $G'' = cf^b + df$. The slope b was found to be the same for controls and HUVECs in 2:3 dilution ECGM-T24 ($b = 0.1$) and similar for the 1:10 dilution case ($b_{control}$=0.1, $b = 0.16$). For both experiments, the control G' values were higher than those of HUVECs in T24-ECGM. The ratios $r_{G'} = G'_{control}/G'$ showed that the high dilution case was closer to the control curve ($r_{G'}$=1.1, f=20Hz) than the low one ($r_{G'}$= 1.5, f=20Hz). HUVECs became softer with decreasing the dilution of ECGM-T24. Previous studies on endothelial cells co-cultured with cancer cells also showed a decrease in their stiffness (Mierke 2011). Based on our findings, culturing HUVECs in cancer cell medium was sufficient to observe differences in their microrheology. Nevertheless, more experiments are needed, including fluorescence imaging to analyze the cytoskeleton.

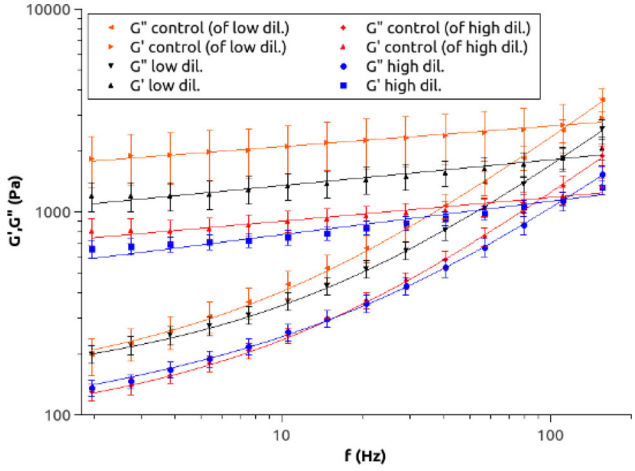


Figure 2. Moduli G'(f) and G''(f) as a function of frequency for HUVECs cultured in (a) high and (b) low dilution. The data displayed are averaged over $n = 26$ for low and $n = 20$ cells for high dilution, as well as $n = 8$ and $n = 20$ for their controls respectively. The error bars correspond to SEM.

4. Conclusions

Elastic and microrheological measurements showed that endothelial cells were softer when cultured in cancer cell conditioned medium. Our results of the elastic moduli E and G' showed that the more concentrated (secreted substances) the medium was, the softer HUVECs became. In the future, these findings will be compared with the co-culture of HUVECs and T24 cells, to better assess the impact of cancer cell-secreted molecules and the physical attachment of cancer cells on the alteration of endothelial cell properties.

Acknowledgements

V.M.L. and C.V. are members of the LabeX Tec 21, France (Investissements d'Avenir: grant agreement No. ANR-11-LABX-0030).

References

Abidine Y, Constantinescu A, Laurent VM, Sundar Rajan V, Michel R, Laplaud V, Duperray A, Verdier C. 2018. Mechanosensitivity of cancer cells in contact with soft substrates using AFM. Biophys J. 114(5):1165–1175. doi: 10.1016/j.bpj.2018.01.005.

Alcaraz J, Buscemi A, Grabulosa M, Trepat X, Fabry B, Farre R, Navajas D. 2003. Microrheology of human lung epithelial cells measured by atomic force microscopy. Biophys J. 84(3):2071–2079. doi:10.1016/S0006-3495(03)75014-0.

Mierke CT. 2011. Cancer cells regulate biomechanical properties of human microvascular endothelial cells. J Biol

Chem. 286(46):40025–40037. doi:10.1074/jbc.M111.256172.

Mierke CT. 2012. Endothelial cell's biomechanical properties are regulated by invasive cancer cells. Mol Biosyst. 8(6):1639–1649. doi:10.1039/c2mb25024a.

Ritchie S, Reed DA, Pereira BA, Timpson P. 2021. The cancer cell secretome drives cooperative manipulation of the tumour microenvironment to accelerate tumourigenesis. Fac Rev. 10:4. doi:10.12703/r/10-4.

Sundar Rajan V, Laurent VM, Verdier C, Duperray A. 2017. Unraveling the receptor-ligand interactions between bladder cancer cells and the endothelium using AFM. Biophys J. 112(6):1246–1257. doi:10.1016/j.bpj.2017.01.033.

KEYWORDS Endothelial cells; viscoelasticity; AFM; cancer cell transmigration; microrheology

georgiamk864@gmail.com

Corneal mechanics for the early detection of the keratoconus using patient-specific geometry and microstructural data

C. Giraudet[a,b], J. Diaz[b,a], P. Le Tallec[a,b] and J.-M. Allain[a,b]

[a]Laboratoire de Mécanique des Solides, CNRS, Ecole Polytechnique, Institut Polytechnique de Paris, Palaiseau, France; [b]Inria, Palaiseau, France

1. Introduction

Cornea is the front part of the eye providing two thirds of its optical power through its lens shape. In keratoconus disease, the cornea shape is progressively altered to become conical, leading to optical aberration (Sedaghat et al. 2018). A late detection imposes a surgery, explaining the need of early diagnosis.

Keratoconus origin is not clearly determined (Najmi 2019). While it is associated with a cornea thinning and a decrease of the mechanical properties, it is not clear which of these two effects is the driving one.

We propose a modeling approach in which we change independently the cornea geometry and mechanical properties from healthy to keratoconic ones.

2. Methods

We simulate the response of the cornea for variations of the intra-occular pressure using a home-made finite element code (MoReFEM). To do so, we first reproduce the cornea geometry. This is done by starting from a generic mesh mimicking an average cornea (Pandolfi and Manganiello 2006). This mesh is then adjusted to reproduce clinical observations (see Figure 1).

The cornea behavior is assumed to be hyperelastic, and contains an isotropic contribution (matrix), and an anisotropic part (collagen lamellae). Orientations and fractions of each component come from experimental observations (Aghamohammadzadeh et al. 2004; Winkler et al. 2013). The collagen lamellae are described by a microsphere model, in which each lamella has its own orientation and is mechanically characterized described by its 1D elastic response. The total contribution is then:

$$\psi_{aniso} = \int\int \rho_{lam}\psi_{lam}d\theta d\varphi$$

with the individual lamellae response

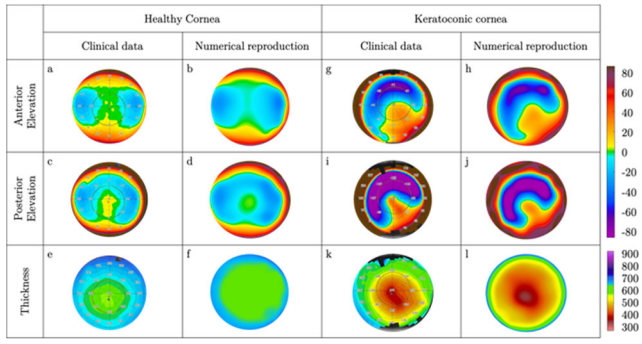


Figure 1. Elevation and thickness maps of healthy and keratoconic cornea (clinical and numerical reproduction, anterior and posterior). color bar in µm. Figure from Giraudet et al. (2022).

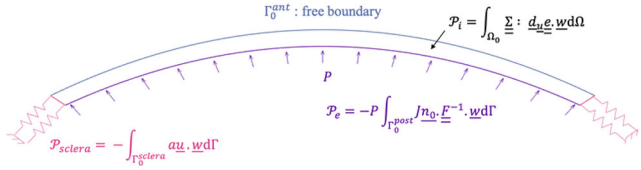


Figure 2. 2D Schematic view of the 3D mechanical problem of an inflation test. A pressure *P* is applied on the posterior surface, while the anterior surface cornea is stress-free, and the lateral fixation is treated as an elastic boundary condition of high stiffness *a*. Figure from (Giraudet et al. 2022).

Table 1. Mechanical parameters of the healthy case. Note that the energies also contain the density of lamellae and of matrix.

Symbol	Contribution	Value
k	Single lamellae stiffness	65 Pa
λ_u	'Unfolding' elongation	1.02
κ_1	Matrix stiffness	60 Pa
κ_2	Matrix stiffness	15 Pa
K	Matrix compressibility	80 kPa

$$\psi_{lam} = \frac{1}{2}k\left(\frac{\lambda}{\lambda_u} - 1\right)_+^2$$

with $(x)_+ = 0$ for $x \leq 0$, and $(x)_+ = x$ for $x \geq 0$.

The non-collagenous components are described by a quasi-incompressible isotropic Mooney–Rivlin model:

$$\psi_{iso} = \rho_{iso}\kappa_1\left[(\bar{I}_1 - 3) + \kappa_2(\bar{I}_2 - 3)\right]$$

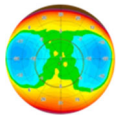
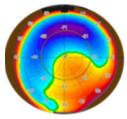
and

$$\psi_{vol} = K\left(J^2 - 1 - 2\log J\right)$$

Mechanical parameters are then determined by fitting experimental inflation data from the literature (Elsheikh et al. 2008) (see Figure 2 for a scheme of the mechanical problem). This gives a reference set of parameters for healthy cornea, given on Table 1.

The keratoconus origin is studied by using first the geometry of keratoconic cornea with reference

Table 2. Evolution of the SimK (in diopter) in function of the geometry (left: healthy, right: keratoconic) and the mechanical parameters used (top: healthy, bottom: weakened lamaellae).

Geometry		
'Healthy' parameters	∼0D	∼0D
'Keratoconic' parameters	+2D	+2D

mechanical parameters, and second the geometry of healthy cornea with altered mechanical parameters. We compared the evolution with pressure of the SimK (a measure of cornea curvature) with the literature (McMonnies and Boneham 2010).

3. Results and discussion

Our simulations of healthy cornea show that the mechanical response comes mainly from the collagen, and in particular its prestretch.

Experimental observations have shown that the SimK doesn't change with an increase of the intraocular pressure for healthy cornea, while it increases by 2 diopters (+2D) for keratoconic cornea. This variation in SimK cannot be reproduced without changing the mechanical parameters, whatever the initial geometry. At the same time, changing the mechanical parameters is sufficient to recover the keratoconic response, even for a healthy geometry. Table 2 shows the variation of the SimK as a function of the mechanical parameters and of the geometry. The parameters for the kerotoconus are the same as the ones of Table 1, except the lamellae stiffness k, which become 40 Pa.

We also computed the shape of a cornea, starting from a relaxed healthy cornea (without pressure) and the parameters of a keratoconic cornea: we observe a cornea similar to a keratoconus at a very early stage.

4. Conclusions

Our work shows that the keratoconic response is primary controlled by a weakening of the mechanical parameters (Giraudet et al. 2022). More precisely, it is the collagen stiffness which seems the most critical parameter. This is consistent with the classical idea that collagen-rich tissues mechanical response is controlled by the collagen fibers. Our result show then the interest of cross-linking treatments, which stiffen the collagen lamellae.

Acknowledgements

We thank A. Pandolfi for the 3D mesh code, K. M. Meek and S. Hayes for the X-ray experimental data, and J. Knoeri and V. Borderie for clinical maps.

References

Aghamohammadzadeh H, Newton RH, Meek KM. 2004. X-Ray Scattering Used to Map the Preferred Collagen Orientation in the Human Cornea and Limbus. Structure. 12(2):249–256. doi:10.1016/j.str.2004.01.002.

Elsheikh A, Alhasso D, Rama P. 2008. Assessment of the epithelium's contribution to corneal biomechanics. Exp Eye Res. 86(2):445–451. doi:10.1016/j.exer.2007.12.002.

Giraudet C, Diaz J, Le Tallec P, Allain J-M. 2022. Multiscale mechanical model based on patient-specific geometry: application to early keratoconus development. J Mech Behav Biomed Mater. 129:105121. doi:10.1016/j.jmbbm.2022.105121.

McMonnies CW, Boneham GC. 2010. Corneal responses to intraocular pressure elevations in keratoconus. Cornea. 29(7):764–770. doi:10.1097/ICO.0b013e3181ca2b75.

Najmi H. 2019. The correlation between keratoconus and eye rubbing: a review. Int J Ophthalmol. 12(11):1775–1781. doi:10.18240/ijo.2019.11.17.

Pandolfi A, Manganiello F. 2006. A model for the human cornea: constitutive formulation and numerical analysis. Biomech Model Mechanobiol. 5(4):237–246. doi:10.1007/s10237-005-0014-x.

Sedaghat M-R, Askarizadeh F, Narooie-Noori F, Rakhshandadi T, Ostadi-Moghadam H, Rajabi S. 2018. Comparative evaluation of tomographic and biometric characteristics in bilateral keratoconus patients with unilateral corneal Vogt's striae: a contralateral eye study. Clin Ophthalmol. 12:1383–1390. doi:10.2147/OPTH.S169266.

Winkler M, Shoa G, Xie Y, Petsche SJ, Pinsky PM, Juhasz T, Brown DJ, Jester JV. 2013. Three-dimensional distribution of transverse collagen fibers in the anterior human corneal stroma. Invest Ophthalmol Vis Sci. 54(12):7293. doi:10.1167/iovs.13-13150.

KEYWORDS Cornea; keratoconus; microstructure; FEM model; patient-specific

jean-marc.allain@polytechnique.edu

Estimation of soft-tissue stiffness using ultrasound indentation for pressure ulcer prevention

A. Segain[a], PY. Rohan[a], M. Matray[a], G. Sciumé[b], B. Keenan[c] and H. Pillet[a]

[a]IBHGC, ENSAM, Paris, France; [b]ENSAM, Univ. of Bordeaux, CNRS, Bordeaux INP, INRAE, I2M, Pessac, France; [c]Cardiff School of Engineering, UK Cardiff, Wales

1. Introduction

Biomechanical modelling has been identified as a potential tool to estimate Pressure Ulcer (PU) risk. Several Finite Element models have been proposed to provide healthcare giver a patient specific estimate of pressure ulcer's risk development. However, currently several barriers exist to the clinical translation of these tools. Amongst these the application of subject-specific tissue material parameters is an important issue, recognizing that there will be inter-subject variations in many factors, including local tissue tolerance and fat content. Different methods have been proposed in the literature to estimate soft tissue properties *in vivo* (Makhsous et al. 2008). Most of these methods model the experiment as an indentation test of a single layer of soft tissue. However, as soft tissue of the thigh and the ischial region is composed of two different materials (muscle and fat), it seems relevant to estimate the stiffness of each tissue separately.

In a previous study (Fougeron et al. 2020), we proposed an ultrasound-based methodology for investigating inter-individual variability of soft-tissue stiffness *in vivo* assuming a single layer. The methodology was applied to seven healthy volunteers. This system presented relatively high values of dispersion between the curves due to the 'handheld' aspect of the indentation system. To overcome these limitations, the aim of this study is to experimentally characterise *in vivo* and *in situ* the local stiffness of soft tissues using an improved version of an US-based indentation device described in (Fougeron et al. 2020) 1/ assuming a bilayer homogeneous isotropic material for the soft tissues 2/ . by fixing the ultrasound probe on a linear guide.

2. Methods

2.1. Indenting system

The indentation system is adapted from the one previously proposed in (Fougeron et al. 2020). Briefly, the system combines a 200 N force sensor (3134—Micro-Load Cell (0–20 kg)—CZL635, GoTronic, Paris, France), and a linear ultrasound probe (SuperLinear^{TM} SL 15-4, Aixplorer; SuperSonic Imagine, Aix-en-Provence, France). In this study, the ultrasound probe was mounted on a linear guide.

2.2. Protocol

Thirteen healthy young volunteers (8 men, 5 women, *mean age* $= 27 \pm 2$, $BMI = 22.4 \pm 2.2$ kg/m^2), participated in the study. The system was used to realize at least 10 compression/relaxation cycles of thigh soft tissue. Each volunteer was instructed to lie supine on a massage desk on one side and to put his/her shanks on a school desk, so the thigh laid unsupported. The system was placed on a stool positioned in the middle of the right thigh. A picture of the experimental setup can be found in Figure 1.

First, the ultrasound probe was positioned above the soft tissues in a thick layer of gel (no contact with the skin). This setting allowed to acquire a first ultrasound image in an unloaded undeformed reference configuration. Tare calibration was also performed in this (the weight of the custom setup in this conference was set as a reference zero force). The probe was then placed in contact with the skin. This setting was the starting point of the indentation cycles, with a known deformation state and a known load. Force data was recorded using the force sensor and an



Figure 1. Experimental setup. The ultrasound-based indentation system was placed on a stool positioned in the middle of the right thigh.

ultrasound video was recorded during the whole acquisition.

2.3. Data post-processing

Data were processed using a custom MATLAB routine developed at the IBHGC. The thickness of the muscle and fat layers was estimated on each frame of the ultrasound clip. The compression state of the tissue was estimated for each frame as the difference between the initial and current thickness. After synchronizing the force and displacement data using peak detection, the force-displacement curves were estimated for each compression/relaxation cycle. For each exam, a mean force/displacement curve was computed for the muscle, fat and total soft tissue layer from all the loading curves of each cycle. The relaxation curves were not studied.

As it is the case for most biological tissue, the force/displacement relationship was non-linear and was approximated using a bilinear model as proposed in (Makhsous et al. 2008). The curves were described by 3 parameters: small deformation stiffness K_{small}, large deformation stiffness K_{large} and a transition point Xs. As described in (Frossard et al. 2019), the transition point was defined as the point furthest to the straight line passing through the first and the last points of the force/displacement curve. The peak force and displacement were also extracted from the curves.

3. Results and discussion

The results for the small deformation stiffness K_{small}, the large deformation stiffness K_{large} and the transition point Xs are shown in Figure 2 below. The results of reported in the literature in (Makhsous et al. 2008) and (Fougeron et al. 2020) have also been added for comparison. Since the authors did not have access to the raw data published in (Makhsous et al. 2008), these were displayed as horizontal lines, showing mean value, and the $\pm 1\sigma$ and $\pm 2\sigma$ corridors. The peak force applied in our protocol were higher than those applied in (Makhsous et al. 2008). To facilitate the comparison with the literature, the results obtained in this study have been restrained to 5 N.

The small deformation stiffness K_{small} and the transition point X_s were respectively 0.33 ± 0.02 N and 3.30 ± 0.25 mm. These results are in accordance with those reported by (Makhsous et al. 2008) for the middle thigh. The small deformation stiffness K_{small} values obtained in this study are also of the same order of magnitude as those reported in (Fougeron et al. 2020). The large deformation stiffness K_{large} and the transition point Xs obtained however are respectively

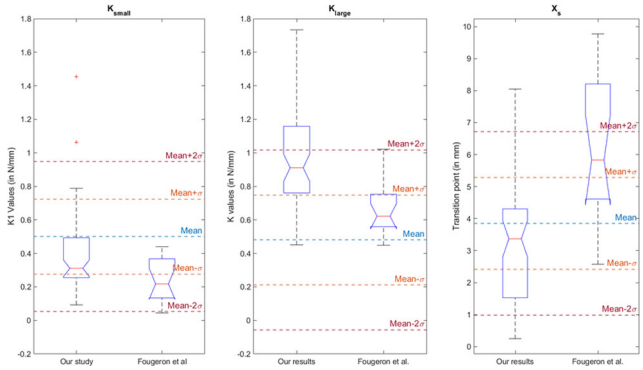


Figure 2. Comparison of the curves' parameters Ksmall, Klarge and Xs (left boxplots) with those published in (Fougeron et al. 2020) (right boxplots) and in (Makhsous et al. 2008) shown as straight horizontal lines representing the normality corridors.

higher and lower than those reported in (Fougeron et al. 2020). These differences could be explained by the variations in soft tissue distributions (the fat to muscle thickness ratio was higher in our population 0.33 versus 0.23 on average).

Another important limitation of this work is that it only estimates the force-displacement relationship, which is not sufficient to extract directly material properties. A common methodology allows to estimate apparent Young's modulus using an analytic solution of the Hertz contact model. However, some limitations of this method make the use of this methodology questionable to estimate the material properties of the human thigh soft tissue *in vivo*. An alternative is to use an experimental/numerical procedure like the Inverse Finite Element approach applied in our previous work (Fougeron et al. 2020).

4. Conclusions

The methodology proposed in this contribution allows to estimate material properties of each soft tissue layer *in vivo*. This is an important challenge since inter-subject variations have a big impact on Finite Element results. Perspective work will focus on adapting the proposed protocol to characterise soft-tissue stiffness in at risk populations and to estimate hyperelastic constitutive parameters from the force-displacement curves at large strains.

References

Fougeron N, Rohan P-Y, Haering D, Rose J-L, Bonnet X, Pillet H. 2020. Combining freehand ultrasound-based indentation and inverse finite element modeling for the identification of hyperelastic material properties of thigh soft tissues. Trans ASME J Biomech Eng. 142(9):091004. doi:10.1115/1.4046444.

Frossard L, Leech B, Pitkin M. 2019. Automated characterization of anthropomorphicity of prosthetic feet fitted to bone-anchored transtibial prosthesis. IEEE Trans Biomed Eng. 66(12):3402–3410. doi:10.1109/TBME.2019.2904713.

Makhsous M, Venkatasubramanian G, Chawla A, Pathak Y, Priebe M, Rymer WZ, Lin F. 2008. Investigation of soft-tissue stiffness alteration in denervated human tissue using an ultrasound indentation system. J Spinal Cord Med. 31(1):88–96. doi:10.1080/10790268.2008.11753987.

KEYWORDS Soft tissue biomechanics; in vivo; material characterization; pressure ulcer

alexandre.segain@ensam.eu

Experimental study of the different layers of the human oesophagus

G. Chagnon[a], C. Durcan[a,b], M. Hossain[b], D. Perić[b] and E. Girard[c,d]

[a]CNRS, UMR 5525, VetAgro Sup, Grenoble INP, TIMC, Univ. Grenoble Alpes, Grenoble, France; [b]Zienkiewicz Centre for Computational Engineering, Faculty of Science and Engineering, Swansea University, Swansea, UK; [c]CNRS, UMR 5525, VetAgro Sup, Grenoble INP, CHU Grenoble Alpes, TIMC, Univ. Grenoble Alpes, Grenoble, France; [d]Laboratoire d'Anatomie des Alpes Françaises, Grenoble, France

1. Introduction

The human oesophagus is a primarily mechanical organ, and its function depends on both the passive and active properties of its tissue wall. It is composed of a superposition of layers, with a muscular layer and a mucosa-submucosa layer with different functional properties. Knowledge of these properties can be used to investigate the effect of pathophysiology on the oesophagus' function; to determine the tissue's material parameters for the development of medical devices and for the understanding of illnesses. These properties can be used in finite element modelling and necessitate the most accuracy to represent the physiological conditions.

The human oesophagus has been little studied in the literature, particularly with regard to the characterisation of each of its layers (Egorov et al. 2003; Vanags et al. 2003). The authors have recently proposed a study on the mechanical behaviour of the different layers of the human oesophagus (the muscular one and the mucosa-submucosa one), the samples having been taken from formaldehyde bodies (Durcan, Hossain, Chagnon, Peric, Bsiesy, et al. 2022; Durcan, Hossain, Chagnon, Peric, Karam, et al. 2022).

It is known that the preservation conditions of tissues influence their mechanical properties. In the study proposed here, the experimental study focused on fresh bodies, i.e. they were not formalized or frozen before tissue harvesting to give the most representative mechanical properties possible.

2. Methods

Three oesophagus were used for this study, they were extracted by means of dissection from fresh cadavers at the Laboratoire d'Anatomie Des Alpes Françaises, Grenoble, France. The three oesophagus specimens were from two women and one man, and the three individuals were 89, 96 and 97 years old respectively.

After death and before dissection, the cadavers were stored in a 4 °C refrigerated room. The precise procedure for dissection is as outlined in our previous studies (Durcan, Hossain, Chagnon, Peric, Bsiesy, et al. 2022; Durcan, Hossain, Chagnon, Peric, Karam, et al. 2022). Once removed from the cadavers, the oesophagus were taken immediately for sample preparation for the mechanical tests. The protocol for this study was approved by a local scientific committee at Université Grenoble Alpes, and the study was performed in compliance with French regulations on postmortem testing. Due to constraints regarding the time and number of tests carried out, all tests were conducted within 5 days of explantation, during which, other than when testing, the tissue was stored in physiological saline solution (0.9% NaCl) at 4 °C. The tests were performed on both layers of the oesophagus, the muscular layer and the mucosa layer. The two layers, i.e. the mucosa-submucosa and the muscularis, were separated for testing. An illustration of the division is shown in Figure 1.

The oesophagus shows structural anisotropy due to the orientation of the fibres in the two tissue layers. To measure this anisotropy, mechanical tests are performed in the axial and circumferential directions of the oesophagus. Uniaxial tensile specimens were cut from the different oesophagus available. Different types of mechanical tests (cyclic, interrupted by relaxation, at different speeds) were performed to evaluate the overall mechanical properties of the tissues. The tests were carried out on an MTS machine with a 25 N transducer. As the tests were not too long, they were carried out at room temperature.

3. Results and discussion

As an example, a cyclic tensile test with increasing cycles is shown in Figure 2 for both directions of mechanical loading for the muscle layer and the mucosa layer. The non-linear behaviour of the tissues is clearly visible with the phenomenon of stiffening of the tissues with deformation, as well as the stress-softening phenomenon after a first loading and the viscoelastic behaviour with the presentation of large hysteresis loops.

The results of these tests can be compared with similar tests we have performed in a previous study on formulated tissue (Durcan, Hossain, Chagnon, Peric, Bsiesy, et al. 2022; Durcan, Hossain, Chagnon, Peric, Karam, et al. 2022). The shapes of the behaviour curves are similar with the same phenomena visible. However, the levels of the phenomena are different depending on how the fabrics are stored. It

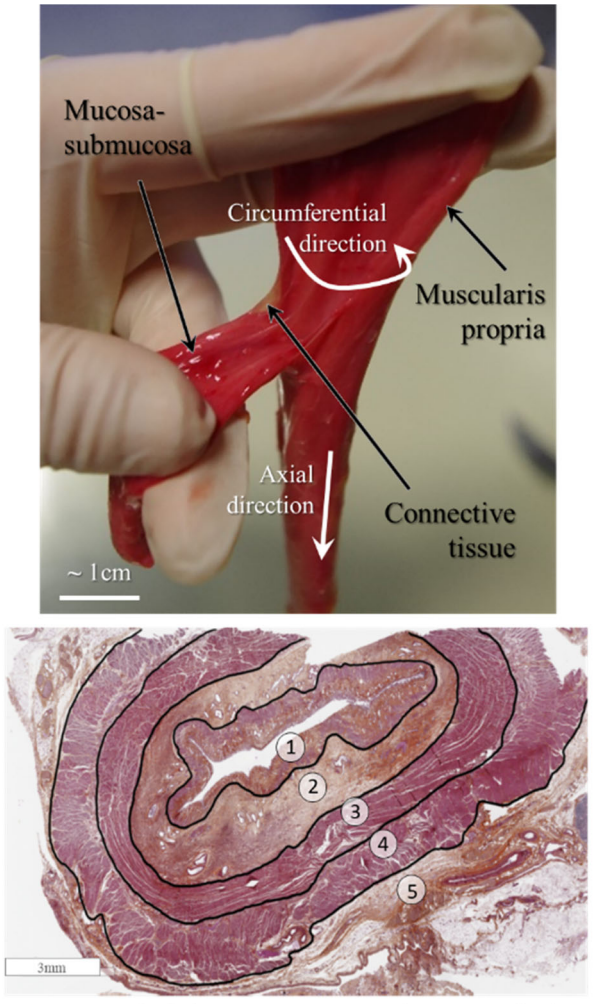


Figure 1. Cutting of an oesophagus with separation of the two layers.

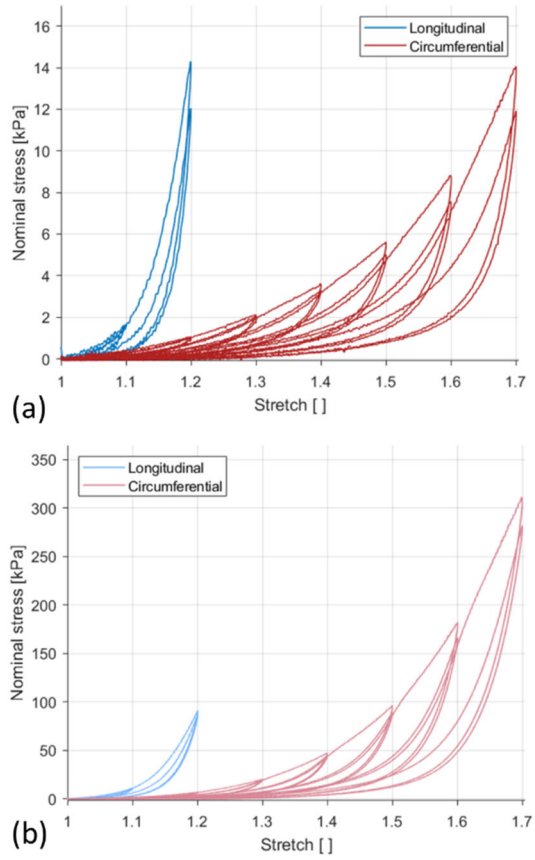


Figure 2. Mechanical behaviour of the oesophagus tissues: (a) muscular layer, (b) mucosa-submucosa layer.

was found that for almost all of the characteristics considered, the magnitude was statistically higher for the embalmed tissue compared to the fresh tissue The rupture stretches, however, was statistically higher for the fresh tissue compared to the embalmed tissue. An analysis of the beginning of the tensile curves allows us to identify the initial modulus of the tissues. It was identified that the modulus of the muscle layer was multiplied by 3 or 6 depending on the direction due to embalming. The phenomenon is more marked for the mucosa-submucosa layer where the ratio between the moduli is in the order of 10–12. Even if the phenomena are similar from a trend point of view, it is clear that the numerical differences obtained between fresh and formalised subjects present very important differences that cannot be explained by differences between anatomical subjects alone (the bodies all came from elderly subjects in the two studies), but rather by a very important effect of embalming on the tissue. These results will make it necessary to adapt the constitutive equations as the phenomena present different relative importance.

4. Conclusions

This study presents results on the mechanical properties of both layers of the human oesophagus. The mechanical tests were performed on fresh tissue. The results obtained show qualitatively similar results to the results of tests performed on embalmed biological tissues but numerically very different with a very marked effect of embalming on the mechanics of the tissues.

Acknowledgements

This work was supported by the Swansea University Strategic Partnerships Research Scholarships (SUSPRS).

References

Durcan C, Hossain M, Chagnon G, Peric D, Bsiesy L, Karam G, Girard E. 2022. Experimental investigations of

the human oesophagus: anisotropic properties of the embalmed muscular layer under large deformation. Biomech Model Mechanobiol. 21(4):1169–1186. doi:10.1007/s10237-022-01583-4.

Durcan C, Hossain M, Chagnon G, Peric D, Karam G, Bsiesy L, Girard E. 2022. Experimental investigations of the human oesophagus: anisotropic properties of the embalmed mucosa–submucosa layer under large deformation. Biomech Model Mechanobiol. 21(6):1685–1702. doi:10.1007/s10237-022-01613-1.

Egorov VI, Schastlivtsev IV, Prut EV, Baranov AO, Turusov RA. 2002. Mechanical properties of the human gastrointestinal tract. J Biomech. 35(10):1417–1425. doi:10.1016/s0021-9290(02)00084-2.

Vanags I, Petersons A, Ose V, Ozolanta I, Kasyanov V, Laizans J, Vjaters E, Gardovskis J, Vanags A. 2003. Biomechanical properties of oesophagus wall under loading. J Biomech. 36(9):1387–1390. doi:10.1016/s0021-9290(03)00160-x.

KEYWORDS Oesophagus; mechanical properties; ex vivo experimental testing; fresh human tissue

gregory.chagnon@univ-grenoble-alpes.fr

Friction when changing neighbours: adhesion-regulated junction slippage controls cell intercalation dynamics in living tissue

Alexander Nestor-Bergmann[a], Guy B. Blanchard[a], Nathan Hervieux[a], Alexander G. Fletcher[b], Jocelyn Étienne[c] and Bénédicte Sanson[a]

[a]PDN, Univ Cambrige, UK; [b]Maths Dept, Univ Sheffield, UK; [c]LIPHY, Univ Grenoble Alpes—CNRS, France

1. Introduction

During development, tissues undergo dramatic shape changes to build and reshape organs. In many instances, these tissue-level deformations are driven by the active reorganisation of the constituent cells. This intercalation process involves multiple cell neighbour exchanges, where an interface shared between two cells is removed and a new interface is grown (Bertet et al. 2004). The key molecular players involved in neighbour exchanges, such as contractile motors proteins and adhesion complexes, are now well-known. However, how their physical properties facilitate the process remains poorly understood. For example, how do cells maintain sufficient adhesive contact while actively uncoupling from one another? Then, how does a new interface grow in a contractile environment? Many existing biophysical models cannot answer such questions (Fletcher et al. 2014.1), due to representing shared cell interfaces as discrete elements that cannot uncouple.

2. Methods

Here, we develop a model where the junctional actomyosin cortex of every cell is modelled as a continuous viscoelastic rope-loop, explicitly representing cortices facing each other at bicellular junctions and the adhesion molecules that couple them (Nestor-Bergmann et al. 2022).

Namely, the cortex of each cell is represented by a mechanical rod, forming a closed loop, and whose energy is the sum of stretch and bending energy. Following the theory of morphoelasticity (Goriely 2017), the elastic stretch α is relative to a virtual configuration. The virtual configuration is obtained by applying a pre-stretch γ to the undeformed configuration without taking into account the contingencies of material continuity and external forces. The total stretch with respect to the initial configuration is $\lambda = \alpha\gamma$, see Figure 1, taking into account the periodic boundary conditions on each cortex and the adhesion forces cortices exert on one another, modelled by discrete elastic bonds between two points on neighbouring cortices. To this instantaneous elastic equilibrium, we add two relaxation

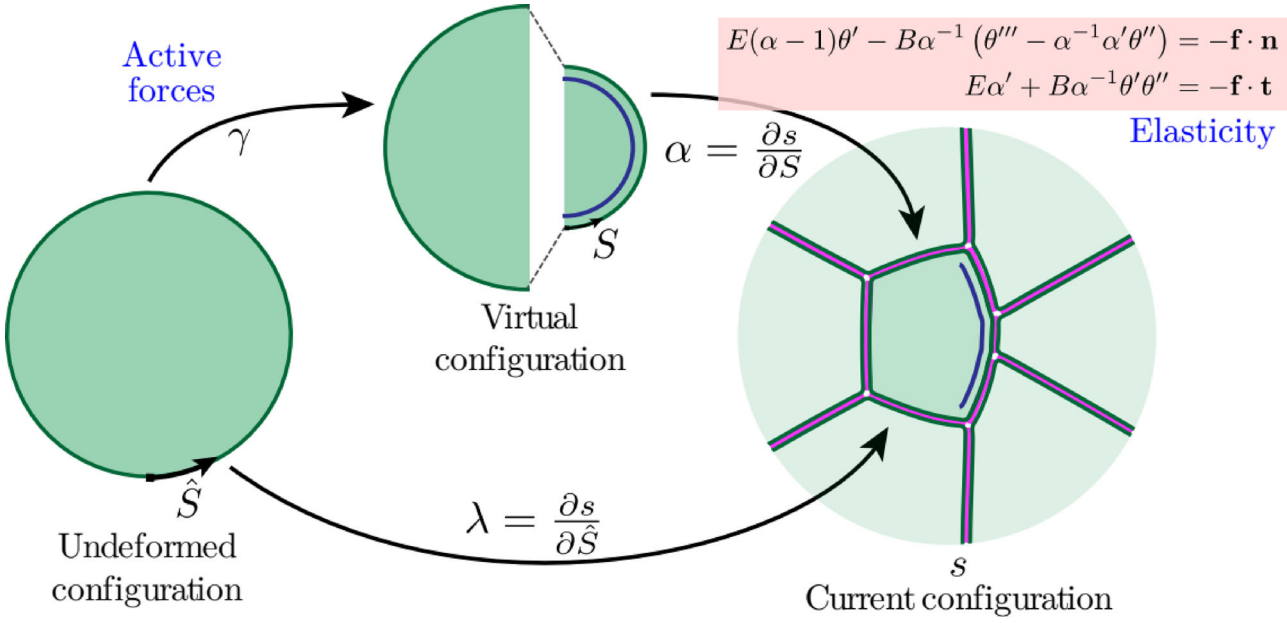


Figure 1. Morphoelastic approach of the ACAM model. $\hat{S}$, S and s are curvilinear coordinates and θ is the angle with respect to x axis of the cortex (green curve). the prestretch γ is an imposed field, symbolised by the blue highlight close to the cortex. E and B are the *stretch* and bending moduli, **f** *is the adhesion force exerted on one cortex by adhesion with other cortices (discrete springs in the magenta regions).*

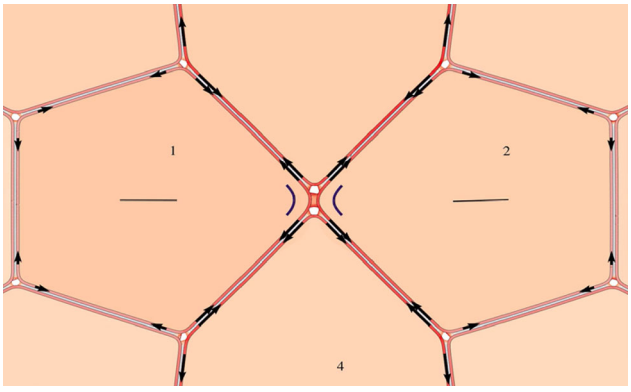


Figure 2. Mechanical balance during neighbour exchange in large cell–cell friction conditions. The junction outlined in dark blue is actively contracting. Black arrows, tension in the cortices of each cell. Cortices interact *via* spring-like adhesions. Observe that tension propagates across tissue, this is due to adhesion resistance to shear.

processes: a viscoelastic relaxation (time τ_{cortex}) of elastic stresses within the cortices, and a turnover time (time τ_{adhesion}) of adhesion bonds which detach in a force-independent fashion and rebind in a relaxed configuration, thereby dissipating adhesion energy.

The model parameters thus relate directly to the properties of the key subcellular players that drive dynamics, providing a multi-scale understanding of cell behaviours. The code is distributed as an open-source free software (Nestor-Bergmann 2022) and allows to reproduce and control the phenomenon of active intercalation, in which active pre-stretch (due to actomyosin) drives the shrinkage of the junction between two cells and is followed by a tissue-cell relaxation in which those cells become separated by the two cells that were neighbouring that junction (Bertet et al. 2004).

3. Results and discussion

We show that active cell neighbour exchanges can be driven by purely junctional mechanisms. Active contractility and cortical turnover in a single bicellular junction are sufficient to shrink and remove a junction. Next, a new, orthogonal junction extends passively. Our Apposed-Cortex Adhesion Model (ACAM) reveals how the turnover of adhesion molecules regulates tension transmission and junction deformation rates by controlling slippage between apposed cell cortices.

The model additionally predicts that rosettes, which form when a vertex becomes common to many cells, are more likely to occur in actively intercalating tissues with strong friction from adhesion molecules.

4. Conclusions

Our approach allows to describe the process of cell intercalation, akin to T1 transitions in foam mechanics, using parameters which are relevant to the microstructure of epithelial tissue. In Nestor-Bergmann et al. (2022), we show that the interplay of the two timescales lead to nontrivial effects: indeed, the shirnkage of the contracting junction is faster when the adhesion turnover time is longer. This is due to the emergence of long-range chains of forces within the model tissue. It will be of interest to explore this emergent effect and characterise it *in vivo*.

Acknowledgements

The authors thank Philippe Beys who manages the cluster.

References

Bertet C, Sulak L, Lecuit T. 2004. Myosin-dependent junction remodelling controls planar cell intercalation and axis elongation. Nature. 429(6992):667–671. doi:10.1038/nature02590.

Fletcher AG, Osterfield M, Baker RE, Shvartsman SY. 2014. Vertex Models of Epithelial Morphogenesis. Biophys J. 106(11):2291–2304., In: doi:10.1016/j.bpj.2013.11.4498.

Goriely A. 2017. The mathematics and mechanics of biological growth. Vol. 45. Cham: Interdisciplinary Applied Mathematics. Springer.

Nestor-Bergmann A, Blanchard GB, Hervieux N, Fletcher AG, Étienne J, Sanson B. 2022. Adhesion-regulated junction slippage controls cell intercalation dynamics in an Apposed-Cortex Adhesion Model. PLoS Comput Biol. 18(1):e1009812. doi:10.1371/journal.pcbi.1009812.

Nestor-Bergmann A., 2022. ACAM – Apposed Cortex Adhesion Model. Tech. Rep. Open-source free software. doi:10.5281/zenodo.5838249.

KEYWORDS Biomechanics; biophysics; actomyosin; adhesion; divided matter

jocelyn.etienne@univ-grenoble-alpes.fr

Hematocrit profile relaxation after a T-shaped bifurcation

K. Useo, F. Risso, P. Duru and S. Lorthois

Institut de Mécanique des Fluides de Toulouse, UMR 5502, CNRS et Universités de Toulouse, Toulouse, France

1. Introduction

Blood circulation in capillary networks allows the diffusion of oxygen to living tissues and the discharge of wastes, including carbon dioxyde. In particular, O_2 and CO_2 are carried by the hemoglobin contained in red blood cells (RBCs). A heterogeneous distribution of RBCs can impair the oxygenation of tissues and is known to play a role in the growth of conditions such as tumors (Bernabeu et al. 2019). White blood cells (WBCs) as well, being larger and stiffer than RBCs, sometimes occlude vessels. The resulting flow modifications may contribute to the redirection of RBCs and thus to an abnormal spatial distribution of O_2 which is involved in Alzheimer's disease development (Cruz Hernández et al. 2019). In summary, heterogeneities in the distribution of both red and white cells at capillary scale, impact the exchange of solutes between blood and tissues and can play an important role in the genesis of some pathologies.

In vivo and *in vitro* studies have allowed a better description of the micro-channel flow phenomenology, and in particular the segregation of cells at bifurcations which leads to heterogeneities in their distribution. This phenomenon, called phase separation, depends on the ratio of blood flow rates between the mother and daughters branches, and impacts the distribution of RBCs at the network scale. However it is not sufficient to explain all the heterogeneities observed experimentally (Merlo et al. 2022).

After each network bifurcation, the RBC transverse concentration profile depends on the phase separation effect, the RBC concentration profiles in the upstream branch and the behavior of RBCs at the bifurcation (cell-cell and cell-wall interactions). This leads to downstream asymmetrical concentration profiles that subsequently relax to symmetric ones along the channel. A better understanding of the physics of this phenomenon is needed to explain the relationships between the architecture of micro-vascular networks and the dynamics of blood flows, at all scales.

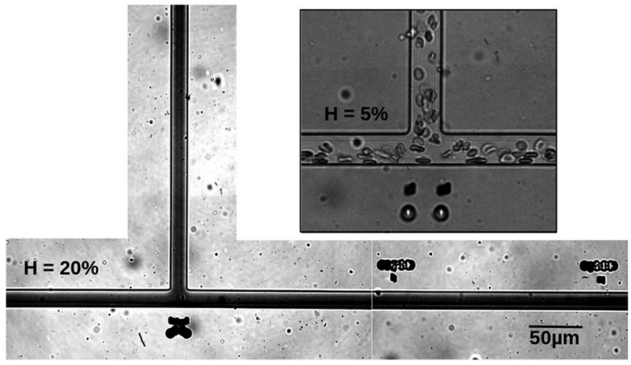


Figure 1. Average image at $H = 20\%$ (lower left panel) and snapshot at $H = 5\%$ (upper right panel) of RBC flow after a T-shape bifurcation.

2. Methods

2.1. Experimental method

We investigate the flow of dilute and concentrated suspensions of RBCs (from a few to 25%), after T-bifurcations of square cross-section microchannels (20 µm). To do so, we re-suspend RBCs in phosphate-buffered saline (PBS) and Optiprep to obtain a density-matched solution (Merlo et al. 2023). We then inject the RBC suspension in a pressure-controlled glass/PDMS microfluidic device, and record the suspension behavior thanks to a high-speed camera (PCO Dimax) connected to the microscope (Leica DMRXA2). A typical image at a 5% RBC concentration is shown in the upper right panel of Figure 1. One can notably observe some RBCs, that are brought by the vertical mother flow, close to the wall facing the incoming top channel. They linger close to the bottom walls of the horizontal daughter microchannels while moving downstream of the bifurcation, and migrating laterally towards the center of the microchannels, under the effects of lift and shear-induced forces. In the lower left panel of Figure 1, an image obtained by averaging over all the images of a recorded sequence is shown, for a 20% RBC concentration. Asymmetry in the RBC distribution in the daughter branches is clearly visible.

2.2. Determination of hematocrit profiles

Hematocrit profiles, i.e. RBC concentration profiles, are measured to characterize this relaxation behavior. First, the optical density is obtained by measuring the ratio between an averaged image (over a sequence of 2000 images, Cf. lower left panel of Figure 1) and the background image (without RBCs). Then the relationship between optical density and local hematocrit is obtained using Leja slides, which are microfluidic

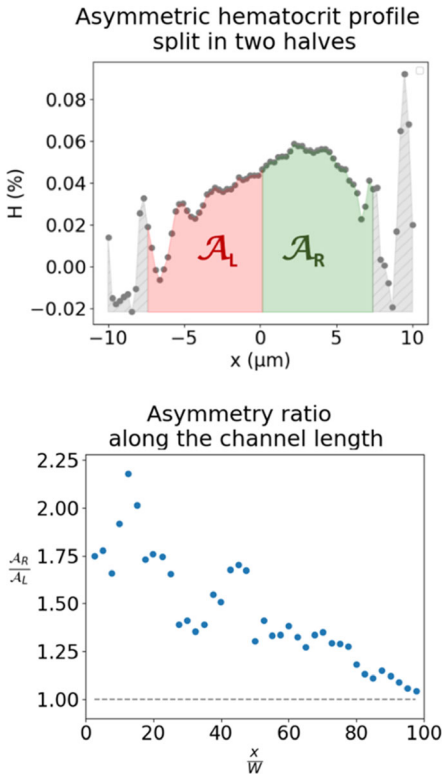


Figure 2. Example of an asymmetric profil (top panel) and evolution of the asymmetry ratio along the channel (bottom panel).

Hele-Shaw cells allowing direct measurement of optical density. If slowly filled and with a small RBC suspension volume, the hematocrit within the Leja slide is homogeneous and equal to the known feed hematocrit. Transverse hematocrit profiles can then be obtained from local optical density values measured across the channel width, owing to the calibration law.

2.3. Asymmetry ratio

To track the relaxation of the hematocrit profiles after a bifurcation, we focus on the evolution of their asymmetry downstream of the bifurcation. Each profile is split into two parts, each one associated with one half of the channel width and we compute the ratio of the areas beneath these half-profiles along the channel length.

3. Results and discussion

As we can see in Figure 2, the asymmetry ratio decreases with increasing distance, in the daughter channel, from the bifurcation. It reaches 1, showing recovery of symmetry after 100 channel width for a dilute case of $H = 5\%$. This result is to mirror with Losserand et al. (2019) experiments made on 17.5 μm channel width, that show it takes over 1500 channel width for an *isolated* red blood cell to relax toward the center of the channel. Such a difference is certainly due to the interactions between RBCs that occur in our experiments and suggests that collective effects in a confined environment strongly accelerate RBC relaxation after bifurcation.

4. Conclusions

We have developed an experimental method to characterize the relaxation of hematocrit profiles after a T-shaped bifurcation in confined cases and over a wide hematocrit range. Experiments performed at higher hematocrit still need to be analyzed to highlight the variation of the relaxation distance with respect to the hematocrit and to lay the foundation for a model describing it.

Acknowledgements

We gratefully acknowledge Y. Abidine, S. Cazin, F. Colombies, J. Lefort and M. Ogier for technical support as well as M. Rondeau and the Etablissement Français du Sang (EFS) for providing blood samples.

References

Bernabeu MO, Köry J, Grogan JA, Markelc B, Beardo A, d'Avezac M, Enjalbert R, Kaeppler J, Daly N, Hetherington J, et al. 2019. Abnormal morphology biases haematocrit distribution in tumour vasculature and contributes to heterogeneity in tissue oxygenation. bioRxiv.

Cruz Hernández JC, Bracko O, Kersbergen CJ, Muse V, Haft-Javaherian M, Berg M, Park L, Vinarcsik LK, Ivasyk I, Rivera DA, et al. 2019. Neutrophil adhesion in brain capillaries reduces cortical blood flow and impairs memory function in Alzheimer's disease mouse models. Nat Neurosci. 22(3):413–420. doi:10.1038/s41593-018-0329-4.

Losserand S, Coupier G, Podgorski T. 2019. Migration velocity of red blood cells in microchannels. Microvasc Res. 124:30–36. doi:10.1016/j.mvr.2019.02.003.

Merlo A, Berg M, Duru P, Risso F, Davit Y, Lorthois S. 2022. A few upstream bifurcations drive the spatial distribution of red blood cells in model microfluidic networks. Soft Matter. 18(7):1463–1478. doi:10.1039/d1sm01141c.

Merlo A, Losserand S, Yaya F, Connes P, Faivre M, Lorthois S, Minetti C, Nader E, Podgorski T, Renoux C, et al. 2023. Influence of storage and buffer composition on the mechanical behavior of flowing red blood cells. Biophys J. 122(2):360–373. doi:10.1016/j.bpj.2022.12.005.

KEYWORDS Red blood cells; bifurcation; relaxation; radial concentration profiles

klervia.useo@imft.fr

Imaging small intestinal motility at macro and micro scales

D. I. Yánez Martín[a], F. Ahmad[a], R. Vernekar[a], S. Tanguy[b] and C. de Loubens[a]

[a]CNRS, Grenoble INP, LRP, Univ. Grenoble Alpes, Grenoble, France; [b]CNRS, CHU Grenoble Alpes, Grenoble INP, TIMC, Univ. Grenoble Alpes, Grenoble, France

1. Introduction

The motility of small intestine (SI) has a fundamental role on the absorption of nutrients (Kisielinski et al. 2002) and the spatio-temporal organisation of gut microbiota (Cremer et al. 2016). Furthermore, mixing and propulsion of the chyme (digested food) at macroscopic scales is achieved thanks to standing or propagating contractions of circular and/or longitudinal smooth muscles (Lentle and de Loubens 2015).

At sub-millimetric scales, small intestinal mucosa is covered by finger-like or leaf-like structures, the so-called villi. Further experiments have indicated that the villi are moved by the transfer of mechanical stress from the smooth muscles layers to the mucosa layer (Lentle et al. 2013) and that their structure is rigid (Lim et al. 2014). Furthermore, recent simulations show that their motility could enhance mixing and mass transfers (Lim et al. 2015). However, simulations with realistic boundary conditions extracted from experiments remain challenging.

At the organ level, various techniques have been used to characterize *in-vivo* the contractions of the smooth muscles using MRI (Ailiani et al. 2009). *Ex-vivo* experiments has also been done using portions of the SI submerged on Krebs while the movement was recorded (Melville et al. 1975). However, it is not well understood how this complex movements may affect the movement of the villi and thus the resulting flow and mixing conditions.

Our main objective is to develop an image technique that permit the quantification of the small intestine motility at the scale of the organ and at the scale of the villi in order to understand the interplay between smooth muscle motility and villi movement.

2. Methods

2.1. Preparation of the duodenal segments

Adult male Wistar rats (300–400 g) were euthanised by heart excision following an injection of Pentobarbital (180 mg/kg). An incision was then made on the abdomen to access the intestine. The initial 15 mm of the SI, corresponding to the duodenum, was resected from the pylorus and immediately immersed in a Tyrode buffer at room temperature.

The mesenteric part was then removed from the excised segment and the duodenal digesta contain was cleaned. Graphite marks were done on the duodenal surface with a 25 G needle to improve the contrast for image analysis. The segment was then attached to the set up and immerged in 80 mL of oxygenated Tyrode buffer at 36 °C without pre-load during 20 min for stabilization.

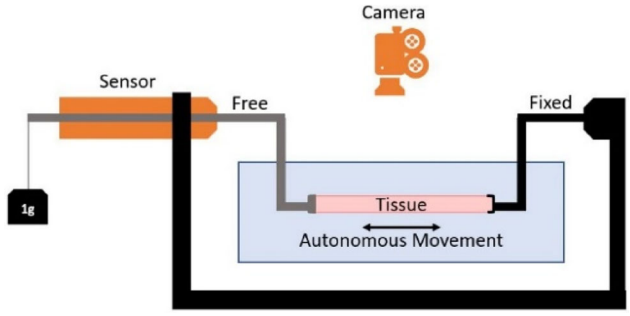


Figure 1. Diagram of the set-up used to make the experiments.

2.2. Experimental set-up

A custom setup was developed for simultaneous deformation measurements and imaging, Figure 1. One end of the duodenum was connected to the sensor that had a weight to produce a tension closer to the physiological state, while the other end was fixed. A macroscope was fixed over it to simultaneously record the motion at the micro scale.

A pre-load of 0.25 g was added every 5 min until 1.5 g was reached. Once this was achieved, another 5 min were waited before finishing the experiment.

2.3. Image analysis

The image analysis was performed following a previous publication (Lentle et al. 2007). Briefly, we tracked 20 sections (20×20 px) of the frames by cross-correlation to obtain the displacement versus time data. The velocity of each portion was obtained with central difference scheme and interpolated using spline over the positions for which displacement were calculated. The derivative of this interpolation gave us the strain-rate.

3. Results and discussion

At macroscopic scale, strain-rate maps were done at different pre-loads, an example is seen in Figure 2a. ST maps shows cyclic contraction (red) or relaxation

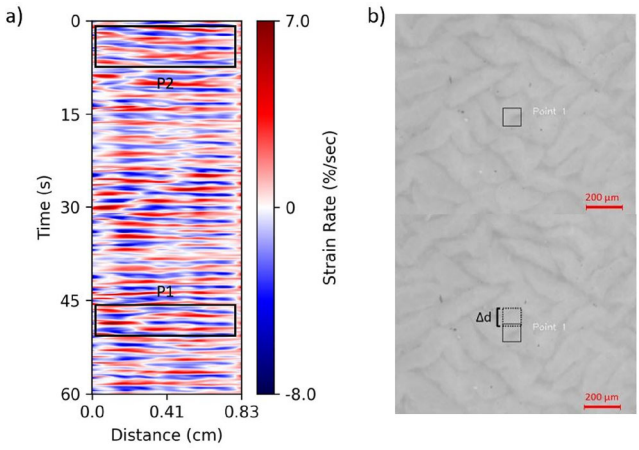


Figure 2. (a) Strain-rate map showing the organisation of longitudinal contractions during 60 s at 1 g. The tissue length analysed was less than 1 cm, where 0 is the closest point to the sensor. Propagating contractions are visible in P1. Non propagating (localized) contractions are visible on P2. (b) Example of tracking of small intestine villi displacement between two consecutive image, Δd after 1s.

(blue) of smooth muscles. Two patterns of organization were observed. The first one is related to propagating longitudinal contractions along the length of the duodenum (e.g. between 45 and 60 s, box P1). In the second one, contractions are organized into fixed domains. Between 15 s and 30 s (box P2), ST maps shows columnar organization which correspond to localized domains of contractions.

Propagating contractions were correlated to higher amplitude of the strain rate than localized contractions. The occurrence of localized contractions was more evident when the applied load was small (<0.5 g). The frequency (0.45±0.03 Hz) was independent on the applied load. The strain rate amplitude decreased when the load was larger than 1 g.

To assess the movement of the villi, a strip of small intestine tissue was used instead of the closed duodenum. The movement of each villi could be resolved and tracked thanks to cross-correlation techniques, Figure 2b.

4. Conclusions

The set-up allowed to characterize the motility of the duodenum in iso-tonic conditions. The spatio-temporal organization was dependent on the applied load. The set-up made possible also to track the movements of the villi. Future experiments will focus on the tracking of villi in *ex-vivo* situations and correlated it to smooth muscle motility.

Acknowledgements

The authors thank also Mohamed Karrouch and Didier Bleses for the development of the experimental bench and the software.

References

Ailiani AC, Neuberger T, Brasseur JG, Banco G, Wang Y, Smith NB, Webb AG. 2009. Quantitative analysis of peristaltic and segmental motion in vivo in the rat small intestine using dynamic MRI. Magn Reson Med. 62(1): 116–126. doi:10.1002/mrm.21982.

Cremer J, Segota I, Yang C, Arnoldini M, Sauls JT, Zhang Z, Gutierrez E, Groisman A, Hwa T. 2016. Effect of flow and peristaltic mixing on bacterial growth in a gut-like channel. Proc Natl Acad Sci USA. 113(41):11414–11419. doi:10.1073/pnas.1601306113.

Kisielinski K, Willis S, Prescher A, Klosterhalfen B, Schumpelick V. 2002. A simple new method to calculate small intestine absorptive surface in the rat. :5.

Lentle RG, Janssen PWM, Asvarujanon P, Chambers P, Stafford KJ, Hemar Y. 2007. High definition mapping of circular and longitudinal motility in the terminal ileum of the brushtail possum Trichosurus vulpecula with watery and viscous perfusates. J Comp Physiol B. 177(5): 543–556. doi:10.1007/s00360-007-0153-8.

Lentle RG, Janssen PWM, DeLoubens C, Lim YF, Hulls C, Chambers P. 2013. Mucosal microfolds augment mixing at the wall of the distal ileum of the brushtail possum. Neurogastroenterol Motil. 25(11):881–e700. doi:10.1111/nmo.12203.

Lentle RG, de Loubens C. 2015. A review of mixing and propulsion of chyme in the small intestine: fresh insights from new methods. J Comp Physiol B. 185(4):369–387. doi:10.1007/s00360-015-0889-5.

Lim YF, Lentle RG, Janssen PWM, Williams MAK, Loubens C, de Mansel BW, Chambers P. 2014. Determination of villous rigidity in the distal ileum of the possum (*Trichosurus vulpecula*). PLoS One. 9(6): e100140. doi:10.1371/journal.pone.0100140.

Lim YF, de Loubens C, Love RJ, Lentle RG, Janssen PWM. 2015. Flow and mixing by small intestine villi. Food Funct. 6(6):1787–1795. doi:10.1039/c5fo00285k.

Loubens CD, Lentle RG, Hulls C, Janssen PWM, Love RJ, Chambers JP. 2014. Characterisation of mixing in the proximal duodenum of the rat during longitudinal contractions and comparison with a fluid mechanical model based on spatiotemporal motility data. PLoS One. 9(4): e95000. doi:10.1371/journal.pone.0095000.

Melville J, Macagno E, Christensen J. 1975. Longitudinal contractions in the duodenum: their fluid mechanical function. Am J Physiol. 228(6):1887–1892. doi:10.1152/ajplegacy.1975.228.6.1887.

KEYWORDS Duodenum; motility; villi; image analysis; bio-mechanics

dacil-idaira.yanez-martin@univ-grenoble-alpes.fr

Investigating human defecation by coupling fluid mechanical modeling and X-ray video-defecography

C. de Loubens[a], F. Ahmad[a], G. Maitrejean[a] and S. Tanguy[b]

[a]CNRS, Grenoble INP, LRP, Univ. Grenoble Alpes, Grenoble, France; [b]UMR5525 TIMC, Univ. Grenoble Alpes, CNRS, Grenoble INP, Grenoble, France

1. Introduction

Defecation is a complex physiological process involving multiple systems, including neural, muscular, hormonal, and cognitive functions (Heitmann et al. 2021). Abdominal and rectal contractions trigger defecation, which is followed by rectal evacuation through the anal canal. Defecation disorders, such as constipation or incontinence, affect approximately 15% of the global population (Higgins and Johanson 2004). Because of limited understanding of defecation, it is challenging for physicians to distinguish aetiologies from symptoms (Scott and Gladman 2008).

There are many possible causes of defecation disorders, including slow bowel transit, structural obstructive phenomena, anal sphincter injuries. However, a significant proportion of patients with impaired defecation do not have a well-defined anatomic disorder (Faucheron and Dubreuil 2000). Although many testing tools are available to diagnose anorectal function (e.g. manometry, video defecography, MRI), methodologic issues limit physicians' understanding of pathophysiological defecation (Carrington et al. 2018).

To gain new insights on the biomechanics of human defaecation, we developed patient-specific simulations of rectal evacuation of yield stress fluids based on X-ray video-defecographies with a neostool. First, we segmented automatically X-ray videos with a Convolutional Neural Network. Then, flow, pressure and stress fields were simulated by lattice-Boltzmann methods for yield stress fluids. Lastly, we applied the model to simulate normal defecation, and impaired defecations in absence or in presence of obstructive phenomena (rectocele).

2. Methods

2.1. Video defecographies

X-ray video-defecographies were carried out with the patient in sitting position, Figure 1. The rectum was filled with a standardized radio-opaque neostool (Faucheron and Dubreuil 2000). The neostool was prepared by mixing barium sulfate with a suspension of potato starch and cooked to obtain a paste with a yield stress τ_0 of 350 Pa, which matched to the yield stress of soft regular human feces (de Loubens et al. 2020). All the patients underwent X-ray defecographies during their health care pathways. The procedures performed in this study complied with the requirements of the ethical standards research committee and with the Helsinki declaration. Ethics approval is not required for this retrospective study.

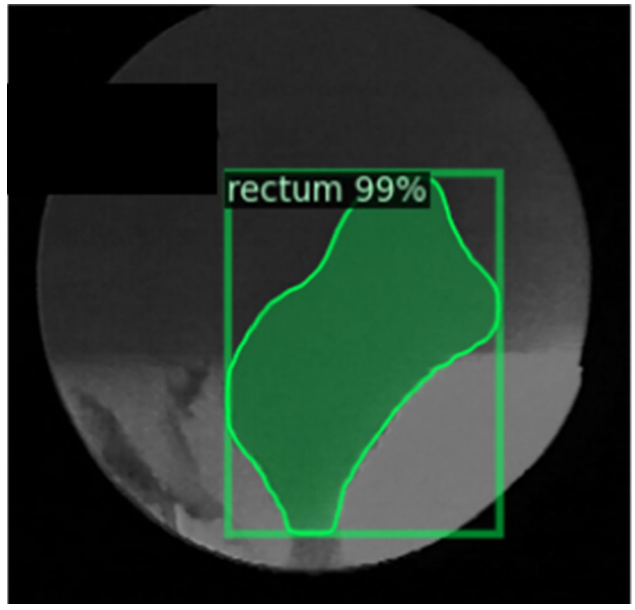


Figure 1. Automatic segmentation of the rectum from X-ray video defecography by a region-based Convolutional Neural Network (RCNN).

2.2. Image segmentation

The RCNN (Region-based Convolutional Neural Network) architecture, and specifically the R50-FPN Mask R-CNN variant, was utilized for the automatic segmentation of X-ray defecography images, Figure 1. R-CNN works by generating region proposals, extracting features using a convolutional neural network, and then classifying the proposed regions and refining their bounding boxes if necessary. Despite the limited dataset of only 200 manually segmented rectum instances, the R50-FPN Mask R-CNN model achieved impressive results with an average precision of 83%.

2.3. Lattice-Boltzmann solver

As the neostool was very viscous and the Reynolds number very small, the flow was modelled using the

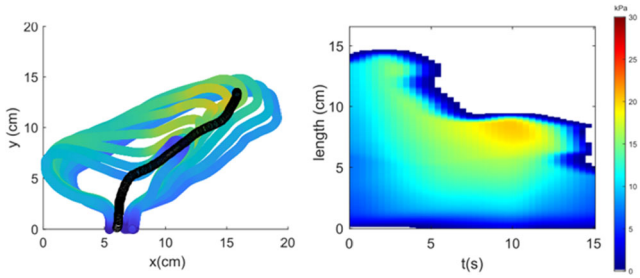


Figure 2. Example of wall normal stress during the defecation of patient with a rectocele (left) and spatio-temporal map of the pressure along the black line (right).

incompressible Stokes equations in 2D for Herschel–Bulkley fluid. The smoothed position of boundary nodes extracted from the video and their velocity were used as boundary conditions along the moving wall of the rectum. The set of equations was solved by lattice-Boltzmann methods for yield stress fluids and moving boundary conditions, see details in Ahmad et al. 2022. We computed flow, pressure and stress fields and also the stress applied in the normal direction by the fluid over the boundaries of the rectum, i.e. the wall normal stress (WNS). By integrating the WNS along the boundaries of the rectum, we calculated also the effective evacuation force F.

3. Results and discussion

We calculated flow, pressure, and stress in the rectum for three types of patients: (i) normal evacuation, (ii) impaired defecation without obstruction, and (iii) anatomical obstruction. In Figure 2, we provide an example of the rectum's squeezing action during defecation. The WNS was highest at the proximal moving part and decreased at the static anorectal junction. Similarly to high resolution manometry (Scott and Gladman 2008), the spatio-temporal evolution of the pressure along a mid-line going from the anal to the proximal ends is shown for one example in Figure 2. In this example, the pressure dropped from 15 to 0 kPa between 5 cm and 0 cm, and increased up to 10 s towards the anorectal junction.

For normal patients, we found that viscous stress was significantly higher than the yield stress of the neostool in the anal canal and the anorectal junction. The flow of the neostool was restricted by these anatomical parts and governed by its shear-thinning properties (see Ahmad et al. 2022 for details). The relationship between the outlet velocity through the anal canal and the evacuation force was strongly nonlinear due to the shear-thinning properties of the neostool. In patients wiith impaired defecation without any obvious anatomical disorder, the WNS and the applied force were only half of what they were in normal patients. This led to a dominance of the yield stress on the flow of the neostool, resulting in a flow rate that was 10 times smaller than for normal patients. Lastly, in patients with an anatomical disorder such as rectocele (Figure 2), the initial phase of defecation had a normal development of the WNS. However, it was unable to sustain the maximum force (pressure) during the second phase of defecation, leading to partial evacuation.

4. Conclusions

In this study, a fluid mechanics analysis of video defecography was introduced as a potential tool to complement clinical investigations of anorectal function. This approach could help better understand normal and pathologic defecation, and identify the origin of disorders such as rectoanal discoordination. By combining medical imaging and fluid dynamics, a new pathophysiological classification of evacuation disorders could be established.

Acknowledgements

The authors thank Agence Nationale de la Recherche for its financial support of the TransportGut project, ANR-21-CE45-0015. The authors would also like to thank Prof. Jean-Luc Faucheron and Dr. Alain Dubreuil for all the data and in-depth discussions.

References

Ahmad F, Tanguy S, Dubreuil A, Magnin A, Faucheron JL, de Loubens C. 2022. Flow simulations of rectal evacuation: towards a quantitative evaluation from video defaecography. Interface Focus. 12(6):20220033. doi:10.1098/rsfs.2022.0033.

Carrington EV, Scott SM, Bharucha A, Mion F, Remes-Troche JM, Malcolm A, Heinrich H, Fox M, Rao SS. 2018. Advances in the evaluation of anorectal function. Nat Rev Gastroenterol Hepatol. 15(5):309–323. doi:10.1038/nrgastro.2018.27.

de Loubens C, Dubreuil A, Lentle RG, Magnin A, Kissi NE, Faucheron JL. 2020. Rheology of human faeces and pathophysiology of defaecation. Tech Coloproctol. 24(4):323–329. doi:10.1007/s10151-020-02174-0.

Faucheron JL, Dubreuil A. 2000. Rectal akinesia as a new cause of impaired defecation. Dis Colon Rectum. 43(11):1545–1549. doi:10.1007/BF02236736.

Heitmann PT, Vollebregt PF, Knowles CH, Lunniss PJ, Dinning PG, Scott SM. 2021. Understanding the physiology of human defaecation and disorders of continence and evacuation. Nat Rev Gastroenterol Hepatol. 18(11):751–769. doi:10.1038/s41575-021-00487-5.

Higgins PD, Johanson JF. 2004. Epidemiology of constipation in North America: a systematic review. Am J Gastroenterol. 99(4):750–759. doi:10.1111/j.1572-0241.2004.04114.x.

Scott SM, Gladman MA. 2008. Manometric, sensorimotor, and neurophysiologic evaluation of anorectal function. Gastroenterol Clin North Am. 37(3):511–538, vii. doi:10.1016/j.gtc.2008.06.010.

KEYWORDS Rectum; motility; rheology

clement.de-loubens@univ-grenoble-alpes.fr

Mechanical analysis of tumor cell of glioblastoma by combining confocal microscopy, Digital Volume Correlation, Scanning ion confocal microscopy and finite element model

A. Gangneux[a], A. Gaboriau[b], L. Caille[a], V. Valle[a], N. Defamie[b], M. Mesnil[b], S. Sebille[c], T. Vendeuvre[a,d] and A. Germaneau[a]

[a]Institut PPrime UPR 3346 CNRS, Université de Poitiers, Poitiers, France; [b]CoMeT Laboratory, UR 24344, Université de Poitiers, Poitiers, France; [c]PRéTI Laboratory, UR 24184, Université de Poitiers, Poitiers, France; [d]Department of Orthopaedic Surgery and Traumatology, University Hospital of Poitiers, Poitiers, France

1. Introduction

The spread of malignant cells from the primary tumor is the principal cause of cancer-related deaths. The initial stage of this invasive process is characterized by the formation of specific membrane protrusions known as invadopodia. (Murphy and Courtneidge 2011). These micrometric structures are capable of breaching and degrading the extracellular matrix (ECM), thereby facilitating the invasion of cells into the adjacent tissues surrounding the tumor (Wolf et al. 2007). This study proposes a method to analyze the mechanical fields inside and outside cells that are responsible for invadopodia formation. For that, we proposed an original approach by using complementary methods:

- Confocal microscopy coupled with Digital Volume Correlation (DVC) to measure displacement fields;
- Scanning Ion Confocal Microscopy (SICM) to identify mechanical properties of cells and substrate;
- Specific Finite Element (FE) model to compute strain and stress fields in cell structures.

2. Methods

2.1. Cell preparation and observation

The study was performed on a human glioblastoma cell line, specifically Ln229 cells, acknowledged for their high invasiveness and ability to create invadopodia. A red lipophilic fluorochrome was used to label the plasma membrane of the cells before they were seeded on Oregon Green 488 conjugated gelatin, a green fluorescent ECM. The development of invadopodia was monitored using a confocal microscope (Olympus FV3000) by taking volume images of the cells and ECM every 6 min during 20 h, corresponding to the development of tumor invasion.

2.2. Displacement field measurement

The Digital Volume Correlation (DVC) method (XDVCorrel) (Bokam et al. 2020) was used to evaluate the displacement fields in volume images of the ECM damaged by invadopodia, as well as the cell in each image voxel. This method consists in analyzing and comparing grey levels in sub-volume domains between images acquired at different transformation states. The voxel size of the images was $0.4\,\mu m \times 0.4\,\mu m \times 0.4\,\mu m$. Full-field displacements were measured with a subset size of 32^3 voxels in each voxel to obtain a full spatial resolution. Finally, the strain fields were calculated from the displacement fields.

2.3. Mechanical characterization of cell and substrate

The mechanical properties of both glioblastoma cells and substrates can be retrieved locally using scanning ion confocal microscopy (SICM) (Zhu et al. 2021). In this method, the height between a hopping probe and the substrate or cell membrane is measured by controlling an ion current passing from the probe to a sensor located in the cell culture medium. By applying different pressures and measuring the local deformation, it is then possible to identify the stiffness properties of the materials analyzed. Based on this technique, the assumption of a linear behaviour law was considered for the measurement of Young's modulus.

2.4. FE simulation

The geometries of cells and substrates were extracted from confocal microscopy images using segmentation techniques. A hexahedral mesh of voxel size was applied to these geometries in order to put the results from DVC as boundary conditions of the model. The behavior laws obtained from SICM were also integrated into the modelling. By using FE simulation techniques, it becomes possible to compute stress and strain fields on the cell and substrate from this model.

3. Results and discussion

Figure 1 shows an example of volume displacement fields measured by DVC on a cell at the beginning of the transformation involved by culture. The internal

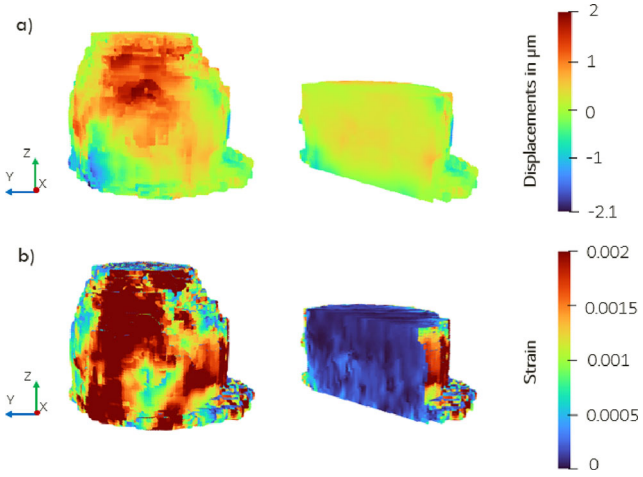


Figure 1. Kinematics fields measured inside a cell by DVC (6–12 min): (a) global displacement; (b) strain.

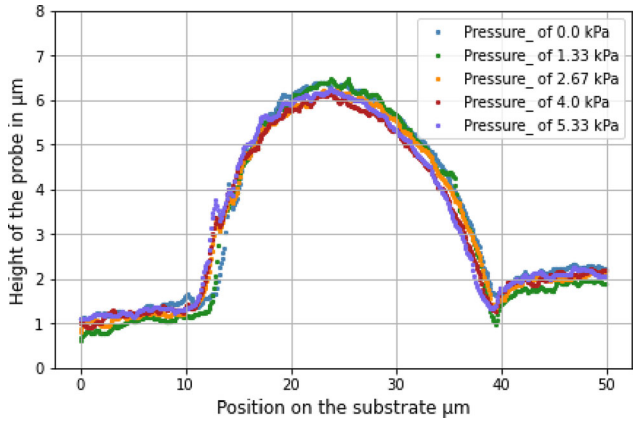


Figure 2. SICM cell and substrate Profiles.

displacements vary in the volume with continuous evolution. The mean and maximum values were respectively 2 µm and −2.1 µm for this first step. The strain fields were calculated from the FE analysis. It can be observed that the strain of the cell is localized at the boundaries, with relatively less strain in the center. This observation is consistent with the confocal microscopy images obtained, which revealed the presence of the nucleus of the cell at its center.

Figure 2 shows an example of Young's modulus measured by SICM on a 2D profile of the cell. Results are summarized in Table 1. Both the cell and the substrate show a slight flattening according to pressure. SICM provides a local value of Young's modulus, which is relatively constant for the substrate. In contrast, the cell presents variations probably due to its constituents.

Displacement measurements performed by DVC inside the cells are in accordance with the results reported in previous studies that used Traction Force Microscopy (TFM) to measure displacement fields at the cell and substrate interface (Maskarinec et al. 2009).

Table 1. Young's modulus results from SICM.

	Substrate	Cell and substrate			Substrate
Position (µm)	(0–10)	(11–20)	(21–30)	(31–40)	(41–50)
Mean Young's modulus (kPa)	12.4	28.1	25.1	22.8	17.5

Regarding the measurements of mechanical properties, the observations are also consistent with previous studies that used SICM (Pellegrino et al. 2012), AFM (Shan-Shan et al. 2021) and confirmed that the stiffness of the cell is influenced by its internal organization and the stiffness of the substrate.

In this preliminary study, only kinematics results have been presented. However, from the displacement fields, image processing and measurements of mechanical properties, it is possible to perform a full FE analysis to compute the stress fields within the cells and substrate and the reaction forces at the interface between the two.

4. Conclusions

This study demonstrated the possibility to characterize mechanical fields in cells during tumor invasion using confocal microscopy and DVC techniques. We visualized and quantified displacement and strain fields at the cell/ECM interface, within the cell and ECM. These measurements can then be coupled with finite element methods to create a digital twin of the cell. The integration of the material properties measured by SICM can lead to the development of a cellular model that is very useful for reproducing cell evolution.

Acknowledgements

The authors would like to thank the platform ImageUp for providing confocal microscope. Interactive LabEx (ANR-11-LABX-0017-01), Ansys, and Ligue contre le Cancer supported this work.

References

Bokam P, Germaneau A, Rigoard P, Vendeuvre T, Valle V. 2020. Evaluation of fracture properties of cancellous bone tissues using digital image correlation/wedge splitting test method. J Mech Behav Biomed Mater. 102: 103469. doi:10.1016/j.jmbbm.2019.103469.

Maskarinec SA, Franck C, Tirrell DA, Ravichandran G. 2009. Quantifying cellular traction forces in three dimensions. Proc Natl Acad Sci U S A. 106(52):22108–22113. doi:10.1073/pnas.0904565106.

Murphy DA, Courtneidge SA. 2011. The 'ins' and 'outs' of podosomes and invadopodia: characteristics, formation and function. Nat Rev Mol Cell Biol. 12(7):413–426. doi: 10.1038/nrm3141.

Pellegrino M, Pellegrini M, Orsini P, Tognoni E, Ascoli C, Baschieri P, Dinelli F. 2012. Measuring the elastic properties of living cells through the analysis of current–displacement curves in scanning ion conductance microscopy. Pflugers Arch. 464(3):307–316. doi:10.1007/s00424-012-1127-6.

Shan-Shan L, You-An S, Mei-Chun Cand Ya-Wen L. 2021. Probing invadosomes: technologies for the analysis of invadosomes. FEBS J. 289(2022):5850–5863.

Wolf K, Wu YI, Liu Y, Geiger J, Tam E, Overall C, Stack MS, Friedl P. 2007. Multi-step pericellular proteolysis controls the transition from individual to collective cancer cell invasion. Nat Cell Biol. 9(8):893–904. doi:10.1038/ncb1616.

Zhu C, Huang K, Siepser NP, Baker LA. 2021. Scanning Ion Conductance Microscopy. Chem Rev. 121(19): 11726–11768. doi:10.1021/acs.chemrev.0c00962.

KEYWORDS Cell invasion; digital volume correlation; finite element; confocal microscopy; scanning ion confocal microscopy

aurelie.gangneux@univ-poitiers.fr

Mechanical and microstructural characterization of the tunica albuginea: a preliminary study

C. Luet[a], P. Neuville[b], D. Carnicelli[b], C. Parat[b], N. Morel-Journel[b] and K. Bruyère[a]

[a]Université Claude Bernard Lyon 1, Univ Gustave Eiffel, IFSTTAR, LBMC UMR_T9406, Univ Lyon, Lyon, France; [b]Hospices Civils de Lyon, Hôpital Lyon Sud, Service d'Urologie, 165, Chemin du Grand-Revoyet, Pierre-Bénite, France

1. Introduction

The tunica albuginea is the fibrous connective membrane that surrounds the cavernous tissue of the penis; its mechanical rigidity contributing to the erection mechanism. Its integrity and its mechanical role can be compromised by various conditions (cancer, Peyronie's disease, trauma) (Chung 2020); its reconstruction could also be required for some specific interventions (phalloplasty) (Harris et al. 2020). Beyond these clinical observations, the mechanical behavior of the albuginea has been little quantified. Only (Bitsch et al. 1990) reported values of elastic modulus and ultimate stress obtained by inflation tests, while (Hsu et al. 1994) measured ultimate stress by punching. The microstructure of the human albuginea has already been described from light and electron microscopy (Bitsch et al. 1990; Hsu et al. 1994; Loreto et al. 2012); it is a bilayered structure with an inner circular layer and an outer longitudinal layer of collagen bundles, with elastic fiber inside and outside collagen bundles. Yet, these studies did not detail precisely these layer's arrangement and thicknesses. The aim of the work reported here is to quantify the mechanical behavior of the tunica albuginea under uniaxial tensile load and to illustrate the thicknesses and the microstructure of the layers that may play a role in the mechanical behavior of the TA.

2. Methods

2.1. Material

Two tunica albuginea (TA) were collected from two Post Mortem Human Subjects, respectively for mechanical tests (#248, 90 yo male) and histology analysis (#212, 85 yo male). Each TA was cut along the corpus spongiosum path, the septum and the cavernous tissue were removed as much as possible. Each TA was then kept frozen at −18 °C. For mechanical tests, when the TA #248 thawed, Buck's fascia was removed and 8 samples were cut using die-cut with two different I-shapes according to the cut map given on Figure 1a): 4 samples were cut in the longitudinal direction of the penis and 4 in the circumferential direction. For histological analysis, biopsies were taken from the TA #212 and placed in histology cassettes with a special care regarding direction and side of the biopsies.

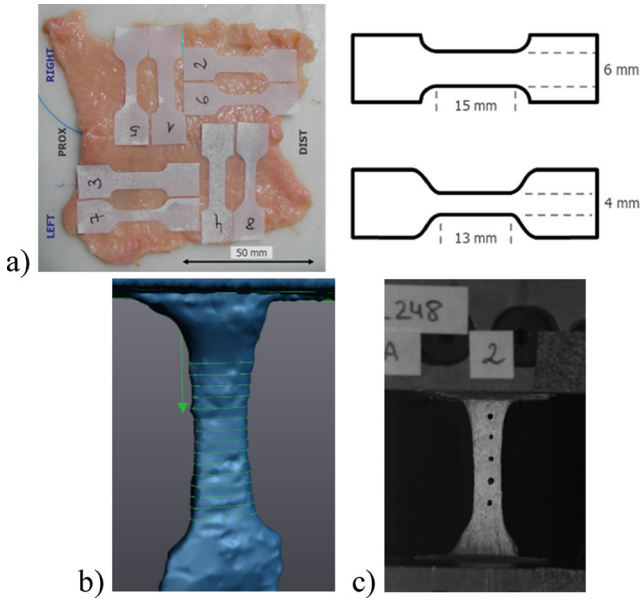


Figure 1. (a) Cut-out plan of the TA samples for tensile tests (subject #248, view of the internal side) and main dimensions of samples, (b) 3D reconstruction of a sample realised with a go!Scan3D^{TM} system, (c) a sample during test.

2.2. Tensile tests

Tensile tests were performed using an INSTRON 8802 (High Wycombe, England) machine. In order to prevent any slippage, the shoulder part of the samples was first martyrized and then clamped with emery cloth. Before clamping in the lower grip, a 3D scanner of the sample was used to measure an average of its section area along its gauge length (15 sections measured) (Figure 1c). To avoid accommodation effect, no cycling was applied and a stretch of the sample was applied at 0.01 s^{-1} strain rate, up to failure.

The stretch of the samples was measured using video and the tracking of points marked at the extremities of their gauge length. Load was measured using a 250 N cell.

2.3. Microstructure observations

Rectangular biopsies were taken from the frozen TA #212 at various locations (proximal, distal, right, left). They were directly immersed 24-h in 10% buffered formol for fixation. Then, these biopsies were

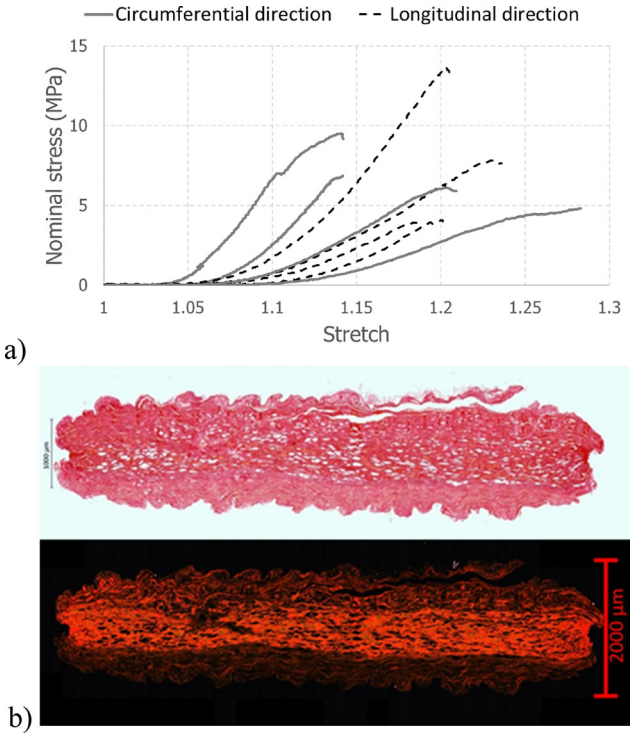


Figure 2. (a) Stress-stretch curves, (b) microscopic view of a transverse plane slice under white light (top) and circular polarized light (bottom), internal side of the TA is located at the bottom of the images.

embedded and 5 µm slices were cut along the transversal or the longitudinal planes of the TA. Some slices were stained with Picrosirius red stain for collagen observation. Slices were observed at various magnification and mosaics of images were reconstructed in order to illustrate the whole section of each biopsy. These mosaics where acquired under white light microscopy and also under circular polarized light to highlight the orientation of collagen fibres.

3. Results and discussion

3.1. Mechanical behaviour

Stress-stretch curves show J-shapes, typical of the nonlinear mechanical behaviour of biological fibrous membranes (Figure 2a). A larger variability of the curves is observed in the transversal direction compared to the longitudinal one. On these two sets of 4 samples, no clear difference of the mechanical behaviour is observed between the two directions of loading. The average modulus in the linear parts of the curves and the average maximal nominal stress are respectively equal to 82 ± 43 MPa and 7 ± 2 MPa in the circumferential direction and to 70 ± 36 MPa and 7 ± 5 MPa in the longitudinal direction.

3.2. Microstructural arrangement

The images of a TA section in a transversal plane are shown in Figure 2b. The remaining cavernous tissue is easily identified on both views under ordinary or polarized lights, at the bottom of the images. Despite its removal in the TA preparation, its thickness is not negligible according to the whole section thickness. The external and internal layers, described respectively as made of longitudinally oriented and circumferentially oriented collagen fibres are not easily discriminated on PS stained section images. The stronger refractivity of the circumferential fibres of the internal layer on images under circular polarized light allows to identify it. This stronger refractivity is due to the higher density and the specific orientation of the circumferential collagen fibres along the horizontal direction on this transversal section image.

4. Conclusions

This preliminary study is a first step towards the evaluation of the TA mechanical behaviour up to failure. A large variability in the stress-stretch curves is observed and the expected mechanical anisotropy is not clearly seen. Images of the microstructure showed the difficulty to characterize the isolated TA, as the cavernous tissue is difficult to remove. This suggests that a characterization of the mechanical behaviour of the cavernous tissue would be useful, and that for further tensile tests, the observation of the microstructure of each tested sample will be essential.

Additional work will also be pursued to complete the analysis of the arrangement of the TA microstructure and its mechanical behaviour under different types of loading.

Acknowledgements

This work is funded by 'France Relance' program, action 4, as MIMAS project. We thank Novotec and the Centre d'Imagerie Quantitative Lyon-Est (CIQLE) for their contribution respectively for the preparation and the observation of the histological slices. We also thank Leïla Ben Boubaker for her technical assistance during mechanical testing.

References

Bitsch M, Kromann-Andersen B, Schou J, Sjøntoft E. 1990. The elasticity and the tensile strength of tunica albuginea of the corpora cavernosa. J Urol. 143(3):642–645. doi:10.1016/S0022-5347(17)40047-4.

Chung E. 2020. Penile reconstructive surgery in peyronie disease: challenges in restoring normal penis size, shape,

and function. World J Mens Health. 38(1):1–8. doi:10.5534/wjmh.170056.

Harris KT, Wu WJ, Manyevitch R, Haney NM, Burnett AL, Bivalacqua TJ, Gearhart JP. 2020. Outcomes of inflatable penile prosthesis insertion using a neotunica allograft in neophalluses of patients on the bladder exstrophy-epispadias complex spectrum. J Pediatr Urol. 16(5):659.e1-659–e6. doi:10.1016/j.jpurol.2020.07.004.

Hsu GL, Brock G, Martínez-Piñeiro L, von Heyden B, Lue TF, Tanagho EA. 1994. Anatomy and strength of the tunica albuginea: its relevance to penile prosthesis extrusion. J Urol. 151(5):1205–1208. doi:10.1016/S0022-5347(17)35214-X.

Loreto C, Orlandi A, Ferlosio A, Djinovic R, Basic D, Bettocchi C, Rutigliano M, Barbagli G, Vespasiani G, Caltabiano R, et al. 2012. Cryopreserved penile tunica albuginea for allotransplantation: a morphological and ultrastructural investigation. J Sexual Med. 9(9):2378–2388. doi:10.1111/j.1743-6109.2012.02789.x.

KEYWORDS Tunica albuginea; tensile test; histology; microstructure

karine.bruyere-garnier@univ-eiffel.fr

Mechanical behavior of stomach tissue: a preliminary study

F. Fournier[a], W. Wei[a], T. Bege[a,b] and C. Masson[a]

[a]LBA UMRT24, Aix Marseille Université / Université Gustave Eiffel, Marseille, France; [b]Service de chirurgie générale et digestive, CHU Nord AP-HM, Marseille, France

1. Introduction

Over the past 2 decades, the number of bariatric surgeries in France has significantly increased from 2800 in 1997 to 52,500 in 2018 (Oberlin and de Peretti 2020), with a majority of sleeve gastrectomy. However, sleeve gastrectomy induces post op complications linked to the stomach mechanics. Therefore, to understand these complications, a FE model using gastric material properties needs to be developed. Although several studies have investigated this material behavior using various specimens (e.g. cadaveric or fresh human/porcine) and different testing methods (e.g. uniaxial and biaxial tensile test, membrane indentation, inflation …) (Zhao et al. 2008; Toniolo et al. 2022), there is no consensus on the most effective way to model its material mechanical behavior.

Indeed, once experimental data is recovered, an actual challenge is to select the most appropriate computational law to fit the observed mechanical behavior during testing, such as hyperelastic isotropic or anisotropic models, with or without viscosity.

In this preliminary study, our aim is to present a complete workflow, from experimental to numerical to determine the mechanical characteristics of porcine stomach tissue using uniaxial tensile test and compare two computational models, using an inverse analysis from Fung and Ogden's third order strain energy functions.

2. Methods

2.1. Materials

Eight porcine stomachs were collected at the Centre d'Enseignement et de Recherche Chirurgical (CERC) at Aix-Marseille University, France (*sus scrofa domesticus*, 30–34 kg, 5 months old). All experiments took place within 12 h after euthanasia.

They were first emptied and cleaned with water. A total of 29 strips were taken from these resected stomachs, 16 circumferential (in the fundus region) and 13 longitudinal (in the corpus region). Each sample was cut to have a size of 105×25 mm (65×25mm after clamping). It was decided to keep intact the samples as a first approach and not split muscle and mucosal layers, as they might be harder to split with human tissue.

2.2. Uniaxial tensile test

For each sample, the testing protocol was a preload of around $1\,\mathrm{N}(0.01 \pm 0.002\,\mathrm{MPa})$ defining zero-strain state, a sinusoidal preconditioning (10 cycles, 10 mm/s and 6 mm amplitude) and the tensile test, at 10 mm/s, for a maximal displacement of 100 mm (stretch around 2.4 depending on the sample). Force and crosshead displacement were measured with a frequency of 128 Hz.

2.3. Computational law

Two strain energy functions were used to fit experimental data, leading to two different expressions for first Piola–Kirschoff stress along the first axis (tensile test direction). Both models are hyperelastic isotropic models, as used by Zhao et al. (2008).

For Fung model (Fung 1993):

$$\Pi_{11} = \frac{1}{2}c\left[\lambda exp\left(2a_1(\lambda^2-1)+a_{10}\left(\frac{1}{\lambda}-1\right)\right) - \frac{1}{\lambda^2}exp\left(2a_9\left(\frac{1}{\lambda}-1\right)+a_{10}(\lambda^2-1)\right)\right]$$

And for third order Ogden model (Ogden 1972):

$$\Pi_{11} = 3\sum_{k=1}^{3}\mu_k\left[\lambda^{(\alpha_k-1)} - \lambda^{\left(-\frac{1}{2}\alpha_k-1\right)}\right]$$

With 4 materials parameters for Fung model (c, a_1, a_9, a_{10}) and 6 for third order Ogden model (μ_k and α_k, $k = 1, 2, 3$).

2.4. Post processing and fitting

Computational models were fitted on nominal stress (or PK1 stress)-stretch curve.

As described by Toniolo et al. (2022), two sections were identified on the stress-stretch curves: a linear toe region and a stiffer linear region before the beginning of damage. A bilinear law was identified on each curve giving two elastic moduli per sample. Corridors were obtained with a mean curve, and plus or minus standard deviation. The same linear fitting process was done on corridors to detect beginning of damage, which corresponds to the loss of linearity after the stiffer linear region. Once damage detected, computational laws were fitted using an interior-point algorithm on corridors, until damage.

A comparison of linear fitting parameters between longitudinal and circumferential samples was done using a Welch two sample *t*-test.

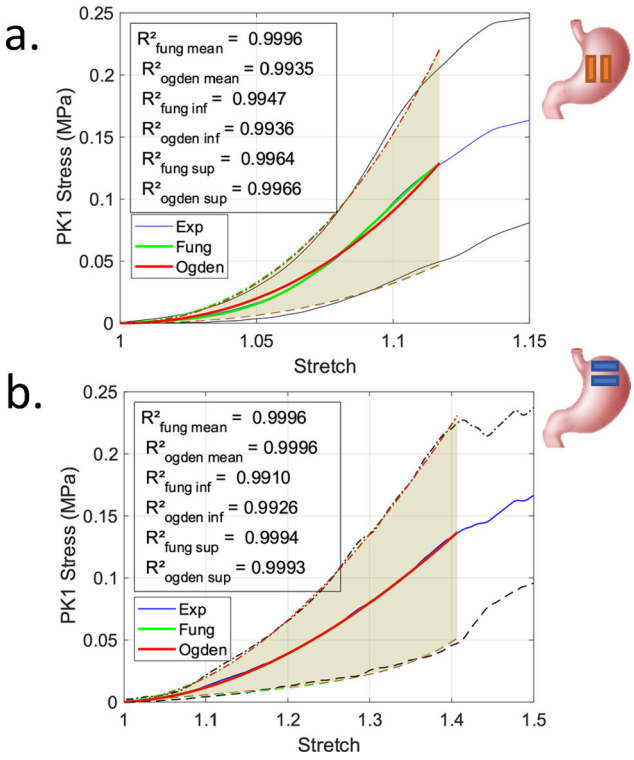


Figure 1. Fitting of the average and corridor stress-stretch curves, obtained for longitudinal strips from the gastric corpus region (a.), circumferential strips from the gastric fundus region (b.). (corridors created from mean curve and ± standard deviation).

3. Results and discussion

Within 29 tests done, 27 were considered valid and post processed (14 circumferential and 13 longitudinal). One excluded test did not go until damage, and one slipped from the clamps.

Material parameters were determined for each computational laws, for longitudinal and circumferential corridors (Table 1). Experimental and fitted corridors are presented on Figure 1 up to the point of initial damage. The correlation coefficients (R^2) for each fitted curves and each model are provided, enabling a performance comparison. A mean thickness of 4.09 ± 0.75 mm was measured on samples, using a laser probe. Tensile tests were carried out at a mean strain rate of 0.15 ± 0.02/s.

Toe and linear elastic moduli, toe and damage elongations and toe stress means were found to be statistically different for longitudinal (from the corpus region) and circumferential (from the corpus region) samples (respectively, $t(17) = 2.7\ p < 0.015$; $t(17) = 7.3$ P < 1e-5; $t(19) = -5.6$ P < 1e-4; $t(22) = -7.3$ P < 1e-6; $t(17) = -2.3\ p < 0.03$). We didn't find a significant difference between circumferential and longitudinal damage stress (t(21) = −0.5 $p = 0.637$).

Table 1. Fung and Ogden Material parameters for longitudinal and circumferential corridor curves.

		Longitidinal			Circumferential		
		Mean	Inf	Sup	Mean	Inf	Sup
Fung	C MPa	0.0011	0.1524	1.6993	0.2036	0.0125	0.1704
	a1	−43.3703	−0.1579	0.6400	0.0610	1.8750	0.0926
	a9	−117.3639	−12.9575	−5.6857	−3.3461	9.7537	−4.8966
	a10	−256.3558	−7.8553	−1.9585	−1.3069	6.2349	−2.4792
Ogden	μ_1 MPa	−0.2161	−1.8320	−2.2050	−0.0656	−0.1807	−0.1499
	μ_2 MPa	−8.5964	2.4359	3.0075	0.7550	−0.6706	1.2702
	μ_3 MPa	4.0879	0.0857	0.2898	0.0886	0.0097	0.1543
	a1	−5.9781	2.1556	2.5598	0.8694	0.4612	0.4591
	a2	1.4455	1.3416	1.0864	−0.2744	−0.0598	−0.3005
	a3	2.7251	8.0030	8.2199	3.0631	5.0072	2.9909

Since elastic moduli are statistically different depending on orientation and location, samples from different orientations need different material parameters to model them properly.

Fitting of both Fung's and Ogden's third order computational models revealed that they can both be used to model hyperelastic mechanical behavior of porcine stomach.

However, we observed several areas for improvements. First, during testing, samples were taken in one direction only for each selected region of the stomach. A complementary study on the opposite direction for each region should be conducted to compare anisotropy for each region. We also decided to fit two phenomenological laws, which does not include any consideration regarding tissue microstructure. It could be interesting to compare this modeling to a structural based modeling, using fiber reinforced models for example.

4. Conclusions

In this study, we first proposed a method on tensile testing and model fitting, identified material parameters of two commonly used hyperelastic isotropic material models and compared their efficiency in the conditions described above. We also compared the mechanical response of samples from two orthogonal orientations. We showed that both models are fitting well stomach wall behavior. We also showed different material parameters has to be used for each couple region-orientation.

References

Fung Y-C. 1993. Biomechanics. New York, NY: Springer New York.

Oberlin P, de Peretti C. 2020. Bariatric surgery in France from 1997 to 2018. Surg Obes Relat Dis. 16(8):1069–1077. doi:10.1016/j.soard.2020.04.022.

Ogden RW. 1972. Large deformation isotropic elasticity – on the correlation of theory and experiment for incompressible rubberlike solids. Proc R Soc Lond. A.326(1567):565–584.

Toniolo I, Giulia Fontanella C, Foletto M, Carniel EEL. 2022. Coupled experimental and computational approach to stomach biomechanics: towards a validated characterization of gastric tissues mechanical properties. J Mech Behav Biomed Mater. 125:104914. doi:10.1016/j.jmbbm.2021.104914.

Zhao J, Liao D, Chen P, Kunwald P, Gregersen EH. 2008. Stomach stress and strain depend on location, direction and the layered structure. J Biomech. 41(16):3441–3447. doi:10.1016/j.jbiomech.2008.09.008.

KEYWORDS Uniaxial tensile test; stomach biomechanics; computational law; constitutive analysis

francois.fournier@univ-eiffel.fr

Mechanical properties of spinal nerve roots along the cervical spine

Audrey Berriot[a,b,c,d], Morgane Evin[a,b], Elisabeth Laroche[b,c,d], Jasdeep Bhinder[b,c,d] and Eric Wagnac[b,c,d]

[a]Laboratoire de Biomécanique Appliquée, UMRT24 AMU/IFSTTAR, Marseille, France; [b]LiLab-Spine – Laboratoire International en Imagerie et Biomécanique du Rachis, Marseille France & Montréal Canada; [c]Department of Mechanical Engineering, Ecole de Technologie Supérieur, Quebec, Canada; [d]Research Center, Hôpital du Sacré-Cœur de Montréal, Montréal Québec, Canada

1. Introduction

Biofidelic modeling of spinal nerve roots (NR) located within the subarachnoidal space are critical to study spinal cord trauma as well as cerebrospinal fluid dynamic (Beauséjour et al. 2022; Heidari Pahlavian et al. 2014; Tangen et al. 2015). In most studies, NR have been modeled as linear springs with no differentiation of their mechanical properties between cervical spinal level. To alleviate this possible limitation, a mechanical characterization of cervical NR has been performed to better understand their mechanical behavior along the cervical spine and to potentially provide comprehensive mechanical properties to improve their modeling, notably at failure.

2. Methods

2.1. Sample preparation

Thirty-five NR samples (Table 1) were collected on six porcine spinal cords (pigs aged 3–6 months, weighing 36–96 kg). Bundles of fibers of 0.62 mm ±0.24 mm diameter and 12.72 ± 4.90 mm length were excised from the subarachnoidal space, conserved in saline solution at 20 °C and tested within 12 h after extraction. The initial length and the diameter of each sample were measured with a caliper and an optical microscope respectively in order to compute the engineering stress and strain.

2.2. Mechanical test set up

Tensile tests comprising 10 sinusoidal cycles of preconditioning at a frequency of 0.125 Hz and a displacement of ±1 mm (approximatively 8% of strain) followed by a final stretch up to failure at a strain rate of 0.1 s^{-1} (quasi-static) were performed on a Mach-1 V500cst mechanical tester (Biomomentum, Canada) equipped with a 17 N load cell (Figure 1). A preload of 0.1 N (approximatively 0.03 MPa) was applied to the specimen prior to testing. NR were fixed to the testing device using needles and suture thread with a drop of cyano-acrylate glue.

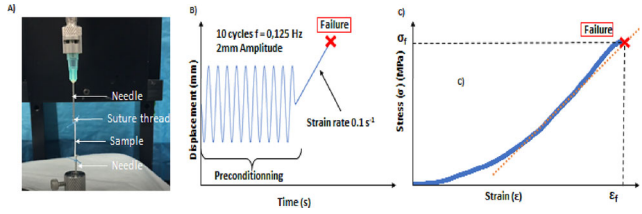


Figure 1. (A) Mechanical setup. (B) test protocol. (C) Typical mechanical response of a sample subjected to uniaxial stretch.

2.3. Post-processing and statistical analysis

Failure stress (σ_f), failure strain (ε_f) and modulus of elasticity were extracted from the engineering stress-strain curves and used to compute the mean values by cervical level. Strain was reset to zero after preconditioning. The resulting curves were typical of biological soft tissues. A toe region was observed in which fibers align in early loading followed by a linear region in which the fibers straighten. The modulus of elasticity was defined as the slope of the second portion of the bilinear fitted curve (Matlab algorithm, Maltab R 2020b) that results from each stretched specimen. Kruskal-Wallis tests have been performed with R (RStudio V1.2.1335) in order to test if cervical levels have an influence on the elastic moduli, the failure strain (σ_f) and the failure stress values (ε_f).

3. Results and discussion

The mean values for the elastic modulus vary from 1.00 MPa at C6/C7 to 3.45 MPa at C2/C3 level. The average failure strain goes from 0.09 for C2/C3 to 0.14 for C5/C6 and the mean of failure stress varies between 0.16 MPa for C6/C7 to 0.32 MPa for C5/6. For all the other samples it is around 0.20 (Table 1).

No significant influence was found between the elastic modulus, the failure strain nor the failure stress at the different cervical levels : all *p*value were above 0.05 (respectively 0.36, 0.43 and 0.74).

Elastic moduli ranging from 0.9 to 1.4 MPa have been reported for murine NR at the lumbar level under quasi-static tensile conditions (Singh et al. 2006). Elastic moduli of 13.8 and 13.2 MPa were also reported for cervical and lumbar porcine NR, respectively, under similar conditions (Tamura and Sakaya 2018). The results of this study are within the range of literature with a global elastic modulus of 2.76 MPa. Previous studies on NR did not show a

Table 1. Mechanical parameters per spinal level (mean ± SD).

	N	Elastic Modulus (MPa)	ε_f	σ_f (MPa)
Global	33	2.25 ± 1.56	0.12 ± 0.04	0.17 ± 0.13
C1/C2	6	3.45 ± 2.27	0.11 ± 0.05	0.19 ± 0.12
C2/C3	4	3.02 ± 1.99	0.09 ± 0.02	0.16 ± 0.86
C3/C4	4	2.15 ± 1.33	0.09 ± 0.02	0.11 ± 0.04
C4/C5	6	2.23 ± 145	0.12 ± 0.04	0.20 ± 0.16
C5/C6	4	1.48 ± 0.74	0.13 ± 0.06	0.18 ± 0.20
C6/C7	3	1.00 ± 1.15	0.12 ± 0.02	0.32 ± 0.11
C7/T1	6	2.22 ± 1.63	0.13 ± 0.03	0.17 ± 0.13

N is the number of samples.

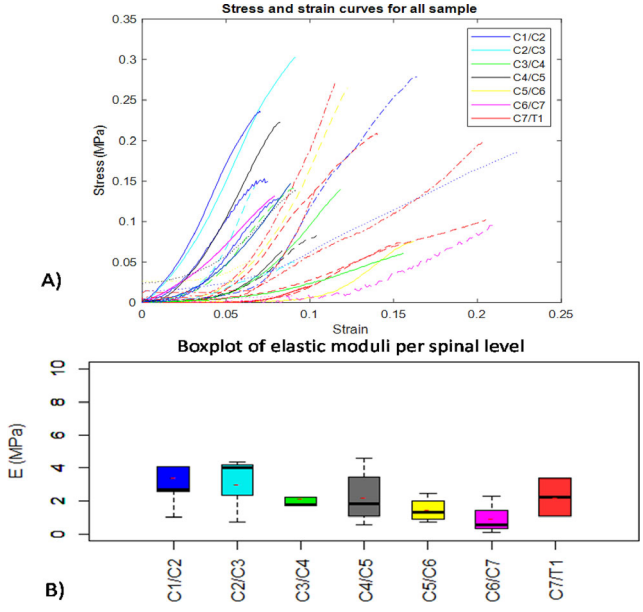


Figure 2. (A) Plot of the stress-strain curves for all samples, samples from the same animal have the same line style. (B) Boxplot of the elastic modulus per spinal level.

statistically significant difference between the mechanical properties of NR between the cervical, thoracic and lumbar levels. However, they suggest an association between NR location and mechanical strength of the bundles. A trend implying that lumbar NR are weaker than cervical NR in term of tensile strength at failure has been highlighted (Tamura and Sakaya 2018). While our results did not show any difference in the mechanical properties of the different cervical levels, trends could be highlighted with higher values of elastic moduli at the C2/C3 level. Such variations could be explained by the range of motion of the cervical spine, which varies significantly between its lower and upper segment (Yang et al. 2000).

4. Conclusions

While not reaching significance in their differences, the elastic modulus of NR within the subarachnoidal space presented trends at the different cervical levels, with upper level having a higher modulus. Viscoelastic characterization and constitutive modeling of these structures should be the subject of future research to further improve their biofidelity in numerical models.

Acknowledgements

The authors would like to greatly acknowledge the support of Boris Chayer from 'Laboratoire de Biorhéologie et d'Ultrasonographie Médicale' of the CHUM in Montréal as well as the team from CR CHUM's animal house.

References

Beauséjour M-H, Wagnac E, Arnoux P-J, Thiong J-MM, Petit Y. 2022. Numerical investigation of spinal cord injury after flexion-distraction injuries at the cervical spine. Trans ASME, J Biomech Eng. 144(1):011011. doi: 10.1115/1.4052003.

Heidari Pahlavian S, Yiallourou T, Tubbs RS, Bunck AC, Loth F, Goodin M, Raisee M, Martin BA. 2014. The impact of spinal cord nerve roots and denticulate ligaments on cerebrospinal fluid dynamics in the cervical spine. Sleegers K, editor. PLoS One. 9(4):e91888. doi:10.1371/journal.pone.0091888.

Singh A, Lu Y, Chen CM, Cavanaugh J. 2006. Mechanical properties of spinal nerve roots subjected to tension at different strain rates. J Biomech. 39(9):1669–1676. doi:10.1016/j.jbiomech.2005.04.023.

Tamura A, Sakaya M. 2018. Dynamic tensile behavior of fiber bundles isolated from spinal neve roots: effects of anatomical site and loading rate on mechanical strength. J Eng Sci Med Diagn Ther. 1(3):031001. doi:10.1115/1.4039560.

Tangen KM, Hsu Y, Zhu DC, Linninger AA. 2015. CNS wide simulation of flow resistance and drug transport due to spinal microanatomy. J Biomech. 48(10):2144–2154. doi:10.1016/j.jbiomech.2015.02.018.

Yang JK, Lövsund P, Cavallero C, Bonnoit J. 2000. A human-body 3D mathematical model for simulation of car-pedestrian impacts. J Crash Prev Inj Control. 2(2): 131–149. doi:10.1080/10286580008902559.

KEYWORDS Spinal cord; cervical; nerve roots; mechanical testing

audrey.berriot@univ-eiffel.fr

Modeling of bulge test of the fascia lata using the discrete element modeling method

A. Lagache[a,b], S. Laporte[a], C. Vergari[a], C. Muth-Seng[a] and J. Girardot[b]

[a]Arts et Métiers Institute of Technology, Université Sorbonne Paris Nord, IBHGC – Institut de Biomécanique Humaine Georges Charpak, HESAM Université, Paris, France; [b]Arts et Métiers Institute of Technology, University of Bordeaux, CNRS, Bordeaux INP, INRAE, I2M Bordeaux, Bordeaux, France

1. Introduction

Numerical modelling of human tissues is increasingly used in research, both for clinical applications and for the improvement of safety systems. It is therefore essential to continue to develop models to better understand the biomechanical behavior of these tissues, for both physiological and non-physiological loading. The biomechanical behavior of the fascia fata is still poorly understood. However, this connective tissue surrounding the thigh muscles has a function as a stabilizer of the lateral cavity (Peabody and Bordoni 2022) making muscle contraction more efficient.

Few mechanical characterization tests have been performed on this tissue, mostly with unphysiological boundary conditions (Pancheri et al. 2014; Otsuka et al. 2018). Bulge inflation tests could reproduce *in vivo* loading of fascia lata, and such tests showed promising results for the characterization of anisotropic tissues (Jayyosi et al. 2016). In a previous study, Muth-Seng et al. (2017) proposed a Discrete Element Modelling (DEM) approach to simulate the fascia under uni-axial tensile tests.

Based on this previous work, the objective of this study is to develop the DEM approach for bulge tests of the fascia lata for its elastic behavior.

2. Methods

2.1. Microstructure of the fascia lata

The fascia lata is a well-organised tissue consisting of bundles of collagen fibres bound together by a soft proteoglycan matrix. The fibres are organised into two layers called the longitudinal and transverse layers, each oriented in a distinct fibre direction. The angle between the two fibre directions is approximately 70° and the longitudinal fibres are about four times larger than the transverse fibres. The collagen fibre bundles are wavy when the tissue is relaxed.

2.2. Discrete element model – geometry

Based on this microstructure, a discrete element model was developed, adapted from previous work on living tissues (Roux et al. 2015; Muth-Seng et al. 2017). A 6 mm diameter disc of fascia lata was implemented in the model. The distance between the layers was 0.335 mm. The model consisted of two types of nodes and three types of links.

The first type of node was longitudinal. These nodes had a diameter of 246 µm, which corresponds to the average fibre diameter measured by Pancheri et al. (2014). The second type of node was the transverse node, which had a diameter of 61.3 µm. The distance between the centre of two nodes of the same fibre was set to 0.8 times the diameter of a node. The distance between the centre of two fibres was set at 0.05 mm plus the diameter of the nodes of the layer. The angle between the two fibre families was 70°.

The three types of links were the matrix links connecting both layers and the fibers of the same layer and the longitudinal and transverse links. Matrix links were generated using three different Delaunay triangulation algorithms. Two of these algorithms were used to realise a 2D triangular mesh on both layers. The third Delaunay was used to connect the two layers. The geometry was generated using Python.

2.3. Discrete element model – material properties

The links were modelled as springs. The collagen fiber springs had a randomly distributed slack strain. The spring stiffness of the matrix was equal to the spring stiffness of the collagen fibers when two fibers were in contact. The collagen properties were taken from the literature (Muth-Seng et al. 2017) and the proteoglycan behavior was taken from previous studies (Roux et al. 2015). The mechanical parameters are shown in Table 1.

2.4. Boundary conditions and simulation

The simulations were performed on the software GranOO (Granular Object Oriented, www.granoo.org).

Table 1. Mechanical parameters of the fibers.

Parameters	Stiffness (Nm)	Slack strain	Max strain
Longitudinal	132830	0.02 ± 25%	0.20
Transverse	33477	0.02 ± 25%	0.20
Matrix	1506		0.30

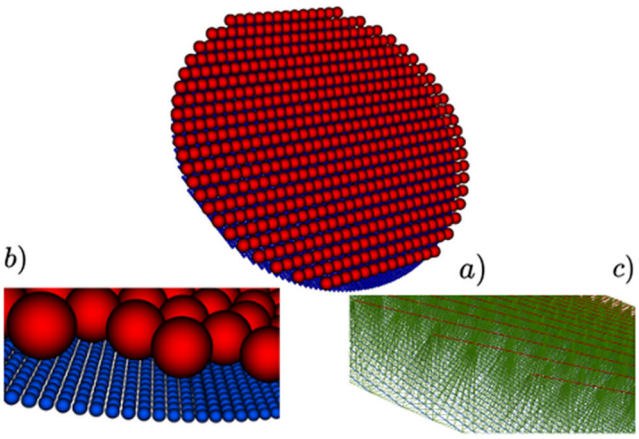


Figure 1. Longitudinal nodes and links are in red, transversal nodes and links are in blue and matrix links are in green. (a) Sample used for the simulation. (b) Zoom on the different nodes. (c) Zoom on the links.

To simulate a bulge test, the perimeter of both layers was fully constrained so that they did not move, like it occurred in the experiments.

The sample was loaded by computing a force normal to each triangular face of the inner layer. A third of the computed force was then applied to the three nodes of the considered triangle. Thus, the actual force applied to any given node was the sum of the third of the force applied to each face around the node. The pressure applied to the sample started at atmospheric pressure and gradually ramped up to 2.5 bars.

2.5. Model evaluation

To assess the model validity, we compared qualitatively it to the experimental bulge tests pretest data conducted. The first point of validation was the deflection induced by the anisotropy. As the longitudinal fibers are stiffer than the transverse one, the deflection should be greater in the transverse direction than in the longitudinal direction. The second point of validation was the distribution of the superficial displacement and the max deflection obtained in both the experiment and the simulation.

3. Results and discussion

The model, shown in Figure 2, was made up of 9245 nodes and 41,820 bonds. Preliminary bulge tests were simulated on the sample. The bulge of the sample exhibited heterogeneous deflection as expected. The displacement field was similar to the one obtained during the pretests. The maximal deflection was 0.6 mm.

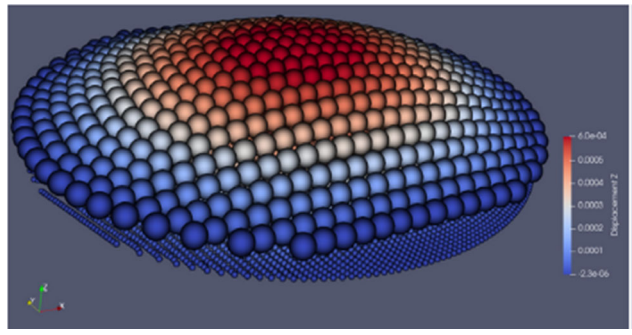


Figure 2. Displacement along Z axis in meter for a bulge test simulation.

During the pretest the maximal deflection was 4 mm for a 6 cm sample. The simulation returned us a 0.6 mm deflection for a 6 mm sample. Although both deflections are close, the main difference between the tests are the loading time. The simulation loaded the sample with 2.5 bar in 0.01s in order to keep the computation time low and not in 30s like in the pretest. The absence of relaxation in the springs may explain the difference in the results. By keeping the experiment time in mind preliminary simulation model can be validated.

4. Conclusions

The results obtained from the preliminary tests are promising. The method developed during this research should be adaptable to any human fibrous and layered tissue. As long as the mesostructure of a tissue is known, this modeling technique is possible and could contribute to a better understanding of its biomechanical properties.

References

Jayyosi C, Coret M, Bruyère-Garnier K. 2016. Characterizing liver capsule microstructure via in situ bulge test coupled with multiphoton imaging. J Mech Behav Biomed Mater. 54:229–243. doi:10.1016/j.jmbbm.2015.09.031.

Muth-Seng C, Gras LL, Roux A, Laporte S. 2017. Modelling of fascia lata rupture duringtensile tests via the discrete element method. Comput Methods Biomech Biomed Eng. 20:147–148.

Otsuka S, Yakura T, Ohmichi Y, Ohmichi M, Naito M, Nakano T, Kawakami Y. 2018. Site specificity of mechanical and structural properties of human fascia lata and their gender differences: a cadaveric study. J Biomech. 77:69–75. doi:10.1016/j.jbiomech.2018.06.018.

Pancheri FQ, Eng CM, Lieberman DE, Biewener AA, Dorfmann L. 2014. A constitutive description of the anisotropic response of the fascia lata. J Mech Behav Biomed Mater. 30:306–323. doi:10.1016/j.jmbbm.2013.12.002.

Peabody T, Bordoni B. 2022. Anatomy, bony pelvis and lower limb, fascia lata. St. Petersburg (FL): StatPearls Publishing.

Roux A, Haen T-X, Lecompte J, Iordanoff I, Laporte S. 2015. Rupture of the muscle-tendon complex in tensile test. comparison between experimentations and discrete element modeling. Comput Methods Biomech Biomed Engin. 18(Suppl 1):2046–2047. doi:10.1080/10255842.2015.1069616.

KEYWORDS DEM; fascia lata; bulge test; fibers

alexandre.lagache@ensam.eu

Modeling spheroids rheology

C. Verdier[a] and L. I. Palade[b]

[a]CNRS, LIPhy, Université Grenoble-Alpes, Grenoble, France;
[b]Institut Camille Jordan, CNRS, INSA-Lyon, Université de Lyon, Villeurbanne, France

1. Introduction

Cancer tumours are synonyms of poor vital prognostic and vary in size and aspect, depending on the location, cell invasiveness and neighboring tissues. They can also contain extracellular matrix (ECM) in different amounts, while cells can possibly synthesize their own matrix. Recent research has focused on tumour models, known as spheroids, obtained using cell culture in controlled conditions. They are good models since they are simple to obtain, have a round geometry and allow to test various drugs. Previously several authors tried to understand the effect of internal stresses within the spheroid (Ambrosi et al. 2017; Guillaume et al. 2019) and others studied the effect of an osmotic pressure (Dolega et al. 2021) applied to the spheroid. An important aspect of such spheroids is to determine their macroscopic behaviour, i.e. whether they can be considered as simple elastic media or poro-visco-elastic systems. Recently data on the viscoelastic properties of spheroids containing various collagen content was obtained (Tsvirkun et al. 2022) and reinforcement of the viscoelastic properties was observed. Here we analyze this data further and present an emulsion model (Palierne 1990) capable of predicting the global rheology of the spheroid based on the individual components, e.g. cells and the collagen matrix.

2. Methods

2.1. Cells, collagen and spheroids

Cells were epithelial bladder cancer cells (invasive type, ATCC, HTB-4, Manassas, VA). They were cultured in T25 flasks using RPMI 1640 medium (Gibco, St Aubin, France) in an incubator at 37 °C, in a 5% CO_2 humid atmosphere. Note that they had been transfected for actin-GFP using a plasmid, therefore they can be visualized when using fluorescence.

Collagen I gels (2 mg/mL) were prepared from rat tail solutions (BD Biosciences) and mixed with culture medium. NaOH (0.1 M) was added to adjust the pH at 7.4 at 4 °C. Then polymerization was achieved at 37 °C during 30 min.

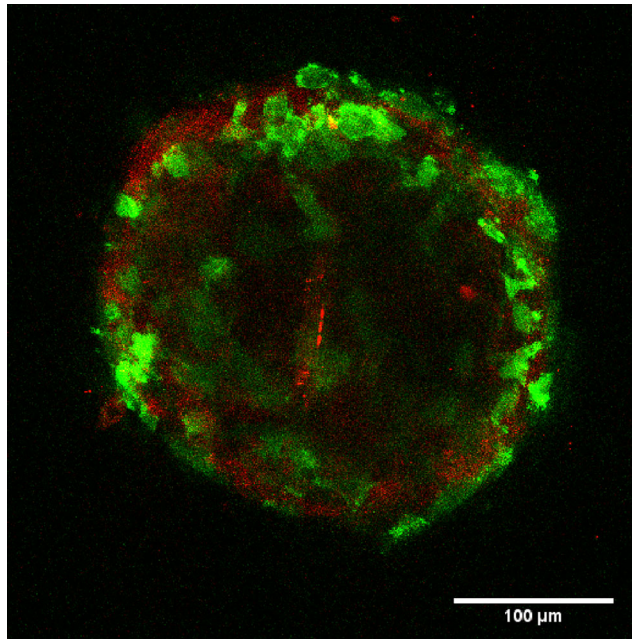


Figure 1. Confocal microscopy image of a spheroid prepared in culture medium containing 0.01 mg/mL collagen. T24 cells are in green, collagen in red.

Spheroids were prepared as described previously (Tsvirkun et al. 2022) in hanging droplets of culture medium. Rat tail collagen (type I) was also included in the RPMI medium at lower concentrations (from 0 to 0.03 mg/mL) until 5000 cells were added to the solution. Spheroids formed after 3 days with a nice round shape, although it seemed that spheroids were more difficult to prepare without collagen. A characteristic confocal microscopy image is shown in Figure 1 where the spheroid showed a compact shape with fluorescent cells in green and collagen (0.01 mg/mL) could be observed in the red channel, using reflectance confocal microscopy. This showed in particular that cells could collect the collagen to make bonds like in a scaffold.

2.2. Rheology characterization

Rheological data of collagen gels was gathered from previous works using low frequency (0.1 Hz–10 Hz) classical plate-plate rheometry (Iordan et al. 2010) and complementary AFM experiments in the higher frequency range (1 Hz–1 kHz). AFM force modulation mode (JPK, Nanowizard NWII, Berlin, Germany) was used as described previously (Abidine et al. 2021). Pyramidal tips (Bruker, MLCT, half angle 20°) were chosen to obtain pyramid-plane contact using Hertz model. Altogether, this allowed to cover several decades in frequency from 0.1 Hz to 1 kHz. The data is typical of a gel behavior with a plateau at low

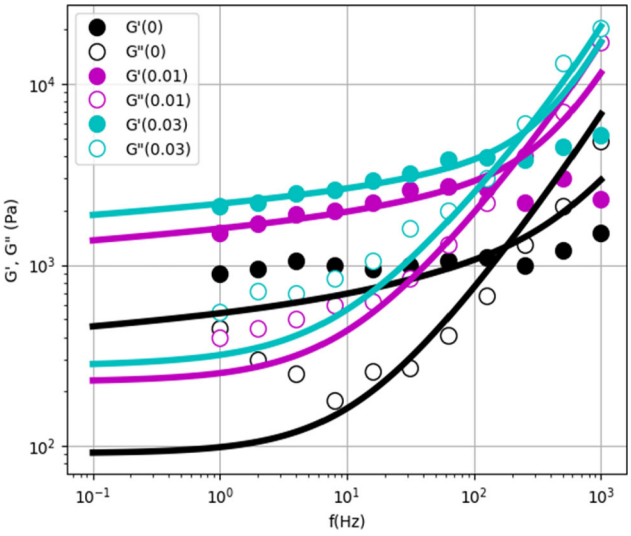


Figure 2. Rheological data and model predictions for three initial concentrations (0–0.01–0.03 mg/mL).

frequencies and a slowly increasing behavior as a function of frequency. This rheology was predicted using power-law behaviours (data not shown).

Cell microrheology was also carried out using AFM as well and exhibited also power law behaviours as reported before (Abidine et al. 2018).

Finally spheroids at three initial collagen content were characterized (0–0.01 mg/mL–0.03 mg/mL). In this case, large flat cantilevers (TL-NCL, Nanosensors, 38 µm width) were put in contact with the spheroids (Tsvirkun et al. 2022). Here we only show the data for spheroids with these initial collagen contents in Figure 2. Full points represent the elastic shear modulus (G') whereas open symbols correspond to the loss shear modulus (G").

2.3. Emulsion model for viscoelastic systems

From the knowledge of viscoelastic data for collagen and cells, we can assume, based on the images obtained (Figure 1), that there are two phases, one is the collagen one (similar to a gel), and the other one consists of the cells with radius R. Previous work on viscoelastic emulsions are available and have been considered to predict accurately the behaviour of such systems. In particular, Palierne (1990) proposed a model based on the rheology of both phases and interfacial tension was also included. The model reads as follows, in the large concentration case:

$$G^*(\omega) = (1 + 3\phi H^*(\omega))/(1 - 2\phi H^*(\omega)) \text{ where}$$
$$H^* = \{4\alpha/R(2G^*_m + 5G^*_i) + (G^*_i - G^*_m)D^*\}/\{40\alpha/R(G^*_m + G^*_i) + (2G^*_i + 3G^*_m)D^*\}$$
$$\text{and } D* = 16G^*_m + 19G^*_i.$$

$G^*_m(\omega)$ and $G^*_i(\omega)$ are respectively the viscoelastic properties of the matrix and the cells, whereas α is the adhesion energy per unit area, and R the cell radius.

3. Results and discussion

Based on this model, we tested our system using single cell viscoelastic properties, as well as collagen ones. Interfacial tension α was found to have little effect therefore a typical value of the adhesion energy was used (30 mN/m) for the simulations. On the contrary, $G^*_m(\omega)$ plays an important role and an optimal collagen concentration was found to be around 2 mg/mL, which could be related to the one in the extra-cellular space. Then the effect of cell content ϕ was studied and showed to play an important role. The best fits are found below.

Cell concentration was found to be optimal at respective values $\phi = 0.82$, 0.95 and 0.97, and the initial collagen content was increased to ~2 mg/mL. Thus it seemed that collagen addition reinforced the bonds between cells and reduced the intercellular spacing, which is an important finding of this work.

4. Conclusions

A viscoelastic emulsion model was used to predict the rheology of different spheroids. It was shown to be in good agreement with data obtained using AFM, after taking into account the properties of both phases measured separately. It could be a useful tool for further studies on the influence of the Extra-cellular matrix within tumours.

References

Abidine Y, Constantinescu A, Laurent VM, Sundar Rajan V, Michel R, Laplaud V, Duperray A, Verdier C. 2018. Mechanosensitivity of cancer cells in contact with soft substrates using AFM. Biophys J. 114(5):1165–1175. doi: 10.1016/j.bpj.2018.01.005.

Abidine Y, Giannetti A, Revilloud J, Laurent VM, Verdier C. 2021. Viscoelastic properties in cancer: from cells to spheroids. Cells. 10:1704. doi:10.3390/cells10071704.

Alcaraz J, Buscemi L, Grabulosa M, Trepat X, Fabry B, Farré R, Navajas D. 2003. Microrheology of human lung epithelial cells measured by AFM. Biophys J. 84(3):2071–2079. doi:10.1016/S0006-3495(03)75014-0.

Ambrosi D, Pezzuto S, Riccobelli D, Stylianopoulos T, Ciarletta P. 2017. Solid tumors are poroelastic solids with a chemo-mechanical feedback on growth. J Elast. 129(1–2):107–124. doi:10.1007/s10659-016-9619-9.

Dolega M, Zurlo G, Le Goff ML, Greda M, Verdier C, Joanny JF, Cappello G, Recho P. 2021. Mechanical behavior of multi-cellular spheroids under osmotic

compression. J Mech Phys Solids. 147:104205. doi:10.1016/j.jmps.2020.104205.

Guillaume L, Rigal L, Fehrenbach J, Severac C, Ducommun B, Lobjois V. 2019. Characterization of the physical properties of tumor-derived spheroids reveals critical insights for pre-clinical studies. Sci Rep. 9(1):6597. doi:10.1038/s41598-019-43090-0.

Iordan A, Duperray A, Gérard A, Grichine A, Verdier C. 2010. Breakdown of cell-collagen metworks through collagen remodeling. Biorheology. 47(5–6):277–295. doi:10.3233/BIR-2010-0575.

Palierne JF. 1990. Linear rheology of viscoelastic emulsions with interfacial tension. Rheol Acta. 29(3):204–214. doi:10.1007/BF01331356.

Tsvirkun D, Revilloud J, Giannetti A, Verdier C. 2022. The intriguing role of collagen on the rheology of cancercell spheroids. J Biomech. 141:111229. doi:10.1016/j.jbiomech.2022.111229.

KEYWORDS Spheroid; rheology; two-phase model

claude.verdier@univ-grenoble-alpes.fr

Quantitative analysis of the fibrous microstructure of 3D collagen gels

J. Romero Bhathal[a,b], L. Orgéas[b], M. Bouzid[b], L. Bailly[b], C. Verdier[a] and V. M. Laurent[a]

[a]CNRS, Liphy, Univ. Grenoble Alpes, Grenoble, France; [b]CNRS, Grenoble INP, 3SR, Univ. Grenoble Alpes, Grenoble, France

1. Introduction

Predicting and understanding cancer cell migration in the extracellular matrix is one of the most exciting and difficult problem in biophysics, biology or in medicine. For that purpose, 2D analyses of cell migration on collagen-coated substrates have been extensively carried out (Dembo and Wang 1999), but 3D studies represent a major technological and scientific challenge today. The first step is to characterize the collagen gels from morphological and mechanical standpoints. For example, Roeder et al. (2002) investigated how the collagen morphogenesis could be altered by the incubation temperature: some of the microstructural changes were detected such as fibril diameter or length observed using confocal reflection microscopy (CM), and related to the mechanical behavior of the collagen gels. However, the evolution of the microstructure (collagen volume fraction or fibril orientation) during mechanical testing of the gel still needs to be analyzed. Therefore, this study aims to process various synthetic collagen gels, and to analyze their 3D microstructure using confocal microscopy in order to determine precisely collagen volume fraction and fibril diameter for gels prepared at two different polymerization temperatures.

2. Methods

2.1. Collagen gels preparation

Collagen gels were prepared using type I collagen from rat tail collagen solution (Corning, USA) at a concentration of 2 mg/mL to mimic human ECM. To ensure the gelation process, the solution was homogenized at 4 °C by slow stirring to obtain a pH of 7.4. Two temperature conditions were used during the collagen network morphogenesis: 37 °C and 23 °C. These two conditions are prone to induce different microstructures (Yang 2009), therefore they present an interest for this study. The gels were incubated for 1 h in a humid chamber (approximately 99% humidity). Two samples, of 25 µL each, were analyzed for each condition.

2.2. Confocal microscopy

Confocal reflectance microscopy (Leica TCS SP8) was used to visualize the microstructure of the collagen gels with the 63X magnification objective (Iordan 2010). The 633 nm HeNe laser was used for reflectance. For each sample, two stacks of images were acquired at two different spatial resolutions (2X and 4X) to analyze the distribution of the volume fraction of collagen fibrils, i.e. with voxel sizes of $0.18 \times 0.18 \times 0.36$ µm^3 and $0.09 \times 0.09 \times 0.36$ µm^3 respectively.

2.3. Image processing

The images obtained with the collagen gels were very noisy (Figure 1), and the standard segmentation tools (based on a fixed greyscale threshold) were not able to achieve proper fibril segmentation. Instead, we used the Trainable Weka Segmentation 3D plugin of Fiji, based on machine learning algorithms (Arganda-Carreras 2017). No preatreatment of the images was done before using Weka. By manually training the plugin to segment objects with various contrast and diameters, we could isolate the fibrils from the rest of the gels. We could then estimate the volume fraction of collagen fibril, obtained by dividing the number of voxels of the fibrous phase by the total number of voxels in the regions of interest. As a first rough approximation, we validated this value by comparing the diameter of the fibrils in the binary image and the CM image.

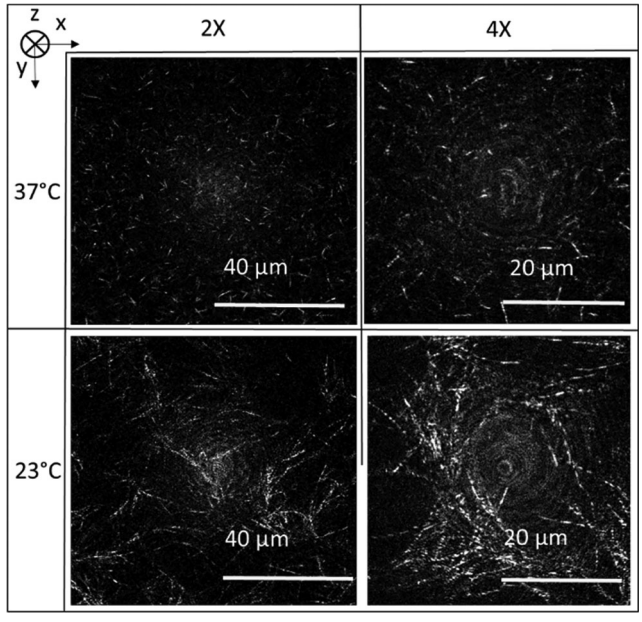


Figure 1. 2D in-plane slices of the collagen gels observed at two different scales and two gelation temperatures.

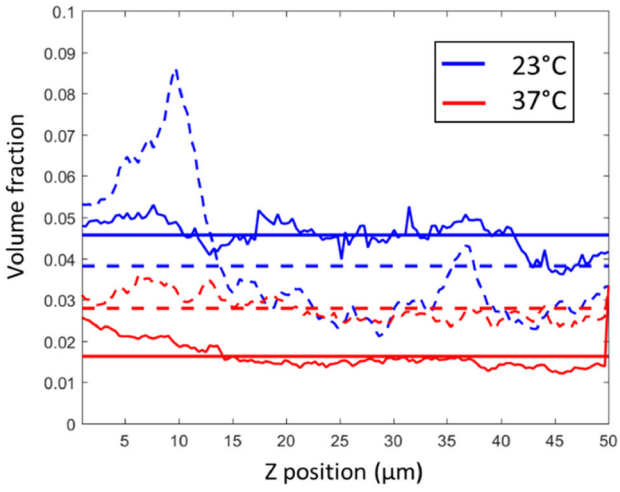


Figure 2. $\varphi_m$of the two samples calculated for each condition for each image of the stack (50 μm). the Dotted line presents the results for 4X, whereas the continuous line is for 2X. Finally, the straight line presents the mean over the volume (2X and 4X).

3. Results and discussion

3.1. Visual morphological analysis

Figure 1 shows typical 2D slices obtained by using confocal microscopy, emphasizing rather well the multiscale architecture of the synthetized nanoscale collagen fibrils, assembling to form micron-scale fibril bundles (or fibers). We showed the grayscale images because observing the fibrils is easier for the eye than with the binary images. The top image shows a gel sample incubated at 37 °C at two different scales. The bottom image shows the gels incubated at 23 °C. The collagen gel polymerized at 37 °C contain short and individual fibrils, homogeneously distributed in the gel. At 23 °C, collagen fibrils are longer and thicker. These results are in agreement with the literature (Yang 2009). The typical diameters of fibrils were measured around 371 ± 53 nm and 488 ± 57 nm for 37 °C and 23 °C (mean + std), which is coherent with the literature data (Roeder 2002).

3.2. Quantification of volume fraction

Figure 2 shows the evolution of the mean volume fraction of collagen fibrils (φ_m) along the thickness of the gel, for the two imaged samples at two different scales, i.e. with two different ROIs: φ_m is higher for the gels polymerized at 23 °C, whatever the ROI. Note that variations obtained around the mean values at either 23 °C or 37 °C are small.

In addition, we observe a difference between the observation at 2X and 4X for each condition. For example, at 37 °C, φ_m is close to 0.016 at 2X, while it is 0.028 at 4X. There are two hypotheses to explain this effect. First, the segmentation itself may be the source of the problem. The image quality at 2X is not the same as at 4X, so the trainable Weka segmentation method could have an effect. Indeed, the major limitation of this technique comes from the user, as the thinner and lighter fibrils are lost in the training. The second hypothesis is that the volume fraction distribution is highly heterogeneous. Such a heterogeneous spatial distribution could have an impact on the mechanical properties of the gels and requires a deeper study of the volume fraction distribution at different scales, and the use of more relevant structural descriptors.

4. Conclusions

In this study, we prepared collagen gels at two different polymerization temperatures and proposed a method to analyze their 3D microstructure through image processing techniques. The results show significant differences in microstructure. At 23 °C, the collagen gels have longer and thicker fibrils with a high fibril content. At 37 °C, the fibril bundles are thinner, shorter and exhibit a lower fibril content. We also observed an improved fibril distribution at a smaller scale and need further analysis to determine the size of the Representative Elementary Volume (REV) to later analyze the macroscopic mechanical properties. Work is currently on-going to complete such analyses and probe other microstructural observables such as length distribution and 3D orientation of fibrils. Next step will be to subject these fibrous media to various physiological loadings and to study the strain-induced variations of all these 3D microstructural descriptors.

Acknowledgements

JRB is thankful for financial support from LabEx Tec21 (Investissements d'Avenir: grant agreement No. ANR-11-LABX-0030). The other authors are members of LabEX Tec21.

References

Arganda-Carreras I, Kaynig V, Rueden C, Eliceiri KW, Schindelin J, Cardona A, Sebastian Seung H. 2017. Trainable Weka Segmentation: a machine learning tool for microscopy pixel classification. Bioinformatics. 33(15):2424–2426. doi:10.1093/bioinformatics/btx180.

Dembo M, Wang Y-L. 1999. Stresses at the cell-to-substrate interface during locomotion of fibroblasts. Biophys J. 76(4):2307–2316. doi:10.1016/S0006-3495(99)77386-8.

Iordan A, Duperray A, Gérard A, Grichine A, Verdier C. 2010. Breakdown of cell-collagen networks through

collagen remodeling. Biorheology. 47(5–6):277–295. doi: 10.3233/BIR-2010-0575.

Yang YL, Leone LM, Kaufman LJ. 2009. Elastic moduli of collagen gels can be predicted from two-dimensional confocal microscopy. Biophys J. 97(7):2051–2060. doi:10.1016/j.bpj.2009.07.035.

Roeder BA, Kokini K, Sturgis JE, Robinson JP, Voytik-Harbin SL. 2002. Tensile mechanical properties of three-dimensional type I collagen extracellular matrices with varied microstructure. J Biomech Eng. 124(2):214–222. doi:10.1115/1.1449904.

KEYWORDS Collagen; 3D gels; image processing; microstructural description; confocal microscopy

julia.romero-bhathal@univ-grenoble-alpes.fr

Quasi-static brain dura mater biaxial tensile testing: preliminary results

M. Evin[a], N. Bailly[a], C. Delteil[a,b], A. Melot[c] and L. Tuchtan[a,b]

[a]Laboratory of Applied Biomechanics, Marseille, France; [b]Lab affiliation; [c]Clairval Hospital, Marseille, France

1. Introduction

Characterization of the dura mater is needed in order to provide accurate material properties for numerical simulations in both traumatic and physiological application especially in the spinal cord (Bailly et al. 2020; Beauséjour et al. 2022). Biaxial mechanical characterization of the dura mater has been reported in human brain dura samples by De kegel et al. (2018) using an anisotropic Gasser–Ogden–Holzapfel (GOH) model and in ovine spinal cord dura by Shetye et al. (2014) using transverse isotropic Gasser and anisotropic Gasser model. Both studies used three different tested ratio of strain rate between axis (1:1,1:0.5,0.5:1 and 1:1,1:2,2:1 respectively). Comparison of constitutive model on an equi-biaxial tensile test study has also be provided in the spinal cord (Evin et al. 2022).

While identification of constitutive model coefficient is using optimisation methods which has been greatly optimised in the recent years (Roux et al. 2020), analysis of biaxial tensile test with different strain ratio between axis is rarely described in the literature apart from its use in constitutive model identification.

This study provides preliminary results of biaxial tensile testing of porcine brain dura mater with identification of anisotropic Gasser constitutive model.

2. Methods

2.1. Samples preparation and thickness measurements

Extraction of dura mater from one porcine brain (domestic pig, 90–100 kg, 8 months) was performed with care in removing the top part of the skull bone avoiding ear structures.

Thickness measurements was performed according with Sudres et al. (2020) as measurement of the side of the cut sample included in agar at three location of the dura (posterior, center and anterior) at an equal distance from the crania fossa (15.4 ± 3.1 mm, 12*10 thickness measurements).

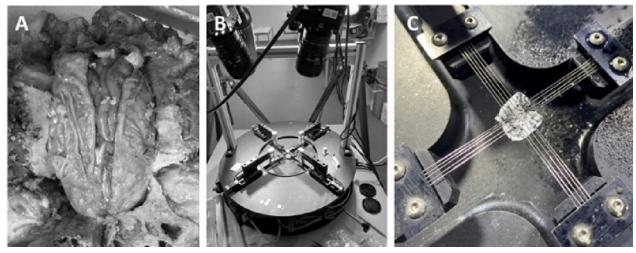


Figure 1. Sampling preparation (a), biaxial tensile test set up (B) and sample on the test system (C).

2.2. Biaxial tensile tests

Biaxial tensile test system consists in four step motors (Zaber, Vancouver, Canada) attached to 5 rakes and four load cells (50 N, sensitivity 0.001 N) controlled by a HBM PMX system (HBM).

Biaxial tensile testing consisted in tensile velocity of 0.1 mm/sec with 5 different axis ratio tests: 1:1, 1:2, 2:1, 1:4 and 4:1 (c11, c12, c21, c14, c41), randomized for each sample and with a threshold of 0.6 mm (8.57%) for each axis. Initial length between rake is 7 mm resulting in strain rates between 0.014 to 0.057 s^{-1}.

2.3. Data post-processing and statistical analysis

Piecewise bi-linear fit was performed on each of the strain-stress curves computed as engineering strain and stresses insuring maximum of r^2 criteria for both part of the fit. Elastic modulus is then computed as the slope of the second linear fit (the first depicting the toe region). The engineering stress and strain were computed respectively computed as the ratio of the tensile force and the initial cross-section area taking into account the thickness of the sample and the elongation at time t along one axis direction divided by the initial length in this direction. Definition of the anisotropic Gasser model is reported as per (Shetye et al. 2014) two fibre populations are considered with (β, γ) describing the orientation of the fibres with respect to circumferential axis and ($\kappa 1$, $\kappa 2$) the degrees of fibre dispersion for each population. Additionally, invariants of the right Cauchy Green tensor are defined as follows: $I_4 = \lambda_1^2 cos^2\beta + \lambda_2^2 sin^2\beta; \quad I_6 = \lambda_1^2 sin^2\gamma + \lambda_2^2 cos^2\gamma.$ The strain energy function of the constitutive model is defined as follow:

$$W = C_{10}(I_1 - 3) + C_{20}(I_1 - 3)^2 + \frac{k_1}{2k_2}\left[e^{k_2\{\kappa_1(I_1-3)+(I_1-3\kappa_1)(I_4-1)\}^2} - 1\right] + \frac{k_3}{2k_4}\left[e^{k_4\{\kappa_2(I_1-3)+(1-3\kappa_2)(I_6-1)\}^2} - 1\right] \quad (1)$$

Table 1. Elastic moduli on each axis and anisotropic Gasser model coefficients (averaged on all tests).

Piecewise bi-linear fitting					
	c11	c12	c14	c21	c41
Elong (Mpa)	7.96	7.86	10.42	5.42	3.87
Ecirc (Mpa)	6.69	2.61	3.73	9.37	8.62
Gasser model coefficients					
C_{10} (MPa)	C_{20}(MPa)	k_1(MPa)	k_2(-)	κ_1(-)	β (rad)
0.017 ± 0.006	0.297 ± 0.06	0.31 ± 0.14	123.5 ± 92.8	0.196 ± 0.05	0.227 ± 0.09
k_3(MPa)	k_4(-)	κ_2 (-)	γ (rad)	r^2	Rmse (MPa)
0.89 ± 0.74	117.32 ± 109.7	0.24 ± 0.09	0.51 ± 0.41	0.98 ± 0.007	0.02 ± 0.02

The matrix part of the constitutive model is a Yeoh hyperelastic model characterized by C_{10} and C_{20} in the anisotropic Gasser model (1) (Shetye et al. 2014). Coefficient identification was performed using lsqcurve fit from Matlab (Mathworks, Natick, USA).

3. Results and discussion

Thickness measurements ranged from 0.04 to 0.1 mm, mean value of 0.07 ± 0.02 mm. This was 3–6 time smaller compared to the reported 0.3 mm in dura spinal cord (Sudres et al. 2020). According to De Kegel et al. (2018), human brain dura mater thickness varies according with distance to the crania fossa tissue and was found 10 times higher than the reported values in swine. Thickness measurements should be furtherly investigated on several specimens.

Seven specimen were tested with the c11 (1:1) biaxial tensile testing condition and six with all five conditions resulting in 30 tests. Table 1 depicts the averaged coefficient value for anisotropic Gasser constitutive model fitted for all of the biaxial test.

Strain stress curves of the equi-axial tested condition are depicted in Figure 2 highlighted variability of the sample behavior. Constitutive model coefficient also presented in Table 1 resulted of the average of all fit of constitutive model for all tests. Differences in elastic modulus between axis should be noticed as well as changes in value depending on the tested strain rate applied to the other axis.

The changes in elastic modulus according with the tested condition and the non symmetry of the condition (c12 vs c21 and c14 vs c41) is highlighting the anisotropy of the material which should be furtherly investigating in both micro-structures and mechanical behavior. Additionally, viscoelasticity of the dura mater should be questioned and considered for further modelling of such structure.

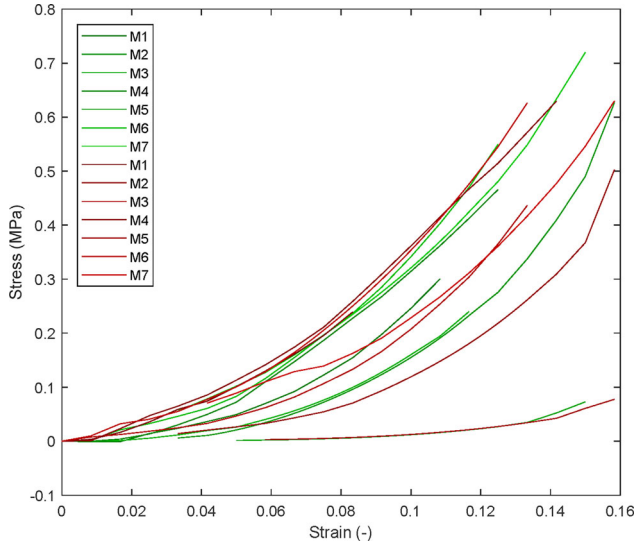


Figure 2. Experimental strain and stress curve for c11 condition (equi-axial tensile test) for both axis (longitudinal in green and circumferential in red).

Limitations of this work consist in the identification of constitutive model coefficient which depends on initial parameters and could depict local minimum. The number of samples is also a limitation of this study.

4. Conclusions

This work provides preliminary findings on bi-axial mechanical characterization of bovine dura mater.

Changes in elastic modulus according with strain rate used in the opposite ratio highlight the anisotropy and the viscoelasticity of the dura mater.

Acknowledgements

The authors thank Yannick Tillier and MathExpert for the development of the biaxial tensile test system.

References

Bailly N, Diotalevi L, Beauséjour M-H, Wagnac É, Mac-Thiong J-M, Petit Y. 2020. Numerical investigation of the relative effect of disc bulging and ligamentum flavum hypertrophy on the mechanism of central cord syndrome. Clin Biomech. 74:58–65. doi:10.1016/j.clinbiomech.2020.02.008.

Beauséjour M-H, Wagnac E, Arnoux P-J, Thiong J-MM, Petit Y. 2022. Numerical investigation of spinal cord injury after flexion-distraction injuries at the cervical spine. J Biomech Eng. 144:011011. doi:10.1115/1.4052003.

De Kegel D, Vastmans J, Fehervary H, Depreitere B, Vander Sloten J, Famaey N. 2018. Biomechanical characterization of human dura mater. J Mech Behav Biomed Mater. 79:122–134. doi:10.1016/j.jmbbm.2017.12.023.

Evin M, Sudres P, Weber P, Godio-Raboutet Y, Arnoux P-J, Wagnac E, Petit Y, Tillier Y. 2022. Experimental Biaxial tensile tests of spinal meningeal tissues and constitutive models comparison. Acta Biomater. 140(21)00777–7):446–456. doi:10.1016/j.actbio.2021.11.028.

Roux É, Tillier Y, Kraria S, Bouchard P-O. 2020. An efficient parallel global optimization strategy based on Kriging properties suitable for material parameters identification. Arch Mech Eng. 67(2). doi:10.24425/ame.2020.131689.

Shetye SS, Deault MM, Puttlitz CM. 2014. Biaxial response of ovine spinal cord dura mater. J Mech Behav Biomed Mater. 34:146–153. doi:10.1016/j.jmbbm.2014.02.014.

Sudres P, Evin M, Wagnac E, Bailly N, Diotalevi L, Laroche E, Melot A, Arnoux P-J, Petit Y. 2020. Quasi-static tensile mechanical properties of the porcine spinal meninges. Submitted at Journal of the Mechanical Behavior of Biomedical Materials.

KEYWORDS Dura mater; brain; biaxial tensile tests; anisotropic gasser

morgane.evin@univ-eiffel.fr

Reproducibility of a finite element model of the human femur in torsional load

Marc Gardegaront[a,b], Joshua Johnson[c], Audrey Auvinet[a], François Bermond[b], Cyrille Confavreux[d], Jean-Baptiste Pialat[d], Aurélie Levillain[b], Benjamin Miller[c], Jessica Goetz[c], David Mitton[b] and Hélène Follet[a]

[a]Univ Claude Bernard Lyon 1, INSERM, LYOS UMR 1033, Univ Lyon, Lyon, France; [b]Univ Eiffel, Univ Claude Bernard Lyon 1, LBMC UMR_T9406, Univ Lyon, Lyon, France; [c]Department of Orthopedics and Rehabilitation, University of IA Carver College of Medicine, Iowa City, IA, USA; [d]Centre Hospitalier Lyon Sud, Hospices Civils de Lyon, Lyon, France

1. Introduction

In 2020, there were an estimated 19.3 million new cases of cancer worldwide (Sung 2021), and around 80% of patients with malignant tumors will develop a bone metastasis (Du et al. 2010). Bone metastases affect the strength of bone, which may lead to fractures during daily activities. Accurate fracture risk assessment is crucial to give patients with bone metastases the best treatment. The current clinical gold standard for fracture prediction is the Mirels' score (Mirels 1989). However, this score has been proven to lack specificity (Piccioli et al. 2014). Hence, other failure prediction methods have been evaluated, mostly within the context of femoral metastases. Among these is CT-scan based finite element (FE) analysis, which allows for computation of failure load based on the geometry and bone density of the patient's femur. Most published FE models give good predictive results, though few have endured a reproducibility study (Gardegaront 2022). As FE models may be sensitive to operator-dependant variables and uncertainties in their experimental validation (Taddei et al. 2006; Amini et al. 2023), this study aims to explore the inter-institutional reproducibility of a FE model previously validated for prediction of femoral fracture under torsional load (Johnson et al. 2020).

2. Methods

Irregularly shaped defects were created in a series of eleven *ex vivo,* cadaveric specimens to mimic lytic femoral metastatic lesions. All femurs were scanned using a SOMATOM CT-scanner (Siemens Medical Systems, Forchheim, Germany, 120 kVp, 52 mA, field of view 11.5 cm, pixel size 0.2246 mm, slice thickness 0.75 mm) together with a calibration phantom to convert Hounsfield units to hydroxyapatite equivalent densities. Femurs were tested to failure in torsion, and a linear FE model with failure criteria was created and cross-validated using these femurs and associated experimental data (Johnson et al. 2020). FE models of these experiments were reproduced by an external lab using the information contained in the paper.

Some changes were made as some software and methods could not be strictly reproduced as mentioned below:

- CT segmentation was performed in different software (3D Slicer vs Mimics).
- Diaphysis constraint was modelled as null displacement for distal femur nodes vs in contact with a constrained distal support.
- Models were loaded with a constraint of nodal load to the nodes of the femoral head vs displacement of femoral head nodes in contact with the loading platen. The rigid rotation of these nodes was not constrained.
- The orientation method was different (diaphysis and neck axes were defined differently).
- The FE software was different (Ansys vs Abaqus).

The results of the original model were then compared to the results of the reproduced model. Furthermore, two different segmentations of each femur from two different operators were used with the reproduced model to quantify the influence of the inter-operator variability of the segmentation.

Agreement between experimental failure loads from each model were evaluated with the coefficient of determination (r^2). Accuracy between model and experimental failure loads was quantified with the mean of differences. Precision between each model (original and reproduced) and experimental failure loads was quantified with the standard deviation of the differences.

3. Results and discussion

There was a strong relationship between the predicted failure loads of the original models and those of the reproduced models ($r^2 > 0.84$, Figure 1 and Table 1). However, both operators of the reproduced model obtained systematically higher failure loads than the original models. There was good agreement in failure loads computed by both operators using the reproduced model ($r^2 = 0.98$, cf. Table 1).

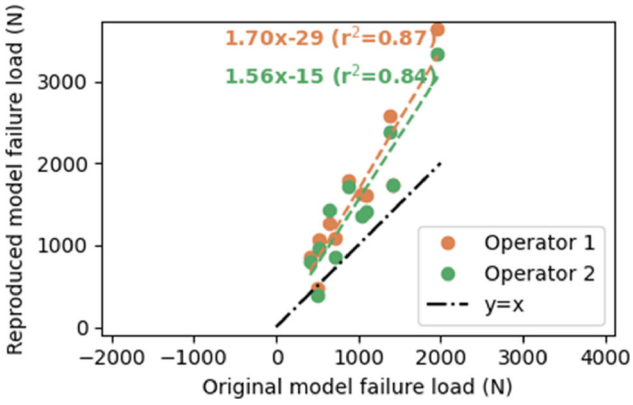


Figure 1. Relationship between original model results and reproduced model results for both operators.

Table 1. Coefficients of determination (r^2) between the experiment (exp.), the models and operators. Orig: Original; rep: Reproduced; Op: Operator.

	Exp.	Orig. Model	Rep. Model Op. 1	Rep. Model Op. 2
Exp.	1	0.88	0.93	0.88
Orig. Model	0.88	1	0.87	0.84
Rep. Model Op. 1	0.93	0.87	1	0.98
Rep. Model Op. 2	0.88	0.84	0.98	1

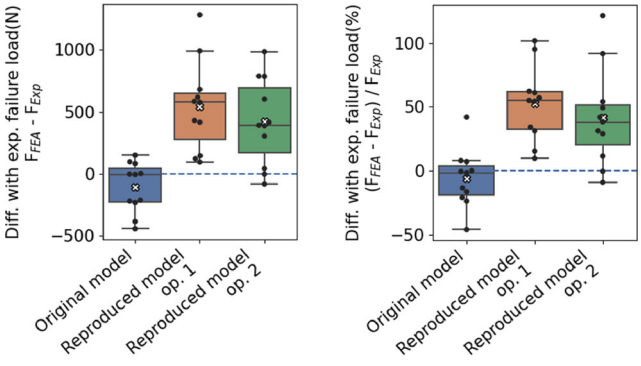


Figure 2. Differences between experimental failure load and predicted failure load for original model and reproduced model (both operators). left: Difference in newtons. Right: Relative difference in % of the experimental failure load.

The accuracy of the original model was −108 N, while for operators 1 and 2 of the reproduced model, it was 539 N and 419 N, respectively. The precision of the original model was 202 N, while for operators 1 and 2 of the reproduced model, it was 366 N and 348 N, respectively (Figure 2).

In a previous study (Gardegaront 2022), a non-linear model of femur failure load was reproduced with strong agreement between the original and reproduced models on the same dataset (r^2 = 0.95). The regression slope in that comparison was closer to 1 (slope =1.07) than for this study (slope >1.56, Figure 1). Even if there are methodological discrepancies between original and reproduced models (orientation, segmentation, etc.) in both studies, the previous study was done in compression and current one in torsion. This suggests that torsional load tests may be more sensitive to segmentation and orientation methods, and boundary conditions.

The results from both operators of the reproduced model suggests an operator dependent segmentation method gives variations on the predicted failure load (there is a difference of 14% between the regression slopes of both operators). However, both operators still obtain systematically higher failure loads than the original model, hinting at a significant contribution of other parameters such as the orientation method or the boundary conditions, on the model predictions.

4. Conclusions

This study aimed to reproduce a linear FE model of the torsional loading of the femur. A relationship between failure load from the original and reproduced model was found, but failure loads of the reproduced model were systematically higher. This suggests that the model may be sensitive to divergent modelling methods of the boundary conditions, segmentation, orientation methods or even the software used. In addition, variations of the predicted failure loads were found when using segmentations from different operators on the reproduced model. A global sensitivity study may explain which variables most affect the predicted failure load of the model, and thus yield information about which variables have to be carefully chosen to avoid inter-institutional reproducibility issues.

References

Amini M, Reisinger A, Synek A, Hirtler L, Pahr D. 2023. The predictive ability of a QCT-FE model of the proximal femoral stiffness under multiple load cases is strongly influenced by experimental uncertainties. J Mech Behav Biomed Mater. 139:105664. doi:10.1016/j.jmbbm.2023.105664.

Du Z, Zang J, Tang X, Guo W. 2010. Experts' agreement on therapy for bone metastases. Orthop Surg. 2(4):241–253. doi:10.1111/j.1757-7861.2010.00095.x.

Gardegaront M. 2022. ESB 2022. https://hal.science/hal-03739888.

Johnson JE, Brouillette MJ, Permeswaran PT, Miller BJ, Goetz JE. 2020. The effect of coordinate system selection on wrist kinematics. J Biomech. 106:109825. doi:10.1016/j.jbiomech.2020.109825.

Mirels H. 1989. Metastatic disease in long bones a proposed scoring system for diagnosing impending pathologic

fractures. Clinical Orthopaedics and Related Research®. 249:256–264. doi:10.1097/00003086-198912000-00027.

Piccioli A, Spinelli MS, Maccauro G. 2014. Impending fracture: a difficult diagnosis. Injury. 45(Suppl 6):S138–S141. doi:10.1016/j.injury.2014.10.038.

Sung H, Ferlay J, Siegel RL, Laversanne M, Soerjomataram I, Jemal A, Bray F. 2021. Global Cancer Statistics 2020: GLOBOCAN estimates of incidence and mortality worldwide for 36 cancers in 185 countries. CA Cancer J Clin. 71(3):209–249. doi:10.3322/caac.21660.

Taddei F, Martelli S, Reggiani B, Cristofolini L, Viceconti M. 2006. Finite-element modeling of bones from CT data: sensitivity to geometry and material uncertainties. IEEE Trans Biomed Eng. 53(11):2194–2200. doi:10.1109/TBME.2006.879473.

KEYWORDS Finite element model; bone; femur; fracture; reproducibility

helene.follet@univ-lyon1.fr

Skin-to-bone interaction: destructive and non-invasive mechanical characterization and modeling of porcine scalp

Y. Vallet[a], A. Baldit[a], C. Bertholdt[b,c], R. Rahouadj[a], O. Morel[b,c] and C. Laurent[a]

[a]CNRS UMR 7239 LEM3 – Université de Lorraine, Nancy, France; [b]CHRU-NANCY, Pôle de la Femme, Université de Lorraine, Nancy, France; [c]INSERM U1254, IADI, Vandoeuvre-lès-nancy, France

1. Introduction

Fasciae are collagenic tissues permitting a large but finite sliding between organs, but also between skins and its underlying elements (Camomilla et al. 2017). These tissues can be found at many scales, and in particular directly underneath the skin. Testing such materials remains a challenge due to high softness and hasty dehydration. The suction testing may constitute a suitable experimental procedure to characterize such tissues. However, the separation of these fibrous tissues contribution from the skin's is not simple at first and performing *ex vivo* experiment upstream is required. Although the peeling test is currently used in the industry, it has been rarely employed to assess the adhesion strength between two living tissues until recently (Larose et al. 2020) and on aorta (Brunet et al. 2021). Despite the strong interest in the modelling in these ubiquitous fibrous tissues, they remain mainly considered as a continuum media (Ganghoffer et al. 2022), or neglected. However, closer observations show a web-like structure and motivate the need of a more descriptive approach (Guimberteau and Delage 2012). The objective of the present study is threefold: we firstly show the feasibility of using a destructive peeling test as a new route to measure the skin-to-bone interaction. Secondly, we propose a geometric and computational approach to model the experimental peeling response of the tested biological tissues, with the help of an associated finite element (FE) model. Lastly, with the use of the proposed skin-to-bone model, we suggest the feasibility of using a non-invasive suction experiment to assess a *in vivo* quantification of the outermost fasciae rigidity.

2. Methods

2.1. Destructive experiments: peel tests

The developed peeling device consists in an *ad hoc* PMMA (Polymethyl methacrylate) translatable tank mounted on a tensile machine (Zwicki Z0.50 TN). The excised specimen of porcine scalps were thin bands composed of three different layers, the skin, the underlying tissues and the skull, and were harvested from two fresh pig heads coming from a local butcher shop. The excision zone was the region between ears, from the back of the head to the nose of the animal. The skull layer of each specimens was fixed at the bottom of the tank, and the skin layer was pulled upward by the tensile machine cross-head, at a speed of 1 mm s^{-1} till the total separation of skin from skull (see Figure 1A)). Two different specimens' widths and lengths were used, permitting to modify the skin-to-skull interface. The peeling force needed to separate the skin and skull layers was then assessed as a function of the prescribed displacement. These experimental data were then used in the geometric and computational approach to model the skin to bone interaction described below.

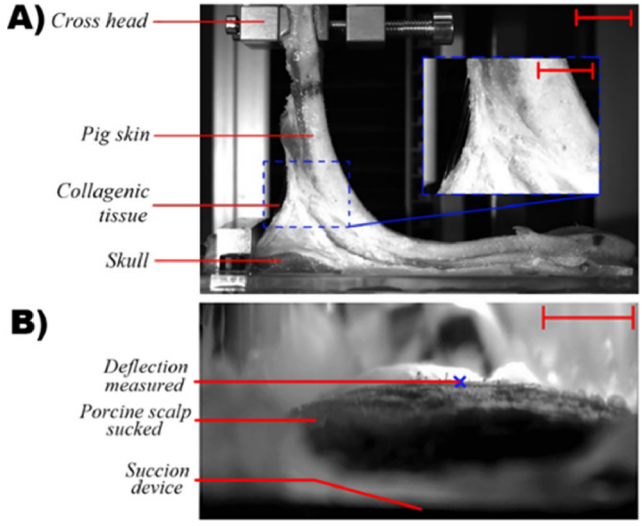


Figure 1. (A) Peeling test performed on porcine scalp. Scale: 20 mm, inset scale: 10 mm. (B) Suction test image. Scale: 10 mm.

2.2. Geometric and computational approach

The proposed geometric model took its essence in the peel-zone model (Pesika et al. 2007) where the adhesion strength is given by the zone where the separation occurs. We assumed that this adhesion strength was due to a population of spring-like elements whose behaviours were constituted of two intrinsic parameters, their stiffness and their length of failure. These two later parameters were identified with the help of an associated FE model (Abaqus/implicit, Figure 2A)) associated to the peeling test and with the help of the experimental dataset. The spring-like elements were modelled by a population of connectors (CONN3D2

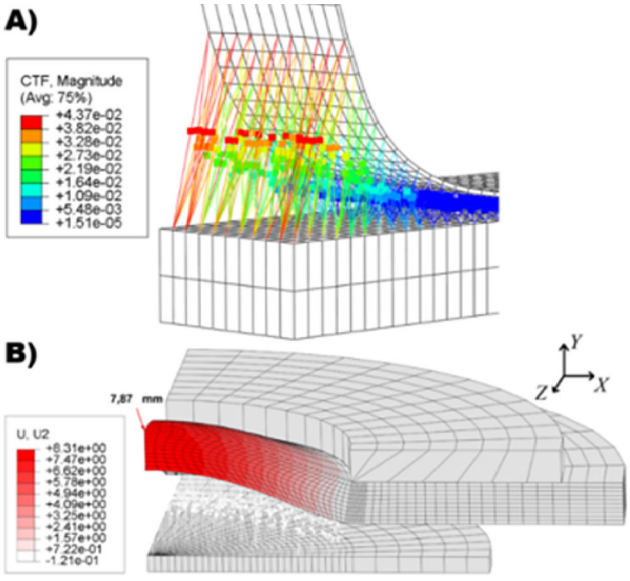


Figure 2. (A) Peeling simulation results exemple. CTF: Connector force (N). (B) Computational result of the suction test including the skin-to-bone interface. U2: nodes displacement along Y axis.

elements) randomly generated *via* an *ad hoc* MATLAB® code. These elements lied between two solid parts representing the scalp's skin and the skull. The two identified parameters were then used in a FE model associated with the non-invasive suction tests described below.

2.3. Non-invasive experiments: suction tests

The suction experiments were done with the help of a dedicated device made of a transparent PMMA cylinder emptied by a 60 mm diameter (coaxial) hole.

The pressure differential was established and maintained few seconds to permit the reading of its value on a manometer (*RS PRO, Germany)*. The deflection of the sucked tissues was filmed aside with a camera (*Allied Vision, Germany*) and then assessed manually from the processed images (MATLAB®).

2.4. Finite element modelling of the scalp's suction

The feasibility of the non-invasive characterization of the skin to bone interaction was assessed through the use of an associated FE model of the suction experiment, which included a population of connectors elements with their two identified intrinsic parameters. The model was composed of two rigid parts representing the porcine's skull and the suction device, together with the deformable scalp's skin. The connectors lied between the later solid and the skull. The material properties of the porcine scalp's skin were identified once separated from the skull using an Ogden constitutive law (order 1, with parameters identified from subsequent destructive tensile tests). A differential of pressure was applied to the skin and the deflection (i.e. numerical) was compared with experimental data.

3. Results and discussion

The separation of skin and bone induced a progressive tear at the skin interface or within the conjunctive tissues (as seen on Figure 1A)). To compare the results from both campaigns, the measured peeling force was normalized by the specimen width while the cross-head displacement was normalized by the skin-to-bone interface length (Figure 2A)). The variability of the experimental data measured may be attributed to the different specimen locations (i.e. in the scalp region), or the tearing point that varied within the thickness of the conjunctive tissues. The identification of the two connector parameters led to a good prediction of the normalized plateau-like experimental curves, commonly reported for adhesive interfaces. The experimental suction test on the porcine head led to a measured deflection of 7.1 mm (Figure 1B)), while the associated FE model (Figure 2B)) predicted 7.87 mm. Despite the errors associated with manual deflection measurement and from the identification of the connector's two parameters, the proposed FE model satisfyingly reproduced the experimental data.

4. Conclusions

By performing an upstream destructive experiment to fuel a geometric and computational modelling of the skin-to-bone interaction, a method for the non-invasive *in vivo* quantification of the underneath soft tissues contribution has been proposed and confronted.

Acknowledgements

The authors would like to thanks Maison Wagner from Marange-Zondrange, FRANCE for providing samples.

References

Brunet J, Pierrat B, Badel P. 2021. Review of current advances in the mechanical description and quantification of aortic dissection mechanisms. IEEE Rev Biomed Eng. 14: 240–255. doi:10.1109/RBME.2019.2950140.

Camomilla V, Dumas R, Cappozzo A. 2017. Human movement analysis: the soft tissue artefact issue. J Biomech. 62:1–4. doi:10.1016/j.jbiomech.2017.09.001.

Ganghoffer J-F, Reda H, Berkache K. 2022. 3 – Generalised continuum mechanics of random fibrous media. In: Silberschmidt VV, editor. Mechanics of fibrous networks. Amsterdam: Elsevier; p. 49–73. doi:10.1016/B978-0-12-822207-2.00003-9.

Guimberteau J-C, Delage J-P. 2012. Les tendons et le système de glissement multifibrillaire. Ann Chir Plast Esthet. 57(5):467–481. doi:10.1016/j.anplas.2012.07.002.

Larose AE, Dakiw-Piaceski A, Barbier MA, Larouche D, Gauvin R, Caruso M, Pope E, Germain L. 2020. Peel test to assess the adhesion strength of the dermal–epidermal junction in tissue-engineered skin. Tissue Eng C Methods. 26(3):180–189. doi:10.1089/ten.tec.2019.0268.

Pesika NS, Tian Y, Zhao B, Rosenberg K, Zeng H, McGuiggan P, Autumn K, Israelachvili JN. 2007. Peel-zone model of tape peeling based on the gecko adhesive system. J Adhes. 83(4):383–401. doi:10.1080/00218460701282539.

KEYWORDS Soft tissue testing; skin-to-bone modelling; peeling; suction; fasciae

yves.vallet@univ-lorraine.fr

Spatial resolution and repeatability of the human brain magnetic resonance elastography

S. Kurtz[a,b], C. L. Johnson[c], D. R. Smith[c], E. E. W. Van Houten[b] and B. Wattrisse[a]

[a]Laboratoire de Mécanique et Génie Civil, CNRS, Université de Montpellier, France; [b]Département de Génie Mécanique, Université de Sherbrooke, Sherbrooke, Canada; [c]Department of Biomedical Engineering, University of DE, Newark, DE, USA

1. Introduction

Magnetic Resonance Elastography (MRE) is a non-invasive, *in-vivo*, phase contrast MRI-based technique used to quantify material properties of soft tissues. Over the past decade, MRE has shown promising results in using stiffness as a biomarker of the brain. It captures small changes in the viscoelasticity of the tissue structure caused by neurodegenerative conditions such as multiple sclerosis (Millward et al. 2015) and Alzheimer's disease (Hiscox et al. 2020).

Estimates of heterogeneous material properties are provided using a nonlinear inversion (NLI) method. The associated algorithm uses a subzone decomposition to handle parallel computing and stabilization of the material properties estimates (Van Houten et al. 1999). This iterative identification method has been recently updated to a novel formulation where the indirect influence of noise through applied boundary conditions is avoided (Kurtz et al. 2023). The method has shown promising results on simulated and *in-vivo* data, demonstrating a significant improvement in the ability to obtain viable property maps in difficult configurations.

The aim of this study is to investigate the nearly-incompressible viscoelastic, isotropic mapping of the human brain using MRE and to provide updates on shear stiffness quantification with improved spatial resolution and repeatability using the novel, BC-free, isotropic NLI formulation. This study discusses optimal parametrization of the method and the outcomes for detecting smaller heterogeneities.

2. Methods

2.1. Data acquisition

The dataset from a previous study (Smith et al. 2022) was used in this study. The same healthy subject (F, 21 y) completed imaging sessions on a Siemens 3 T Prisma MRI scanner, with multi-excitation MRE scans performed in both anterior-posterior (AP) and left-right (LR) directions. Vibrations of each excitation were applied at 50 Hz. MRE acquisition used a 3D multiband, multishot spiral sequence (Johnson et al. 2014) with a $2.0 \times 2.0 \times 2.0\,mm^3$ isotropic resolution grid and a field-of-view of 240×240 x $128\,mm^3$. The acquisition protocol was repeated three times for each excitation direction scan. Shear wave displacement fields were calculated by unwrapping phase images and filtering with a Fourier transform. Further details regarding the acquisition, excitation protocol, and displacement calculation can be found in the study by Smith et al. (2022).

2.2. Biomechanical property estimation

Viscoelastic material properties maps ($\sim 3.2 \cdot 10^6$ points) associated to shear stiffness (μ) and damping ratio (ξ) were estimated for each dataset using the BC-free, isotropic NLI formulation. To investigate spatial resolutions gains, reconstructions were processed using two different regularization strategies: total variation (TV) minimization and spatial filtering (SF) smoothening. TV acts as a direct influencer during the inverse problem minimization process by assuming local homogeneity of the tissue which leads a softening of the sensitivity to noise without penalizing large gradients (Goenezen et al. 2011). On the other hand, SF has an indirect impact on the reconstructions process: it stabilizes the iterative progression by applying a Gaussian smoothening on the identified material properties (Van Houten et al. 1999). Regularizations were realized by coupling four sizes of SF sizes (σ_{SF}), and seven TV weights (α_{TV}). Optimal regularizations parameters are obtained using both statistical and visual assessment.

3. Results and discussion

The optimal TV parameter is first selected through visual assessment, by fixing the SF size to its minimum value for each reconstruction of a single dataset. When the TV weighting is low, reconstructed regions tend to overestimate stiffness ($\mu > 6\,kPa$), while highly TV-weighted maps exhibit abnormally high levels of homogeneity due to over-regularization. An intermediate parameter ($\alpha_{TV} = 1 \cdot 10^{-16}$) is chosen. This investigation is extended by analyzing the SF influence, as shown in Figure 1. Individual reconstructions of SF sizes lead to satisfying repeatability. Indeed, in this case, with a fixed SF size, the maximum absolute difference of the identified shear modulus averaged over the entire volume between repetitions is less than 25 Pa. The highest SF size presented in the figure ($\sigma_{SF} = 1.5\,mm$) is selected because it provides clear distinctions of heterogeneities while being coherent with the brain's structural topology. Figure 2 shows a

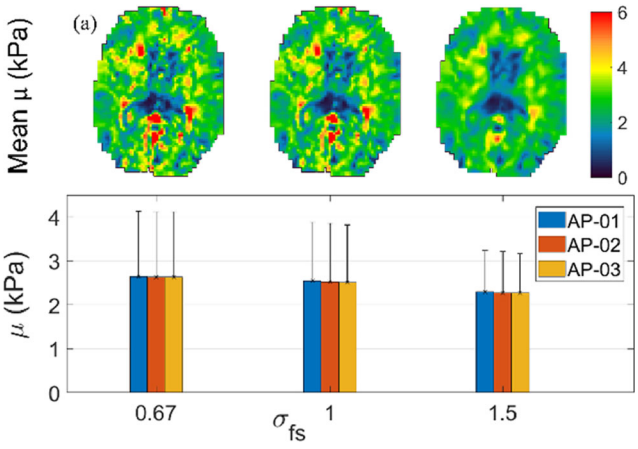


Figure 1. Reconstructions of shear stiffness for 3 SF sizes at the selected TV weight. (a): averaged maps. (b): mean and standard-deviation of each 3 AP excitations individual reconstructions (entire volume).

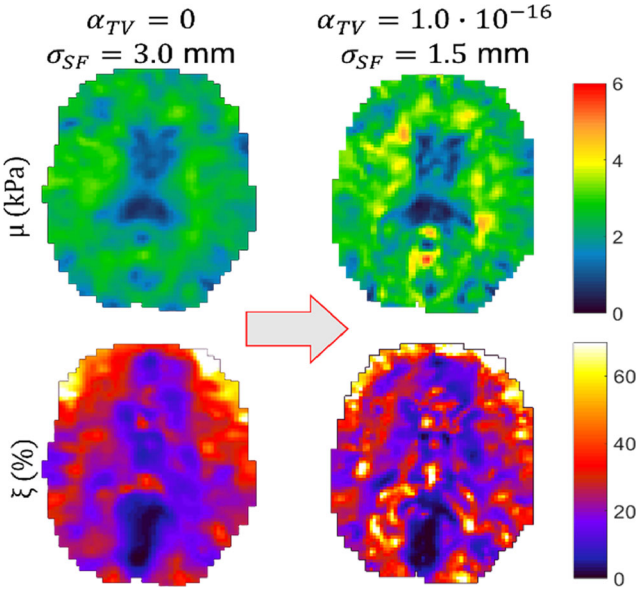


Figure 2. Reconstructed material properties of a single dataset using previous (left) and updated (right) regularization parameters.

visual synthesis of the identified moduli between the previous and updated parametrization. In the previous parametrization, the stability of the identifications was ensured by a large SF size ($\sigma_{SF} = 3$ mm). The updated parametrization reduces the SF by a factor of 2, indicating better tolerance to small gradients while limiting the presence of overestimated regions. These visual results allow for sharper stiffness-based distinctions of cortical and subcortical gray matter.

4. Conclusions

This study builds on stability gains achieved through recent updates in MRE data acquisition and NLI methods, to propose a new set of regularization standards that guarantee satisfying repeatability between reconstructions. Sub-centimeter heterogeneity appears to be detectable with high stability in this configuration. Analysis of noisier data could extend the scope of this study and allow for the eventual implementation of different regularization setup scenarios. Segmentation of brain regions of interest could greatly enhance the precision of these analyses.

Acknowledgements

This research was enabled in part by support provided by Calcul Québec and the Digital Research Alliance of Canada. The subject provided informed, written consent to participate in the study approved by the University of Delaware (DE, USA) Institutional Review Board.

References

Goenezen S, Barbone P, Oberai AA. 2011. Solution of the nonlinear elasticity imaging inverse problem: the incompressible case. Comput Methods Appl Mech Eng. 200(13–16):1406–1420. doi:10.1016/j.cma.2010.12.018.

Johnson CL, Holtrop JL, McGarry MDJ, Weaver JB, Paulsen KD, Georgiadis JG, Sutton BP. 2014. 3D multislab, multishot acquisition for fast, whole-brain MR elastography with high signal-to-noise efficiency: 3D multislab, multishot whole-brain MRE. Magn Reson Med. 71(2):477–485. doi:10.1002/mrm.25065.

Kurtz S, Houten EV, Wattrisse B, Laboratoire M. 2022. Bias restrictions for the MRE nonlinear inversion problem. MRE Study Gr ISMRM. 324:178521.

Hiscox LV, Johnson CL, McGarry MDJ, Marshall H, Ritchie CW, Van Beek EJR, Roberts N, Starr JM. 2020. Mechanical property alterations across the cerebral cortex due to Alzheimer's disease. Brain Commun. 2(1):fcz049. doi:10.1093/braincomms/fcz049.

Millward JM, Guo J, Berndt D, Braun J, Sack I, Infante-Duarte C. 2015. Tissue structure and inflammatory processes shape viscoelastic properties of the mouse brain. NMR Biomed. 28(7):831–839. doi:10.1002/nbm.3319.

Smith DR, Caban-Rivera DA, McGarry MDJ, Williams LT, McIlvain G, Okamoto RJ, Van Houten EEW, Bayly PV, Paulsen KDand, Johnson CL. 2022. Anisotropic mechanical properties in the healthy human brain estimated with multi-excitation transversely isotropic MR elastography. Brain Multiphys. 3:100051. doi:10.1016/j.brain.2022.100051.

Van Houten EEW, Paulsen KD, Miga MI, Kennedy FE, Weaver JB. 1999. An overlapping subzone technique for MR-based elastic property reconstruction. Magn Reson Med. 42(4):779–786. doi:10.1002/(SICI)1522-2594(199910)42:4<779::AID-MRM21>3.0.CO;2-Z.

KEYWORDS Elastography; brain; nonlinear inversion; regularization; viscoelasticity

samuel.kurtz@umontpellier.fr

Strain measurement by digital volume correlation applied to optical coherence tomography images: detection and monitoring of retina pathologies

M. Lelouarn[a], J.-B. Marcel[a], J.-C. Dupré[b], P. Doumalin[b] and N. Leveziel[a]

[a]CHU Poitiers Service d'ophtalmologie; [b]Institut Pprime, UPR 3346, Université de Poitiers-CNRS, Poitiers, France

1. Introduction

Optical Coherence Tomography (OCT) is an observation technique that has many applications in medicine such as gastroenterology, dermatology, gynecology or neurosurgery. Ophthalmologists are increasingly using this device to observe the retina and detect changes associated with the onset or treatment of pathologies such as age-related macular degeneration, diabetic retinopathy and glaucoma. This device provides a series of cross-sectional images of the retina which creates a 3D image and gives a volume representation of the retina. It is then possible to use Digital Volume Correlation (DVC) to measure displacement and deformation fields inside the retina. There are some studies in the literature about the use of DVC with OCT images but transfer this measurement technique to image series obtained from a commercial OCT device commonly used by ophthalmologists was not done. The proposed 3D strain measurement opens the possibility to enrich medical examinations with a quantitative evaluation of local strains of retinal tissues allowing (i) to finer detect transformations of tissues initiating a pathology, (ii) to know the mechanical state of tissues. The determination of the geometry and the thickness of the retina layers on slices are currently available on OCT but they do not provide this data.

DVC was adapted to the morphology and local contrasts of retinal layers and applied to images from the commercial device used by ophthalmologists at Poitiers hospital. The first results showed the potential of the approach and quantified mechanical solicitations due to a surgery.

2. Methods

2.1. OCT, samples and volumes acquisition

The tests have been realized with HRA + OCT SPECTRALIS device from Heidelberg Engineering company (Marcel 2021). This system allows to observe the retina around the fovea on an area of 9×9 mm2 and a depth up to 2 mm.

2.2. Strain measurement inside the retina

Displacement and strain measurements of retina are made using DVC technique (Tran 2013). As the retina has a basin-shaped morphology and these tissues are a stack of layers with different contrasts, DVC has been adapted to ensure a possible and reliable measurement. The developed technique includes a preliminary detection of lower and upper retinal layers in both images (initial and deformed, Figure 2a,b) and allows to automatically determine the area of interest between these two lines, the measurement points and the initial displacement values necessary for DVC.

3. Results and discussion

3.1. Measurement performance

The technique has been applied in-vivo to healthy retinas as shown Figure 1a. Two volumes are successively recorded without motion. Figures 1b and c show an example of displacement fields obtained by DVC with and without adaptation. The adapted method gives a more regular displacement field than with usual DVC. The obtained field is not a random field centered on zero because of the motion of the patient during the acquisition. Nevertheless, it is

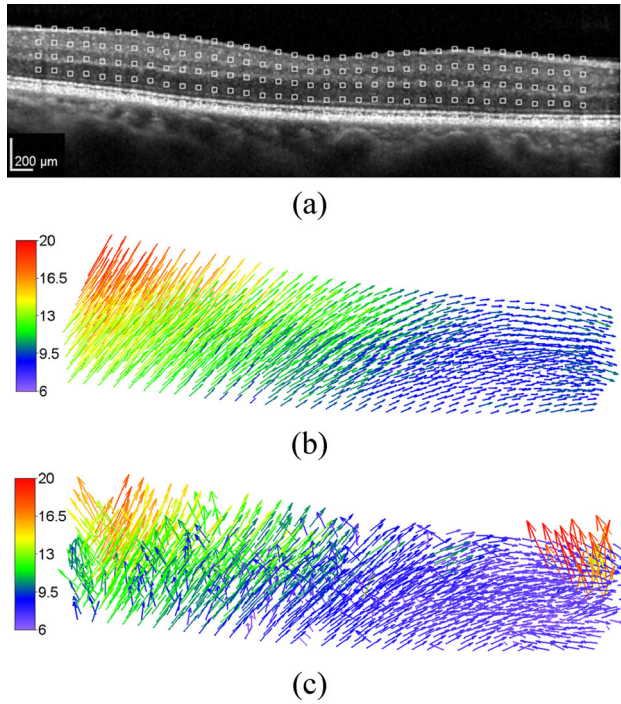


Figure 1. (a) Measurement points in a slice, displacement field (in voxels, 1 voxel =6 µm) obtained (b) by adapted DVC (c) by usual DVC.

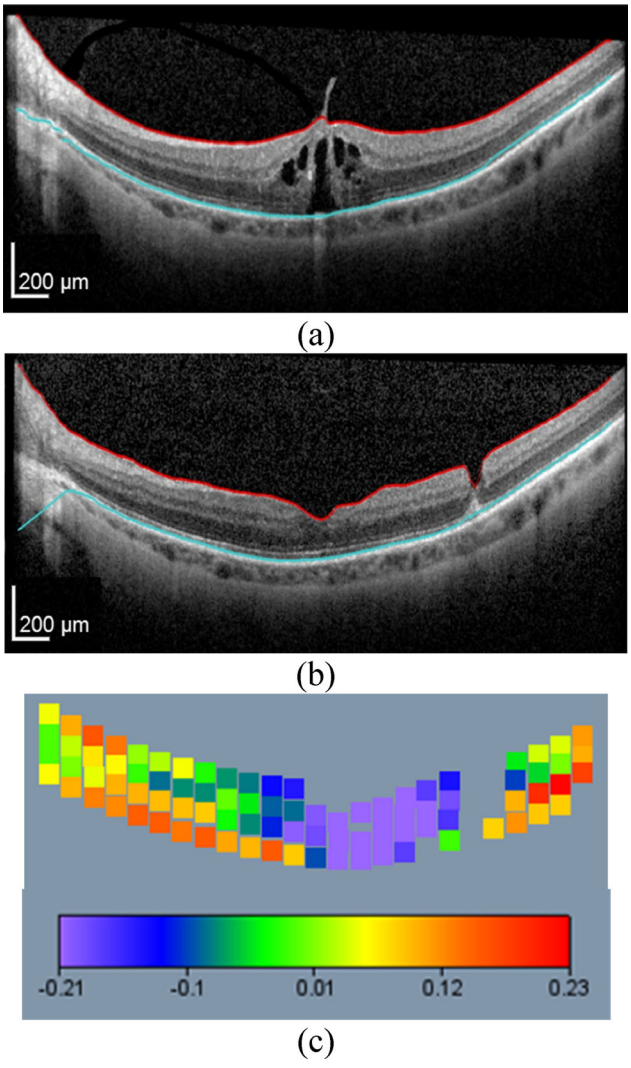


Figure 2. median plane of retina, (a) before surgery and (b) after surgery, detection of layers (blue RPE, red ILM), (c) vertical deformations.

possible to evaluate the absolute strain uncertainty (strains supposed null for two successive scans). of the same order in the three directions, about 3%.

3.2. An example of application

Figure 2a shows the case of vitreo-macular traction, a pathology that deforms the retina and therefore leading to a distorted image for the patient. In this case, this traction could have been eliminated by vitreo-retinal surgery (Figure 2b). Figure 2c shows vertical deformations (Ascan direction) between both states in the median plane. We are then able to quantify thickness variations in this slice: in the center the retina shrinks (negative deformations of 21%) and resumes a normal thickness while on the edges the thickness of the retina increases more weakly (positive deformations of 10 to 15%). This analysis shows that the surgery has freed the tension stresses in the retina, the architecture of the tissue is modified and the thickness is more homogeneous.

4. Conclusions

This first work on 3D strains measurement inside the retina shows that adapting DVC to OCT images makes measurement possible and reliable. The precision obtained by each direction allows, for example, to quantify the transformations that retinal tissues undergo following repair surgery. This approach is then currently applied to know mechanical state of tissues after surgery and will be soon used to monitor the stretching of tissues for exudative age-related macular degeneration.

References

Marcel JB. 2021. Suivi et quantification des déformations rétiniennes par tomographie à cohérence optique, utilisation de la corrélation d'images numériques. thèse de docteur en médecine septembre.

Tran H, Doumalin P, Delisée C, Dupré JC, Malvestio J, Germaneau A. 2013. 3D mechanical analysis of low-density wood-based fiberboards using X-ray microcomputed tomography and Digital Volume Correlation. J Mater Sci. 48(8):3198–3212. doi:10.1007/s10853-012-7100-0.

KEYWORDS OCT; DVC; strain field; retina; ophtalmology

pascal.doumalin@univ-poitiers.fr

The role of mechanical damage in abdominal wall incisional hernia: mechanical characterization and finite element modelling

B. Pillet[a], A. Bel-Brunon[b], G. Molnár[c], J. Molimard[a], Anicet Le Ruyet[d] and B. Pierrat[a]

[a]Mines Saint-Etienne, Univ Jean Monnet, Etablissement Francais du Sang, INSERM, U1059 Sainbiose, Centre CIS, Saint-Etienne, France; [b]INSA Lyon, CNRS, LaMCoS, UMR5259, Univ Lyon, Villeurbanne, France; [c]CNRS, INSA Lyon, LaMCoS, UMR5259, Univ Lyon, Villeurbanne, France; [d]Medtronic – Sofradim Production, Trévoux, France

1. Introduction

Abdominal wall (AW) incisional hernia (AWIH) is one of the most frequent complications in visceral surgery. This condition, associated with poor incisional healing, has been correlated with environmental and genetic risk factors (Liang et al. 2017) (e.g. diabetes, obesity), but also with the surgical closure technique. In addition, the use of a prophylactic mesh has become the standard of care. Despite tremendous advances in treatment, complications remain and reported recurrence rates are still high for high-risk patients, up to 30% (Gignoux et al. 2021). To better understand the causes of occurences and improve treatment outcomes, this study investigates the mechanical behaviour of mesh-reinforced AWs after midline laparotomy closure. There are still significant gaps in our understanding of the causes of occurence and the factors that contribute to repair failure, which involves damage mechanics. Furthermore, the success of the midline closure depends on both patient-specific factors (e.g. body mass index (BMI), age, risk factors such as diabetes) and surgical decisions (e.g. use of a mesh, suturing technique). To address this challenge, this study proposes a parametric computational model of a repaired AW based on the finite element (FE) method. We assume that the development of incisional hernia is directly related to damage phenomena in the tissue or mesh, and since weak areas are not known *a priori*, a phase-field damage formulation is used to predict possible initiation sites. Previous studies have provided mechanical data to identify the mechanical parameters of the intact AW (Astruc et al. 2018). However, damage and rupture of these tissues have not been studied experimentally. As our model requires such data, the mechanical parameters were determined by an extensive experimental campaign including an animal study. Tissues were collected and tested at different times after surgery to obtain the necessary data.

The objective of this study is to better understand the mechanical behaviour of mesh-reinforced AWs after hernia repair and to identify potential factors that contribute to recurrence. This research is significant in improving the current understanding and treatment of AWIH, and ultimately in reducing the rates of recurrence and associated complications.

2. Methods

2.1. Mechanical characterization

An *ex vivo* animal study was designed to replicate as closely as possible the conditions of midline laparotomy closure. The study was conducted on female white pigs (weight range: 43–47 kg). The pigs were divided into four groups ($N = 23$): a first control group did not undergo any surgery. A 15-cm incision of the midline was performed on all other animals as well as the dissection of a 12×12 cm retro muscular space. These animals were divided in three groups: a group with an unrepaired ventral hernia, and 2 repair groups. The first repair group was sutured with the short bite technique, while the second group had an 23×8 cm additional mesh implanted in onlay. Mechanical characterisation was performed at three different time points: 2 days, 4 weeks, and 12 weeks after surgery. Tensile and peeling tests were carried out to quantify the mechanical properties of the AW tissues and the repair. The different components of the wall were tested: lateral and rectus muscles, Linea Alba (intact and sutured), the original and integrated mesh, the neo-tissues. Mechanical quantities, such as maximum load, tangent stiffness, cohesive and fracture energies, were extracted from the tests and analysed between the different groups at each time point. Assuming that the mechanical behaviour of the tissues is not species dependent, these properties were used to feed an FE model of the AW.

2.2. Finite element modeling

The repaired AW model consists of a region of interest including the Linea Alba (LA), segmented from the Visible Human Project, surrounded by the rectus muscles (RM). The different components (LA, RM, mesh, neo-tissues) of the AW were modelled using a hyperelastic anisotropic formulation. Damage was included using a phase field approach. The model was implemented in 2D in the Fenics FE framework.

The geometry was parametrised to describe different populations and surgeries. In the first category,

Table 1. Ultimate transverse tension T_{max} obtained from uniaxial tension for the different repair modalities at different integration times.

Tissue	Post-op. time	T_{max} (N/mm)
LA	Intact	6.0 ± 2.2
Sutured LA	2 days	1.5 ± 1.2
	4 weeks	6.2 ± 2.7
	12 weeks	2.6 ± 1.5
Sutured LA + mesh	2 days	4.5 ± 2.2
	4 weeks	7.7 ± 1.0
	12 weeks	4.4 ± 1.2

LA size and thickness as well as constitutive parameters can effectively represent different virtual patients (e.g. different BMIs). In the second category, four surgical cases can be generated: healthy, incision repaired with suture or mesh, and unrepaired incision. Initial suture tension, incision length, bite depth and bite width were also parametrised.

The loading scenario consisted of a preliminary closure of the AW incision by increasing the suture tension for sutured cases, followed by the application of longitudinal and transverse tensions to the boundaries of the model. These tensions were extracted from a full-scale 3D AW model for three loading conditions (supine, standing and coughing) which were simulated by increasing the abdominal pressure and activating the muscles for the latter case.

3. Results and discussion

Mechanical characterisation revealed the following highlights:

- The anisotropic nature of the intact LA was confirmed (stiffer in the transverse direction). No significant differences between supra- and infra-umbilical were found.
- The repair technique had a significant effect on the strength of the repaired LA, as shown in Table 1. Indeed, both ultimate transverse tensions (i.e. ultimate tensile force divided by sample width) and rupture energies were higher with the use of a mesh than with sutures alone at 2 days, 4 weeks and 12 weeks postoperatively.
- Peeling tests between the mesh and the underlying tissues showed that cohesive energy increased from 2 days to 4 weeks after surgery and then remained stable. This shows that integration is already almost complete at 4 weeks post-op.

Using this data, the FE model was used to observe the location and magnitude of the damage field, as shown in Figure 1. None of the cases resulted in a complete rupture for the simulated daily physiological activities. We found that the large-bite suture technique resulted in more damage than the small-bite technique, confirming clinical studies indicating higher recurrence for the former (Liang et al. 2017). The damage patterns found near the suture holes (Figure 1) were consistent with the comet's tail phenomenon due to suture migration. The use of a mesh helped to reduce damage in the covered area, although damage remained at the mesh-tissue interfaces. Finally, high BMI was associated with significantly higher damage at all postoperative time points, as reported in the clinical literature (Liang et al. 2017).

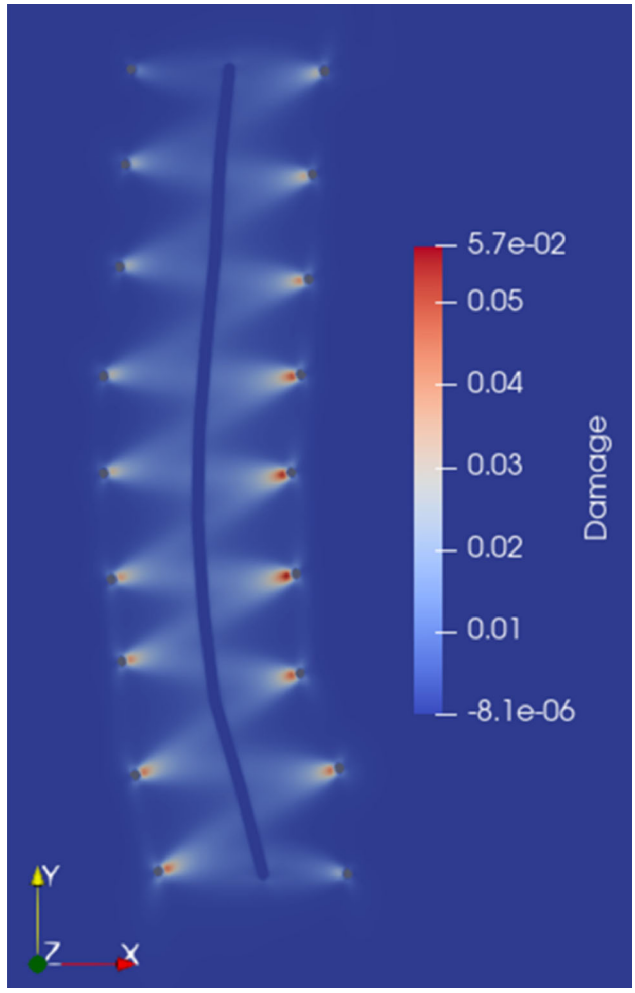


Figure 1. Damage field near sutures 2 days after surgery during a cough, obtained from the FE model.

4. Conclusions

This work provides the necessary tools and data to evaluate surgical techniques in terms of potential damage initiation in the AW tissues. The originality lies in the complete preliminary characterisation of the tissue behaviour, in particular during rupture, and the absence of a predefined failure path. This fully parametrised

model may become a patient-specific tool for visceral surgeons to reduce the recurrence of AWIH.

References

Astruc L, De Meulaere M, Witz JF, Nováček V, Turquier F, Hoc T, Brieu M. 2018. Characterization of the anisotropic mechanical behavior of human abdominal wall connective tissues. J Mech Behav Biomed Mater. 82:45–50. doi:10.1016/j.jmbbm.2018.03.012.

Gignoux B, Bayon Y, Martin D, Phan R, Augusto V, Darnis B, Sarazin M. 2021. Incidence and risk factors for incisional hernia and recurrence: retrospective analysis of the French national database. Colorectal Dis. 23(6):1515–1523. doi:10.1111/codi.15581.

Liang MK, Holihan JL, Itani K, Alawadi ZM, Gonzalez JRF, Askenasy EP, Ballecer C, Chong HS, Goldblatt MI, Greenberg JA, et al. 2017. Ventral Hernia Management: expert Consensus Guided by Systematic Review. Ann Surg. 265(1):80–89. doi:10.1097/SLA.0000000000001701.

KEYWORDS Incisional hernia; damage; characterisation; finite element modelling

pierrat@emse.fr

The soft tissues tension-compression asymmetry: challenges and solutions

N. Kamaei[a], A. Kazemi[a], M. A. Nazari[a,b], P. Perrier[c] and Y. Payan[b]

[a]School of Mechanical Engineering, University of Tehran, Tehran, Iran; [b]CNRS, Grenoble INP, TIMC, Univ. Grenoble Alpes, Grenoble, France; [c]CNRS, Grenoble INP, GIPSA-Lab, Univ. Grenoble Alpes, Grenoble, France

1. Introduction

Skeletal muscles behave in tension when activated. It is often supposed that they do not resist in compression (Liu et al. 2019) whereas such muscles and their surrounding soft tissues exert a passive resistance when compressed. Therefore, characterizing the muscle tissues' behavior under compression is essential. This was done for example by Nagle et al. (2014) who showed that the response of skeletal muscle tissue in tension/compression plays an important role in biomechanical simulations. Soft tissues have nonlinear and anisotropic elastic properties along with viscoelastic behavior (Takaza et al. 2014). Existing data from skeletal muscle tissue under tensile and compressive deformation has shown a significant tension-compression asymmetry (TCA) (Böl et al. 2022). Many researchers have worked on tensile deformations of soft tissues but only a few of them studied TCAand TCA has not been yet captured by current constitutive models using a unique set of material parameters (Takaza et al. 2014).

The aim of this paper is to study the deformation response of chicken pectoralis muscle under tension and compression and to investigate the capability of various hyperelastic models to represent the corresponding asymmetric behavior.

2. Methods

2.1. Experimental setup

Six specimens were harvested from pectoralis muscle of a two-month-old female chicken with an average body weight of 3 kg within 20 h post-mortem. Samples were cut to a proper size along the fiber directions for the corresponding tests. The three compression samples were cut to the size of $10 \times 10 \times 5$ mm to prevent buckling and the three tension samples were cut to the size of $27 \times 10 \times 10$ mm for having slender specimens. Load-to-failure tests were conducted on Santam STM-1 testing machine. Tests were performed at 1% per minute strain rate to minimize viscoelastic effects. No pre-tension was applied on tensile samples. Force data was recorded using a 6-kg ZEMIC load cell, MODEL L6D Class C3.

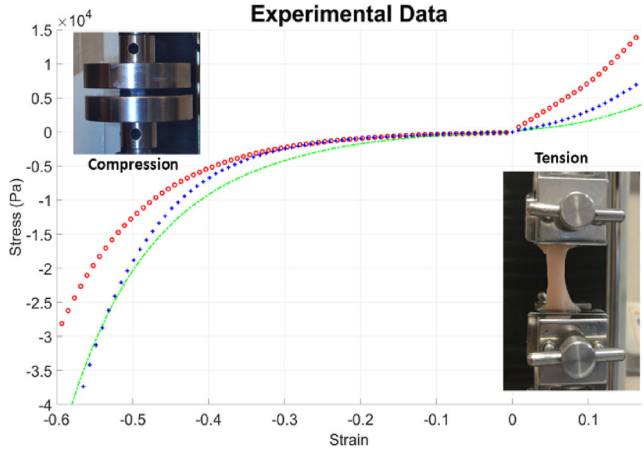


Figure 1. A sample uniaxial test data of pectoralis muscle along muscle fibers (tension and compression loadings were combined).

Ink lines were drawn at the muscle-clamp interface to confirm that the tests were performed without sample slipping.

2.2. Data processing

The strain was calculated as the elongation divided by the initial gauge length and the first Piola-Kirchhoff stress was computed as the force divided by the initial cross-sectional area. Ultimate stress and ultimate strain were taken as the stress and strain values at the point of material failure. The tensile data were combined with compression data. This combination was done for the samples harvested at same location and along the same fiber directions. The experimental stress-strain data is shown in Figure 1.

To find a suitable constitutive law, capturing the tissue behavior, different hyperelastic models available in the ANSYS© library were studied. This library is limited to isotropic models.

3. Results and discussion

As it can be seen on Figure 1, there is an obvious tension-compression asymmetry in uniaxial test. We picked up the most prominent asymmetric data to have their mechanical properties.

The chicken pectoralis muscle shows nonlinear behavior as most biological soft tissues. The apparent stiffnesses in tension and in compression at the same strain show large different orders of magnitude. For

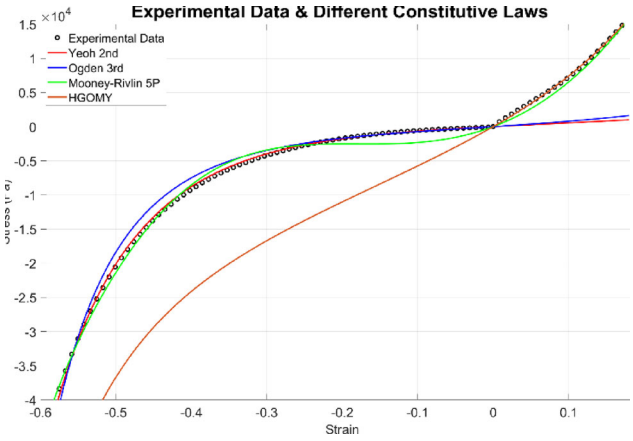


Figure 2. Three isotropic hyperelastic models to represent the TCA: 2nd order Yeoh, 3rd order Ogden and 5-parameter Mooney–Rivlin and a proposed transversely isotropic model (HGOMY).

example, at the maximum tensile stretch, the stress is about 12.4 kPa while at the equivalent compressive stretch, the magnitude of stress is about 0.68 kPa. This shows that the apparent stiffness in tension is about (12.4/0.68≈) 18 times higher than for compression.

To capture the tissue' behavior and its mechanical properties, we tried to fit our experimental data with most isotropic hyperelastic models available in ANSYS© library. Whereas hyperelastic models can well represent the tension and compression deformation responses separately, it seems necessary to check if such models can capture the tension-compression asymmetry with a unique set of material parameters. It is however evident that none of them can fully capture the slopes asymmetry observed at the origin (Figure 1) since such models have first order continuity at all points.

For fitting experimental data with different constitutive models, ANSYS© Workbench 2021 R1 was used. Among all the models tested, three are reported in this paper: 2nd order Yeoh, 3rd order Ogden and 5-parameter Mooney–Rivlin. Most of these models cannot capture the tension and compression behaviors at the same time with a unique set of parameters (Figure 2). Only the 5-parameter Mooney–Rivlin model provides a nice account of the tension-compression asymmetry.

The 5-parameter Mooney–Rivlin constitutive law is described by the following equation for strain energy density with respect to initial configuration:

$$\psi = C_{10}(I_1 - 3) + C_{01}(I_2 - 3) + C_{11}(I_1 - 3)(I_2 - 3) + C_{20}(I_1 - 3)^2 + C_{02}(I_2 - 3)^2$$

Table 1. 5-Parameter Mooney–Rivlin material constants.

C_{01} [kPa]	C_{02} [kPa]	C_{10} [kPa]	C_{11} [kPa]	C_{20} [kPa]
−49.0	14.5	54.4	−56.5	73.4

where I_1 and I_2 are the first and second invariants of Cauchy-Green strain tensor respectively. The corresponding obtained material parameters are given in Table 1.

In fitting the experimental results, the program assumed a fully incompressible hypothesis. This assumption needed to be verified. For this purpose, we have computed the Poisson ratio using DIC imaging and assuming isotropy. This ratio was found to be equal to 0.3 which seemed not realistic since muscular soft tissues are mostly composed of water with a ratio that should be near to 0.5. This meant that the hypothesis of isotropy is probably wrong. To overcome this difficulty, a new method was proposed to model the material behavior, with a transversely isotropic material and an exponential behavior along fibers, inspired from the HGO strain energy density:

$$\psi = c_1(I_1 - 3) + c_2(I_1 - 3)^2 + \frac{k_1}{2k_2}\left(e^{k_2(I_4-1)^2} - 1\right)$$

in which I_4 is the square of stretch ratio along fiber directions. The first term represents the matrix behavior and the second term shows the fiber properties. It is known that the fibers do not resist much in compression. Therefore, to estimate the parameters of ψ, the values c_1 and c_2 were first estimated using compression data only. Then, while keeping these values constant, the parameters describing fiber direction were estimated using tension data only.

Using the above algorithm, c_1 and c_2 were found equal to 1.12 kPa and 0.705 kPa respectively assuming full incompressibility. Keeping these constants fixed and using tension experimental data, the material constants k_1 and k_2 were found equal to 14.1 kPa and 0.79 respectively.

4. Conclusions

Fitting experimental data with constitutive laws that include many parameters is not classical. This can end to an oscillating behavior as it can be seen with the 5 parameters Mooney–Rivlin law. The fitted models first assumed an isotropy of the tissue. This assumption had to be revoked since the quasi-incompressibility of the tissue could not be guaranteed in that case. A new anisotropic constitutive law was introduced to take into account muscle fibre directions, but this law still lack to represent the strong

tension-compression asymmetry observed during the tests.

References

Böl M, Kohn S, Leichsenring K, Morales-Orcajo E, Ehret AE. 2022. On multiscale tension-compression asymmetry in skeletal muscle. Acta Biomater. 144:210–220. doi:10.1016/j.actbio.2022.03.034.

Liu H, Holzapfel GA, Skallerud BH, Prot V. 2019. Anisotropic finite strain viscoelasticity: constitutive modeling and finite element implementation. J Mech Phys Solids. 124:172–188. doi:10.1016/j.jmps.2018.09.014.

Nagle AS, Barker MA, Kleeman SD, Haridas B, Douglas Mast T. 2014. Passive biomechanical properties of human cadaveric levator ani muscle at low strains. J Biomech. 47(2):583–586. doi:10.1016/j.jbiomech.2013.11.033.

Takaza M, Cooney GM, McManus G, Stafford P, Simms CK. 2014. Assessing the microstructural response to applied deformation in porcine passive skeletal muscle. J Mech Behav Biomed Mater. 40:115–126. doi:10.1016/j.jmbbm.2014.08.019.

KEYWORDS Tension-compression asymmetry; soft tissues; finite deformation; transversely isotropic

manazari@ut.ac.ir

Cardiovascular and respiratory biomechanics

1D modelisation in retinal microvascular network: sensivity analysis, validation and application to stenosis in vascular diseases, page S103.
3D simulation of active thin structures in a viscous fluid and application to mucociliary transport, page S106.
A micro-poro-mechanical model of the lung parenchyma, page S108.
A numerical model to study the coupling between lung biomechanics and physiology, page S111.
Characterization of ciliary beating in chronic rhinosinusitis, page S114.
Comparison of mechanical and hemodynamic properties of custom-made silicone mitral valves, page S117.
Computational characterization of venous valve dynamics and associated hemodynamics, page S120.
Computational simulation of respiration-induced deformations of the renal arteries in AAA patients, page S123.
Contrast-enhanced micro-CT protocol for in-situ mechanical experiments of aortic thrombi, page S125.
How magnetic resonance elastography (MRE) could provide biomechanical property to complete computed tomography (CT) scan lung diagnostic?, page S128.
Improvement of the prediction of the vascular structure deformation induced by tools insertion in EVAR, page S130.
Increase of Wall Shear Stress in a vessel due to curvature, page S133.
Intracardiac hemodynamics: a preliminary parametric study, page S136.
Noninvasive estimation of pressure drop in arterial stenoses with color Doppler ultrasound, page S139.
Numerical and experimental investigation of the hemodynamics of surgical repair in severe pediatric coarctation, page S142.
Numerical hemodynamics simulation of 4D flow magnetic resonance imaging, page S145.
Numerical study of the deployment of a femoral artery self-expanding nitinol stent, page S148.
Uncertainty Quantification in Personalized Pulmonary Mechanics, page S150.

1D modelisation in retinal microvascular network: sensivity analysis, verification and application to stenosis in vascular diseases

L. Julien[a,b], S. Bonnin[c], M. Paques[b,d] and J.-M. Fullana[a]

[a]CNRS, Institut Jean le Rond d'Alembert, Sorbonne Universités, Paris, France; [b]INSERM, CNRS, Institut de la Vision, Sorbonne Universités, Paris, France; [c]Department of Ophthalmology, Rothschild Foundation Hospital, Paris, France; [d]CHNO des Quinze-Vingts, INSERM-DGOS CIC 1423, Paris, France

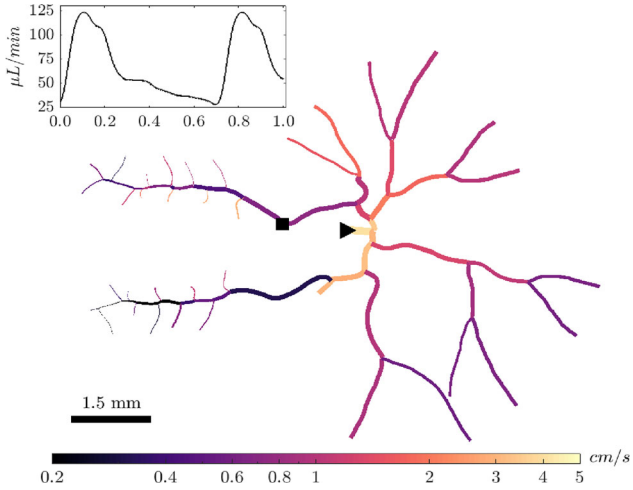


Figure 1. Snapshot of the velocity at time 0.5 s.

1. Introduction

Modeling techniques are an essential complement to clinical studies of the retina, as they provide access to non- measurable parameters through the network and enable the simulation of controlled disturbances or pathologies. In this work, we propose the development of a patient-specific 1D model of the arterial circulation in the retina. Our model is based on conservation laws and utilizes morphometric and velocimetric data obtained through clinical multimodal imaging to construct the network topology and impose realistic boundary conditions. Specifically, our model simulates blood flow from the Central Retina Artery (CRA, in the center of the network in Figure 1) ($144\mu m$) to the terminal smallest arterioles (10 μm). To validate our model, we perform a sensitivity analysis and compare its results to published data. Finally, we use our model to investigate the hemodynamic consequences of focal stenosis on retinal arteries.

Insert indicates the flow rate as function of time(s) in the CRA. Square : position of the stenosis.

2. Methods

2.1. Clinical flow and morphological data

We combine data from Adaptive Optic Ophthalmoscopy (AOO) and confocal Scanning Laser Ophtalmoscopy (cSLO) to build the retinal network of Figure 1. The network skeleton is extracted from AOO (resolution : 1 µm), cSLO (resolution : 8 µm) and some part are constructed numerically. There is 73 vessels, one input, and 35 outputs. Experimental Doppler Ultrasound data have been used to impose the flow at the entrance to the network, in the CRA (placed on the black triangle in Figure 1).

2.2. One dimensional flow modelisation

The 1D model derives from the Navier-Stokes axi-symmetrics equations integrated over the section:

$$\partial_t A + \partial_x Q = 0, \tag{1}$$

$$\partial_t Q + \partial_x \left(\frac{Q^2}{A}\right) + \frac{A}{\rho}\partial_x p = -8\pi\frac{\mu}{\rho}\frac{Q}{A}, \tag{2}$$

where A is the cross-sectional area, Q the flow rate, $\rho = 1$ g cm^{-3} the fluid density and µ the viscosity. The viscosity model is a combination of the Cross and Kiani models (Kiani and Hudetz 1990) to take in account non-Newtonian and Fahraeus-Lindqvist effects. We consider elastic vessels and junctions with a rigidity of $K = 1,8.10^9 g.s^{-2}cm^{-2}$. Area is related to pressure

$$\text{with : } \quad p = K\left(\sqrt{(A)} - \sqrt{(A_0)}\right). \tag{3}$$

More details can be found in Julien et al. (2023).

2.3. Senvitivity analysis of output boundary conditions

We present a modelisation for the output boundary conditions with a tree connecting the arterial network to the capillary bed. We computed the total resistance R_{term} of the tree to set purely resistive conditions for each terminal vessel. Thus imposed output pressure P_{out} is, depending of the output flow rate Q_{out} :

$$r \leq r_{cut} : P_{out} = P_c$$

$$\text{and } r > r_{cut} : P_{out} = P_c + R_{term}Q_{out} \tag{3}$$

The capillary pressure P_c is constant. The tree is constructed using geometric laws for the radii of daughter vessels (r_{D1}, r_{D2}) at junctions : $r_{D1} = \alpha r_M$

Table 1. Sobol indices and values use in simulations for output boundary condition variables.

Variables	α	r_{cut}	P_c
1st order Sobol – A	0.05	0.05	0.92
1st order Sobol – Q	0.45	0.26	0.16
Use in simulation	0.6	10 µm	11 mmHg

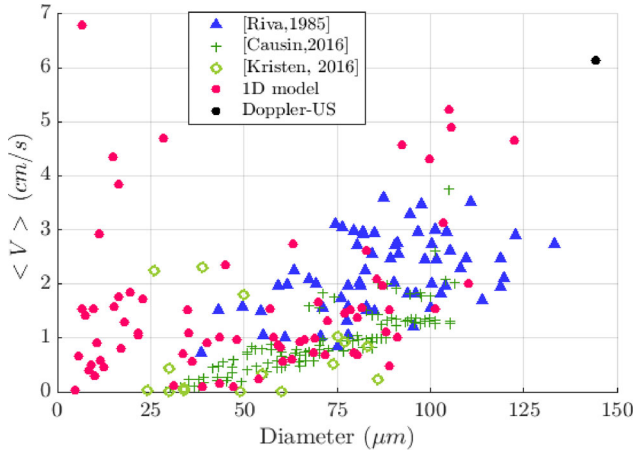


Figure 2. Mean velocity (cm/s) as diameter (µm). data from the 1D model compared to literature.

and $r_{D2} = \alpha\sqrt{0.4}r_M$ where r_M is the mother vessel's radius. Tree is constructed until reaching a cutoff radius r_{cut}. Then, we compute the resistance of each vessel of the tree using Poiseuille law.

The Sobol analysis provides a quantitative measure of the sensitivity of the model output (area and flow rate) to boundary conditions variables (α,r_{cut}, P_c). Mean values (on all vessels) of the 1st order Sobol analysis are presented in Table 1. Output flow rate is sensivitive to α and r_{cut}. The relative changes in output pressure causes multiple redistributions of flows. For the area, major changes are caused by P_c, indeed, they are directly linked in the model (3). So P_c takes over and crushes the effects of flow redistributions.

3. Results and discussion

3.1. Healthy case verification

We choose the network of a healthy patient. A result of the model is showed on Figure 1. It's a mapping of the velocity in the network at 0.5s of the cardiac cycle. This provides help to visualize how blood is distributed through the network. We will assess the performance of the 1D model by comparing it to published data. Figure 2 displays mean blood velocity for the 1D models' predictions, *in-vivo* experimental data (Riva et al. 1985) and data obtained from other models (Causin et al. 2016; Kristen et al. 2016).

3.2. Stenosis in vascular diseases

Stenosis is a common vascular anomaly in vascular diseases. For the pathological simulations we applied single and multiple stenosis to a third branch level vessel with a diameter of 87.9μm. For different lengths and degrees of severity, we observe consequences after the diameter constriction. As the severity or the length increases, a fall in time averaged blood flow appears. Initial results show that several consecutive stenoses have the same effect as a single stenosis of a length equal to the cumulative length of all stenoses ; if all stenoses have the same degree of severity.

4. Conclusions

The computational 1D model presented provides a tool to the study of the patient-specific blood flow in the retina. We also proposed a cap- illary connection model based on a structured tree. We showed that the flow distribution was rather sensitive to the boundary conditions parameters. Our verification of the model involved comparison with experimental and numerical data. The model values show the same order of magnitude and growth as the literature data for diameters above 25 μm. For the smallest diameters, the lack of data on a comparable system in the literature means that we cannot verificate the orders of magnitude obtained. Note the ongoing development of an experimental device to test this range of values.

We have studied pathological cases, single and multiples unilateral stenosis. The associated decrease in flow, localised after the stenosis, is sensitive to the geometry of the stenosis. Through this study, we hope to provide clinicians with clues for assessing the severity of microcirculatory pathologies affected by stenoses.

Acknowledgements

We wish to acknowledge Florence Rossant (ISEP), Philippe Bonnin (Hôpital Lariboisière) and Céline Chaumette (CIC-CHNO des XV-XX).

References

Causin P, Guidoboni G, Malgaroli F, Sacco R, Harris A. 2016. Blood flow mechanics and oxygen transport and delivery in the retinal micro- circulation: multiscale mathematical modeling and numerical simulation. Biomech Model Mechanobiol. 15(3):525–542. doi:10.1007/s10237-015-0708-7.

Julien L, Bonnin S, Paques M, Fullana JM. 2023. One dimensional modeling of microvascular hemodynamics in the retina using multimodal imaging. Phys Fluids. 35(6):061901. doi:10.1063/5.0152499.

Kiani M, Hudetz A. 1991. A semi-empirical model of apparent blood viscosity as a function of vessel diameter and discharge hematocrit. BIR. 28(1–2):65–73. doi:10.3233/BIR-1991-281-207.

Kristen A, Kelsey L, Wintermantel E, Doyle B. 2016. Fundus image based blood flow simulation of the retinal arteries. In: Joldes G, Doyle B, Wittek A, Nielsen P, Miller K, editors. Computational biomechanics for medicine. Cham: Springer. doi:10.1007/978-3-319-28329-6_13.

Riva C, Grunwald J, Sinclair S, Petrig B. 1985. Blood velocity and volumetric flow rate in human retinal vesels. Inv Oph Vis Sci. 26:1124–1132.

KEYWORDS Microvascular; retina; model 1D; hematocrit; vascular diseases; visual disorders

laureline.julien@dalembert.upmc.fr

3D simulation of active thin structures in a viscous fluid and application to mucociliary transport

A. Decoene[a], S. Martin[b] and C. Meziane[c]

[a]MAP5 (CNRS UMR 8145), Université Paris Cité, Paris, France; [b]IMB (CNRS UMR 5251), Université de Bordeaux, Bordeaux, France; [c]LMO (CNRS UMR 8628), Université Paris Saclay, Orsay, France

1. Introduction

This work deals with the mathematical modelling and the numerical simulation of active thin structures in a viscous fluid and its application to mucociliary clearance. Direct simulation aims at getting a better understanding of some of the mechanisms involved in mucociliary transport, in the perspective of analyzing the collective dynamics arising in the flow due to cilia beating, as well as their impact on the efficiency of the mucus transport.

The human lung is protected from inhaled particles, and allergens, by a thin liquid layer lining the surface of airways. This airway surface liquid (ASL) is composed of mucus, a Newtonian viscous fluid secreted by the epithelium, and a thin layer less viscous than the mucus, called periciliary layer (PCL) also secreted by the epithelium. Considering cilia as 1D structure, we investigate the velocity distribution of the mucus flow. We developed an original model which is based on a Stokes problem with nonlocal singular source terms: let V be the velocity of the fluid, and p its pressure, the equations in a 3D domain Ω are:

$$-div(\mu\nabla V) + \nabla p = \sum_{(i=1)}^{N} f_i[V]\delta_{\Gamma_i}, div(V) = 0$$

where μ represents the viscosity of the bifluid, and N the number of cilia. Here Γ_i denotes the 1D curve describing the centerline of the i-th cilia, and δ_{Γ_i} denotes the lineic Dirac distribution at Γ_i which makes the source term singular. Note that involved parameters have a physical significance and values are taken from the literature.

2. Methods

2.1. Slender-Body theory

In order to define the distribution of forces f along the thin structures immersed in the fluid, we use the so-called slender-body theory (Cox 1970; Mori et al. 2019). If $s \to \xi(s,t)$ is a parametrization of the position of the structure at time t in curvilinear coordinates, the expression of the force is defined by

$$f(\xi) = M_\xi\left(\partial_t\xi - \begin{pmatrix} u_b \\ 0 \\ 0 \end{pmatrix}\right),$$

where M_ξ is a matrix that depends (among other parameters) on ξ, and u_b is a term called 'bulk-flow' that models the damping of the flow onto the cilia. We approximate the bulk flow by the mean axial velocity of the fluid. This assumption makes the 3d system *nonlocal*.

2.2. Bifluid

The fluid is composed of two layers: in the lower part of the domain the periciliary layer (PCL) whose viscosity is similar to that of water ; in the upper part, mucus whose viscosity is 50–10,000 higher than in the PCL. Cilia beating mostly occurs in the PCL but it can reach the mucus during the effective stroke. The two layers are separated by an interface that is stable due to surface tension.

2.3. Surface tension

Surface tension acts on the mucus–PCL interface, it is associated to the following constraint: at the interface, normal velocity is zero, preventing fluid mass transfer between both phases and ensuring the stability of the interface between the PCL and the mucus.

2.4. Resolution

Existence and uniqueness of a solution to the nonlocal singular Stokes problem is derived in suitable functional spaces (using Babuska-Lax-Milgram theorem). As for the numerical resolution, the nonlocal property of the source term, induced by the bulk flow, makes the straightforward computation difficult. To skip this difficulty, we first compute the mean axial velocity $\overline{u}$. Through an averaging process we can find the ODE satisfied by $\overline{u}$ (interestingly, the reduced 1D model includes all the 3D features). Then we insert the mean axial velocity $\overline{u}$ into the source term of the 3D Stokes equations. This process reduces the computational cost, since the previous step now allows us to solve a classical Stokes problem (with singular source terms and velocity constraint at the PCL-Mucus interface).

3. Results and discussion

We have computed the flow produced by a dense forest of cilia, with data given by Table 1: we consider a

Table 1. Summary of data for fluid and cilia in the lungs (Fulford and Blake 1986).

Fluid			
Domain dimension:			
Axial direction	L_x	30.0	μm
Azimuthal direction	L_y	4.8	μm
Radial direction	L_z	10.0	μm
PCL viscosity	μ_1	1.0	mPa s
Mucus viscosity	μ_2	50.0	mPa s
Mucus-PCL interface	H	4.8	μm
Cilia			
Length of cilium	L	6.0	μm
Cross-sectional radius	a	0.1	μm
Beat frequency	f	15.0	Hz
Cilia spacing	l_0	0.3	μm
Methachronal wavelength	λ	30.0	μm

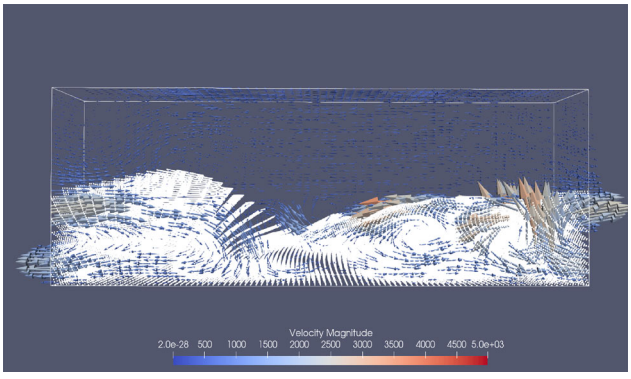


Figure 1. Velocity distribution associated to a dense forest of cilia. All data from Table 1.

3D box, with an axial length equivalent to the length of one metachronal wave. A 100×16 array of cilia is attached to the bottom of this box. At the bottom of the domain, no-slip boundary conditions are considered ($V = 0$), while at the top of the domain, free-slip conditions are prescribed. On the four lateral boundaries, biperiodic conditions on the solution of the Stokes equations are imposed, in order to mimic the configuration of a periodic 'infinite' forest of cilia. The simulation of the 3D flow, based upon biophysical parameters, allows us to get an order of magnitude of the mucus velocity which is consistent with the one obtained in experimental works (Sleigh et al. 1988). Moreover we observe important recirculations in the PCL, while the flow is almost homogeneous and axial in the mucus. Mucus is thus like a block 'sliding' over the PCL, and it is transported at nearly constant velocity to the right of the domain. To our knowledge, the description of the velocity distribution (in particular its difference between PCL and mucus) through

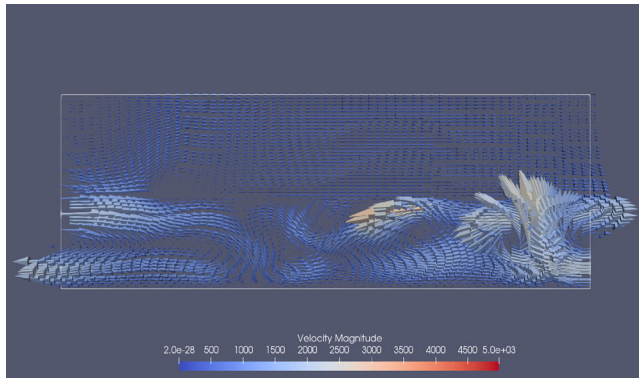


Figure 2. 2D slice of the domain associated to the fluid velocity.

direct simulation is original and provides a new insight in the understanding of the collective ciliary beating upon the velocity distribution.

4. Conclusions

In this work we aim to give a realistic representation of the velocity in the mucus, so we can get better understanding of mucus. Notice that in the non-pathological case, the order of magnitude of the velocity in the mucus is about $300\mu m$, which is the same as found in our work. Nevertheless several difficulties should be overcome in order to get a realistic model: (1) viscoelastic properties of the mucus should be taken into account; (2) in a more critical way, the main limitation relies on the ciliary movement which is prescribed although it should emerge from a fluid-structure interaction problem.

References

Cox RG. 1970. The motion of long slender bodies in a viscous fluid. Part 1. General theory. J Fluid Mech. 44(04): 791–810. doi:10.1017/S002211207000215X.

Mori Y, Ohm L, Spirn D. 2019. Theoretical justification and error analysis for slender body theory with free ends. Arch Ration Mech Anal. 235(3).

Fulford GR, Blake JR. 1986. Muco-ciliary transport in the lung. J Theor Biol. 121(4):381–402.

Sleigh M, Blake JR, Liron N. 1988. The propulsion of mucus by cilia. Am Rev Respir Dis. 137(3):726–741. doi: 10.1164/ajrccm/137.3.726.

KEYWORDS Mucociliary transport; nonlocal stokes problem; thin structures

chabane.meziane@universite-paris-saclay.fr

A micro-poro-mechanical model of the lung parenchyma

M. Genet[a,b], M. Manoochehr Tayebi[a,b] and A. Bel-Brunon[c]

[a]Laboratoire de Mécanique des Solides (LMS), École Polytechnique/IPP/CNRS, France; [b]MΞDISIM team, INRIA, France; [c]Laboratoire de Mécanique des Contacts et des Structures (LaMCoS), INSA-Lyon/CNRS, France

1. Introduction

To better understand the link between the macroscopic behavior of the lung parenchyma and its microscopic geometrical and mechanical features, we developed a micromechanical (alveolar scale) model and studied its global response (in terms of average stress/strain as well as pressure/porosity) to various loadings (average stress, strain or pressure). We also compared its global response to the one of a macroscopic (tissue scale) poromechanical model which we recently proposed for the lung parenchyma (Patte, Genet, et al. 2022). In fine, the microscopic model will help us derive a better macroscopic model, hence performing more physiological organ scale breathing simulations for clinical applications (Patte, Brillet, et al. 2022; Laville et al. 2023) while maintaining a link to the state of the tissue at alveolar scale, opening the door for explicitly modeling alveolar scale phenomena such as surface tensions, remodeling mechanisms, etc.

2. Methods

2.1. Microstructure and micromechanics

We considered a 2D hexagonal periodic microstructure, as shown in Figure 1, whose walls obey a generic hyperelastic constitutive law with neohookean and Ogden-Ciarlet-Geymonat potentials.

2.2. Micro-poro-mechanics problem formulation

To formulate the problem, we start by decomposing the total displacement into an affine part and a periodic perturbation:

$$\underline{U}(\underline{X}) := \underline{\underline{\tilde{\epsilon}}} \cdot \left(\underline{X} - \underline{X_0}\right) + \underline{\hat{U}}(\underline{X}),$$

where $\underline{\underline{\tilde{\epsilon}}}$ is a symmetric second order tensor, i.e. the macroscopic strain, $\underline{X_0}$ an arbitrary reference point and $\underline{\hat{U}}$ a periodic displacement field. Let us introduce another variable, namely the macroscopic stress:

$$\underline{\underline{\tilde{\sigma}}} := \frac{1}{|\omega|}\left(\int \underline{\underline{\sigma}} d\omega_s - |\omega_f| p_f \underline{\underline{1}}\right),$$

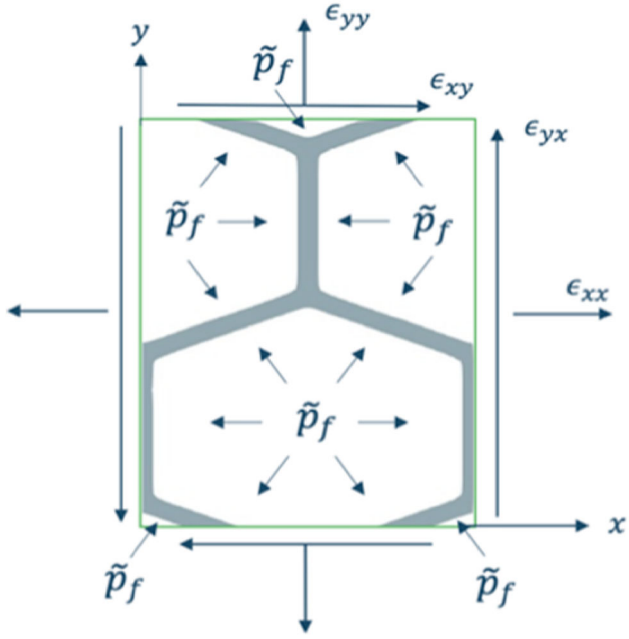
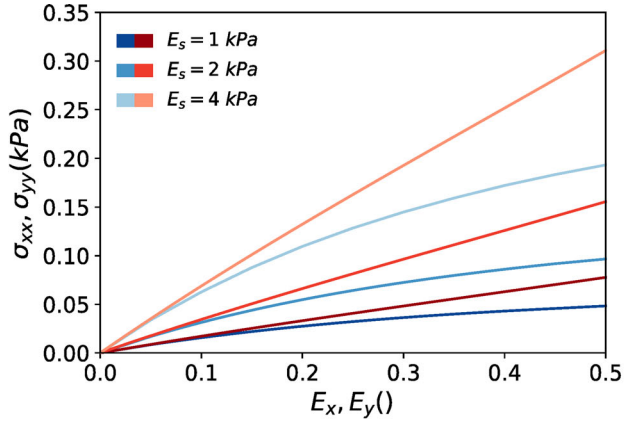


Figure 1. Generic porous microstructure.

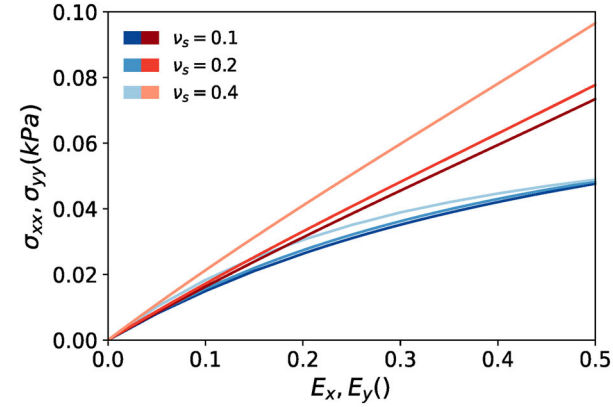
where $\omega = \omega_s \cup \omega_f$ is the deformed domain, composed of solid and fluid parts, $\underline{\underline{\sigma}}$ is the Cauchy stress tensor, p_f is the fluid pressure. The strong form of the general micro-poro-mechanics problem is thus:

$$\textit{Find } (\underline{\underline{\tilde{\epsilon}}}, \underline{\hat{U}}) \textit{ such that } \begin{cases} \underline{\hat{U}} \textit{ is periodic} \\ \underline{div}(\underline{\underline{\sigma}}) = 0 \textit{ in } \omega_s \\ {}^t\underline{\underline{\sigma}} = \underline{\underline{\sigma}} \textit{ in } \omega_s \\ \underline{\underline{\sigma}} \cdot \underline{n} = -p_f \underline{n} \textit{ on } \partial\omega_s \backslash \partial\omega \\ \underline{\underline{\sigma}} \cdot \underline{n} = 0 \textit{ on } \partial\omega_s \cap \partial\omega \\ \underline{\underline{\Sigma}} = \underline{\underline{\Sigma}}(\underline{U}) \textit{ in } \Omega_s \\ \tilde{\epsilon}_{ij} = \tilde{\epsilon}'_{ij}. \\ \tilde{\sigma}_{kl} = \tilde{\sigma}'_{kl} \end{cases},$$

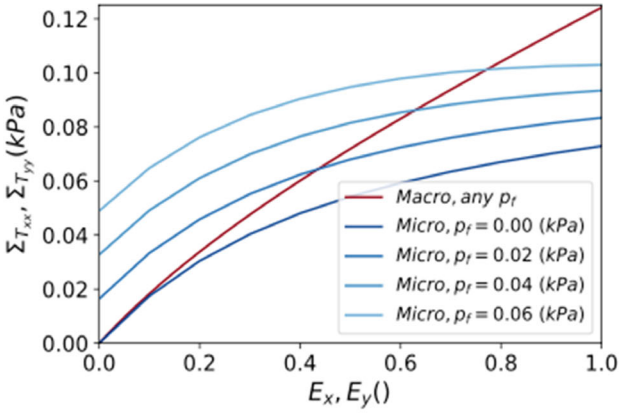
Where $\underline{\underline{\Sigma}}$ is the second Piola–Kirchhoff stress tensor. This system describes the balance of linear momentum, the balance of angular momentum, the applied pressure on the inner surface, the periodicity of the stress field, the constitutive relation, the constraint of some component of the macroscopic strain to a given value $\tilde{\epsilon}_{ij}'$, and the constraint of some component of the macroscopic stress to a given value $\tilde{\sigma}_{kl}'$. In practice we pull all equations back to the reference configuration, and formulate the problem in weak form. Compared to (Álvarez-Barrientos et al. 2021), we explicitly express the macroscopic stress, which make the formulation valid for any microstructure. This general formulation allows to impose various types of loading to the microstructure: fluid pressure and/or macroscopic strain and/or macroscopic stress.



(a) Cauchy stress-strain response to an imposed equi-biaxial strain for different values of the solid Young modulus.



(b) Cauchy stress-strain response to an imposed equi-biaxial strain for different values of the solid Poisson coefficient.



(c) Terzaghi stress-strain response to an imposed equi-biaxial strain for different fluid pressure values.

Figure 2. Global response of the micro-poro-mechanical model (blue) vs. a macro-poro-mechanical model (Patte, Genet, et al. 2022) (red). (a) Cauchy stress-strain response to an imposed equi-biaxial strain for different values of the solid Young modulus. (b) Cauchy stress-strain response to an imposed equi-biaxial strain for different values of the solid Poisson coefficient. (c) Terzaghi stress-strain response to an imposed equi-biaxial strain for different fluid pressure values.

3. Results and discussion

We systematically compared the global response of the microscopic model to the one of our poromechanical model. Some results are shown in Figure 2. Figure 2a,b shows the stress-strain response to an imposed equi-biaxial strain for different values of the solid Young modulus and Poisson coefficient. The material parameters of both models are chosen such that the linearized response match, which is apparent on the plots. For larger levels of deformation, the responses of the micro- and macro-models differ. Also, as expected, the response is much more sensitive to the Young modulus than the Poisson coefficient. Figure 2c shows the Terzaghi stress as a function of strain, for different levels of fluid pressure. In the context of our micro-model, we define the Terzaghi stress as:

$$\underline{\underline{\sigma_T}} := \underline{\underline{\tilde{\sigma}}} + \frac{|\omega_f|}{|\omega|} p_f \underline{\underline{1}}.$$

In the very construction of our poromechanical model, the Terzaghi stress is independent from the fluid pressure (Chapelle and Moireau 2014). On the contrary, our micromodel shows a strong coupling between the applied strain and fluid pressure.

4. Conclusions

We have developed a micro-poro-mechanical model of the lung parenchyma, based on a general formulation that allows to compute the response of the microstructure to fluid pressure, macroscopic strain and/or macroscopic stress. This model allows to investigate the fundamental hypothesis underlying macroscopic poromechanical models. We now plan to introduce additional mechanisms (e.g. surface tension, fibrosis, etc.) within our micromodel, as well as develop a model reduction approach to be able to perform organ scale simulations directly based on this micro-model.

References

Álvarez-Barrientos F, Hurtado DE, Genet M. 2021. Pressure-driven micro-poro-mechanics: a variational framework for modeling the response of porous materials. Int J Eng Sci. 169:103586. doi:10.1016/j.ijengsci.2021.103586.

Chapelle D, Moireau P. 2014. General coupling of porous flows and hyperelastic formulations–from thermodynamics principles to energy balance and compatible time schemes. Eur J Mech B Fluids. 46:82–96. doi:10.1016/j.euromechflu.2014.02.009.

Laville C, Fetita C, Gille T, Brillet P-Y, Nunes H, Bernaudin J-F, Genet M. 2023. Comparison of optimization parametrizations for regional lung compliance estimation using personalized pulmonary poromechanical modeling. Biomech Model Mechanobiol. https://doi.org/10.1007/s10237-023-01691-9.

Patte C, Brillet P-Y, Fetita C, Gille T, Bernaudin J-F, Nunes H, Chapelle D, Genet M. 2022. Estimation of regional pulmonary compliance in idiopathic pulmonary fibrosis based on personalized lung poromechanical modeling. J Biomech Eng. 144(9):091008. doi:10.1115/1.4054106.

Patte C, Genet M, Chapelle D. 2022. A quasi-static poromechanical model of the lungs. Biomech Model Mechanobiol. 21(2):527–551. doi:10.1007/s10237-021-01547-0.

KEYWORDS Micro-mechanics; poro-mechanics; pulmonary mechanics; finite element method

martin.genet@polytechnique.edu

A numerical model to study the coupling between lung biomechanics and physiology

C. Bruna-Rosso[a] and S. Boussen[a,b]

[a]Laboratoire de Biomécanique Appliquée, Aix-Marseille Univ., Gustave Eiffel Univ, Marseille, France; [b]Department of Anaesthesiology and Critical Care Medicine, University Hospital la Timone, AP-HM, Aix-Marseille Univ, Marseille, France

1. Introduction

The Acute Respiratory Distress Syndrome (ARDS) is a critical condition. For patients suffering from this pathology, mechanical ventilation (MV) is needed to ensure their sufficient ventilation and oxygenation. Intensivists have several therapeutic tools at their disposal to design a correct MV. The most diffused are recruitment maneuvers with Positive End Expiratory Pressure (PEEP) and prone positioning (Meyer et al. 2021). However, practitioners face several issues when confronted to ARDS and using these two techniques:

- High variability between patients
- Limits in the understanding of the underlying mechanisms

This leads to a mostly experienced-based decision-making for physicians. Considering both the down-side effects and the resources required to implement the recruitment maneuvers and prone positioning, being able to evaluate the probability to respond to different therapeutic approaches would be of high clinical significance. Moreover, better understanding the biomechanical and physiological phenomena underlying the patient response could inform new MV strategies to deal with ARDS. In order to tackle these issues, a coupled physio-mechanical computational framework was conceived and implemented.

2. Methods

2.1. Global framework

The global framework that was used to implement the physio-mechanical model is illustrated in Figure 1. Part of this framework, corresponding to the mechanical model, was presented is a previous publication (Bruna-Rosso and Boussen 2022). The model is a so-called multi-compartment model, which represents the lung as several 'balloons' able to inflate and deflate according to a non-linear compliance. These compartments also have the ability to exchange gases with external capillaries. This later phenomenon, which extends the previously published model, is further detailed in the next subsection.

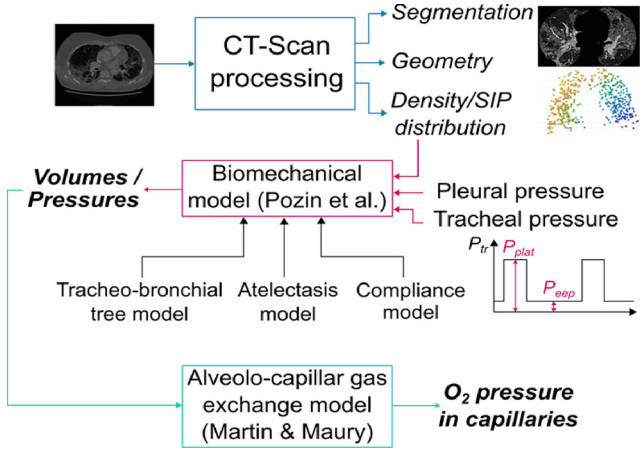


Figure 1. Physio-mechanical model workflow.

2.2. Physiological model

The physiological model aims at simulating the gas exchanges between the alveoli and the blood consecutive to an inspiration that is modelled within the mechanical part of the computational framework.

The physiological model computes two main variables, namely the dioxygen fraction within the alveoli c_A and the partial pressure of O_2 P_c within the capillaries.

The equations that were used are based on the model from Martin & Maury (Martin and Maury 2013) and are the following:

- Variation of O_2 volume inside a compartment

$$\frac{d}{dt}(c_A V) = c_A^0 \dot{V} H(\dot{V}) + c_A \dot{V}(1 - H(\dot{V})) - Q$$

Where V is the total compartment volume (computed by the mechanical model) [L], $c_{O_2}^0$ is the fraction of dioxygen in the inhaled air (0.2), H is the Heaviside function and Q is the flow of oxygen through the alveolar-capillary membrane [L s^{-1}]. The first term of the right-hand side represents the inspiration, the second the expiration and the last one the oxygen that diffuses to the blood through the alveolar-capillary membrane.

- Variation of O_2 quantity in the capillary blood

$$\frac{d}{dt}\left(V_c\left(\sigma P_c + 4Cf(P_c)\right)\right) = Q = D_m(P_A - P_c)$$

Table 1. Simulation parameters.

P_{eep}	P_{plat}	τ_b	Respiratory rate	D_m
16 cmH_2O	26 cmH_2O	0.45s	20 min^{-1}	$3.5e^{-6}$

Where V_c is the volume of capillary blood for one compartment [L], σ is the oxygen solubility in plasma [mol^{-1} L^{-1} $mmHg^{-1}$], C is the concentration of hemoglobin [mol L^{-1}], P_A is the partial pressure of oxygen within the alveoli [cmH2O] and D_m is the membrane diffusing capacity [mol s^{-1} $mmHg^{-1}$]. f represents the Hill's curve given by the following relationship: $f(P) = \frac{P^n}{\tilde{P}^n + P^n}$ where n=2.5 and $\tilde{P} \approx$ 26 mmHg. $D_m$was weighted with a coefficient z ($z = 1$: healthy tissue, $z = 0$: non aerated tissue) according to the corresponding voxel HU in the patient CT-scan to simulate a lower diffusion in pathological tissue. To close this system of equation, we need a relationship between P_A and c_A. According to (Jbaily et al. 2020), we have:

$$P_A = c_A \times \frac{M_G}{M_O}(P_A - P_{vap} + P_{atm}),$$

where M_G and M_O are respectively the gas mixture and oxygen molar masses [g mol^{-1}], P_A, P_{atm} and P_{vap} are respectively the alveolar (retrieved from the mechanical model), atmospheric and vapor pressures [cmH_2O]. M_G was deemed constant throughout the respiratory cycle. To simulate the heart beats that have a frequency that differs from the respiration one, the variable P_c was set to 40 mmHg (venous blood O_2 partial pressure) at every τ_b, the heart period.

2.3. Implementation and simulation

Following the mechanical model framework, the physiological model was implemented using the Julia language. A simulation of an ARDS patient MV throughout 10 respiratory cycles was performed on $N = 512$ compartments. The main parameters of this simulation are regrouped in Table 1.

3. Results and discussion

The volume, alveolar O_2 fraction and capillary oxygen partial pressure time evolutions on 10 respiratory cycles are given in Figure 2. Theses curves clearly show the influence of the weighting parameter z, and thus the pathology, on both the ability of the lung to expand and diffuse gases through the alveolar-capillary membrane. We can see that the blood oxygenation stabilizes at a much lower value (76 mmHg against 120 mmHg for maximal P_c value on a respiratory cycle).

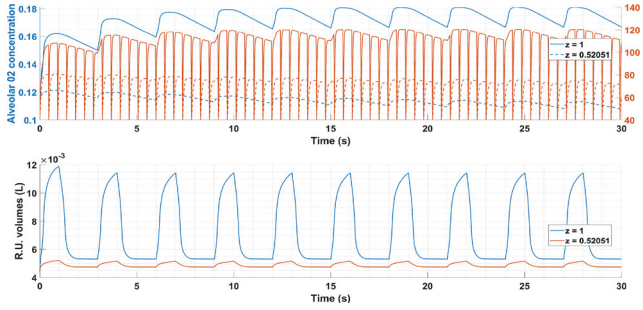


Figure 2. Respiratory unit volume (bottom), O_2 concentration and capillary partial pressure (top) for 10 respiratory cycles.

This figure also illustrates the interplay between lung biomechanics and physiology, since it shows how impaired inflation of a respiratory unit decreases the quantity of oxygen it diffuses. It reveals the potential of the model to investigate either the effect of MV parameters, such as Peep or prone positioning, on the patient oxygenation, and thus the potential of such a model to assist the clinicians in their decision-making process. This is further supported by the low computational cost of a simulation (around 10 min for the simulation presented here). However, the diffusion model that is currently implemented is very simplistic. Discrepancies in the blood flow between respiratory units is not represented while it is known to be inhomogeneous throughout the lung, especially in case of ARDS (Cressoni et al. 2014). Future works should consider a spatial distribution for V_c, the capillary blood volume. Moreover, the way in which the pathology is modeled, i.e. through the weighting coefficient of both the compartments' compliance and diffusivity coefficient should be improved. Indeed, while it reproduces tendencies clinically observed, it is too simplistic to inform clinical decisions.

4. Conclusions

A homegrown computational framework designed to simulate pathological lung biomechanics was extended with a gas exchange model to describe the physio-mechanical coupling inside the respiratory system. Simulation on an ARDS patient was performed. Results were in accordance with tendencies observed in a clinical context, however the simplistic nature of the model implemented does not allow to make quantitative predictions. Future works will aim at making the diffusion model more sophisticated.

References

Bruna-Rosso C, Boussen S. 2022. A computational framework to study pathological lung biomechanics. In:

Computer Methods in Biomechanics and Biomedical Engineering Volume 25, Issue sup1: 47th congress of the Société de Biomécanique. Vol. 25.

Cressoni M, Cadringher P, Chiurazzi C, Amini M, Gallazzi E, Marino A, Brioni M, Carlesso E, Chiumello D, Quintel M, et al. 2014. Lung inhomogeneity in patients with acute respiratory distress syndrome. Am J Respir Crit Care Med. 189(2):149–158. doi:10.1164/rccm.201308-1567OC.

Jbaily A, Frank S, Szeri AJ. 2020. Pulmonary mechanics and gas exchange: a mathematical framework. Int J Eng Sci. 154:103276. 154. doi:10.1016/j.ijengsci.2020.103276.

Martin S, Maury B. 2013. Modeling of the oxygen transfer in the respiratory process. Esaim: m 2an. 47(4):935–960. doi:10.1051/m2an/2012052.

Meyer NJ, Gattinoni L, Calfee CS. 2021. Acute respiratory distress syndrome. Lancet. 398(10300):622–637. doi:10.1016/S0140-6736(21)00439-6.

KEYWORDS Lung biomechanics; gas exchanges; numerical modeling; acute respiratory distress syndrome

claire.bruna-rosso@univ-eiffel.fr

Characterization of ciliary beating in chronic rhinosinusitis

M. Renaud[a], E. Escudier[b], R. Mitri-Frangieh[a,c], M. Filoche[a], J.-F. Papon[a,d], V. Fournier[a], A. Coste[a,e], B. Louis[a] and E. Béquignon[a,e]

[a]INSERM-UPEC U955, CNRS EMR, Créteil, France; [b]INSERM U933, Paris, France; [c]CHIC, Service d'Anatomopathologie, Créteil, France; [d]AP-HP, Hôpital Bicêtre, Service d'Oto-Rhino-Laryngologie et de Chirurgie cervico-faciale, Le Kremlin-Bicêtre, France; [e]CHIC, Service d'Oto-Rhino-Laryngologie et de Chirurgie cervico-faciale, Créteil, France

1. Introduction

Mucociliary clearance is one of the major lines of defense in the respiratory system. Goblet cells produce mucus which traps unwanted airborne particles. The mucus layer containing the trapped particles is carried away along the airway tree towards the pharynx where it is swallowed. This transport is insured by the constant beating of the cilia covering the epithelial cells (diameter ~0.2 µm, length ~6 µm and ~200 cilia per ciliated cell). Cilia beating results from the combination of the complex motion of each individual cilium, with an asymmetric pattern, into a highly coordinated motion forming the so-called metachronal wave. Dysfunction of ciliary beating is a hallmark of several genetic diseases such as primary ciliary dyskinesia. In addition, ciliary dysfunction may result in chronic airway inflammation and infection causing injury and structural changes to the airway epithelium, leading to a variety of diseases, including bronchiectasis and primary diffuse chronic rhinosinusitis. The latter is a frequent condition (~10% of general population) is still poorly characterized. *In situ* observation of ciliary beating and mucociliary clearance is almost impossible in patients at present stage. Therefore, one currently lacks a reliable and general method for evaluating mucociliary clearance in the clinical field. Light microscopy (often associated with high-speed camera) observation of ciliated edge obtained by nasal or bronchial brushing is the most common method used to evaluate ciliary beating by measuring the cilia beating frequency associated to a subjective description of the cilia beating pattern (Bricmont et al. 2021). Recently, a new method was proposed to assess the shear stress induced in the neighboring fluid, by tracking the motion of microbeads used as markers of the fluid displacement generated by the beating (Bottier, Blanchon, et al. 2017). Here the relevance of this method was appraised by comparing the values of the induced shear stress as well as the reference index (the cilia beating frequency) used in video microscopy to characterize the ciliary beating between a group of chronic rhinosinusitis and a control group.

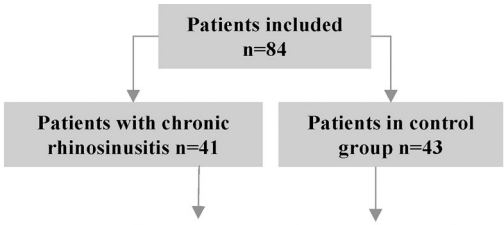
2. Methods

2.1. Study population

All patients were referred to our clinical centers for a diagnosis and management for nasal obstruction complain. Chronic rhinosinusitis and control groups were defined after diagnosis establishment. In the control group, free of chronic rhinosinusitis, patients had an indication of endonasal surgery for nasal obstruction or for unilateral nasal pathology. Patient with primary ciliary dyskinesia were excluded.

2.2. Ciliary beating evaluation

Suspended nasal epithelial cells were obtained by nasal brushing. Cells and polystyrene microbeads (Polybead © Microspheres, Polysciences, Inc., Warrington, PA, USA) suspended in a cell survival medium were deposited on a microscope slide, observed on an inverted microscope with a x40 objective and recorded with a digital camera (PixeLINK® A741, Ottawa Canada) at a rate of 358 frames/s. A 2D model was used to interpret the velocity field around the ciliated cells observed *via* the microbeads (Bottier, Pena Fernandez, et al. 2017). This 2D model is an envelope model where the tips of the cilia compose an undulating continuous surface allowing normal and tangential deformation. In this model the main inputs where the cilia beating frequency, the relative cilia density related to a slip length, the cilia amplitude, the cilia length and the metachronal wavelength. The computational model predicts a steady contribution for the profile of velocities that is essentially parabolic. In this case the shear stress at the ciliated wall is easy to infer: $\tau_w = (2\mu/h)U_w$ where µ is the known viscosity of the survival medium. U_w and h are respectively the velocity at the ciliated wall and the distance where the velocity vanishes. U_w and h can be experimentally inferred from the velocity profile determined by the microbeads. The shear stress appears as a global index of the potential ciliary beat efficiency. The cilia beating frequency, the relative cilia density, the cilia length, and the metachronal wavelength were also determined from the recorded movie. Cilia beating frequency was inferred *via* Fast Fourier Transform and relative density by comparing areas with and without cilia. The



Parameter: mean±SD (total number)	Chronic Rhinosinusitis	Control group	p
Ciliary beat frequency (Hz)	7.1 ± 1.7 (n=30)	7.1 ± 2 (n=38)	0.917
Cilia length (µm)	6.1 ± 1 n=30	6.8 ± 0.8 n=38	0.001
Relative density (%)	61.8 ± 14 (n=30)	70.7 ± 9.3 (n=38)	0.003
Wavelength (µm)	5.8 ± 2.7 (n=22)	8.5 ± 3.5 (n=20)	0.010
Shear stress (mPa)	0.27 ± 0.15 (n=21)	0.66 ± 0.3 (n=28)	2.E-06

Figure 1. Flow chart and parameters results.

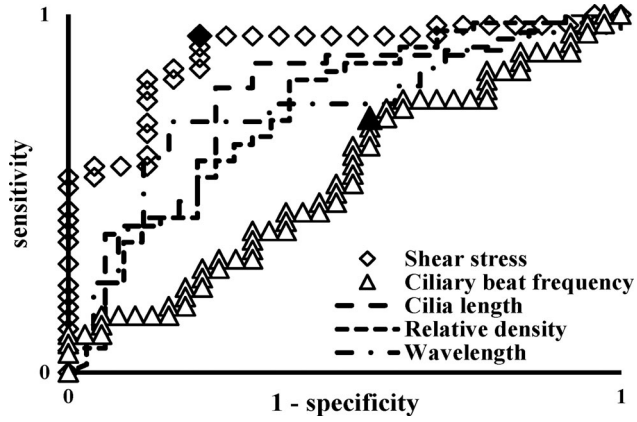


Figure 2. Receiver operating characteristic. For shear stress and frequency, the filled symbols correspond to the youden index, i.e. the threshold optimizing both the sensitivity and the specificity.

wavelength was estimated by measuring the phase change of the cilia beats along the ciliated edge. The wavelength was the distance separating 2 loci with a phase variation of 2π. Cilia length was estimated by direct observation and pixel size calibration.

2.3. Statistical analysis

The comparison of the different parameter in the two groups was done with the Mann–Whitney test. Receiver operating characteristic curve and area under the curve (AUC) were used to evaluate the discriminating power of each parameter.

3. Results and discussion

Flow chart and parameters mean values are showed in Figure 1. The shear stress is significantly lowered in the rhinosinusitis group whereas the frequency is not modified. In terms of ciliary beat frequency, the scarce results of the literature are very heterogeneous, ranging from normal to decreased or increased. In our relatively large groups ciliary beat frequency does not significantly differ between the chronic rhinosinusitis group and the control group, while all other parameters (cilia length, relative density wavelength and shear stress) are significantly different between the two groups (Figure 1). All these variations, except for the wavelength, induce a decrease of the efficiency in the 2D model. Nevertheless, the decrease of the wavelength may also be induced by an alteration of the beating coordination with a decrease of the area where cilia seem coordinated.

The shear stress appears as the best parameter to discriminate between the 2 groups with a sensitivity of 94% and a specificity of 76% with AUC of 89% (Figure 2). By contrast the ciliary beat frequency is the worst parameter with a sensitivity of 71% and a specificity of 45% with an AUC close to a random statistical model. Clearly ciliary beat frequency, that is the historical and classical parameter used to evaluate the ciliary beating, does not appear as an interesting parameter to get a global view of the cilia beating. This point was already notified by expert of the primary ciliary dyskinesia even if a combination of ciliary beating frequency and beating pattern was found useful in the primacy ciliary dyskinesia diagnosis (Stannard et al. 2010). The main limit of the shear stress measurement lies in its feasibility since the measurement requires to record at the same time microbeads and beating ciliated edge. It explains why it was only possible to measure the shear stress in 49/68 (72%) patients where beating ciliated edge were present.

4. Conclusions

The shear stress appears as a promising parameter to evaluate the severity of the effects of pathology on cilia beating and mucociliary clearance. Interestingly this parameter is measurable without modification of the human data collection.

References

Bottier M, Blanchon S, Pelle G, Bequignon E, Isabey D, Coste A, Escudier E, Grotberg JB, Papon JF, Filoche M, et al. 2017. A new index for characterizing micro-bead motion in a flow induced by ciliary beating: part I, experimental analysis. PLoS Comput Biol. 13(7): e1005605. doi:10.1371/journal.pcbi.1005605.

Bottier M, Pena Fernandez M, Pelle G, Isabey D, Louis B, Grotberg JB, Filoche M. 2017. A new index for characterizing micro-bead motion in a flow

induced by ciliary beating: part II, modeling. PLoS Comput Biol. 13(7):e1005552. doi:10.1371/journal.pcbi.1005552.

Bricmont N, Alexandru M, Louis B, Papon JF, Kempeneers C. 2021. Ciliary videomicroscopy: a long beat from the European Respiratory Society guidelines to the recognition as a confirmatory test for primary ciliary dyskinesia. Diagnosis. 11(9):1700.

Stannard WA, Chilvers MA, Rutman AR, Williams CD, O'Callaghan C. 2010. Diagnostic testing of patients suspected of primary ciliary dyskinesia. Am J Respir Crit Care Med. 181(4):307–314. doi:10.1164/rccm.200903-0459OC.

KEYWORDS Ciliary beating efficiency; mucociliary clearance; shear stress

bruno.louis@inserm.fr

Comparison of mechanical and hemodynamic properties of custom-made silicone mitral valves

K. Delanoë[a], V. Stanová[a], E. Salaun[a], R. Rieu[b] and P. Pibarot[a]

[a]Québec Heart and Lung Institute, Laval University, Québec, Canada; [b]Aix-Marseille Univ / Gustave Eiffel University, Marseille, France

1. Introduction

Significant mitral valve regurgitation affects over 2% of the total population worldwide (Coleman et al. 2017). No drug treatment has been proven efficient in reducing the progression of the disease and cardiac surgery, or more recent, percutaneous techniques remain the only option of treatment. The hemodynamic consequences of these techniques as well as the mechanical stress applied on the mitral valve leaflets need to be considered. Recently, 3D printing has been used to assist cardiac surgeons in planning procedures for complex surgery. However, while commercially available 3D printers are capable of printing soft, tissue-like material, they cannot replicate the complex anatomy of the mitral valve while achieving the mechanical and rheological properties as well as echogenicity of the native mitral valve suitable for *in vitro* testing. In this context, the objective of this study was to develop a silicone valve reproducing the anatomical and physiological characteristics of the native mitral valve.

2. Methods

2.1. Mitral valve models

To compare the comportment of different materials under chosen hemodynamic conditions *in vitro*, mitral valve models based on the Lifelike mitral valve (Lifelike BioTissue Inc.,Ontario, Canada) were created (Figure 1a). The Lifelike valve was imaged with desktop micro-CT scanner (NanoScan PET-CT, Mediso). The high-resolution images were imported into 3D Slicer (open-platform for subject-specific image analysis). The finalized model was imported into MeshMixer (Autodesk Inc., San Francisco, CA, USA) to create a negative mold. This mold was then 3D printed (Figure 1b) with Lulzbot Taz Pro Dual Extruder printer (North Dakota, USA) using NinjaFlex material (NinjaTek 3D, PA, USA). Silicone was applied layer by layer on mold to ensure homogenous curing of the silicone. For each silicone a specific number of layers have been poured to obtain a leaflet thickness (2 mm) comparable to the thickness of native mitral valve leaflets (Grande-Allen et al. 2005). The chordae were created using six braided strings (100% polyester, Gütterman GmbH, ermany) per valve (Figure 1c). Each string was divided into three pieces, providing 18 points of tensile force application. Chordae were placed between two layers of silicone, ensuring the tension during cardiac cycle. The silicone models were then left to dry for several hours before being removed from their molds (Figure 1d).

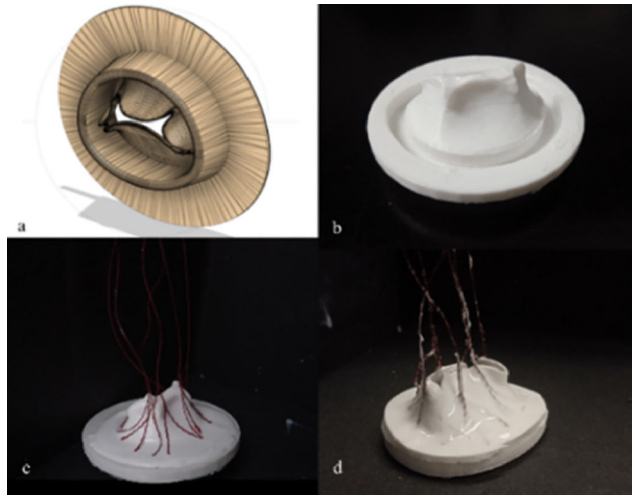


Figure 1. Creation of silicon valves. (a) 3D model, (b) 3D printed mold, (c) Chordae added between silicon layers, (d) Final custom-made mitral valve.

2.2. Material properties

In this study, four different silicone elastomers (i.e. EcoFlex 00-30 (EF30), EcoFlex 00-50 (EF50), DragonSkin 10 Very Fast (DS10), DragonSkin 20 (DS20) (Smooth-On Inc., Easton, PA, USA) with different mechanical properties were used to create mitral valve models and compared to identify which imitates the tissue comprising the leaflets most closely. These elastomers (EF30, EF50, DS10, DS20) were chosen due to their mechanical properties referred in literature, i.e. a Young's Modulus of 0.1 MPa, 0.1 MPa, 0.5 MPa and 0.34 MPa respectively, an Ultimate Tensile Stress of 1.2, 1.7, 3.28 and 3.79 MPa respectively, Tear Strength of 6.66, 8.44, 17.9 and 21 kN/m respectively and different harnesses (00-30, 00-50, 10 A and 20 A respectively).

2.3 Hemodynamic testing

For the purpose of this study, a double activation left heart duplicator system was used. Each of the silicone

mitral valves was tested under three experimental conditions replicating the stroke volume (SV) usually found in clinical trials. A SV of 70 mL correspond to an healthy hemodynamic condition whereas a SV of 50 mL and 30 mL stands for low flow conditions. For each experimental condition, the heart Rate (HR) and mean aortic pressure were held constant at 70 bmp and at 100 mmHg respectively. Doppler Mitral Valve Area (MVA) was estimated using Gorlin Equation (Gorlin and Gorlin 1990).

$$(MVA)\ (cm^2) = \frac{CO}{31 * \sqrt{MPG} * HR * SEP}$$

Where CO = Cardiac Output (mL/min), MPG = Mean Pressure Gradient (mmHg), SEP = Systolic Ejection Period (%). Physiological responses: E/A ratio (characterized by early-filling period (E) followed by an atrial filling period (A)) and mean pressure gradient (MPG) of each model were analyzed from doppler continuous waves collected by transthoracic echocardiography (Vivid 7, GE Healthcare). Determination of Geometric Orifice Area (GOA) was done using custom-coded Matlab program.

Table 1. Silicone valves' MPG, MVA, GOA.

Silicone	SV (ml)	N	MPG (mmHg)	MVA (cm²)	GOA (cm²)	E/A
DS 20	30	5	4.5±0.4	1.3±0.1	0.9±0.1	1.2±0.1
	50	15	7.2±0.5	1.8±0.1	1±0.1	1.4±0.1
	70	15	11.6±1.7	1.9±0.1	1.2±0.1	1.4±0.1
DS 10	30	14	3.4±0.4	1.5±0.1	1.0±0.1	1.4±0.1
	50	9	3.7±0.5	2.5±0.2	1.3±0.1	1.5±0.1
	70	15	8.4±0.9	2.2±0.1	1.3±0.3	1.5±0.1
EF 50	30	7	4.3±0.6	1.3±0.1	0.9±0.1	1.2±0.1
	50	5	5.3±0.7	2.1±0.2	1.2±0.2	1.3±0.1
	70	14	7.3±1.3	2.4±0.2	1.5±0.1	1.3±0.1
EF 30	30	9	2.6±0.3	1.7±0.1	1.2±0.1	1.2±0.1
	50	20	4.1±0.7	2.4±0.7	1.4±0.2	1.4±0.1
	70	21	5.3±0.9	2.8±0.2	1.8±0.4	1.8±0.1

Continuous variables were presented as mean values ± sd and were compared using Student *t*-test (*p*-value< 0.05 considered statistically significant).

3. Results and discussion

Comparing the mechanical properties of different silicones found in literature points out reserved conclusions. Indeed, due to a Young's Modulus and a Shore Hardness lower than in DragonSkin elastomers, EcoFlex polymers seemed to be more elastic and softer, which is also characteristic for mitral valve leaflets ($E = 0.06$ MPa ((Richards et al. 2012)). However, tensile stress and tear strength of DragonSkin series are higher, advantaging them to face higher stroke volumes and tensile strengths applied by chordae. Hemodynamic values of healthy mitral valve under normal flow conditions are MPG <5 mmHg, MVA >2 cm^2 and induced a ventricular filling characterized by E/A ratio between 1.0 and 1.5. Table 1 presents values of MPG, E/A, MVA and GOA of different silicone valves under different hemodynamic conditions. Under normal flow conditions (Figure 2) EF 30 and EF 50 presented lower MPG than DS10 and DS20 (Table 1). MVA was higher for EF 30 and EF 50 compared to DS 10 and DS 20 (Figure 2). All valves presented non-to-mild regurgitation with regurgitation fraction of <20%.

4. Conclusions

In this study we sought to compare different silicone materials mimicking native mitral valve anatomy and its properties. Silicones presented in this study had different mechanical behaviors and hemodynamic responses. EF30 presented the lowest MPG, highest MVA and GOA in most experimental conditions indicating to be the material that most closely imitates the native mitral valve. The validation of the

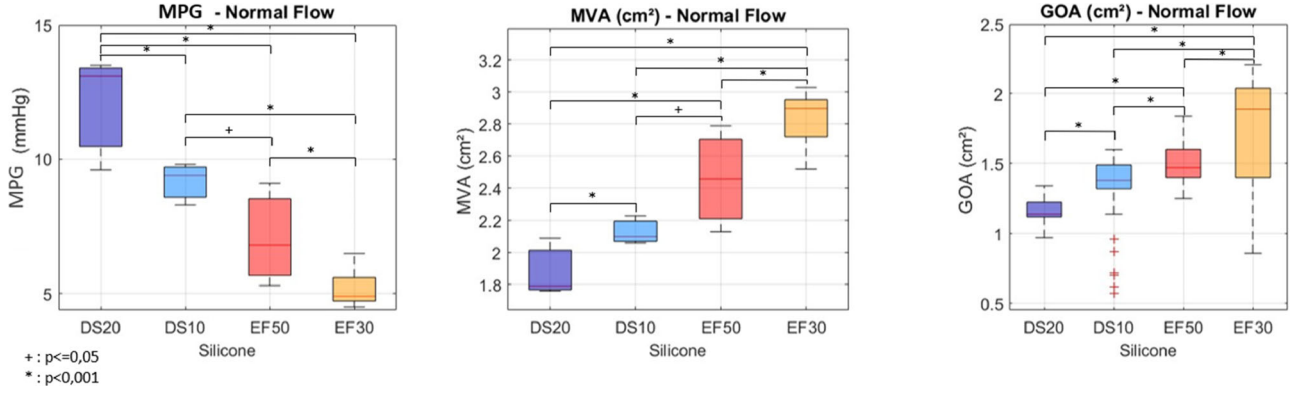


Figure 2. Hemodynamic data of mitral valves models collected under normal conditions (SV 70 mL).

mitral valve models was done under normal condition, data collected for SV 50 mL and 30 mL were added as they replicate major hemodynamic conditions seen in patients undergoing mitral valve surgery. This study shows that the custom-made silicone valve can provide the necessary means of dynamical evaluation, and in future could be used to plan mitral valve repair in order to eliminate the mitral valve regurgitation and assure the best hemodynamic outcomes. Furthermore, diseased, or degenerative mitral valves could also be developed to improve the understanding of the pathological behavior of these valves. These silicone models were implanted in a prototype of left ventricle with limited tensile strength applied on the chordae which could induce mild regurgitation. We are currently developing more suitable model with precise control of the chordae tension.

References

Coleman W, Weidman-Evans E, Clawson R. 2017. Diagnosing and managing mitral regurgitation. JAAPA. 30(6):11–14. doi:10.1097/01.JAA.0000516342.41351.6d.

Gorlin WB, Gorlin R. 1990. A generalized formulation of the Gorlin formula for calculating the area of the stenotic mitral valve and other stenotic cardiac valves. J Am Coll Cardiol. 15(1):246–247. doi:10.1016/0735-1097(90)90210-g.

Grande-Allen KJ, Barber JE, Klatka KM, Houghtaling PL, Vesely I, Moravec CS, McCarthy PM. 2005. Mitral valve stiffening in end-stage heart failure: evidence of an organic contribution to functional mitral regurgitation. J Thorac Cardiovasc Surg. 130(3):783–790. doi:10.1016/j.jtcvs.2005.04.019.

Richards JM, Farrar EJ, Kornreich BG, Moïse NS, Butcher JT. 2012. The mechanobiology of mitral valve function, degeneration, and repair. J Vet Cardiol. 14(1):47–58. doi:10.1016/j.jvc.2012.01.002.

KEYWORDS Mitral valve; silicone; Young's modulus

katell.delanoe.1@ulaval.ca

Computational characterization of venous valve dynamics and associated hemodynamics

B. Thibaud[a], S. Mendez[a], E. Faure[b,c], A. Perez-Martin[b,c], J. C. Gris[b,c] and F. Nicoud[a]

[a]IMAG, Univ Montpellier, CNRS, Montpellier, France; [b]Department of Vascular Medicine, University Hospital, Nimes, France; [c]UMR UA11 INSERM IDESP – Montpellier University, France

1. Introduction

Deep vein thrombosis (DVT) is a major problem in western society. As demonstrated by Sevitt (1974), DVT mostly forms in valvular bags and is linked to stresses applied on endothelial cells (ECs). These stresses are caused by blood flow or mechanical deformation. Accessing information on the valve dynamics would help understanding the onset mechanism of DVT. Venous valves dynamics results from the interaction between an incompressible fluid (blood) flow and a deformable structure (valve and vein tissues). In the previous studies on venous valve, as in Narracott et al. (2015), assumptions made on leaflets geometry force them to stretch. This report explores the hypothesis that leaflets mainly buckle, as supported by medical images. The present study proposes the use of a fluid-structure interaction (FSI) computational method to assess hemodynamics markers such as shear stress and time of residence in the perivalvular region. Section 2 describes briefly the FSI method. Section 3 presents the validation of the method, the valve model, and results on the 3D model followed by discussion. The fourth section gives a quick sum up of this abstract.

2. Methods

2.1. Numerics

Blood is modeled as an incompressible fluid following the Navier-Stokes equations in the ALE framework. The fluid density and kinematic viscosity are 1050kg m^3 and 3.3×10^{-6} m^2 s^{-1} respectively. At the inlet, velocity is imposed as a Dirichlet condition, and a convective outward flow condition is imposed on the outlet. The structural dynamic equilibrium of the valve is solved thanks to a finite element method solving the structural mechanics equations for a neo-Hookean material, while the vein itself is considered rigid. Contact between leaflets is handled by a penalization method. Because of the strong added mass effect ($\rho_s/\rho_f = 1$), the two sets of equations are strongly coupled in the framework of a partitioned solver with body-fitted meshes. To accelerate the convergence algorithm, the Aitken dynamic relaxation method is used (Mok 2001).

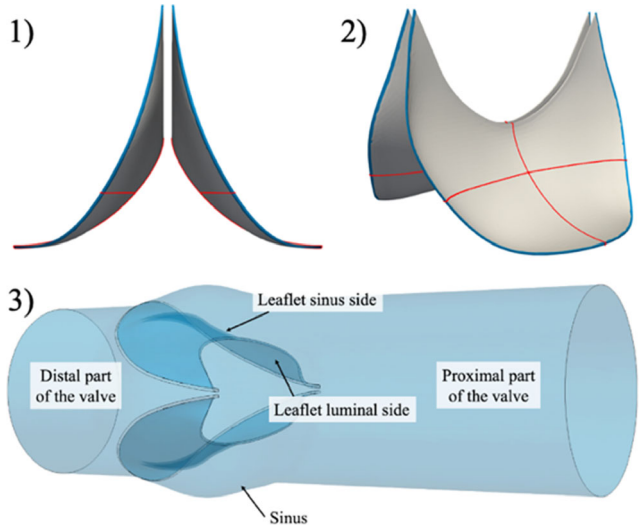


Figure 1. (1) Side view of the leaflets. (2) Three Quarter view of the leaflets. (3) Fluid geometry and notations.

2.2. Venous valve geometry

The geometry of the valve has been designed in the closed configuration based on the description of the geometry provided by Hofferberth et al. (2020). The size of the valve was selected to reproduce a common femoral vein valve (1 cm diameter). The resulting geometry is presented in Figure 1. The blue line on the leaflets shows the location of the insertion of the leaflets on the vein wall while the red lines show the 3D curvature of the model. The thickness of the leaflets and the valve heigh equal 70μm and 1cm respectively. With the model of the valve explained, an inflow must be determined to match medical observations. The signal retained is the following:

$$u(\mathrm{t}) = u_{\max}\ \left(1.01 + \left|\cos^5(\pi \mathrm{t}/\mathrm{T})\right|\right)$$

where u_{max} is the bulk velocity which equals 0.2 $m.s^{-1}$ corresponding to $Re = 303$. Given the geometry, a transitory flow is expected. The period T is chosen to be 1s reproducing a shortened breathing cycle. The corresponding flowrate equals 315 mL s^{-1} which falls into the physiological range for the common femoral vein. The fluid mesh contains 11 M cells.

3. Results and discussion

3.1. Validation of the method

The numerical benchmark used to validate the method is a 2D valve case, where a vertical elastic

Table 1. Max and min displacement of the flap tip.

	Max (mm)	Min (mm)
Present study	5.841	3.003
Boilevin-Kayl et al. (2019)	5.766	3.146

Comparison with Boilevin-Kayl et al. (2019).

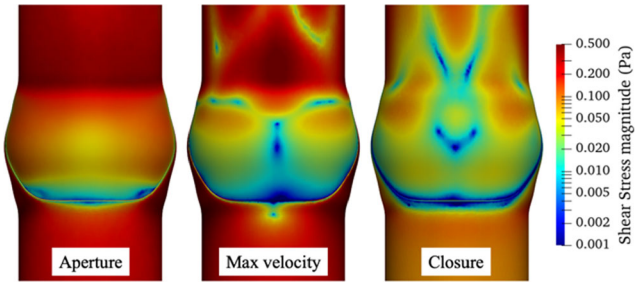


Figure 2. Shear stress magnitude on the vein wall at different moment of the valve cycle coloured by a log scale.

beam is plunged into a horizontal crossflow (for more details, Boilevin-Kayl et al. (2019)). Validation is done by reproducing the movement of the beam, the displacement of the beam tip is thus compared. The results are gathered in Table 1. Only the maximum and minimum displacements along the x-axis are reported to remain concise. The results of the present method are in good agreement with Boilevin-Kayl et al. (2019).

3.2. Venous valve

Three cycles of this signal were simulated. The results shown hereafter are taken on the third cycle to ensure initial conditions are completely flushed. At maximum bulk velocity, the pressure gradient acting on the leaflets equals 22Pa, which is consistent with a dynamic pressure caused by an incident flow velocity of 0.2 m s^{-1}. By opening the valve, this pressure gradient causes a reduction of cross-sectional area of 56%. Medical observations report a reduction of the order of $30-40\%$ (Lurie and Kistner 2012). Figure 2 displays valve sacs hemodynamics at 3 instants of the valve cycle: opening, maximum bulk velocity and closure. One common feature from the 3 views is that shear stress is lower in the center of the sinus along the vertical axis and close to the insertion. Overall, the shear stress is 10 times higher during opening than during the other two stages of the valve cycle and remains very low at the bottom of the sac. Compared to the shear stress observed further from the valve, the intra-saccular shear stress is at least 5 times lower. This last remark is coherent with the observations made by Welsh et al. (2019) and showing that the antithrombotic phenotype of the ECs depends on their location and is more expressed in perivalvular ECs. Concerning low shear stress at the bottom of the sacs, this is due to a lack of movement of the leaflets in this region. On echography, the angle of attachment of the leaflets on the insertion seems to change during the cycle which is not the case in the simulation.

4. Conclusions

This study characterizes shear stress acting on perivalvular endothelial cells under physiological flow. At first, a validation study of the FSI method under simpler conditions has been performed and leads to good agreement with reference results. Then the FSI method has been used to simulate valvular sacs dynamics submitted to a physiological inlet flow velocity signal. The cross-section reduction at maximum opening of the valve is higher than medical observation, 56% against 30–40%. Concerning the angle of attachment, considering the vein wall deformation, or adjusting the leaflet geometry could help reproduce this behavior. Moreover, simulation shows higher shear stress in the perivalvular area during opening than the rest of the cycle. Shear stress level stays lower in the sacs than in other parts of the vein which means endothelium in this region would be more sensitive to blood stasis and explains why DVT forms mostly in valvular sacs.

References

Boilevin-Kayl L, Fernández MA, Gerbeau J-F. 2019. A loosely coupled scheme for fictitious domain approximations of fluid-structure interaction problems with immersed thin-walled structures. SIAM J Sci Comput. 41(2):B351–B374. doi:10.1137/18M1192779.

Hofferberth SC, Saeed MY, Tomholt L, Fernandes MC, Payne CJ, Price K, Marx GR, Esch JJ, Brown DW, Brown J, et al. 2020. A geometrically adaptable heart valve replacement. Sci Transl Med. 12(531):eaay4006. doi:10.1126/scitranslmed.aay4006.

Lurie F, Kistner R. 2012. The relative position of paired valves at venous junctions suggests their role in modulating three-dimensional flow pattern in veins. Eur J Vasc Endovasc Surg. 44(3):337–340. doi:10.1016/j.ejvs.2012.06.018.

Mok DP. 2001. Partitionierte Lösungsansätze in der Strukturdynamik und der Fluid-Struktur-Interaktion [Internet].

Narracott A, Keijsers J, Leguy C, Huberts W. 2015. Fluid-structure interaction analysis of venous valve haemodynamics. Computational and Mathematical Biomedical Engineering Proceedings.

Sevitt S. 1974. The structure and growth of valve-pocket thrombi in femoral veins. J Clin Pathol. 27(7):517–528. doi:10.1136/jcp.27.7.517.

Welsh JD, Hoofnagle MH, Bamezai S, Oxendine M, Lim L, Hall JD, Yang J, Schultz S, Engel JD, Kume T, et al. 2019. Hemodynamic regulation of perivalvular endothelial gene expression prevents deep venous thrombosis. J Clin Invest. 129(12):5489–5500. doi:10.1172/JCI124791.

KEYWORDS Fluid-structure interaction; deep venous valve; venous flow; shear stress

barthelemy.thibaud@umontpellier.fr

Computational simulation of respiration-induced deformations of the renal arteries in AAA patients

A. Corvo[a], F. Chassagne[a], A. Aliseda[b], S. Haulon[c] and S. Avril[a]

[a]Mines Saint-Etienne, Univ Lyon, Univ Jean Monnet, INSERM, Saint-Etienne, France; [b]Department of Mechanical Engineering, University of WA, Seattle, WA, USA; [c]Aortic Center, Marie Lannelongue Hospital, Groupe Hospitalier Paris Saint Joseph, Paris Saclay University, Le Plessis-Robinson, France

1. Introduction

During human respiration, the diaphragm contraction and relaxation induce the motion of organs such as the liver, pancreas, duodenum, kidneys, especially in the cranio-caudal direction. This phenomenon implies translation, bending or axial deformation of the visceral arteries, such as left (LRA) and right renal arteries (RRA). Studies reporting cranio-caudal kidney motion have been published and, specifically, Suh et al. (2013) reported the values of changes in curvature, and branching angles associated with respiration, for patients with an Abdominal Aortic Aneurysm (AAA). AAA is a dilatation of the lowest anatomical section of the aorta, which can be treated through open surgery repair (OSR) or endovascular aneurysm repair (EVAR). This second treatment is a minimally invasive surgical intervention that consists of stent-graft deployment inside the abdominal aorta to prevent blood flow from entering the AAA, minimizing the surgical trauma and recovery for the patients. Numerical simulations of stent-graft deployment for AAA patient-specific cases have been performed. Tran et al. (2021) and Cheng et al. (2019) were the first to evaluate the respiration-induced changes in branch vessels for patients undergoing EVAR, with fenestrated and snorkel stent-grafts, respectively. The latter also showed how deformation induced by respiration is more significant than deformation associated with cardiac pulsatility (Cheng et al. 2019). Possible bending of the renal arteries could affect renal stent and could induce complications like restenosis and renal occlusions. However, no studies have ever been published concerning numerical simulations of renal artery movement due to breathing and, additionally, its impact on stent-graft deployment, despite their potential to accurately predict the hemodynamic impacts on renal artery deformations during respiration. The goal of this study is to address this lack with numerical simulations starting from an idealized geometry.

2. Methods

2.1. Abdominal aorta and renal artery modeling

The idealized geometrical model including an AAA located below renal arteries (Figure 1) was created on Onshape (Onshape, Boston, MA, USA), on the basis of the following geometrical parameters representative of human anatomy: 30.8 mm neck aortic diameter, 6.66 mm renal artery diameter, 44.6 mm RRA and 35.1 mm LRA length (Tran et al. 2021). The hyperelastic Yeoh model was first used to describe the aorta and renal arteries' mechanical behaviour. Then, material properties from the Holzapfel-Gasser-Ogden model were applied to the aorta and renal arteries, after dividing them into different sections to each of which is assigned a system of cylindrical co-ordinates, necessary for the orientation of the material anisotropy (Perrin et al. 2015).

2.2. Implementation of the computational simulation

Mechanical simulations were achieved with Abaqus (Simulia, Dassault Systemes, Providence, RI, USA) which already includes both the Yeoh and Holzapfel model. The idealized geometry was imported on Abaqus and meshed with 0.5 mm triangular shell elements with a thickness of 1.5 mm for the aorta and 0.5 mm for renal arteries. For the boundary conditions, displacements in the cranio-caudal, right-left, and anterior-posterior directions were applied at the distal extremities of the renal arteries, according to the kidney movements reported in the literature for free-breathing patients (Tai et al. 2013).

2.3. Measuring geometrical parameters

Vessel centrelines were extracted on *3D Slicer* with the *Vascular Modelling ToolKit* extension for LRA and RRA after inspiration and expiration (Figure 1).



Figure 1. RRA and LRA centrelines at the end of expiration (green and blue, respectively) and inspiration (red and orange, respectively).

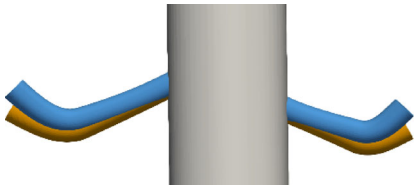


Figure 2. Idealized model of a section of the aorta with configurations of LRA and RRA at the end of expiration (blue) and inspiration (orange).

Subsequently, the difference in branching angle from inspiration to expiration, as well as the difference in renal artery mean and maximum curvature, were measured in *MATLAB*. Data collected were then compared with the literature results for the same metrics; no changes in renal artery diameter and/or displacement of renal arteries' ostium have been reported in previous publications (Suh et al. 2013).

3. Results and discussion

During the simulation including the expiration and inspiration phases, the kinetic energy was checked and remained under the fixed threshold of 10% of internal energy, to ensure a quasi-static regime. The final configuration of the renal artery at the end of expiration (blue) and inspiration (orange) phases are shown in Figure 2, with the aorta and AAA idealized geometry.

The motion of the renal artery during respiration was found to be in agreement with the physiological conditions. For the validation of the outcomes of the simulation, a comparison of geometrical metrics against data extracted from the literature is reported in Table 1.

The data obtained from our simulation workflow are in agreement with the measurements reported in the literature (Suh et al. 2013) and conducted on AAA patient-specific CT scans, especially for the changes in branching angle, for both tested material properties. Although the RA displacements are in the order of millimeters, they can significantly alter the RA geometry, causing deformations, which can be decisive for a successful outcome of the surgery following the SG insertion and can potentially impact the blood flow, possibly inducing complications.

4. Conclusions

The simulation workflow predicts accurately the physiological motion of renal arteries, under the conditions selected for this first case. The obtained results were in agreement with renal artery deformations reported in the literature and they emphasized that the variation in branching angle is the most important aspect of respiratory motion.

Table 1. Comparison between computational results and Suh et al. patient measurements for the difference in branching angle (degrees), in mean and maximum curvature (mm^{-1}), from inspiration to expiration.

ΔBranching angle	LRA	RRA
Suh et al. 2013	−7.5 ± 7.8	− 4.9 ± 5.3
Numerical results (Yeoh model)	−6.33	−4.63
Numerical results (Holzapfel model)	−6.35	−4.30
|ΔMaximum curvature|		
Suh et al. 2013	0.07 ± 0.03	0.04 ± 0.03
Numerical results (Yeoh model)	0.0103	0.0156
Numerical results (Holzapfel model)	0.0206	0.0327
|ΔMean curvature|		
Suh et al. 2013	0.01 ± 0.01	0.01 ± 0.01
Numerical results (Yeoh model)	0.0103	0.0104
Numerical results (Holzapfel model)	0.0068	0.0102

The next step will be to simulate renal artery stenting, evaluating the influence of breathing, and assessing if respiration can affect the stenting effectiveness, first in the idealized geometry and then, for future developments, in patient-specific geometries.

Acknowledgments

This study is part of the interdisciplinary project (EndovX), funded by the RHU program in France, aimed at developing novel technologies for personalized medicine in aortic disease.

References

Cheng CP, Suh GY, Kim JJ, Holden A. 2019. Cardiac pulsatility– and respiratory-induced deformations of the renal arteries and snorkel stents after snorkel endovascular aneurysm sealing. J Endovasc Ther. 26(4):556–564. doi: 10.1177/1526602819856363.

Perrin D, Badel P, Orgéas L, Geindreau C, Dumenil A, Albertini JN, Avril S. 2015. Patient-specific numerical simulation of stent-graft deployment: validation on three clinical cases. J Biomech. 48(10):1868–1875. doi:10.1016/j.jbiomech.2015.04.031.

Suh GY, Choi G, Herfkens RJ, Dalman RL, Cheng CP. 2013. Respiration-induced deformations of the superior mesenteric and renal arteries in patients with abdominal aortic aneurysms. J Vasc Interventional Radiol. 24(7): 1035–1042. doi:10.1016/j.jvir.2013.04.006.

Tai A, Liang Z, Erickson B, Li XA. 2013. Management of respiration-induced motion with 4-dimensional computed tomography (4DCT) for pancreas irradiation. Int J Radiat Oncol Biol Phys. 86(5):908–913. doi:10.1016/j.ijrobp.2013.04.012.

Tran K, Suh GY, Mougin J, Haulon S, Cheng C. 2021. Respiratory-induced changes in renovisceral branch vessel morphology after fenestrated thoracoabdominal aneurysm repair with the BeGraft balloon-expandable covered stent. J Vasc Surg. 74(2):396–403. doi:10.1016/j.jvs.2020.12.093.

KEYWORDS Computational simulation; renal artery; respiration; aneurysm; EVAR

alessandra.corvo@emse.fr

Contrast-enhanced micro-CT protocol for *in-situ* mechanical experiments of aortic thrombi

J. Léonet[a], J. Vicente[b], M. de Masi[a,c] and V. Deplano[a]

[a]CNRS, Centrale Méditerranée, IRPHE UMR7342, Aix-Marseille Univ, Marseille, France; [b]CNRS, Aix-Marseille Univ, Marseille, France; [c]AP-HM, Service de chirurgie vasculaire hôpital de la Timone, Aix -Marseille Univ, Marseille, France

1. Introduction

Intraluminal thrombus (ILT) is a porous structure made of a fibrin matrix with an aggregation of cellular elements such as platelets, blood cells and blood proteins that is present in most abdominal aortic aneurysms (AAAs). The ILT is composed by 3 distinct layers that differ by their composition and structure depending notably on ILT ageing and leading to permeability gradients. Only few studies were conducted on ILT characterization and its involvement in AAA biomechanics is still under debate. More experiments are needed to define a reliable model. We proposed a protocol to obtain the 3D morphology using X-rays microtomography (μ−CT) (Léonet et al. 2022) but the dehydration process and phosphotungstic acid (PTA) staining alter the microstructure and the mechanical properties of the tissue (Pétré et al. 2022). The objectives of the present study are therefore (i) to propose a new μ−CT protocol to prepare the tissues (ii) to perform *in-situ* experiments of ILT preserving their properties and compare the obtained results with those performed using PTA (iii) to numerically determine microscopic permeability from μ-CT images and compared to macroscopic experimental values and finally, (iv) to perform preliminary compression tests to define parameters for future *in-situ* tests.

2. Methods

2.1. Specimens

Thrombus were removed from 2 AAAs of human donor (average age 60) and preserved in DMEM solution. Four cylindrical samples, 7 disk samples and 6 cubic samples were used to perform μ−CT, macroscopic permeability and mechanical tests respectively.

2.2 X-ray microtomography protocol

A new staining agent named sodium polytungstate (SPT) preserving ILT properties was chosen (Pétré et al. 2022). Cylindrical samples of 3 mm were cut into the ILTs thickness using a scalpel keeping the 3 layers. Samples were then stained during 6 days in a solution of DMEM and SPT with a concentration of 15 g/L at 4 °C. After staining, each sample was then immersed in DMEM and placed in the μ−CT (Easytom XL, RX Solutions). The microfocus 150 kV source used in our previous study was replaced by a nanofocus 160 kV source for future *in-situ* mechanical testing. A total of 1120 images was taken at 3 μm resolution with a voltage of 55 kV and a current of 131 μA. Morphological parameters that are porosity, interconnectivity and permeability were calculated using iMorph software from the μ−CT images.

2.3. Macroscopic permeability

The macroscopic permeability was evaluated using the same experimental setup and protocol as our previous study (Léonet et al. 2022). A total of seven samples were obtained including 5 luminal, 1 abluminal and 1 luminal/medial disk.

2.4. Compression testing

Cubic samples with different dimensions were cut into one ILT using a scalpel keeping the 3 layers. Samples were then immersed in DMEM solution at 4 °C until testing. Each sample was placed in a rheometer (Thermo Scientific HAAKE MARS III) for unconfined-compression testing. The loading was applied until 40% of compression of the initial thickness at a velocity of 0.0295 mm/s followed by the unloading with the same conditions. To evaluate the preconditioning effect, several cycles were applied on 2 samples.

3. Results and discussion

3.1. μ−CT study

Figure 1 shows the μ−CT images obtained using PTA (Figure 1a, protocol 1) and SPT protocol (Figure 1b, protocol 2) for 2 different thrombus samples. The

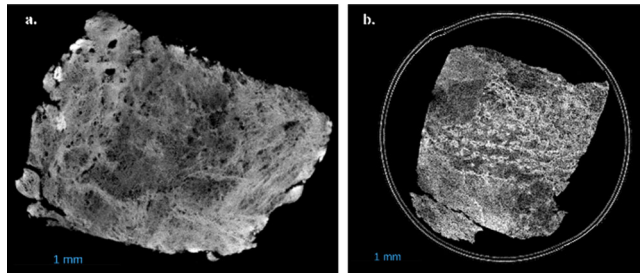


Figure 1. Comparison between μ−CT images of luminal layers obtained using PTA (a) and SPT (b).

Table 1. Comparison between morphological parameters obtained using PTA protocol (n°1) and SPT protocol (n°2).

	Luminal		Medial		Abluminal	
Protocol	1	2	1	2	1	2
Porosity (%)	7.4	13.2	8.2	13	4	4.3
Dp (µm)	8.8	11.4	28.8	11.1	28.8	9.8
Dist (µm)	55	21.6	80	21.2	150	17
I (%)	88	82	–	–	–	–

results show that the new SPT protocol allows to visualize the morphology of ILT even if the contrast is less important than with the PTA.

Table 1 shows the comparison between the mean morphological properties obtained for both protocols 1 and 2. Dp corresponds to the mean pore diameter, Dist the mean distance between pores and I to the level of pore interconnection between the top and the bottom of the layer. Considering a maximal representative elementary volume, a higher porosity is obtained for the thrombus samples stained with SPT. Dp and Dist obtained with SPT differ from the ones with PTA with similar values for all layers by preserving the biological properties. Only the luminal layer was found fluid-permeable numerically with values range between $1.9.10^{-14}$ m^2 and $1.7.10^{-15}$ m^2 that are closed to the ones found macroscopically for the same thrombus ($5.26.10^{-13}$ m^2).

3.2. Permeability study

Macroscopic permeability values were obtained for each type of tested layer. For the luminal layers, permeability values ranged between $5.26.10^{-13}$ m^2 and $9.62.10^{-23}$ m^2 depending on the ILT studied. No perfusion was reported for one luminal disk. Concerning the luminal/medial disk, a permeability of $9.13.10^{-14}$ m^2 was obtained during the first 65 min then the perfusion stopped until the end of the test. Finally, no perfusion was reported for the abluminal disk. These findings are in accordance with the results found in our previous study (Léonet et al. 2022) suggesting a permeable luminal layer with high heterogeneity. Moreover, the results confirm that the abluminal layer is fluid impermeable.

3.3. Mechanical study

Figure 2 showed the Piola–Kirchoff stress-strain curves obtained from the unconfined-compression tests. A visco-hyperelastic behavior of the tissues is observed with maximum stresses comprised between 10 to 32.5 kPa at 40% of deformation. The variations can be notably explained by the high heterogeneity of the thrombus. The preconditioning effect was

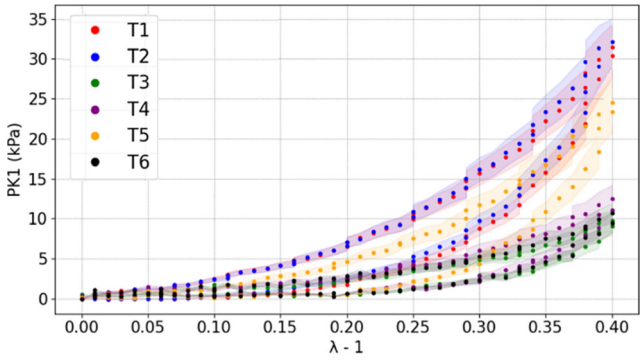


Figure 2. Stress-strain curves from unconfined-compression tests (Tx = thrombus 1 to 6).

evaluated and results show that after 5 loading-unloading cycles, the mechanical response is stabilized. Only 2 studies performed unconfined-compression tests on ILTs but the 3 layers were tested separately. The study of Boschetti et al. (2007) obtained a maximum mean Young's Modulus E of 22.5 kPa for the abluminal layer at 45% of deformation while we obtained a mean secant modulus of 50.4 kPa at 40% of deformation. The difference can be firstly explained by the difference of the experimental protocol but also by the fact that we tested all 3 layers simultaneously.

3.4. Discussion

Different morphological parameters were obtained using SPT explained by the removal of fixation and dehydration processes. In addition, SPT staining preserves tissue properties avoiding shrinkage as caused by PTA staining. Macroscopic and microscopic permeability values are comparable even if only few measurements were performed. Finally, the unconfined-compression tests revealed a visco-hyperelastic response of the tissue where a preconditioning of 5 cycles would have to be performed.

4. Conclusions

A new experimental protocol which conserves biological properties of ILT was developed for µ−CT experiments. For the first time, mechanical response under compression was obtained for ILT with all layers. This work is ongoing increasing the ILT sample number. Moreover, *in-situ* compression tests will be performed to link morphological and mechanical properties and build a reliable ILT model.

Acknowledgements

Initiative d'Excellence d'Aix-Marseille Université- AMIDEX (AMX-19-IET-010).

References

Boschetti F, Di Martino EM, Giota G. 2007. A poroviscoelastic model of intraluminal thrombus from abdominal aortic aneurysms. 2007 Summer bioengineering conference, Keystone CO. doi:10.1115/SBC2007-176341.

Léonet J, Baudouard M, De Masi M, Guivier−Curien C, Bertrand E, Lepidi H, Vicente J, Deplano V. 2022. Morphological and poro−mechanical characterization of thrombi from aortic aneurysm. Comput Methods Biomech Biomed Eng. 25:sup1, S186–S188. doi:10.1080/10255842.2022.2116885.

Pétré M, Balcaen T, El Aazmani W, Pyka G, Kerckhofs G. 2022. Effect of X-Ray contrast-enhancing staining agents on the mechanical properties of blood vessels. Tomography for Scientific Advancement Society Conference (ToScA).

KEYWORDS Thrombus; CT; permeability; compression

valerie.deplano@univ-amu.fr

How magnetic resonance elastography (MRE) could provide biomechanical property to complete computed tomography (CT) scan lung diagnostic?

M. K. Chakouch[a], P. Pouletaut[a], F. Charleux[b] and S. F. Bensamoun[a]

[a]Sorbonne University, Université de Technologie de Compiègne, UMR CNRS 7338 Biomechanics and Bioengineering, Compiègne, France; [b]ACRIM-Polyclinique Saint Côme, Radiologie Médicale, Compiègne, France

1. Introduction

Currently, the detection of pulmonary fibrosis is performed with computed tomography (CT) scan that uses radiation. From this test, subjective morphological data, with inter and intra operator variability, is obtained (Chassagnon et al. 2018). There is an important need to objectively and non-invasively quantify pulmonary fibrosis to better observe the effect of treatment and undertake the follow-up of disease. Thus, one alternative is Magnetic Resonance Elastography (MRE) that is a non-invasive technique, based on the application of motion encoding gradients (MEG) to estimate the shear modulus parameter, allowing the quantification of the biomechanical properties of different soft tissues. Other MRE parameters such as the damping ratio, the attenuation, etc. have been correlated to the physiological and structural properties of the tissue, demonstrating that additional MRE markers could provide complementary information. While the liver is the first organ approved for clinical MRE test (Pouletaut et al. 2023), additional MRE research protocols are extensively developed for the brain, kidney, prostate, muscle (Debernard et al. 2011; Chakouch et al. 2022). The COVID-19 pandemic has spurred research in the characterization of the lung tissue (Chakouch et al. 2022). Thus, the purpose of the study is to combine different imaging techniques to demonstrate the relevant biomechanical property that can be provided by MRE test.

2. Methods

2.1. Computed tomography (CT) scan

Patients ($N = 10$) had a CT scan to monitor a cough, the impacts of tobacco, asbestos, etc. Lung CT images have been acquired with multi-detector row on General Electric (GE) machine (Figures 1A-1B). Patients were examined during a single breath-hold and the following parameters were applied for the thoracic CT acquisition: FOV: $43 \times 43\,cm^2$; matrix: 512×512; voxel size: $0.84 \times 0.84 \times 0.625\,mm^3$; slice thickness: 0.625 mm; 100–140 kV according to the patient's weight. A radiologist read all CT acquisitions.

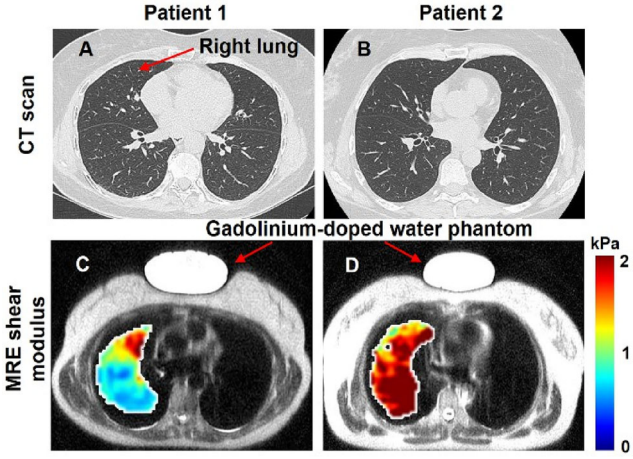


Figure 1. Example of two patients among the cohort with lung axial CT scans (A,B) and MRE shear modulus cartographies (C,D) of the right lungs. Red arrows show the localization of the gadolinium-doped water phantom.

2.2. Magnetic Resonance Elastography (MRE)

MRE tests were performed, at the same slice level as the CT scan, by using spin-echo echo-planar imaging (SE-EPI) sequence on a 1.5 T MRI GE machine to obtain 4 axial slices of the lungs.

The scan time was 22 s at breath-hold. A round pneumatic driver, used for MRE liver (Leclerc et al. 2013), was placed on the right lung. It is connected to a plastic tube where an air pressure is induced at a frequency of 50 Hz using an acoustic speaker system.

The MRE pulse sequence including a motion-encoding gradient, which oscillated in the Z direction, was used to image the displacement of the shear waves. The phase images were recorded with the following parameters: FOV: $48 \times 48\,cm^2$; TR: 250 ms; slice thickness: 15 mm; number of axial slices: 4; voxel size: $3.75 \times 3.75 \times 15\,mm^3$; matrix: 128×128; 4 phase offsets.

To measure the lung biomechanical properties different steps are followed: (1) a region of interest is drawn to select only the right lung to avoid the heart motion, (2) the apparent lung shear modulus is calculated from the phase images using multi-model direct inversion (MMDI) and a specific post- processing

(Silva et al. 2015), and then (3) corrected with the cartography of the density hereafter described.

2.3. Lung density

The shear modulus being proportional to the density, a cartography of lung density for each patient is necessary to obtain a true cartography of the shear modulus (Figure 1C,D).

MRI was performed at breath-hold, at the same slice level as the CT scan, with a fast gradient recalled echo (GRE) sequence (Holverda et al. 2011) and a TR: 15 ms, from which the initial signal of the lung was estimated. Then, the lung density was obtained in reference to a Gadolinium-doped water phantom (Figures 1C,D) placed on the chest. The MRI acquisition is realized with: FOV: $48 \times 48\,cm^2$; voxel size: $7.5 \times 7.5 \times 15\,mm^3$; matrix: 64×64; slice thickness: 15 mm; and flip angle: 10°.

3. Results and discussion

Figure 1A,B shows an example of CT scan results obtained for two patients with unknown lung disease. No detectable solid mass or any other lung disease was identified on both CT scans, leading to the conclusion that the two patients have healthy lungs.

Figure 1C,D shows the results of the true MRE cartographies of the shear modulus tests obtained for the two patients. The mean shear modulus for patient 1 and patient 2 are 1.15 ± 0.58 kPa and 2.40 ± 0.82 kPa, respectively. The value obtained for patient 1 is in agreement with the literature for healthy lung (Fakhouri et al. 2022). However, patient 2 revealed a higher shear modulus indicating a pathological biomechanical property of the tissue.

To summarize, the CT scans for both patients had healthy structural properties but the MRE tests have highlighted different biomechanical behaviors. This result shows possible benefits of the MRE tests which can provide complementary information to better diagnose the lung tissue.

4. Conclusions

This study has showed that MRE test could become a non-invasive lung diagnostic tool, allowing the quantification of the lung shear modulus, a potential biomechanical marker of lung disease. In perspective, the CT scan parameters could be correlated to the MRE parameters to predict the evolution of the lung disease. In addition, MRE protocol must be further enhance for the biomechanical characterization of the both right and left lungs. The present study shows the potential interest of MR elastography in the regular care of lung disease and paves the way for other lung applications.

Acknowledgements

This work was supported by the European React'EU recovery plan.

References

Chakouch M, Charleux F, Pouletaut P, Bensamoun SF. 2022. MR elastography of the human lung. State Art Bioeng. 2(1):hal-03562216.

Chassagnon G, Martin C, Burgel PR, Hubert D, Fajac I, Paragios N, Zacharaki EI, Legmann P, Coste J, Revel MP. 2018. An automated computed tomography score for the cystic fibrosis lung. Eur Radiol. 28(12):5111–5120. doi:10.1007/s00330-018-5516-x.

Debernard L, Robert L, Charleux F, Bensamoun SF. 2011. Characterization of muscle architecture in children and adults using magnetic resonance elastography and ultrasound techniques. J Biomech. 44(3):397–401. doi:10.1016/j.jbiomech.2010.10.025.

Fakhouri F, Kannengiesser S, Pfeuffer J, Gokun YD, Kolipaka A. 2022. Free-breathing MR elastography of the lungs: an in vivo study. Magnetic Resonance Med. 87(1):236–248. doi:10.1002/mrm.28986.

Holverda S, Theilmann RJ, Sá RC, Arai TJ, Hall ET, Dubowitz DJ, Prisk GK, Hopkins SR. 2011. Measuring lung water: ex vivo validation of multi-image gradient echo MRI. J Magn Reson Imaging. 34(1):220–224. doi:10.1002/jmri.22600.

Leclerc GE, Charleux F, Robert L, Ho Ba Tho MC, Rhein C, Latrive JP, Bensamoun SF. 2013. Analysis of liver viscosity behavior as a function of multifrequency magnetic resonance elastography (MMRE) postprocessing. J Magn Reson Imaging. 38(2):422–428. doi:10.1002/jmri.23986.

Pouletaut P, Boussida S, Ternifi R, Miette V, Audière S, Fournier C, Sandrin L, Charleux F, Bensamoun SF. 2023. Impact of hepatic iron overload in the evaluation of steatosis and fibrosis in patients with nonalcoholic fatty liver disease using vibration controlled transient elastography (VCTE) and MR imaging techniques: a clinical study. Innov Res Biomed Eng. 44(3):100750. doi:10.1016/j.irbm.2022.100750.

Silva AM, Grimm RC, Glaser KJ, Fu Y, Wu T, Ehman RL, Silva AC. 2015. Magnetic resonance elastography: evaluation of new inversion algorithm and quantitative analysis method. Abdom Imaging. 40(4):810–817. doi:10.1007/s00261-015-0372-5.

KEYWORDS Lung; biomechanical properties; magnetic resonance elastography; computed tomography; shear modulus

sabine.bensamoun@utc.fr

Improvement of the prediction of the vascular structure deformation induced by tools insertion in EVAR

H. Mozahem[a], M. Chastre[b], F. Lalys[b], S. Esneault[b], A. Kaladji[c] and A. Bel-Brunon[a]

[a]CNRS, LaMCoS, UMR 5259, F-69621, Univ. Lyon, INSA Lyon, Villeurbanne, France; [b]Therenva, F-35000, Rennes, France; [c]CHU Rennes, Inserm, LTSI, UMR 1099, Univ. Rennes, Rennes, France

1. Introduction

Endovascular aneurysm repair (EVAR) is the most popular treatment for abdominal aortic aneurysm (AAA). During this procedure, the arterial deformation caused by endovascular devices can cause intra and postoperative complications. Thanks to advances in fusion imaging, surgeons can reduce these complications risk with proper planification during the preoperative step. Yet, estimating the deformations induced by tools insertion during the procedure is mainly based on surgeon's experience.

During the last ten years, biomechanical models have been used in finite-element simulation to predict the tools effects on the arterial wall. Gindre et al. (2017) developed a parametric model of the aorto-iliac structure and its surrounding, and simulated its deformation due to the guidewire insertion. The model parameters were tuned and validated with 28 patient cases for which intraoperative and simulated guidewire positions were compared.

This was the only validation data as only the tools could be observed on intraoperative images. Since then, fluoroscopy images quality improved and the validation can now rely on the vascular wall position. This more comprehensive measure was used by recent studies to predict ostia displacement due to arterial deformations (Dupont et al. 2021). Predicting the ostia displacement instead of the tools position can provide useful information to the surgeon during the planning phase, for instance to prevent the risk of the stent-graft covering the renal ostia.

In this study, we tested Gindre parametrization with a validation including both the guidewire position (for iliac deformations) and the renal ostia position, and proposed a new parametrization to improve the simulation predicting performances.

2. Methods

2.1. Patient data

In this study, 21 patient cases with AAA and undergoing EVAR between January 2016 and December 2017 were selected. For each patient, preoperative CT-scan and intraoperative fluoroscopy image were acquired. 19 patient cases were selected for renal ostia position validation, among which 6 patient cases could also be used for iliac guidewires position validation. 2 more patient cases with intraoperative iliac guidewires position only were also selected. The selected patients experienced large ostia displacement according to clinicians.

2.2. Simulation

The biomechanical model and the simulation process used in this study were the same as Gindre et al. (2017), as described in their publications. The preoperative CT-scans of the patient data were used to construct the biomechanical model of the vascular structure. The patient-specific geometry is segmented with the clinical planning software ENDOSIZE® (Therenva, Rennes, France).

The mesh is composed of discrete Kirchhoff triangular (DKT) shell elements, with a homogeneous thickness of 1.5 *mm* for the aorta, and 1.2 *mm* for the iliac arteries. To simulate the mechanical behaviour of the arterial wall, a polynomial nonlinear isotropic hyperelastic potential of Yeoh second order is used:

$$W = C_{10}(I_1 - 3) + C_{20}(I_1 - 3)^2$$

This model only represents the arterial wall, the effect of the surrounding tissues and environment is modeled by an external load on the wall with three terms, an elastic spring term, a viscosity term and a pressure one:

$$\overrightarrow{f_{ext}} = (-k\vec{u} - c\vec{v} + p\vec{n}) \cdot dS$$

The model was simulated with Ansys LS-DYNA explicit finite-element solver (Ansys, Inc., Canonsburg, PA, USA). The model geometry corresponds to a pre-stressed state of the model due to arterial pressure. Therefore, a stress-free geometry, called 'zero-pressure geometry' was applied with a controlled internal blood pressure. Then the insertion of a stiff guidewire is simulated. The guidewire is represented with 189 4 *mm* two-nodes beam elements with linear elastic properties: $E = 180\ GPa,\ \upsilon = 0.3$.

2.3. Validation methodology

The new validation method includes landmark points of the vascular wall (renal ostia) and guidewire position on the iliac arteries (from P7/P8 to P4). The positions obtained from simulation are compared to those obtained from intra-operative fluoroscopy

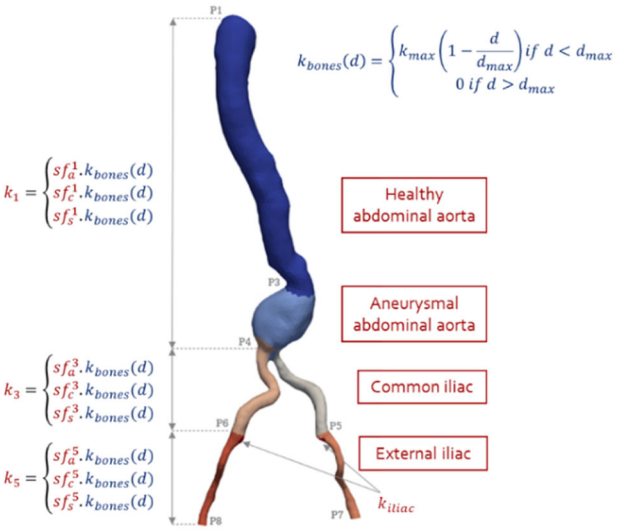


Figure 1. Elastic stiffness distribution of the external support on the vascular wall.

images. The Modified Hausdorff Distance (MHD) was used to measure the position error of the guidewire:

$$MHD(G_{real}, G_{simu}) = \max[\text{moy}d(p, G_{simu})_{p \in S_{real}}, \text{moy}d(p, G_{real})_{p \in S_{simu}}]$$

With p, G_{simu} and G_{real} representing points of simulated and intraoperative guidewire respectively and d the node-to-node distance.

This error is calculated the same way between the preoperative and intraoperative configurations.

2.4. Sensitivity analysis

In order to improve the model parametrization, trial and error method was privileged over optimization methods. This choice is explained by the long-time simulation and the large number of parameters. Based on observations of Lalys et al. (2019), clinicians expertise as well as Gindre parametrization results, four parameters of elastic stiffness were adapted: (sf_c^1, sf_s^1) were decreased from (1, 0.25) to (0.7, 0) so that renal ostia were more free to move; (sf_a^5, k_7) were increased from (0, 0.2) to (0, $1E-6\ MPa.mm^{-1}$) so that iliac arteries were more constrained.

3. Results and discussion

Nineteen patient cases with large displacement of the renal ostia were simulated with Gindre parametrization and the proposed new parametrization, based on their preoperative CT-scans. The obtained results showed a mean reduction of the error from

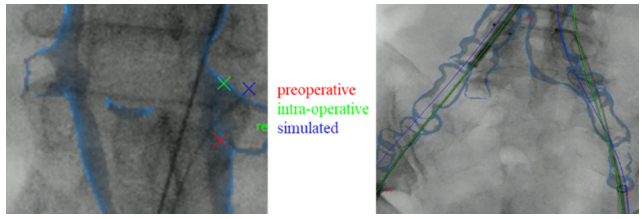


Figure 2. Position of renal ostia and guidewires obtained from preoperative CT-scan (red), intraoperative fluoroscopy (green), and simulation (blue) on fluoroscopy images.

10.58 ±5.99 *mm* (intra vs preoperative configurations) *to* 3.90 ±3.61mm (intraoperative vs simulated configurations) for the left renal ostium and from 10.39 ±5.07mm (intra vs preoperative configurations) to 4.04 ±3.47mm (intraoperative vs simulated configurations) for the right renal ostium.

For the 8 patient cases with intraoperative guidewires positions, the obtained position error of the guidewire with the new parametrization was below 5 mm, with a MHD value of 4.96 ±2.20mm for the left guidewire and 2.95 ±1.60mm for the right guidewire.

Those promising results show that it is possible to accurately predict both the iliac deformations and renal ostia displacements, which are both quantities of interest for the surgeons, especially for patients experiencing large deformations. The proposed parametrization does not result from a proper optimization due to computational cost and parametrization complexity; besides the number of considered patients is rather small. However, the validation images which field of view include both the renal ostia and the iliac arteries are rare.

4. Conclusions

The reduction of the mean displacement error of renal ostia as well as guidewires position shown in this study improves the accuracy of the biomechanical model. It needs confirmation on more patient data. Predicting the deformation induced by insertion of endovascular tools could provide the surgeon more information during the preoperative planning for the EVAR procedure, improve image fusion and potentially increase the success rate of the surgery.

References

Dupont C, Kaladji A, Rochette M, Saudreau B, Lucas A, Haigron P. 2021. Numerical simulation of fenestrated graft deployment: anticipation of stent graft and vascular structure adequacy. Int J Numer Method Biomed Eng. 37(1):e03409.

Gindre J, Bel-Brunon A, Rochette M, Lucas A, Kaladji A, Haigron P, Combescure A. 2017. Patient-specific finite-element simulation of the insertion of guidewire during an EVAR procedure: guidewire position prediction validation on 28 cases. IEEE Trans Biomed Eng. 64(5):1057–1066. doi:10.1109/TBME.2016.2587362.

Lalys F, Barré A, Kafi M, Benziane M, Saudreau B, Dupont C, Kaladji A. 2019. Identification of parameters influencing the vascular structure displacement in fusion imaging during endovascular aneurysm repair. J Vasc Interv Radiol. 30(9):1386–1392. doi:10.1016/j.jvir.2019.02.022.

KEYWORDS Finite element simulation; patient-specific; endovascular navigation; abdominal aorta; validation

hussein.mozahem@insa-lyon.fr

Increase of wall shear stress in a vessel due to curvature

Y. Chen[a,b,c], J. C. Béra[a,c], X. Escriva[b,c], T. Castelain[b,c] and B. Gilles[a,c]

[a]LabTAU U1032 Inserm, Lyon, France; [b]LMFA, Lyon, France; [c]Université de Lyon, Lyon, France

1. Introduction

Arterial endofibrosis is a non-atheromatous vascular pathology specific to athletes. It is defined histologically by an intimal fibrosis leading to wall thickening and to the reduction of the artery lumen caliber (Feugier and Chevalier 2004). Numerous etiological hypotheses have been proposed to explain the pathological development but no dedicated study has yet tested these hypotheses on *in vitro* / *in vivo* or in silico experiments. Hemodynamic alteration as one of the etiological factors has been proposed by several authors (Chevalier et al. 1986; Kral et al. 2002). The increased cardiac output and arterial hypertension at maximal strain, contribute to generating an abnormal levels of wall shear stress (Kral et al. 2002). According to Chevalier et al. (Chevalier et al. 1986), the majority of subjects with endofibrosis have excess iliac artery length, which promotes the arterial curvature. In addition, the damage is often observed on the outer bend of the vessels. Our research hypothesis is that in the absence of bifurcation and significant stenosis, the vessel flow structure is locally dominated by the centrifugal forces due to curvature, which causes the fluid particles to change their main direction of motion and Dean vortices to appear, with an increase of the wall shear stress, which is the main factor of artery injury.

Under the flow conditions in resting subjects, the peak Reynolds number ranges from 300 to 700 (volume flow rate ~0.3 l/min) (Stein et al. 1979), while it can reach 2000 during exercise. The objective of this preliminary work is to study the wall shear stress distribution in the curved part of the artery depending on different value of Reynolds number (Re), using numerical simulations (CFD—computational fluid dynamics). While several numerical studies have investigated pipe bends with curvature angles ranging from 90 degrees to 180 degrees (see Cox et al. 2019 for instance), our focus lies on a lower curvature angle more relevant to the iliac artery, for which the secondary flow might not be fully developed.

2. Methods

2.1. Artery model and flow conditions

The study deals with the flow in a simplified geometry consisting of a circular tube of constant diameter $D = 1$ cm, with a straight pipe (length 3.5D) followed by a bent part (curvature radius R = 3D, curvature angle of 55°), and ended by a straight pipe (length 10.5D). Geometry parameters were extracted from medical imaging data obtained from a set of four patients' morphological parameters with arterial endofibrosis, including the determination of the curvature radius in the region where the artery lumen caliber is reduced.

Assuming a quasi-permanent flow regime in such a constant section vessel, a continuous flow confined by rigid walls is considered for this preliminary work. The Reynolds number (Re) varies from 275 to 2000 and the corresponding Dean number $\left(Dn = Re\sqrt{\frac{D}{2R}}\right)$ varies from 112 to 816.

2.2. Numerical simulations

The numerical computations have been performed with the finite volume-based open-source toolbox OpenFOAM®, using the SIMPLE procedure for coupling the velocity and pressure fields.

A paraboloid profile is taken as inflow velocity conditions, and a zero-gradient boundary condition is applied at the outflow cross section. A hexahedral mesh structure is arranged in the cross section of the geometry. The mesh is based on a O-grid structured pattern in the cross-section of the geometry with additional refinement near the curved section to ensure equivalent fineness of the mesh in upstream and downstream sections compared to the curved section. The resulting final hexahedral mesh, after a thorough mesh convergence study at Re =2000, comprises 436,080 cells.

The Reynolds numbers are adjusted to accommodate a Newtonian model of blood fluid with a kinematic viscosity of 3.8 10^{-6} m^2/s.

The simulation model was first validated using experimental results from Enayet et al. (1982) obtained in a configuration corresponding to a 90° bend with a diameter of 48 mm at Re =500. A Laser Doppler Velocimetry (LDV) experimental setup is being developed in order to compare and validate our numerical observations in the configuration of our study.

3. Results and discussion

In order to understand the flow structure in the area of curvature, the contour plots of the longitudinal velocity component U is presented at Re = 550 in

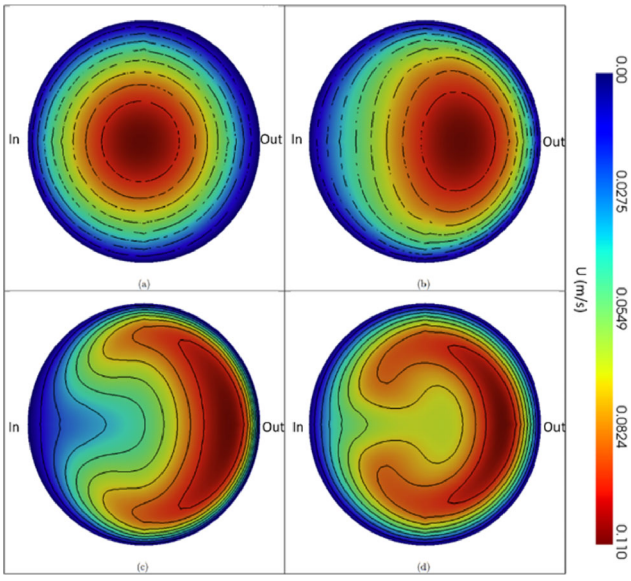


Figure 1. Contour plots of longitudinal velocity U at four places along the pipe Re =550: a) at the entrance of the bend, b) at the Middle of the bend, c) at the end of the bend, d) at 3D downstream of the bend.

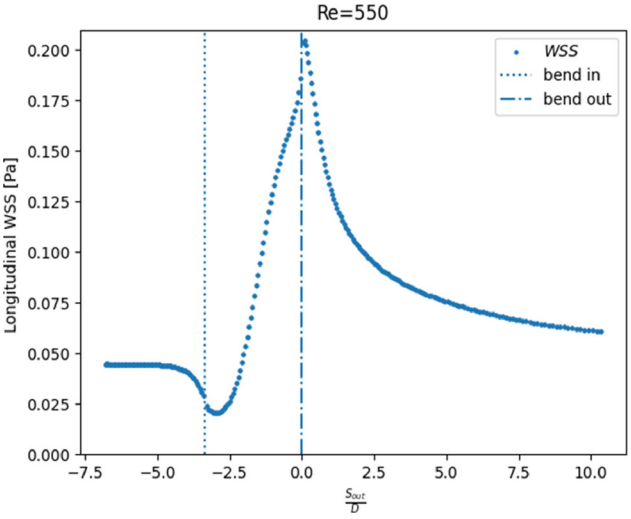


Figure 2. Longitudinal WSS along the outer curvilinear abscissa sout/D at Re =550.

Figure 1. The corresponding volume flow rate is 0.26 l/min, the mean velocity is 0.055 m/s. As a paraboloid velocity profile penetrates the bend (Figure 1a), the fluid in the center of the pipe is swept towards the outer side of the bend due to centrifugal forces as shown in Figure 1b.

The fluid near the pipe wall returns towards the inside of the bend, creating a pair of counter-rotating cells classically denoted as Dean vortices (Figure 1c). This secondary flow is persistent at a distance 3D downstream of the bend (Figure 1d).

Table 1. Maximum WSS values.

Re	275	550	690	960	1370	2000
Dn	112	225	282	392	559	816
Max WSS (Pa)	0.06	0.20	0.29	0.48	0.81	1.42

The maximum velocity gradient in the outer side of the bend is observed. Figure 2 shows the longitudinal Wall Shear Stress (WSS) along the outer curvilinear abscissa Sout/D at Re = 550. The straight part upstream corresponds to Sout/D = [−6.8,−3.36], the bend corresponds to Sout/D = [−3.36,0], and the straight part downstream to Sout/D = [0,10.5].

A sharp maximum of longitudinal WSS is observed at the end of the bend. Its value reaches 0.2 Pa at Re = 550, but it increases rapidly with Re and exceeds 0.5 Pa as soon as Re is larger than 1000, as shown in Table 1. The results also reveal that the maximum WSS is consistently located at the end of the bend.

4. Conclusions

This study presents the flow under normal hemodynamics conditions. Dean vortices are observed in the area of curvature, where the longitudinal WSS is sharply increased along the outer side of the pipe. The maximum value is reached at the end of the bend. The position of the maximum WSS remains unchanged despite an increase in Reynolds number, but exhibiting a clear correlation with the curvature of the vessel. Further investigation is necessary to explore the relationship between the position of the maximum WSS and the localization of endofibrotic plaque.

Acknowledgements

The authors would like to thank P. Feugier for the fruitful discussions and assistance with the morphological data.

References

Chevalier J-M, Enon B, Walder J, Barral X, Pillet J, Megret A, Lhoste P, Saint-AndrC J-P, Davinroy M. 1986. Endofibrosis of the external iliac artery in bicycle racers: an unrecognized pathological state. Ann Vasc Surg. 1(3): 297–303.

Cox C, Najjari MR, Plesniak MW. 2019. Three-dimensional vortical structures and wall shear stress in a curved artery model. Phys Fluids. 31(12):121903. doi:10.1063/1.5124876.

Enayet MM, Gibson MM, Taylor AMKP, Yianneskis EM. 1982. Laser-Doppler measurements of laminar and turbulent flow in a pipe bend. Int J Heat Fluid Flow. 3(4): 213–219. doi:10.1016/0142-727X(82)90024-8.

Feugier P, Chevalier J-M. 2004. Endofibrosis of the iliac arteries: an underestimated problem. Acta Chirurgica Belgica. 104(6): 635–640. doi:10.1080/00015458.2004.11679635.

Kral CA, Han DC, Edwards WD, Spittell PC, Tazelaar HD, Cherry KJ. 2002. Obstructive external iliac arteriopathy in avid bicyclists: new and variable histopathologic features in four women. J Vasc Surgery. 36(3):565–570. doi: 10.1067/mva.2002.126558.

Stein PD, Sabbah HN, Anbe DT, Walburn FJ. 1979. Blood velocity in the abdominal aorta and common iliac artery of man. BIR. 16(3):249–255. doi:10.3233/BIR-1979-16313.

KEYWORDS Vascular flow; wall shear stress; dean vortices; arterial endofibrosis

yuling.chen@inserm.fr

Intracardiac hemodynamics: a preliminary parametric study

S. Bru[a], S. Mendez[a], D. Garcia[b] and F. Nicoud[a]

[a]IMAG, Univ Montpellier, CNRS, Montpellier, France; [b]CREATIS, University Lyon 1, INSA Lyon, France

1. Introduction

Heart failure is the cardiomyopathy that will have the greatest impact on the lives of European citizens in the next decades (Timmis et al. 2019). Early detection and accurate prediction of heart failure is challenging, but recent advances in numerical simulation techniques and exploitation of imaging raise new hopes by making it possible to study blood flow in the heart. One such tool is Ultrasound (US) Doppler imaging, which is a fast and non-invasive way to investigate the intracardiac hemodynamics. However, US Doppler imaging provides only partial information about the blood flow, and the lack of complete data hampers accurate diagnoses. To address this challenge, an algorithm named 4D-*i*VFM has been developed by Assi et al. (2017); Vixege et al. (2021) to reconstruct the two missing velocity components from the radial component of the velocity. To validate the 4D-*i*VFM algorithm, a virtual echo doppler exam was performed on a numerical flow model to reproduce the blood flow, and the reconstructed intra cardiac flow was compared against the ground truth CFD solution to test the accuracy of the method (Assi et al. 2017; Vixege et al. 2022).

So far, the 4D-iVFM algorithm was tested by considering only one cardiac geometry and operating condition. This study explores the numerical simulation of a left heart and some variations of several key features for a better understanding of their influence on the cardiac hemodynamics. Section 2 describes briefly the numerical method used to simulate the intracardiac flow, and the parametric study that has be done. Section 3 discusses some of the results obtained so far.

2. Methods

2.1. Numerical method

A numerical framework to compute the blood flow within patient-specific human hearts was developed by Chnafa et al. (2014). The geometry of the heart cavities and their wall dynamics were extracted from medical images of a patient, and the simulations were made using the in-house YALES2BIO solver (Mendez et al. (2022)). The geometric domain is composed by the four pulmonary veins, the left atrium, the left ventricle and the aorta. The valves are modeled using an immersed boundary method.

Blood is modeled as an incompressible fluid of density 1000kg m^{-3} and kinematic viscosity 4×10^{-6} $m^2 s^{-1}$. The flow equations are written on a conformal moving computational domain, using an Arbitrary Lagrangian-Eulerian framework, and solved numerically with a fourth-order finite-volume technique available in YALES2BIO.

Table 1. Summary of the different cases.

	Bpm	C_{dilat}	Reynolds
Reference	60	1	5000
Case 1	45	1	3900
Case 2	80	1	6700
Case 3	60	0.85	3600
Case 4	60	1.2	7200

2.2 A Preliminary parametric study

To investigate the impact of different parameters on the intracardiac blood flow, a number of key variables were selected for manipulation in this study.

- Heartbeat (from 45 to 80 beats per minute (bpm))
- Isotropic volume change: from Cdilat =0.85 (15% compression) to 1.2 (20% dilatation)

The main characteristics of the simulations performed are provided in Table 1.

2.3 Study of the effects of the mitral valve

The mitral valve plays a critical role in regulating blood flow. In the model from Chnafa et al. (2014), the position of the mitral valve was extracted from medical images but, due to the bad resolution of those images the exact shape was not reproduced. Instead, the valve was modelled by a thick cone, and assumed to open and close instantaneously, with no intermediate positions. A crude penalty method was used to model the effects of this valve on the fluid, driving the flow velocity to zero in the valve region.

A more accurate valve model has been developed in the course of this study, which accounts for a more localized description of the valve, its intermediate position as well as its shape. The geometry of this model is based on the work of Domenichini and Pedrizzetti (2015) and reads:

$$\begin{cases} x_v(\theta,s) = R\cos\theta(1 - s\cos\varphi) - \varepsilon R s\cos\varphi \\ y_v(\theta,s) = R\sin\theta(1 - sk\cos\varphi) \\ z_v(\theta,s) = -s^2\left(\dfrac{1+k}{2} + \varepsilon\cos\theta + \dfrac{1-k}{2}\cos 2\theta\right)R\sin\varphi \end{cases}$$

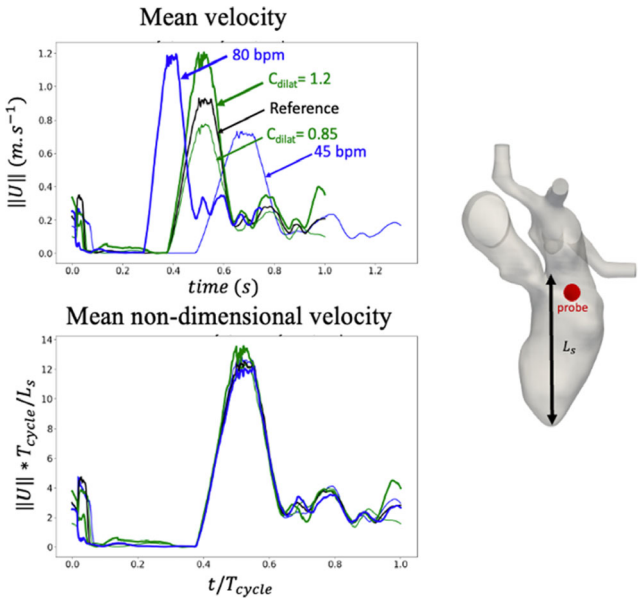


Figure 1. Comparison of the velocity (mean velocity of 30 cycles) of a probe close to the mitral valve.

with R representing the radius, ε denoting the asymmetry of the valve, and k representing the curvature of the leaflets. In this model, the coordinates θ and s span the ranges $[0, 2\pi]$ and $[0, 1]$, respectively, whereas φ allows for continuous evolution from closed ($\varphi = 0$) to open ($\varphi = \varphi_{max}$) geometry.

The localization of the valve and the computation of the effects of the latter on the fluid flow were also improved by using the immersed boundary method detailed in Siguenza et al. (2016) instead of the crude penalization method used in Chnafa et al. (2014).

This novel model is used to explore four distinct scenarii: the baseline (normal) case where $\varphi_{max} = 1.1$, $\varepsilon = 0.25$, $k = 0.6$, on top of three anormal situations with either a larger leaflet asymmetry ($\varepsilon = 0.45$), an increased ($\varphi_{max} = 1.3$) or reduced ($\varphi_{max} = 0.9$) opening angle. The latter case mimics a pathological condition corresponding to the calcification of the anterior leaflet of the mitral valve.

3. Results and discussion

For the first parametric study, the velocity signal recorded at a probe located downstream of the mitral valve are shown in Figure 2, which also displays the probe location. Although the different cases considered in Table 1 lead to very different signals (Figure 1a), all the results overlap very nicely (Figure 1b) once properly scaled by the period of a cycle (T_{cycle}) and the length of the ventricle at the end of systole (L_s).

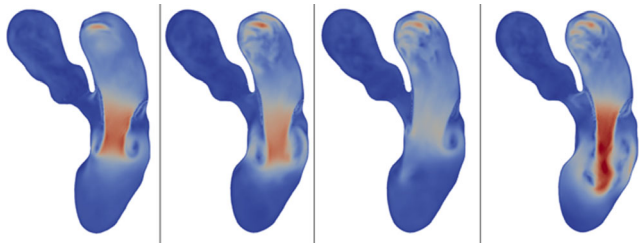


Figure 2. Flow in the left heart at $t/t_{cycle} = 0.55$ for 4 mitral valve model. From left to right: Reference case, $\varepsilon = 0.45$, $\varphi_{max} = 1.3$, anterior leaflet impaired.

Thus, the flows in the five cases appears to be very similar, up to a scaling factor. This outcome is consistent with the study of other parameters (vorticity, Q criterion), where the effects of changes are minimal.

In contrast, modifications to the mitral valve model exert a significant influence on the flow dynamics within the ventricle, notably altering the properties of the jet and vortices, as illustrated in Figure 2. To assess the 4D-iVFM's ability to accurately reproduce the intra cardiac flow in a variety of situations, the reconstruction algorithm is being applied to the four cases presented. This will be discussed in the presentation.

References

Assi KC, Gay E, Chnafa C, Mendez S, Nicoud F, Abascal JFPJ, Lantelme P, Tournoux F, Garcia D. 2017. Intraventricular vector flow mapping-a Doppler-based regularized problem with automatic model selection. Phys Med Biol. 62(17):7131–7147. doi:10.1088/1361-6560/aa7fe7.

Chnafa C, Mendez S, Nicoud F. 2014. Image-based large--eddy simulation in a realistic left heart. Comput Fluids. 94:173–187. doi:10.1016/j.compfluid.2014.01.030.

Domenichini F, Pedrizzetti G. 2015. Asymptotic model of fluid–tissue interaction for mitral valve dynamics. Cardiovasc Eng Technol. 6(2):95–104. doi:10.1007/s13239-014-0201-y.

Mendez S, Bérod A, Chnafa C, Garreau M, Gibaud E, Larroque A, Lindsey S, Martins Afonso M, Mattéoli P, Méndez Rojano R, et al. 2022. YALES2BIO: a general purpose solver dedicated to blood flows.

Sigüenza J, Mendez S, Ambard D, Dubois F, Jourdan F, Mozul R, Nicoud F. 2016. Validation of an immersed thick boundary method for simulating fluid–structure interactions of deformable membranes. Comput Phys. 322:723–746. doi:10.1016/j.jcp.2016.06.041.

Timmis A, Townsend N, Gale CP, Torbica A, Lettino M, Petersen SE, Mossialos EA, Maggioni AP, Kazakiewicz D, May HT, et al. 2019. European society of cardiology. Cardiovascular Disease Statistics Eur Heart J. 41(1):12–85.

Vixege F, Berod A, Sun Y, Mendez S, Bernard O, Ducros N, Courand P, Nicoud F, Garcia D. 2021. Physics-constrained intraventricular vector flow mapping by color Doppler. Phys Med Biol. 66:245019. doi:10.1088/1361-6560/ac3ffe.

Vixege F, Berod A, Courand P, Mendez S, Franck N, Blanc-Benon P, Vray D, Garcia D. 2022. Full-volume three-component intraventricular vector flow mapping by triplane color Doppler. Phys Med Biol. 67(9):095004. doi:10.1088/1361-6560/ac62fe.

KEYWORDS Intracardiac hemodynamic; blood flow

salome.bru@umontpellier.fr

Noninvasive estimation of pressure drop in arterial stenoses with color Doppler ultrasound

S. Choupani[a], F. Varray[a], B. Gilles[b], J. C. Béra[b] and D. Garcia[a]

[a]CREATIS U1294 UMR5220; [b]LabTAU U1032, Lyon, France

1. Introduction

Vascular stenosis, in which a vessel narrows, results in reduced blood flow to the tissues it supplies. Assessing the severity of vascular stenosis is critical to making therapeutic decisions. A conventional method is to scan the affected region with vascular ultrasound and use anatomic criteria to grade the severity. These measurements provide limited information about the hemodynamic function of the stenosis. To address this issue, measuring the total pressure drop induced by the stenosis is an effective solution. Intravascular pressure can be assessed by catheterization, which is an invasive medical procedure with potential complications, making noninvasive methods preferable.

Phase-contrast magnetic resonance imaging can provide 3-D + time blood velocities. However, its use is primarily for research purposes, not routine examination. On the other hand, Doppler ultrasound is a widely used clinical modality for real-time blood flow analysis. Doppler ultrasound combined with fluid dynamics equations can accurately estimate pressure drops in significant aortic stenoses (diverging jets) or pressure gradients in the left ventricle (Euler-type flow). In parallel, various techniques have been proposed to derive vector velocity fields based on color Doppler imaging.

Estimating pressure drops in arterial stenoses is another matter: (1) the ultrasound beam cannot be aligned with the flow axis; (2) the pressure drop arises from both wall friction and the downstream divergent jet. The purpose of our study was to estimate the pressure drop in mild to moderate arterial stenosis, using conventional clinical color Doppler, for earlier diagnosis. The approach that we developed allows (1) recovering intravascular velocity vector fields from color Doppler images, then (2) estimating pressure drops induced by a stenosis. We validated our innovative method in axisymmetric models of carotid stenosis from (i) multiphysics simulations that included fluid dynamics and ultrasound, and (ii) *in vitro* phantoms in which color Doppler velocities and pressures were measured.

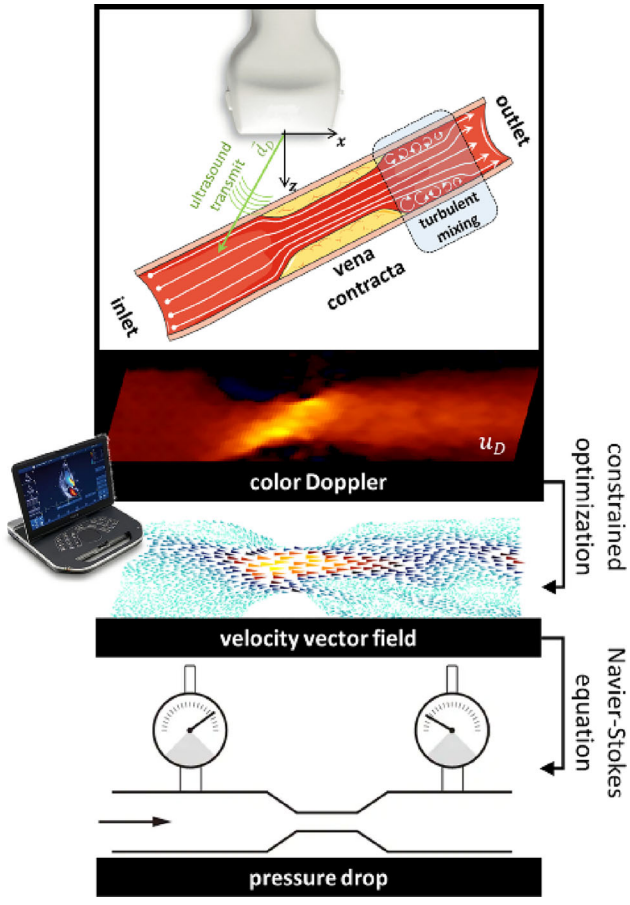


Figure 1. From color Doppler to pressure drop.

2. Methods

2.1. Optimization method: from color Doppler to trans-stenotic pressure drop

The methodological approach was two-fold (Figure 1):

A vascular vector flow mapping (***v*VFM**) method recovered the 2-D velocity vector field $\vec{v} = \{v_x, v_z\}$ from the scalar Doppler field u_D.

The trans-stenotic pressure drop was estimated from $\vec{v}$ by integrating the Navier-Stokes equations.

1 – We note $\vec{d}_D$ the direction vector of the ultrasound beam pointing from the transducer to the blood flow (Figure 1). To estimate $\vec{v}$ from u_D, we solved the constrained least-squares minimization problem:

$$\vec{v} = \text{argmin}_{\vec{u}} \left(\| \vec{u} \cdot \vec{d}_D - u_D \|^2 + \alpha \| \boldsymbol{D} \vec{u} \|^2 \right),$$

$$\text{subject to} \begin{cases} \text{div}_{axisymmetric}(\vec{v}) = 0, \\ \vec{v} \cdot \vec{n}_{wall} = 0. \end{cases}$$

The matrix $\boldsymbol{D}$ refers to second-order partial derivatives and induces spatial smoothing whose level is

tuned by the positive scalar α. $\overrightarrow{n}_{wall}$ stands for the unit vector normal to the vessel walls. The constraints ensure incompressibility and no-penetration boundaries.

2 – Pressure drops were derived from the estimated velocity fields $\overrightarrow{v}$. In an arterial stenotic constriction, the flow converges down to the vena contracta and then diverges to regain its initial geometry. Most of the energy loss occurs in the divergent zone as a result of turbulent mixing. We estimated the ΔP pressure drops ($= P_{\text{outlet}} - P_{\text{inlet}}$) by using the Bernoulli equation (no energy dissipation) between the inlet and the vena contracta and by integrating the Navier-Stokes equation between the vena contracta and the outlet. The estimated pressure drops were compared with the ground-truth pressure drops (see subsections 2.2 and 2.3).

2.2. Validations through multiphysics simulations

We simulated blood flow and color Doppler in axisymmetric models of carotid stenoses (8-mm ⌀). Cosine- and Gaussian-shaped stenoses were created, each with degrees of stenosis of 60% and 70% in ⌀ reduction. Steady flow rates were studied (up to 1 L/min) by using COMSOL Multiphysics assuming a Newtonian fluid and k-ϵ turbulent regime. The simulated flow fields were seeded with 50,000 scattering particles to compute ultrasound simulations using SIMUS (Garcia 2022; Cigier et al. 2022): 7.6-MHz linear array, focused beams, beam-to-flow angle = 15°, Doppler packet size = 6. The simulated ultrasound signals were post-processed using the MATLAB ultrasound MUST toolbox (Garcia 2021) to obtain color Doppler velocities. The velocity vector fields were then estimated by using the vVFM method from which we deduced the trans-stenotic pressure drops (see Subsection 2.1).2.3. Validations through *in vitro* experiments. Blood-mimicking fluid flowed into four homemade carotid stenosis phantoms. Cosine- and Gaussian-shaped stenoses were created with 50% and 60% degrees of stenosis to mimic mild to moderate grades. Steady flow rates ranged from 0.2 to 1.2 L/min. Color Doppler velocities were obtained with a clinical ultrasound system (GE Vivid iq). Velocity vector fields were estimated using the vVFM method, from which we derived trans-stenotic pressure drops (see Subsection 2.1). Upstream and downstream pressures were measured with pressure guidewires (ComboWire XT, Philips Volcano) to obtain ground-truth pressure drops.

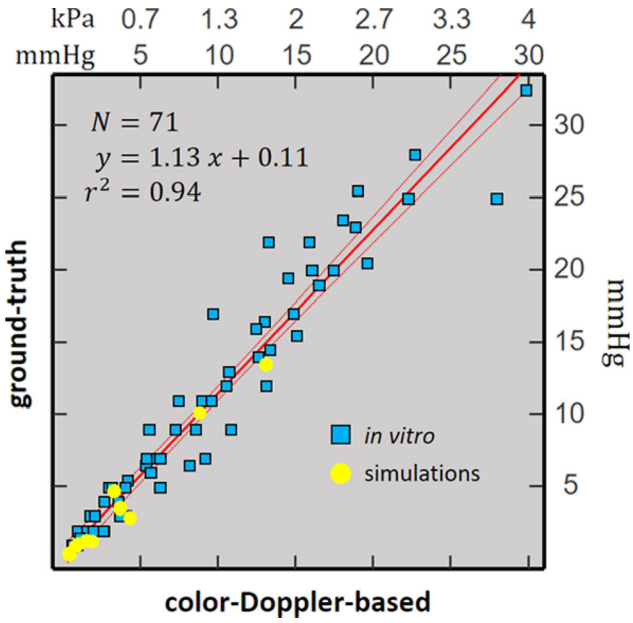


Figure 2. Estimated vs. ground-truth pressure drops.

3. Results and discussion

3.1. In silico and in vitro results

Both problems were reduced to linear matrix systems whose solutions were computed in a fraction of a second. When stacking *in silico* and *in vitro* data experiments, pressure drops estimated by color Doppler ranged from 1 to 30 mmHg (4000 Pa) for steady flow rates between 0.2 and 1.2 L/min. The two-step method showed good agreement between Doppler-based and ground-truth pressure drops ($r^2 = 0.94$, $y = 1.1x + 0.1$, $N = 71$, Figure 2). Our results tend to confirm that pressure drop in arterial stenoses can be estimated noninvasively with clinical color Doppler ultrasound.

3.2. Limitations and perspectives

In this work, we have considered the conditions of a quasi-axisymmetric steady flow. The study will be generalized to pulsatile flows by time averaging the equations over a cardiac cycle. We will also investigate the effect of geometry asymmetry on the pressure drop estimates, as well as the effect of ultrasound probe misalignment with respect to the mid-plane of the flow. Note, however, that our flows were not axisymmetric due to experimental hazards (stenosis phantom not straight, wall roughness, flow instability, upstream flow not fully developed, etc.). This tends to show that our method can also work in non-axisymmetric flows. These analyses will be performed using simulations and *in vitro* experiments. One approach would be to update the equations to 3-D and use

volume ultrasound imaging with a matrix array. Once validated, the clinical feasibility of pressure drop measurements by our *v*VFM-based approach will be investigated.

4. Conclusions

In contrast to other ultrasound studies that evaluated static-dynamic pressure conversions only (Olesen et al. 2018), our results show that it is possible to estimate turbulent pressure losses in arterial stenoses using conventional color Doppler ultrasound. The next step will be to generalize our method to asymmetric pulsatile stenotic flows.

Acknowledgements

This work was supported by LABEX CeLyA (ANR-10-LABX-0060) and EUR MANUTECH SLEIGHT (ANR-17-EURE-0026), *Investissements d'Avenir* program (ANR-16-IDEX-0005)

References

Cigier A, Varray F, Garcia D. 2022. SIMUS: an open-source simulator for medical ultrasound imaging. Part II: comparison with four simulators. Comput Methods Programs Biomed. 220:106774. doi:10.1016/j.cmpb.2022.106774.

Garcia D. 2021. Make the most of MUST, an open-source Matlab UltraSound Toolbox. 2021 IEEE International Ultrasonics Symposium (IUS); p. 1–4.

Garcia D. 2022. SIMUS: An open-source simulator for medical ultrasound imaging. Part I: theory & examples. Comput Methods Programs Biomed. 218:106726. doi:10.1016/j.cmpb.2022.106726.

Olesen JB, Villagomez-Hoyos CA, Moller ND, Ewertsen C, Hansen KL, Nielsen MB, Bech B, Lonn L, Traberg MS, Jensen JA, et al. 2018. Noninvasive estimation of pressure changes using 2-D vector velocity ultrasound: an experimental study with in vivo examples. IEEE Trans Ultrason Ferroelectr Freq Control. 65(5):709–719. doi:10.1109/TUFFC.2018.2808328.

KEYWORDS Arterial stenosis; pressure drop; ultrasound

damien.garcia@inserm.fr

Numerical and experimental investigation of the hemodynamics of surgical repair in severe pediatric coarctation

F. Chassagne[a], S. Buddhe[b], L. C. Permut[b], D. M. Mc Mullan[b], S. P. Seslar[b] and A. Aliseda[c]

[a]Mines Saint-Etienne, SAINBIOSE INSERM U1059, Saint-Etienne, France; [b]Seattle Children's Hospital, Seattle, USA; [c]Department of Mechanical Engineering, University of Washington, Seattle, USA

1. Introduction

Coarctation of the aorta is a localised reduction of the diameter of the descending aorta, i.e. a stenosis of the aortic lumen. It results in an unphysiological pressure gradient (ΔP), increasing with disease severity. Surgery is recommended for a ΔP higher than 20 mmHg. This gradient results in a strong reduction of the flow through the descending aorta, supplying the abdominal organs and lower limbs.

Aortic coarctation can be associated with arch hypoplasia. For these patients, the stenosis is combined with a reduced diameter of the aortic arch, requiring surgical repair within their first months of life. This surgical treatment consists of a combination of resection of the coarcted area (*via* an end-to-end anastomosis) and the suture of a patch (i.e. patch angioplasty) to enlarge the diameter of the aorta along the arch. Current standard care is to design and cut this aortic patch in the operating room, increasing the length of the surgery and the risk of complications.

Recently, *in vitro* (Ghisiawan et al. 2016) and *in silico* (Ju et al. 2019; Swanson et al. 2020) models have been used to help the planning of the aortic coarctation's surgical repair. Building on this, this project aims at, first, developing a method to evaluate the effect of the surgical treatment on an *in vitro* model, and then test whether the design of the patch could be optimized for each patient prior to surgery.

2. Methods

2.1. In vitro model creation

Two patient-specific *in vitro* models were created from MRIs of newborns with severe coarctation associated with arch hypoplasia, who underwent surgery at Seattle Children's Hospital. The aortic lumen was segmented and 3D printed (Form3, Formlabs Inc.). A second mold for the outer envelope of the vessel (thickness of 1.5 mm) was created and 3D printed. Using these 2 molds, a thin-wall silicone model (Ecoflex 00-20, Smooth On) was created using the lost wax technique (Chivukula et al. 2019) (Figure 1).

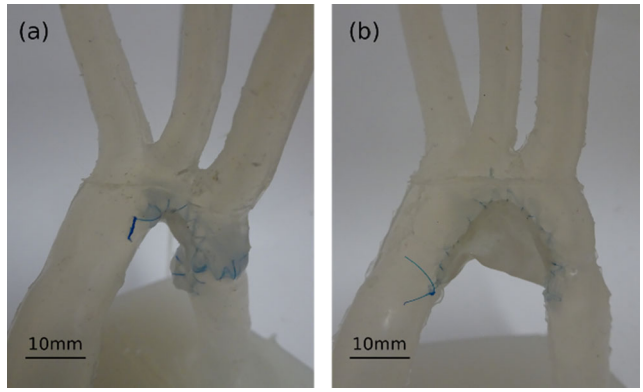


Figure 1. Examples of 2 types of *in vitro* repairs for the same silicone model: (a) end-to-end anastomosis and patch aortoplasty (designed *in silico*) and (b) patch aortoplasty only (designed by the surgeon).

2.2. In vitro model repair

The silicone models were repaired by surgeons from Seattle Children's Hospital following a procedure that mimics the real operation. They were asked to perform their preferred repair (Figure 1b), as well as an end-to-end anastomosis combined with patch angioplasty (Figure 1a). For this last procedure, they were provided with an optimal patch design, based on a 'virtual repair' created with an in-house code (Matlab, MathWorks). This *in silico* repair was created with inputs from the surgeons: the length of the coarcted aorta that would be surgically removed and the starting point for the widening of the arch lumen. Its efficacy at restoring physiological flow (no jet and smooth pressure gradient across the arch) was checked with CFD simulation. The geometries of the lumen for these repaired models were reconstructed *via* micro-CT imaging of the phantoms.

2.3. Evaluation of the surgical repair efficacy

The micro-CT images were segmented and meshed (StarCCM+, Siemens) to perform unsteady CFD simulations. Inlet velocity waveforms were extracted for each patient from US Doppler measurements, part of clinical care. Windkessel elements were used for the outlet boundary conditions. The resistance values were computed based on the cross-sectional area of each outlet. CFD simulations (Fluent, Ansys) resolving the spatial and temporal fluctuations in the flow were run for 3 cardiac cycles, with the first two discarded for transient effects and the last cycle used in

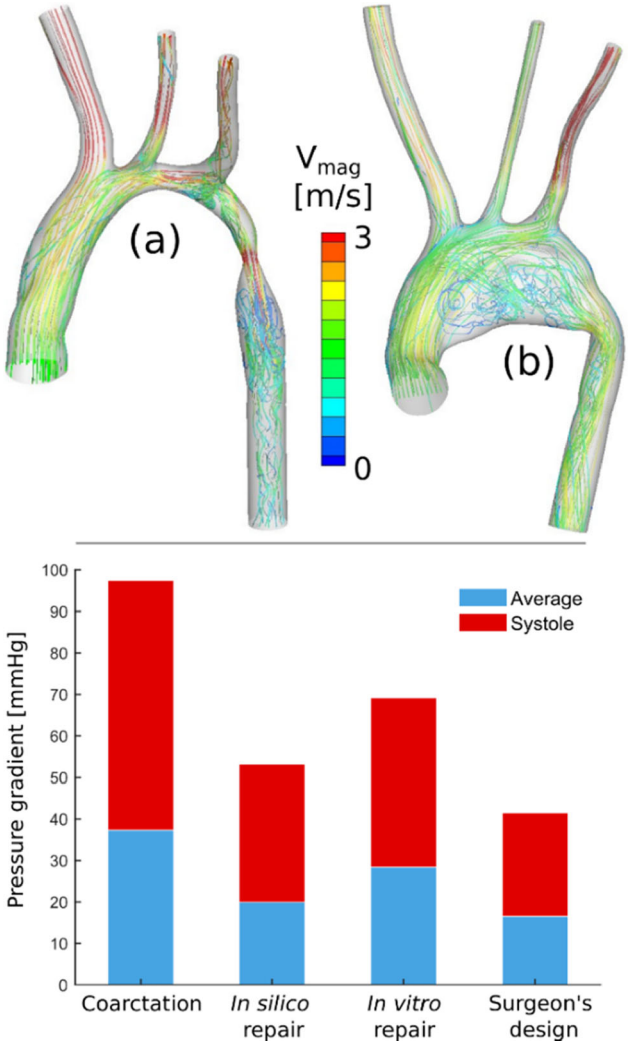


Figure 2. Top: Streamlines at peak systole for the coarctation (a) and the surgeon's patch repair geometry obtained from microCT (b); Bottom: Pressure gradient for the coarctation geometries, the *in silico* repair, the actual *in vitro* realization of the *in silico* repair, and the *in vitro* surgeon's repair.

the analysis. Two main metrics were used to assess the effect of the treatment: the flow splits between the different branches and the pressure gradient.

3. Results and discussion

The coarctation geometries exhibited high pressure gradients through the stenosis and severely reduced flow through the descending aorta ($\sim$ 15% of the total cardiac output). In addition to the increase in resistance, the stenosis led to a strong jet and recirculation areas post-stenosis (Figure 2a). The optimal *in silico* repair showed streamlined flow across the aortic arch with lower pressure gradient and elimination of the stenotic jet. The two *in vitro* repairs performed by the surgeons successfully removed the jet and reduced the pressure gradient.

However, the flow patterns were very different between the repairs. For instance, as shown in Figure 2b, the surgeon's 'preferred' repair led to a large recirculation area in the 'pouch' created by the patch angioplasty. Independently of the type of repair, the flow in the descending aorta increased to about 45% of the total cardiac output, demonstrating the effectiveness of the surgical treatment. However, results differ between the different repair types, when focusing on the pressure gradient. The surgeon's patch repair shows the strongest reduction of the pressure gradient (Figure 2 – bottom), equivalent to the *in silico* result for optimized patch. However, for the actual *in vitro* repair with the *in silico* patch design, the pressure gradient remains higher and does not completely match the *in silico* prediction from the simulations. This can be explained by significant differences between the *in silico* and *in vitro* repair geometries, mostly due to the sutures and the difference in stiffnesses between the silicone and the patch.

4. Conclusions

This combination of numerical and experimental investigations demonstrated the evaluation of different surgical repair strategies for severe pediatric coarctation of the aorta. The results showed that in addition to restoring physiological pressure gradient and flow splits, the optimal repair can restore streamlined flow in the aortic arch.

Further studies are needed to conclude on the optimal *in silico* design of the patch before surgery.

Acknowledgements

The authors want to thank Dr. Sabine Rolland du Roscoat and the laboratory 3SR, Grenoble, for access to the microCT and their help to scan the *in vitro* repaired models.

References

Chivukula VK, Levitt MR, Clark A, Barbour MC, Sansom K, Johnson L, Kelly CM, Geindreau C, Rolland Du Roscoat S, Kim LJ, et al. 2019. Reconstructing patient-specific cerebral aneurysm vasculature for in vitro investigations and treatment efficacy assessments. J Clin Neurosci. 61:153–159. doi:10.1016/j.jocn.2018.10.103.

Ghisiawan N, Herbert CE, Zussman M, Verigan A, Stapleton GE. 2016. The use of a three-dimensional print model of an aortic arch to plan a complex percutaneous intervention in a patient with coarctation of the aorta. Cardiol Young. 26(8):1568–1572. doi:10.1017/S1047951116001827.

Ju S, Abdullah I, Lin S, Gu L. 2019. Hemodynamics and wall mechanics after surgical repair of aortic arch:

implication for better clinical decisions. Applied Sciences. 9(4):807. doi:10.3390/app9040807.

Swanson L, Owen B, Keshmiri A, Deyranlou A, Aldersley T, Lawrenson J, Human P, De Decker R, Fourie B, Comitis G, et al. 2020. A patient-specific CFD pipeline using doppler echocardiography for application in coarctation of the aorta in a limited resource clinical context. Front Bioeng Biotechnol. 8:409. doi:10.3389/fbioe.2020.00409.

KEYWORDS Aortic coarctation; CFD; pediatric surgery; surgical planning

fanette.chassagne@emse.fr

Numerical hemodynamics simulation of 4D flow magnetic resonance imaging

M. Garreau[a,b], R. Moreno[c,d], T. Puiseux[b,d], S. Toupin[e], D. Giese[f], S. Mendez[a] and F. Nicoud[a]

[a]IMAG, Univ. Montpellier, CNRS, Montpellier, France; [b]Spin Up, ALARA Group, Strasbourg, France; [c]ALARA Expertise, ALARA Group, Strasbourg, France; [d]I2MC, INSERM/UPS UMR 1297, Toulouse, France; [e]Siemens Healthcare France, Saint-Denis, France; [f]Magnetic Resonance, Siemens Healthcare GmbH, Erlangen, Germany

1. Introduction

4D Flow Magnetic Resonance Imaging (MRI) is an imaging technique, which allows to quantify blood flow dynamics inside a 3D volume over the cardiac cycle (Markl et al. 2003). It has gained interest over the recent years, yet its clinical use remains limited due to its low spatio-temporal resolution and various potential sources of errors: imaging artifacts, complexities inherent to the MRI acquisition procedure… To numerically simulate the MRI process could be an interesting way to investigate and decompose errors related to hardware issues from errors originating from the acquisition process itself. Another modality to predict hemodynamics is Computational Fluid Dynamics (CFD), which could be coupled with MR physics. The present study proposes a CFD-MRI simulation framework, where Navier-Stokes and Bloch equations are solved simultaneously in an Eulerian-Lagrangian formalism (Puiseux et al. 2021). An application is presented on a rigid flow phantom, whose geometry produces complex flow patterns as can be observed in the cardiovascular system.

2. Methods

Figure 1 presents the geometry and the pulsatile inflow, which comes from in-vitro experimental 4D flow MRI data based on the same phantom (Garreau et al. 2022). Besides the mesh and boundary conditions, the MR pulse sequence is another input into our simulation, corresponding to the chronogram of the external magnetic field. The MR sequences used in this work are based on a constructor sequence (WIP 4D Flow Siemens). The CFD tetrahedral-based mesh (2 mm characteristic size) is seeded with Lagrangian particles (8/cell), which are massless tracers carrying a magnetization vector that evolves with

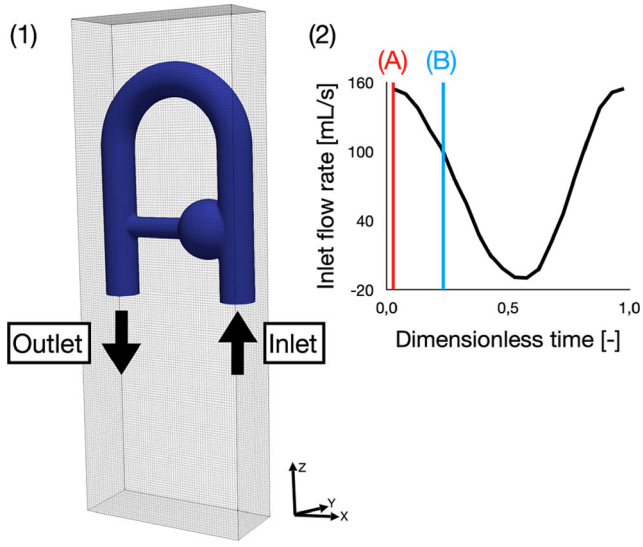


Figure 1. (1) Geometry and MRI field-of-view (FOV). (2) Inflow – lines indicate time instants for Figure 2.

their position and the effective magnetic field they experience. The first step of our solver is to compute the CFD velocity field. This velocity field is then interpolated on the position of particles. Bloch equations are solved for each fluid particle according to the current magnetic events. At particular time instants specified in the sequence, the global magnetization is computed and collected in the so-called k-space, which can be interpreted as the 3D Fourier transform of the image. The synthetic images (SMRI) are then reconstructed from k-space with in-house Python scripts.

In the present work, two 4D flow MRI sequences are compared, a conventional one and another using partial echo (PE). PE consists in acquiring only a fraction of the k-space, relying on its symmetric properties. Here, the first 25% of the k-space is not acquired for the 2nd sequence. Whereas sequences can be designed so that position- and velocity-encoding occur simultaneously along two directions (here X and Y), there is an inevitable time delay between the velocity and spatial-encoding along the last direction (here Z), as the latest has to occur during signal collection around the echo time TE. This delay, called displacement time TD, is known to be related with common misregistration artifacts (Steinman et al. 1997). More than reducing the acquisition time, PE allows to reduce TD. In the present work, the acquisition time has been kept equal for both sequences. TE is reduced from 4.20 to 4.16 ms, but TD decreases from 1.99 to 1.52 ms. Other sequence parameters are equivalent in both simulations. The images of the 2nd

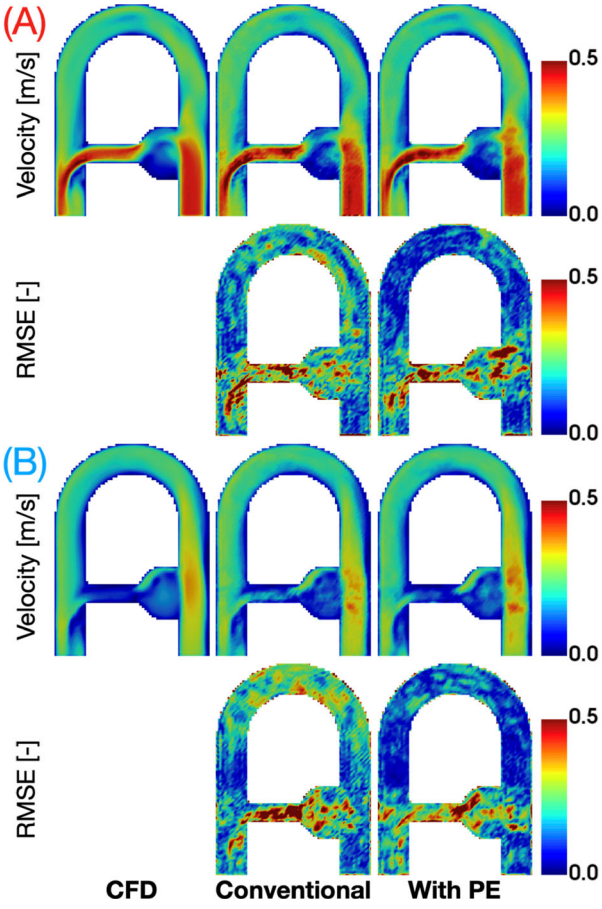


Figure 2. Velocity field and RMSE maps for the cardiac cycle instants (A) and (B) in Figure 1.

simulation are reconstructed according to the zero-filling method (Dyverfeldt et al. 2015).

3. Results and discussion

Reconstructed velocity maps are obtained for SMRI and compared with phase-averaged CFD velocity fields, downsampled to the MRI spatial resolution (2 mm isotropic). Qualitatively, good agreement is found between SMRI and CFD, where the main flow structures are preserved in all directions and for all cardiac phases, as illustrated in Figure 2. Errors maps are computed based on the Root-Mean Square Error:

$$\mathrm{RMSE}(\boldsymbol{r}) = \frac{\sqrt{\sum_{i\in x,y,z}\left(u_{SMRI,i} - u_{CFD,i}\right)^2}}{\overline{||\boldsymbol{u}_{MRI}||}}$$

where $u = (ux,uy,uz)$ is the velocity vector associated to the voxel at the position r, and uMRI is the in-vitro experimental time-averaged bulk velocity at the inlet used for normalization.

In Figure 2A, errors are found under the jetting flow after the junction between the collateral tube and the descending main pipe. The associated recirculation could account for the discrepancy. In the decelerating phase (Figure 2B), the errors are mainly located in the collateral branch. The change of sign of *ux* in this narrow section could explain the misregistration of the SMRI velocity. The RMSE averaged over the cardiac cycle is 0.28 for conventional SMRI and 0.24 for PE. As a reference, the averaged RMSE computed for the matching conventional experimental MRI was found to be around 0.25 (Garreau et al. 2022). Thereby even though less signal is collected for the PE sequence, the shortened TD seems to improve the quality of the reconstructed SMRI velocity fields.

4. Conclusions

A numerical CFD-MRI solver is presented. The effect of the MR sequence parameter TD in the context of partial echo is investigated in a flow phantom with pulsatile inflow. In the present setup, to have a short TD despite less k-space data collected seems to improve the reconstructed velocity fields. Some perspectives are to impose an inflow closer to physiological conditions, to study different geometries (e.g. stenosis to investigate acceleration-induced artifacts) and to implement additional sources of artifacts such as gradient non-linearities.

Acknowledgements

Simulations with YALES2BIO were performed using HPC resources from GENCI-CINES (grant numbers A0080307194 and A0100307194) and with the support of the MESO@LR-Platform at the University of Montpellier.

References

Dyverfeldt P, Bissell M, Barker AJ, Bolger AF, Carlhäll C-J, Ebbers T, Francios CJ, Frydrychowicz A, Geiger J, Giese D, et al. 2015. 4D flow cardiovascular magnetic resonance consensus statement. J Cardiovasc Magn Reson. 17(1):72. doi:10.1186/s12968-015-0174-5.

Garreau M, Puiseux T, Toupin S, Giese D, Mendez S, Nicoud F, Moreno R. 2022. Accelerated sequences of 4D flow MRI using GRAPPA and compressed sensing: a comparison against conventional MRI and computational fluid dynamics. Magnetic Resonance in Med. 88(6):2432–2446. doi:10.1002/mrm.29404.

Markl M, Chan FP, Alley MT, Wedding KL, Draney MT, Elkins CJ, Parker DW, Wicker R, Taylor CA, Herfkens RJ, et al. 2003. Time-resolved three-dimensional phase-contrast MRI. J Magn Reson Imaging. 17(4):499–506. doi:10.1002/jmri.10272.

Puiseux T, Sewonu A, Moreno R, Mendez S, Nicoud F. 2021. Numerical simulation of time-resolved 3D phase-contrast magnetic resonance imaging. Borazjani I, editor. PLoS ONE. 16(3):e0248816. doi:10.1371/journal.pone.0248816.

Steinman DA, Ethier CR, Rutt BK. 1997. Combined analysis of spatial and velocity displacement artifacts in phase contrast measurements of complex flows. J Magn Reson Imaging. 7(2):339–346. doi:10.1002/jmri.1880070214.

KEYWORDS Computational fluid dynamics (CFD); hemodynamics; magnetic resonance imaging (MRI)

morgane.garreau@umontpellier.fr

Numerical study of the deployment of a femoral artery self-expanding nitinol stent

E. Parpaillon[a,b], T.-H. Nguyen[a], H. Louche[a], V. Huon[a], D. Chauvey[b], A. Jeanjean[b] and F. Jourdan[a]

[a]LMGC, CNRS-Université de Montpellier, Montpellier, France; [b]ANSM, Vendargues, France

1. Introduction

Peripheral Artery Disease (PAD) can be treated through surgery or endovascular revascularization with or without stenting. Stents provide a mechanical support aiming to regain lumen in the artery. Self-expanding nitinol stents are common in the treatment of PAD in the superficial femoral artery as their super elasticity allows them to withstand large deformations. However, its efficacy can be impaired by fracture of the device which in a recent study was evaluated at 33% (Daher et al. 2020), the risk of fracture increases with the length of the stented segment (Scheinert et al. 2005). The pulsatile mechanical loading of the stent will have an impact on the fatigue of the device and its eventual fracture as previously studied (Pelton et al. 2008).

The goal of this paper is to create a numerical model of a superficial femoral artery stent to get preliminary results on the deployment of the stent. Thanks to a simple elastic material model, we can thus estimate the pressure and the stress applied on the stent.

2. Methods

2.1. Microscopy

The modelling of the self-expanding peripheral stent was based on a medical device from the brand B. Braun. To be able to have a truthful model, the geometry of the stent was first determined with an optical microscope calibrated at the micrometer at different magnification allowing us to have a global as well as a local geometry of the device. Those pictures were taken all along the stent to observe the presence of a specific pattern, the resulting geometry are precise to the pixel (6.4 µm)

2.2. Geometrical modelisation

Based on the results from the microscopy, the full 3D geometry of the stent has been modelled with a CAD software.

2.3. Finite element modelisation

A static finite element analysis (Ansys software), with small deformation assumption, has been used with a linear elastic isotropic material model. A fine mesh of 852,000 hexahedra finite elements have been used. The Young modulus ($E = 53$ GPa), Poisson ratio (0.3) values were taken according to (Concannon et al. 2021). When implanted in a patient, the stents are oversized. In this study, the stent is devoted to being implanted in a phantom artery with an inner diameter of 8 mm. The oversize ratio is then equal to $10.3/8 = 1.288$, right within the optimal range (Bernini et al. 2022). A known initial pressure was firstly applied on the external surface of the stent to simulate the compression state loading imposed by the artery (supposed to be rigid). Displacement boundary conditions were applied on three specific small surfaces of the stent to avoid rigid solid motion while providing radial compression. Then, the diameter variation of the stent after deformation was obtained using the coordinates of several points on the perimeter and through the calculation of their center of gravity. Thanks to the linearity of the mechanical problem, we can finally calculate the applied pressure necessary to reach the targeted diameter after deformation and get the maximum principal stress as well as their locations.

3. Results and discussion

The self-expanding stents observed are 120 mm long and have an inner diameter of 10 mm and a thickness of 150 µm. They are composed of 32 rings and each of those rings count 12 struts in a V shape. The integrity of the device is made through bridges binding rings, with 3 bridges per ring.

Figure 1 shows the stent at different magnifications. The microscope had previously been calibrated at each of those magnifications making it possible to make quantitative measurements. Microscopic pictures were taken all along the stent. V shaped struts patterns were observed, depending on if they are next to a bridge or not. The base of a strut on the right of a bridge is 2.89 ± 0.21 mm, the ones on the left are 2.35 ± 0.24 mm and the ones not neighboring a bridge are 2.45 ± 0.24 mm.

Pressure loading of 64 kPa was calculated in order to get the diametral targeted deformed shape, i.e. a diametral reduction of (10.3–8) 2.3 mm.

In Figure 2, we can see that the maximal principal stress is localized to the peak of a V shaped strut. The reduction of diameter happening with the application

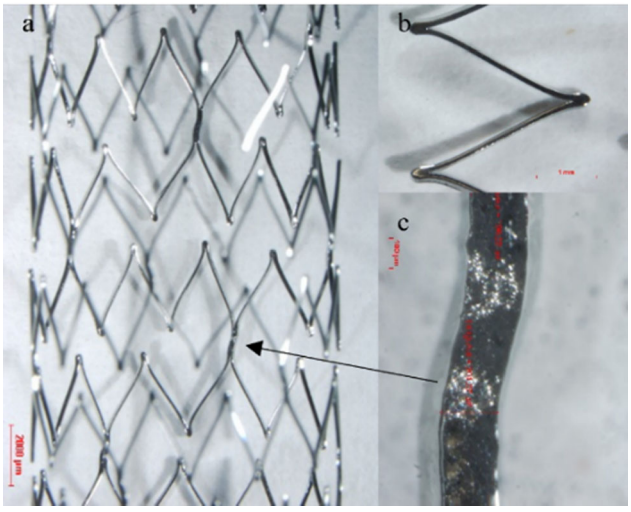


Figure 1. Optical microscopic imagery with an optical lens (×10). (a) Magnification 0.75× of the global stent. (b) Magnification 3× of a single V shaped strut. (c) Magnification 11.25 of a bridge.

of an external pressure is possible thanks to the reduction of the angle at the summit of each strut. Those results have been observed in FEA studies (Pelton et al. 2008) as well as experimental studies (Høl et al. 2019).

The value of the maximal principal stress, calculated with the linear elastic model, is 590 MPa. This high stress is a consequence of the linear elasticity condition, it exceeds the value of the start of the transformation loading stress of 434 MPa (Concannon et al. 2021). This means that the region of the stent of high stress is submitted of phase transformation. The elastic material model can't be used in these regions and had to be replaced by a super elastic one in future work.

4. Conclusions

This study generated a self-expanding stent model in his globality. Without focusing on a single strut, we have been able to observe a pattern in the geometry of the device. With an elastic model we've been able to show that while in its physiological functioning the stent will be in its transformation phase. In the future those results could be confirmed by an experimental approach and should be studied with a 3D superelastic model. This work presented is part of a more global work where other influences such as the corrosive environment the device is in contact with will be studied in order to get a full understanding of the ageing of this medical device.

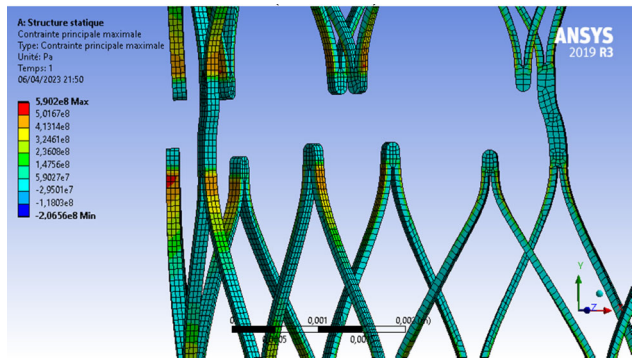


Figure 2. Finite element analysis of the resulting stress (maximum principal stress) from a 64 kPa pressure applied on the external surface of the stent.

Acknowledgements

This study was made possible by the cooperation of B. Braun.

References

Bernini M, Colombo M, Dunlop C, Hellmuth R, Chiastra C, Ronan W, Vaughan TJ. 2022. Oversizing of self-expanding Nitinol vascular stents – a biomechanical investigation in the superficial femoral artery. J Mech Behav Biomed Mater. 132:105259. doi:10.1016/j.jmbbm.2022.105259.

Concannon J, Moerman K, Hynes N, Sultan PS, McGarry J. 2021. Influence of shape-memory stent grafts on local aortic compliance. Biomech Model Mechanobiol. 20(6): 2373–2392. doi:10.1007/s10237-021-01514-9.

Daher MDA, Lopez GE, Duarte PV. 2020. Stents in the femoropopliteal territory: prevalence of fractures and their consequences. Rev Col Bras Cir. 47:e20202481. doi: 10.1590/0100-6991e-20202481.

Høl PJ, Gjerdet NR, Jonung T. 2019. Corrosion and metal release from overlapping arterial stents under mechanical and electrochemical stress – an experimental study. J Mech Behav Biomed Mater. 93:31–35. doi:10.1016/j.jmbbm.2019.02.001.

Pelton A, Schroeder V, Mitchell M, Gong X, Barney M, Robertson S. 2008. Fatigue and durability of Nitinol stents. J Mech Behav Biomed Mater. 1(2):153–164. doi: 10.1016/j.jmbbm.2007.08.001.

Scheinert D, Scheinert S, Sax J, Piorkowski C, Bräunlich S, Ulrich M, Biamino G, Schmidt A. 2005. Prevalence and clinical impact of stent fractures after femoropopliteal stenting. J Am Coll Cardiol. 45(2):312–315. doi:10.1016/j.jacc.2004.11.026.

KEYWORDS Stent; nitinol; FEA; femoral artery

emilie.parpaillon@umontpellier.fr

Uncertainty quantification in personalized pulmonary mechanics

A. Peyraut[a,b] and M. Genet[a,b]

[a]Laboratoire de Mécanique des Solides (LMS), École Polytechnique/IPP, /CNRS, France; [b]MΞDISIM team, INRIA, France

1. Introduction

Idiopathic Pulmonary Fibrosis (IPF) is an uncurable interstitial lung disease, characterized by a stiffening of the lung tissues and causing breathing difficulties in patients. Its mechanisms of appearance and evolution are still poorly understood, making it difficult to diagnose, classify and treat (Wells 2018). The development of an in-silico model of the lungs, able to integrate patient data, could prove useful for the investigation of IPF and provide doctors with an efficient tool for diagnosis, prognosis and treatment optimization.

We recently proposed a lung model based on a poromechanical behavior and specific boundary conditions (Patte, Genet, et al. 2022), as well as an associated personalization pipeline that can incorporate clinical imaging data (Patte, Brillet, et al. 2022; Laville et al. 2023), e.g. in our model CT scans from patients. One of the main challenges of the development of our personalized model is to estimate the constants involved in the poromechanical law representing the constitutive behavior of the lungs – involving Ciarlet-Geymonat and Neohookean potentials – as well as the constants involved in the loading such as the pleural pressure. Those constants are highly patient-dependent. The question of the actual identifiability of these parameters based on clinical data, as well as the question of the bias introduced by image noise and model error during the estimation process, are therefore central for the development of a reliable personalized lung model. This question is all the more fundamental that the values of those parameters could have a predictive power on the evolution of the disease, and all the more difficult that there is very little experimental data available for validation. We therefore developed a statistical pipeline to perform a quantitative study of the identifiability of various model parameters based on synthetic data including measurement and/or model error.

2. Methods

Many approaches have been proposed to estimate material and/or loading parameters from imaging data (Avril et al. 2008). We plan to quantitatively investigate the performance of various identification methods. However, as a first approach, we established our identifiability quantification pipeline using solely the 'displacement' identification method, a.k.a. FEMU. The FEMU method consists in finding the parameters minimizing a cost function that characterizes the distance between the displacement given by the model, which depends on the different model parameters, and the measured displacement, which is extracted from the clinical images. However, using a displacement field extracted from clinical images does not give information on the error made on the identified parameters, since the ground truth for these parameters is unknown. To investigate the identifiability of our parameters, we therefore generate synthetic data with various levels of model and/or measurement error, and then perform the same cost function minimization as with real data. Our synthetic measure is obtained by running the model with reference parameters, chosen at physiological values. We then add Gaussian noise to the displacement obtained to induce random measurement errors. The resulting displacement consists in our synthetic measure. The estimation is then performed by optimizing the cost function, here using the standard direct search Nelder-Mead method, starting from a random value. The optimization is performed for many realizations of noise, until convergence of the obtained distribution.

3. Results and discussion

The distribution of the error on the estimated stiffness parameter in the case of a highly identifiable problem -a simple spring under tension- is presented in Figure 1 as a function of the Signal to Noise Ratio (SNR). In this example, the force of tension of the spring is assumed to be known exactly, the displacement is assumed to be measured with a given level of noise, and the estimated parameter is the spring stiffness. For any level of noise, our method provides the estimation error for the stiffness. For SNR, the optimization always converges towards the exact parameter value; whereas for small SNR, the obtained parameters are far away from the ground truth. The smaller the SNR, the higher the impact of the noise and the higher the error made on the estimated parameter. Our pipeline thus allows to quantify the identifiability of the stiffness depending on the noise on the measures. These results are consistent with the expected error distribution in the case of a linear

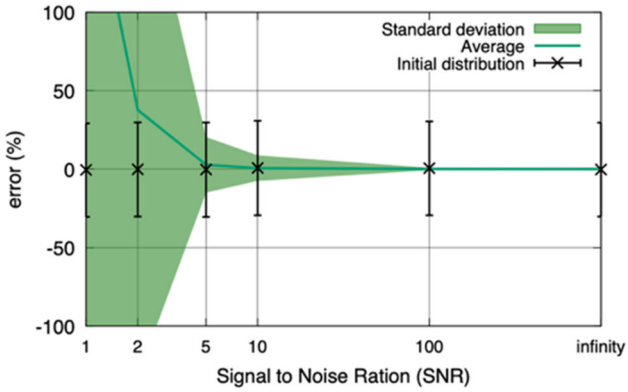


Figure 1. Distribution of the estimation error for the stiffness parameter as a function of SNR for a simple spring under tension.

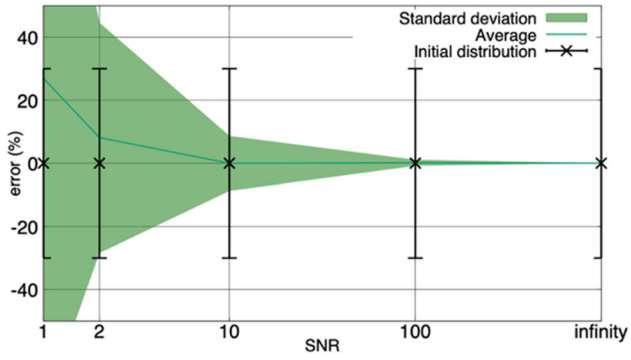


Figure 2. Distribution of the estimation error for the stiffness parameter as a function of SNR for our poromechanical problem.

spring and therefore provide a first element of validation of our pipeline.

The distribution of the error on the estimated stiffness of the tissues in the case of our poromechanical framework is presented in Figure 2 as of function of the SNR. All other parameters of the model are assumed to be known. As for Figure 1, this Figure presents the error made on the identified parameter depending on the SNR. Our pipeline therefore allows to quantify the identifiability of the stiffness depending on the noise present on the measures for our poromechanical framework. The identified stiffness is here also close to ground truth for large SNR, while the error made during the estimation process increases for smaller SNR. Figure 2 also allows to quantify the level of confidence we have on our estimated parameters. For this example, physiological levels of SNR are around 10. From our results, it is therefore possible to say that the stiffness of our model can be estimated with a confidence of about 8%. Our method therefore allows us to have quantitative information on the reliability of the identified parameters, by providing a confidence interval on the error made on the estimated parameters, depending on the noise.

The results presented in Figures 1 and 2 focus on the identifiability of only one parameter, the stiffness. Our pipeline however does not restrict to the study of the identifiability of one parameter only but also applies to the quantification of the error of all the parameters estimated in our model, including loading parameters such as the pleural pressure. The uncertainty on parameters typically increasing as the number of identified parameters increases, the pipeline will therefore also give information on how many parameters can be identified in practice.

4. Conclusions

Our results provide a first element of validation of our incertitude quantification pipeline, as well as a first application to personalized pulmonary poromechanics. They illustrate that this pipeline can be used as a tool to improve our model and the estimation process, by studying the identifiability of the different parameters for different modeling choices, model parametrizations, identification approaches, etc. This pipeline is therefore an important step towards improving the reliability of our personalized lung model.

References

Avril S, Bonnet M, Bretelle A-S, Grédiac M, Hild F, Ienny P, Latourte F, Lemosse D, Pagano S, Pagnacco E, et al. 2008. Overview of identification methods of mechanical parameters based on full-field measurements. Exp Mech. 48(4):381–402. doi:10.1007/s11340-008-9148-y.

Laville C, Fetita C, Gille T, Brillet P-Y, Nunes H, Bernaudin J-F, Genet M. 2023. Comparison of optimization parametrizations for regional lung compliance estimation using personalized pulmonary poromechanical modeling. Biomech Model Mechanobiol. doi:10.1007/s10237-023-01691-9.

Patte C, Brillet P-Y, Fetita C, Bernaudin J-F, Gille T, Nunes H, Chapelle D, Genet M. 2022. Estimation of regional pulmonary compliance in idiopathic pulmonary fibrosis based on personalized lung poromechanical modeling. Trans ASME J Biomech Eng. 144(9):091008. doi:10.1115/1.4054106.

Patte C, Genet M, Chapelle D. 2022. A quasi-static poromechanical model of the lungs. Biomech Model Mechanobiol. 21(2):527–551. doi:10.1007/s10237-021-01547-0.

Wells AU. 2018. IPF diagnosis: flexibility is a virtue. Lancet Respir Med. 6(10):735–737. doi:10.1016/S2213-2600(18)30374-6.

KEYWORDS Pulmonary biomechanics; Image-Processing; parameter estimation; uncertainty quantification; finite element method

alice.peyraut@polytechnique.edu

Motion analysis and simulation

A comparison of force plates data and derivative of momenta during stepping, page S153.
Accuracy of 2D-markerless upper-limb anatomical landmark identification using DeepLabCut, page S156.
Anterior-posterior margins of stability when stepping in/out of a moving walkway, page S159.
Anticipatory landing strategies differ between the lower and the upper limbs, page S162.
Backpack carriage effect on joint torques computed from a range of models: a preliminary study, page S165.
Balance control adjustment when load impact perturbation – A transfer function model-based analysis, page S167.
Changes in knee joint pivot pattern after unicompartmental arthroplasty; impact on clinical outcomes, page S170.
Comparison of two confidence-based methods for markerless motion capture, page S172.
Development of a pipeline of 3D underwater motion capture: application to the analysis of horse swimming, page S175.
Is hip subluxation risk influenced by the femoral head geometry and cup orientation?, page S178.
KneeKG Manual Gait Initiation Detection Repeatability Experiment, page S180.
Simulated increase in monoarticular hip muscle strength reduces the first peak of knee compression forces during walking, page S183.
Transmission of vibration from the instrument to the fingers during guitar playing, page S186.
Upper-Limb Joint Angles Estimation from Two RGB Cameras and a Markerless Skeleton Tracker Algorithm, page S189.
Vertical Ground Reaction Force Analysis for Elderly Fall Detection, page S192.

A comparison of force plates data and derivative of momenta during stepping

B. Watier[a,b], H. Pillet[c], J. Begue[d] and T. Caderby[d]

[a]LAAS-CNRS, CNRS, UPS, Toulouse, France; [b]JRL, AIST-CNRS, IRL, Tsukuba, Japan; [c]Arts et Métiers Sciences et Technologies, IBHGC, Paris, France; [d]IRISSE, UFR SHE, Le Tampon, France

1. Introduction

The external forces and moments applied during locomotion are classically measured using force plates which remain the gold standard of laboratory conditions. In classical mechanics, the derivatives of linear and angular momenta are equal to the total external force and moment respectively. The momenta could be determined by modelling the body of the subjects by a multi-segments chain. Therefore, the combination of the inverse kinematics process and anthropometric data of the segments permits the calculation of whole-body momenta. However, due to large uncertainties regarding both anthropometric data and kinematics data, authors found several differences between force plate data with respect to the center of pressure trajectories or the net joint torques computed using top down methodology (Ren et al. 2008).

Recently, authors (Neptune and Vistamehr 2019; Begue et al. 2021) proposed locomotion instability criteria based on the whole-body momenta or its derivative computed at the Body Center of Mass (BCOM) of the subjects. The authors used both methodologies: force plates or multi-segments chain kinematics. Nevertheless, to the best of our knowledge, no study compared both.

In this context, the aim of this research consists in comparing external forces and moments measured by force plates and the derivative of momenta computed at the BCOM. As gait initiation is well known (Halliday et al. 1998) to increase the instability of the subjects due to large dynamics variations, this comparison was performed during the first phase of the initiation of the gait. Moreover, we hypothesized that due to larger inaccuracies of the measured kinematics in dynamic conditions, the slower the gait speed, the smaller the differences between both methods.

2. Methods

Data collection methods have been previously described (Begue et al. 2021) and are briefly summarized here.

2.1. Participants

Twenty-nine adults (46.8 y.o. [19–77]; 60.5 kg [77 − 37], 164 cm [147 − 186]) participated to this research. The study protocol was in accordance with the Declaration of Helsinki and approved by the local institutional review board.

2.2. Experimental procedure

Initially, the volunteers stood motionless on a force plate and were asked to initiate a first step. The subjects were equipped with 49 reflective passive markers. Both, ground reaction forces and moments and kinematics were measured with the force plate (1000 Hz) and a Vicon system (200 Hz) respectively until the end of the first step. The participants performed this first step at spontaneous speed and at fast speed. For each participant, at least 9 trials were achieved at each speed.

2.3. Data analysis

The participants were modelled as a 19 multi-chain rigid body segments with 42 degrees of freedom. Anthropometric data were mostly extracted from the regression table of (Dumas et al. 2007).

The inverse kinematics process was performed with Opensim software which made it possible to calculate momenta and their derivatives at the BCOM. Concomitantly, ground reaction forces and moments were transferred to the BCOM according to the Varignon theorem. All the parameters were normalised from 0 (movement onset) to 100% (heel contact). Medio-lateral, antero-posterior, vertical and norms of the ground reaction forces and moments were then compared to the equivalent component of the derivatives of the momenta. To this end, RMSE where computed according to the following equation:

$$RMSE = \sqrt{\sum_{i=0}^{i=100\%} \frac{\left(y_i - \hat{y}_i\right)^2}{101}}$$

where y_i is the force or the moment component and $\hat{y}_i$ the equivalent component of the derivative of the momenta.

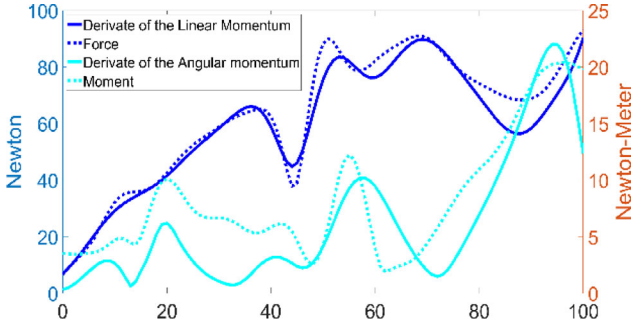


Figure 1. Comparison of the norms of the forces (N – left axis) and moments (Nm – right axis) and the derivative of the norms of the momenta.

Table 1. Mean RMSE ± Std between medio-lateral (F_ML, M_ML), antero-posterior (F_AP, M_AP), vertical (F_VERT, M_VERT), norm (F_norm, M_norm) of the forces (N) and moments (Nm) and the equivalent components of the derivative of the momenta at spontaneous and fast speed.

	Spontaneous	Fast
F_ML	4.7 ± 1.5	7.0 ± 2.0*
F_AP	7.6 ± 2.6	12.9 ± 3.5*
F_VERT	8.6 ± 3.2	15.2 ± 3.8*
F_Norm	7.3 ± 2.6	12.5 ± 3.2*
M_ML	16.3 ± 14.3	19 ± 12.0*
M_AP	5.5 ± 2.2	6.2 ± 2.3*
M_VERT	1.5 ± 0.4	2.6 ± 0.9*
M_Norm	14.3 ± 12.4	15.3 ± 9.9

* indicates a significant ($p < 0.05$) difference between both speeds.

2.4. Statistical analysis

A *t*-test was performed to compare RMSE at spontaneous and fast speed. The level of statistical significance was set at $p < 0.05$.

3. Results and discussion

An example of the profiles of the norm of the forces and moments and the norm of the derivative of the momenta are presented in Figure 1.

Mean RMSE highlights that the maximal differences at spontaneous speed are 8.6 N for the vertical force and 16.3Nm for the medio lateral moment (Table 1). At fast speed, the differences increase to 15.2 N and 19Nm.

In accordance with our hypothesis, we found a significant speed effect for seven of the eight computed parameters with larger differences at fast speed. It confirms that dynamics effect decreases the quality of the inverse dynamics process due, among other things, to larger soft tissue artefacts.

The derivative of the momentum remains close to the forces measured by the force plate with a maximum RMSE of 12.5 N at fast speed. This is an interesting result as the forces are directly measured with high accuracy by the force plate. On the opposite, the moments appear to have important differences with a mean RMSE close to 15Nm. These differences are particularly significant along the medio-lateral axis reflecting the flexion-extension moments applied to the joints. These differences represent a significant proportion of the torques usually measured by inverse dynamics process during gait at the lower limbs. In this context, the use of the derivative of the angular momentum appear to be an important source of error in the inverse dynamic process.

However, in our work, both moments were transferred at the BCOM to be compared. Thus, it remains unclear if the observed differences are due to the calculation of the derivative of the angular momentum of each segment or the location of the BCOM. Indeed, the measured forces on the force plate, transferred to the BCOM, could create non-negligible moments if the BCOM is non-accurately determined. In this regard, an inverse kinematics process is always necessary to determine the location of the BCOM. Further investigation is therefore required to determine if the differences in both moments are due to the bad location of the BCOM or the computation of the derivative of the segment's angular momenta.

4. Conclusions

This work aims at comparing external forces and moments applied during gait initiation with the equivalent component of the derivative of the momenta according to the classical dynamics' equations. The results show good consistency of the estimated derivate of the linear momentum and the forces. However large differences were observed between the moments and the derivative of the angular momentum. Moreover, in line with our hypothesis, our results show increasing differences when the speed increases.

Acknowledgements

This work is part of the ANR projects BAC2WALK (ref. ANR-22-CE19-0003-01) and e-WALKING (ANR-22-CE19-0009-01).

References

Begue J, Peyrot N, Lesport A, Turpin NA, Watier B, Dalleau G, Caderby T. 2021. Segmental contribution to whole-body angular momentum during stepping in

healthy young and old adults. Sci Rep. 11(1):19969. doi:10.1038/s41598-021-99519-y.

Dumas R, Chèze L, Verriest J-P. 2007. Adjustments to McConville et al. and Young et al. body segment inertial parameters. J Biomech. 40(3):543–553. doi:10.1016/j.jbiomech.2006.02.013.

Halliday SE, Winter DA, Frank JS, Patla AE, Prince F. 1998. The initiation of gait in young, elderly, and Parkinson's disease subjects. Gait & Posture. 8(1):8–14. doi:10.1016/S0966-6362(98)00020-4.

Neptune RR, Vistamehr A. 2019. Dynamic balance during human movement: measurement and control mechanisms. J Biomech Eng. 141(7):0708011–07080110. doi:10.1115/1.4042170.

Ren L, Jones RK, Howard D. 2008. Whole body inverse dynamics over a complete gait cycle based only on measured kinematics. J Biomech. 41(12):2750–2759. doi:10.1016/j.jbiomech.2008.06.001.

KEYWORDS Forces; moments; momentum; angular momentum; gait initiation

bruno.watier@univ-tlse3.fr

Accuracy of 2D-markerless upper-limb anatomical landmark identification using DeepLabCut

F. Lefebvre[a,b], I. Rogowski[a], N. Long[b] and Y. Blache[a]

[a]Laboratoire Interuniversitaire de Biologie de la Motricité, Univ Lyon, Université Claude Bernard Lyon 1, Villeurbanne, France; [b]TRINOMA, Villefort, France

1. Introduction

The assessment of upper-limb kinematics is of great interest for sport biomechanics, orthopaedics or ergonomics. Nevertheless, non-invasive methods using skin markers are affected by soft tissue artefacts, leading to inaccurate evaluation of movements, especially for the scapula (Lempereur et al. 2014).

The development of markerless pose estimation tools, such as DeepLabCut (DLC; Mathis et al. 2018) using deep learning to identify markers or body parts, are a great opportunity to overcome the impracticability and inaccuracy of skin marker approaches. Studies about markerless performance for estimating kinematics have emerged with promising results (Lahkar et al. 2022; Vafadar et al. 2021). Unfortunately, they focus on tracking joint centres and none of them consider the shoulder complex, including the scapula.

This study aimed to evaluate the performance of a DLC model for identifying upper-limb anatomical positions on 2D frames during analytical movements as a step towards markerless estimation of the full upper-limb kinematics, including the shoulder complex.

2. Methods

2.1. Participants

Two females and 11 males (age 24.9 ± 4.1 yrs, height 175.5 ± 5.9 cm, body mass 69.8 ± 7.6 kg) volunteered to participate to this study after giving their informed consent (CER-UDL 2022-10-13-002) and reported no upper-body injury for at least 6 months from the test.

2.2. Data collection and procedure

Five video cameras (Miqus Video Color, 2Mpx, 85 Hz, Qualisys AB, Göteborg, Sweden) captured participant, while performing five movements: humerothoracic elevations in the frontal, scapular and sagittal planes, inferomedial to supero-medial elevation, and humerothoracic internal rotation with arm abducted at 90° and elbow flexed at 90°. The first three motions were decomposed in five static poses, and the two latter in three static poses, maintained by the participant while hanging a vertical bar. For each pose, a markerless (ML) frame was recorded, thereafter the experimenter palpated and marked 17 body landmarks on the thorax ($n = 2$), clavicle ($n = 1$), scapula ($n = 5$), humerus ($n = 3$), forearm ($n = 3$) and hand ($n = 3$), and a markerfull frame (MF) was recorded.

2.3. Labelling

The 17 markers of each MF frame were manually labelled on images to identify their coordinates (DLC; v. 2.2.1.1). To ensure model training was unaffected by skin markers, coordinates of labelled markers obtained from MF frame were reported to ML frames. An optical flow algorithm was used to compensate for participant movement between MF and ML frames (Farnebäck 2003). Markers on ML frames were finally visually controlled to prevent from any computational errors.

2.3. Model training and evaluation

For training, default ResNet-50 architecture and default image augmentation were used. Networks from three shuffles with a training set fraction of 0.80 were trained from the 1298 frames dataset. Each network was trained for 150,000 iterations starting from the default initial weights, and evaluated every 10,000 iterations, by computing the root mean square error (RMSE) between ground truth and prediction coordinate whose confidence value were above 0.6 for each marker (Figure 1). For each shuffle, the snapshot that produced the minimum error across all markers on test frames was selected for further analysis.

2.4. Performance analysis

Global performance considering all markers together of selected snapshot for each shuffle was computed and the median performing one was selected for deeper analysis. RMSE on test frames was computed for each marker. Lastly, test frames were grouped by movement and global RMSE was computed for each of them. To help interpreting results, mean calibration residual for each camera was computed and averaged in pixels (px) and mm to estimate the mm/px ratio.

3. Results and discussion

Training performance of each selected snapshot for all shuffles are presented in Table 1. Shuffle 3 was

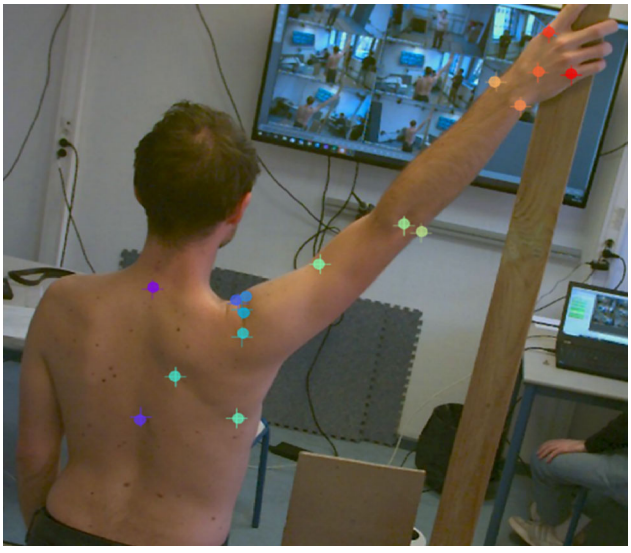


Figure 1. Training image with annotated evaluation results. '+' represent ground truth and '●' DLC predictions.

Table 1. Global RMSE (mean ± SD, in px) on train and test frames for each shuffle.

Shuffle	Train error	Test error
1	2.8 ± 1.5	6.4 ± 5.2
2	3.0 ± 1.7	6.6 ± 5.6
3	2.8 ± 1.5	6.5 ± 5.5

picked for further analysis as showing median test error.

Mean and standard deviation of test error was larger than train error (Table 1). Dataset could be improved to reduce the gap between train and tests, quantitatively by increasing the number of images and by fine tuning training parameters, such as network architecture, data augmentation method or training fraction. Nevertheless, obtained test errors were smaller than test errors reported by Moore et al. (2022) on a similar experiment for estimating torso and upper body landmarks on marmosets.

Smallest mean RMSE were reported for 2nd and 5th metacarpal markers (M2, M3) with 4.2 ± 5.0 px and 4.9 ± 4.5 px, respectively. Acromion markers also presented small RMSE (5.4 px on average for A1, A2, A3 and A4). For scapula markers, RMSE increased with 8.2 ± 7.2 px for trigonum spinae (S1) and 8.9 ± 5.8 px for inferior angle (S2) (Figure 2).

Relatively to movement performed, global error was similar for all studied motions with smallest mean RMSE of 6.1 ± 5.2 px for frontal elevation, 6.3 ± 5.9 px for scaption, 6.5 ± 4.7 px for sagittal elevation, 6.8 ± 5.9 px for infero-to-supero-lateral elevation up to 7.6 ± 5.9 px for humerothoracic internal rotation.

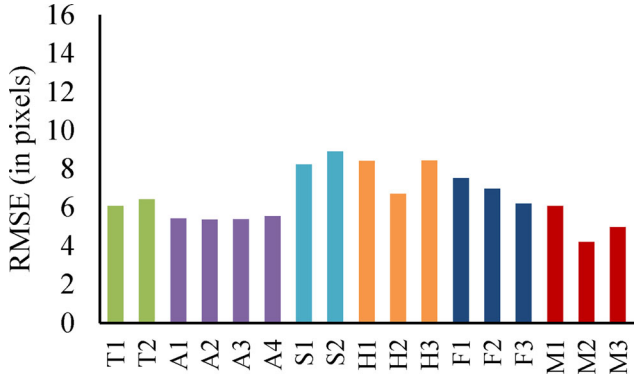


Figure 2. Mean + SD of RMSE for each marker on all test frames (T: thorax, A: acromion, S: scapula, H: humerus, F: forearm, M: hand).

To further interpret data, the ratio of 2.0 ± 0.7 mm/px was given as qualitative estimation of accuracy in focal plane, where subject was located. Our results were then similar to those presented by Vafadar et al. (2021) who found error on shoulder joint center around 21 mm in sagittal plane during gait. Nakano et al. (2020) reported even higher errors during throwing with up to 47.3 mm for elbow joint center with equivalent method and materials. Comparably, marker movement distance for scapula markers in elevated position ranged from 30.4 to 70.0 mm (Yoshida et al. 2022). Considering our results were preliminary work on uniform population, they highlighted the potential of accuracy and versatility of our method if the improvements raised are addressed and applied to a more diverse cohort.

4. Conclusions

Deep learning method for markerless identification of upper-limb anatomical landmarks in 2D showed promising results for a diversity of positions and movements. Sources of improvements are multiple, allowing for even better performance and in future studies. Furthermore, expected works to use this method for 3D motion analysis would enhance its interest and potential use.

Acknowledgements

The authors are grateful to Gaëtan Lopez and Louis Chauvet for their help in this study.

References

Farnebäck G. 2003. Scandinavian conference on image analysis. Lect Notes Comp Sci. 2749:363–370.

Lahkar BK, Muller A, Dumas R, Reveret L, Robert T. 2022. Accuracy of a markerless motion capture system in

estimating upper extremity kinematics during boxing. Front Sports Act Living. 4:939980. doi:10.3389/fspor.2022.939980.

Lempereur M, Brochard S, Leboeuf F, Rémy-Néris O. 2014. Validity and reliability of 3D marker based scapular motion analysis: a systematic review. J Biomech. 47(10): 2219–2230. doi:10.1016/j.jbiomech.2014.04.028.

Mathis A, Mamidanna P, Cury KM, Abe T, Murthy VN, Mathis MW, Bethge M. 2018. DeepLabCut: markerless pose estimation of user-defined body parts with deep learning. Nat Neurosci. 21(9):1281–1289. doi:10.1038/s41593-018-0209-y.

Moore DD, Walker JD, MacLean JN, Hatsopoulos NG. 2022. Validating markerless pose estimation with 3D X-ray radiography. J Exp Biol. 225(9) jeb243998. doi:10.1242/jeb.243998.

Nakano N, Sakura T, Ueda K, Omura L, Kimura A, Iino Y, Fukashiro S, Yoshioka S. 2020. Evaluation of 3D markerless motion capture accuracy using openpose with multiple video cameras. Front Sports Act Living. 2:50. doi:10.3389/fspor.2020.00050.

Vafadar S, Skalli W, Bonnet-Lebrun A, Khalifé M, Renaudin M, Hamza A, Gajny L. 2021. A novel dataset and deep learning-based approach for marker-less motion capture during gait. Gait Posture. 86:70–76. doi:10.1016/j.gaitpost.2021.03.003.

Yoshida Y, Matsumura N, Yamada Y, Yamada M, Yokoyama Y, Miyamoto A, Nakamura M, Nagura T, Jinzaki M. 2022. Three-dimensional quantitative evaluation of the scapular skin marker movements in the upright posture. Sensors. 22(17):6502. doi:10.3390/s22176502.

KEYWORDS Deep learning; upper body; markerless tracking

felix.lefebvre@univ-lyon1.fr

Anterior-posterior margins of stability when stepping in/out of a moving walkway

V. Gibeaux[a], N. Pronost[b], A. Naaim[a], T. Robert[a] and R. Dumas[a]

[a]LBMC UMR T_9406, Univ Lyon, Univ Gustave Eiffel, Univ Claude Bernard Lyon 1, Lyon, France; [b]CNRS LIRIS UMR 5205, Université de Lyon, Université Claude Bernard Lyon 1, Villeurbanne, France

1. Introduction

The ability to adapt one's gait to a changing environment is a critical skill for a safe locomotion. Stepping in and out of a moving walkway is as a very simple experimental paradigm to assess this ability. It is also an ecological task that reproduces real-life situations, notably encountered in public transportations. However, if adaptations to other type of perturbations (stepping over obstacles, reaction to unexpected perturbations …) have already been studied, there is almost no literature about stepping in/out a moving walkway. Only Hsu et al. (2015) reported adaptations of the spatiotemporal parameters when stepping in the moving walkway (Hsu et al. 2015). No study present results about the margins of stability (MoS) although it is a well-known and consistent method to analyse such adaptations (Hof et al. 2005).

Therefore, the aim of this paper was to study the MoS during the transition step when the participant has one foot on the steady ground and the other on the moving walkway. Our hypothesis is that the anterior-posterior MoS will reveal adaptations to the change of speed.

2. Methods

Sixteen adults, 10 males and 6 females (27.9 ± 7.2 years old, 69.5 ± 11.9 kg, and 1.73 ± 0.08 m) with no self-declared gait impairment, gave their written consent to participate in the study. The experimental protocol was approved by the Gustave Eiffel University ethics committee.

A setup composed of an instrumented split-belt treadmill (Treadmetrix, Park City, USA) and two 2-m platforms positioned at each end of the treadmill was designed to replicate a moving walkway. The belt velocity was set at 0 m/s for a walking condition and at 0.5 m/s for the stepping in/out conditions. Participants were asked to walk across the walkway at their comfortable walking speed. Each condition was repeated at least seven times after a familiarisation period (the participants performed as many trials as necessary until they felt comfortable with the task).

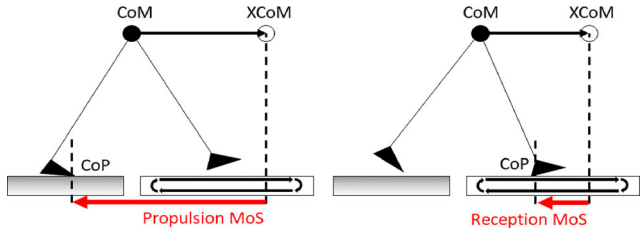


Figure 1. Definition of propulsion and reception MoS when stepping in the moving walkway.

The force data was captured from three force plates, two in the treadmill and one (Bertec, Columbus, USA) implemented in one of the platforms. The kinematics data was captured with 10 optoelectronic cameras (Qualisys, Göteborg, Sweden) using 13 markers for centre of mass (CoM) calculation (Tisserand et al. 2016).

The extrapolated centre of mass (XCoM) and its position with respect to the centre of pressure (CoP) (Hof et al. 2005) were used to compute the MoS vector (Equations 1 and 2):

$$\overrightarrow{\mathbf{MoS}} = \overrightarrow{\mathbf{CoP}} - \overrightarrow{\mathbf{XCoM}} \quad (1)$$

$$\overrightarrow{\mathbf{XCoM}} = \overrightarrow{\mathbf{CoM}} + \frac{\overrightarrow{\mathbf{v}_{/stance}}}{\sqrt{g/_l}} \quad (2)$$

with l being the leg length, g the gravitational acceleration and $\overrightarrow{v_{/stance}}$ the velocity of the CoM expressed in the stance foot frame (i.e. corrected by the belt velocity if the stance foot was on the moving walkway). The anterior-posterior component of the MoS vector (Equation 1) was computed at two instants of time (Figure 1): just before contralateral heel-strike for the trailing leg (named propulsion MoS) and just after contralateral toe-off for the leading leg (reception MoS). The propulsion and reception MoS captured the overall body dynamics just before (i.e. anticipation) and just after (i.e. adaption) the transition in/out the moving walkway. Note that the MoS must be negative to ensure a steady gait.

After checking for non-normal distributions of the averages across trials for each participant, Dunn–Sidak's tests were used to perform multiple comparisons between the propulsion/reception MoS in the walking condition and the stepping in/out conditions ($p < 0.05$).

3. Results and discussion

The self-selected walking speed of the participants, computed as the CoM velocity over three steps, was

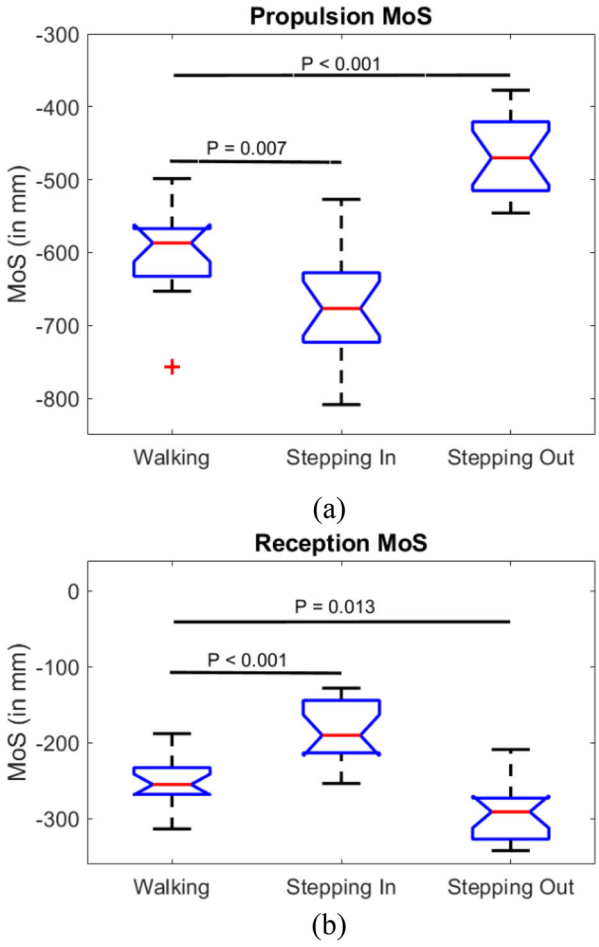


Figure 2. Propulsion (a) and reception (b) MoS during the walking, stepping in, and stepping out conditions.

1.22 ± 0.05 m/s for the walking condition. In this condition, the median propulsion and reception MoS were −587 mm and −254 mm, respectively. As shown on Figure 1, it was expected to have a reception MoS of smaller amplitude.

Figure 2a shows that propulsion MoS for stepping in and out of the moving walkway were significantly different from the walking condition. The XCoM was placed, respectively, more anterior and less anterior from the CoP than during walking, resulting in an acceleration (stepping in) and deceleration (stepping out) of the CoM at the beginning of the transition step.

Figure 2b shows that reception MoS for stepping in and out of the moving walkway were significantly different from the walking condition. Conversely to the propulsion, the XCoM was placed, respectively, less anterior and more anterior from the CoP than during walking, resulting in a deceleration (stepping in) and an acceleration (stepping out) of the CoM at the end of the transition step.

The results demonstrate that the participants have anticipated the speed change, but that the adaptations needed further adjustments. Our hypothesis was therefore confirmed. Interestingly, for all participants, the adaptations tended to over-control the CoM velocity (i.e. more acceleration or deceleration than needed). The adjustments therefore corresponded to opposite variations of the CoM acceleration with respect to the walking condition. These adaptations and adjustments seem to correspond to mechanisms that can be captured with an inverse pendulum model (i.e. studying CoP, CoM, XCoM, and MoS) but other balance mechanisms such as angular momentum can be present in case of gait perturbations and these mechanisms were not studied here. The control of the swing foot while stepping in moving surface has been already studied in the literature (Hsu et al. 2015). The reported increased speed of the leading foot to match the belt velocity seems consistent with the increased propulsion MoS found in the stepping in condition of the current study.

Although the participants were young, healthy, and got familiarised with the task, stepping in and out of a moving walkway with a belt speed at 0.5 m/s remained a quite challenging task. This belt speed is a standard speed for moving walkway, i.e. about half the speed of a natural walking pace. Previous ergonomic studies of moving walkway operating in airports (Hawkins and Atha 1976) have reported potential balance problems (e.g. slight sway, convulsive jerks).

4. Conclusions

Adaptations of the anterior-posterior MoS were required to efficiently step in and out of a moving walkway. These adaptations tended to over-control the CoM velocity during the propulsion and needed further adjustments during the reception of the transition step. These results provide baseline data for future studies in the fields of transport (e.g. adequate belt speed for a moving walkway) or clinics (e.g. personalized training protocols for patients with stability/balance impairments).

References

Hawkins NM, Atha J. 1976. A study of passenger behaviour on a slow speed travellator system. Ergonomics. 19(4): 499–517. doi:10.1080/00140137608931561.

Hof AL, Gazendam MGJ, Sinke WE. 2005. The condition for dynamic stability. J Biomech. 38(1):1–8. doi:10.1016/j.jbiomech.2004.03.025.

Hsu W-C, Wang T-M, Lu H-L, Lu T-W. 2015. Anticipatory changes in control of swing foot and lower limb joints when walking onto a moving surface traveling at constant speed. Gait Posture. 41(1):185–191. doi: 10.1016/j.gaitpost.2014.10.003.

Tisserand R, Robert T, Dumas R, Chèze L. 2016. A simplified marker set to define the center of mass for stability analysis in dynamic situations. Gait Posture. 48:64–67. doi:10.1016/j.gaitpost.2016.04.032.

KEYWORDS Extrapolated centre of mass; centre of pressure; pedestrian conveyor; gait perturbation

raphael.dumas@univ-eiffel.fr

Anticipatory landing strategies differ between the lower and the upper limbs

R. Bechet[a], R. Tisserand[a], A. Péneaud[a], L. Fradet[a] and F. Colloud[b]

[a]Institut Pprime, UPR 3346, CNRS – University of Poitiers, France; [b]Institut de Biomécanique Humaine Georges Charpak, Arts et Métiers Institute of Technology, Paris, France

1. Introduction

Movement execution relies on a complex coordination controlled by the central nervous system (CNS). During voluntary movements, the CNS programs anticipatory muscular activations preceding predictable motor changes, based on an internal representation of both internal and external constraints (Wolpert and Kawato 1998). However, the functional role of these anticipatory activations remains unclear.

In motor tasks with large momentum like landing, lower-limb muscular anticipations have been mostly characterized through co-activation patterns using EMG (Peng et al. 2011). According to these studies, muscular anticipations are thought to adjust muscular stiffness, to a level neither excessive nor insufficient, to avoid large joint angular velocities. This stiffness adjustment would serve a key purpose: slow down the center of mass velocity during ground contact (GC) to reduce the risk of functional instability and protect the skeletal system (Butler et al. 2003). However, the kinematic consequences of these anticipatory activations have been poorly described, and may clarify their functional role. Indeed, during both landing and drop-jumping, we found a knee flexion starting before GC (Bechet et al. 2023), and questioned whether this would be specific to the lower-limb.

When landing on the ground after a fall, humans often use their upper limbs for cushioning. Anatomical similarities between the lower and the upper limbs (i.e. three main joints allowing similar degrees of freedom) suggest they may be used similarly during landing. Anticipatory muscular co-activations were recorded in humans landing on their hands following externally-applied falls, with a slight elbow extension preceding GC, thought to prevent elbow buckling (Borrelli et al. 2020). However, this has not yet been verified in a voluntary landing context.

The aim of this study was to compare the kinematic consequences of anticipatory muscular activations in the upper limbs with that of the lower limbs when mobilized in a comparable landing task, before and after GC. We hypothesized that the anticipatory muscular activations would not provoke the same kinematic consequence between the elbow and knee joints in anticipation, resulting in different landing coordination.



Figure 1. Initial (left) and final (right) states of the upper-limbs landing task.

2. Methods

2.1. Participants and procedure

In a first experiment, 15 participants (7 females, 25 ± 4 years old, 173 ± 8 cm, 67 ± 8 kg) landed on their feet from a 35 cm elevated platform on two force plates (Sensix) recoding the 3D ground reaction forces (GRF) at 2000 Hz. In a second experiment, 16 males (23 ± 3 years old, 177 ± 5 cm, 76 ± 14 kg) landed on their hands from a 35 cm elevated platform on the same force plates, with feet on the ground (Figure 1). Participants were instructed to keep their arms alongside their trunk, to limit shoulder abduction, and were allowed to familiarize with the task. A motion analysis system composed by 19 infrared cameras (Vicon) recorded at 200 Hz the 3D trajectories of 64 and 16 reflective markers, respectively.

2.2. Data analysis

GRF and marker trajectories were low pass filtered at 50 and 20 Hz, respectively, with a zero lag critically damped filter. For both experiments, flexion-extension angles were computed, and time-derived to obtain angular velocities. The onset of joint flexion was defined as the first instant during which the angular velocity was positive and GC was defined as the first instant when the vertical GRF exceeded 20 N. Rate of force development (RFD) was used to quantify the impact on the ground, defined as the variation of the vertical GRF over time, from GC to the first peak of vertical GRF. For each task, the trial with the lowest peak of vertical ground reaction force was analyzed.

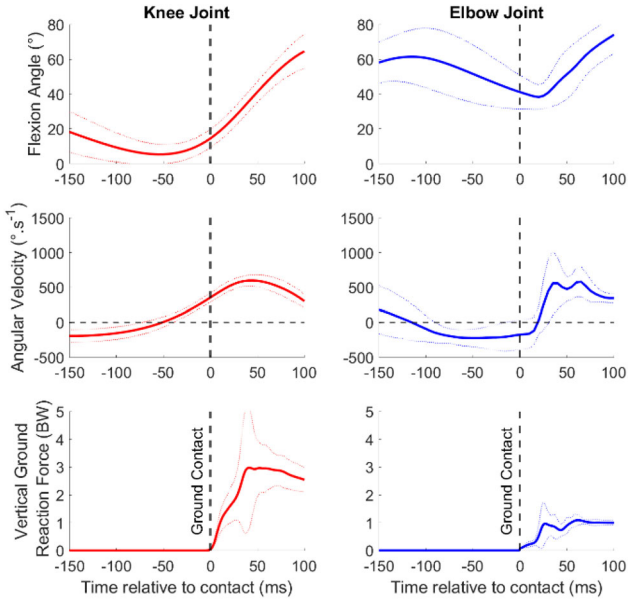


Figure 2. Results for the knee (left) and elbow (right) joints. Flexion angle (+) (top), flexion angular velocity (middle) and normalised vertical ground reaction force (bottom) during both tasks. Solid lines represent the mean and dotted lines represent one standard deviation. BW = body weight.

2.3. Statistical analysis

Because they were all normally distributed, the dependent variables were compared between the lower and the upper-limb using an independent Student *T*-test, with a threshold set at $p < 0.05$.

3. Results and discussion

The force results showed that the landing was globally similar, with smaller GRF when landing on the hands than on the feet (Figure 2). Consecutively, the RFD was smaller for the upper limb (33.3 ± 15.2 BW s^{-1}) than for the lower-limb (82.9 ± 61.1 BW s^{-1}) ($p < 0.01$). For the kinematics, the knee flexion started systematically before GC (-52 ± 17 ms), and before the elbow flexion (25 ± 14 ms after GC) ($p < 0.001$). The angular velocity peak was larger and occurred sooner for the elbow joint after GC ($963 \pm 170°$ s^{-1} at 32 ± 16 ms) compared to the knee joint ($609 \pm 84°$ s^{-1} at 43 ± 7 ms) ($p < 0.001$ and <0.01 for the peak timing, respectively).

The aim of the study was to quantify the kinematic consequences of anticipatory muscular activations from the lower and upper limbs during landing. As hypothesized, the kinematic consequences were different in terms of joint angles and angular velocity for the knee and the elbow (Figure 2).

The anticipated knee flexion may be the reason why there was no abrupt change in the knee angle after GC (Figure 2): the knee flexion velocity increased smoothly, and was not modified despite the large GRF amplitude. This strategy probably allows to control a smooth lowering of the whole-body centre of mass and protects the knee joints (Bechet et al. 2023).

Similar to what was found in reactive hand landing (Borrelli et al. 2020), the elbow joint was extending before and at GC (Figure 2). However, contrary to the knee joint, the elbow angle displayed an abrupt change almost immediately after GC, resulting in a large elbow flexion angular velocity, and a large change of angular velocity. It was previously suggested that elbow extensors are largely activated before GC, to slow down the elbow flexion during GC and protect the head (DeGoede and Ashton-Miller 2003). This may explain why the elbow did not flex prior to GC. However, even if an anticipatory flexion was not achieved, and the mobilizing body mass was smaller compared to lower-limb landing, the upper-limb strategy still limited the impact force and the RFD, probably to protect the skeletal system from injuries. The differences can also come from our protocol, with an unusual task performed with the upper-limbs, that can explain the large variations in the results. Moreover, the large angular velocity for the elbow joint suggest the upper limbs may not be suitable for this kind of task, with the absence of strong antigravity muscles compared to the lower-limbs.

4. Conclusions

Even though lower and upper limb anticipatory muscular activations may look similar at first glance, their kinematic consequences differ during landing. For the knee joint, the flexion that would have been induced by ground contact is anticipated, whereas an extension was recorded for the elbow joint. However, both seem to serve the same purpose: protect the skeletal system. This suggests that the CNS adapts the motor behavior to the anatomical constraints of each joint.

These specificities highlight that the kinematic consequences of muscular activations should be described when characterizing the motor consequences of anticipatory activations, to better describe how the CNS coordinates movements with large momentum.

Acknowledgements

This work was funded by the Region Nouvelle-Aquitaine and PPrime laboratory (France).

References

Bechet R, Tisserand R, Fradet L, Colloud F. 2023. Invariant kinematic consequences of muscular anticipation during landing and drop-jumping. Paper presented at: CMBBE 2023. Proceedings of the18th International Symposium on Computer Methods in Biomechanics and Biomedical Engineering; May 3–5; Paris, France.

Borrelli J, Creath R, Rogers MW. 2020. Protective arm movements are modulated with fall height. J Biomech. 99:109569. doi:10.1016/j.jbiomech.2019.109569.

Butler RJ, Crowell HP, Davis IM. 2003. Lower extremity stiffness: implications for performance and injury. Clin Biomech. 18(6):511–517. doi:10.1016/s0268-0033(03)00071-8.

DeGoede KM, Ashton-Miller JA. 2003. Biomechanical simulations of forward fall arrests: effects of upper extremity arrest strategy, gender and aging-related declines in muscle strength. J Biomech. 36(3):413–420. doi:10.1016/s0021-9290(02)00396-2.

Peng H-T, Kernozek TW, Song C-Y. 2011. Quadricep and hamstring activation during drop jumps with changes in drop height. Phys Ther Sport. 12(3):127–132. doi:10.1016/j.ptsp.2010.10.001.

Wolpert DM, Kawato M. 1998. Multiple paired forward and inverse models for motor control. Neural Netw. 11(7–8):1317–1329. doi:10.1016/s0893-6080(98)00066-5.

KEYWORDS Coordination; anticipation; landing

romain.tisserand@univ-poitiers.fr

Backpack carriage effect on joint torques computed from a range of models: a preliminary study

A. Schuster, A. Tomezzoli, C. Pontonnier and G. Dumont

Inria, CNRS, IRISA, M2S, Univ Rennes, France

1. Introduction

In a military framework, it could be interesting to predict biomechanical quantities such as joint torques and ground reaction forces while walking and carrying heavy loads. Indeed, these quantities could help to study injuries mechanism of low back pain or stress fractures related to the mass of the soldier's equipment carried on the field, which has nearly doubled since World War I (Knapik et al. 2004). The aim of this study is thus to determine to what extent it is possible to predict the influence of different load carriage conditions, on flexion/extension joint moments, with a baseline kinematic acquisition combined with predicted ground reaction forces and moments (GRF&Ms) as inputs.

2. Methods

2.1. Experimental data

Data have been collected from French army soldiers who participated to a previous study (Puchaud 2020) (CPP n° 2018-A00484-51). Motion for 5 walking tasks without backpack and with 10, 20 and 30 kg was recorded for 9 soldiers. We thus chose to focus this study on a single soldier (height =174 cm, weight =75,4kg) who performed ten gait trials: 1 without backpack, 3 carrying 10 kg, 4 carrying 20 kg and 2 carrying 30 kg with the selected gait cycle (first left heel strike on the force platform to the next) (Figure 1). The marker set used was a full body marker set based on ISB recommendations. Three markers were hidden by the backpack (T10 and 2 PSIP) and removed from the marker set. Technical markers placed on the pelvis and thorax were used to reconstruct the trajectories of the markers in these areas.

2.2. Modelling

A generic osteoarticular model of the entire body with 18 segments linked by ball joints was designed in CusToM (Muller, Pontonnier, Puchaud, et al. 2019), then scaled to the subject (Puchaud et al. 2020). The inertial parameters (mass, center of mass, inertia matrix) of the thoracic body segment have been modified to virtually represent the mass of the backpack as a point mass. The ground reaction forces and moments (GRF&Ms) from experience and kinematics associated to the loading condition were firstly conserved (EXPE). Secondly,

GRF&Ms were predicted thanks to a motion-based prediction method (PRE1) (Muller, Pontonnier, Dumont 2019). Then, only no-load gait motion and predicted GRF&Ms (PRE2) were used to compute joint moments for each loading condition.

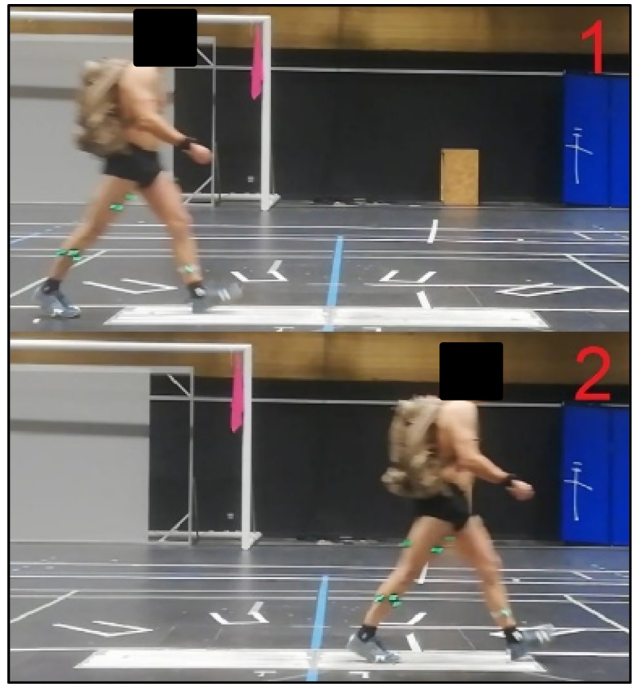


Figure 1. Heel-to-heel gait cycle description.

Table 1. Comparison of the RMSE of PRE1 and PRE2 with respect to EXPE.

	RMSE between EXP and PRE1 (N.m)			
Load (kg)	L5/S1	Hip	Knee	Ankle
0	0	17.5	10.6	7.0
10	0	35.7	24.2	18.5
20	0	36.8	**24.8**	22.8
30	0	45.9	**34.1**	32.3
	RMSE between EXP and PRE2 (N.m)			
Load (kg)	L5/S1	Hip	Knee	Ankle
10	22.7	**35.0**	**23.2**	**18.3**
20	33.2	**33.3**	29.8	**15.8**
30	46.9	**30.9**	39.6	**20.7**

In Bold: lowest RMSE.

2.3. Post-processing

A comparison between each method was made for flexion/extension joint torques at the L5/S1, left hip, knee, and ankle joints. All cycles were normalised

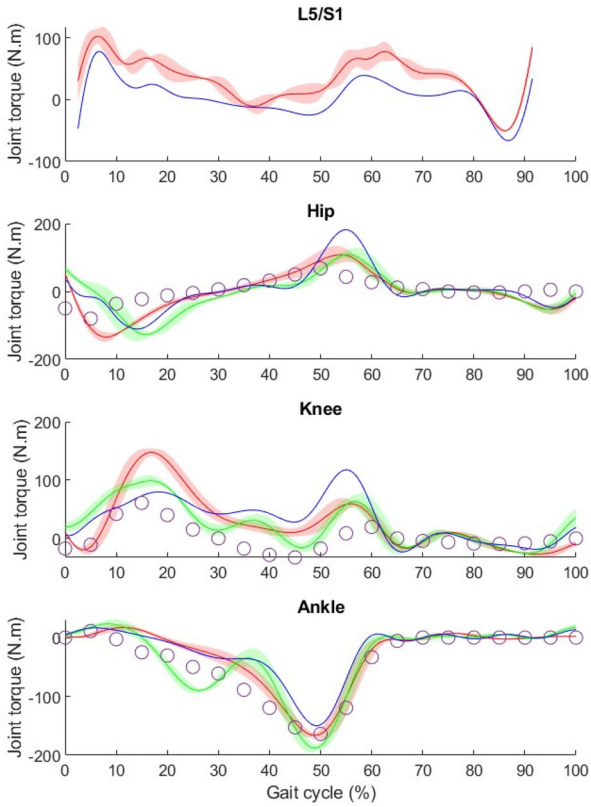


Figure 2. Flexion joint torques for a loading of 20 kg (in red: EXPE, in green: PRE1, in blue: PRE2. Circles: Joint torques from Harman et al. 2000).

according to cycle length. For repetitive sessions (10, 20, 30 kg), joint torques were averaged between trials. In addition, the RMSE of joint torques between the EXPE and PRE1 methods, and between the EXPE and PRE2 methods were computed over the gait cycles.

3. Results and discussion

Results from PRE2 displayed a lower RMSE for the left hip and left ankle flexion/extension joint torque than PRE1. This was not entirely the case for left knee flexion/extension joint torques. Hence, in this case and for this subject, PRE2 led to a similar level of approximation as PRE1 for lower limbs levels. Quantitative results from flexion joint torques RMSE at L5/S1 (PRE2) will be compared to other subjects in a future in-depth study. Moreover, similar results in terms of shape and peak joint torques were obtained in the literature (Harman et al. 2000) where lower limbs joint torques for 20 kg backpack carriage were computed for 16 subjects (height $=181.2 \pm 7.5$cm, weight $=76.8 \pm 8.9$ kg) (Figure 2). However, the number of samples used for this study is not sufficient to assess the repeatability of the results. The model of the backpack used is limited. Indeed, the backpack tends to deform during walking, which was not considered in this first study. In addition, only the kinematics unaffected by wearing a backpack were used in the PRE2 method and results obtained could differ depending on the baseline kinematics chosen. Finally, walking speed was not controlled which led to a temporal shift. This could be compensated by a dynamic time warping method.

4. Conclusions

The purpose of this study was to assess if it is possible to predict the influence of load carriage on joint torques with a baseline gait (here carrying-free) and a virtually heavier model. Altering a generic biomechanical model and keeping baseline kinematics offers the possibility of inverse dynamics computation for multiple configurations of load carriage. Results emphasized that such a prediction (PRE2) is possible for specific loading conditions. A future parametric study could investigate the choice of baseline kinematics, for an inverse dynamics method based on GRF&Ms prediction, on joint torques with respect to experimental results from multiple subjects.

Acknowledgements

We would like to thank P. Puchaud for sharing his database for the purpose of this study.

References

Harman E, Hoon K, Frykman P, Pandorf C. 2000. Military Performance Division U.S. Army Research Institute of Environmental Medicine Natick, MA.

Knapik JJ, Reynolds KL, Harman E. 2004. Soldier load carriage: historical, physiological, biomechanical, and medical aspects. Mil Med. 169(1):45–56. doi:10.7205/milmed.169.1.45.

Muller A, Pontonnier C, Puchaud P, Dumont G. 2019. CusToM: a Matlab toolbox for musculoskeletal simulation. JOSS. 4(33):927. doi:10.21105/joss.00927.

Muller A, Pontonnier C, Dumont G. 2019. Motion-based prediction of hands and feet contact efforts during asymmetric handling tasks. IEEE Trans Biomed Eng. 67(2): 344–352. doi:10.1109/TBME.2019.2913308.

Puchaud P. 2020. Modélisation musculo-squelettique générique et spécifique en vue du support de l'activité physique du soldat [doctoral dissertation]. École normale supérieure de Rennes.

Puchaud P, Sauret C, Muller A, Bideau N, Dumont G, Pillet H, Pontonnier C. 2020. Accuracy and kinematics consistency of marker-based scaling approaches on a lower limb model: a comparative study with imagery data. Comput Methods Biomech Biomed Eng. 23(3):114–125. doi:10.1080/10255842.2019.1705798.

KEYWORDS Dynamics; load carriage; joint torques; gait

aurelien.schuster@ens-rennes.fr

Balance control adjustment to load impact perturbation – a transfer function model-based analysis

Olivier Martin[a,b], Emmanuel Witrant[a,b] and Sufiyan N'Yo[a,b]

[a]GIPSA-lab, Grenoble, France; [b]Grenoble-Alpes University, Grenoble, France

1. Introduction

When upright standing equilibrium is impaired by an external perturbation, balance is maintained using the central integration of sensory signals. Adaptive postural commands are computed on-line, automatically or intentionally, from the sensory inputs regulating the motor outputs. This study focuses on the effects of a push-like perturbation on stance reactive control. Experiments are carried out to provide a real balance dataset, which is used to derive a linear dynamical system (after some transformations) parameterized as an autoregressive model with exogenous input (ARX). Our goal is to propose a data-based model of adaptive balance behaviour using a system identification method. Mixed balance perturbations are considered, as met in everyday life, sports, or therapy, as previously experienced with vestibular patients (Voda et al. 2019). Although identification studies usually challenge static standing posture maintenance with external forces (e.g. Engelhart et al. 2015), our purpose specifically concerns the intentional balance control in response to an anticipated external load perturbation in a predictive-reactive equilibrium control in normal subjects.

2. Methods

The experimental conditions and data acquisition were obtained in 2019 and are briefly described here (see N'Yo 2019, Master's thesis, for more details).

2.1. Participants

Four males and one female, aged 25–56 years old, participated in the experiment and gave their informed consent according to ethical research standards. Two subjects were Tai Chi Chuan (TCC) experts, three had no previous experience.

2.2. Postural task

The participants stand upright on a force plate in a TCC posture with a defence attitude, i.e. an arm-hand segment placed forward at shoulder height to resist the load impact (Figure 1). The postural task implies controlling the whole-body equilibrium despite a load perturbation applied at hand level by a passive inertial pendulum device. It produces an impact load on the hand-arm segment and is discharged after impact using a manually activated quick-release device. The subjects have to control the imbalance while maintaining their posture.

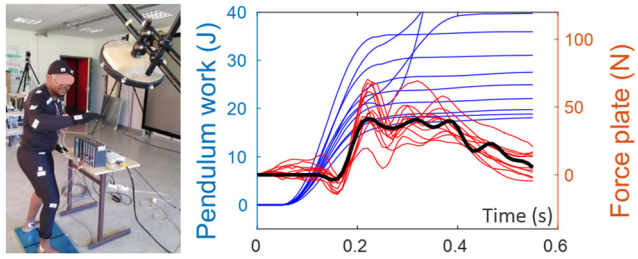


Figure 1. Left: subject standing on the force plate, facing the load perturbation device. Right: Time plot of the input values (pendulum work in Joule (J), blue left scale), the output data (GRF in newton (N), red right scale), and the simulated response from the transfer function (black large line).

2.2. Protocol

The standardized postural tasks sequence consists of a VISION x LOAD crossed-protocol. The two VISION conditions, Closed-Eyes vs. Open-Eyes, are repeated in the two LOAD conditions: No Load on the pendulum vs. With Load (with an additional 5 kg load). The tasks sequence is ordered as follows, with 10 trials per task: 1. Opened Eyes, No load; 2. Opened Eyes, With Load; 3. Closed Eyes, No load; 4. Closed Eyes, With Load. This design generates a trial-dependant level of work and constraint on the balance, once the load is suddenly applied to the subject's hand-arm segment.

2.3. Data acquisition

A MOCAP Qualysis system records both the pendulum (load) trajectory to calculate the force impact value in terms of the input (pendulum work in Joule (J)) and the impact time, as well as the hand-arm and whole-body anatomical landmarks (Figure 1). A Kistler force plate records the ground reaction force (GRF) to compute the resultant force from the 6 DoF components (Force plate (N)) (Figure 1). All data acquisitions are time-synchronized.

2.4. Data analysis

The relation between the perturbation characteristics and the postural behaviour is characterized by the ARX transfer function model (Figure 1, black thick

line). Reasonable fits for each position and for each subject are obtained with ARX models of order 10 and by choosing the optimal fit (minimizing the least squares error) for a time-delay varied between 10 and 200 ms. The model input is the time evolution of the perturbation, characterized by the work of the load applied on the hand-arm segment. The model output corresponds to the GRF time sequence (Figure 1, force plate values). The transfer function is determined for each specific postural task (Load x Vision conditions). We consider a class of autoregressive models with exogenous inputs (ARX) that writes as:

$$y(k) = -a_1 y(k-1) - \ldots - a_{na} y(k-n_a) + b_1 u(k-1) + \ldots + b_{nb} u(k-n_b),$$

where y(k) is the square root of the sum of the squared components of the reactive force measured by the force plate, u(k) is the work done by the pendulum force on the wrist, k is the time instant of the data sample, n_a and n_b define the number of past samples (outputs and inputs, respectively) used to compute the model, and $\{a_1, ., a_{na}, b_1, ., b_{nb}\}$ are constant parameters that are optimized to minimize the expectancy of the squared modelling error.

3. Results and discussion

3.1. Results

At a behavioural level, the comparative analysis of the pendulum work vs. force plate time-series for all the postural conditions shows both LOAD and VISION main effects (comparison between lines and columns in Figure 2) and their interaction. The postural reaction is correlated with the intensity of the balance perturbation; the augmentation of the pendulum work applied to the hand-arm segment significantly increases the GRF values. Additionally, time-series comparison shows a significant increase in the GRF in the 'Closed-Eyes' condition, with a cumulative interaction effect in the 'With Load' condition.

The transfer function (TF) results obtained from the identification procedure show that the model results fit well with the behavioural data (Figure 2, black large line), as a representative mean estimation of the overall trials effect for each condition of Load and Vision. The TF response captures both the amplitude and transient behaviour of the response (GRF). These results demonstrate that the complexity of the adaptive postural reaction in response to load and vision perturbations can be captured by a simple linear model with a reasonable number of degrees of freedom.

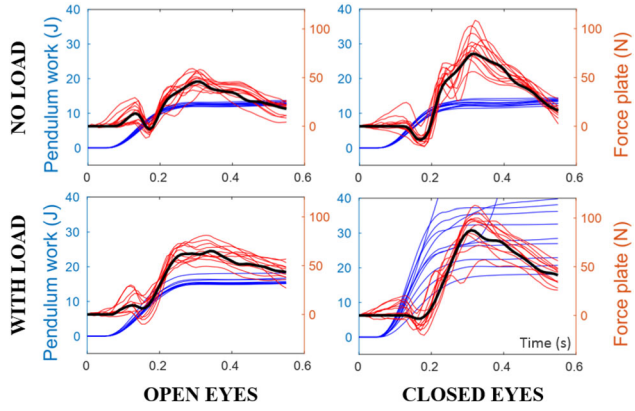


Figure 2. Comparison between the pendulum work (perturbation values as input; blue right scale), the force plate data (GRF as output; left red scale), and the transfer function model (black large line), for LOAD (No/with load) and VISION (closed/open eyes) conditions. Data for a Tai-Chi expert.

3.2. Discussion

From a neuro-biomechanical point of view, this study shows that during the external perturbation of balance, the compensatory postural adjustments rely (1) on the related characteristics of both the sensorimotor disturbances (load and vision) and the biomechanical constraints (reaction force) and (2) on the on-line reactive strategies used to maintain balance control.

In this analytic framework, the TF based on the ARX model is able to characterize and estimate both the perturbation constraints and the effectiveness of the associated postural adjustments. Consequently, the optimized parameters in the TF model allow us to clearly characterize and clarify the impact of sensory and physical constraints on adaptive balance control. Finally, this study demonstrates that context-related balance control can be appropriately modelled by input-output identification.

4. Conclusions

The use of TF methods for an in-depth analysis of postural control processes is of real interest, as is questioning the processes of balance impairment restoration or optimization. Exploring the identification parameters could give us additional knowledge for further assumptions about the adaptive stimulus-response trade-off in balance control.

Acknowledgements

The authors wish to thank the participants, the MiSCIT students at University Grenoble-Alpes and the Gipsa-lab technical team.

References

Engelhart D, Schouten AC, Aarts RG, van der Kooij H. 2015. Assessment of multi-joint coordination and adaptation in standing balance: a novel device and system identification technique. IEEE Trans Neural Syst Rehabil Eng. 23(6):973–982. doi:10.1109/TNSRE.2014.2372172.

N'Yo S. 2019. Adaptation to a push-like perturbation in a Tai-Chi posture. Master thesis, Université Grenoble Alpes. https://hal.science/hal-04061769.

Voda A, Martin O, Neto PR, Gascuel JD, Schmerber S. 2019. Visual-vestibular compensation in balance recovery: a transfer function model-based analysis. 8th IFAC Conference on Systems Biology in Engineering, Papers Online 52–26:88–93. doi:10.1016/j.ifacol.2019.12.241.

KEYWORDS Balance control; external perturbation; adaptive behaviour; transfer function model

olivier.martin@gipsa-lab.grenoble-inp.fr

Changes in knee joint pivot pattern after unicompartmental arthroplasty; impact on clinical outcomes

R. Courteille[a], L. Chèze[b], C. Batailler[b,c], S. Lustig[b,c] and N. Hagemeister[a]

[a] LIO, École de technologie supérieure, Montréal, Canada; [b]Univ Eiffel, Univ Lyon 1, Lyon, France; [c]Hôpital de la Croix Rousse, Lyon, France

1. Introduction

Knee osteoarthritis (OA) is a common and disabling pathology. Patients often experience pain as well as reduced mobility and stability (DiBonaventura et al. 2011; Bytyqi et al. 2014). Unicompartmental knee arthroplasty (UKA) can be recommended as a treatment for advanced knee OA. A UKA is preferred in young patients, because it needs less bone resection and allows for potential revision surgery at an older age (Foissey et al. 2022). UKA is a less invasive procedure, as it keeps most of the native anatomical structures. On cadaver knees, it has been shown that UKA reproduces normal knee kinematics (Bandi et al. 2022). The aim of this study was to assess if indeed UKA reproduces native kinematics in terms of knee joint pivot motion. We also wanted to determine if reproducing native motion would imply better outcomes.

2. Methods

Fifty-six (56) participants were included in this study. All patients received UKA using the same implant (HLS Uni Evolution, Tornier®) at the orthopedic service of the Croix Rousse hospital (Lyon, France). Knee landmarks and kinematics were captured during gait using the KneeKG® system (Emovi Inc., Canada) before and 6 months after surgery. Intra and inter-operator attachment system's reliability has been assessed by Lustig et al. (2012).

Joint pivot motion pattern was determined independently during loading, mid stance, end stance, push off and swing phases. Joint pivot motion was assessed by projecting consecutive transepicondylar axis positions in the transverse plane (i.e. tibial plateau) throughout the gait cycle (Banks and Hodge 2004).

Four pivot categories have been determined. Category I presents no rotation (pure antero-posterior (AP) translation). Categories II to IV present a rotation around a lateral pivot point (II), a medial pivot point (III) or a central pivot point (IV) (see Figure 1). Patients were classified based on their predominant pattern in each phase. All calculations were performed using MatLab (Mathworks, MA).

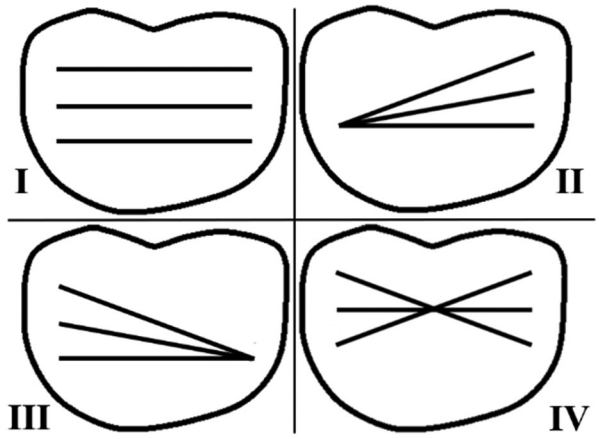


Figure 1. Joint pivot motion patterns – Superior view of the transverse plane with anterior side at the top (left knee).

All patients filled out the Forgotten Joint Score (FJS) score 6 months after their surgery. This questionnaire is a standard assessment tool to evaluate joint pain and stability and the perception of the patient (Adriani et al. 2020). A higher FJS score is indicative of better quality of life and overall clinical outcomes.

Participants who presented the same pivot motion pattern pre- and post-operatively were classified as 'non-changers'. Those who changed their pivot motion pattern were classified as 'changers'. This was done for each sub-phase independently. FJS scores were compared between changers and non-changers. Student *T*-tests (i.e. one for each phase) were used to compare FJS scores between changers and non-changers (significance level of $\alpha = 0.05$).

3. Results and discussion

During loading phase, 32 out of 56 (57%) participants were non-changers (i.e. they presented the same joint pivot motion pattern before and after UKA). During mid stance, 29 out of 56 (52%) were non-changers, Non-changers represent 20 participants (36%) during end stance, 31 (55%) during push off and 35 (63%) during swing phase. Mean FJS scores for changers and non-changers and associated *p*value are presented in Table 1.

Post-operative FJS scores were significantly higher in non-changers compared to changers for the push off phase ($p < 0.05$). There was no significant

Table 1. Post-operative FJS scores comparison between changers and non-changers during stance and swing phase.

Phase (% of GC)		Mean FJS score	Standard deviation	*p*
Loading	Changers	71.44	23.53	0.92
(0–15%)	Non-changers	72.00	19.58	
Mid stance	Changers	69.90	21.80	0.53
(15–30%)	Non-changers	73.59	21.92	
End stance	Changers	68.28	22.83	0.12
(30–45%)	Non-changers	77.80	18.64	
Push off	Changers	64.80	25.94	0.03*
(45–60%)	Non-changers	77.22	16.40	
Swing phase	Changers	74.91	21.66	0.39
(60–100%)	Non-changers	69.74	21.86	

differences between both groups for each other phases. FJS scores between each pattern were not significantly different.

This result suggests that significant differences in outcomes appear during weight-bearing activities.

4. Conclusions

This study extends the work done by Banks and Hodge (2004) and Koo and Andriacchi (2008) who presented methods to estimate the knee pivot point from fluoroscopic images or optoelectronic sensors. The method presented in this abstract uses a medical device to assess knee dynamic 3D function (KneeKG® system) which is used in clinical settings (Lustig et al. 2012) without any radiations for the patient. Results suggest that participants who do not change their joint pivot motion pattern during push off with the surgery may have better outcomes post-UKA. These results come from a preliminary study. The proposed method has to be assessed in future studies conducting similar analyses on a cohort of asymptomatic participants. This method is promising to better understand the different outcomes after knee surgeries (sport medicine or arthroplasty).

References

Adriani M, Malahias M-A, Gu A, Kahlenberg CA, Ast MP, Sculco PK. 2020. Determining the validity, reliability, and utility of the forgotten joint score: a systematic review. The Journal of Arthroplasty. 35(4):1137–1144. doi:10.1016/j.arth.2019.10.058.

Bandi M, Benazzo F, Batailler C, Blatter I, Siggelkow E, Parratte S. 2022. A morphometric fixed-bearing unicompartmental knee arthroplasty can reproduce normal knee kinematics. an in vitro robotic evaluation. Arthroplast. Today. 16:151–157. doi:10.1016/j.artd.2022.02.023.

Banks SA, Hodge WA. 2004. 2003 Hap Paul Award paper of the International Society for Technology in Arthroplasty. The Journal of Arthroplasty. 19(7):809–816. doi:10.1016/j.arth.2004.04.011.

Bytyqi D, Shabani B, Lustig S, Cheze L, Karahoda Gjurgjeala N, Neyret P. 2014. Gait knee kinematic alterations in medial osteoarthritis: three dimensional assessment. International Orthopaedics (SICOT).). 38(6):1191–1198. doi:10.1007/s00264-014-2312-3.

DiBonaventura MD, Gupta S, McDonald M, Sadosky A. 2011. Evaluating the health and economic impact of osteoarthritis pain in the workforce: results from the National Health and Wellness Survey. BMC Musculoskelet Disord. 12(1):83. doi:10.1186/1471-2474-12-83.

Foissey C, Batailler C, Shatrov J, Servien E, Lustig S. 2023. Is combined robotically assisted unicompartmental knee arthroplasty and anterior cruciate ligament reconstruction a good solution for the young arthritic knee? Int Orthop (SICOT). 47(4):963–971. doi:10.1007/s00264-022-05544-5.

Koo S, Andriacchi TP. 2008. The knee joint center of rotation is predominantly on the lateral side during normal walking. J Biomech. 41(6):1269–1273. doi:10.1016/j.jbiomech.2008.01.013.

Lustig S, Magnussen RA, Cheze L, Neyret P. 2012. The KneeKG system: a review of the literature. Knee Surg Sports Traumatol Arthrosc. 20(4):633–638. doi:10.1007/s00167-011-1867-4.

KEYWORDS Knee; pivot motion pattern; FJS score; osteoarthrisis

remi.courteille.1@ens.etsmtl.ca

Comparison of two confidence-based methods for markerless motion capture

A. Chaumeil, A. Muller, R. Dumas and T. Robert

LBMC UMR_T 9406, Univ Lyon, Univ Eiffel, Univ Claude Bernard Lyon 1, Lyon, France

1. Introduction

Most video-based human pose estimation software provide results in the 2D coordinate system of the input image or video. However, studies in biomechanics often require 3D information. One commonly used method to obtain 3D points from 2D points and calibrated cameras is the direct linear transform (DLT) (Abdel-Aziz and Karara 1971).

Most pose estimation software associates each pixel with a value between 0 and 1, which corresponds to the confidence that the investigated keypoint is located at this particular pixel. It transforms the image into a confidence heatmap. The most common approach uses this confidence information in a binary way: the 2D point of interest corresponds to the pixel with the maximal confidence over the whole heatmap. Yet, Iskakov et al. (2019) obtained promising results by using the whole confidence information: both temporal continuity and accuracy increased, especially when using a small set of video cameras. However, these results were obtained using specifically trained neural networks. It would then be interesting to test if such improvement could also be obtained using the same idea applied to more generic tools, e.g. using confidence heatmaps generated by OpenPose (Cao et al. 2019). Two approaches can be envisaged, according to Iskakov et al. (2019): one consists in using a classical binary 2D point estimation for each camera view and then to compute the 3D point using a weighted DLT based on their confidence given by the heatmaps. The second approach, which is recommended by Iskakov et al. (2019), consists in projecting the 2D heatmaps to obtain 3D confidence volumes, from which a 3D point is extracted.

In this study, we propose an approach that allows exploiting the whole information from the confidence heatmaps provided as output of OpenPose. The goal of this study is therefore to compare the two previously presented confidence-based methods for markerless 3D reconstruction.

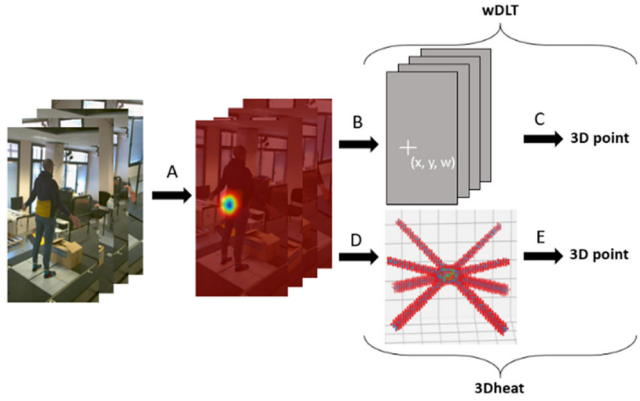


Figure 1. Visual representation of the confidence-based methods.

2. Methods

2.1. Participants

For this study, eight participants were recruited (3 women), with age: 28.3 ± 2.8 years old, height: 1.70 ± 0.09 m and mass: 63.1 ± 6.36 kg. Participants had no history of musculoskeletal problems. They signed an informed consent form and the study was approved by our institutional review board.

2.2. Experimental setup

Data was collected using 10 Qualisys Miqus Video cameras at 60 Hz which were synchronized and calibrated using Qualisys Track Manager (v2021.1.2 – average residual after calibration: 0.38 mm). Participants wore their usual clothes. A box (approximately 60x40x30 cm) was put in front of them on the ground. Participants were asked to stand still and then squat, grab the box, stand up with the box, squat again and then put the box back in front of them. Three repetitions per participant were performed.

2.3. Data processing

Videos were processed using Theia3D (v 2022.1), which was used as reference in the absence of markers. A visual explanation of the two confidence-based methods is displayed in Figure 1. Both methods were used to obtain 3D position of the main joint centres of interest in this study (left (L) and right (R) shoulders, elbows, wrists, hips, knees and ankles). OpenPose (v 1.7.0) was applied to a subset of four evenly distributed cameras. It provided the confidence heatmap of each keypoint (Figure 1A) from which the position (x, y) and associated confidence (w) of the keypoints were extracted (Figure 1B).

First (Figure 1C), 3D positions were estimated using a confidence-based weighted DLT (wDLT)

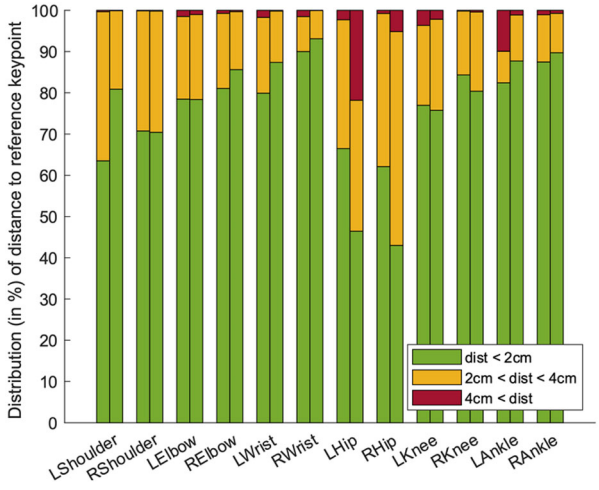


Figure 2. Distribution, in percent, of the Euclidean distance between wDLT and Theia3D (left bar) and between 3Dheat and Theia3D (right bar), for each keypoint.

(Pagnon et al. 2021). Second, 3D heatmaps (3Dheat) were built for each point (Figure 1D). 3D space was discretized with a point every 3 mm in all 3 directions. Then, using the intrinsic and extrinsic parameters of the cameras, the points were projected on the heatmaps for each camera and associated with the corresponding confidence value. The 4 confidence values associated with each camera were then summed. The 3D point with the maximum summed confidence was selected as the position of the keypoint for the studied frame (Figure 1E).

2.4. Data analysis

Euclidean distances between joint centre positions estimated with wDLT and 3Dheat and Theia3D were computed. Associated root mean square errors (RMSE) and standard deviation were computed for each keypoint for both methods. Euclidean distances were classified according to their values (under 2 cm, between 2 cm and 4 cm and above 4 cm). Threshold values were selected based on the differences observed in the literature between marker-based and markerless for keypoint detection (Kanko et al. 2021): below 2 cm, the distance is considered to be due to measurement noise, and above 4 cm it is considered to be a major difference.

3. Results and discussion

The RMSE is below 2 cm for all keypoints except 3Dheat LHip (3.3 ± 1.9 cm), wDLT and 3Dheat RHip (2.0 ± 0.7 cm and 2.4 ± 0.9 cm respectively) and wDLT LAnkle (2.4 ± 1.7 cm). For both hips, RMSE and standard deviation are higher for 3Dheat than wDLT (LHip: 1.9 ± 0.9 cm for wDLT). For wDLT LAnkle, RMSE is higher than 2 cm with a bigger standard deviation than for 3Dheat (1.59 ± 0.80 cm for 3Dheat).

Figure 2 displays the distribution of differences. For the hips, there are fewer differences that are below 2 cm and more differences above 4 cm for 3Dheat than for wDLT. For LAnkle, the proportion of differences above 4 cm is higher for wDLT (9.9%) than for 3Dheat (1.1%), while the proportion of differences below 2 cm remains similar (87.5% for wDLT and 89.6% for 3Dheat). For the other keypoints, there is not a clear trend for one method generating smaller differences than another.

For the hips, the observed differences between the methods can be explained by several factors. Firstly, the movement itself makes it difficult to estimate the position of the hip joint centers, especially during the squat movement. Hip keypoints obtained with OpenPose thus have a medium or low confidence. Moreover, differences in hip joint center definition and detection between Theia3D and OpenPose could generate systematic errors between the two confidence-based 3D reconstruction methods and Theia3D. However, both Theia3D and OpenPose provide limited information about biomechanical definition of the keypoints, thus systematic errors can only be evaluated experimentally. Secondly, 3Dheat is a completely different approach. For wDLT, the point that is reconstructed is the point that is closest to all projection lines. For 3Dheat, the selected point is the one with maximum confidence. Heatmaps create beams in 3D space by projecting zones of confidence instead of points, and the point with the maximum summed confidence is at the crossing of two or more beams. For example, for the hips, beams do not often cross all together at some point in space, or they only cross two by two. Thus, the maximum summed confidence is not in the middle of a beam-crossing area (where the point given by the wDLT results lies) but somewhere on the periphery of this area.

For LAnkle, 3Dheat provides better results, especially regarding differences above 4 cm. One factor explaining this difference is the high number of inconsistent detections generated by OpenPose, which sometimes detects LAnkle where it is absolutely not (typically when LAnkle is occluded). In this case, the inconsistent beam crosses the other beams far from where they intersect and has thus little influence on the maximum summed confidence. However, the

point that is selected by wDLT is influenced by the inconsistent point, even if it has low confidence.

4. Conclusions

Comparison of two confidence-based methods for markerless motion capture has been performed. Overall, the two methods provide similar results. Yet, they seem to be robust against different situations: 3Dheat in the case of one wrongly detected point, wDLT in the case of uncertain points. Nonetheless, both approaches rely on OpenPose keypoint detection quality.

References

Abdel-Aziz YI, Karara HM. 1971. Direct linear transformation from comparator coordinates into object space coordinates in close-range photogrammetry. Photogramm Eng Remote Sens. 81(2):103–107.

Iskakov K, Burkov E, Lempitsky V, Malkov Y. 2019. Learnable triangulation of human pose. 2019 IEEE/CVF International Conference on Computer Vision (ICCV). doi:10.1109/ICCV.2019.00781.

Cao Z, Hidalgo G, Simon T, Wei S-E, Sheikh Y. 2019. OpenPose: realtime multi-person 2D pose estimation using part affinity fields.

Kanko RM, Laende EK, Davis EM, Selbie WS, Deluzio KJ. 2021. Concurrent assessment of gait kinematics using marker-based and markerless motion capture. J Biomech. 127:110665. doi:10.1016/j.jbiomech.2021.110665.

Pagnon D, Domalain M, Reveret L. 2021. Pose2Sim: an end-to-end workflow for 3D markerless sports kinematics—part 1: robustness. Sensors. 21(19):6530. doi:10.3390/s21196530.

KEYWORDS Markerless motion capture; confidence heatmaps; triangulation; 3D point reconstruction

thomas.robert@univ-eiffel.fr

Development of a pipeline of 3D underwater motion capture: application to the analysis of horse swimming

C. Giraudet[a], C. Hatrisse[b,c], C. Macaire[a,b,d], P. Gaulmin[b], C. Moiroud[b], K. Ben Mansour[a], F. Audigié[b], H. Chateau[b] and F. Marin[a]

[a]UTC, BMBI, UMR 7338, Compiègne, France; [b]EnvA, CIRALE, USC 957 BPLC, Maisons-Alfort, France; [c]Univ Gustave Eiffel, Univ Claude Bernard Lyon 1, LBMC UMR_T 9406, Univ Lyon, Lyon, France; [d]LIM France, Labcom LIM-ENVA, Nontron, France

1. Introduction

Limbs and tendon injuries are primary causes of activity loss in racehorses and sport horses. Aquatic training is an effective method to maintain and strengthen the cardiorespiratory system while minimizing the impact of gravity on the musculoskeletal and joint systems. Although swimming pool training offers clinical advantages, the biomechanics of horse swimming has received little attention (Santosuosso et al. 2021) and remain poorly understood. Biomechanics research typically employs motion capture and analysis (Roberson et al. 2013). The objective of this study is to develop a pipeline for capturing and reconstructing underwater 3D motion, estimate the accuracy of the process and to apply it to the 3D motion of a horse during a complete swimming cycle.

2. Methods

2.1. Acquisition system

The acquisition system comprises six GoPro Hero 8 Black cameras, each capable of capturing 120 frames per second at a resolution of 2.7K. These cameras are strategically placed on one side of the swimming pool, as shown in Figure 1 – up, with overlapping fields of view to enable tracking over a distance of 2.6 meters (Figure 1 – bottom). On the horse, 24 anatomical markers were drawn by the veterinary team with cattle markers (Raidex) of contrasting colors with respect to the horse's color, on six anatomical locations on each limb: the scapula, the shoulder, the elbow, the carpus, the fetlock, and the hoof for the front limb (Figure 2 – left) and the tuber coxae, the hip, the stifle, the tarsus, the fetlock, and the hoof for the hind limb (Figure 2 – right). Only one side of the horse is visible to the cameras at each recording.

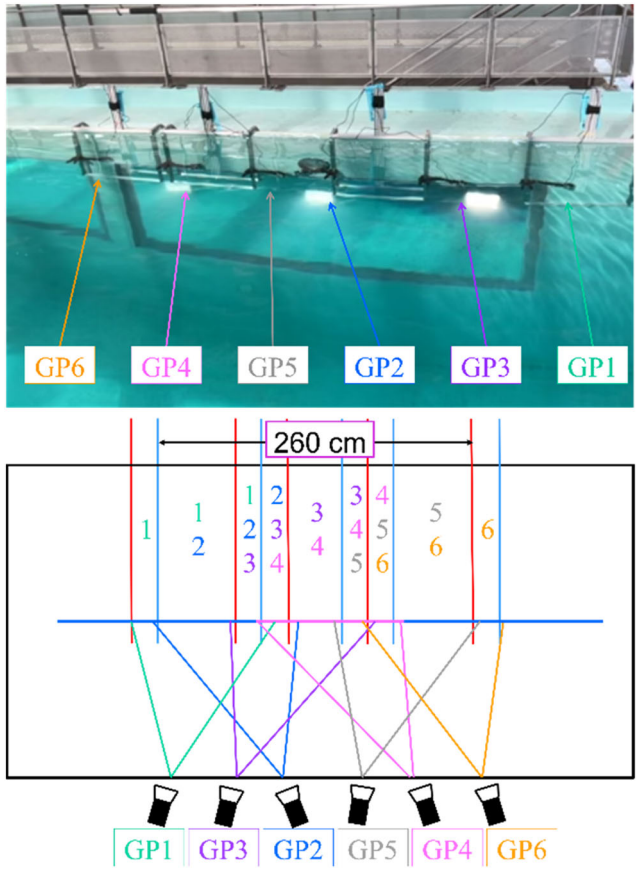


Figure 1. Camera disposition and field of view (GP = GoPro camera). the total field of view is around 260 cm, and each camera belongs to one (GP1 and GP6) or two pairs (GP2 to GP5) for the 3D reconstruction.

To date, the experiments have been conducted on four horses, representing 113 records.

2.2. Pre-processing of the video

Six preprocessing steps are necessary before performing the 3D reconstruction of the anatomical points:

- convert the videos to H264 format;
- segment the videos and synchronize them using successive shutdowns of the spotlights, which can be clearly seen on the videos;
- calibrate the cameras to determine their intrinsic and extrinsic parameters using images of a checkerboard and camera calibrator app (Matlab);
- correct the fisheye of the videos using camera parameters;
- compute the camera positioning with respect to each other using images of the checkerboard on each pairs of cameras and stereo-camera calibrator app (Matlab);
- track semi-automatically the anatomical points on the six videos using the video-labeler app (Matlab).

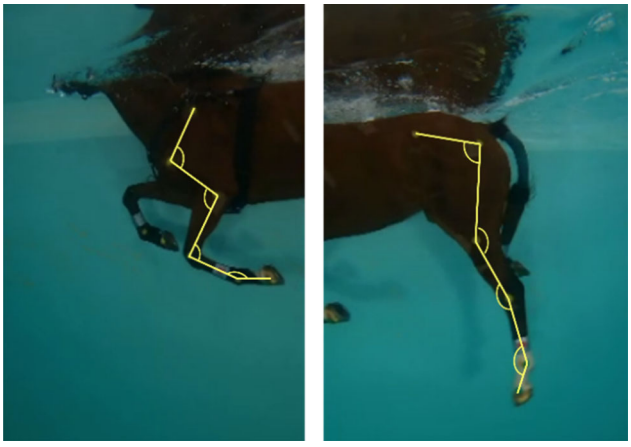


Figure 2. View of the 2nd and 5th camera at the same time. The anatomical points are from top to bottom: front limb (left): mid-length of scapular spine, shoulder, elbow, carpus, front fetlock and front foot. Hind limb (right): tuber coxae, hip, stifle, tarsus, hind fetlock and hind foot.

2.3. Post-processing of the video

By combining the tracked points and camera positioning, a 3D reconstruction is performed in local reference frames (reference frame of the first camera of each pair), using the Direct Linear Transformation (DLT) algorithm. A global reference frame of the swimming pool is established to enable the 3D reconstruction to be computed in a common reference frame with respect to the five pairs of cameras.

2.4. Error estimation

An error estimation has been computed on the checkerboard. We considered eight segments whose dimension is known by construction (between 34 and 60 mm) and five angles between 34 and 102°, which correspond to the dimension found on horses for the anatomical segments of the limbs. The absolute error is less than 10 mm for the reconstructed segments and less than 1° for the different angles computed.

3. Results and discussion

3.1. Horse reconstruction and angle computation

The 3D reconstruction of 24 anatomical points (12 on each side of the horse) allows for the computation of eight different angles of the front (Figure 2 – left) and hind (Figure 2 – right) limbs:

- (a) left: the shoulder angle formed by the anatomical points of the scapula, the shoulder and the elbow;
- (b) left: the elbow angle formed by the anatomical points of the shoulder, the elbow and the carpus;

Table 1. Value of the minimum and maximum computed values for the 8 angles.

Front limb	Shoulder	Elbow	Carpus	Front fetlock
Angle range	[100–125°]	[55–145°]	[60–180°]	[120–180°]
Hind limb	Hip	Stifle	Tarsus	Hind fetlock
Angle range	[60–110°]	[75–150°]	[50–170°]	[100–175°]

- (c) left: the carpus angle formed by the anatomical points of the elbow, the carpus and the front fetlock;
- (d) left: the front fetlock angle formed by the anatomical points of the carpus, the front fetlock and the hoof of the front limb;
- (a) right: the hip angle formed by the anatomical points of the tuber coxae, the hip and the stifle;
- (b) right: the stifle angle formed by the anatomical points of the hip, the stifle and the tarsus;
- (c) right: the tarsus angle formed by the anatomical points of the stifle, the tarsus and the hind fetlock;
- (d) right: the hind fetlock angle formed by the anatomical points of the tarsus, the hind fetlock and the hoof of the hind limb.

The first results for the minimum and maximum values of the different reconstructed 3D angles are summarized in Table 1. Based on preliminary results from a single record, the joint range of motion is as follows: shoulder: 100–125°, hip: 60–110°, elbow: 55–145°, stifle: 75–150°, carpus: 60–180°, tarsus: 50–170°, front fetlock: 120–180° and hind fetlock:100–175°.

These values have been compared to the values available for the three classical gaits – walk, trot and canter – (Back et al. 1997). It appears that the amplitude of the range of motion is greater for all angles during swimming, with greater maximum flexion and extension observed in both the front and hind limbs.

4. Conclusions

In summary, we have developed a comprehensive pipeline for capturing and analysing the joint movements of a horse's limbs during a full swimming stride. Our preliminary findings indicate a broader range of motion compared to traditional training, which could result in different muscle activation. This information could be valuable for muscle strengthening or rehabilitation purposes.

References

Back W, Schamhardt HC, Barneveld A. 1997. Kinematic comparison of the leading and trailing fore- and

hindlimbs at the canter. Equine Vet J Suppl. 23(23):80–83. doi:10.1111/j.2042-3306.1997.tb05060.x.

Santosuosso E, Leguillette R, Vinardell T, Filho S, Massie S, McCrae P, Johnson D, Rolian C, David F. 2021. Kinematic analysis during straight line free swimming in horses: part 1 & 2 – forelimbs & hindlimbs. Front Vet Sci. 8:752375. doi:10.3389/fvets.2021.752375.

Roberson EDG, Caldwell GE, Hamill J, Kamen G, Whittlesey SN. 2013. Research method in biomechanics. 2nd ed. Champaign (IL): Human Kinetics.

KEYWORDS Horse swimming; joint angle; 3D reconstruction; underwater motion capture

chloe.giraudet@utc.fr

Is hip subluxation risk influenced by femoral head geometry and cup orientation after THA?

P. Chavet[a], R. Buisson[a], E. Dessyn[b,c], T. Coyle[a] and P. Chabrand[a]

[a]Aix Marseille Université, CNRS, ISM, Marseille, France; [b]Département de chirurgie orthopédique, AP-HM, Institut du mouvement et de l'appareil locomoteur, Hôpital Sainte-Marguerite, Marseille, France; [c]Hôpital privé La Casamance, service d'Orthopédie, Aubagne, France

1. Introduction

By 2030 the volume of total hip arthroplasty (THA) procedures will have increased by 170% for the total world population (Dargel et al. 2014). However, the characteristics of the population needing a THA have changed. Younger active people are seeking complete restoration of motor capacity and seniors over 65 years old are now expecting better quality aging. In this line, improving function, preventing dislocations and avoiding wear might be the focus of the improvement of the advances in THA.

Several studies have denounced improper component positioning, increased wear and early failure after total hip replacement as contributing to instability (Lewinnek et al. 1978). Indeed, the accurate positioning of the acetabular prosthesis is a clear challenge as it is reported as the primary cause of THA dislocation (Biedermann et al. 2005). The optimal range of acetabular cup angle so as to minimize dislocation risk after primary THA has been commonly accepted since Lewinnek et al. in 1978 first put forward the idea of a 'safe zone'. This safe zone is delimited by a cup inclination of 40° ±10° and an anteversion of 15° ±10°. These margins are still widely recognized in the orthopedic community.

The general purpose of the study was first to characterize precisely the cup positioning and then to document the 3D range of hip joint motion considering various prosthetic femoral head diameters. Only the kinematics of the bony structures associated to the prosthetic parts were tested. It was hypothesized that an intermediate 45° abduction-15° anteversion positioning of the cup for the smallest femoral head diameters would best meet criteria of a safe range of motion.

2. Methods

2.1. Materials

Sawbone® pelvis and femur bones were used. Dual mobility THA implants (Adler Orthopaedics®) were used in the study. Four femoral heads of 28, 32, 36, and 40 mm diameter associated to a Modula® modular neck (Adler Orthopaedics®) were tested. The bones were prepared for the insertion of the hip prosthesis implants. The femoral head was resected, and the pelvis acetabulum was milled before impaction with the ancillary device to position the acetabular cup at 15° (±5°) ANT angle. An adjustable stand was used hold the pelvis immobile with the sacral plateau horizontal.

The VICON (Oxford, UK) optoelectronic motion capture system with 7 MXT40 CCD cameras was used to acquire ($f = 125$ Hz) the kinematic data of a maximum of 13 semi-hemispherical reflective markers of 4 mm in diameter fixed onto the bone segments.

2.2. Protocols

Static Data Acquisition was performed to calculate the distance between the center of the femoral head and the inner center of the cup.

The femur was manually moved in 3 orthogonal planes to correspond to Euler sequence i.e. flexion-extension (FLEX-EXT), adduction-abduction (ADD-ABD), and medial-lateral rotation (M-L). The six rotations were performed continuously and slowly, taking care to remain within the approximate physiological range.

The movement of the femur was continued until impingement occurred (component to component, bone to bone or bone to component).

Three Anteversion * 3 Abduction angles were combined for the cup positioning resulting in 9 configurations : $A = 30°_{ABD}\text{-}0°_{ANT}$; $B = 45°_{ABD}\text{-}0°_{ANT}$, $C = 60°_{ABD}\text{-}0°_{ANT}$, $D = 30°_{ABD}\text{-}15°_{ANT}$, $E = 45°_{ABD}\text{-}15°_{ANT}$, $F = 60°_{ABD}\text{-}15°_{ANT}$, $G = 30°_{ABD}\text{-}30°_{ANT}$, $H = 45°_{ABD}\text{-}30°_{ANT}$, and $I = 60°_{ABD}\text{-}30°_{ANT}$.

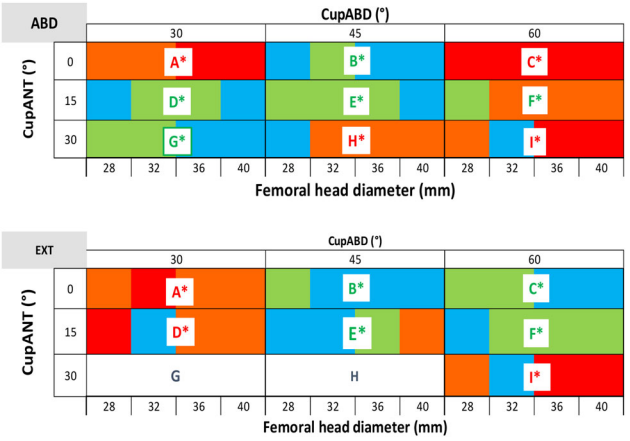
Each configuration was tested for each head diameter (total of 36 acquisitions).

2.3. Data analysis

Kinematic data were filtered with a 10 Hz Butterworth lowpass filter. The calculation of the joint ROM resulted from the 3D kinematics of the hip joint using Euler angles. The distance between the center of the femoral head and the center of the cup (DC-FH) was computed as it can constitute a relevant parameter to express the subluxation risk.

Nonparametric tests were run to characterize the DC-FH according to three factors i.e. 3D rotations (FLEX-EXT, ABD-ADD, M-L) of the femur, and 9 cup orientation (anteversion-inclination configurations), and 4 femoral head diameters. Spearman ρ was used to compute the correlation between DC-FH and the 3D rotation factor. Subsequently a

Table 1. Overview of the 36 combinations of hip movement, abduction (top) and extension (bottom). blue area = very low risk, green area = low risk ; orange area = intermediate risk, and red area = high risk.



The worst statistical combinations are identified with a red *, and the best favourable with a green *.

Kruskal-Wallis analysis tested the influence of cup orientation and femoral head diameter involved in the correlation. Finally, a Mann and Whitney test serves as post-hoc analysis. The threshold of the statistical significance (p) was set at 0.05.

3. Results and discussion

Only abduction (ρ =0.46, $\pi = 5.9.\ 10^{-3}$) and extension ($\rho = 0.48$, $p = 3.5.10^{-3}$) revealed a significant variation of DC-FH with the increase of joint amplitude (factor 3D rotation). DC-FH, key parameter of subluxation, is linked to two interacting factors: the diameter of the femoral head associated with combinations of orientation of the cup embedded in the coxal acetabulum. Our results reveal that only abduction and extension predict DC-TF values even if the strength of the link is moderate ($\rho = 0.46$ and $\rho = 0.48$ respectively).

No statistical effect of the head diameter was reported whatever the 6 types of rotations whereas the orientation of the cup did influence the maximal value of the ROM amplitude ($8.\ 10^{-4} < p > 2.1.\ 10^{-2}$).

Our results reported more favorable accepted orientations and wider angular configurations than those identified by Kosashvili et al. (2013). We proposed a new representation in the form of a table, for each of the two relevant rotations. To highlight the orientation combinations that are more or less favorable, we established a four-color code sharing proportional DC-FH which is similar to an indication of the risk of subluxation (Table 1).

Our hypothesis is partially refuted as DC-FH, potential key indicator of hip subluxation, is relevant for only two hip joint movements. Recently Sadhu et al. (2017) re-affirmed the interest of the safe zone established by Lewinnek by reporting a higher percentage of prosthetic hip dislocation when the surgery was performed out of the safe zone. In this line our study extends the study of Lewinnek; as we associate the orientation of the cup with the criterion defined clinically and measured, the DC-FH.

4. Conclusions

The multifactorial aspect of the subluxation was confirmed by this study, as it was classically reported in the literature. Considering only the bone– prosthetics interactions we revealed the importance of hip abduction and extension as the distance between the acetabulum and the femoral head increased which may intensify the risk of a subluxation. These data should help the development of finite element model of the mechanical efficiency of the THA. Even if muscular insertions and periarticular tissues are absent it can help the surgeon positioning the prosthesis according to the cup orientation to optimize the effectiveness of THA surgery.

Acknowledgements

We would like to thank Adler®Ortho company for the donations of prosthesis and sawbones.

References

Biedermann R, Tonin A, Krismer M, Rachbauer F, Eibl G, Stöckl B. 2005. Reducing the risk of dislocation after total hip arthroplasty – the effect of orientation of the acetabular component. Bone Joint J. 87-B(6):762–769. doi:10.1302/0301-620X.87B6.14745.

Dargel J, Oppermann J, Bruggemann GP, Eysel P. 2014. Dislocation following total hip replacement. Dtsch Arztebl Int. 111(51–52):884–890. doi:10.3238/arztebl.2014.0884.

Lewinnek GE, Lewis JL, Tarr R, Compere CL, Zimmerman JR. 1978. Dislocations after total hip-replacement arthroplasties. J. Bone Joint Surg. Am. 60(2):217–220. doi:10.2106/00004623-197860020-00014.

Kosashvili Y, Omoto D, Backstein D, Safir O, Lakstein D, Gross AE. 2013. Acetabular alignment and primary arc of motion for minus, skirtless, and skirted 28-, 32-, 36-, and 40-mm femoral heads. J. Arthroplasty. 28(2):279–285.e2. doi:10.1016/j.arth.2012.06.005.

Sadhu A, Nam D, Coobs BR, Barrack TN, Nunley RM, Barrack RL. 2017. Acetabular component position and the risk of dislocation following primary and revision total hip arthroplasty: a matched cohort analysis. J. Arthroplasty. 32(3):987–991. doi:10.1016/j.arth.2016.08.008.

KEYWORDS Hip joint; total hip replacement; kinematics; subluxation; safe zone

pascale.chavet@univ-amu.fr

KneeKG manual gait initiation detection repeatability experiment

D. Sweidy[a], M. Coleman[b], P. Landry[c], L. Beckman[c], A. Cagnin[c], H. Pillet[a], M. M. Lefevre-Colau[d], N. Hagemeister[e], P.-A. Vendittoli[f] and A. Roren[d]

[a]Ecole Supérieure Nationale des Arts et Métiers, Paris, France; [b]Service de MPR, Hôpital Cochin, Paris, France; [c]EMOVI, Montréal, Canada; [d]Faculté de Santé, UPC, Paris, France; [e]École de Technologie Supérieure, Montréal, Canada; [f]Université de Montréal, Canada

1. Introduction

The KneeKG® system (EMOVI, Canada) is a validated medical device assessing three-dimensional (3D) knee motion during gait on a conventional treadmill. This device provides accurate and reliable quantification of 3D knee kinematics after normalizing all cycles having various speeds (Labbe et al. 2008; Lustig et al. 2012). It has been used to assess dynamic knee movements in several pathologies (e.g. osteoarthritis, etc.).

With the absence of ground reaction force data, the KneeKG software uses an alternative method to define the initiation of the gait cycle (i.e. the first minimum of the flexion-extension curve corresponding to the heel strike). This event detection process combines an automated suggestion and requires a manual validation: a cursor indicates the first minimum by averaging the minimum values (i.e. in flexion), and a manual adjustment is made by the observer who visually assesses the first minimum on the knee flexion-extension curve. The reliability of this detection depends on the shape of the curve which may differ according to the knee pathology. Patellofemoral pain syndrome (PFPS) is defined as pain in the retro- or peri-patellar area during different types of physical activities, such as gait, squatting, running and prolonged sitting. Despite being commonly diagnosed, its exact pathophysiology and the biomechanical factors involved in patients suffering from PFPS remain incompletely elucidated (Sisk and Fredericson 2019).

The repeatability of the manual process of defining the gait initiation event within the KneeKG system was never reported, and the definition of the initiation of the gait cycle impacts the phases of the gait cycle. The main objective of this study was to evaluate the intra- and inter-observer repeatability of defining the initiation of the gait cycle in both asymptomatic and PFPS individuals. The second objective was to evaluate the impact of potential variation of the event detection process on the maximum values in the three planes of movement in both populations.

2. Methods

The repeatability study was retrospective using previously collected 3D knee kinematic measurements from 15 asymptomatic participants [7 females, 33.6 (6.6) years old, 24.5 (2.7) kg m^{-2}, total of 30 asymptomatic knees] and 14 participants with PFPS [8 females, 32.6 (11.7) years old, 23.5 (3.2) kg m^{-2}, total of 17 knees (3 bilateral PFPS)]. The 3D knee measurements were performed at Maisonneuve Rosemont Hospital and at EMOVI Headquarters in Montréal (Canada), and at Cochin Hospital in Paris (France). Patients gave written informed consent for data collection and usage in all sites. Four observers, of which two are experts (LB, PL) and two are novices (DS, MC), participated in the study. For intra-observer repeatability, DS determined the gait cycle initiation for the 47 knees two separate times. The first session from DS (DS1) and the only session from LB, PL and MC were used to assess inter-observer repeatability. Prior to the repeatability tests, a training course was provided to both novice observers by EMOVI technical team to standardize the method for detecting gait initiation (Figure 1). The data of interest was the first minimum knee flexion angle manually selected (i.e. gait cycle initiation) and the maximal value for knee flexion, adduction-abduction and external-internal rotation during gait, in both groups of participants. For each observer, different random sequences of the kinematic recordings for the 47 knees were generated. The Kolmogorov-Smirnov test showed the normality of the data distribution. Intraclass correlation coefficients (ICC (3,1) and ICC (2,1)) were used to assess intra-observer and inter-observer repeatability, respectively. ICC <0.5 indicates poor reliability. $0.5 \leq$ ICC <0.75 indicates moderate reliability, $0.75 \leq$ ICC <0.9 indicates good reliability,

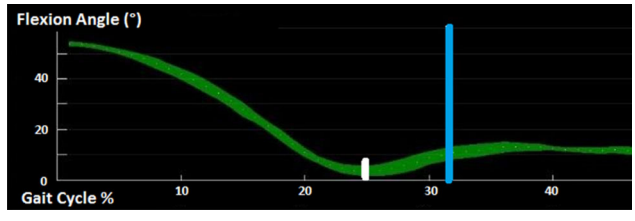


Figure 1. Knee flexion curve with the automatic cursor (small white line) at the first minimum and the manual cursor (long blue line) to its right.

Table 1. ICC values of inter-observer repeatability in asymptomatic and PFPS populations.

Observer	DS1-LB	DS1-PL	DS1-MC
Asymptomatic	0.98	0.93	0.75
PFPS	0.99	0.92	0.93

and ICC $\geq$0.9 indicates excellent reliability (Koo and Li 2016). The Bland and Altman plot was used to assess the agreement between measurements. Student paired *t*-tests were used to compare the maximum angle values for all degrees of freedom.

3. Results

For intra-observer repeatability, the observer (DS) repeated the test 3 days after the 1st session. The ICC was over 0.99 for the manually selected gait cycle initiation (i.e. the first minimum knee flexion angle) in both asymptomatic and PFPS participants. The maximum angle values for all degrees of freedom did not statistically vary between the first and second session (asymptomatic population: $p = 0.982$, $p = 0.367$ and $p = 0.539$, for flexion-extension, adduction-abduction, and external-internal rotation, respectively; PFPS population: $p = 0.657$, $p = 0.402$ and $p = 0.521$). For the inter-observer repeatability, ICC values were all $\geq$0.92 except for one (i.e. 0.75, see Table 1). For the 3 inter-observers sessions, in the asymptomatic population, the maximum flexion-extension, adduction-abduction and external-internal rotation angles did not statistically vary ($0.144 \leq p \leq 1.0$). In the PFPS population, the maximum knee abduction-adduction angle was significantly different, compared to DS1, between LB ($p = 0.04$) and MC ($p = 0.043$).

The Bland and Altman plot showed a good concordance between the tests (Figure 2). The mean of the differences was close to zero, the point cloud was horizontal and the majority of values were inside the confidence interval.

4. Discussion

The current study shows excellent intra-observer repeatability and good to excellent inter-observer repeatability of the choice of the gait initiation threshold. The results confirm the excellent reliability of the KneeKG measurements (Hagemeister et al. 1999). The difference in maximal knee adduction-abduction angles between two observers in participants with PFPS could be explained by their experience level (LB was an expert, MC was a novice) and the small range of motion (RoM) of knee adduction-abduction. The maximal knee angles are in agreement with the knee RoM used during gait (Kadaba et al. 1990).

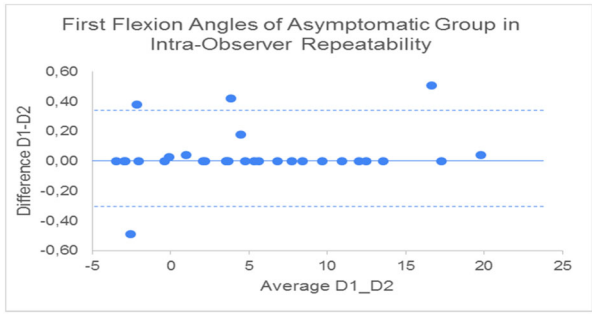


Figure 2. Example of Bland and Altman plot: intra-observer repeatability for first minimum flexion angle in the asymptomatic group.

For only 3 out of the 47 knees assessed (1 asymptomatic and 2 PFPS), the selected percentage for the gait cycle initiation varied between the 4 observers. These 3 kinematic patterns were characterized by the flat aspect of the knee flexion-extension curve during the loading phase, making it more difficult to accurately assess gait initiation.

Our study has some limitations: the automatic cursor could have influenced the observer's choice when selecting the first minimum knee flexion angle. The gait speed may have differed between participants. The difference in screen sizes between the observers could have altered the accuracy of the identification of the first minimum. In the absence of detection of gait initiation (i.e. by force plates), we could not compare the actual event detection instance with the actual gait initiation.

5. Conclusion

The KneeKG procedure showed good to excellent intra- and inter-observer repeatability in detecting gait cycle initiation allowing its use for clinical practice and research. In the future, we should find a way to make gait initiation detection automatic in order to save observers' time and increase measurement accuracy.

Acknowledgements

The authors do not have specific acknowledgements to report.

References

Hagemeister N, Yahia L, Duval N, de Guise JA. 1999. In vivo reproducibility of a new non-invasive diagnostic tool for three-dimensional knee evaluation. The Knee. 6(3):175–181. doi:10.1016/S0968-0160(99)00004-6.

Kadaba MP, Ramakrishnan HK, Wootten ME. 1990. Measurement of lower extremity kinematics during level walking. J Orthop Res. 8(3):383–392. doi:10.1002/jor.1100080310.

Koo TK, Li MY. 2016. A guideline of selecting and reporting intraclass correlation coefficients for reliability research. J Chiropractic Med. 15(2):155–163. doi:10.1016/j.jcm.2016.02.012.

Labbe DR, Hagemeister N, Tremblay M, de Guise J. 2008. Reliability of a method for analyzing three-dimensional knee kinematics during gait. Gait Posture. 28(1):170–174. doi:10.1016/j.gaitpost.2007.11.002.

Lustig S, Magnussen RA, Cheze L, Neyret P. 2012. The KneeKG system: a review of the literature. Knee Surg Sports Traumatol Arthrosc. 20(4):633–638. doi:10.1007/s00167-011-1867-4.

Sisk D, Fredericson M. 2019. Update of risk factors, diagnosis, and management of patellofemoral pain. Curr Rev Musculoskelet Med. 12(4):534–541. doi:10.1007/s12178-019-09593-z.

KEYWORDS Repeatability; gait initiation; KneeKG; intra/inter-observer

doriansweidy@gmail.com

Simulated increase in monoarticular hip muscle strength reduces the first peak of knee compression forces during walking

E. Jolas[a,b,c], M. B. Simonsen[a,b] and M. S. Andersen[a,b]

[a]Department of Materials and Production, Aalborg University, Aalborg, Denmark; [b]MathKOA, Aalborg University, Aalborg, Denmark; [c]Ecole Normale Supérieure de Rennes, Bruz, France

1. Introduction

Knee osteoarthritis (KOA) is a leading cause of disability worldwide. Although the relationship between knee loading and KOA progression is debated, reducing knee loading with conservative treatments is often recommended and may alleviate symptoms (Brophy and Fillingham 2022). This load is often quantified using the first and second peaks in knee joint compressive forces during gait (KCF_{p1} and KCF_{p2}; Stoltze et al. 2018). Studies have focused on identifying simple changes in muscle coordination through modeling to reduce KCF_{p2} by reducing the gastrocnemius activation in favor of the soleus (Uhlrich et al. 2022). The reduction of KCF_{p1}, on the other hand, has not achieved the same amount of attention. A previous study indicated that the KCF_{p1} could be reduced by applying a hip flexion/extension moment (MH_{FE}; Stoltze et al. 2018). However, studies found significant inter-individual variability in the magnitude of net joint moments during healthy walking (Simonsen and Alkjær 2012). These differences must be considered as they could affect the outcome of simulations targeting muscle coordination and KCF. Therefore, this study aimed to identify which monoarticular hip muscles could compensate for the MH_{FE} to reduce KCF_{p1} while considering different walking strategies using musculoskeletal modeling.

2. Methods

2.1. Experimental data

Twenty-four healthy participants (12 males and 12 females, 23.3 ± 3.2 years) performed three walking trials at their own pace. An eight-camera Qualisys system (Qualisys, Gothenburg, Sweden) recording at 100 Hz, 32 reflective markers placed on the lower extremity, and two force plates recording at 1000 Hz (AMTI, Watertown, USA) were used to collect data from gait trials. The study was conducted in accordance with the Declaration of Helsinki and the Danish law on ethics in research.

2.2. Musculoskeletal models

The anatomical landmark scaled musculoskeletal model (Lund et al. 2015) was applied using the AnyBody Modelling System (AMS; AnyBody Technology, Aalborg, Denmark). Then, AMS was used to perform an inverse dynamic analysis of each gait trial without an applied moment (Normal) and with an externally applied moment to compensate 100% for the moment generated by the muscles creating flexion/extension rotation around the hip joint ($Comp100\%MH_{FE}$). This moment allows the muscles responsible for creating the flexion/extension rotation around the hip joint to be unloaded in that direction during the gait trial. The force data of all hip muscles, the total compressive knee joint force (tKCF), the moments (MH_{FE}, MK_{FE}, MA_{PD}), and joint angles in the sagittal plane for the hip, knee, and ankle joints were computed during the stance phase for both load cases. These initial results were used to select potential muscles for further study, i.e. those whose force at KCF_{p1} reduces the most between the two load-cases. Thus, the same type of inverse dynamics analysis was performed with a 30% and 40% increase in the maximum isometric strength of the previously selected muscles to see the effect on KCF_{p1}.

2.3. Data processing and statistical analysis

The data were normalized to the percentage of body weight (%BW) and, only for the joint moments, to the percentage of body height (%BW·BH). After identifying KCF_{p1}, each variable's values corresponding to this peak were retrieved. MH_{FE} and MK_{FE} during the KCF_{p1}, considered relevant in studies that characterize healthy walking using cluster analyses (e.g. Simonsen and Alkjær 2012), were used as input to a K-means clustering algorithm (Hruschka and Covões 2005). The KCF_{p1} value and all muscle forces contributing to the peak were compared using a two-way analysis of variance with clusters and load-cases as factors. For the Normal condition, cluster differences in joint moments and angles were assessed over the stance phase using the statistical parametric mapping version of the two-sample *t*-test (SPM).

3. Results and discussion

3.1. Comparison of clusters in Normal condition

As in previous studies (Simonsen and Alkjær 2012), the cluster analysis revealed two clusters:

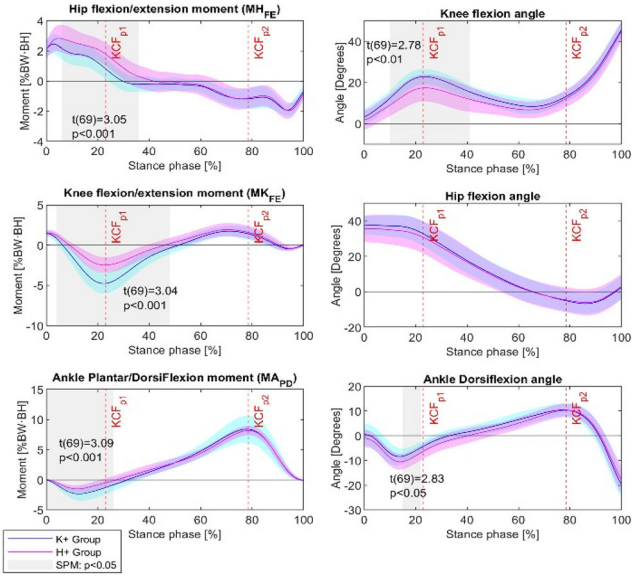


Figure 1. Comparison of K+/H + groups for kinematic and Kinetic variables during stance phase in *Normal* condition.

Table 1. Evolution of KCF_{p1} (in %BW) compared to *Normal* condition according to the load-cases.

Load-case	K+ Group	H+ Group	
Normal	**367.59±87.31**	**270.46±61.76**	*
Comp100%MH_{FE}	**347.61±96.51** -19.97±3.35 (-6.03±6.68%)	**211.13±53.31**# -59.34±27.12% (-21.82±8.71%)	*
+30%F0GlutMax	**362.09±87.66** -5.50±2.46% (-1.59±0.96%)	**261.99±60.69** -8.47±2.84 (-3.21±1.09%)	*
+30%F0GlutMed	**361.52±87.84** -6.07±3.65 (-1.76±1.04%)	**262.12±59.07** -8.35±3.38 (-3.00±0.89%)	*
+40%F0GlutMax and +30%F0GlutMed	**356.97±88.68** -10.62±6.78 (-3.09±1.95%)	**253.95±58.38** -16.51±5.44 (-6.12±1.69%)	*

Difference between groups: p<0.05*
Difference from the Normal condition: p<0.05#

K + consisted of 9 participants with a significantly higher MK_{FE} in early stance (mean difference: 1.38%BW·BH, $p < 0.001$), and H + of 15 participants with a significantly higher MH_{FE} (mean difference: 0.79%BW·BH, $p < 0.001$; Figure 1). In addition, MA_{PD}, knee flexion angle, and ankle dorsiflexion angle were significantly higher for K + group during KCF_{p1} ($p < 0.01$; Figure 1), highlighting different walking strategies between the two groups.

3.2. Analysis of load cases

The values of KCF_{p1} according to the load-cases (e.g. Comp100%MH_{FE}) and the group (i.e. K+, H+) are presented in Table 1.

In all load-cases, the K + group had a significantly higher KCF_{p1} than the H + group. This is in agreement with the literature, which has shown that the amplitude of the KCFs depends mainly on the forces developed by the quadriceps for KCF_{p1} (Uhlrich et al. 2022). Indeed, the K + group predominantly used the quadriceps to contribute to the support moment walking with the knees more bent, creating a higher KCF_{p1}. MH_{FE} compensation resulted in a reduction in KCF_{p1} for both groups, as in the study by Stoltze et al. (2018), but this was significant for the H + group (-59.34 ± 27.12, −21.82 ± 8.71%; $p < 0.01$) and not for the K + group (−19.97 ± 22.46%BW, −6.03 ± 6.68%; $p = 0.99$). This reduction of KCF_{p1} can be explained by the total unloading of the hamstrings. Thus, strengthening of the gluteus medius (GlutMed) and gluteus maximus (GlutMax) was performed to redistribute the relative loads of the mono and biarticular muscles crossing the hip. This increase in strength reduced KCF_{p1} compared to the Normal condition for both groups. Again, this reduction was greater for the H + group for all three strengthening conditions tested. The participants with a larger MK_{FE} (K + group) walk with less hamstring activation and, therefore, have less potential to reduce KCF_{p1} by strengthening the glutes.

4. Conclusions

The present study provides new information about strengthening the gluteus effect on reducing the KCF_{p1}. Simulations revealed that the reduction is larger in individuals with a high MH_{FE} and a relatively low MK_{FE}. Thus, a new training approach could be to strengthen these muscles and minimize hamstring activation. Specifically for the K + group, modifying their walking strategy to approach that of the H + group could be a first step in reducing KCF_{p1}. However, as this study is a simulation, we cannot determine whether the increased strength of the proposed muscles will lead to reduced symptoms of KOA. Secondly, it is challenging to assert that muscle adaptation induced by strength training on the gluteus will change the relative activation of these muscles and the hamstrings during walking. Thus, future studies could investigate the effect of specific training of the hip muscles on tKCF, kinematic gait data and patient-reported outcomes.

References

Brophy RH, Fillingham YA. 2022. AAOS clinical practice guideline summary: management of osteoarthritis of the knee (nonarthroplasty), third edition. J Am Acad Orthop Surg. 30(9):e721–e729. doi:10.5435/JAAOS-D-21-01233.

Hruschka ER, Covoes TF. 2005. Feature selection for cluster analysis: an approach based on the simplified silhouette criterion. International Conference on Computational

Intelligence for Modelling, Web Technologies and Internet Commerce (CIMCA-IAWTIC'06). Vol. 1; p. 32–38.

Lund ME, Andersen MS, Zee MD, Rasmussen J. 2015. Scaling of musculoskeletal models from static and dynamic trials. Int Biomech. 2(1):1–11. doi:10.1080/23335432.2014.993706.

Simonsen EB, Alkjær T. 2012. The variability problem of normal human walking. Med Eng Phys. 34(2):219–224. doi:10.1016/j.medengphy.2011.07.013.

Stoltze JS, Rasmussen J, Andersen MS. 2018. On the biomechanical relationship between applied hip, knee and ankle joint moments and the internal knee compressive forces. Int Biomech. 5(1):63–74. doi:10.1080/23335432.2018.1499442.

Uhlrich SD, Jackson RW, Seth A, Kolesar JA, Delp SL. 2022. Muscle coordination retraining inspired by musculoskeletal simulations reduces knee contact force. Sci Rep. 12(1):9842. doi:10.1038/s41598-022-13386-9.

KEYWORDS Knee osteoarthritis; musculoskeletal modeling; gait; muscle strengthening; cluster analysis

elisa.jolas@ens-rennes.fr

Transmission of vibration from the instrument to the fingers during guitar playing

R. Caron[a], N. Forier David[b], A. Paté[a] and D. Chadefaux[b]

[a]UMR 8520 – IEMN, Univ. Lille, CNRS, Centrale Lille, Univ. Polytechnique Hauts-de-France, Junia, Lille, France; [b]Université Sorbonne Paris Nord, Arts et Metiers Institute of Technology, IBHGC-Institut de Biomécanique Humaine Georges Charpak, HESAM Université, F-75013 Paris, France

1. Introduction

For decades, the physics of musical instruments has mostly focused on sound, highlighting how the mechanical vibrations in the instrument produce the sound and how this sound is perceived by the player and the audience. Music playing however involves sensory modalities beyond audition only, electric guitar players for example are able to report on the tactile perception of their instrument during playing with a great precision (Cambourian et al. 2022). Vibrotactile cues are known to be used by players to evaluate the quality of their instrument (Fontana et al. 2017), or to have an effect on the perception of audio-related attributes (Wollman et al. 2014). The vibrotactile interaction between the player and the instrument has however scantly been studied. Many questions remain, from the purely physical understanding of how the vibration is transmitted from the instrument to the body of the player, to how the player perceives the transmitted vibration, and to higher-level biomechanical concerns. The musicians' adaptations to instruments with different vibratory characteristics, e.g. in terms of posture or muscular activity, and their relationships with 'playing-related musculoskeletal disorders' (PRMD) are still to be addressed. This paper is part of a broader project aiming at answering these questions in the case of the electric guitar, an instrument on which the auditory feedback (from a distant amplifier) is to some extent uncoupled from the vibratory feedback (on the instrument). This paper proposes a first investigation of the transmission of vibration from an instrument to its player's body.

2. Methods

2.1. Experimental procedure

One guitar player was asked to perform a 250-BPM scale on an electric guitar (Squier Telecaster Classic Vibe '50s). This tempo (one note per beat) corresponds to a medium tempo which is easily played by the guitar player (male, 24 years old, 10 years of practice, mostly in heavy metal style) without prior training. The scale is an E-mixolydian, with three notes per string, combining open strings and fretted notes with the forefinger, the middle finger, the ring finger, and the little finger (see Figure 2). Such a scale was chosen for its being a classical and ergonomic fingering. In the following, the fretting finger refers to the finger, on the left hand, that presses the string against the fret of the note to be played. In practice, other fingers may be pressed against the strings, with no effect on the note. Finally, the scale has been repeated three times. Simultaneously, the vibration response of the guitar was measured using a three-axis accelerometer (PCB Piezotronics M352A32, ± 50 g pk; [1–4000] Hz; sampling rate 52.1 kHz) fixed to the instrument's neck. Two one-axis accelerometers (PCB Piezotronics M352A24, ± 50 g pk; [1–8000] Hz; sampling rate 52.1 kHz) were fixed as close as possible to the base of the second and third metacarpal bones to quantify the vibration transmission to the player's left hand.

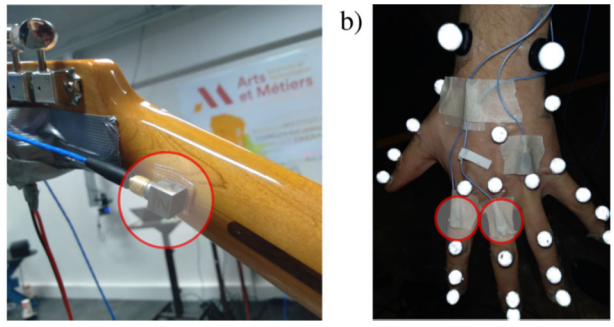


Figure 1. (a) Back of the neck of the guitar, with the 3-axis accelerometer placed near the normal position of the left-hand thumb during playing. (b) Left-hand of the player, equipped with accelerometers on the base of the second and third metacarpal bones. Note that reflective markers were not used in this study.

2.2. Data analysis

The collected signals were segmented into single notes according to a simple onset detection algorithm (search for maxima in the RMS-envelope of the neck acceleration signal). In order to characterize the transmission of vibration between the instrument and the fingers, the analysis was carried out on the signals from the three accelerometers mentioned above (only the out-of-plane axis of the neck accelerometer is used). For each note of the scale, 4096-point windows (1-point hop size) were extracted for the first 100 ms of the signals. The spectrum and the RMS value were

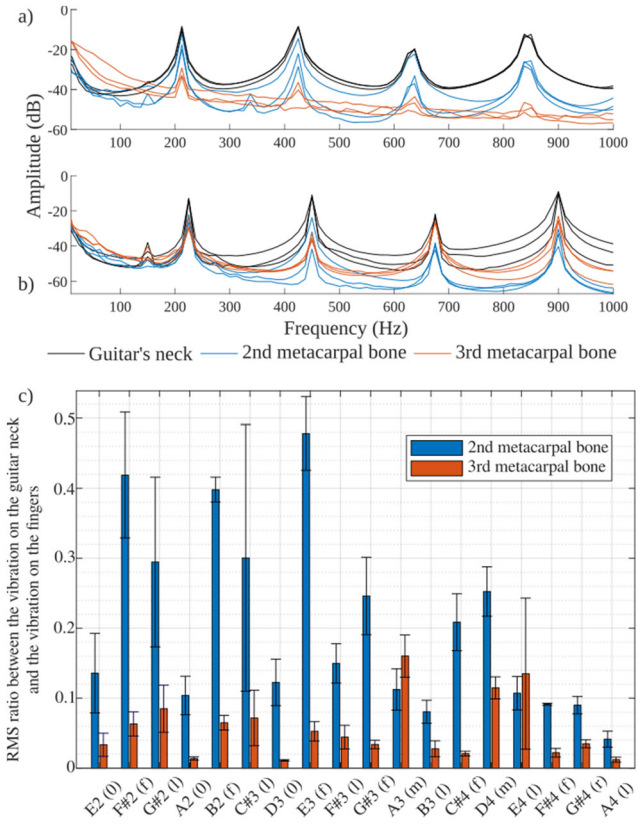


Figure 2. (a) Acceleration spectra for note G#3 (fretting finger = forefinger). (b) Acceleration spectra for note A3 (fretting finger = middle finger). (c) RMS ratio between the acceleration signal on the neck and on the forefinger, resp. middle finger (blue bar, resp. orange bar), computed for three trials. X-axis indicates: note (fretting finger, where forefinger, middle, ring and little fingers are respectively abbreviated f, m, r, and l).

computed from each window, and then averaged in order to obtain one spectrum and one RMS value for each of the 18 notes and each of the 3 accelerometers.

3. Results and discussion

Acceleration spectra measured for the notes G#3 (fundamental frequency 207.7 Hz) and A3 (220 Hz) are presented in Figure 2a,b. Although the vibration level was higher at the guitar's neck, all three signals were of similar order of magnitude. The note's fundamental frequency and harmonics were observable in all signals up to 1000 Hz (usually taken to be the upper limit of vibration perception (Verrillo 1992). These outcomes are in accordance with data reported by Xu et al. (2011).

The vibration transmission was more important to the 2nd than the 3rd metacarpal bone when playing G#3 since the forefinger was used to fret and was the only finger in contact with the instrument. As the middle finger was used to fret A3, the vibration level was slightly higher at the 3rd than the 2nd metacarpal bone. Interestingly, the vibration level at the 2nd metacarpal bone is still relatively high even for A3. This can be explained by the fact that the fingering scheme on each string always consists in a 2-finger or 3-finger sequence starting with the forefinger: it is possible that the forefinger is still in contact with the string and neck even when another finger frets the string.

To generalize these observations, Figure 2c presents, for each note, the ratio of the RMS values of the neck accelerometer signal and each of the finger accelerometer signals. Results confirmed that in general, more energy is transmitted to the fingers that are in contact with the neck, whether they are the fretting finger (e.g. notes G#3 fretted with the forefinger, or A3 fretted with the middle finger), or if they stayed in contact with the neck after having fretted a previous note (e.g. note A3 where the forefinger, still in contact with the neck, gets a high amount of vibration energy from the instrument). A higher amount of energy to a non-fretting finger can sometimes be observed (e.g. note D4, fretted with the middle finger, but with a higher energy transmitted to the forefinger). Besides, the general trend seems to be that energy is better transmitted from the instrument to the fingers at low frequencies.

4. Conclusions

This paper aimed at describing the vibration transmission from the electric guitar to the player's metacarpal bones when playing a simple scale. Results revealed that the vibration transmitted to the fingers is similar to the neck's vibration, the vibration content being transmitted up to the upper limit for vibrotactile perception. Further work will address the player's perception of such transmitted vibration (including the thumb as well in the future), as well as the postural and muscular adjustments to various vibration characteristics.

References

Cambourian P, Paté A, Cance C, Navarret B, Vasseur J. 2022. Vocabulary to speak about touch: analysis of the discourse of electric guitar players. Acta Acust. 6(2):2. doi:10.1051/aacus/2021052.

Fontana F, Papetti S, Järveläinen H, Avanzini F. 2017. Detection of keyboard vibrations and effects on perceived piano quality. J Acoust Soc Am. 142(5):2953–2967. doi:10.1121/1.5009659.

Verrillo RT. 1992. Vibration sensation in humans. Music Perception. 9(3):281–302. doi:10.2307/40285553.

Wollman I, Fritz C, Poitevineau J. 2014. Influence of vibrotactile feedback on some perceptual features of violins. J Acoust Soc Am. 136(2):910–921. doi:10.1121/1.4889865.

Xu XS, Welcome DE, McDowell TW, Wu JZ, Wimer B, Warren C, Dong RG. 2011. The vibration transmissibility and driving-point biodynamic response of the exposed to vibration normal to the palm. Int J Ind Ergon. 41(5): 418–427. doi:10.1016/j.ergon.2011.05.007.

KEYWORDS Vibration; transmission; electric guitar

delphine.chadefaux@sorbonne-paris-nord.fr

Upper-limb joint angles estimation from two RGB cameras and a markerless skeleton tracker algorithm

M. Adjel[a,b], R. Dumas[c], S. Mohammed[a] and V. Bonnet[d]

[a]Laboratoire Images Signaux et Systèmes Intelligents, Créteil, France; [b]NaturalPad, Montpellier, France; [c]Laboratoire de Biomécanique et de Mécanique des Chocs, Bron, France; [d]Laboratoire d'Analyse et d'Architecture des Systèmes-CNRS, Toulouse, France

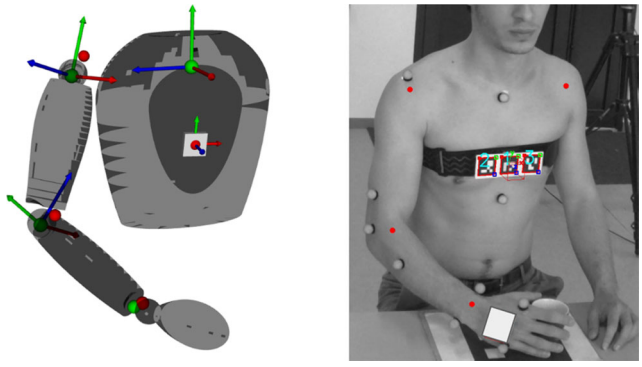


Figure 1. Participant performing the pick and place task (right) and the reconstructed kinematics with our method (left)

1. Introduction

Monitoring upper limb motricity evolution during rehabilitation of post-stroke patients can be done through several clinical indexes. Lavernia et al. (2008) showed that the quantitative visual evaluation of a multi-segment motion can lead to inter/intra-clinician variability up to 9 deg in the estimation of joint angles. The proper monitoring of motricity evolution requires an accurate and repeatable assessment of joint angles, which could be done using a gold standard Stereophotogrammetric Systems (SS); however, their cost and complexity do not allow their use for observation in real life situations. Several studies proposed to use a mechanical model and Joint Center Positions (JCP) obtained from skeleton tracking algorithm with RGB (Lahkar et al. 2022) and with RGB-D (Colombel et al. 2020) cameras to estimate the joint angles with an Inverse Kinematics (IK) algorithm. However, the Root Mean Square Error (RMSE) obtained by Colombel et al. (2020) was superior to 20 deg for several joints, while Lakhar et al. (2022) obtained an RMSE going from 6.3 deg for the shoulder to 20 deg for the wrist. Moreover, the latter was obtained using a costly commercial system with 10 high speed cameras. In this context, we propose to develop and evaluate a low-cost system based on a reduced set of two RGB cameras and a skeleton tracking algorithm and a sliding windows IK algorithm, used to impose temporal continuity and thus reduce outliers influence, to estimate shoulder and elbow flexion/extension joint angles.

2. Methods

The proposed method consists of using 3D JCP of shoulder, elbow and wrist obtained from MediaPipe skeleton tracking algorithm introduced by Lugaresi et al. (2019) to estimate the joint angles of the 4 first degrees-of-freedom of the arm during a pick and place task.

2.1. Mechanical model

The mechanical model was described by $N_L = 3$ rigid links articulated with $N_j = 4$ joints. The successive local poses (positions and orientations) of segments Coordinates Systems (CS) were determined through an anatomical calibration based on a wand relying on a fiducial marker, as introduced by Bisi et al. (2015). the trunk position and orientation with respect to the camera coordinates system R_c were also estimated using a fiducial marker through the Aruco library introduced by Romero-Ramirez et al. (2018). The upper-arm was linked to trunk through three successive hinge joints representing the shoulder flexion/extension, internal/external rotation and abduction/adduction respectively. The lower-arm was linked to the upper-arm through a hinge joint representing the elbow flexion/extension. The wrist joint was not considered in this study. The vector $\boldsymbol{\theta}$ containing the joint angles was used in the forward kinematics model to calculate the 3D JCP $\boldsymbol{p}_s$, $\boldsymbol{p}_e$ and $\boldsymbol{p}_w$ of shoulder, elbow and wrist, respectively, with respect to the camera coordinate system R_c as following $[\boldsymbol{p}_s,\ \boldsymbol{p}_e,\ \boldsymbol{p}_w] = FKM.(\boldsymbol{\theta})$

2.2. Sliding window inverse kinematics

The 2D JCP provided by the skeletal tracker were triangulated using a direct linear transform to obtain the 3D JCP. The noise and discontinuities of these measurements were compensated by a sliding window IK algorithm to ensure the dynamical consistency of the estimated joint angles. The state vector $\boldsymbol{X} = [\boldsymbol{\theta}_1,\ \ldots,\ \boldsymbol{\theta}_{N_s},\ \dot{\theta}_1,\ \ldots, \dot{\theta}_{N_S}]$ was defined as containing the successive vectors of joint angles $\boldsymbol{\theta}_i$ and joint velocities $\dot{\boldsymbol{\theta}}_i$, $(i = 1,\ \ldots, N_s)$ for a window of 1s

Table 1. Joint angles comparison between the ones calculated from markerless measurements with the ones obtained from SS measurements.

	RMSE [deg]	RMSE offset removed [deg]	Correlation coefficient
Shoulder flex./ext.	20.2	5.7	0.56
Shoulder int./ext. rot.	7.5	7.1	0.54
Shoulder abd./add.	10.9	3.8	0.78
Elbow flex./ext.	6.7	5.9	0.62
Average	11.3	5.7	0.63

divided in $N_s = 30$ samples. The vector of estimated successive joint angles $\hat{\boldsymbol{X}}$ over a window were determined to minimize the measurement tracking error as follows:.

$$find\ \hat{\boldsymbol{X}}\ \min_{\hat{\boldsymbol{X}}} \sum_{i=1}^{i=N_s} \|FKM(\hat{\boldsymbol{\theta}}_i) - \boldsymbol{y}_i\|^2 \tag{2a}$$

$$\text{subject to}\quad \theta_j^- \leq \theta_j \leq \theta_j^+,\ \forall j = 1...N_j, \tag{2b}$$

$$\boldsymbol{\theta}_{i+1} = \boldsymbol{\theta}_i + T_s\dot{\boldsymbol{\theta}}_i, \forall i = 1...N_s, \tag{2c}$$

where $T_s = \frac{1}{N_s}$ is the sampling time, $\boldsymbol{y}_i$ represents the $i-th$ measurement vector of the window, containing the shoulder, elbow and wrist 3D JCP. θ_j^- and θ_j^+ represent the upper and lower joint limits of the $j-th$ joint.

3. Experimental validation

Three healthy male and two healthy female participants (72 ± 13 kg, 25 ± 1 years, 1.78 ± 0.02 m) were asked to perform three repetitions of a pick and place task that is the core of several rehabilitation exercises for upper arm. The proposed method was experimentally validated using a reference SS. Reflective markers of the SS were placed on 8 anatomical landmarks as proposed by Wu et al. (2005). Corresponding reference joint angles were calculated using an extended Kalman filter (Fohanno 2014). The two cameras were placed front to the participant.

4. Results and conclusions

The average RMSE for all the joint angles was of 11.3 deg including the calibration offset and of 5.7 deg when the calibration offset was removed, with a mean correlation coefficient of 0.63 (Table 1). These results are comparable to those obtained by Lakhar et al. (2022) that used an expensive multi-camera markerless system.

The segment lengths were accurately estimated thanks to anatomical calibration. The use of a wand resulted in a mean error of $6 * 10^{-3}m$ on pointed anatomical landmarks, with respect to SS. The relatively poor correlation coefficient can be explained by the noisy data provided by the skeleton tracking algorithm. Further studies should focus on the increasing the accuracy of shoulder joint angles estimates and introducing the use of functional calibration method to estimate the segment lengths and relative segment CS poses, to avoid the requirement of an external operator.

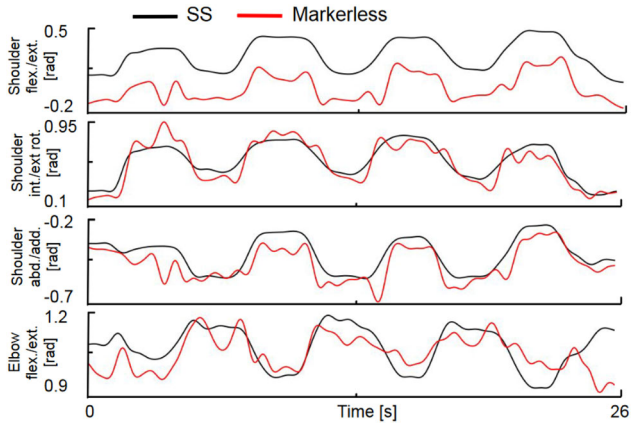


Figure 2. Comparison of joint angles estimated from the markerless and SS measurements.

References

Bisi M, Stagni R, Caroselli A, Cappello A. 2015. Anatomical calibration for wearable motion capture systems: video calibrated anatomical system technique. Med Eng Phys. 37(8):813–819.

Colombel J, Bonnet V, Daney D, Dumas R, Seilles A, Charpillet F. 2020. Physically consistent whole-body kinematics assessment based on an rgb-d sensor: application to simple rehabilitation exercises. Sensors. 20(10): 2848. doi:10.3390/s20102848.

Fohanno V, Begon M, Lacouture P, Colloud F. 2014. Estimating joint kinematics of a whole body chain model with closed-loop constraints. Multibody Syst Dyn. 31(4): 433–449. doi:10.1007/s11044-013-9366-7.

Heller A. 1987. Arm function after stroke – measurement and recovery over the 1st 3 months. J Neurol Neurosurgery Psychiatry. 50(6):714–779.

Lahkar B, Muller A, Dumas R, Reveret L, Robert T. 2022. Accuracy of a markerless motion capture system in estimating upper extremity kinematics during boxing. Front Sports Act Living. 4:939980. doi:10.3389/fspor.2022.939980.

Lavernia C, D'Apuzzo M, Rossi MD, Lee D. 2008. Accuracy of knee range of motion assessment after total knee arthroplasty. J Arthroplasty. 23(6 Suppl 1):85–91. doi:10.1016/j.arth.2008.05.019.

Lugaresi C, Tang J, Nash H, McClanahan C, Uboweja E, Hays M, Zhang F, Chang C-L, Yong MG, Lee J, et al.

2019. MediaPipe: a framework for building perception pipelines. https://arxiv.org/abs/1906.08172

Romero-Ramirez FJ, Muñoz-Salinas R, Medina-Carnicer R. 2018. Speeded up detection of squared fiducial markers. Image Vis Comput. 76:38–47. doi:10.1016/j.imavis.2018.05.004.

Wu G, van der Helm FCT, Veeger HEJD, Makhsous M, Van Roy P, Anglin C, Nagels J, Karduna AR, McQuade K, Wang X, et al. 2005. Isb recommendation on definitions of joint coordinate systems of various joints for the reporting of human joint motion – part II: shoulder, elbow, wrist and hand. J Biomech. 38(5):981–992. doi:10.1016/j.jbiomech.2004.05.042.

KEYWORDS Markerless; estimation; joint kinematics

adjelmohamed@gmail.com

Vertical ground reaction force analysis for elderly fall detection

T. Rezgui[a,b], S. R. Kamate[b], S. Arbi[b], S. Helaili[a] and F. Najar[a]

[a]Ecole Polytechnique de Tunisie, Applied Mechanics, and Systems Research Laboratory (LASMAP), University of Carthage, Tunis, Tunisia; [b]National Engineering School of Bizerte, University of Carthage, Tunisia

1. Introduction

Maintaining a balanced posture is crucial for daily activities and is achieved by integrating visual, vestibular, and somatosensory systems. The natural decline of human body abilities and functions with aging is highly associated with an increased risk of falls. Consequently, insufficient balance control is considered as a major cause of increased injuries and mortality rates for the elderly because of the loose of independency and the decreased quality of life (WHO 2021). As a significant public health and societal concerns for the aged population, it is crucial to accurately evaluate balance ability and assess the risk of falls for healthy individuals and rehabilitation purposes. In clinical practice, a large variety of tests can be conducted to describe postural balance, based on questionnaires (fear of falling FES, History of fall in the 12 months prior, IPAQ) or functional tests (BESTest, Mini-BESTest, …), and Stabilography evaluation (Nnodim and Yung 2015). Performing quantitative balance assessments can be a time-consuming process involving costly equipment like force plate platforms or motion capture systems. Additionally, these assessments can be challenging due to patient physical limitations and fear of injury. The most common quantitative measurement to characterize body balance is the displacement of the center of pressure (COP) extracted from a force pressure plate for a short recording time (Quijoux et al. 2021). However, there is no consensus on the required experimental protocols (tasks, duration, instruments), and the techniques to analyze COP displacement for balance assessment. In recent years, using artificial intelligence algorithms in combination with physiological signals became increasingly common tool for clinical diagnosis. Several studies have focused on predicting fall risk in older adults using machine learning (ML) based on features extracted from COP signals as an effective tool for classification (Giovanini et al. 2018; Liao et al. 2021; Savadkoohi et al. 2021). However, little attention has been devoted to the ground reaction force measurements for balance assessment (Cetin and Bilgin 2019). In fact, during upright stance, the center of mass (COM) oscillates to maintain balance. These small oscillations are controlled by muscle activations and its dynamic resultants are recorded as ground reaction forces (Sozzi et al. 2022). In this study, it is proposed to assess the contribution of Vertical Ground Reaction Forces (vGRF) in detecting risks of fall among elderly groups, using an ML-based approach.

2. Methods

2.1. Database and extracted features

vGRF measurements, used in this study, were derived from the public database for human balance assessment (Santos and Duarte 2016). The subjects performed a quiet standing test for 60 s on an AMTI force platform under four conditions: eyes-open and eyes-closed on a rigid surface (OR–CR); and eyes-open and eyes-closed on a soft surface (OS–CS). COP and GRF measurements were collected and stored in a text file format. Among the 163 subjects of the database, only 76 participants aged over 60 years were included in the study. Based on various clinical balance scores for each participant, participants were divided into a 'fall' and a 'non-fall' groups. To define the fall-risk group in this study, at least one of three main risk factors must be verified: (i) History of falls in the past 12 months (F12M); (ii) High fear of falling (score FES$>=$ 14); (iii) a lower score of Mini-BESTest functional test (score $<=$16). Consequently, fallers and non-fallers groups comprise 40 and 36 subjects, respectively. MATLAB scripts were developed for postprocessing data and extract features. First, the data were normalized with respect to the body weight after subtracting the corresponding mean value. Second, 10 vGRF features were extracted: Mean amplitude, Maximum amplitude, Standard Deviation, RMS, Power Spectrum Density (PSD), 50% of PSD, 95% of PSD, Mean frequency, Centroidal frequency and Frequency dispersion of PSD.

2.2. Machine learning classification model

ML classifications algorithms considered in this study are as follows: K-Nearest Neighbors (KNN), Random Forest (RF), Support Vector Machine (SVM), Logistic regression (LR), Linear Discriminant Analysis (LD) and Kernel Naïve Bayes (NB). The ML models are tested using five-fold cross-validation. All computations were performed using the classification learner tool in Matlab software. To evaluate the performance

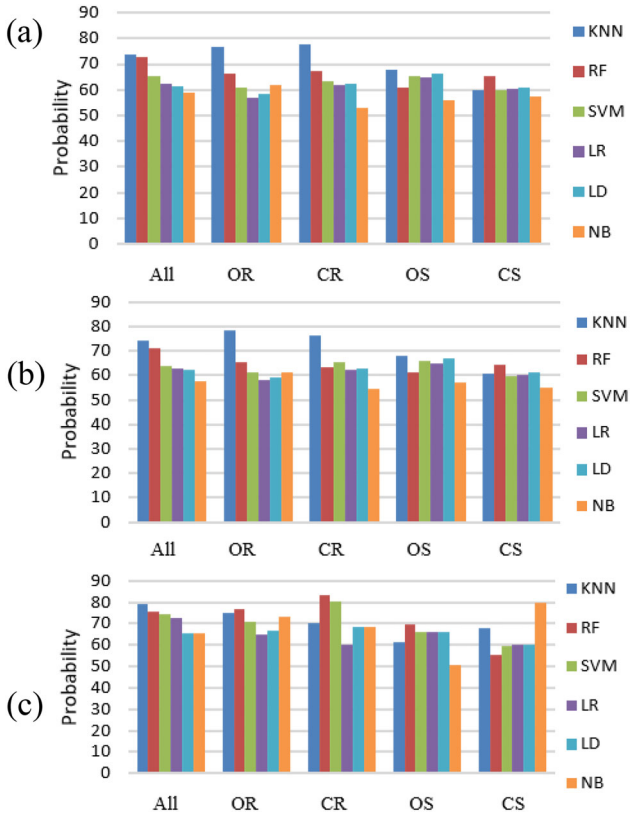


Figure 1. Performances of classifiers for fall group detection during different upright standing conditions: (a) accuracy (b) precision (c) recall.

of different classifiers, accuracy, precision, and recall were considered as evaluation criteria.

3. Results and discussion

The accuracy, recall and precision of KNN, RF, SVM, LR, LD and NB algorithms for faller and non-faller group classification are illustrated in Figure 1. Taking all upright standing condition (All) together, KNN and RF classifiers present the highest accuracy (73.9% and 72.9%), precision (74.3 and 71.3%), and recall (75.3% and 79%).

Under rigid surface balance tests, the KNN remains the best classifiers for fall risk detection among older populations for eyes-open and closed conditions in terms of accuracy and precision. However, it shows less accuracy and precision in detecting fallers under soft surface tests ($68 \pm 0.3\%$ and $60.1 \pm 0.5\%$ respectively). This result was predictable, since KNN was reported to be inconsistent with time domain signals having high variability. An interesting result of our study is the performance of RF and KNN to predict the risk of falls among elderly populations when applied to vGRF of eyes-open and eyes closed under rigid surface test balance conditions (mean accuracy: 71.5 ± 7.5 vs 72.6 ± 7.4; mean precision: 72.2 ± 9.1 vs 71.1 ± 7.8 and recall: 75.8 ± 1.2 vs 81.8 ± 1.8). No significant effect of vision was detected for those classifiers, except for recall performance.

Predictor importance analysis with KNN and RF classifiers was conducted for further investigation. Among all studied features, Power Spectrum Density and the Mean Frequency obtained the highest scores for classifying fallers and non-fallers groups. This result is in coherence with the findings of (Sozzi et al. 2022).

4. Conclusions

As a preliminary study on the performance of ML classification algorithms in the Elderly detection of risk of falls based on Vertical Ground Reaction forces, results have shown that KNN and RF outperform the other classifiers, particularly for upright tests under a rigid surface. It may suggest that for only standing over rigid surface is recommended clinical balance tests as it is safer for elderly. However, the maximum accuracy found for all tested algorithms is less than 80%, suggesting two hypotheses to further study in future works. First, the number of features extracted from vGRF may not be sufficient to predict falls. Second, the ML results highly depend on the definition of the 'fall group' based on clinical score threshold. In sum, this study can be useful to select the suitable classifier for detecting risk of fall among the older population based on vGRF. In addition, findings suggest that focusing on vGRF measurements, with appropriate features and ML algorithms, may substantially reduce the cost of clinical balance evaluations.

References

Cetin E, Bilgin S. 2019. Investigating effects of force and pressure centre signals on stabilogram analysis. IET Sci Meas Technol. 13(9):1305–1310. doi:10.1049/iet-smt.2019.0078.

Giovanini LH, Manffra EF, Nievola JC. 2018. Discriminating postural control behaviors from posturography with statistical tests and machine learning models: does time series length matter? International Conference on Conceptual Structures.

Liao F, Wu C, Wei Y, Chou L, Chang K. 2021. Analysis of center of pressure signals by using decision tree and empirical mode decomposition to predict falls among older adults. J Healthc Eng. 2021:6252445. doi:10.1155/2021/6252445.

Nnodim JO, Yung RL. 2015. Balance and its clinical assessment in older adults – a review. J Geriatric Med Gerontol. 1(1):003. doi:10.23937/2469-5858/1510003.

Quijoux F, Nicolaï A, Chairi I, Bargiotas I, Ricard D, Yelnik A, Oudre L, Bertin-Hugault F, Vidal P-P, Vayatis

N, et al. 2021. A review of center of pressure (COP) variables to quantify standing balance in elderly people: algorithms and open-access code. Physiol Rep. 9(22):e15067. doi:10.14814/phy2.15067.

Santos DA, Duarte M. 2016. A public data set of human balance evaluations. PeerJ. 4:e2648. doi:10.7717/peerj.2648.

Savadkoohi M, Oladunni T, Thompson LA. 2021. Deep neural networks for human's fall-risk prediction using force-plate time series signal. Expert Syst Appl. 182: 115220. doi:10.1016/j.eswa.2021.115220.

Sozzi S, Do MC, Schieppati M. 2022. Vertical ground reaction force oscillation during standing on hard and compliant surfaces: the 'postural rhythm'. Front Neurol. 13: 975752. doi:10.3389/fneur.2022.975752.

World Health Organization. 2021. WHO global report on falls prevention in older age. Geneva: WHO.

KEYWORDS Older adults; vertical ground reaction forces; balance assessment; classification

taysir.rezgui@ept.ucar.tn

Biomechanics of human-system interaction, ergonomics and robotics

Automatic Generation of Patient-Specific Finite Element Meshes of Oral Cavity and the Face for Orofacial Digital Twins, page S196.
Biomechanical effects of using a passive upper-limb exoskeleton to assist firefighters during vehicle extrication maneuver, page S199.
Biomechanical model of the human face for surgical assistance, page S202.
Comparison of EMG-to-torque models using an upper-limb exoskeleton, page S205.
Does wearing a virtual reality head-mounted display affect balance in healthy young adults?, page S208.
Dynamics aware Cartesian wrench polytope estimation based on human musculoskeletal models, page S210.
Effect of exoskeleton characteristics on EMG activities during a repetitive manual lifting task, page S213.
Effect of mass addition on upper limb joint torques during meat cutting tasks: a parametric study, page S215.
Genetic algorithms for force polytopes prediction, page S218.
Impact of 3D unload orthosis on tibiofemoral contact forces in relation to adduction moment and contact locations, page S221.
Perineal tissue deformation under bicycle saddle pressure, page S223.
Simulation of maximum isometric and isokinetic elbow actuation torques based on zonotopes, page S226.
Subject specific biomechanical model identification as a clinical routine, page S229.

Automatic generation of patient-specific finite element meshes of the face and oral cavity for orofacial digital twins

M. Calka[a,b], M. C. Picard[a,b,c], P. Perrier[b], M. Rochette[c] and Y. Payan[a]

[a]CNRS, Grenoble INP, TIMC-IMAG, Univ. Grenoble Alpes, Grenoble, France; [b]CNRS, Grenoble INP, GIPSA-lab, Univ. Grenoble Alpes, Grenoble, France; [c]ANSYS, Villeurbanne, France

1. Introduction

Digital Twins, i.e. digital models that precisely simulate the behavior of physical systems, are increasingly used to better understand the properties of the systems and predict how they would behave under unknown conditions (Jones et al. 2020). This concept is particularly useful in the *a priori* evaluation and planning of clinical treatments, which impacts can be simulated in a patient-specific manner, by using Digital Twins that are specifically adapted to reproduce the physical characteristics of each patient (Lauzeral et al. 2019).

In this paper we present a method for the design of patient-specific biomechanical models of the orofacial region (oral cavity and face) starting from a thoroughly validated reference Finite Element (FE) model. This method is based on an iconic image registration process (Bijar et al. 2016). Some anatomical landmarks are introduced to improve the registration while the human face and the entire oral cavity are transformed with the method.

2. Methods

2.1. General process

The segmentation of the different mechanical structures of the orofacial region on 3D medical images is particularly difficult and long lasting, because many of them are made of soft tissues and are in contact with each other. This is why our approach in designing patient-specific biomechanical models of these structures consists in applying a non-rigid geometric transformation on a reference biomechanical model that has been designed from carefully segmented MR and CT 3D images recorded from a male subject. Our method uses patterns of grey levels as well as anatomical landmarks on bone structures in both images to determine the best geometrical transformation that registers the reference image into the patient-specific one. The registration process uses the Elastix library (Klein et al. 2010). It returns a 3D displacement field that can be in turn applied to the FE mesh of the reference subject (Calka et al. 2023), using the library called Transformix, part of the Elastix library, in order to obtain a patient-specific mesh.

2.2. Registration parameters

A non-rigid landmark assisted B-Spline transformation is used. The optimization process consists of 5 steps that rely on 5 different image resolutions, with a grid size varying from 256 mm to 16 mm (256 mm, 128 mm, 64 mm, 32 mm, 16 mm). A multi-metric approach is used made of a normalized cross correlation (NCC) commonly used for images of the same modality and a landmark mapping based on Euclidean distance (SCP) for rigid alignment such as:

$$S = \alpha NCC + \beta SCP$$

During the 5 steps the parameters α and β vary: in the 1st step only the SCP metric is used and only the NCC metric is used during the last two steps; for steps 2 and 3 a ratio 0.95/0.05 is chosen for α and β. A Gaussian pyramid ($\sigma =$ 16.0, 8.0, 4.0, 2.0, 1.0) is used during the different steps to subsample the image.

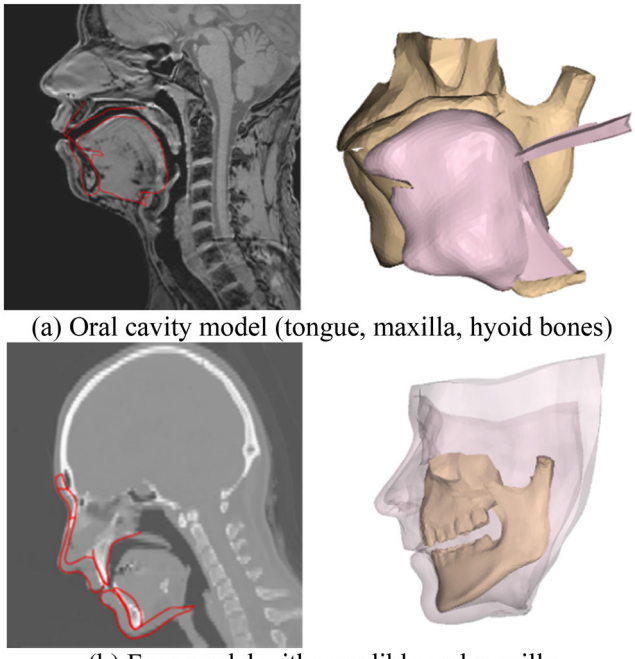
A random sampling extracted 5000 voxels samples, which corresponds to about 0.0005% of the image. It allows us to drastically reduce the computation time. The interpolation is performed using a B-Spline interpolator of order 3. Finally, the optimization of the transformation is done using a stochastic gradient descent method as advised in Klein et al. (2010).

3. Results and discussion

3.1. Registration result

Figure 1a represents the different meshes of a patient-specific oral cavity obtained through our iconic registration process. These meshes are superimposed on a mid-sagital MR image of the patient. The tongue and the mandible obtained are rather precise. The hyoid bone is not perfectly positioned. The maxilla is precise at the level of the teeth but less so on the palate area. We can note that all the contacts tongue/mandible and tongue/hyoid-bone seem to be preserved.

Figure 1b represents the same process applied to the face, the mandible and the maxilla of a second patient. The meshes are superimposed on CT scan images. These two examples show the ability of our registration method to be used for different type of mono-modal transformations (MRI/MRI and CT/CT).



(a) Oral cavity model (tongue, maxilla, hyoid bones)

(b) Face model with mandible and maxilla

Figure 1. Generated patient-specific FE model. Left: Patient-specfic mesh superimposed on MRI data; right: patient-specific FE model.

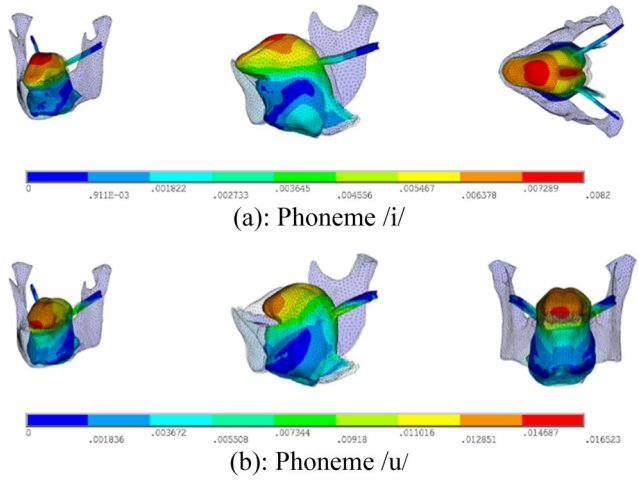
Table 1. Mean, standard deviations, min, max for different quality mesh criteria.

Criteria	Mean	Sd	Min	Max
Aspect ratio (AR)	2.157	0.554	1.197	7.435
Skewness (SN)	0.378	0.164	0.003	0.953
Orthogonal quality (OQ)	0.621	0.161	0.048	0.983
Maximum angle (MA)	102°	12°	72°	153°

Table 1 shows the quality of the generated FE meshes according to several quality criteria. According to ANSYS criteria, an element is considered to be of poor quality if: AR >20, SN >0.95, OQ <0.14, MA >165°. We can see that some elements exceed the quality thresholds, but these remain in small quantities and do not prevent simulations even if they might reduce their accuracy.

3.2. Patient-specific FE model simulation

Figure 2 shows simulations (ANSYS MAPDL) performed with the patient-specific tongue model generated with our method. These simulations represent two French phonemes (/i/, /u/) involving lingual, mandibular ($\simeq$ 2 mm) and bonded and sliding contacts. In the phoneme /i/, the tongue slides along the mandible toward the teeth. The hyoid bone advances as a result of the genioglossus advancing the tongue. In the phoneme /u/, the tongue has an important backward movement. The hyoid bone lowers due to the action of the sternohyoid muscle allowing the base of the tongue to compress more. All these movements show that the generated patient-specific models are usable in simulations that will be used in the future to generate interactive time simulations.



(a): Phoneme /i/

(b): Phoneme /u/

Figure 2. French phonemes /i/ and /u/ pronounced with the generated patient-specific FE tongue model. The color bar corresponds to the displacements of tongue tissues.

4. Conclusions

The patient-specific mesh generation method based on iconic image registration using the Elastix library shows real capacities to generate quality meshes usable in accurate and realistic FE simulations. These preliminary works need to be validated on several patients. The next step is to generate a reduced order model from the biomechanical model in order to speed up simulations Such a digital twin could then be used in a clinical application like a preoperative simulator for orofacial surgery planning.

References

Bijar A, Rohan P-Y, Perrier P, Payan Y. 2016. Atlas-based automatic generation of subject-specific finite element tongue meshes. Ann Biomed Eng. 44(1):16–34. doi:10.1007/s10439-015-1497-y.

Calka M, Rochette M, Perrier P, Payan Y. 2023. Modélisation biomécanique de la langue humaine. In: Laurent C, editor. Mécanique de Tissus Biologiques. Paris: ISTE Editions.

Jones D, Snider C, Nassehi A, Yon J, Hicks B. 2020. Characterising the digital twin: a systematic literature review. CIRP J Manuf Sci Technol. 29:36–52. doi:10.1016/j.cirpj.2020.02.002.

Klein S, Staring M, Murphy K, Viergever MA, Pluim J. 2010. Elastix: a toolbox for intensity-based medical image

registration. IEEE Trans Med Imaging. 29(1):196–205. doi:10.1109/TMI.2009.2035616.

Lauzeral N, Borzacchiello D, Kugler M, George D, Rémond Y, Hostettler A, Chinesta F. 2019. A model order reduction approach to create patient-specific mechanical models of human liver in computational medicine applications. Comput Methods Progr Biomed. 170:95–106. doi:10.1016/j.cmpb.2019.01.003.

KEYWORDS Face and oral cavity; patient-specific; finite element model; image registration; biomechanical models

maxime.calka@univ-grenoble-alpes.fr

Biomechanical effects of using a passive upper-limb exoskeleton to assist firefighters during vehicle extrication maneuver

P. Maurice[a], S. Lemonnier[b], N. Kohili[c], L. Cavagnac[b] and G. Mornieux[c]

[a]CNRS, Inria, Loria, Université de Lorraine, Nancy, France; [b]PerSEUs, Université de Lorraine, Metz, France; [c]Faculty of Sport Sciences, Université de Lorraine, DevAH, Nancy, France

1. Introduction

Firefighters' work involves numerous strenuous tasks, which often lead to the development of musculoskeletal disorders (MSDs) (Frost et al. 2015; Kodom-Wiredu 2019; Nazari et al. 2020). Among these tasks, vehicle extrication is particularly demanding because it requires the manipulation of heavy cutting tools (20–30 kg) in constrained and non-ergonomic postures. While adequate physical training is of utmost importance and can help reduce MSDs risk, it is not sufficient alone, especially with the current aging of the workforce.

In industry, occupational exoskeletons have been proposed as a potential solution to alleviate the physical load on workers, and thereby reduce MSDs risk (De Looze et al. 2016; Theurel & Desbrosses 2019). While exoskeletons are envisioned as a promising solution for firefighters as well (Taborri et al. 2021), their benefit is strongly task-dependent. So far, exoskeletons for firefighters have mainly been developed as whole-body powered devices for strength enhancement in load carrying tasks (Osipov 2019). However, the use of lighter and less cumbersome exoskeletons with MSDs reduction in mind has, to the best of our knowledge, not been studied. This work therefore investigates the biomechanical effects of using a passive upper-limb exoskeleton during a simulated vehicle extrication maneuver.

2. Methods

2.1. Participants and protocol

Twelve male firefighters (7 professionals and 5 volunteers; age: 31 ± 9 yrs; experience: 11 ± 9 yrs; height: 175 ± 5 cm; mass 73 ± 6 kg) performed a vehicle extrication maneuver (Figure 1), both with (WE) and without (NE) the exoskeleton. The maneuver consisted in a timed sequence of three subtasks performed at different heights on the vehicle (heights: rocker panel, middle of the door, top of the vehicle), with two different cutting tools (about 22 kg each), for a total duration of 3 min. The two conditions were performed in random order, with a 15 min break in between. The study was approved by INRIA's ethical committee COERLE (#2022-49) and was conducted in accordance to the Declaration of Helsinki.

2.2. Instrumentation

The participants were equipped with the Xsens MVN Link inertial motion capture system (capture rate 240 Hz) to record whole-body kinematics. Fourteen Delsys Trigno Snap-Lead EMG sensors were placed according to the Seniam recommendations bilaterally on the erector spinae (ES), latissimus dorsi (LD), anterior deltoid (AD), upper trapezius (TR), biceps brachii (BB), triceps brachii (TB) and brachioradialis (BR) to record back, shoulder and arm muscle activity (capture rate 1926 Hz). Finally, a Garmin Forerunner 345 sensor was placed on the participants' chest to monitor heart rate (capture rate 1 Hz).

At the end of each condition, participants answered a Borg CR10 questionnaire to evaluate the effort perceived in five body areas: shoulders, upper-arms, forearms, abdominal and lumbar (Borg 1998).

2.3. Exoskeleton

The exoskeleton used in this study is the MATE-XT (Comau, Torino, Italy). It is a lightweight (3 kg) passive upper-limb exoskeleton designed to provide shoulder support in tasks involving arm elevation (Pacifico et al. 2020). The MATE was selected as a test candidate following a preliminary study of the non-assisted extrication maneuver, in which the shoulder was identified as the primary joint to assist. Among commercially available exoskeletons for shoulder support, the MATE was deemed a good



Figure 1. Firefighters equipped with the MATE exoskeleton performing a vehicle extrication maneuver.

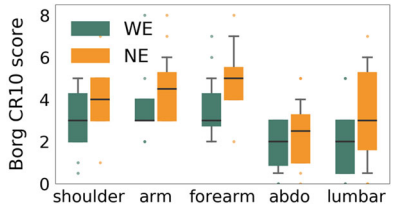


Figure 2. Distribution across participants of the Borg CR10 scores of the 5 body areas, with and without exoskeleton.

compromise between the level of assistance provided and the device compactness imposed by the task.

In the present study, the firefighters wore the exoskeleton over their work clothes, and the highest level of assistance was always used (6 kg per arm). The exoskeleton was fitted on each participant according to the designer's guidelines. Before starting the task, participants could move around and manipulate the cutting tools during a few minutes (about 2–3 min) to familiarize with the exoskeleton.

2.4. Data analysis

The following dependent variables were analyzed: average cardiac cost (current minus rest heart rate) over the last 3 sec of the task; root mean square value of the filtered EMG signal (Butterworth 4th order band-pass with 10–500 Hz cut-off frequency) over the whole task for each of the 14 recorded muscles; percentage of time spent in the different zones inspired from the RULA ergonomics assessment method (McAtamney and Corlett 2004) for the back (<20 deg; 20–60 deg; >60 deg), left arm and right arm (<45 deg; 45–90 deg; >90 deg) flexion/extension; perceived effort (Borg score) for each of the five body areas.

Due to the non-normality of the data, Wilcoxon signed-rank tests were conducted for all dependent variables to evaluate the effect of the exoskeleton. A significance level of 5% was used.

3. Results

3.1. Kinematics

When using the exoskeleton, participants spent more time with their left arm in the 45–90 deg elevation zone and less in the 0–45 deg zone, compared to without it (+7% in average). There was no significant difference for the right arm or back.

3.2. Muscle activity

The use of the exoskeleton caused a significant increase in the activity of the right BB (by 10% in average). All other muscles were unaffected. Even the activity of the left shoulder muscles remained similar, despite more time spent with the arm elevated when using the exoskeleton.

3.3. Heart rate

The cardiac cost was not significantly affected by the use of the exoskeleton.

3.4. Perceived effort

A significant reduction was observed for the shoulder (by 22% in average), upper-arm (by 22% in average), and forearm (by 26% in average) areas when using the exoskeleton (Figure 2). For the abdominal and lumbar areas, the exoskeleton also reduced the perceived effort, but not significantly.

4. Discussion and conclusion

This study suggests that there is no physiological benefit in using the MATE exoskeleton for the extrication maneuver, except possibly a mild assistive effect on the left shoulder (similar muscle activity despite higher arm elevation). This may be due to the low arm elevation angle adopted by most participants (<45 deg during most of the task), where the MATE provides only limited assistance, especially compared to the weight of the cutting tools. Interestingly though, participants reported a reduction of perceived effort with the exoskeleton, which suggests either a placebo effect of the device, or biomechanical changes that are too small to be detected with the proposed methodology, given the large task's degree of freedom.

Acknowledgement

This work has received funding from the Université de Lorraine Interdisciplinary Program (Pompexo).

References

Borg G. 1998. Borg's perceived exertion and pain scales. Champaign (IL): Human Kinetics.

de Looze MP, Bosch T, Krause F, Stadler KS, O'Sullivan LW. 2016. Exoskeletons for industrial application and their potential effects on physical work load. Ergonomics. 59(5):671–681. doi:10.1080/00140139.2015.1081988.

Frost DM, Beach TAC, Crosby I, McGill SM. 2015. Firefighter injuries are not just a fireground problem. WOR. 52(4):835–842. doi:10.3233/WOR-152111.

Kodom-Wiredu JK. 2019. The relationship between firefighters' work demand and work-related musculoskeletal disorders: the moderating role of task characteristics. Safety and Health at Work. 10(1):61–66. doi:10.1016/j.shaw.2018.05.004.

McAtamney L, Corlett N. 2004. Rapid upper limb assessment (RULA). In: Handbook of human factors and ergonomics methods. Boca Raton (FL): CRC Press.

Nazari G, MacDermid JC, Sinden K, D'Amico R. 2020. Prevalence of musculoskeletal symptoms among Canadian firefighters. WOR. 67(1):185–191. doi:10.3233/WOR-203264.

Osipov A. 2019. Fire exoskeleton to facilitate the work of the fireman. E3S Web Conf. 126:00015. doi:10.1051/e3sconf/201912600015.

Pacifico I, Scano A, Guanziroli E, Moise M, Morelli L, Chiavenna A, Romo D, Spada S, Colombina G, Molteni F, et al. 2020. An experimental evaluation of the proto-MATE. IEEE Robot Automat Mag. 27(1):54–65. doi:10.1109/MRA.2019.2954105.

Taborri J, Pasinetti S, Cardinali L, Perroni F, Rossi S. 2021. Preventing and monitoring work-related diseases in firefighters: a literature review on sensor-based systems and future perspectives in robotic devices. Int J Env Res Public Health. 18(18):9723.

Theurel J, Desbrosses K. 2019. Occupational exoskeletons: overview of their benefits and limitations in preventing work-related musculoskeletal disorders. IISE Trans Occup Ergo Human Factors. 7(3–4):264–280. doi:10.1080/24725838.2019.1638331.

KEYWORDS Exoskeleton; ergonomics; physiological measures

pauline.maurice@loria.fr

Biomechanical model of the human face with a perspective of surgical assistance

MC. Picard[a,b,e], M. Cotton[a], N. Briot[a], M. Nazari[a,c], D. Poisbleau[d], P. Perrier[b], G. Chagnon[a], M. Rochette[e] and Y. Payan[a]

[a]CNRS, Grenoble INP, TIMC, Univ. Grenoble Alpes, Grenoble, France; [b]CNRS, Grenoble INP, GIPSA-Lab, Univ. Grenoble Alpes, Grenoble, France; [c]School of Mechanical Engineering, University of Tehran, Tehran, Iran; [d]CHU Grenoble Alpes, La Tronche, France; [e]ANSYS France, Lyon, France

1. Introduction

Our group has been working on the biomechanical modeling of the human face soft tissue for more than 20 years, with two main applications: surgical assistance (Chabanas et al. 2003) and speech production (Nazari et al. 2011).

The first version of our face model was designed to predict the aesthetic and functional consequences of bone repositioning in the context of maxillofacial surgery (Chabanas et al. 2003). It included a hexahedral-dominant Finite Element (FE) mesh made of two layers representing the dermis and hypodermis tissues. Muscle activations used for speech production or for facial mimics were functionally modeled through a set of external forces applied to nodes along the muscle courses.

Twenty years later, we must unfortunately admit that such kind of modeling tools are still not used by surgeons in their clinical practice. Some commercial products such as Materialise® software propose modeling options for predicting passive and active face tissue deformations after bone repositioning. However, such options are currently not used by most surgeons who consider them as not sufficiently realistic.

This paper aims to address this limitation, coming back to the design of a patient-specific face model, with a special focus on the accuracy of the model, including:

- 1) the identification and differentiation of anatomical structures involved in face deformations, skin, muscles and hypodermis tissues, in which we include in a first approximation as a whole fat and connective tissue;
- 2) the meshing of the volume represented by each of these anatomical structures with a full tetrahedrons FE mesh which convergence has been studied;
- 3) the accurate design of the course of each face muscle, based on muscle contours observed on a CT and an MRI exams of the patient, to study as a perspective the functional aspect of the patient's soft tissues after surgery;
- 4) the definition of accurate boundary conditions with the face FE mesh fixed onto specific locations of the skull and with sliding contacts between lips and teeth.
- 5) experimental tensile tests carried out on tissues extracted from a human cadaver head, in order to propose constitutive laws as inputs to the FE model.

2. Methods

2.1. Finite element (FE) face model

The global geometry of the FE face model, extracted from 3D CT images of the patient's head, represents a 3D FE mesh composed of tetrahedral elements that are supposed to model the hypodermis and muscle tissues. On the top of this FE volume are defined shell elements that represent the skin (with a thin thickness of 1 mm). Bony surfaces (mandible and maxilla) are added and modeled by shell elements.

The volumetric and surface FE meshes were generated using Hypermesh® software, making sure that the elements were of good quality. Indeed, a poor quality mesh can lead to numerical errors during a FE analysis and thus to distorted visual results. In order to check the quality of the mesh, geometrical criteria such as the ones proposed by ANSYS® FE solver were used. A convergence analysis was performed to determine what element sizes to put in our FE model in order to find a good compromise between accuracy and computation time. A mesh that includes 132,736 elements and 27,696 nodes was therefore used for the simulations.

2.2. Muscles inserted into the FE mesh

Starting from this 3D tetrahedral mesh, the courses of most muscles involved in the human face were defined as follows. A set of points along muscle tracks were manually positioned in 3D using information from the literature (Hutto and Vattoth 2015) but also with the use of CT images of the patient, on which it was possible to distinguish the contours of some muscles. Eleven muscles were then implemented by selecting the sets of elements along the course of these points: zygomaticus major and minor, orbicularis oris peripheral and marginal, levator anguli oris, buccinator, levator labii superioris alaeque nasi, risorius,

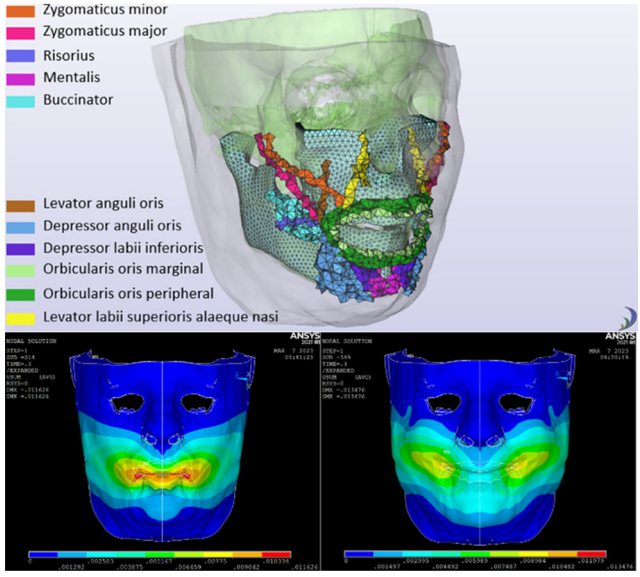


Figure 1. Top panel: Model of the human face (gray: soft tissues, light blue: mandible and maxilla, light green: skull, other colors: muscles). Lower panel: Face deformations during the contraction of the orbicularis oris peripheral OOP, responsible for smiling (left) and the zygomaticus ZYG major and minor, responsible for lip protrusion (right). Simulations are provided by the ANSYS software with the material parameters of Barbarino et al. (2009).

depressor anguli oris, depressor labii inferioris, and mentalis, represented in Figure 1 (top panel).

Muscle activations are modeled using the ANSYS UserMat element designed by Nazari et al. (2022). Such a model generates active stress along muscular fibers assuming a transverse isotropic behavior for the muscle.

2.3. Experimental tensile tests

To the best of our knowledge, no mechanical *ex vivo* experimental test has been provided in the literature as concerns the human facial tissues. We propose here preliminary tests on a single specimen. In accordance with French regulations on post-mortem testing, a face anatomical dissection was performed at the Anatomy Laboratory, Grenoble Faculty of Medicine, on a female cadaver head (95 years old, 160 cm tall and 55 kg). The dissection occurred 8 days after the death. Samples from skin, hypodermis tissue and muscles (zygomaticus and masseter) were extracted and dog-bone shape samples were used to carry out tensile tests in a 37 °C bath of saline solution (MTS criterion model 41 machine, Figure 2). Since this work is preliminary, a single sample was tested for each tissue, without any details as concerns variability.

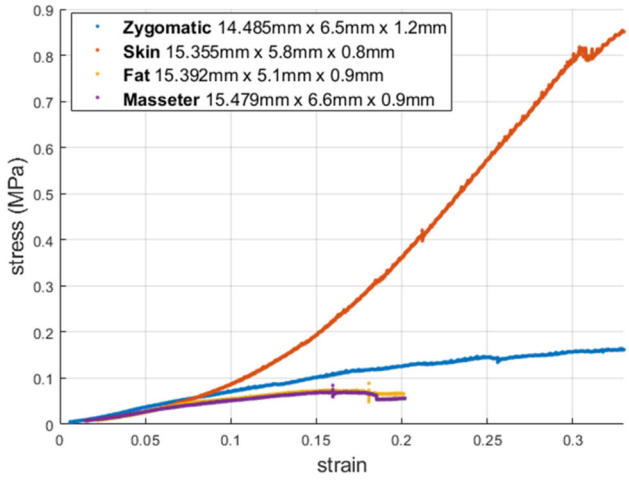


Figure 2. Experimental stress/strain measurements of skin, fat, zygomatic and masseter muscles. Strain rate was 10%/min.

3. Results and discussion

The lower panel of Figure 1 plots face deformations after the activation of two muscles, namely the orbicularis oris peripheral (left) and the zygomaticus (right). The corresponding face deformations are coherent with what is expected from these muscles, namely lip closing and protrusion from OOP, and a smile from ZYG (Nazari et al. 2011).

Figure 2 plots the nominal stress-strain curves recorded for four tissue samples corresponding to skin, fat, and the zygomatic and masseter muscles. As expected (Barbarino et al. 2009), skin appears stiffer in tension than fat and muscles.

Finally, it seems important to note that the various steps described in this paper to generate a generic subject-specific FE model of the face have to be done one time only. For any new patient to study and to model, an automatic image-based non-rigid registration technique will be used to morph the generic FE model to the anatomy of that new patient.

References

Barbarino GG, Jabareen M, Trzewik J, Nkengne A, Stamatas G, Mazza E. 2009. Development and validation of a three-dimensional finite element model of the face. Journal of Biomechanical Engineering. 131(4):041006. doi:10.1115/1.3049857.

Chabanas M, Luboz V, Payan Y. 2003. Patient specific finite element model of the face soft tissue for computer-assisted maxillofacial surgery. Med Image Anal. 7(2):131–151. doi:10.1016/S1361-8415(02)00108-1.

Hutto JR, Vattoth S. 2015. A practical review of the muscles of facial mimicry with special emphasis on the superficial musculoaponeurotic system. Am J Roentgenol. 204(1): W19–W26. doi:10.2214/AJR.14.12857.

Nazari M, Perrier P, Payan Y. 2022. Interwoven muscle fibers: a 3D two-fiber muscle active model. Comput Methods Biomech Biomed Eng. 25(sup1): S226–S22.

Nazari MA, Perrier P, Chabanas M, Payan Y. 2011. Shaping by stiffening: a modeling study for lips. Motor Control. 15(1):141–168. doi:10.1123/mcj.15.1.141.

KEYWORDS Finite element model (FEM); human face; biomechanical model

marie-charlotte.picard@univ-grenoble-alpes.fr

Comparison of EMG-to-torque models using an upper-limb exoskeleton

L. Quesada[a,b,c], D. Verdel[a,b,c], O. Bruneau[c], B. Berret[a,b], M.-A. Amorim[a,b] and N. Vignais[a,b]

[a]CIAMS, Université Paris-Saclay, Orsay, France; [b]CIAMS, Université d'Orléans, Orléans, France; [c]LURPA, ENS Paris-Saclay, Gif-sur-Yvette, France

1. Introduction

Work-related musculoskeletal disorders (MSDs) pose significant challenges to society. To reduce the incidence of MSDs, current solutions rely on developing ergonomic workplaces or adapting work tasks. A promising alternative aims to compensate for MSD-causing efforts by using active exoskeletons. However, an accurate estimation of the operator's intention is crucial for providing timely and appropriate assistance (Bi et al. 2019). One potential method is to utilize electromyographic (EMG) signals for estimating joint torques and determining suitable assistance (Treussart et al. 2020). The present study aims to compare the ability of different EMG-to-torque models to estimate elbow torque.

2. Methods

2.1. Participants

Ten healthy participants (3 F, 29.4 ± 6.6y, 72.6 ± 11.0 kg, 175.7 ± 4.4 cm) participated in this study and signed a written informed consent. The protocol was approved by an ethics committee (CER-PS-2021-048/A1).

2.2. Material

EMG signals were recorded from seven muscle heads at a frequency of 2 kHz (MiniWave, Cometa, Italy). Electrodes were placed following SENIAM recommendations on the lateral, medial, and long triceps, the long and short biceps, the brachialis, and the brachioradialis. The elbow axis of the ABLE upper limb exoskeleton (Garrec et al. 2008) was used in resistive mode, applying a viscous force field during flexion and extension movements to impose a torque perturbation on the elbow (based on a normalized subjective effort using a Borg scale). The participant was attached to the exoskeleton at wrist level through an adapted orthosis under which a 6-axis force/torque (FT) sensor allowed the measurement of the perturbation applied by the exoskeleton on the forearm. Kinematic data were recorded using an optoelectronic system (Qualisys, Sweden). Target trajectory and elbow angle visual feedback were projected onto a screen in front of the participant.

2.3. Procedure

EMG sensors were placed on the participant's muscles, and maximal voluntary contraction (MVC) was performed after verifying sensor location. Reflective markers were placed on anatomical landmarks for limb measurement and kinematics. After being attached in the exoskeleton with their arm immobilized, the participant was asked to track a 30s randomized trajectory projected on the screen, implying elbow flexion and extension. Each participant performed ten trials.

2.4. Data processing

EMG signals were processed using a 20–450 Hz band-pass filter, a rectification, and a 3 Hz low pass filter (Lotti et al. 2022). They were then normalized with MVC. Interaction torque ($\boldsymbol{\tau_i}$) was computed using inverse dynamics from the exoskeleton's FT sensor. Dynamic torques of the forearm ($\boldsymbol{\tau_{dyn}}$, gravitational and inertial) were estimated using inertial data from anthropometric tables. The net human torque $\boldsymbol{\tau_h}$ is then $\boldsymbol{\tau_h} = \boldsymbol{\tau_{dyn}} + \boldsymbol{\tau_i}$ and is the reference value.

2.5. Model validation

A cross-validation method was used to evaluate EMG-to-torque models: they were each first calibrated on one trial and then used to estimate torques (i.e. $\hat{\tau}_h$) on the other nine trials. A normalized root mean square error (NRMSE) was computed for each of the nine estimates, comparing τ_h and $\hat{\tau}_h$. This process was repeated for each of the ten trials in turn, with one serving as calibration and the others as validation. The mean NRMSE for each model was then computed.

2.6. Statistical analysis

Normality was first assessed (Shapiro-Wilk), and a repeated measures analysis of variance (RmANOVA) was performed to test model differences. A post hoc test was then performed using a Bonferroni correction.

3. EMG-to-torque models

In the following section, EMG-to-torques models are described using k muscles and j degrees of freedom.

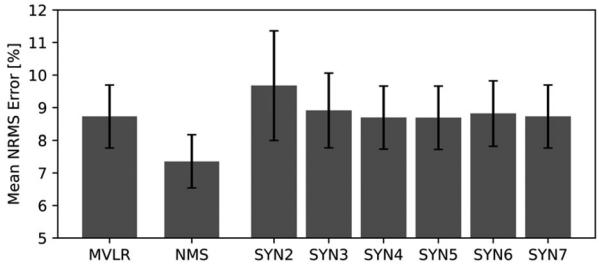


Figure 1. Mean normalized root mean square error of validation trials for each model. Error bars represent the 95% confidence interval.

Data matrices contain n samples. Models were chosen based on common occurrences in literature.

3.1. Multivariate linear regression

The multivariate linear regression (MVLR) model was used as a baseline for comparison (Camardella et al. 2021). It is a linear relationship between muscle excitations and torques:

$$\boldsymbol{\tau}(t) = \boldsymbol{C} \cdot \boldsymbol{m}(t)$$

where $\boldsymbol{C} \in \mathbb{R}^{j*k}$ is the muscle mapping matrix, $\boldsymbol{\tau} \in \mathbb{R}^{j}$ the torque vector and $\boldsymbol{m} \in \mathbb{R}_{+}^{k}$ the muscle excitation vector. The muscle mapping matrix is computed using multivariate regression on calibration data matrices $\boldsymbol{T_c} \in \mathbb{R}^{j*n}$ and $\boldsymbol{M_c} \in \mathbb{R}_{+}^{k*n}$ containing respectively torque and muscle excitation sample vectors.

3.2. Synergies

Synergy-based models (SYN) are described as a coherent activation in space and time of groups of muscles (Delis et al. 2014). Spatial synergies can be extracted from muscle excitations using non-negative matrix factorization:

$$\boldsymbol{M_c} = \boldsymbol{W} \cdot \boldsymbol{H_c} + \boldsymbol{\varepsilon}$$

with $\boldsymbol{H_c} \in \mathbb{R}_{+}^{s*n}$ the synergy activation matrix corresponding to the calibration data, and $\boldsymbol{W} \in \mathbb{R}_{+}^{k*s}$ the synergy matrix, mapping a synergy activation to a group of muscles. In this formulation, s is the number of extracted synergies and $\boldsymbol{\varepsilon} \in \mathbb{R}^{k*n}$ is the matrix of factorization residuals. After factorization, the torque is computed in a similar way to the MVLR model:

$$\boldsymbol{\tau}(t) = \boldsymbol{C_s} \cdot \boldsymbol{W}^{+} \cdot \boldsymbol{m}(t)$$

with $\boldsymbol{C_s} \in \mathbb{R}^{j*s}$ the synergy mapping matrix computed using multivariate regression on calibration data matrices $\boldsymbol{T_c}$ and $\boldsymbol{H_c}$, and $\cdot^{+}$ is the pseudo inverse. This model was tested with two to seven synergies.

3.3. Neuromusculoskeletal

Neuromusculoskeletal (NMS) models combine musculoskeletal and Hill-type neuromuscular models. A generic OpenSim model (Holzbaur et al. 2005) is first scaled using kinematic data. Muscle activation a is then derived from excitations *via* a non-linear shape factor and each muscle force is computed from a Hill-type model (Buchanan et al. 2004):

$$F_m = F_0\left(af^L(\tilde{l})f^V(\tilde{v}) + f^{PE}(\tilde{l})\right)\cos(\alpha)$$

where F_0 is the maximum isometric force, f^L and f^V are respectively the force-length and force-velocity relationships, $\tilde{l}$ and $\tilde{v}$ are the normalized length and velocity of the muscle fiber, and α is the muscle pennation angle. The passive elastic behavior of the muscle fiber is represented by f^{PE}. Finally, the joint torque τ was obtained by summing muscle forces weighted by the muscle's moment arm projected on the joint axis. A genetic algorithm was used to optimize five parameters per muscle from calibration data: max isometric force, tendon slack length, optimal pennation angle, optimal fiber length, and shape factor.

3. Results and discussion

Calibration took an average of ten minutes for NMS and less than one second for MVLR and SYN. Estimation time was several milliseconds for NMS and less than one millisecond for MVLR and SYN. The NMS and MVLR models produced a mean NMRSE of 7.35% ± 1.2 and 8.73% ± 1.4, respectively. SYN models ranged from 9.68% ± 2.5 to 8.69% ± 1.4. (Figure 1). Overall, the NMS model allowed for significantly ($p < 0.01$) better torque reconstruction than any other model with a large effect size (Cohen's $d > 0.8$). MVLR and SYN models did not show significant differences. While the NMS model is more accurate than the other models, other criteria such as calibration and estimation times should be considered for application purposes (Bi et al. 2019). In this context, the performance of the NMS model may not be worth its computational cost against MVLR. To ensure applicability in industrial settings, it is crucial to expand these findings to multiple joints, considering the potential influence of biarticular muscles on the results. Additionally, it is important to investigate the impact of EMG signal degradation caused by factors such as sweat, fatigue, and electrode displacement.

4. Conclusions

In the present preliminary study, we compared three EMG-to-torque models using a specific *in situ* procedure. We showed that the NMS model was significantly more accurate than MVLR and SYN models. Future work will extend this study to include more degrees of freedom and criteria to guide the selection of models for real-time applications.

References

Bi L, Feleke A, Guan C. 2019. A review on EMG-based motor intention prediction of continuous human upper limb motion for human-robot collaboration. Biomed Signal Process Control. 51:113–127. doi:10.1016/j.bspc.2019.02.011.

Buchanan TS, Lloyd DG, Manal K, Besier TF. 2004. Neuromusculoskeletal modeling: estimation of muscle forces and joint moments and movements from measurements of neural command. J App Biomech. 20(4):367–395.

Camardella C, Barsotti M, Buongiorno D, Frisoli A, Bevilacqua V. 2021. Towards online myoelectric control based on muscle synergies-to-force mapping for robotic applications. Neurocomputing. 452:768–778.

Delis I, Panzeri S, Pozzo T, Berret B. 2014. A unifying model of concurrent spatial and temporal modularity in muscle activity. J Neurophysiol. 111(3):675–693. doi:10.1152/jn.00245.2013.

Garrec P, Friconneau JP, Measson Y, Perrot Y. 2008. ABLE, an innovative transparent exoskeleton for the upper-limb. 2008 IEEE/RSJ International Conference on Intelligent Robots and Systems.

Holzbaur K, Murray W, Delp S. 2005. A model of the upper extremity for simulating musculoskeletal surgery and analyzing neuromuscular control. Ann Biomed Eng. 33(6):829–840. doi:10.1007/s10439-005-3320-7.

Lotti N, Xiloyannis M, Missiroli F, Bokranz C, Chiaradia D, Frisoli A, Riener R, Masia L. 2022. Myoelectric or force control? A comparative study on a soft arm exosuit. IEEE Trans. Rob. 38(3):1363–1379.

Treussart B, Geffard F, Vignais N, Marin F. 2020. Controlling an upper-limb exoskeleton by EMG signal while carrying unknown load. IEEE ICRA.

KEYWORDS Electromyography; intention detection; torque estimation; exoskeleton

lucas.quesada@universite-paris-saclay.fr

Does wearing a virtual reality headmounted display affect balance in healthy young adults?

Valentin Ruiz, Emilie Simoneau-Buessinger, Christophe Gillet, Dimitri Elie and Laura Wallard

Univ. Polytechnique Hauts-de-France, LAMIH, CNRS, UMR 8201, F-59313 Valenciennes, France

1. Introduction

Virtual reality (VR) headset has been increasingly used in clinical settings in recent years for balance and gait rehabilitation in patients with neurological conditions (Cano Porras et al. 2018) or older adults (Soltani and Andrade 2020). However, this device was not specifically developed for rehabilitation and balance assessment but for video games.

Consequently, the specificity of this device could lead to a modification of the user balance. In fact, some authors (Akizuki et al. 2005) assessed the effect of virtual reality on balance in healthy adults compared to non-VR headset condition. They concluded that VR headset negatively impacts balance in healthy adults. However, the effect of VR headset on balance could be attributed to two main factors: the specificity of the projection of the virtual environment as nonfamiliar visual clues and visual-vestibular conflict, and the added mass of the headset that, is actually distributed towards the front of the head. However, to achieve postural stability, the nervous system notably relies on head stabilization within space (Wallard et al. 2012). In addition, perception from cutaneous and kinesthetic receptors can influence postural stability (Jeka and Lackner 1995). Some studies (Robert et al. 2016) have analyzed the effect of VR headset on balance and found no significant difference compared to the non-VR headset condition. However, the mass, its repartition and the sensory feedback may vary from a headset to another. These differences can lead to different effects of the device on balance. In addition, another study (Gotardi et al. 2020) evaluated the impact of a headset eye tracker and observed that the device's mass and sensory feedback contributed to enhance user stability.

To our knowledge, no study has evaluated the effect of the HTC VIVE^{TM} on postural stability, control and leaning. This headset is currently the most commonly used in clinical practice. Therefore, this study aimed to assess the effects of the mass (380 g) of the HTC VIVE^{TM} on postural stability, control and leaning. It was hypothesized that the mass of this headset and its distribution over the head modifies these postural parameters during upright standing.

2. Methods

1.1. Participants

The study involved 10 healthy young males (age: 24.7 ± 4.2 years, height: 1.76 ± 0.06 m, and body mass: 70.0 ± 11.3 kg). All included participants were informed of the objectives and the progress of the study, and gave written consent.

1.2. Protocol

The experimental task consisted of a 30 s stabilometric measurement. Between each acquisition, the participants were invited to complete a rest period of at least one minute outside the force platform. They were asked to stand still upright in a standard standing position on the force platform, on an A3 sheet of paper, with feet at hip-width and arms along the side of the body (Figure 1). For the following trials, participants had to position their feet according to their drawn footprints. From then, two conditions with eyes closed were used to analyze the effects of the mass of the HTC VIVE^{TM} headset: with VR headset (Headset) and without VR headset (No headset).

1.2. Data analysis

The postural stability (antero-posterior (AP) and medio-lateral (ML) ranges of the center of pressures

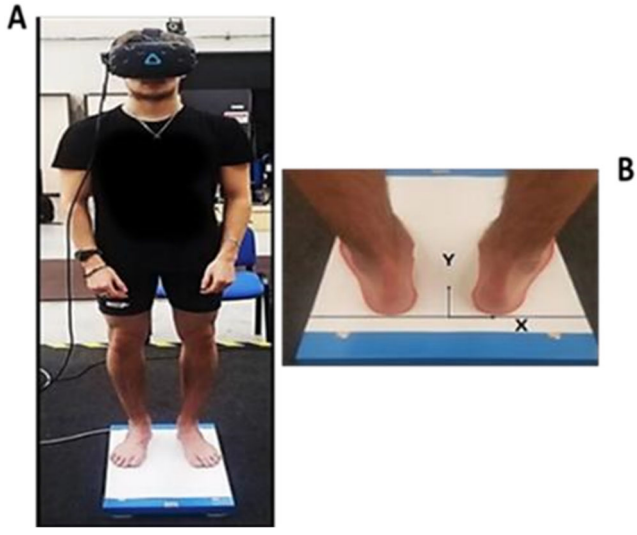


Figure 1. The experimental setup – standard position on the force platform with the VR headset(a). standardization of feet placement on an A3 sheet of paper (B).

Table 1. CoP parameters with (Headset) and without (no headset) headset with eyes closed.

	Headset	No headset	p-value
RangeAP (mm)	16.3 ± 3	16.3 ± 3.9	0.98
RangeML (mm)	11.8 ± 3.7	10.7 ± 3.35	0.20
EC90 (mm^2)	121.8 ± 56.9	113 ± 54.8	0.59
$Velocity_{GL}$ ($mm\ s^{-1}$)	10.5 ± 1.2	10.7 ± 2.2	0.71
$Velocity_{AP}$ ($mm\ s^{-1}$)	7.9 ± 1.4	8.0 ± 1.6	0.66
$Velocity_{ML}$ ($mm\ s^{-1}$)	4.7 ± 1.1	4.6 ± 1.6	0.95
StdAP (mm)	3.3 ± 0.7	3.3 ± 0.8	0.93
StdML (mm)	2.5 ± 0.8	2.3 ± 0.7	0.35
CoP mean $position_{AP}$ (mm)	−74.9 ± 12.6	−73.6 ± 12.6	0.59
CoP mean $position_{ML}$ (mm)	1.5 ± 6.4	2.5 ± 4.3	0.55

(CoP), 90% confidence ellipse area (EC_{90})), postural control (CoP velocity (global, AP and ML)) and standard deviation of the CoP mean position (Std)), and postural leaning (AP/ML CoP mean position) were assessed. The statistical analysis was done using a paired sample *t*-test with JASP (V0.14) software. The significance level α was set at $p \leq 0.05$.

2. Results and discussion

The spatiotemporal parameters characterizing postural stability, postural control and postural leaning were not significantly different with and without headset (all $p \geq 0.55$) (Table 1).

Our findings, consistent with a previous study on postural balance using a different VR headset (Robert et al. 2016), contradict the results of another study that showed balance improvements with a 395 g headset eye tracker (Gotardi et al. 2020). This difference may be attributed to variations in mass distribution around the head. While the eye tracker had a relatively uniform mass distribution, the VR headset concentrated most of its mass on the forehead. This could explain our disagreement in two ways. Firstly, the additional sensory information provided by the VR headset mass may have been countered by mechanical degradation induced by the VR headset mass. Secondly, the concentration of the VR headset mass predominantly on the forehead could lead to a reduction in degrees of freedom. Previous studies have shown that the ability to control and suppress biomechanical degrees of freedom allows the postural control system to adapt postural strategies without compromising balance (Buchanan and Horak 2001).

3. Conclusions

The mass of the VR headset did not significantly affect postural balance in young and healthy users. These results should be confirmed in vulnerable populations.

In the perspective of future research, it would be intriguing to investigate the impact of VR headset usage on Kinematic parameters, focusing on degrees of freedom, specifically utilizing the uncontrolled manifold theory. Studying the impact of VR on human movement and coordination, specifically the coordination between controlled and uncontrolled components, can provide valuable insights for optimizing VR-based rehabilitation.

References

Akizuki H, Uno A, Arai K, Morioka S, Ohyama S, Nishiike S, Tamura K, Takeda N. 2005. Effects of immersion in virtual reality on postural control. Neurosci Lett. 379(1): 23–26. doi:10.1016/j.neulet.2004.12.041.

Buchanan JJ, Horak FB. 2001. Transitions in a postural task: do the recruitment and suppression of degrees of freedom stabilize posture? Exp Brain Res. 139(4):482–494. doi:10.1007/s002210100798.

Cano Porras D, Siemonsma P, Inzelberg R, Zeilig G, Plotnik M. 2018. Advantages of virtual reality in the rehabilitation of balance and gait: systematic review. Neurology. 90(22):1017–1025. doi:10.1212/WNL.0000000000005603.

Gotardi GC, Rodrigues ST, Barbieri FA, Brito MB, Bonfim JVA, Polastri PF. 2020. Wearing a headmounted eye tracker may reduce body sway. Neurosci Lett. 722: 134799. doi:10.1016/j.neulet.2020.134799.

Jeka JJ, Lackner JR. 1995. The role of haptic cues from rough and slippery surfaces in human postural control. Exp Brain Res. 103(2):267–276. doi:10.1007/BF00231713.

Robert MT, Ballaz L, Lemay M. 2016. The effect of viewing a virtual environment through a headmounted display on balance. Gait Posture. 48:261–266.doi:10.3389/fspor.2020.531535.

Soltani P, Andrade R. 2020. The influence of virtual reality head-mounted displays on balance outcomes and training paradigms: a systematic review. Front Sports Act Living. 2:531535. doi:10.3389/fspor.2020.531535.

Wallard L, Bril B, Dietrich G, Kerlirzin Y, Bredin J. 2012. The role of head stabilization in locomotion in children with cerebral palsy. Ann Phys Rehabil Med. 55(9–10): 590–600. doi:10.1016/j.rehab.2012.10.004.

KEYWORDS Balance; headset; postural sway; virtual reality

Valentin.ruiz@uphf.fr

Dynamics aware Cartesian wrench polytope estimation based on human musculoskeletal models

A. Skuric[a], N. Rezzoug[a,b], D. Daney[a] and V. Padois[a]

[a]AUCTUS Team, INRIA Bordeaux, Bordeaux INP, Talence, France; [b]Institut PPrime, CNRS-Université de Poitiers-ENSMA, Poitiers, France

1. Introduction

Cartesian wrench capacity, the range of achievable forces and moments that a human, with different parts of his body, can generate in different directions of space, is an important tool for analyzing human physical abilities in various fields such as sport and rehabilitation (Rezzoug et al. 2021). However, obtaining this information through empirical means is time-consuming and often limited to static conditions. Musculoskeletal models provide an efficient way of calculating Cartesian wrench capacity metrics, such as Cartesian wrench polytopes, enabling real-time applications (Skuric et al. 2022; Carmichael and Liu 2011). However, when using these metrics on the fly, it is essential to consider the dynamic factors related to gravity and inertia. Therefore, in this paper, we propose a new extended formulation of Cartesian wrench capacity polytope based on musculoskeletal models accounting for these motion and gravity related effects.

2. Methods

The dynamical model of the human musculoskeletal model can be expressed as

$$\boldsymbol{M}(\boldsymbol{q})\ddot{\boldsymbol{q}} + \boldsymbol{C}(\boldsymbol{q},\dot{\boldsymbol{q}})\dot{\boldsymbol{q}} + \boldsymbol{g}(\boldsymbol{q}) = -\boldsymbol{L}^{\boldsymbol{T}}(\boldsymbol{q})\boldsymbol{t} - \boldsymbol{J}^{\boldsymbol{T}}(\boldsymbol{q})\boldsymbol{F}$$

where $M(q)$ and $\boldsymbol{C}(\boldsymbol{q},\dot{\boldsymbol{q}})$ are state $q,\dot{q}$ dependent inertia and Coriolis and centrifugal matrix, $g(q)$ is the vector of gravity induced joint torques. Matrix $-L(q)^T$is the muscle moment arm matrix describing the relationship between muscular forces and generated joint torques $\tau = -L^T(q)t$ and $J(q)$ is the jacobian matrix relating joint velocities $\dot{q}$ and the cartesian velocity $\dot{x} = J(q)\dot{q}$. Vector t is a vector of muscular tension forces and F is the generated cartesian wrench.

2.1. Influence of dynamic on the wrench generation

The generation of the Cartesian wrench F involves two main factors: muscular forces t and the effects of rigid body dynamics. These effects can be represented as a state-dependent bias joint torque vector.

$$\boldsymbol{\tau_b}\ (\boldsymbol{q},\ \dot{\boldsymbol{q}},\ \ddot{\boldsymbol{q}}\ ) = \boldsymbol{M}(\boldsymbol{q})\ddot{\boldsymbol{q}} + \boldsymbol{C}(\boldsymbol{q},\dot{\boldsymbol{q}})\dot{\boldsymbol{q}} + \boldsymbol{g}(\boldsymbol{q})$$

If assuming kineto-static conditions, where velocity and acceleration is approximately zero $\dot{\boldsymbol{q}},\ddot{\boldsymbol{q}} \approx 0$, the bias vector corresponds to the gravity vector $g(q)$.

The influence of dynamical movements is present in the range of available muscular forces as well

$$\boldsymbol{t} \in [\boldsymbol{t}_{min}(q,\dot{q}),\ \boldsymbol{t}_{max}(q,\dot{q})]$$

as they depend on the muscle lengths and contraction velocities which can be known from q and $\dot{q}$. t_{max} and t_{min} correspond to the muscular forces produced by fully activated (activation a=1) and unactivated (a=0) muscle correspondingly.

2.2. Cartesian wrench polytope formulation

For given joint position q_k, velocity $\dot{q}_k$ and acceleration $\ddot{q}_k$, jacobian J_k=$J(q_k)$ and moment arm L_k=$L(q_k)$ matrices can be determined, as well as the range of available muscle tension forces $t_{k,min}, t_{k,max}$ and the bias vector $\tau_{k,b}$. Finally, the resulting set of all achievable Cartesian wrenches F can be represented as a convex polytope

$$\boldsymbol{P} = \{\boldsymbol{F} | \boldsymbol{t} \in [\boldsymbol{t}_{k,min}, \boldsymbol{t}_{k,max}],\ \boldsymbol{J}_k^T\boldsymbol{F} = -\boldsymbol{L}_k^T\boldsymbol{t} - \boldsymbol{\tau}_{k,b}\}$$

2.2. Polytope evaluation

In order to transform this polytope to the minimal set of vertices (vertex representation) or a set of constraints $HF \leq d$ (half-plane representation) an extension of the *Iterative convex hull method* (ICHM) (Skuric et al. 2022) is proposed. ICHM is defined for families of problems

$$\boldsymbol{P_x} = \{\boldsymbol{x} \mid \boldsymbol{y} \in [\boldsymbol{y_{min}},\ \boldsymbol{y_{max}}],\ \boldsymbol{Ax} = \boldsymbol{By}\ \}$$

To enable this method to evaluate the dynamics aware Cartesian wrench polytope P, it needs to be extended to account for additional bias b

$$\boldsymbol{P_x} = \{\boldsymbol{x} \mid \boldsymbol{y} \in [\boldsymbol{y_{min}},\ \boldsymbol{y_{max}}],\ \boldsymbol{Ax} = \boldsymbol{By} + \boldsymbol{b}\}$$

If the vector $By + b$ belongs to the image $Im\{A\}$ of the matrix A, then the problem can be reformulated as

$$x = A^{+}(By + b)$$

where A^+ is the pseudo-inverse of A. To ensure that $By + b$ does belong to $Im\{A\}$, the equality constraint can be enforced

$$V_2^T By + V_2^T b = 0$$

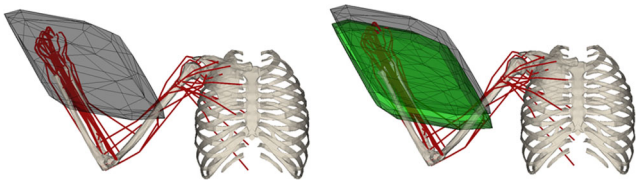


Figure 1. Cartesian wrench polytope with (green) and without (gray) the effect of gravity.

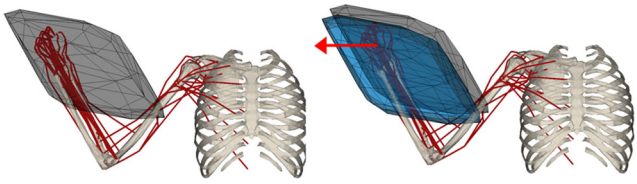


Figure 2. Cartesian wrench polytope with (blue) and without (gray) the effects of dynamics and gravity.

where V_2^T is the projector matrix onto the null-space of A, obtained from its *Singular Value Decomposition* (SVD). This constraint guarantees that any solution x to the equation $x = A^+(By + b)$ also satisfies the original equation $\boldsymbol{Ax} = \boldsymbol{By} + \boldsymbol{b}$.

Finally, the new formulation of the *Linear Program* (LP) used by the ICHM for finding the extreme points (vertices) of the polytope P_x, in the direction of space defined by the vector c, becomes

$$\begin{aligned} &max\ c^T A^+ By + c^T A^+ b \\ &s.t.\ V_2^T By = -V_2^T b \\ &\boldsymbol{y_{min}} \leq \boldsymbol{y} \leq \boldsymbol{y_{max}} \end{aligned}$$

3. Results and discussion

To demonstrate the influence of dynamical effects, a 3D Cartesian force polytope P is calculated for a 50 muscle, 7 degrees of freedom, upper limb musculoskeletal model (Holzbaur et al. 2005), generating forces with its hand. To make these effects more visible the model has been extended to include a mass of 5 kg rigidly fixed to its hand. The joint configuration used for the experiments is

$$\boldsymbol{q_o} = [0,\ 0.76,\ -1.29,\ 1.82,\ 0,\ 0,\ 0]^T$$

The first experiment demonstrates the effect of gravity on the polytope P. For this experiment the kineto-static conditions are assumed $\dot{\boldsymbol{q}}_o, \ddot{\boldsymbol{q}}_o = 0$, where the bias vector becomes $\tau_b(\boldsymbol{q_o}, 0, 0) = \boldsymbol{g}(\boldsymbol{q_o})$.

The influence of the arm's gravity on the polytope P can be seen as a vertical shift of the polytope. As shown on Figure 1, compared to no gravity polytope, the arm is capable of applying a higher force in the gravity direction and a lower force in the opposite direction, while forces in other directions are not impacted.

In the second experiment, the effect of the arm's movement is demonstrated. Joint velocity $\dot{\boldsymbol{q}}_o$ and acceleration $\ddot{q}_o$ are set to ones producing 2 ms^{-1} and 2 ms^{-2} in the x-axis direction.

$$\begin{aligned} \boldsymbol{J}(\boldsymbol{q_o})\dot{\boldsymbol{q}}_o &= [2,\ 0,\ 0]^T \boldsymbol{ms}^{-1},\ \boldsymbol{J}(\boldsymbol{q_o})\ \ddot{\boldsymbol{q}}_o \\ &= [2,\ 0,\ 0]^T ms^{-2} \end{aligned}$$

Figure 2 shows that when considering the effect of the arm's movement in the x-axis (red arrow), the polytope P is shifted in the same direction. This fact confirms that the arm is capable of generating higher forces in the direction of movement.

Average polytope calculation time is around 150 ms. The experiments are implemented in programming language python using biorbd library (Michaud and Begon 2021) and the proposed method is available as a part of the open-source python library called *pycapacity*.[1]

4. Conclusions

In conclusion, this paper presents a new method for calculating human wrench capacity polytopes based on musculoskeletal models that takes into consideration the dynamics of the human body. The method has a potential to be used in real-time applications and could be a useful tool for analyzing human performance online.

However, the method relies entirely on the accuracy of the musculoskeletal model used. Therefore, further work is needed to validate the accuracy of the calculated values against real data to ensure the reliability of the method.

Note

1. https://pypi.org/project/pycapacity/

Acknowledgements

Partially funded by the BPI France project Lichie.

References

Carmichael MG, Liu D. 2011. Towards using musculoskeletal models for intelligent control of physically assistive robots. Annual International Conference of the IEEE Engineering in Medicine and Biology Society. IEEE Engineering in Medicine and Biology Society. Annual International Conference. 2011:p. 8162–8165.

Holzbaur KRS, Murray WM, Delp SL. 2005. A model of the upper extremity for simulating musculoskeletal

surgery and analyzing neuromuscular control. Ann Biomed Eng. 33(6):829–840. doi:10.1007/s10439-005-3320-7.

Michaud B, Begon M. 2021. biorbd: A C++, Python and MATLAB library to analyze and simulate the human body biomechanics. JOSS. 6(57):2562. doi:10.21105/joss.02562.

Rezzoug N, Hernandez V, Gorce P. 2021. Upper-limb isometric force feasible set: evaluation of joint torque-based models. Biomechanics (Basel, Switzerland). 1(1):102–117. doi:10.3390/biomechanics1010008.

Skuric A, Padois V, Rezzoug N, Daney D. 2022. On-line feasible wrench polytope evaluation based on human musculoskeletal models: an iterative convex hull method. IEEE Robot Autom Lett. 7(2):5206–5213. doi:10.1109/LRA.2022.3155374.

KEYWORDS Wrench polytopes; musculoskeletal human model; rigid body dynamics

antun.skuric@inria.fr

Effect of exoskeleton characteristics on EMG activities during a repetitive manual lifting task

M. Schwartz[a], K. Desbrosses[a], J. Theurel[a] and G. Mornieux[b,c]

[a]Working Life Department, French National Research and Safety Institute for the prevention of occupational accidents and diseases (INRS), Vandoeuvre-les-Nancy, France; [b]Université de Lorraine, Nancy, France; [c]Faculty of Sport Sciences, Université de Lorraine, Nancy, France

1. Introduction

Overuse of back muscles induced by repetitive handling tasks can be associated with the development of low back pain (LBP). Several previous studies highlighted that the use of occupational back-support exoskeletons can limit lumbar muscular stress during dynamic work tasks (Theurel and Desbrosses 2019). However, the magnitude of the effects appears to depend on the characteristics of the exoskeleton used (Kermavnar et al. 2021). On average, the use of active systems could decrease the muscle activity of the erector spinae by an average of 25%, whereas for passive systems, this reduction was only 18%. If these results generally come from work tasks of short duration (with few repetitions), the question also exists for longer repetitive tasks, potentially generating neuromuscular fatigue. Indeed, Dos Anjos et al. (2022) recently showed a significant interaction between exoskeleton technologies and task duration. They observed an effect of the passive exoskeleton with lower muscle activity only at the beginning of a repetitive task. Having evaluated only one exoskeleton, it is difficult to say whether this observation is linked or not to the model tested or it can be generalized.

The objective of this study was therefore to assess the consequences of the use of different models of back-support exoskeletons on the activities of spine and hip extensor muscles, during a 5-min repetitive manual lifting task.

2. Methods

2.1. Participants

Twenty-seven volunteers without musculoskeletal disorders participated in this study. Before the experimentation, the participants realized a training protocol to familiarize them with the use of the exoskeletons.

Table 1. Participant characteristics.

Sex	*N*	Age (years)	Height (m)	Weight (kg)
Women	14	24 ± 6	1.66 ± 0.06	63.6 ± 13.3
Men	13	25 ± 5	1.80 ± 0.04	75.5 ± 7.9

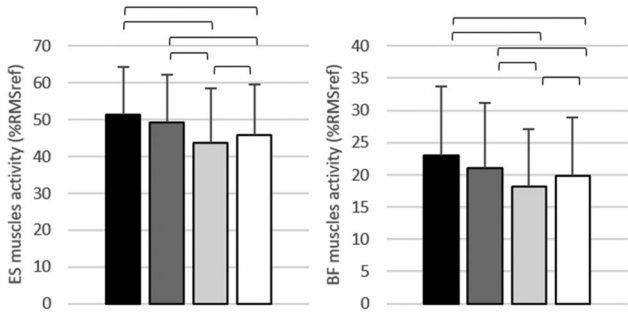


Figure 1. Mean EMG activities ± standard deviations of erector spinae (ES) and biceps femoris (BF) muscles on the whole task. The control condition (CON) is in black, P-EXO in dark gray, A-EXO1 in light gray and A-EXO2 in white. A significant difference between two conditions ($p < 0.05$ is represented by a bracket.

2.2. Experimental condition

Participants performed a standardized repetitive manual lifting task in the sagittal plane with a 10 kg load, during 5 min at an imposed rhythm of 15 cycles/minutes. The lifting task was realized with the stoop technique without equipment (CON) and with three exoskeletons: 1 passive (P-EXO, BackX from SuitX) and 2 actives (A-EXO1, Exoback from RB3D and A-EXO2, CrayX from German Bionic). Surface EMG activity of erector spinae (ES) and biceps femoris (BF) was recorded continuously during the task and normalized as a percentage of a reference value determined with isometric contraction (%RMSref). Data were analysed using generalized linear mixed model with exoskeletons, sex and time as main effects, as well as their interaction effects ($p < 0.05$). Normality of the residuals was checked.

3. Results and discussion

Statistical analyses firstly showed a main exoskeleton effect ($p < 0.05$). Considering the whole task, the use of active exoskeletons (A-EXO1 and A-EXO2) significantly decreased the muscle activity of ES by −15 and −11% and BF by −21 and −14% respectively, compared to the control condition without equipment. These results are in agreement with previous studies showing reduced muscle activity with the use of active exoskeletons. There was also a decrease in muscle activity of −6 to −14% compared to passive systems when using active ones. This result is in agreement

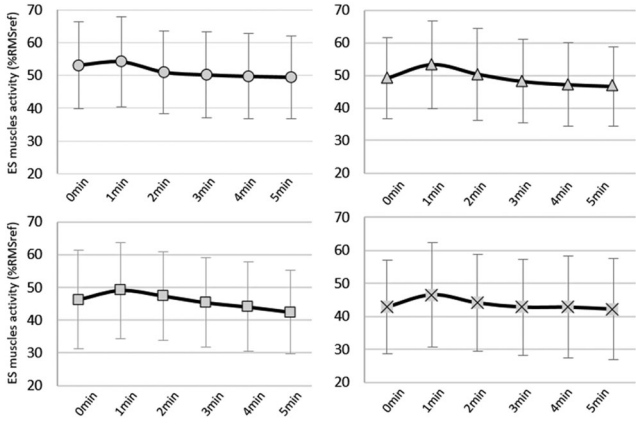


Figure 2. Mean EMG activities ± standard deviations of erector spinae (ES) muscle over time. The control condition (CON) is presented at the top left, P-EXO at the top right, A-EXO1 at the bottom left and A-EXO2 at the bottom right.

with the review of Kermavnar et al. (2021), who reported greater benefits on ES muscle activity with active compared to passive systems. These differences between technologies could be explained by the assistance level, which is higher for active systems. In our study, the passive exoskeleton theoretically allowed a maximum assistive torque of 41Nm while the active exoskeletons allowed 72Nm. However, our results also shown a difference between the two active systems on ES and BF muscle activity, with larger decreases (-5 and 8%, respectively) for A-EXO1. As active systems have been settled to an identical assistive torque, these differences could be explained by different design characteristics, in terms of weight, transfer points of the assistance or joints number. Indeed, a lower weight (8 kg versus 11 kg) and a higher level of anthropomorphism (2 joints at the lower back and hip level versus one at the hip level) could explain the greater EMG reductions induced by the A-EXO1 compared to A-EXO2. These hypotheses have previously been advanced to explain differences observed for cardiorespiratory parameters (Schwartz et al. 2021).

In this study, the exoskeleton-time interaction was not significant for the both ES and BF muscles activity. This result means that the beneficial effects induced by the exoskeletons are not modified over the time of the task performed. This is not in agreement with Dos Anjos et al. (2022), who showed that the EMG activity of ES muscles was reduced by 5% only at the beginning of the task when using a passive system. This difference with our study could be induced by different experimental protocols. For example, the task duration was 5 min in the present study while it was 10 min in the study of Dos Anjos et al. (2022). So it is possible that in the present study the task was not sufficiently long to induce muscle fatigue, which could have modulated the consequences of exoskeletons on the muscle activities. Other studies must be carried out during longer or more complex tasks inducing neuromuscular fatigue to confirm this hypothesis.

4. Conclusions

The objective of this study was to evaluate the evolution of the muscular consequences of the use of various models of back-support exoskeletons during a repetitive manual lifting task. Our results showed that the use of active occupational back-support exoskeletons could reduce the EMG activity of the erector spinae and biceps femoris muscles. The benefits provided by these systems appear however to depend on various characteristics of their design. It was also observed that there was no differences in temporal evolution of EMG activities during the task between the different exoskeleton conditions. In conclusion, active back-support exoskeletons could help reduce the risk of low back pain (LBP) related to repetitive handling tasks.

Acknowledgements

We thank G. Reno, O. Remy and O. Morel for their technical support. C. Gaudez for providing medical assistance, and I. Urmes for her statistical support.

References

Dos Anjos FV, Ghislieri M, Cerone GL, Pinto TP, Gazzoni M. 2022. Changes in the distribution of muscle activity when using a passive trunk exoskeleton depend on the type of working task: a high-density surface EMG study. J Biomech. 130:110846. doi:10.1016/j.jbiomech.2021.110846.

Kermavnar T, de Vries AW, de Looze MP, O'Sullivan LW. 2021. Effects of industrial back-support exoskeletons on body loading and user experience: an updated systematic review. Ergonomics. 64(6):685–711. doi:10.1080/00140139.2020.1870162.

Schwartz M, Theurel J, Desbrosses K. 2021. Effectiveness of soft versus rigid back-support exoskeletons during a lifting task. Int J Environ Res Public Health. 18(15):8062.

Theurel J, Desbrosses K. 2019. Occupational exoskeletons: overview of their benefits and limitations in preventing work-related musculoskeletal disorders. IISE Trans Occup Ergon Human Factors. 7(3–4):264–280. English. doi:10.1080/24725838.2019.1638331.

KEYWORDS EMG; lifting tasks; wearable assistive devices; low back pain

mathilde.schwartz@inrs.fr

Effect of mass addition on upper limb joint torques during meat cutting tasks: a parametric study

A. Tomezzoli, A. Schuster, G. Dumont and C. Pontonnier

Inria, CNRS, IRISA, Univ Rennes, France

1. Introduction

Musculoskeletal disorders (MSDs) are a major public health issue. In the meat processing industry, elbow and hand MSDs are over-represented, neck and shoulder MSDs prevalence still being high (Nordander et al. 2009). To mitigate the exposure to physical risk factors of MSDs, especially to forceful exertions, the use of a wrist exoskeleton delivering an assistive force to the user during the task performance can be considered (Chander et al. 2022). During the development process of wrist exoskeletons, the risk of increasing physical load by the addition of a given mass, depending on its position on the forearm, arose. To investigate this effect in biomechanical terms, the intensity of the user-generated torques associated with the exertion *versus* rest duration can be used (Potvin 2012). The goal of the study was to identify, based on these criteria, areas of maximum increase in joint torques of a mass added to the forearm, during a real meat cutting task.

2. Methods

2.1. Data collection

A previous dataset, described by Chander et al. (2022), was reused. A meat cutting task consisting in pork belly deboning was performed by a professional butcher (INRIA ethics committee COERLE, n° 2021-07). The butcher's motion was recorded with an opto-electronic motion capture system (Qualisys, 200 Hz). Knife and table forces were recorded using 6 degree of freedom (dof) force sensors (ATI Mini45-E Transducer, 500 Hz, and HBM MCS10-005-6C, 1000 Hz, respectively).

2.2. Joint torques computation

The cutting task was defined as the part of the trial with a cutting force intensity higher than 3 N. A biomechanical model of the upper limb (3 segments, 7 dofs) was designed in CusToM (Muller et al. 2019), following the International society of biomechanics

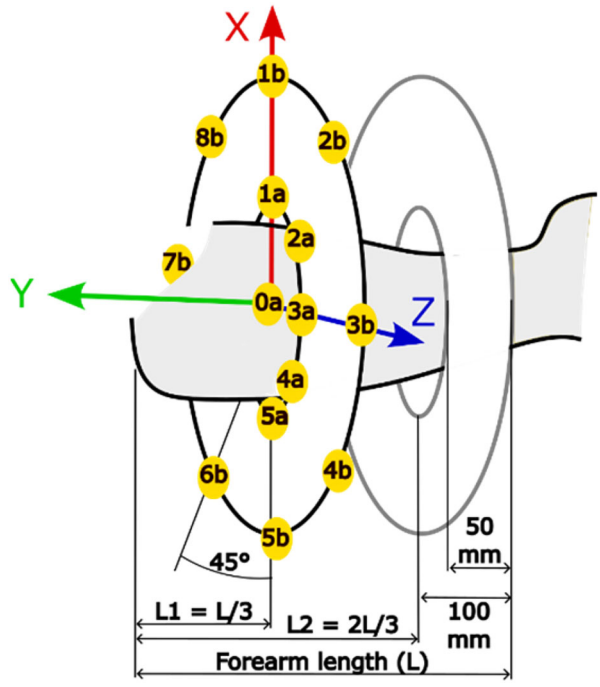


Figure 1. Positions of the additional mass on the forearm. Related model names (in yellow) on the proximal transversal plane (black circles).

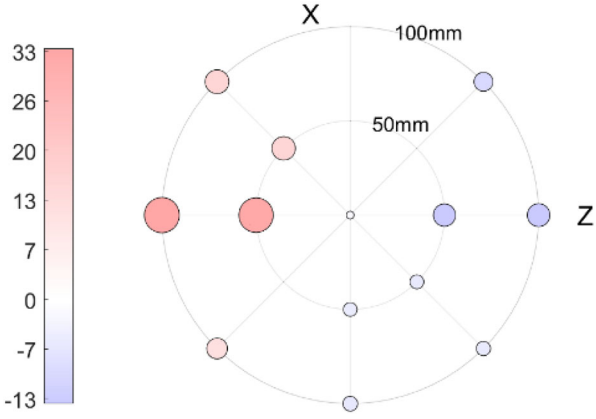


Figure 2. Pronation peak torque variations (%) for different proximal mass locations.

recommendations, and using body segment inertial parameters of Dumas et al. (2007) scaled to the participant. This baseline biomechanical model was modified to provide a range of models integrating a 0.5 kg additional point mass at successive locations on the forearm, to simulate the mass of an exoskeleton and realistic positions of its center-of-mass. Three parameters were combined: distance along the forearm $\overrightarrow{Y}$ longitudinal axis ($n = 2$), distance from this axis ($n = 3$), angular position on the transversal plane ($n = 8$), for a total of 34 locations (Figure 1). Inverse

Table 1. Maximum effect of mass addition, in terms of joint torque increase: magnitude, mass position, and associated effect on exposure duration.

	Baseline model		Maximum effect of mass addition		
	Duty cycle (%)	Peak torque (N.m)	Peak torque variation (%)	Model name	Difference in duty cycle (%)
Shoulder plane of elevation +/-	61.8/38.2	18.4/−4.2	1.0/−23.0	5bL1/5bL2	0.2/6.0
Shoulder depression/elevation	44.5/55.5	15.1/−9.5	5.6/−13.1	7bL2/5bL2	−3.0/4.0
Elbow flexion/extension	85.0/15.0	16.7/−7.4	6.1/−0.0	7bL1/2aL1	1.7/0.0
Pronation/supination	32.3/67.7	1.5/−1.4	38.0/−38.3	1bL2/5aL1	36.9/12.3

kinematics and dynamics were computed, under the assumption of unmodified task performance, in terms of upper limb kinematics and external forces.

2.3. Postprocessing

Peak torques were computed, for each dof, as the 97.5 and 2.5 percentile of torque distributions across time, to prevent measurement artifacts exceeding 2 standard deviations from the mean. The peak torque variations were computed as $(\tau_{i,a,j} - \tau_{i,b})/\tau_{i,b}$, i being the different dofs, a,j the different altered models, and b the baseline model. The duty cycle (DC) was computed as the percentage of frames exhibiting positive torques (e.g. elbow flexion) or negative torques (e.g. elbow extension). Differences between the baseline model ($DC_{i,b}$) and each altered model ($DC_{i,a,j}$) were computed as ($DC_{i,a,j} - DC_{i,b}$). As internal/external rotation of the arm can hardly be interpreted clinically, this result is not reported.

3. Results and discussion

3.1. Effects of mass location

Areas of maximum increase in joint torques were identified. Firstly, peripherical positionings resulted in larger joint torques than positioning close to the longitudinal forearm axis, for shoulder elevation, elbow flexion and, in case of distal positioning, for shoulder elevation plane (-). Secondly, proximal ulnar positionings resulted in larger joint torques than proximal radial ones, for shoulder elevation plane (-), shoulder elevation and pronation (Figure 2). Maximum joint torques were increased at most by 38.3%, 38.0%, and 23.0% for supination, pronation, and shoulder elevation plane (-), respectively (Table 1). The associated DC were increased by 12.3%, 36.9%, 6.0%, respectively. This increase of torques, especially when combined with increased exposition durations (Potvin 2012), seems large enough to increase the risk of forearm and shoulder MSDs, which is already high among butchers (Nordander et al. 2009).

3.2. Limitations

Firstly, kinematics was assumed to be unmodified; in real life, kinematics might be influenced by a mass addition (Latash and Zatsiorsky 2016). Secondly, the forearm diameter varies depending on people anthropometry and along the longitudinal forearm axis, which will influence the position of an exoskeleton; this should be accounted for accurate prediction of the effect of a specific exoskeleton. Finally, as high inter-personal and inter-task kinematics variability has been reported during meat cutting tasks (Chander et al. 2022), more kinematics records should be analyzed to conclude about the best mass positioning. Moreover, an active exoskeleton is expected to induce motion adaptations that were not considered in the current study.

4. Conclusions

The effect of diverse mass positions on upper limb joint torques was assessed, by virtually adding a 0.5 kg mass at different locations on a butcher's forearm, during a real meat cutting task. Proximal ulnar, along with peripherical positionings, increased multiple joint torques. Pronation torques were particularly affected by the choice of the additional mass positioning, in terms of peak torques and exposure duration. Consequently, the efficiency of an exoskeleton can probably be compromised by poor center of mass location, even for relatively light exoskeletons. Inertial parameters must be considered when developing an exoskeleton.

Acknowledgements

This study has been funded by the Région Bretagne, within the frame of the EXOSCARNE 2.0 project, and supported by French government funding managed by the National Research Agency under the Investments for the Future program (PIA) with the grant ANR-21-ESRE-0030 (CONTINUUM project). The authors thank Lab4i company and COOPERL's workers.

References

Chander DS, Marie S, Gréau M, Pontonnier C. 2022. Biomechanical requirements of meat cutting tasks: an overview. Comput Methods Biomech Biomed Eng. 25(S1):S1–S307.

Dumas R, Chèze L, Verriest JP. 2007. Adjustments to McConville et al. and Young et al. body segment inertial parameters. J Biomech. 40(3):543–553. doi:10.1016/j.jbiomech.2006.02.013.

Latash ML, Zatsiorsky VM. 2016. Biomechanics and motor control. New York: Academic Press. Elsevier.

Muller A, Pontonnier C, Puchaud P, Dumont G. 2019. CusToM: a Matlab toolbox for musculoskeletal simulation. JOSS. 4(33):927. doi:10.21105/joss.00927.

Nordander C, Ohlsson K, Akesson I, Arvidsson I, Balogh I, Hansson G-A, Strömberg U, Rittner R, Skerfving S. 2009. Risk of musculoskeletal disorders among females and males in repetitive/constrained work. Ergonomics. 52(10):1226–1239. doi:10.1080/00140130903056071.

Potvin JR. 2012. Predicting maximum acceptable efforts for repetitive tasks: an equation based on duty cycle. Hum Factors. 54(2):175–188. doi:10.1177/0018720811424269.

KEYWORDS Dynamics; butchery; wrist; shoulder; exoskeleton

aurelie.tomezzoli@ens-rennes.fr

Genetic algorithms for force polytopes prediction

G. Laisné[a], J.-M. Salotti[b] and N. Rezzoug[a,c]

[a]INRIA Bordeaux, Université de Bordeaux, Talence, France; [b]CNRS, Bordeaux INP, INRIA, IMS, UMR 5218, Univ. Bordeaux, Talence, France; [c]Institut PPrime, CNRS-Université de Poitiers-ENSMA, UPR 3346, Poitiers, France

1. Introduction

Knowledge of human's force capacities enables the design of physical Human-Robot Interaction (*pHRI*) workspaces. As measuring force capacities for all postures is time consuming, predicting force capacities from a subset of measurements performed in a limited number of postures is crucial. The force capacities can be described as a convex polytope by means of a personalized musculoskeletal (MSK) model (Skuric et al. 2022). However, the tuning of a MSK model is difficult due to the high number of parameters. Thanks to its constraint-free nature on the optimization function, a genetic algorithm is implemented to find a MSK model parameter set, which fits and predicts force polytopes (Van Soest and Casius 2003; Peng et al. 2015).

2. Methods

2.1. Force polytope

The upper-limb is considered as a n degree-of-freedoms kinematic chain actuated by d muscles. In isometric conditions, the (convex) force polytope localized at the center of the hand is defined as:

$$P = \{\mathbf{f} \in \mathbf{R}^3 \mid J^T\mathbf{f} = -L^T\mathbf{t},\ \mathbf{t} \in [\mathbf{t_{min}},\ \mathbf{t_{max}}]\} \quad (1)$$

where $J^T \in \mathbf{R}^{n\times 3}$ and $-L^T \in \mathbf{R}^{n\times d}$ map respectively the forces at the end-effector $\mathbf{f} \in \mathbf{R}^3$ and the muscle tensions $\mathbf{t} \in [\mathbf{t_{min}}, \mathbf{t_{max}}]$ onto the torque space. These mappings and the muscle tensions depend on the joint configuration $\mathbf{q} \in \mathbf{R}^n$. The *Iterative Convex Hull* method with a tolerance of 1 N is used to approximate the polytope vertices (Skuric et al. 2022).

For an arbitrary $k \in \mathbf{N}$, the *discretization* of a polytope is a scaled-down representation in $2k$ vertices. It ensures easier comparisons. The polytope is intersected with lines $L_1, L_2, ..., L_k$ passing through the origin and k points evenly distributed on the upper sphere, with L_1 passing through $(1, 0, 0)$. Each line produces two vertices noted $v^+_{L_i}$ and $v^-_{L_i}$. The discretized polytope is defined as:

$$P^D = \left(v^+_{L_1},\ v^-_{L_1},\ ...,\ v^+_{L_k}, v^-_{L_k}\right) \in \mathbf{R}^{2k} \quad (2)$$

2.2. Musculoskeletal model

A *biorbd*-compatible version of Stanford's upper-limb model (Holzbaur et al. 2005) is used and consists of 50 muscles and 7 degrees-of-freedom. The muscle tensions are computed using Thelen's muscle model.

2.3. Optimization problem

Our goal is to find a MSK model parameter set $\mathbf{M}^*$ which generates discretized forces polytopes close to discretized polytopes computed from an unknown model parameter set in p postures:

$$\mathbf{M}^* = \text{argmin}_{\mathbf{M}}\ f_p(\mathbf{M}) \quad (3)$$

$$\text{with } f_p(\mathbf{M}) = \frac{1}{p}\sum_{i=1}^{p} \text{MSE}\left(\hat{P}_i^D, P_i^D(\mathbf{M})\right) \quad (4)$$

with $\mathbf{M}$ a model parameter set, p the number of postures considered, $\hat{P}_i^D$ the discretized polytope to estimate at posture i, and $P_i^D(\mathbf{M})$ the computed discretized polytope at posture i.

2.4. Genetic algorithm

Genetic algorithms are based on the biological concept of evolution. They are particularly efficient compared to classic optimization methods to find solutions for hard optimization problems, with conditions such as unsteadiness, non-derivability, or noise (Van Soest and Casius 2003). A genetic algorithm begins with randomly or manually initialized solutions called the *initial generation*. The solutions are then assessed according to a cost function. The best solutions, called *parents*, define a new generation by means of small changes called *mutations*. The process is iterated until a terminating criterion is met.

2.5. Simulations

A genetic algorithm is used to minimize (4). A solution is a set of 150 parameters defining Stanford's MSK model. This set includes 3 parameters per muscle (the maximum isometric force, the optimal muscle length at which the muscle creates its maximal isometric force and the tendon slack length). These parameters have direct impact on muscle tensions computed using the force-length relationship. Each generation has 128 solutions. An initial generation is created using uniform random perturbations up to 30% (arbitrarily chosen due to computation considerations) of the Stanford's model parameter set. Small perturbations, up to 5%, are also applied on each

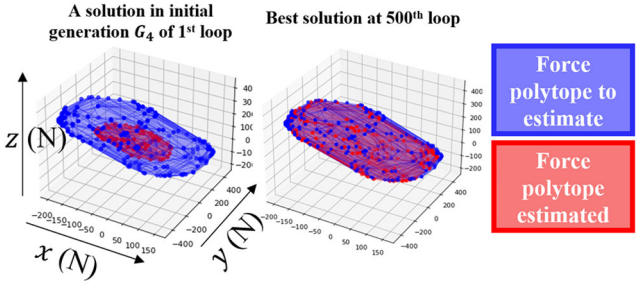


Figure 1. Force polytope fitting for posture $\mathbf{Q}_1$ from loop 1 to loop 500 using the posture set.S_6

Table 1. Mean ± SD of discretized force polytopes RMSEs (N) between stanford's and solutions found for G_1 to G_5 using S_4 and S_6 in fitting postures (white) and in 10 new prediction postures (grey).

	G_1	G_2	G_3	G_4	G_5
S_4	4±1	3±1	4±1	5±1	5±2
S_4	14±7	16±13	32±45	31±39	31±53
S_6	5±2	6±1	6±1	6±2	9±3
S_6	20±14	16±13	11±9	11±8	14±8

muscle origin and insertion points. Five initial generations G_1, G_2, G_3, G_4 and G_5 are defined.

To assess the impact of the number of postures in the optimization process, two sets of postures S_4 and S_6 are considered: S_4 includes 4 common upper-limb postures ($\mathbf{Q}_1, \mathbf{Q}_2, \mathbf{Q}_3$, and $\mathbf{Q}_4$), while S_6 includes 2 more ($\mathbf{Q}_5$ and $\mathbf{Q}_6$). The model is defined in the global reference frame following the ISB recommendations: the x-axis is normal to the coronal plane, the y-axis normal to the transverse plane and the z-axis normal to the sagittal plane. The postures are described by 7 Euler angles in degrees using a y-z'-y'' sequence for the shoulder, a z-y' sequence for the elbow and a x-z' sequence for the wrist: $\mathbf{Q}_1 =$ (31°, 12°, −34°, 74°, 17°, 15°, 15°), $\mathbf{Q}_2 =$ (79°, 54°, -73°, 53°, 90°, 0°, 0), $\mathbf{Q}_3 =$ (124°, 56°, −75°, 32°, 88°, 0°, 0°), $\mathbf{Q}_4 =$ (27°, 66°, −59°, 34°, 88°, 0°, 0), $\mathbf{Q}_5 =$ (-41°, 79°, −6°, 104°, −46°, 6°, 0), and $\mathbf{Q}_6 =$ (108°, 104°, 7°, 31°, −46°, 6°, 0°).

A cost function is defined per posture set and are respectively f_4 and f_6, using (4). The 5 best solutions which minimize the cost function define the parents. An elitist strategy is used to keep the parents in the next generation. For each parent, the mutation process generates 5 new parameter sets randomly selected in the neighbourhood of the parent parameter set. The neighbourhood size varies depending on the number of times a solution has been selected as a parent: below 4 times, the neighbourhood includes up to 10% around the parent parameters. Between 5 and 9 times, up to 1%. Between 10 and 29, up to 0.5% and above 30 times, up to 0.1%. Each generated parameter set also includes up to 1% random perturbations for the muscle origin and insertion points. They induce small perturbations in the generated force polytopes, allowing us to verify the genetic algorithms robustness.

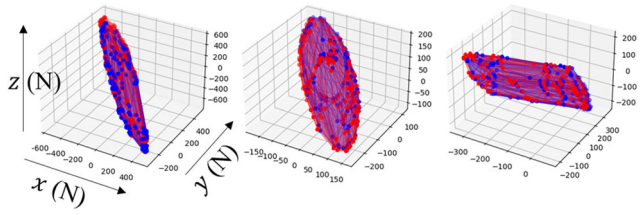


Figure 2. Example of force polytope predictions for 3 new postures.

3. Results and discussion

A genetic algorithm was used to tune a MSK model using force polytopes discretized in 26 vertices. A simplified version of the Stanford's MSK model (Holzbaur et al. 2005) with 7 degree-of-freedoms and 50 muscles was used as the model parameter set to estimate. For the five different initial generations considered using each posture sets, the algorithm converged to a solution (Figure 1). Predictions show better results using 6 postures, due to overfitting when using 4 postures only (Table 1).

Posture number should be optimized to get better results. Also, found solutions were expectedly distant from the model parameter set to estimate, due to redundancy in joint torques generation.

4. Conclusions

Simulation results attest the performance of finding a model parameter set which fits and predicts force polytopes for different postures (Figure 2). The cost functions should be adapted to consider the polytopes geometry. The method was tested *in silico* and will be validated experimentally using a similar protocol for force polytopes measurements as in (Rezzoug et al. 2013).

Acknowledgements

The simulations were carried out using the PlaFRIM experimental testbed (Inria, CNRS, LABRI, IMB, Université de Bordeaux, Bordeaux INP and Conseil Régional d'Aquitaine) (see https://www.plafrim.fr).

References

Holzbaur KRS, Murray WM, Delp SL. 2005. A model of the upper extremity for simulating musculoskeletal surgery and analyzing neuromuscular control. Ann Biomed Eng. 33(6):829–840. doi:10.1007/s10439-005-3320-7.

Peng L, Hou Z-G, Peng L, Wang W-Q. 2015. A practical EMG-driven musculoskeletal model for dynamic torque estimation of knee joint. IEEE International Conference on Robotics and Biomimetics; p. 1036–1040. doi: 10.1109/ROBIO.2015.7418908.

Rezzoug N, Hernandez V, Jacquier-Bret J, Gorce P. 2013. Comparison between model-based and measured force polytopes: towards isometric force capacity evaluation. Comput Methods Biomech Biomed Engin. 16(sup1):172–174. doi:10.1080/10255842.2013.815972.

Skuric A, Padois V, Rezzoug N, Daney D. 2022. On-line feasible wrench polytope evaluation based on human musculoskeletal models: an iterative convex hull method. IEEE Robot Autom Lett. 7(2):5206–5213. doi:10.1109/LRA.2022.3155374.

Van Soest AJK, Casius LJRR. 2003. The merits of a parallel genetic algorithm in solving hard optimization problems. J Biomech Eng. 125(1):141–146. doi:10.1115/1.1537735.

KEYWORDS Force polytope; genetic algorithm; musculoskeletal model

gautier.laisne@inria.fr

Impact of 3D unload orthosis on tibiofemoral contact forces in relation to adduction moment and contact locations

S. Guitteny[a], R. Aissaoui[b], J. Bleau[c] and R. Dumas[a]

[a]LBMC UMR T_9406, Univ Lyon, Univ Eiffel, Univ Lyon 1, Lyon, France; [b]Dépt Génie des systèmes, ETS, Montréal, Canada; [c]Laboratoire Orthopédique Médicus, Montréal, Canada

1. Introduction

Knee osteoarthritis (OA) is a chronic disease characterized by joint cartilage damage which is a major health issue in today's society. Valgus knee orthoses are recommended to improve the quality of life of OA patients and to postpone the arthroplasty. Tibiofemoral (TF) contact forces are important parameters for the follow up of OA progression and the assessment of the orthosis efficiency (Yan et al. 2022).

A reduction of the medial contact forces has been reported using musculoskeletal models but the mechanical action of orthosis was not modelled or simplified to an external adduction moment (Yan et al. 2022). Musculoskeletal models have also shown that medial contact force in OA patients is correlated with inter-segmental moments and contact point locations (Dumas et al. 2020; Amiri et al. 2023).

Using a musculoskeletal model with a personalised modelling of the orthosis mechanical action, this study aims to investigate how wearing an orthosis impacts the medial contact forces and its correlations with internal knee adduction moments and contact point locations.

2. Methods

2.1. Experimental set up

Sixteen patients diagnosed with severe medial OA wore a personalised 3D printed orthosis (Evoke, OssKin) for four weeks prior to the test. The orthosis applies a correction of 4 mm knee medial displacement and 5° knee abduction angle. All patients completed the consent form approved by the institutional Ethics Committees. Low dose biplane x-rays (EOS) were acquired in five weight-bearing squat postures (0°, 15°, 30°, 45°, 70° knee flexion) with and without wearing the orthosis. Two inertial Sensors (Noraxon, Inc) were placed in the sagittal plane of the shank and the thigh to control the knee flexion/extension angle in real-time. An AMTI force platform (ORS-6) was fixed inside the EOS cabinet to measure the forces and moments under the studied foot. A platform was designed to isolate the ground reaction forces under the contralateral foot, while both feet were maintained at the same level.

2.2. Musculoskeletal modelling

A five-segment lower limb model with 5 joint degrees of freedom and 43 muscles lines of action was used in this study. Bone segments and muscles have been scaled to subject anthropometry and positioned in 3D using the biplane x-ray images. Hip joint centre, TF contact point locations (Zeighami et al. 2017), and patellar tendon insertion and tendon length were personalised using the bones 3D reconstructions.

This study used a newly developed method to personalise loads applied by the orthosis on the lower limb. The 3D orthosis forces and moments were computed from the soft tissue stiffness of each segment (K^i_{tj}, K^i_{rj}), where $i = 2,3$ stand for shank and thigh, $j = 1,2,3$ for spatial directions and r,t for rotation and translation mechanical action (Shafiei and Behzadipour 2020):

$$\begin{Bmatrix} F^i_j \\ M^i_j \end{Bmatrix} = \begin{Bmatrix} K^i_{tj} * (u - u_0) \\ K^i_{rj} * (\vartheta - \vartheta_0) \end{Bmatrix} \quad (1)$$

where $(u_0,\ \vartheta_0) = (-4\ mm,\ -5°)$ is the correction values applied at standing posture and (u, ϑ) is the orthosis movement relative to the bone measured in the biplane x-rays of other postures. In order to ensure static orthosis equilibrium, forces and moments on each space axis has been modified as follow:

$$\begin{Bmatrix} |F_j| \\ |M_j| \end{Bmatrix} = \begin{Bmatrix} \left|(F_j{}^3 - F_j{}^2)/2\right| \\ \left|(M_j{}^3 - M_j{}^2)/2\right| \end{Bmatrix} \quad (2)$$

For all of the static squat postures, internal knee adduction and flexion moments (KAM and KFM) and contact forces were calculated *via* inverse dynamics and static optimisation including subject-specific contact point locations (Dumas et al. 2020). The Mann–Whitney statistical test has been performed to study the effect of wearing or not the orthosis on TF contact forces. Linear regression tests have been performed to study the relation between the evolutions of medial force, internal KAM, internal KFM and contact points locations.

3. Results and discussion

Regarding TF contact forces, a major increase of lateral contact force of 26.4% in standing posture and a general but not significant decrease in medial force in all postures were found with the orthosis (Table 1).

Table 1. Average variation (in %) of TF contact forces while wearing orthosis.

	0°	15°	30°	45°	70°
Medial	−9.1	−15.2	−15.2	−12.9	−6.6
Lateral	+26.4	−6.2	−3.9	−3.6	+0.7
Total	+1.3	−10.8	−9.1	−7.3	−2.3

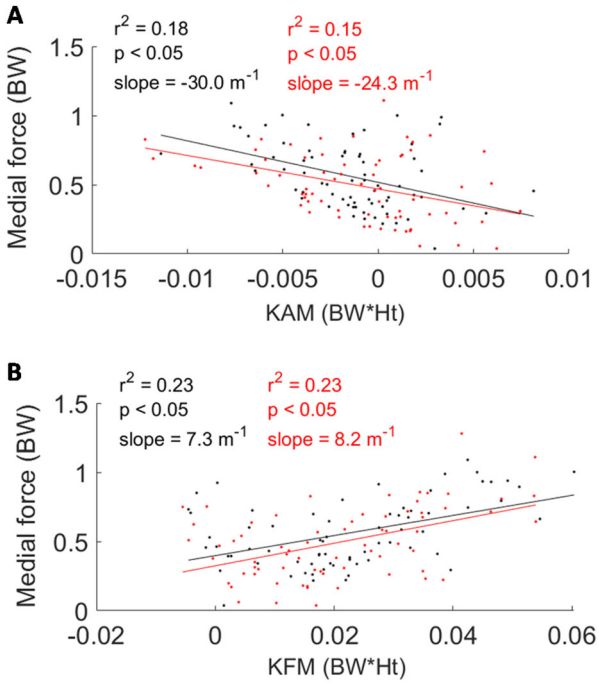


Figure 1. Correlations between medial contact force and internal KAM (A) and internal KFM (B), with (red) and without (black) the orthosis.

Correlations were observed between the medial contact force and the KAM parameters (r^2 = 0.18 and r^2 = 0.15 with and without orthosis, respectively) and the KFM parameters (r^2 = 0.23 both with and without orthosis) (Figure 1) indicating that modelling the orthosis does not impact the relationships identified in the literature for OA patients (Dumas et al. 2020; Amiri et al. 2023). Given the slopes of the correlations, to reduce the medial contact force, the internal KAM should be increased (external KAM reduced) and the internal KFM should be decreased (external KFM increased). No correlations have been found between the medial contact force and the contact point locations neither with or without the orthosis. The literature (Dumas et al. 2020) showed that medial contact forces could be reduced if the contact points are more medial. However, contact points seem already located more medially in OA patients (Zeighami et al. 2017) compared to healthy subjects, and this may not necessarily be the goal to achieve with the orthosis. Besides, it has been observed that the displacement of contact point locations remains close to 0 mm for many patients and postures.

This study reports on the unloading mechanism of the medial compartment of the knee when wearing the orthosis, as previously observed by Yan et al. (2022), and confirmed these observations with the inclusion of the orthosis into the numerical approach. In this study, the orthosis was assumed to be rigid, and the slippage was neglected. The soft tissue stiffness was obtained from the literature (Shafiei and Behzadipour 2020) and was not subject-specific. All these modelling assumptions result in the computation of orthosis loads that can compromise orthosis equilibrium. That is why a control step was implemented in this study.

4. Conclusions

This study evaluates the impact of 3D knee unload orthosis using biplane radiography and musculoskeletal modelling including customized loads applied by the orthosis. Medial contact forces are reduced as the internal adduction moments increased and the internal flexion moments decreased.

Future investigations should now focus on evaluating the orthosis performances on dynamic activities such as walking.

References

Amiri P, Davis EM, Outerleys J, Miller RH, Brandon S, Astephen Wilson JL. 2023. High tibiofemoral contact and muscle forces during gait are associated with radiographic knee OA progression over 3 years. Knee. 41:245–256. doi:10.1016/j.knee.2023.01.012.

Dumas R, Zeighami A, Aissaoui R. 2020. Knee medial and lateral contact forces computed along subject-specific contact point trajectories of healthy volunteers and osteoarthritic patients. Computer Methods Imaging Visualization Biomech Biomed Eng. 36:457–463.

Shafiei M, Behzadipour S. 2020. The effects of the connection stiffness of robotic exoskeletons on the gait quality and comfort. Journal of Mechanisms and Robotics. 12(1):011007. doi:10.1115/1.4044841.

Yan Y, Liu G, Zhang L, Gong R, Fu P, Han B, Li H. 2022. Biomechanical effect of valgus knee braces on the treatment of medial gonarthrosis: a systematic review. Saarakkala S, editor. Appl Bionics Biomech. 2022: 4194472. doi:10.1155/2022/4194472.

Zeighami A, Dumas R, Kanhonou M, Hagemeister N, Lavoie F, de Guise JA, Aissaoui R. 2017. Tibio-femoral joint contact in healthy and osteoarthritic knees during quasi-static squat: a bi-planar X-ray analysis. J Biomech. 53:178–184. doi:10.1016/j.jbiomech.2017.01.015.

KEYWORDS Osteoarthritis; musculoskeletal modelling; knee brace; tibiofemoral contact forces

raphael.dumas@univ-eiffel.fr

Perineal tissue deformation under bicycle saddle pressure

M. Shirzadi, X. Wang, K. Bruyère and L. Dubuis

Univ Lyon, Université Claude Bernard Lyon 1, Univ Gustave Eiffel, IFSTTAR, Lyon, France

1. Introduction

For ecological, economical and public health reasons, sustainable urban mobility such as bicycle commuting has increased in French cities, especially since the Covid-19 pandemic. Nevertheless, despite the advantages, some people are refractory to using bicycle because of the pain from the saddle.

Indeed, due to the time spent on saddle, bicycle commuters, sport cyclists (leisure or competition) or professionals (such as delivery cyclist) may suffer from more serious troubles than discomfort. These troubles can be numbness of the perineal region, apparition of nodules, irritations, erectile troubles, loss of sensibility, oedema, etc (Van der Walt et al. 2014).

Up to now, most of the studies working on bicycle saddle discomfort have focused on the interface pressure between the saddle and the soft tissues of the perineum (Guess et al. 2011). However, even if it shows disparity of the pressure distribution among cyclists, the measure of pressure is not enough to predict discomfort because it does not give information on soft tissue stress.

In order to access to more information, some authors measured the blood flow through the perineum while sitting on a saddle (Piazza et al. 2020). But this measure is not directly liked to discomfort, nor most of the troubles. Another idea from Bressel et al. (2007) was to use MRI in order to directly observe the perineal tissue deformation. Because it was in a conventional MRI, the participants had to be lying on their back. For applying saddle pressure, a device was developed where the participant was harnessed to pull up the saddle toward the perineum. But the position of the participants was far from their position on a bicycle. Consequently, the soft tissue deformation observed in this study may not be relevant due to unrealistic loading conditions.

In this study, we used an open MRI to reproduce upright cycling postures during the image acquisition to measure deformation in different soft tissues of the perineum from image segmentation.



Figure 1. Set up in the open MRI. Left: reference position; middle: top position; right: drop position.

2. Methods

2.1. Experimental setup

An upright MRI scanner (Paramed® 0.5 Tesla, Figure 1), from the European Scanning Centered in Manchester, United Kingdom, was used.

A plastic mockup, composed of a 3D printed saddle, handlebars and supports, was built in order to fit in the MRI which requires non-metallic material to avoid ferrous metal and interferences.

Three male participants, aged 28, 35 and 31 years old, were asked to hold three postures (Figure 1):

- the 'reference' posture, where the participants stood up on their feet, in order to get anatomical images of the unloaded perineum's participants;
- the 'top' posture, where the participants were seated on the saddle, holding the handlebar such as their back is approximately at 45°, corresponding to a cruising posture;
- the 'drop' posture where the participants were seated on the saddle, with their forearm on the arm rests, so their back was approximately at 25°, corresponding to a racing posture.

The resolution of the scans was set to 2 mm slice thickness, and 1 mm slice gap. For this resolution, the field of view was adjusted to be $300 \times 300 \times 300$ mm in sagittal, coronal and transversal planes respectively. Each scan took approximately 8 min. In order to help participants not to move during the acquisitions to avoid blurry scans, two stabilizers allowed the participants to lean their upper body for stability.

The protocol was approved by the ethical committee of Université Gustave Eiffel (formerly the French

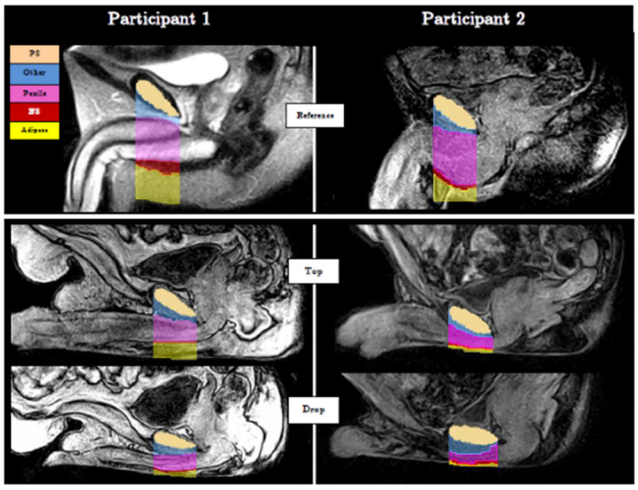


Figure 2. Segmentations in the ROI in the medial sagittal view in the reference, top and drop posture. The four tissue categories are highlighted as well as the pubic symphysis (PS) in peach.

Institute of Science and Technology for Transport, Development and Networks – IFSTTAR).

2.2. Data processing and analysis

The acquired MR images were segmented and processed in 3D slicer. It was desired to compare levels of tissue deformations below the anterior face of the pubis, from the reference to the top and drop postures. This anatomical location was of particular interest, as the peak deformation due to saddle induced forces are observed in this region according to (Bressel et al. 2007). Hence, for each participant, a region of interest (ROI) was subsequently defined as the tissues below the pubis symphysis (perpendicular to the saddle) in between the bilateral pubic tubercle (Figure 2).

The visible tissues identified in the ROI were divided into four categories: adipose tissue (fat and skin), the bulbospongiosus muscle (BS), penile tissues (PT) (comprised of corpus spongiosum and corpus cavernosum), and other (i.e. suspensory ligament of the penile body, etc.). These tissues were then separately segmented within the ROI for all participants' posture scans, and their individual segment volumes were extracted. These volumes were then used for determining the individual and total percentage tissue deformations.

3. Results and discussion

The MRI images of the three postures are shown in Figure 2 where the four tissue categories from the ROI are highlighted. The maximum compression of the tissues in the whole ROI occurs in the drop posture. For the participant 1, this value is approximately 50%, however for the second and third participants it is more than 70%. The BS muscle is the most compressed tissue in the ROI in both postures for participants 1 and 2. This is the case for the adipose tissue in the participants 3's ROI.

Table 1. Percentage of the tissue compression in the ROI for the top and drop postures compared to the reference state.

Tissues	Other	Penile	BS	Adipose
	Participant 1			
Top	26%	32%	80%	45%
Drop	28%	49%	77%	80%
	Participant 2			
Top	12%	69%	70%	83%
Drop	29%	73%	62%	81%
	Participant 3			
Top	12%	71%	31%	55%
Drop	18%	72%	45%	76%

Table 1 shows tissue compression based on volume in the ROI in top and drop postures compared to the reference posture: $1 - V/V_{ref}$. It seems that the penile and the adipose tissues are the most compressed.

It appears clearly that there are disparities in between participants in anatomy as well as in tissue compression (Figure 2 and Table 1). Because the number of participants in this study is small, it is not possible to conclude on the possible cause of discomfort and health trouble due to bicycle saddle. Further work needs to be performed with more participants.

4. Conclusions

Results show a difference between the anatomies and percentage tissue compositions across the participants. Surely these differences have major influence on the manner with which the respective tissues deform in the perineal region, and hence affect the neurovascular vessels they enveloped within them.

With regards to the effect of cycling posture on tissue deformations, the results indicate that the maximum tissue-bundle deformation occurs during the drop posture across all the participants.

In conclusion, pelvic and perineal anatomical structures should be taken account during saddle conception and should be added to the parameters that need to be assessed before choosing a saddle.

Acknowledgements

The authors thank IFSTTAR for the funding, the European Scanning Center and the participants.

References

Bressel E, Reeve T, Parker D, Cronin J. 2007. Influence of bicycle seat pressure on compression of the perineum: a MRI analysis. J Biomech. 40(1):198–202. doi:10.1016/j.jbiomech.2005.11.017.

Guess MK, Partin SN, Schrader S, Lowe B, LaCombe J, Reutman S, Wang A, Toennis C, Melman A, Mikhail M, et al. 2011. Women's bike seats: a pressing matter for competitive female cyclists. J Sex Med. 8(11):3144–3153. doi: 10.1111/j.1743-6109.2011.02437.x.

Piazza N, Cerri G, Breda G, Paggiaro A. 2020. The effect of a new geometric bicycle saddle on the genital-perineal vascular perfusion of female cyclists. Science & Sports. 35(3):161–167. doi:10.1016/j.scispo.2019.07.010.

Van der Walt A, van Rensberg DJ, Fletcher L, Grant CC, Van Der Walt AJ. 2014. Non-traumatic injury profile of amateur cyclists. SA J Sports Med. 26(4):119–122. doi:10.7196/SAJSM.555.

KEYWORDS Bicycle saddle; MRI analysis; perineal tissues; discomfort

laura.dubuis@univ-lyon1.fr

Simulation of maximum isometric and isokinetic elbow actuation torques based on zonotopes

J. Savin[a], D. Haering[b], N. Rezzoug[c] and C. Pontonnier[b]

[a]INRS, Vandoeuvre-lès-Nancy, France; [b]ENS/INRIA/IRISA/M2S MimeTIC, Rennes, France; [c]PPrime Institute, CNRS-University of Poitiers-ENSMA, Poitiers, France

1. Introduction

How can work equipment designers estimate the maximum joint actuation torques that operators can perform at the workstation? These data are essential for ergonomic risk assessment, yet designers usually only have at their disposal the databases provided with digital mannequin software. These are often approximate (Hall et al. 2021), leading to potential under-estimation of occupational risk exposure. This study describes a methodology based on zonotopes and musculoskeletal simulation to provide designers with more comprehensive and more reliable estimates of maximum actuation torques. As a partial validation process, this study also compares such simulated maximum actuation torques to experimental data described in the literature (Frey Law et al. 2012; Haering et al. 2019) focusing on maximum isometric and isokinetic actuation torques of the elbow.

2. Methods

2.1. Mathematical and modelling approach

The upper limb is described as a musculoskeletal system made of m muscles and p rigid bodies linked together by N degrees of freedom (DoF). Let $\boldsymbol{R} = [r_{i,j}]$ be the matrix of the moment arms of muscle j relative to the DoF i. $\boldsymbol{R}$ depends only on the joint angles $\boldsymbol{q}$ of the system. Let $\boldsymbol{t}$ be the vector of individual muscle tensions. Considering a Hill-type muscle model accounting for the active/passive length/velocity force relationships, $\boldsymbol{t}$ depends on joint the angles and velocities $(\boldsymbol{q}, \dot{\boldsymbol{q}})$. Hence the vector $\boldsymbol{\tau}$ of actuation torques is:

$$\boldsymbol{\tau} = \boldsymbol{R}(\boldsymbol{q})\boldsymbol{t}(\boldsymbol{q},\ \dot{\boldsymbol{q}}) \tag{1}$$

The set $\boldsymbol{T}$ of all achievable muscle tensions is a hypercube of dimension m. In this study, its bounds have been computed using OpenSim (Seth et al. 2018) and the musculoskeletal model of the upper limb 'MOBL' described in (Saul et al. 2015). This model represents to a male subject with a height of 1.77 m and a mass of 75 kg. It includes 50 muscles and 7 DoFs.

According to Equation (1), the set of achievable actuation torques is the image of $\boldsymbol{T}$ through the linear mapping defined by $\boldsymbol{R}$. This set, denoted $\mathbf{Z}$, is a special type of convex polytope called a zonotope, which can be computed using the hyper-plane shifting method (Gouttefarde and Krut 2010). Any point on the external surface of $\boldsymbol{Z}$ is an extremum, where at least one joint torque is maximum. Hence, computing maximum joint actuation torques is equivalent to computing intersections or projections of $\boldsymbol{Z}$ with a line or a surface in the space of actuation torques.

2.2. Comparison with experimental data

As a partial validation process, we conducted simulations for two experiments, on the one hand that of (Frey Law et al. 2012), hereafter denoted *FL*, and on the other hand that of (Haering et al. 2019), hereafter denoted *H*. Both concern the joint torque-velocity-angle relationships (JTVAR) of elbow flexion and extension. The first focuses on concentric exertion, the latter addresses eccentric exertion in addition.

3. Results and discussion

3.1. FL-experiment

We used the experimental data corresponding to 30 male subjects (mean height of 1.80 m and mass of 81.5 kg). Figure 1 compares the experimental and simulated maximum actuation torques. The Root Mean Square (RMS) difference in normalized actuation torque is about 27% and 20% for flexion and extension exertion respectively.

3.2. H-experiment

This experiment involved 34 subjects, but we only considered the subject whose height and mass were the most similar to the MOBL model. Figure 2 shows the experimental and simulated normalised maximum flexion and extension joint torques depending on joint velocity. The RMS is about 7% and 16% for flexion and extension exertions.

3.3. Discussion

Simulated and experimental torques show similar trends. This may be a significative benefit of this approach over DHM data that completely neglects the influence of joint velocities on actuation capabilities. However, a normalisation processing is needed because the MOBL model is not parameterised

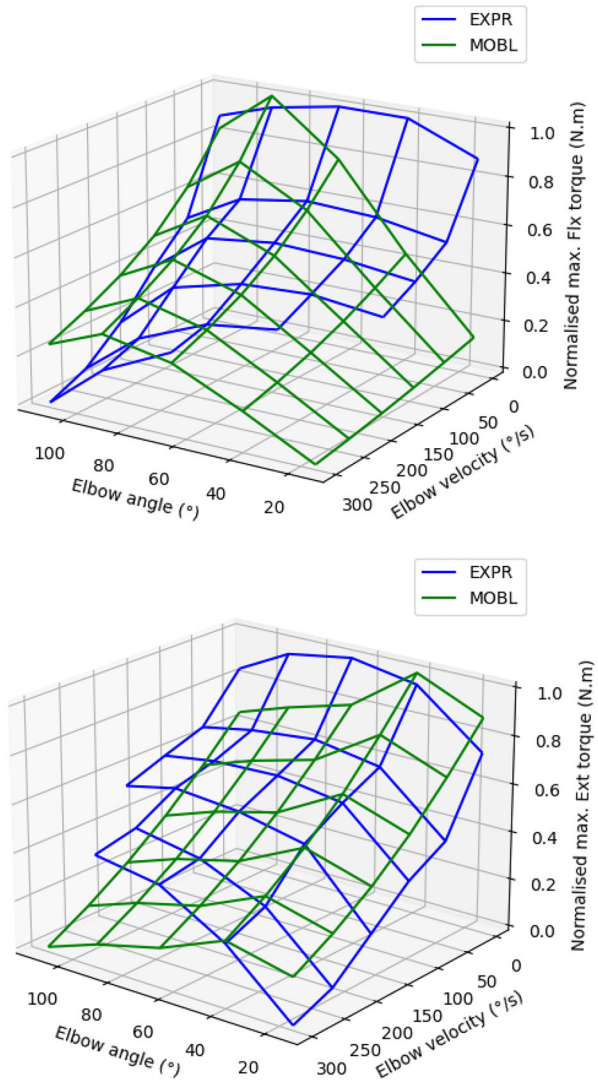


Figure 1. Experimental (blue) and simulated (green) normalised maximum flexion (top) and extension (bottom) actuation torques for the FL-experiment.

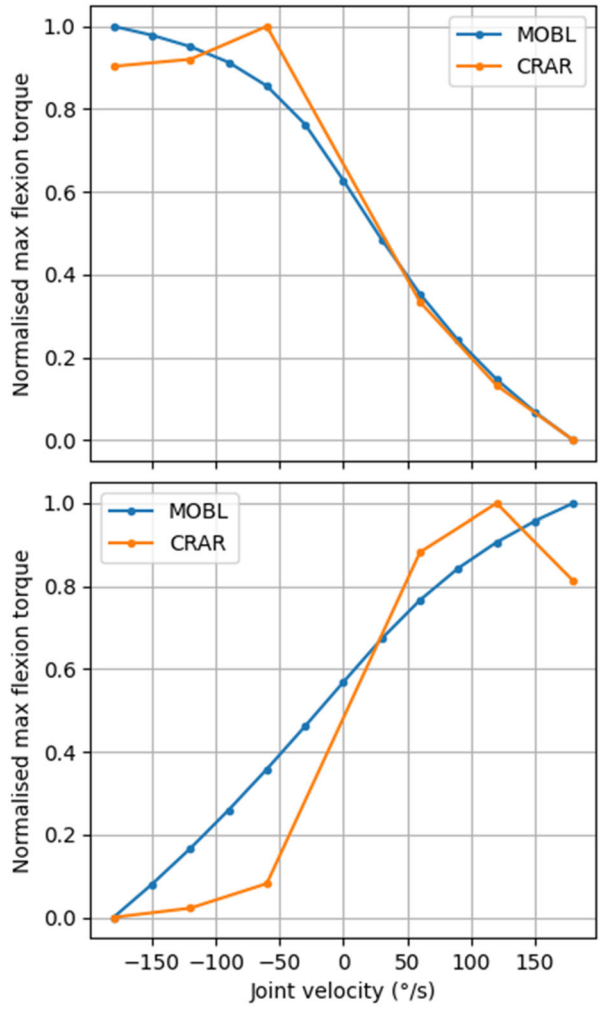


Figure 2. Experimental (Orange) and simulated (blue) normalised maximum joint torques for one subject of the H-experiment.

according to subjects' anthropometry and performance.

4. Conclusions

This paper describes a method to estimate joint actuation performance based on zonotopes and musculoskeletal simulation. This approach can be used to simulate complex experiments, including isokinetic exertions. As a first validation step, this study shows that such simulations account for the global trends observed experimentally, even without any customization of the musculoskeletal model. This parameterisation step is to be explored further to reduce the gap observed between experiments and simulation. Scaling the model anthropometry, the individual muscle capacities and moment arms should be the main levers to play with. If this step is completed, this approach may provide a convenient way to provide work equipment designers with more accurate and comprehensive estimations of maximum actuation performances of operators at the workplace than those at their disposal through current Digital Human Model software tools.

References

Frey-Law LA, Laake A, Avin KG, Heitsman J, Marler T, Abdel-Malek K. 2012. Knee and elbow 3D strength surfaces: peak Torque-angle-velocity relationships. J Appl Biomech. 28(6):726–737. doi:10.1123/jab.28.6.726.

Gouttefarde M, Krut S. 2010. Characterization of parallel manipulator available wrench set facets. In: Lenarcic J, Stanisic MM, editors. Advances in robot kinematics: motion in man and machine. Dordrecht: Springer Netherlands; p. 475–482.

Haering D, Pontonnier C, Bideau N, Nicolas G, Dumont G. 2019. Using torque-angle and torque–velocity models to characterize elbow mechanical function: modeling and applied aspects. J Biomech Eng. 141(8):084501. doi:10.1115/1.4043447.

Hall AD, La Delfa NJ, Loma C, Potvin JR. 2021. A comparison between measured female linear arm strengths and estimates from the 3D Static Strength Prediction Program (3DSSPP). Appl Ergon. 94:103415. doi:10.1016/j.apergo.2021.103415.

Saul KR, Hu X, Goehler CM, Vidt ME, Daly M, Velisar A, Murray WM. 2015. Benchmarking of dynamic simulation predictions in two software platforms using an upper limb musculoskeletal model. Comput Methods Biomech Biomed Eng. 18(13):1445–1458. doi:10.1080/10255842.2014.916698.

Seth A, Hicks JL, Uchida TK, Habib A, Dembia CL, Dunne JJ, Ong CF, DeMers MS, Rajagopal A, Millard M, et al. 2018. OpenSim: simulating musculoskeletal dynamics and neuromuscular control to study human and animal movement. PLoS Comput Biol. 14(7):e1006223. doi:10.1371/journal.pcbi.1006223.

KEYWORDS Ergonomics assessment; workstation design; maximum actuation torques; torque zonotope; musculoskeletal simulation

jonathan.savin@inrs.fr

Subject specific biomechanical model identification as a clinical routine

M. Sabbah[a], B. Watier[a,c], R. Dumas[b] and V. Bonnet[a]

[a]LAAS-CNRS, Université Paul Sabatier, CNRS, Toulouse, France; [b]Université Claude Bernard Lyon 1, IFSTTAR, Univ. Lyon, Lyon, France; [c]JRL, AIST-CNRS, IRL, Tsukuba, Japan

1. Introduction

Studies on human motion dynamics rely heavily on a good knowledge of Segment Inertial Parameters (SIP). Accurate knowledge of those parameters has made it possible to refine medical diagnosis and personalize health-care solutions. Conversely, a poor estimation of those parameters leads to wrong estimate of the external wrench and joint torques. A first estimation of SIP (Dumas 2007) can be obtained from Anthropometric Tables (AT), but they are notoriously inaccurate for people with atypical mass distribution such as infants, athletes or pathological individuals. In this context, Venture (2009) showed a reliable and robust method to estimate the SIP for humans out of motion and external wrench measurements using a real time visual feedback. This is this method that have been revisited here to allow accurate SIP identification for human. This work is based solely on open-source software that will be made available to the community upon request.

2. Methods

2.1. Biomechanical model

The biomechanical model used in this study is composed of $N_j = 42$ DoFs (including a floating base) and $N_s = 16$ body segments. It follows the joint axis definition proposed by the International Society of Biomechanics. The base of the model is located on the pelvis frame from which the upper body and the lower body are connected to. A floating base, represented by 3 translations and 3 rotations, precedes the pelvis frame to move the model in space. The main kinematic tree chains the pelvis to the abdomen through one lumbar cardan joint, the abdomen to the thorax and the thorax to the head with respectively one thoracic and one cervical spherical joint. Both upper-arm segments are connected to the thorax through one spherical joint, lower-arm segments are linked to the upper-arm through a cardan joint, and hand segments are linked to the lower-arm through a cardan joint. Same applies for the legs where upper-leg segments are connected to the pelvis through one spherical joint, lower-leg segments are attached to upper-legs through revolute knee joints and the feet segments are linked to lower-legs thanks to ankles cardan joints.

2.2. Inverse dynamic model (IDM)

The objective is to determine a set of 10 SIP for each segment j that are expressed in the joint frame: $\Phi_j = \left[M_j\ MS_j\ TI_j\right]$, where M_j is the mass of the segment, $MS_j = \left[MSX_j\ MSY_j\ MSZ_j\right]$ is the 3D vector of the first moment of inertia and $TI_j = \left[XX_j\ XY_j\ XZ_j\ YY_j\ YZ_j\ ZZ_j\right]$ is the 6D vector regrouping the element of the tensor of inertia.

It has been demonstrated that the IDM can be written in a linear form with respect to the SIP as:

$$R_d\Phi = \left[0\ \tau\right]^T + \sum_{k=1}^{N_c}\left[J_{0k}^T\ J_{ck}^T\right]^T F_k^{ext} \qquad (1)$$

where:

- $\tau \in \mathbb{R}^{N_j-6}$ is the vector of joint torques.
- N_c is the number of contact point with the environment.
- $F_k^{ext} \in \mathbb{R}^6$ is the vector of external wrench acting on the structure at contact k.
- $[J_{0k}\ J_{ck}] \in \mathbb{R}^{6*N_j}$ are the basic Jacobian matrices of the positions and orientations of the contact link at contact k with respect to q_0 and q_c, the angular configurations of the base and of the rest of the kinematic chain.
- $R_d = [R_{d0}\ R_{dc}]^T \in \mathbb{R}^{N_j*10N_s}$ is the dynamic regressor associated respectively to the base link and to the other segments. They are function of q_0, q_c and their derivatives.
- $\Phi \in \mathbb{R}^{10N_s}$is the vector containing all the segments SIP.

For humans, as we can only measure external wrench acting on the base link, only the upper part of the equation associated to the motion of the base link can be used. Consequently, to identify human SIP during the experiment, one requires the measurement of the structure motion using, for instance, motion capture to retrieve, thanks to Inverse Kinematics (IK), $q_0$and $q_c$and their derivatives and the measurement of external forces F_k^{ext}.

The IDM as well as the forward kinematic model are computed in real-time thanks to the C++ Pinocchio (Carpentier 2019) library that efficiently

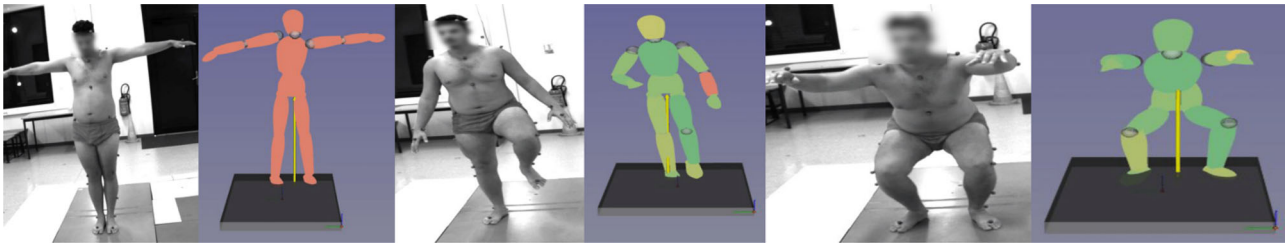


Figure 1. Experimental setup and visual feedback associated to specific pose.

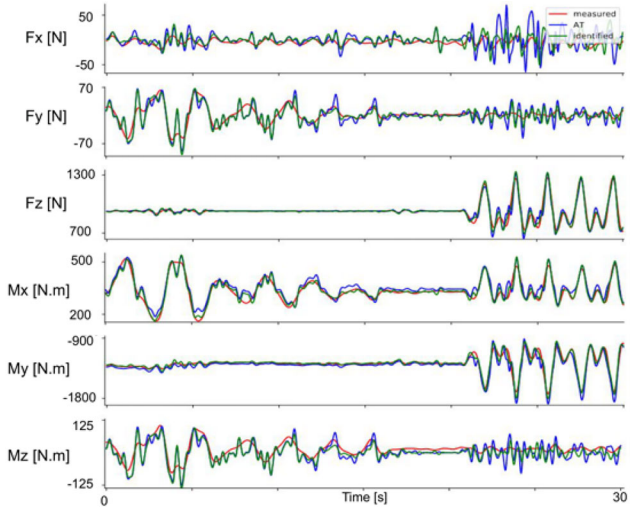


Figure 2. Human external wrench comparison between measurements (red) and its estimation using at model (blue) and the identified model (green).

implements state-of-the-art rigid body algorithms for poly-articulated system.

2.3. Experimental setup

Experiment has been conducted on one healthy subject (26 years, 97 kg) using a 20 cameras Stereophotogrammetric Systems and a force plate (Vero v2.2 Vicon, AMTI OR6 Series) sampled at 100 Hz at CREPS in Toulouse. The popular plug-in gait template based on 35 markers was used to estimate human motion.

The identification process is as follows:

1. The geometric model of human is calibrated, using a static anatomical pose (T-pose).
2. From the motion capture and force-plates measurements, the SIP are identified in real-time.
3. A colored visual feedback (Figure 1) is used to inform the subject about the quality of the identification of each segment. It improves the quality of identification results without the need to prescribe pre-defined exciting motions.

The subject was simply instructed to perform several movements such as squats, or arms and legs rapid flexion/extensions as shown in Figure 1 until the visual feedback showed all segment in the green meaning that the identification was successful. Indeed, the colours were displayed according to the quality of the identification following the relative standard deviation of the error:

$$\sigma_{\phi_j\%} = 100\frac{\sqrt{cov_{i,i}(\phi_j)}}{mean(\phi_j)}.$$

3. Results and discussion

To evaluate the quality of the identification process, the measured forces and the ones estimated with the model were compared. Figure 2 is a comparison between the measured external wrench and its estimate when using a model based on the AT and the identified one. The corresponding averaged RMSE were 19.47N and 33.22N.m for the model based on AT and 16.84N and 16.77N.m for the identified model

4. Conclusions

We have proposed a real time identification method for the whole body segment parameters of humans. We have shown that:

- The identification of all the SIP is possible. The estimated parameters meet the identification results without distortion, and minimize the error of the prior information from data-base. A good way to evaluate the results is to see how well the measured forces are tracked when using the identified model.
- The proposed approach of real-time identification and visualization of identification results during measurement allows to generate optimal persistent exciting trajectories, thus to obtain more accurate results with less data.

Future work will consist in developing the real time algorithm using more affordable sensors to generalize the pipeline. Applications of the method include interfaces for health and rehabilitation monitoring, to be seen as a clinical routine.

References

Carpentier J, Saurel G, Buondonno G, Mirabel J, Lamiraux F, Stasse O, Mansard N. 2019. The Pinocchio C++ library – a fast and flexible implementation of rigid body dynamics algorithms and their analytical derivatives. 2019 IEEE/SICE International Symposium on System Integration (SII).

Dumas R, Chèze L, Verriest P. 2007. Adjustments to McConville et al. body segment inertial parameters. J Biomech. 40(3):543–553. doi:10.1016/j.jbiomech.2006.02.013.

Venture G, Ayusawa K, Nakamura Y. 2009. Real-time identification and visualization of human segments parameters. Annu Int Conf IEEE Eng Med Biol Soc. 2009:3983–3986. doi:10.1109/IEMBS.2009.5333620.

KEYWORDS Humans; visual feedback; identification; motion dynamics; realtime

msabbah@laas.fr

Handicap and rehabilitation biomechanics

Adaptations in Muscle Activation and Glenohumeral Joint Angle During Manual Wheelchair Propulsion Over an Obstacle, page S233.
Evaluation of knee unloader braces and brace design challenges – A literature review, page S235.
Mechanical performances of DREEVEN, a novel motorization unit for custom knee orthosis, page S237.
Numerical simulation of medical compression stockings for venous and lymphatic disease treatment, page S240.
Objective assessment of facial mimicry using motion capture for patient follow-up, page S243.
Reliability assessment of an upper limb manual muscular testing protocol for manual wheelchair users using a hand-held dynamometer, page S245.
Slow anticipatory postural adjustments during gait initiation in autistic children, page S248.
Speed of sound measurement as a tool for assessing tendon functional recovery after an injury in horses, page S251.
Using Artificial Intelligence to Improve the Lives of Wheelchair Users, page S253.
Vision-based interface for grasping intention detection and grip selection: towards intuitive upper-limb assistive devices, page S256.

Adaptations in muscle activation and glenohumeral joint angle during manual wheelchair propulsion over an obstacle

L. Henry[a], N. Assila[a,b], M. Begon[b] and S. Duprey[a]

[a]LBMC UMR T_9406, Univ Lyon, Univ Eiffel, Lyon, France; [b]S2M, University of Montreal, Montreal, Canada

1. Introduction

About 75 million people worldwide require a manual wheelchair (WHO 2018). Within manual wheelchair users, the prevalence of upper limb pain, particularly in the shoulder, is over 70% (Smith 2016). Due to the persistence of pain, their mobility and quality of life are severely compromised (Chow and Levy 2011). Previous studies looking at wheelchair locomotion mainly investigated propulsion on a flat surface (Koontz 2009; Waldford 2019) and to a lesser extent over curbs, slopes, or during other advanced wheelchair skills (Cowan 2008; Nagy 2012; Lalumiere 2013; Rouvier 2022). However, none have focused on the kinematics of wheelchair propulsion over an obstacle (e.g. gutters or tram tracks) despite them being com-mon within urban environments. Assessing propulsion over an obstacle would improve our understanding of the challenges and injury risks wheelchair users face while being mobile within urban environments. Thus, the aim of this study is to identify the adaptations of wheelchair users when propelling over an obstacle.

2. Methods

2.1. Participants

The protocol was approved by the Sainte-Justine University Hospital Center Ethics Committee (MP-21-2020-2533). It included seven manual wheelchair users (six males, average mass 71.77 ± 11.38 kg, height 178.6 ± 8.1 cm, age 20-40 years, four right-handed) who had used a wheelchair for 6 months to 8 years. The participants had no history of right shoulder pain or injury, or neurodegenerative disorders.

2.2. Data collection and analysis

Each participant used his/her wheelchair during the data collection. Thirty-eight reflective markers were used to track the participants' trunk and upper right limb. Additionally, six markers were placed on the wheelchair frame, five on each back wheel, and four on the obstacle. The kinematic data were recorded using Vicon (Vicon Motion Systems, Oxford, UK) at 250 Hz. Muscle activity was recorded at 2000 Hz using surface electromyography (EMG) electrodes for 12 muscles (Delsys, Natick, MA, USA): deltoids (anterior (DA), median (DM), posterior (DP)), trapezius (upper (TI), middle (TM), lower (TS), serratus anterior (SA), latissimus dorsi (LA), pectoralis major (clavicular head) (PS), biceps (BI), and triceps (long (TRB), lateral (TRL). For the six participants who consented, intramuscular EMG electrodes were inserted into the supraspinatus (SUPSP), infraspinatus (INFSP), and subscapularis (SUBSC).

The participants propelled themselves at a constant, comfortable, self-selected speed over a smooth, flat surface (>1 m), starting and stopping propulsion outside of the view of the cameras. The steady-state propulsion was confirmed by evaluating wheelchair velocity. Then they propelled over an obstacle with the dimensions $0.06 \times 0.12 \times 1.3$ m (H × W × L). They began facing the obstacle with the wheelchair axle 1 m from it, and propelled their wheelchair up to 1 m after the obstacle. The participants chose the movement approach while propelling over the obstacle; no technique was imposed.

The 15 muscles' EMG maxima and the joint angle time histories (Wu 2004) were calculated and tested for normality using the Shapero-Wilks test. A paired *t*-test with Bonferroni correction was performed to compare the maxima glenohumeral (GH) joint angles (flexion-extension, abduction-adduction, and external-internal axial rotation) and muscle activation for each condition.

3. Results and discussion

The peak GH flexion-extension angles were significantly lower ($p < 0.017$), and the peak GH joint external rotation angles were significantly higher ($p < 0.017$) during propulsion over an obstacle compared to propulsion on a flat surface (Table 1). Maximum muscle activation was significantly higher ($p < 0.003$) during propulsion over an obstacle compared to propulsion on a flat surface for the following muscles, with the percentage difference: DA (70 ± 20%), DM (32 ± 36%), DP (25 ± 41%), TI (72 ± 19%), TM (39 ± 36%), TS (72 ± 15%), SA (32 ± 33%), LA (75 ± 18%), PS (63 ± 29%), BI (69 ± 16%), SUPSP (19 ± 53%), and INFSP (22 ± 78%) (Figure 1).

Previous studies have found that higher peak shoulder joint angles occur whilst ascending higher curbs compared to lower curbs (Lalumiere 2013; Nagy 2012). In the present study, the flexion-extension angles recorded during propulsion over an obstacle were lower than during propulsion on a flat

Table 1. Mean and SD for the maximum angles of the GH joint angles during propulsion on the flat and over an obstacle.

GH joint angles	Obstacle	Flat surface
Flexion-extension	10.7 ± 7.4*	15.7 ± 5.8*
Abduction-adduction	25.6 ± 6.9	27.7 ± 8.2
Internal-external axial rotation	−5.1 ± 8.9*	−0.1 ± 4.1*

* represents a significant difference ($p < 0.0017$).

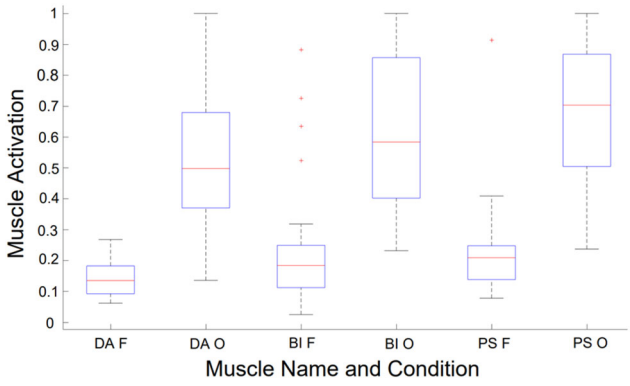


Figure 1. Peak muscle excitation during propulsion on a flat surface (F) and over an obstacle (O) for deltoids anterior (DA), biceps (BI), and pectoralis major (PS).

surface. However, the external rotation (i.e. negative axial rotation) was significantly higher. Given the high SD values for both GH joint angles and muscle activation, these results should be treated carefully. As participants chose their movement approach for the obstacle, the high SD could be due to the variance in technique and strength. Propulsion over an obstacle required a limited GH range of motion compared to flat propulsion. This may be due to the higher levels of control required to complete the obstacle. During propulsion over the obstacle, all muscles showed, on average, over 19% higher peak EMG excitations compared to propulsion on a flat surface. Propulsion over an obstacle may be more strenuous compared to propulsion on a flat surface, as wheelchair users must elevate themselves above the obstacle, counteracting gravity. Indeed, previous studies have found maxima muscle activation of the BI, PS, and DA were significantly higher whilst ascending higher curbs compared to lower curbs (Lalumiere 2013).

4. Conclusions

Overall, GH flexion-extension angles were significantly lower, and GH external rotation angles were significantly higher whilst propelling over an obstacle than over a flat surface, Given the high SD values, it would be beneficial to expand this work by testing more participants. The peak muscle activations were higher during propulsion over an obstacle, indicating that this task is more strenuous than propelling on a flat surface. A perspective is to measure the external efforts, using an instrumented wheel, to also document the GH joint moments.

References

Chow JW, Levy CE. 2011. Wheelchair propulsion biomechanics and wheelers' quality of life: an exploratory review. Disabil Rehabil Assistive Technol. 6(5):365–377.

Cowan RE, Boninger ML, Sawatzky BJ, Mazoyer BD, Cooper RA. 2008. Preliminary outcomes of the SmartWheel users' group database: a proposed framework for clinicians to objectively evaluate manual wheelchair propulsion. Arch Phys Med Rehabil. 89(2):260–268. doi:10.1016/j.apmr.2007.08.141.

Koontz AM, Roche BM, Collinger JL, Cooper RA, Boninger ML. 2009. Manual wheelchair propulsion patterns on natural surfaces during start-up propulsion. Arch Phys Med Rehabil. 90(11):1916–1923. doi:10.1016/j.apmr.2009.05.022.

Lalumiere M, Gagnon DH, Hassan J, Desroches G, Zory R, Pradon D. 2013. Ascending curbs of progressively higher height increases forward trunk flexion along with upper extremity mechanical and muscular demands in manual wheelchair users with a spinal cord injury. J Electromyogr and Kinesiol. 23(6):1434–1445. doi:10.1016/j.jelekin.2013.06.009.

Nagy J, Winslow A, Brown J, Adams L, O'Brien K, Boninger M, Nemunaitis G. 2012. Pushrim kinetics during advanced wheelchair skills in manual wheelchair users with Spinal Cord Injury. Top Spinal Cord Inj Rehabil. 18(2):140–142. doi:10.1310/sci1802-140.

Rouvier T, Louessard A, Simonetti E, Hybois S, Bascou J, Pontonnier C, Pillet H, Sauret C. 2022. Manual wheelchair biomechanics while overcoming various environmental barriers: a systematic review. PLoS One. 17(6): e0269657. doi:10.1371/journal.pone.0269657.

Smith EM, Giesbrecht EM, Mortenson WB, Miller WC. 2016. Prevalence of wheelchair and scooter use among community-dwelling Canadians. Physical Therapy. 96(8): 1135–1142. doi:10.2522/ptj.20150574.

Walford SL, Requejo PS, Mulroy SJ, Neptune RR. 2019. Predictors of shoulder pain in manual wheelchair users. Clin Biomech. 65:1–12. doi:10.1016/j.clinbiomech.2019.03.003.

World Health Organization. 2018. Assistive technology. https://www.who.int/news-room/fact-sheets/detail/assistive-technology.

Wu G, van der Helm FCT, Veeger HEJD, Makhsous M, Van Roy P, Anglin C, Nagels J, Karduna AR, McQuade K, Wang X, et al. 2005. ISB recommendation on definitions of joint coordinate systems of various joints for the reporting of human joint motion—Part II: shoulder, elbow, wrist and hand. J Biomech. 38(5):981–992. doi:10.1016/j.jbiomech.2004.05.042.

KEYWORDS Kinematics; glenohumeral joint; wheelchair; obstacles; muscle activation

lauren.henry@univ-eiffel.fr

Evaluation of knee unloader braces and brace designing challenges – a literature review

L. Boillereaux[a,b], S. Le Floc'h[a], A. Kheddar[b] and F. Jourdan[a]

[a]Laboratoire de Mécanique et Génie Civil, Université de Montpellier, France; [b]Laboratoire d'Informatique, de Robotique et de Microélectronique de Montpellier, Université de Montpellier, France

1. Introduction

To relieve patients suffering cartilage diseases and to facilitate the rehabilitation after an operation, it is necessary to unload the knee during daily living activities. Medical doctors used to prescribe knee orthosis to relieve their patients. These devices are based on various concepts to unload one or both knee's compartments by reducing the tibiofemoral contact force (TFCF) or the abduction-adduction moment. Nevertheless, because it is difficult to measure articular forces *in vivo*, few studies evaluated knee braces in terms of TFCF reduction. This leads us to question their effectiveness. In this paper, we then raises two objectives: to list the various quantitative methods for knee brace evaluation methods in terms of TFCF reduction and then to highlight the current challenges in the design of unloader braces.

2. Methods

This literature review was carried out using the following databases: Scopus, World of Science, Science direct and Google scholar.

The following keywords were used to review the various TFCF evaluation methods: 'tibiofemoral contact force evaluation', 'tibiofemoral contact force *in vivo*'. The brace evaluation results were obtained by typing the keywords 'knee brace evaluation', 'unloader brace evaluation', 'unloader brace effectiveness', 'tibiofemoral contact force reduction'. Finally, 'knee kinematics', '*in vivo* knee kinematics' and 'skin brace interaction' were used to obtain data on knee kinematics *in vivo* and interaction between skin and orthotic devices.

3. Results and discussion

3.1. Methods for quantitative evaluation of the tibiofemoral contact forces

Several methods for qualitative or quantitative evaluation of the effectiveness of knee braces have been developed and reviewed (perception based score, joint geometry modification, knee abduction moment modification) (Parween et al. 2019).

Quantitative measurement of the TFCF have recently been carried out using tools that are still under development in many laboratories. *In vivo*, the TFCF is estimated associating musculoskeletal models and measured electromyography (EMG) signals, associated to Motion Capture (Mocap) measurements (Zeighami et al. 2018). *Ex vivo*, cadaveric knees are placed in a test rig and instrumented with pressure plates. Muscular forces are created with pneumatic cylinders. (Hale et al. 2018).

3.2. Evaluation of knee braces tibiofemoral contact force reductions results

Various mechanical knee braces have been tested using the *in vivo* method presented above.

It shows that the reduction of the tibiofemoral contact force peak by knee braces is weak with orthosis that are just trying to create abduction-adduction moment (max 5% with the Unloader Brace provided by Ossür during gait (Hall et al. 2019)).

Unloader braces are presenting better results in terms of contact force reduction (around 40% for the prototype of Stoltze et al. (2021) and 25% for the Levitation Brace commercialized by Spring Loaded (Bishop et al. 2023). However, these braces are designed to unload the knee during one specific movement and sometimes are effective during one phase of this movement (e.g. first peak of the stance phase during gait).

3.3. Major issues and limiting points in knee brace design

It is necessary to design more efficient orthoses allowing the reduction of the TFCF. However, other

Authors	Method (in/ex vivo)	Movement
Zhou et al.	MRI + fluoroscopy	Squat
Dreyer et al.	Instrumented implants + EMG + Mocap + Fluoroscopy	Downhill walking, squat, sit to stand, stair descent
Taylor et al.	Instrumented implants + fluoroscopy + EMG + Mocap + force plates	Downhill/level walking, squat sit to stand, stair descent
Li and al.	Dual fluoroscopy + CT scans	Box squat, seated knee extension
Kozanek and al.	MRI + Fluoroscopy + force plates (stance phase)	Treadmill walking
Zeighami and al.	Mocap + Force plates + musculoskeletal model	Treadmill walking
Thomeer and al.	MoBix system : Fluoroscopy Mocap + Forces plates	Open-chain flexion,standing, stair descent/ascent, sevel/sownhill walking,

Figure 1. Methods used to determine knee kinematics and contact locations during daily living activities.

parameters must be considered when designing such device:

- The non-linearity of the contact force,
- The patient specific TFCF profile,
- Skin and soft tissue sensitivity to prolonged pressure (pressure sores),
- The complex fine 6 degrees of freedom (6dof) kinematics of the knee, patient specific.

The fine kinematic of the knee according to the 6 degrees of freedom can be determined experimentally, using complex medical imaging devices, recently developed, presented in Figure 30 (Kozanek et al. 2009; Taylor et al. 2017; Zeighami et al. 2018; Thomeer et al. 2021; Zhou et al. 2021; Dreyer et al. 2022; Li et al. 2022)

4. Conclusions

Knee brace effectiveness is complex to evaluate in terms of tibiofemoral contact force reduction. New TFCF measurement methods (*in vivo*) are in development and few braces have been tested using it. Results of this studies are showing that the contact force reduction is generally small. It seems that orthoses aiming to reduce muscular activity have the best results.

Several issues must be considered when designing an orthosis, such as the interaction of the device with the soft tissues or the kinematic constraints imposed by the system at the knee joint.

In conclusion, *in vivo* methods for measuring contact forces and joint kinematics are still under development. Much progress remains to be made both in the design of unloading orthoses and in the quantitative evaluation of their effectiveness.

References

Bishop EL, McGibbon CA, Kuntze G, Clark ML, Cowper-Smith C, Ronsky JL. 2023. Tricompartment offloader knee brace reduces contact forces in adults with multicompartment knee osteoarthritis. J Orthop Res. 41(9): 1925–1933. jor.25556. doi:10.1002/jor.25556.

Dreyer MJ, Trepczynski A, Hosseini Nasab SH, Kutzner I, Schütz P, Weisse B, Dymke J, Postolka B, Moewis P, Bergmann G, et al. 2022. European Society of Biomechanics S.M. Perren Award 2022: standardized tibio-femoral implant loads and kinematics. J Biomech. 141:111171. doi:10.1016/j.jbiomech.2022.111171.

Hale R, Green J, Hausselle J, Saxby D, Gonzalez RV. 2018. Quantified in vitro tibiofemoral contact during body-weight back squats. J Biomech. 79:21–30. doi:10.1016/j.jbiomech.2018.07.002.

Hall M, Diamond LE, Lenton GK, Pizzolato C, Saxby DJ. 2019. Immediate effects of valgus knee bracing on tibiofemoral contact forces and knee muscle forces. Gait Posture. 68:55–62. doi:10.1016/j.gaitpost.2018.11.009.

Kozanek M, Hosseini A, Liu F, Van de Velde SK, Gill TJ, Rubash HE, Li G. 2009. Tibiofemoral kinematics and condylar motion during the stance phase of gait. J Biomech. 42(12):1877–1884. doi:10.1016/j.jbiomech.2009.05.003.

Li P, Li C, Wang C, Kernkamp WA, Yang C-H, Hu H, Tsai T-Y. 2022. In-vivo tibiofemoral kinematics of the normal knee during closed and open kinetic chain exercises: a comparative study of box squat and seated knee extension. Med Eng Phys. 101:103766. doi:10.1016/j.medengphy.2022.103766.

Parween R, Shriram D, Mohan RE, Lee YHD, Subburaj K. 2019. Methods for evaluating effects of unloader knee braces on joint health: a review. Biomed Eng Lett. 9(2): 153–168. doi:10.1007/s13534-019-00094-z.

Stoltze JS, Pallari J, Eskandari B, Oliveira ASC, Pirscoveanu CI, Rasmussen J, Andersen MS. 2021. Development and functional testing of an unloading concept for knee osteoarthritis patients: a pilot study. J Biomech Eng. 144(1):011007. doi:10.1115/1.4051847.

Taylor WR, Schütz P, Bergmann G, List R, Postolka B, Hitz M, Dymke J, Damm P, Duda G, Gerber H, et al. 2017. A comprehensive assessment of the musculoskeletal system: the CAMS-Knee data set. J Biomech. 65:32–39. doi:10.1016/j.jbiomech.2017.09.022.

Thomeer L, Guan S, Gray H, Schache A, de Steiger R, Pandy M. 2021. Six-degree-of-freedom tibiofemoral and patellofemoral joint motion during activities of daily living. Ann Biomed Eng. 49(4):1183–1198. doi:10.1007/s10439-020-02646-2.

Zeighami A, Aissaoui R, Dumas R. 2018. Knee medial and lateral contact forces in a musculoskeletal model with subject-specific contact point trajectories. J Biomech. 69: 138–145. doi:10.1016/j.jbiomech.2018.01.021.

Zhou C, Zhang Z, Rao Z, Foster T, Bedair H, Li G. 2021. Physiological articular contact kinematics and morphological femoral condyle translations of the tibiofemoral joint. J Biomech. 123:110536. doi:10.1016/j.jbiomech.2021.110536.

KEYWORDS Unloader brace; contact force reduction; knee kinematics

lea.boillereaux@umontpellier.fr

Mechanical performances of DREEVEN, a novel motorization unit for custom knee orthosis

L. Colas, K. Giraud-Esclasse and R. Temporelli

REEV SAS, Toulouse, France

1. Introduction

In Europe and the United States, 75 million people suffer from walking disorders: stroke, osteoarthritis, arthritis, sarcopenia, poliomyelitis, cerebral palsy, multiple sclerosis, myopathies, etc. These motor disorders cause increased muscle and/or joint weakness. To reduce the progressive loss of locomotor faculties caused by these pathologies, the health authorities recommend a regular and adapted physical activity: walking. To improve the daily life of people with walking disabilities, restore their mobility and extend their walking perimeter, focusing on the knee joint, REEV develops the DREEVEN solution (Temporelli 2022), a motorization unit for custom knee orthosis.

If many assistive lower limb orthosis are already available on the market (Dollar and Herr 2008), the motorized ones are serial (not custom) exoskeletons which is a problem considering that most people needing motor assistance require custom orthosis. In addition, as presented in (Bernhardt 2006), patients tend to think that actual serial exoskeletons don't cover all desired use cases, are unwieldy and the mass/volume is not well accommodated on the human body. For these reasons existing serial exoskeletons are not suitable and unattractive for a daily use. In addition, they are expensive; hence, they are mostly bought by dedicated rehabilitation centres. Thus, people lack access to the daily assistive rehabilitation/help they require today.

The DREEVEN solution presented in this article is based on an unobtrusive electrohydraulic transmission which can be integrated on any custom orthosis thanks to its specific mechanical interface designed to fit the morphology of the patient. The solution consists in a motorized hydraulic emitter-receptor cylinder derived from (Temporelli 2019). Two hydraulic hoses link the emitter part (the power unit) and the receptor part (transmission mechanism at lower limb level). This principle allows to relocate and spread the mass and volume of the power unit to an appropriate area of the human body (e.g. close to the center of mass for a better body balance) and allows designing a light and slim transmission mechanism at lower limb level. The design of the mechanical transmission also allows to transmits eccentric and concentric torque to the knee, therefore assisting the patient during the entire gait cycle. For these reasons, the DREEVEN solution allows to power custom knee orthosis with an adequate assistive torque and an adequate bandwidth on the knee in various use cases whilst being slimer and lighter than other marketed systems.

Here, we present the mechanical architecture of the DREVEEN solution and the experimental investigation of its mechanical performances: torque capacities and bandwidth.

2. Methods

2.1. Dimensioning and target performances

Understanding the kinematics and kinetics of the lower limbs during the different daily activities is fundamental for developing a robotic orthosis. We established a typical profile of a 80 kg patient with a healthy gait and focused our attention on walking, ascending/descending stairs and sit-to-stand/stand-to-sit movements. Grounding our calculation on the dataset presented in Reznick (2021), we defined our requirements as follows: we aim to assist 30% of the knee torque developed by a 80 kg user (approximation of the mean weight of men in Europe) during a 1-s sit-to-stand movement lasting. The worst load case occurs at the 110° knee flexion where a 110 Nm knee torque is required. Considering the 30% assistance objective that was based on an estimation of the best power-mass ratio respecting the allocated esthetic volume envelope, and the targeted speed, the system was designed to be able to produce a 33 Nm torque at a 0.5 Hz frequency.

2.2. Mechanical design

As previously stated, existing exoskeletons tend to be heavy, bulky, expensive and lack power or use cases coverage. We aim to overcome these drawbacks with our design. After consideration of existing exoskeletons mechanical designs (Shi 2019), we designed a novel mechanical transmission for lower limb exoskeleton inspired by the electromechanical clutch actuator presented in Temporelli (2019). The presented design relies on an hydraulic transmission functioning as described in Figure 1.

The system is divided in two parts: the emitter (the power unit installed in a bag pack close to the center of mass) and the receptor unit (the transmission mechanism installed on a lower limb custom orthosis). At the emitter level, the motor drives in

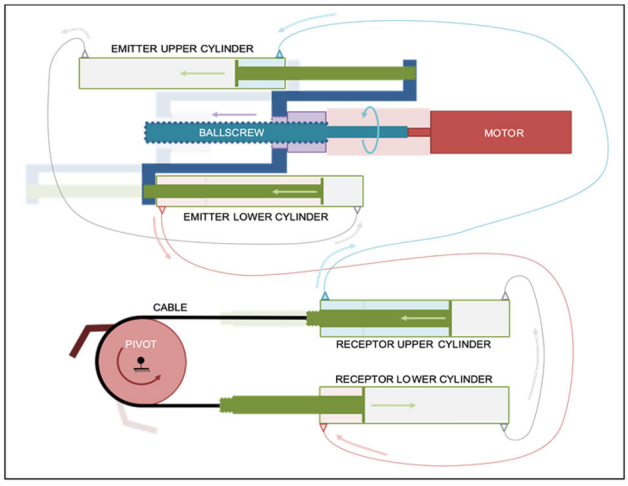


Figure 1. Mechanical architecture of DREEVEN.

rotation a ball screw that pushes the ball nut solidary to two pistons using mechanical blades, therefore opening and closing the emitter cylinders. The small chamber of each emitter cylinder is connected to the small chamber of a receptor cylinder that gets opened or closed by the oil transport, and the pistons in their travels pull on a cable therefore resulting in the rotation of the knee pivot. As the receptor is fixed on a thigh orthosis and the knee pivot is linked to a calf orthosis, the motor rotation leads to a torque being transmitted to the knee, therefore assisting the patient's gait.

The 'Results and Discussion' section describes the test procedure that allowed us to validated the defined mechanical objectives.

3. Results and discussion

In order to evaluate its mechanical performances, the first prototype of the DREEVEN solution was placed on a test bench. A high stiffness spring was attached to it with a cable, creating a return force when the pivot rotated.

A simple back and forth open-loop control was applied with 3 different reference shapes (steps, ramp and sweep sinusoid).

The test bench and experimental results of the 1 Hz loaded step test are presented in Figure 2. The DREEVEN developed a 34.06 Nm torque on the pivot and its response was fast enough to sustain a chirp up to 1 Hz, therefore confirming the system's capacity to reach the desired bandwidth and torque, thus whilst keeping the mass and volume of the mechanical assembly to 2170 cm3 and 1,5kg in the backpack and 1461 cm3 and 1,1kg on the leg These performances can be compared to [Sanchez 2019] and classify

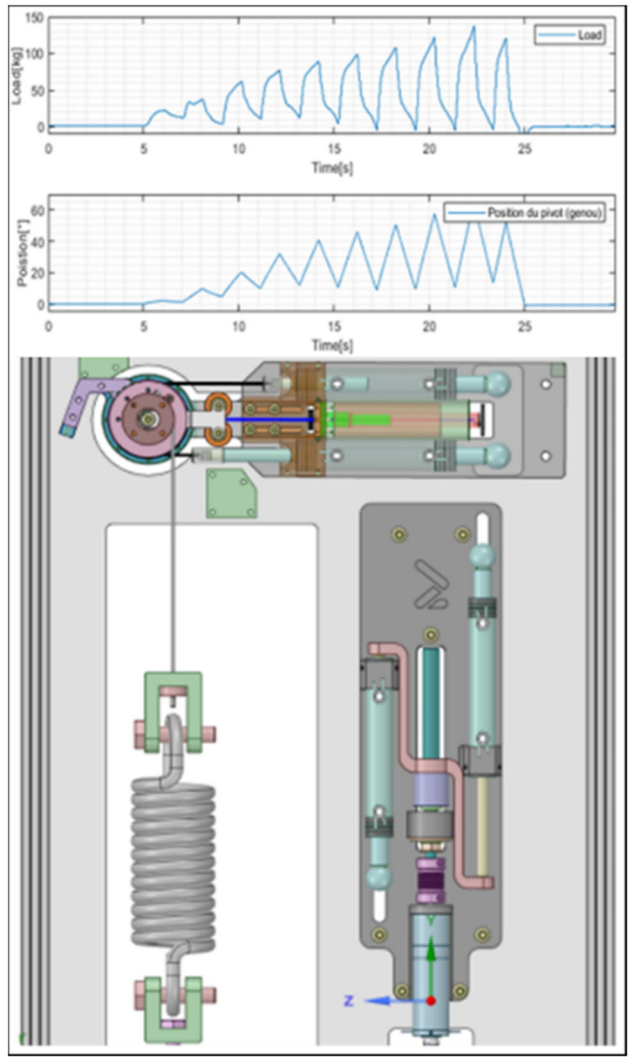


Figure 2. DREEVEN on its test bench and step loaded cycle test results.

DREEVEN has a light exoskeleton for its application and encourages us to follow our development of differentiating features by implementing a novel robust and adaptative control law.

4. Conclusions

We present DREEVEN, a novel concept overcoming the drawbacks of the lower-limb assistive exoskeletons present on the market in order to bring a novel assistive solution to the patients. The electro-hydraulic transmission divided in a power unit placed in a backpack and a receptor mechanism interfaced with a custom leg orthosis allows a better mass spreading and power density. An experimental validation phase allowed us to test the mechanical performances of the system, confirming its ability to assist 30% of the knee torque developed by a 80 kg patient during a 1 s long sit-to-stand movement.

References

Bernhardt KA, Irby SE, Kaufman KR. 2006. Consumer opinions of a stance control knee orthosis. Prosthet Orthot Int. 30(3):246–256. doi:10.1080/03093640600618818.

Dollar AM, Herr H. 2008. Lower extremity exoskeletons and active orthoses: challenges and state-of-the-art. IEEE Trans Robot. 24(1):144–158. doi:10.1109/TRO.2008.915453.

Reznick E, Embry KR, Neuman R, Bolívar-Nieto E, Fey NP, Gregg RD. 2021. Lower-limb kinematics and kinetics during continuously varying human locomotion. Sci Data. 8(1):282. doi:10.1038/s41597-021-01057-9.

Sanchez-Villamañan MDC, Gonzalez-Vargas J, Torricelli D, Moreno JC, Pons JL. 2019. Compliant lower limb exoskeletons: a comprehensive review on mechanical design principles. J Neuroeng Rehabil. 16(1):55. doi:10.1186/s12984-019-0517-9.

Shi D, Zhang W, Zhang W, Ding X. 2019. A review on lower limb rehabilitation exoskeleton robots. Chin J Mech Eng. 32(1):1–11. doi:10.1186/s10033-019-0389-8.

Temporelli R, Boisvert M, Micheau P. 2019. Control of an electromechanical clutch actuator using a dual sliding mode controller: theory and experimental investigations. IEEE/ASME Trans Mechatron. 24(4):1674–1685. doi:10.1109/TMECH.2019.2919673.

Temporelli R. 2022. U.S. Patent Application No. 17/826,157.

KEYWORDS Exoskeleton; biomechanics; control; mechatronics; medical robotics

laurence.colas@reev.care

Numerical simulation of medical compression stockings for venous and lymphatic disease treatment

I. Pita Miguélez, D. Soulat, X. Legrand and A. R Labanieh

Laboratoire GEMTEX, ENSAIT Roubaix – Université de Lille, France

1. Introduction

Lymphoedema and chronic venous insufficiency are among the most common diseases affecting the lower limbs of adults. Compression therapy is the cornerstone of their prevention and treatment, aiming to improve venous and lymphatic return and reduce oedema. Thanks to the manufacturing techniques and their unique structures, compression products can deliver controlled pressure in different areas of the extremity. The different compression zones are obtained by adjusting the manufacturing parameters. In the case of the leg, the effect is greatest at the ankle, where the structure is most compact, and gradually decreases towards the top of the garment. (Kankariya 2022).

Currently, there are different methods to determine the compression exerted by the garment. In addition to direct measurements using pressure sensors, and experimental approaches based on Laplace's law (Siddique et al. 2022), numerical calculations using finite elements are attracting great interest (Lu et al. 2021; Ye et al. 2022). This type of simulation is carried out using digital twins of the limb and the textile. By bringing them into contact, it is possible to determine the pressure distribution and the effect of the garment on venous and lymphatic flow.

While the models of human twins evolve to offer accurate representations of the body tissues, the textile simulations are often based on simple approaches.

The aim of the present work is therefore to offer a new perspective to the modelling of medical compression stockings; the aim is to develop an innovative numerical model that integrates the different components of the knitted structure, highlighting the importance of the production parameters in their final mechanical behaviour.

2. Methods

To design an accurate numerical model of the compression stocking, it is important to study its knitted structure and mechanical properties. For this purpose, tests are carried out on the three primary compression zones of the product: ankle, calf and thigh. After that, the numerical twin of the textile can be designed. The compression distribution can be determined when coupled with the numerical twin of the leg.

2.1. Characterisation of the medical compression stocking

For characterisation, samples from the three compression zones are knitted with a cylindrical shape, similar to that of the real product. The structural properties are determined from the information provided by the manufacturer and by microscopic analysis; the mechanical properties are studied through tensile tests.

2.1.1. Identification of structural parameters

The structural properties of each compression zone determine its mechanical behaviour. This indicates that each zone will have a specific structure according to its mechanical requirements.

The European Standard for compression products (SIST-TP CEN/TR 15831:2009) specifies that the raw material is an elastic yarn, also known as a covered yarn, obtained by overlaying an elastic polyurethane core with other types of fibre (cotton or polyamide). It also specifies the insertion of an inlaid covered yarn in each course of the knitted structure (Figure 1a). This results in a complex structure, based on two components: the base yarn creating the knit, responsible of the shape and comfort, and the inlay yarn, responsible of the compression.

The production parameters are adjusted to obtain a compression that gradually varies along the garment and a specific knitted structure is created.

To complement the manufacturer's information, the samples are analysed under a microscope. (Olympus DSX1000) (Figure 1b,c). The number of courses and wales per cm, the yarn tex for the knit (base yarn) and inlay yarn, and the stitch length and

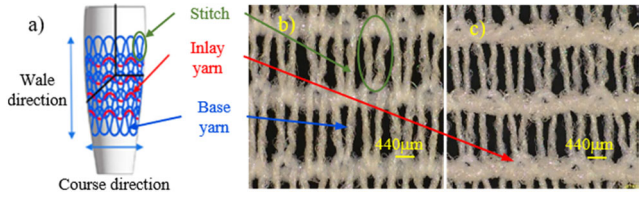


Figure 1. Knitted structure of a medical compression stocking: (a) schematic representation, (b) front side of the calf zone under a microscope, (c) back side of the calf zone under a microscope.

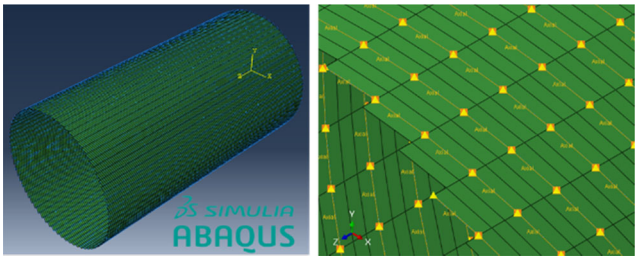


Figure 2. Numerical model of the ankle part of the medical compression stocking.

density are the parameters that define the knitted structure.

2.1.2. Identification of mechanical parameters

To conduct the mechanical characterisation of the compression zones, a tensile test is performed on the cylindrical specimens using a Zwick dynamometer with a 100 N sensor. As required by the NF G 30-102 standard, the products are previously massaged on a normalized wooden leg (Hohenstein), to simulate the wearing over a day. During the test, a sensor located in the central part of the upper jaw registers the force variation associated with the change in perimeter. In addition to the stress-strain curves obtained from the test, the protocol allows the determination of the compression for each perimeter, based on Laplace's law.

Besides, tensile tests are also performed in inlay yarns extracted from medical compression stockings.

2.2. Finite element simulation

After the characterisation of the medical compression stocking, it is possible to design the numerical model. The choice of a hybrid model allows the dissociation of the two components of the knitted structure: the knit (base yarn), and the inlay yarn (Nasri et al. 2022).

The knit is represented by shell elements, in the form of a cylinder with the dimensions of each of the compression zones. Their mechanical properties are defined by the results of the tensile test on the cylindrical specimens.

The inlay yarn is represented by connectors, which, according to the structural and production parameters, describe a helix along the cylinder. Their mechanical properties will be determined by the results of the test on the yarns extracted from the compression product.

The model is coded in Python (Spyder) to be executed in the software Abaqus (Simulia, Dassault Systems) (Figure 2).

3. Results and discussion

The presented characterisation of the compression stockings allows the design of a numerical model, in accordance with the production parameters.

The structural parameters of each compression zone define the geometry of the model through its elements. The distribution of inlay yarn, the main responsible of the compression, will be specific to each zone. This way, we can differentiate the part of the ankle, calf and thigh.

As for the mechanical characterisation, the results of the tensile tests allow us to define the properties of the shell elements for the knit, and the connectors for the inlay yarn. Future work will focus on the integration of these properties in the model, and the validation of the results obtained from the simulation by comparison with the experimental ones.

Further analysis is also suggested to identify the impact of each element on the final behaviour of the medical compression stocking.

4. Conclusions

This study proposes a novel finite element model of a medical compression stocking, based on its knitted structure. It constitutes the first step towards linking the mechanical behaviour of a compression product to its structural parameters. Enriching this model will lead to a better comprehension of how the production influences the behaviour of the final product. By coupling the model with limb twins, it will be possible to obtain the distribution of the compression effect along the leg. This combination will allow to adapt the design and production of compression products to meet the specific needs of each patient.

References

Kankariya N. 2022. Material, structure, and design of textile-based compression devices for managing chronic edema. J Ind Text. 52:152808372211188. doi:10.1177/15280837221118844.

Lu Y, Zhang D, Cheng L, Yang Z, Junyan Li. 2021. Evaluating the biomechanical interaction between the medical compression stocking and human calf using a highly anatomical fidelity three-dimensional finite element model. Text Res J. 91(11–12):1326–1340. doi:10.1177/0040517520979743.

Nasri M, Abbassi F, Garnier C, Labanieh AR, Dalverny O, Zghal A. 2022. Analysis of woven fabrics forming through a comparison between discrete elastic and hypoelastic approaches based on mesoscale structure. Compos Struct. 284:115149. doi:10.1016/j.compstruct.2021.115149.

Siddique HF, Kus Z, Militký J, Havelka A, Mazari AA, Lubos H. 2022. Development of new mathematical models and their comparison with existing models for the prediction of compression pressure using the cut-strip method. Text Res J. 92:004051752210887. doi:10.1177/00405175221088747.

Ye C, Liu R, Wu X, Liang F, Ying MTC, Lv J. 2022. New analytical model and 3D finite element simulation for improved pressure prediction of elastic compression stockings. Mater Des. 217:110634. doi:10.1016/j.matdes.2022.110634.

KEYWORDS Medical compression stocking; mechanical behaviour; finite element simulation; knitted fabric; lymphatic and venous pathologies

ines.pita-miguelez@ensait.fr

Objective assessment of facial mimicry using motion capture for patient follow-up

F. Marcellin[a,c], E. A. Rodríguez M[a,c], H. Leturger[a,c], E. Colin[a,b,c], F.-R. Sarhan[a,b,c] and S. Dakpé[a,b,c]

[a]CHIMERE – UR 7516 UPJV, Amiens, France; [b]Service de Chirurgie Maxillo-Faciale CHU Amiens-Picardie, Amiens, France; [c]Institut Faire Faces, Amiens, France

1. Introduction

Facial mimicry is most commonly analysed clinically in deficit situations, with facial palsy being the most prevalent pathological condition. Peripheral facial palsy refers to the partial or total loss of function in certain facial muscles due to damage to the facial nerve, which can have various aetiologies. Current methods of facial movement analysis rely on clinical assessment, but quantitative methods such as motion capture have been developed on an experimental basis (Zhou and Hu 2008). Several studies have attempted to overcome the lack of objective, reproducible, and sensitive measures for facial movement assessment using these methods (Hontanilla and Aubá 2008; Sforza et al. 2010). Here, our method uses a larger set of markers and the normalised displacement as feature of interest. The primary objective of this research is to use motion capture to measure marker displacement amplitudes, allowing patient monitoring and comparison with reference values obtained from healthy individuals.

2. Methods

One patient with left facial palsy was recruited. She underwent surgery (hypoglossal facial anastomosis) at the end of February 2022 to rehabilitate her facial palsy. A few days before, she performed an initial motion capture acquisition. The follow-up acquisitions were made after 6 months (September 2022) and 12 months (February 2023). These acquisitions followed the same protocol as Sarhan et al., 2023. (Figure 1). She performed five movements: (M1) simple eyelid closure, (M2) forced eyelid closure, (M3) labial protrusion on the [o] sound, (M4) labial protrusion on the [pμ] sound, and (M5) a wide smile revealing the teeth. During the first 6 months, the patient received botulinum toxin injections in May 2022 on the right side of the face, but did not receive any injection between the 6th and 12th months. Movements were recorded using

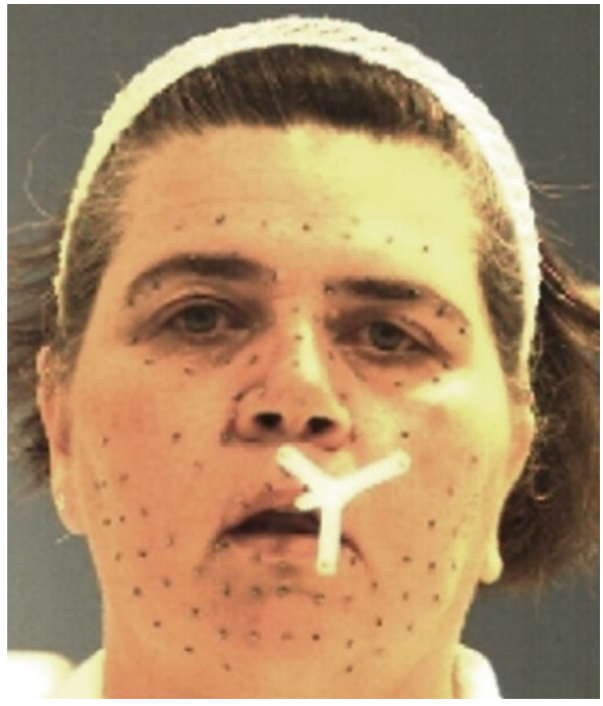


Figure 1. Markers placement and maxillary mouthpiece defining orthonormal reference frame.

a 10-camera Vicon Vantage system (Oxford Metrics, Oxford, UK) recording at 100 Hz.

The healthy reference was calculated using data previously obtained in 30 healthy volunteers (11 men (26.05 ± 2.58 years old) and 19 women (25.40 ± 3.15 years old)). From these sessions, the data were labelled and extracted. To calculate the normalised mean displacement, first, we changed the reference frame from Vicon to maxillary (Figure 1). After that, we used 1D interpolation to bring all the acquisitions to the same number of samples, in a second step, we normalised the displacement from 0 to 1 with respect to the maximum displacement recorded for the subject. The same method was used to calculate the normalised mean displacement for the patient. The data are represented in a graph named Faciograph. For this graph, we reorganised the normalised displacement to show the markers on their corresponding side of the face (mirror view of the face). Finally, the normalised abnormality score was determined by calculating the sum of the absolute values of the differences between the healthy reference and the patient's data (Rodriguez et al. 2023).

3. Results and discussion

Figure 2, named 'Faciograph', shows the mobility tracking of the movement of the wide smile uncovering the teeth (M5) at 12 months. It shows the normalised mean displacement of each marker for the 2

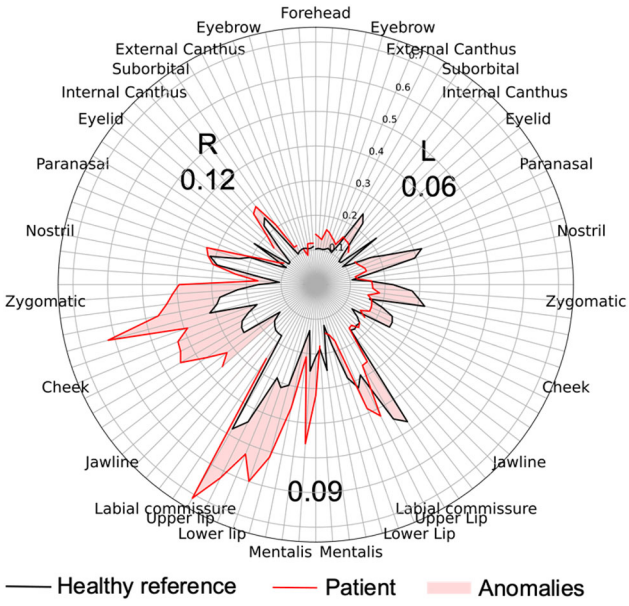


Figure 2. Faciograph for M5 in the 12th month.

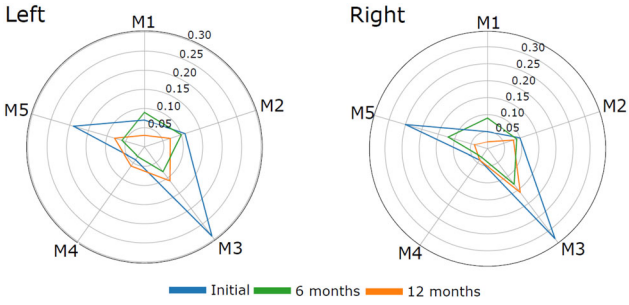


Figure 3. Follow-up of anomaly score by side of face and movement.

populations with the difference between us representing the anomaly. These anomalies are summarised as an average score and by side of the face.

The results of the other movements and follow-ups are detailed Figure 3.

This figure shows us a decrease of the anomalies between the first and the second acquisition and then an increase of these anomalies between the second and the third acquisition for the movements 1 and 2 which both concern the closing of the eyes, for the healthy side and the paralysed side. In movement 3, the anomalies decrease only for the whole face. In movement 4, there is a decrease then an increase of the anomaly for the paralysed side, and a stability then a decrease for the healthy side. Finally, for movement 5 there is a decrease in the anomaly between each acquisition for the paralysed side, whereas for the healthy side there is first a decrease, then an increase.

The decrease in the anomaly score between the initial acquisition and the 6th month, but also an increase between the 6th and the 12th month is due to the fact that the patient was treated with botulinum toxin during the first few months and then stopped. This work initially confirms the benefit of surgery for this patient and in a second time the effect of botulinum toxin in the treatment and rehabilitation of facial palsy (De Sanctis Pecora and Shitara 2021). This study was carried out on a single patient. It would therefore be interesting to include more subjects to confirm this work. Another perspective would be to use deep learning to make predictions of healthy movement using models trained on data from healthy volunteers (Rodriguez et al. 2023).

4. Conclusions

Here we describe the use of photo-reflective markers and the 'Faciograph' representation that allowed for a precise and objective analysis of the patient's facial movements, which is important in the context of evaluating the effectiveness of rehabilitation and treatment. It would indeed be valuable to enlarge the sample size of this study to confirm these initial findings and to evaluate the usefulness of this method in larger populations. Overall, this study provides promising insights into the use of biomechanical analysis to follow-up patients with facial palsy.

References

Hontanilla B, Aubá C. 2008. Automatic three-dimensional quantitative analysis for evaluation of facial movement. J Plast Reconstr Aesthet Surg. 61(1):18–30. doi:10.1016/j.bjps.2007.03.037.

De Sanctis Pecora C, Shitara D. 2021. Botulinum toxin type A to improve facial symmetry in facial palsy: a practical guideline and clinical experience. Toxins. 13(2):159. doi:10.3390/toxins13020159.

Rodríguez Martínez EA, Polezhaeva O, Marcellin F, Colin É, Boyaval L, Sarhan F-R, Dakpé S. 2023. DeepSmile: anomaly detection software for facial movement assessment. Diagnostics. 13(2):254. doi:10.3390/diagnostics13020254.

Sarhan F, Olivetto M, Ben Mansour K, Neiva C, Colin E, Choteau B, Marie J, Testelin S, Marin F, Dakpé S. 2023. Quantified analysis of facial movement: a reference for clinical applications. Clin Anat. 36(3):492–502. doi:10.1002/ca.23999.

Sforza C, Mapelli A, Galante D, Moriconi S, Ibba TM, Ferraro L, Ferrario VF. 2010. The effect of age and sex on facial mimicry: a three-dimensional study in healthy adults. Int J Oral Maxillofac Surg. 39(10):990–999. doi:10.1016/j.ijom.2010.05.011.

Zhou H, Hu H. 2008. Human motion tracking for rehabilitation—a survey. Biomed Signal Process Control. 3(1):1–18. doi:10.1016/j.bspc.2007.09.001.

KEYWORDS Motion capture; facial palsy; follow-up; anomaly quantification; rehabilitation

Marcelin.felix-ext@chu-amiens.fr

Reliability assessment of an upper limb manual muscular testing protocol for manual wheelchair users using a hand-held dynamometer

Y. Poulet[a,b], C. Coffin[a], Y. Xu[a], H. Pillet[b] and C. Sauret[a,b]

[a]Centre d'Etudes et de Recherche sur l'Appareillage des Handicapés, Institution Nationale des Invalides, Créteil, France; [b]Institut de Biomécanique Humaine Georges Charpak (IBHGC), Arts et Métiers Institute of Technology, France

1. Introduction

Manual Muscle Testing (MMT) is a tool commonly used to evaluate muscular capacity of individuals in various fields such as rehabilitation, sport, or research. If the use of an isokinetic dynamometer is considered the gold standard for muscle testing (Romero-Franco et al. 2019), it might not be suitable for all manual wheelchair users (MWU), especially because some users cannot sit upright. In that case, using a hand-held dynamometer (HHD) with the patient in a supine position appears as an alternative. Although recent studies have already demonstrated the validity of HHD versus stationary dynamometers in healthy subjects (Roy et al. 2009), such validation has never been carried out on a MWU-adapted protocol.

With the aim of characterizing MWU muscular strength, the goal of this study was to assess the feasibility, validity, reproducibility, and repeatability of a MWU-oriented upper limb MMT protocol.

2. Methods

2.1. Manual muscle testing protocol

The developed protocol covers the integrality of the measurement session, starting with a standardized warm-up composed of 5 min of wheelchair propulsion at a self-selected but active pace, followed by 4 series of 10 sub-maximal concentric contractions analytically recruiting the muscle groups to be tested. The MWU then transfers to a rehabilitation table where he lies supine with trunk, waist and both legs strapped, and with a support bar available to its non-tested limb to facilitate stabilization with the aim of reducing compensation. The lever arms (i.e. the distances between joint centers and dynamometer/arm contact points) are then measured by the operator and marked on the skin using a dermographic pencil.



Figure 1. Use of a hand-held dynamometer to test shoulder extension with patient strapped to the table.

Finally, a MicroFet2 dynamometer (Hoggan scientific, USA) is used to measure the patient's force at the previously identified points. For each movement tested, the patient was motivated by the operator. The posture of the patient's arm was standardized as follows:

i. Shoulder flexion/extension (SF/SE): shoulder and elbow flexed at 90° with neutral rotation (Figure 1),
ii. Shoulder adduction/abduction (SAdd/SAbd): shoulder abducted at 45° and elbow flexed at 90°,
iii. Shoulder external/internal rotation (SER/SIR): arm in neutral rotation and forearm in intermediate pronation and elbow flexed at 90°,
iv. Elbow flexion/extension (EF/EE): arm against the trunk, elbow flexed at 90° and forearm supinated.

Considering the potential high fatiguability of MWU, only one successful measurement was performed by muscle group. Additional acquisitions were realized if considered necessary by the operator. Measured forces were finally multiplied by their corresponding lever-arms to obtain torque data in N m.

2.2. Data acquisition

For reproducibility and repeatability assessment, four physiotherapists, 2 men (24 y/o, 1.78 m, 79 kg and 27 y/o, 1.85 m, 97 kg) and 2 women (24 y/o, 1.63 m, 61 kg and 23 y/o, 1.53 m, 42 kg), with no to little prior experience in hand-held dynamometric measurement were enrolled and participated both as subject and operator. After one week of training in the use of the HHD, they all tested each other's dominant arm twice, observing at least a 2-days rest period between tests.

For validity and feasibility assessment, 39 healthy subjects, 15 males and 24 females (age 30.6 ± 10 y/o, height 1.71 ± 0.1 m, mass 66.7 ± 12.2 kg), and 14

Table 1. Torque measured per movement (mean [min-max]), repeatability (s_r) and reproducibility (s_R) standard deviations and global uncertainty in percentage of maximal value (I%max).

Movement	Mean torque (Nm)	s_r	s_R	I%max
SF	48 [18–82]	4,15	2,35	11
SE	61 [28–123]	6,35	2,98	11
SAbd	48 [17–97]	3,94	2,82	10
SAdd	57 [23–127]	8,30	8,33	18
SER	48 [16–90]	3,19	4,94	13
SIR	34 [15–54]	1,91	1,87	10
EF	56 [24–99]	2,54	4,25	10
EE	36 [12–73]	1,63	1,55	6
Overall	N/A	4,00	3,64	11

MWU, 6 males and 8 females (age 55.4 ± 16 y/o, height 1.72 ± 0.1 m, mass 73.9 ± 17.3 kg) were tested.

2.3. Data processing

Repeatability (i.e. the ability of an operator to obtain similar data when performing the same test multiple times) and reproducibility (i.e. the ability of a protocol to produce the same results when carried out by different operators) were characterized by their respective standard deviations s_r and s_R, as described in the ISO standards (ISO 5725-2).

Repeatability and reproducibility were first assessed per movement then averaged. Thus, for each movement, s_r was computed as the mean of the standard deviations of each measurement pair. Similarly, for each movement and each subject, s_R was computed as the standard deviations of the mean of the 3 measurement pairs. The average of these standard deviations over the 4 subjects was finally retained. Then, global uncertainty (I) was computed as described in Equation (1) then expressed as percentage of the maximal value of torque measured (I%max).

$$I = 1.96 * \sqrt{s_r^2 + s_R^2} \quad (1)$$

Finally, for feasibility and validity assessment, the average torque data obtained on the dominant arm of healthy and MWU participants were computed and compared to the few articles in the literature providing torque reference values (Mayer et al. 1994, Harbo et al. 2012) (Figure 2).

3. Results and discussion

Repeatability, reproducibility and uncertainty, results for each movement are gathered in Table 1. Smaller values indicate better repeatability and reproducibility. Figure 2 represents the torque obtained on both healthy subjects and MWU's dominant arm sorted by gender.

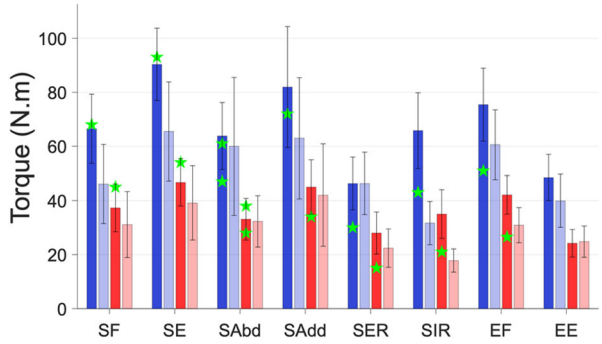


Figure 2. Shoulder and elbow joint torques. Comparison with references values obtained in the literature. (blue: men, red: women, dark: healthy subjects, light: MWU, green stars: reference values).

As expected, worse uncertainty was obtained for the movements in which subjects developed higher torques such as shoulder adduction (I%max =18). In contrast, elbow extension appears to be the most reliable measurement (I%max =6).

Additionally, in accordance with the literature, the detailed results showed that lighter operators had more difficulties in obtaining consistent data from their two measurements, regardless of the movement.

Regarding Figure 2, healthy participants developed torques consistent with data previously reported in the literature and MWU displayed lower strength for most movements. This trend was particularly true for male subjects, but a larger number of MWU should be tested to further investigate this observation.

4. Conclusions

This study assessed the repeatability, reproducibility and validity of a specific protocol using a HHD to measure the maximal isometric strength of MWU's upper limbs. By doing so, it established the feasibility of using such a protocol in a clinical routine and for research involving MWU. However, an overall uncertainty of 11% needs to be considered for individual subject strength analysis using this protocol.

References

Harbo T, Brincks J, Andersen H. 2012. Maximal isokinetic and isometric muscle strength of major muscle groups related to age, body mass, height, and sex in 178 healthy subjects. Eur J Appl Physiol. 112(1):267–275. doi:10.1007/s00421-011-1975-3.

Mayer F, Horstmann T, Rocker K, Heitkamp HC, Dickhuth HH. 1994. Normal values of isokinetic maximum strength, the strength/velocity curve, and the angle at peak torque of an degrees of freedom in the shoulder. Int J Sports Med. 15(SUPPL. 1):S19–S25. doi:10.1055/s-2007-1021105.

Romero-Franco N, Fernández-Domínguez JC, Montaño-Munuera JA, Romero-Franco J, Jiménez-Reyes P. 2019. Validity and reliability of a low-cost dynamometer to assess maximal isometric strength of upper limb: low cost dynamometry and isometric strength of upper limb.J Sports Sci. 37(15):1787–1793. doi:10.1080/02640414.2019.1594570.

Roy JS, MacDermid JC, Orton B, Tran T, Faber KJ, Drosdowech D, Athwal GS. 2009. The concurrent validity of a hand-held versus a stationary dynamometer in testing isometric shoulder strength. J Hand Ther. 22(4):320–326; quiz 327. doi:10.1016/j.jht.2009.04.008.

KEYWORDS Manual muscular testing; hand held dynamometer; manual wheelchair; reproducibility; repeatability

yoann.poulet@invalides.fr

Slow anticipatory postural adjustments during gait initiation in autistic children

A. Benchekri[a,b], R. Tisserand[a,b], C. Bidet-Ildei[b], É. Lemonnier[c], A. Amestoy[d] and L. Fradet[a]

[a]Institut PPRIME, Université de Poitiers, Poitiers, France; [b]CERCA, Université de Poitiers-Tours, Poitiers, France; [c]CRA, CHU Limoges, Limoges, France; [d]INCIA, Université de Bordeaux, Bordeaux, France

1. Introduction

Autism Spectrum Disorders (ASD) are part of neurodevelopmental disorders characterized by persistent deficits in communication and social interaction, and restricted and repetitive behaviors, interests, or activities. Motor disorders are also part of the clinical phenotype of ASD (Mosconi et al. 2015). Yet, because they remain poorly investigated and because the diagnosis still takes time to set up, it remains unknown whether the study of motor tasks may improve the process of identifying ASDs.

By transitioning between posture and movement, gait initiation (GI) is a challenging motor task for balance control. The quality of posture-movement coordination during GI can be estimated by characterizing the anticipatory postural adjustments (APAs), a specific coordination that fulfills two complementary mechanical roles. First, they create a disequilibrium during the loading phase, through a backward and a lateral (towards the future swing foot) displacement of the Center of Pressure (CoP). This initial imbalance provokes a center of mass (COM) motion forward and towards the stance foot. Second, the COM motion is stabilized during the unloading phase, where the CoP moves towards the stance foot. Previous results of APAs performed by ASD children during GI reported a reduced mediolateral (ML) displacement of the CoP, suggesting a reduced ML stability (Fournier et al. 2010). However, the authors did not distinguish the two APAs phases, thus leaving the mechanisms of reduced stability unclear.

The objective of our study was to characterize APAs during GI in ASD and typically developing (TD) children by distinguishing the two phases.

2. Methods

2.1. Population

Twenty-five children diagnosed with ASD (10 girls, 8.7 ± 1.9 years old, 1.33 ± 0.16 m, 28.7 ± 12 kg) were recruited at the Limoges University Hospital and 31 age–matched TD children (15 girls, 8.4 ± 1.4 years old, 1.34 ± 0.90 m, 29.8 ± 6 kg) were recruited in Poitiers.

2.2. Task and equipment

All children completed five GI trials. During each trial, children started from an upright standing posture, with each foot positioned on one force plate and their arms at their side. After at least 3s of quiet standing, children were verbally instructed to start walking at a comfortable speed to reach a ground mark about 3 metres away. Initial position of the feet was marked on the ground to ensure initial position repeatability.

Ground Reaction Forces (GRF) were recorded using two adjacent force plates (Sensix® in Poitiers and Kistler® in Limoges) sampled at 1000 Hz. A Vicon 3D motion-capture system with 20 cameras sampled at 100 Hz recorded the trajectories of four reflective markers placed on foot anatomical landmarks (lateral and medial malleoli, second metatarsal head, and calcaneus).

2.3. Data analysis

The vertical component of the GRF (Fz) extracted from the force plate located underneath the stepping foot was used to identify three key instants (Figure 1, left): APAs Onset (AO), as the first instant when Fz amplitude was larger than its mean +3 SDs measured during the 3s of quiet standing; Foot-Off (FO), as the first instant when Fz was inferior to 2.5% of the child's weight; and Beginning of Unloading (BU), as the instant when Fz was maximal between AO and FO. These instants were then used to compute three durations: the total APAs (between AO and FO); the loading phase (between AO and BU); and the unloading phase (between BU and FO). Also, the trajectory of the CoP was extracted from the two force plates (Figure 1, right). After filtering the CoP using a 2nd order Butterworth filter with a 10 Hz cut-off frequency, its trajectory was characterized by its amplitude, in the AP and ML directions during the loading

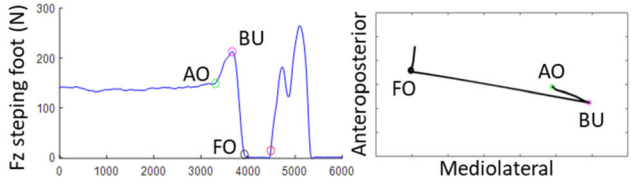


Figure 1. Temporal evolution of the stepping foot GRF during GI with the three key events AO, BU, and FO (left) and a top view of the CoP trajectory during GI (right).

Table 1. Group effect on the different dependent variables.

APAs		Mean (SD) ASD	Mean (SD) TD	*p*-Value (M–W)
APAs duration (ms)		590 (171)	511 (81)	0.05*
Loading	Duration (ms)	306 (157)	292 (59)	0.25
	AP displacement normalized	0.27 (0.26)	0.31 (0.18)	0.16
	ML displacement normalized	0.22 (0.12)	0.32 (0.14)	0.004*
	AP peak velocity ($m\ s^{-1}$)	0.20 (0.14)	0.26 (0.13)	0.06
	ML peak velocity ($m\ s^{-1}$)	0.27 (0.15)	0.45 (0.25)	0.003*
Unloading	Duration (ms)	284 (102)	218 (85)	0.009*
	ML displacement normalized	0.57 (0.31)	0.68 (0.18)	0.07
	ML peak velocity ($m\ s^{-1}$)	1.60 (0.63)	2.04 (0.66)	0.09

SD: standard deviation; M–W: Mann–Whitney test; AP: anteroposterior; ML: mediolateral.

phase, and in the ML direction during the unloading phase. These amplitudes were normalized by the size of the base of support, estimated as the foot length and the feet width, measured from the feet markers, respectively in the AP and ML axes. AP and ML velocity peaks were also extracted during the loading and unloading phases, by taking the maximum of the time-derivative of the trajectory.

2.4. Statistics

Non-parametric Mann–Whitney tests were performed to compare the two groups for each dependent variable, with a threshold set at $p < 0.05$.

3. Results and discussion

ASD children displayed prolonged APAs during GI compared to TD children. This prolongation was principally consecutive to the lengthening of the unloading phase, during which the CoP also tended to move with reduced amplitude and velocity. Despite no duration difference between groups during the loading phase, the CoP of ASD children moved with reduced amplitude and velocity in the ML direction (Table 1).

During the loading phase, laterally moving the CoP towards the future swing foot allows to drive the COM towards the future stance foot, increasing the mediolateral stability conditions at foot-off. With reduced amplitude and velocity during the loading phase, the mechanical consequences of APAs produced by ASD children should drive the COM with reduced velocity towards their stance foot. Consecutively, ASD children may need to wait longer during the unloading phase for the vertical projection of their COM to come close enough to the stance foot to be able to lift the swing foot. This may explain why, in line with previous research, ASD children displayed a prolonged unloading phase with reduced CoP movement compared to TD children (Fournier et al. 2010).

Together, our results suggest that the main difference between ASD and TD children resides in the ML direction for balance control of GI. These results seem to corroborate previous observations reporting differences between ASD and TD children in the ML axis during maintenance of an upright standing posture (Lim et al. 2017). In the control of upright standing postures, it is assumed that hip muscles are mostly responsible for CoP lateral displacements. Therefore, ASD children may have difficulties with hip muscle force production and/or hip muscles coordination control (Lim et al. 2017). Difficulties in coordination control may also come from immature body representations consecutive to altered sensorimotor integration during motor tasks (Assaiante and Schmitz 2009). Among the neural structures involved in motor control, one of the best candidates for ineffective balance control if altered is the cerebellum because it is at the crossroads of ascending and descending sensorimotor functions (Mosconi et al. 2015).

4. Conclusions

In summary, we showed that ASD children have slow APAs during GI. The slowness of these APAs suggest ASD children would end GI with reduced dynamic stability in the mediolateral direction. These balance deficits may be explained by alterations in hip muscles and/or sensorimotor control going through the cerebellum. GI seems to be a relevant paradigm to identify motor alterations in ASD children, yet more research is necessary to disentangle the origins of these impairments.

Acknowledgements

This work was supported by the Region Nouvelle-Aquitaine.

References

Assaiante C, Schmitz C. 2009. Construction des représentations de l'action chez l'enfant : quelles atteintes dans l'autisme ? Enfance. 1(1):111–120. doi:10.3917/enf1.091.0111.

Fournier KA, Kimberg CI, Radonovich KJ, Tillman MD, Chow JW, Lewis MH, Bodfish JW, Hass CJ. 2010. Decreased static and dynamic postural control in

children with autism spectrum disorders. Gait Posture. 32(1):6–9. doi:10.1016/j.gaitpost.2010.02.007.

Lim YH, Partridge K, Girdler S, Morris SL. 2017. Standing postural control in individuals with autism spectrum disorder: systematic review and meta-analysis.J Autism Dev Disord. 47(7):2238–2253. doi:10.1007/s10803-017-3144-y.

Mosconi MW, Mohanty S, Greene RK, Cook EH, Vaillancourt DE, Sweeney JA. 2015. Feedforward and feedback motor control abnormalities implicate cerebellar dysfunctions in autism spectrum disorder. J Neurosci. 35(5):2015–2025. doi:10.1523/JNEUROSCI.2731-14.2015.

KEYWORDS Autism; gait initiation; anticipatory postural adjustment

aurelie.benchekri@univ-poitiers.fr

Speed of sound measurement as a tool for assessing tendon functional recovery after an injury in horses

N. Crevier-Denoix, B. Ravary-Plumioen, F. Munoz-Nates, J.-M. Denoix and P. Pourcelot

INRAE, Ecole Nationale Vétérinaire d'Alfort, Maisons-Alfort, France

1. Introduction

Superficial digital flexor tendon (SDFT) injury is one of the most frequent conditions in racehorses. Management is still controversial, and recovery requires a long period out of work. Rehabilitation based on a gradually increased controlled exercise program is thought to play a prominent part for a successful return to full training. However the outcome of these conditions is still poor and recurrences are frequent (more than 50%; Witte et al. 2016). Ultrasonography is the most used tool to follow-up tendon healing. However, after 4 months, the ultrasonographic images are not so helpful to give a functional assessment of the tendon. Objective tools to assess tendon functional recovery after an injury are lacking.

Speed of sound (SOS) measurement using ultrasonic axial transmission method has been used to follow-up induced SDFT core lesions (Vergari et al. 2012). In this previous study, SOS in the tendon significantly decreased just after lesion induction. From 10 weeks after induction, SOS started to increase, but at the end of the follow-up period (15 weeks) SOS was still significantly lower compared with the healthy tendon (pre-induction) values.

The objective of the present study was to use SOS measurement to follow-up a group of racehorses during their rehabilitation after a spontaneous SDFT injury, and to compare SOS data at the end of rehabilitation with the horses' subsequent performances. It was hypothetized that SOS would be higher at the end of the rehabilitation, or at least would show a larger (positive) variation rate in horses that subsequently had a good outcome.

2. Methods

2.1. Animals

Ten steeplechase racehorses (6 geldings and 4 mares, 4.5 (0.8) years) suffering from a recent (<1 month) fore SDFT injury were included in a rehabilitation program based on controlled exercise only. Ultrasonography was used to initially characterize the lesion and define the maximal severity zone, then for following-up lesion healing through systematic examinations every 4 weeks.

2.2. Speed of sound measurements

SOS measurement (*Tensonics*, axial transmission, 1 MHz) was performed, every 5 weeks in average, during the rehabilitation of each horse. After clipping then depilating the palmar metacarpal area, the probe (1 emitter, 2 receivers 1 cm apart) was placed in an adapted gaiter facing the maximal severity zone as defined ultrasonographically.

During each measurement session, for a given horse (and for each forelimb), SOS between the 2 receivers was measured on 20 (4 series of 5) strides of walk at a fixed and controlled pace (Figure 1).

SOS measurements were performed during 4 trials of 5 strides of walk, the horse being led by hand.

The maximal value of the SOS of each stance phase was determined (Figure 2) then averaged over the 20 strides of each session (i.e. 1 average SOS value per session).

Ten SOS measurement sessions were performed in average on each horse during its rehabilitation program.

2.3. Follow-up of performances

After completion of the rehabilitation program, the 10 horses went back to training (at 4 different trainers). The subsequent outcome (at training, then if applicable, at racing) was followed-up.

Reinjury at training (before racing), or after 3 races or less, was considered 'non successful' (N_S).



Figure 1. The ultrasonic probe is placed facing the maximal severity zone determined during the initial ultrasonographic Examination.

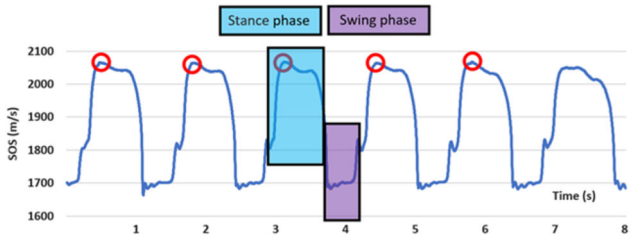


Figure 2. Example of SOS chart. For each of the 4 trials, the first 5 maximal values of SOS (calculated between the 2 probe receivers) during stance were determined then averaged over the 20 strides.

Horses having raced 3 times or more without reinjury were considered 'successful' (S).

2.4. Statistical analysis

Comparison of the SOS variables between the 'S' and the 'N_S' groups was performed using Student *t*-test.

3. Results and discussion

Reinjury appeared at training (before racing) in 4 cases; another horse reinjured after 3 races. For these 5 horses, rehabilitation was considered 'non successful' (N_S). For the other 5 horses, who did 3 to 17 (7.8(5.5)) races without reinjury, rehabilitation was considered 'successful' (S).

Although the final SOS maximal value (value of the last session before returning at training) tended to be higher in the S-group (2067(77) than in the N_S group (1987(100) m/s), this difference was not significant.

Nevertheless, the average SOS variation rate during the last 100 days of rehabilitation was significantly larger in the S-group ($p = 0.006$: +0.09(0.24) m/s/day versus −0.33(0.18) in the N_S group, Table 1).

Table 1. Speed of sound variation rate (m/s/Day) over the last 100 days of rehabilitation in the 10 horses (5 with a 'successful', 5 with a 'non-successful', outcome).

	Successful	Non Successful
	-0.14	-0.33
	0.15	-0.25
	0.01	-0.22
	0.47	-0.22
	-0.04	-0.64
Mean	**0.09**	**-0.33**
S.D.	0.24	0.18

4. Conclusions

Although performance is multifactorial and external factors (e.g. training technique) could have influenced the outcome, these preliminary results are promising. Assessing the functional recovery of a healing tendon is essential to adapt the exercise level and decide when the horse is ready to return to full work.

Further analysis is needed to precise on which minimal period of time the variation rate of SOS is the most relevant as a prognostic indicator of outcome. SOS measurement is a non-invasive, well-tolerated technique. It has the potential of becoming a useful tool for monitoring rehabilitation after tendon injury.

Acknowledgements

Many thanks to Aurélie Montauban, Michèle Prats and Rémi Seznec, for their technical help.

References

Vergari C, Pourcelot P, Ravary-Plumioën B, Dupays AG, Jacquet S, Audigié F, Denoix JM, Laugier P, Mitton D, Crevier-Denoix N. 2012. First application of axial speed of sound to follow-up injured equine tendons. Ultrasound Med Biol. 38(1):162–167. doi:10.1016/j.ultrasmedbio.2011.10.008.

Witte S, Dedman C, Harriss F, Kelly G, Chang YM, Witte TH. 2016. Comparison of treatment outcomes for superficial digital flexor tendonitis in National Hunt racehorses. Vet J. 216:157–163. 2016 doi:10.1016/j.tvjl.2016.08.003.

KEYWORDS Tendinopathy; tendon healing; ultrasound; functional prognosis; equine

nathalie.crevier-denoix@vet-alfort.fr

Using artificial intelligence to improve the lives of wheelchair users

J. Charafeddine[a,b], N. Kicha[a] and E. Monacelli[a]

[a]Université Paris-Saclay-UVSQ; [b]Laboratoire d'Ingénierie des Systèmes de Versailles (LISV EA4048), Vélizy, France

1. Introduction

It is impressive that the virtual wheelchair offers a solution for regaining mobility for people with impairments and that it also offers a training program depending on the user's performance. However, measuring these performances overlooks one factor: the user's posture (Pouvrasseau 2019), which affects his stability and makes him fatigued (Aissaoui et al. 2001). By examining the seated person's behavior and how it relates to muscle fatigue, in this paper we highlight the relationship between wheelchair platform movement and the response of the person sitting on it. We also present a thorough analysis and evaluation of different machine learning algorithms for predicting physical fatigue in a virtual dynamic state scenario. The posture tracking system was implemented in the virtual wheelchair simulator developed at Laboratory of Systems Engineering of Versailles-LISV (Goncalves et al. 2014)

2. Methods

2.1. Data acquisition

We conducted an evaluation of the postural response of eight healthy subjects seated on an immersive simulator (Virtual wheelchair) equipped with a Kinect V2 sensor, which captures parts of the human body at a frequency of 30 Hz, a compact motion platform that reproduces rapid forward and backward movements through a scenario for approximately 10 min of successive ascending and descending slopes generated by the Unity 3D simulator, and a bipolar EMG sensor (Myon 3D) placed on the external oblique muscle of the seated person to measure muscle contraction. The recorded data of muscle activity by EMG sensors and the absolute position relative to the Kinect camera, restored in a CSV format file. Using this data, it is possible to measure the postural response and muscle contraction of the participant using MATLAB.

2.2. Signal processing

The measurements obtained with the EMG sensor must be processed to be usable. For signal processing, we used the root-mean-square method, which is well suited for bipolar EMG sensors because it allows both rectification and smoothing of the signal. They were bandpass filtered between 10 and 500 Hz using a sixth order Butterworth filter. After bandpass filtering, the processed EMG signal was normalized using the maximum voluntary contraction (MVE).

2.3. EMG and muscle fatigue

The Root Mean Square (RMS) values, which are variables related to the amplitude of the EMG signal, and the Median Power Frequency (MPF), which is related to the frequency content of the EMG signal, are often used to evaluate the onset and development of muscle fatigue (Rota 2013).

2.4. EMG classification

The task of moving our wheelchair was repeated three times, and the collected EMG data were divided into training and testing sections. Two sections were used for training the proposed classification model in MATLAB, while one section was used for testing.

(a) Binary indications of fatigue from the user were used to train our model (0 means no fatigue, 1 means fatigue). Thus, a valid set of labels as specified by the user would have the following form: [0,0,0,0,0,0,.,1,1,1,1,1,1,1,1,1], where each label corresponds to a sample detected by the EMG sensor. Therefore, SVM (Super vector machine) and KNN (K-Nearest Neighbors) classifiers can be trained to detect these changes in electrical activity and classify our given EMG signal as representative of a muscle fatigue state or not. This can be achieved by using signal feature extraction techniques (such as power spectral density (PSD), zero crossing rate (ZC), entropy, etc.) to extract relevant features from the EMG signal, which are then used as input to an SVM.

(b) Our model was trained in a different way using the Artificial Neural Networks (ANN-LSTM) (with the XTrain and YTrain data. XTrain stores the binary indications of fatigue from the user the EMG samples and YTrain stores the corresponding EMG label of that sample. The EMG label can be either. non-fatigue or fatigue with a representation of 0 or 1, respectively. The variable XTest stores the test data of the EMG signal classified using the trained neural network, and the estimated label was stored in the variable YPred.

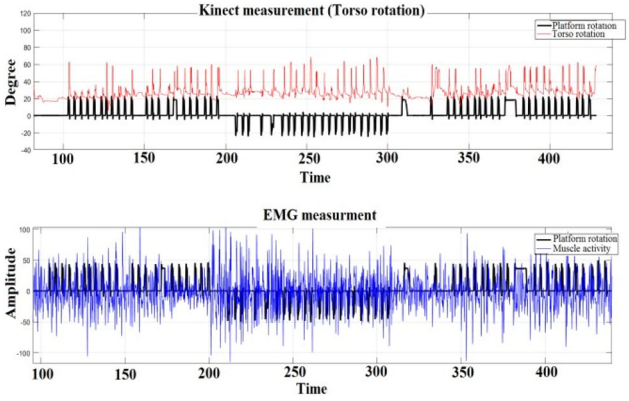


Figure 1. Platform rotation's effect on body movement and EMG measurements.

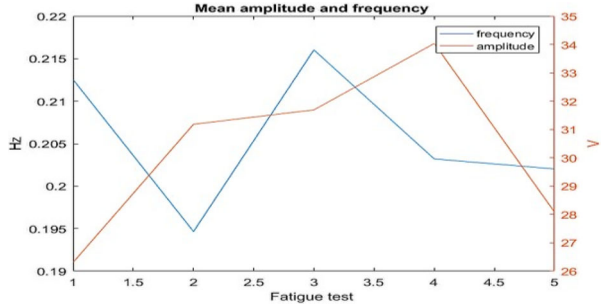


Figure 2. The relationship between frequency content and EMG activity.

The neural model developed here consists of 800 hidden units and trained in an iterative process with epochs of up to 60 iterations. bandpass filtered between 10 and 500 Hz using a sixth order Butterworth filter. After bandpass filtering, the processed EMG signal was normalized using the maximum voluntary contraction (MVE).

3. Results and discussion

(a) Effects of the disorders on postural and muscular behavior: The result presented in the first subgraph (Figure 1) illustrates the relationship between the perturbations of the platform and the measurements acquired by the Kinect as a function of time (seconds). We observe that when the motion imposed by Unity, the platform becomes active and performs backward and forward rotations, which perturbed the camera measurement and shows an amplitude variation over time. This implies a strong relationship between the perturbation motion induced by the platform and the motion induced in the person sitting in the wheelchair, which appears in the balance between torso and platform rotations. that means that the presence of perturbation leads to a loss of balance manifested, among other things, by movements of the upper limbs of this person, which affects his muscle behaviour. The second subgraph of this figure relates the movement of the wheelchair to the EMG data (amplitude in volts as a function of time(s)). We see that the muscle contraction increases proportionally to the rotation of the platform.

Temporal analysis: to better understand the content of this EMG signal, the measurement of the MVE value is used as a reference to evaluate the effects of fatigue on muscle contraction. From the result graph, there is a variation in EMG amplitude when the platform is mobilized, we can conclude that a fast recovery of maximum muscle force indicates that the body has efficiently recovered the energy against muscle fatigue, which means that the muscle is ready to perform another intense effort. In contrast, a slow recovery of maximal muscle force indicates that the body is still fatigued and the muscle (OE) needs more time to recover before it can perform another intense effort.

-Frequency analysis: we carried out fatigue tests, which involved subjecting the sample to varying levels of stress amplitude; which we note variation of EMG activity with frequency content (Figure 2) by calculating average frequency of the EMG power spectrum (MPF), this means that fatigue generally leads to a shift of the EMG power spectrum to lower frequencies, while higher frequencies can provide information about faster and more precise muscle contractions.

The result of this frequency analysis shows that the amplitude of the EMG signal increases with increasing frequency up to the cutoff frequency (fc = 0.217 Hz) and then decreases beyond this frequency. The increase in EMG activity that accompanies the increase or maintenance of frequency content corresponds to greater muscle excitation rather than fatigue. The increase in MPF observed during this exercise can be explained by the activation of fast-twitch muscle fibers involved in high-intensity muscle contractions. Conversely, the frequency of muscle action potentials detected by the EMG signal decreases. This is due to the fact that more easily fatigued muscle fibers tend to discharge more slowly, which may contribute to a decrease in the frequency of the EMG signal.

(b) The results of the training performance of the proposed network have been shown in Table 1.

The accuracy, sensitivity, and specificity of the SVM and KNN algorithms are shown to be 70% in the performance results, but the ANN algorithm

Table 1. Classification performance of models.

Algorithm	Accuracy	Sensitivity	Specificity
SVM%	70	70	70
KNN%	70	70	70
ANN%	85.73	85.73	85.73

stands out with values of 85.73%, suggesting greater predicting capacity.

4. Conclusions

We discussed the postural behavior evaluation performed with the virtual wheelchair using a Kinect v2 camera and EMG sensor. The results show that the wheelchair user becomes unstable when disturbed, which affects his muscle behavior and leads to prolonged fatigue. In the context of muscle fatigue detection, we proposed two methods that allow us to classify the acquired signal into two classes 'fatigue' and 'non-fatigue' using supervised learning techniques such as SVM, KNN and ANN.

At a later stage, after applying the three-dimensional study to the muscles of the upper body, we can infer muscle fatigue from the movement without the need for EMG and develop an improvement strategy.

ORCID

J. Charafeddine http://orcid.org/0000-0001-7732-3578

References

Aissaoui R, Boucher C, Bourbonnais D, Lacoste M, Dansereau J. 2001. Effect of seat cushion on dynamic stability in sitting during a reaching task in wheelchair users with paraplegia. Arch Phys Med Rehabil. 82(2):274–281. 2001 Feb; doi:10.1053/apmr.2001.19473.

Goncalves F, Trenoras L, Monacelli E, Schmid A. 2014. Motion adaptation on a wheelchair driving simulator. 2014 2nd Workshop on Virtual and Augmented Assistive Technology (VAAT). IEEE; p. 17–22. doi:10.1109/VAAT.2014.6799463.

Pouvrasseau F, Charles S, Monacelli E, Routhier F, Malafosse B. 2019. Évaluation posturale sur fauteuil roulant : évaluation de faisabilité de la plateforme Virtual Fauteuil. Neurophysiologie Clinique. 49(6):416. doi:10.1016/j.neucli.2019.10.029.

Rota S, Rogowski I, Champely S, Hautier C, et.al. 2013. Reliability of EMG normalisation methods for upper-limb muscles. J Sports Sci. 31(15):1696–1704. doi:10.1080/02640414.2013.796063.

KEYWORDS Virtual wheelchair; EMG; supervised classifiers; muscle fatigue

jinan.charafedine@lisv.uvsq.fr

Vision-based interface for grasping intention detection and grip selection: towards intuitive upper-limb assistive devices

E. Moullet[a,b], F. Bailly[a], J. Carpentier[b] and C. Azevedo-Coste[a]

[a]CAMIN, INRIA centre d'Université Côte d'Azur, Université de Montpellier, Montpellier, France; [b]WILLOW, INRIA Paris, Département Informatique de l'ENS, Paris, France

1. Introduction

Numerous pathologies may affect upper-limb movements (quadriplegia, stroke, amputation …). In particular, grasping is crucial for many daily activities, and its impairment considerably impacts quality of life and autonomy. Attempts to restore this function may rely on various approaches and devices (functional electrical stimulation, exoskeletons, prosthesis …), and all face two great challenges. First, targeted objects' characteristics are highly variable in shape, weight, and texture, demanding high flexibility from the assistive device in controlling its degrees of freedom (DOFs). Second, individuals with disabilities have a significantly reduced number of DOFs available to express their intent, and current human-machine interfaces provide limited inputs for controlling devices (Azevedo Coste et al. 2022; Jiang and Farina 2014). Current approaches (i.e. myoelectric control) rely on state machines to alternatively set the user's DOF as the control input for a given (potentially synergetic) movement elicited by the device. Yet these command modalities often exert considerable cognitive loads on users and lack controllability and intuitiveness in daily life.

In this work, we propose a novel user interface for grasping movement control in which the user delegates the grasping task decisions to the device, only moving their (potentially prosthetic) hand toward the targeted object. Time before impact is estimated for the device to open or prepare the hand in time for the upcoming grip, which is automatically selected among a set of grips achievable by the assistive device.

2. Methods

2.1. Apparatus and computer vision tools

Required information for assisting an ongoing grasping task is the following: (1) hand position and orientation; (2) object position and orientation; (3) object nature (including shape and potentially weight and texture). Regarding hand pose estimation, markerless motion capture applying convolutional neural network (CNN) to RGB frames is a most active field of research that has consistently been narrowing the accuracy gap that used to separate them from optoelectronic systems, all while relying on less expensive and cumbersome hardware. In the meantime, object pose estimation most active research also relies on CNNs applied to RGB frames.

Thus, an OAK-D S2 (Luxonis) stereoscopic RGB camera was chosen as a data acquisition sensor, prioritizing cost, ease of use, installation and universality, as it may be easily mounted on a wheelchair or a hat. Hand pose estimation was performed using Google's MediaPipe (Zhang et al. 2020), leveraging stereoscopic vision for depth estimation. Object identification and pose estimation were achieved using CosyPose (Labbé et al. 2020), a multi-object 6D pose estimator trained on a set of objects with known 3D models.

2.2. Grasping intention detection

Hand and objects' pose were estimated and represented in a 3D virtual scene for grasping intention detection. Multiple rays formed a virtual cone in the direction of the hand's velocity, with a length and diameter embedding scalar velocity. Ray tracing was used to determine if the user targeted an object by comparing the number of rays intercepting with the object's 3D mesh to a threshold.

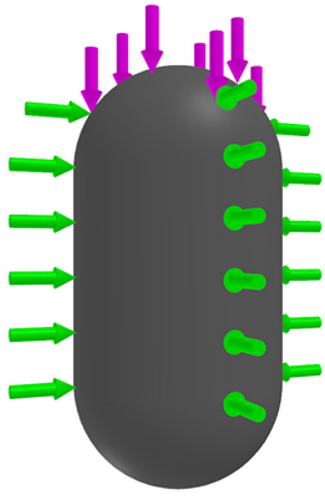


Figure 1. Illustration of the adaptive grip selection: different approach movements (represented as arrows embedding Δ_{imp} and v_{hand}) yield either a palmar grip (green) or a pinch grip (purple).

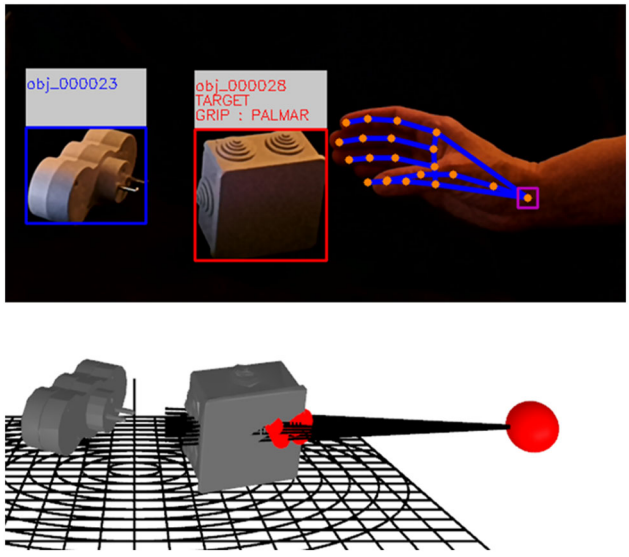


Figure 2. Visualization of the adaptive grasping assistance algorithm.

2.2. Time before impact estimation

We defined the expected area of impact as the mesh triangle intercepted by a ray defined as the barycenter of the intercepting rays. Time before impact was evaluated by integrating the extrapolated velocity of the hand up to the area of impact.

2.3. Grip selection

We chose to select a grip among a predefined set rather than generate a grip on the flight for two reasons: (1) some assistive devices cannot (yet) achieve independent, continuous control over the hand (Azevedo Coste et al. 2022); (2) predefined grips are more likely to be correctly anticipated and exploited by the user. We took inspiration from the concept of documented objects (Dalibard et al. 2010) to select the optimal grip for a given object and a foreseen vector of impact. A 4-dimensional table (illustrated in Figure 1) was constituted for each object of the used set in which a grip is attributed to every tuple formed by the mesh triangle representing the expected area of impact Δ_{imp} and the hand's normed velocity v_{hand}.

3. Results and discussion

In a preliminary study, a participant was instructed to grasp randomly selected objects with a randomly selected grip. Video recordings of the task were analyzed offline to fine-tune the parameters of our grasping intention detection algorithm and build the grip selection table.

Our ongoing study aims at quantifying the real-time performances of our algorithm regarding accuracy and time of impact estimation, which are crucial for practical use. Figure 2 shows a snapshot of the video feed of a grasping task on the upper part and the corresponding virtual scene on the lower part. Object 000028 was correctly detected as the target, while object 000023 was ignored. Area of impact was estimated from the ray intercepts figured as red dots, and a palmar grip was accordingly selected.

An upcoming study in which participants will wear an assistive (FES or prosthetic) device will assess the usability of the proposed approach.

Although this proof of concept used CosyPose, which is restricted to the variety of objects it was trained on, recent work allows for pose estimation of objects unseen during training but with known 3D models. Nonetheless, the fact that our grip selection table was built specifically for our set of objects may present challenges in real-time scenarios where object discovery is required. Despite these limitations, the proposed approach shows potential in controlled environments with known objects, such as home settings, where it can significantly reduce the cognitive load for individuals with upper-limb pathologies.

Additionally, it should be noted that the proposed approach is agnostic of the hand and object pose estimation tool. Any precise and fast enough pose estimation solution could be utilized, allowing for flexibility in choosing appropriate technologies based on specific requirements and constraints.

Finally, while only the 3D position of the palm was used, exploiting the whole hand pose estimation and prolonging the tracking after the object is grasped would allow, for instance, increases in the grip strength if the object is slipping as a substitution to missing sensory feedback.

4. Conclusions

Grasping intention detection and automatic adaptive grip selection were achieved, requiring minimally complex sensors. This proof of concept paves the way for assistive device control modes lightening the cognitive load of impaired people in known environments.

References

Azevedo Coste C, William L, Fonseca L, Hiairrassary A, Andreu D, Geffrier A, Teissier J, Fattal C, Guiraud D. 2022. Activating effective functional hand movements in individuals with complete tetraplegia through neural

stimulation. Sci Rep. 12(1):16189. doi:10.1038/s41598-022-19906-x.
Dalibard S, Nakhaei A, Lamiraux F, Laumond JP. 2010. Manipulation of documented objects by a walking humanoid robot. 2010 10th IEEE-RAS International Conference on Humanoid Robots. IEEE; p. 518–523.
Jiang N, Farina D. 2014. Myoelectric control of upper limb prosthesis: current status, challenges and recent advances. Front Neuroeng. 7(4):7–9.
Labbé Y, Carpentier J, Aubry M, Sivic J. 2020. CosyPose: consistent multi-view multi-object 6D pose estimation. In: Vedaldi A, Bischof H, Brox T, Frahm JM, editors. Computer vision – ECCV 2020. ECCV 2020. Lecture notes in computer science. Vol. 12362. Cham: Springer.
Zhang F, Bazarevsky V, Vakunov A, Tkachenka A, Sung G, Chang CL, Grundmann M. 2020. Mediapipe hands: on-device real-time hand tracking. arXiv preprint arXiv: 2006.10214.

KEYWORDS Grasping; assistive devices; computer vision

etienne.moullet@inria.fr

Sport biomechanics

Biomechanical analysis of the final push of an elite springboard diver, page S260.
Computation of the wheelchair fencers reach space envelop – a preliminary study for assessing functional abilities, page S263.
Impact of holding a racket on upper limbs for para-badminton: a preliminary study, page S265.
Isokinetic assessment of glenohumeral rotator muscle strength endurance: influence of the number of contractions and computational method, page S267.
Quantification of vibration exposure in horseback riders depending on the type of riding saddle: a preliminary study, page S270.
Trunk kinematics in wheelchair badminton: preliminary results, page S273.
Validation of walking events detecting algorithm during Nordic Walking of healthy subjects, page S275.
Wheelchair caster power losses due to rolling resistance, page S278.
Wrist extensor tendon forces during tennis forehand might be modulated by player-specific technique, page S281.

Biomechanical analysis of the final push of an elite springboard diver

L. Demestre[a], N. Bideau[b], G. Nicolas[b], C. Pontonnier[c] and G. Dumont[c]

[a]Institution nationale des Invalides (INI) / Centre d'Etude et de Recherche sur l'Appareillage des Handicapés (CERAH), Créteil, France; [b]Inria, M2S, Univ Rennes, Rennes, France; [c]Inria, CNRS, IRISA, Univ Rennes, Rennes, France

1. Introduction

Springboard diving is a sport which is evaluated by judges. The performance is based on the technique and grace from the starting position to the entry into water (FINA 2017). The interaction between the diver and the springboard, depending on the temporal synchronization between them, may be optimized to improve this performance (Sinclair 2012).

This pilot study focuses on the synchronization between the final push of the diver before take-off and the maximal deflection of the springboard during forward dives. The technical sport manager and the literature (Miller and Munro 1985) agree that this push should be synchronized with the maximal deflection of the springboard. But they also observed that this push was usually performed while the springboard was still deflecting. The current abstract presents a study of the synchronization between this push and the maximal deflection of the springboard for dives with different difficulty levels.

This push was studied according to knee joint coordinates and torques. The synchronization between the knee kinematics and dynamics and the maximal deflection of the springboard was then addressed. A biomechanical model of the diver and motion capture data of the diver and the springboard were used to compute the required mechanical features.

2. Methods

2.1. Motion capture data

Motion capture data were recorded using an optoelectronic system (18 cameras, 200 Hz, Qualisys). A set of 36 reflective markers was placed on an elite diver (1.80 m; 79 kg) following ISB standards for a whole-body study. A set of 51 markers was placed on diving board sides (50 on a side and 1 on the other side)

and spaced 10 cm apart. The diver performed 9 forward dives (3 101 C, 3 105 C and 3 107 C). These types of dives differ in the amount of half somersaults achieved, which corresponds to the last number of the code. These dives were evaluated by another elite diver watching them: the 3 repeats of each type of dive were ranked against each other.

2.2. Diver modelling and IF&M computation

A three-dimensional 18-segment model of the diver was used to compute the interaction forces and moments (IF&M) between the diver and the springboard. Firstly, joint coordinates were computed using an inverse kinematics method. They were filtered using a 4th-order Butterworth low-pass filter with no phase shift and a cut-off frequency of 10 Hz. The IF&M were then computed using these results and motion capture data of the diver and the springboard. Firstly, a contact detection step was performed considering 28 discrete contact points under the diver's feet. This process was suitable for interaction between a human subject and a moving and/or non-horizontal structure. Secondly, the forces were distributed among them using an optimization approach (Demestre et al. 2022). An inverse dynamics step was then carried out using the Matlab toolbox CusToM to compute joint torques (Muller et al. 2019).

2.3. Data analysis

To study the diver's final push on the springboard, the knee kinematics and dynamics were considered. The temporal evolution of joint coordinates and torques of the two knees were computed from touchdown (start of the last contact phase before take-off) to take-off. The two knees were observed separately to verify the hypothesis of a movement in the sagittal plane admitted in the literature.

The touchdown and take-off moments were identified using the contact detection results of the IF&M computation method. The maximal deflection moment was identified using motion capture data of the springboard free end. The flexion-extension angles of the knees were obtained from inverse kinematics results. Maximal extension corresponded to an angle of 0° and maximal flexion to an angle of −180°. The flexion-extension torques of the knees were obtained from the inverse dynamics results. The torque was positive during extension and negative during flexion. The duration between maximal torque and deflection (DT) was computed as the difference between the maximal deflection moment and the maximal torque moment. A negative duration corresponded to a maximal torque happening after maximal deflection. A similar duration was also computed regarding the maximal knee flexion (DF).

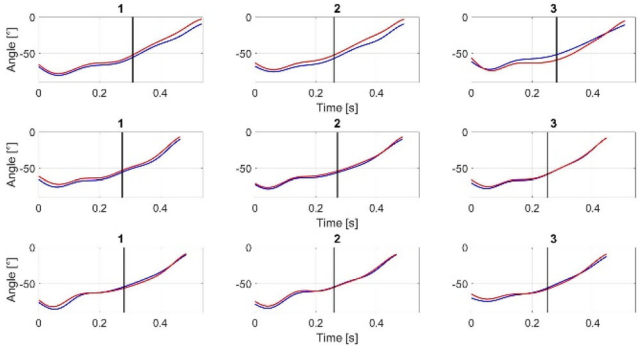


Figure 1. Evolution of the flexion-extension angles of the right (blue) and left (red) knees for 101 C (up), 105 C (middle) and 107 C (bottom) dives. For each line, each graph corresponds to a repeat. The vertical line corresponds to the maximal deflection moment.

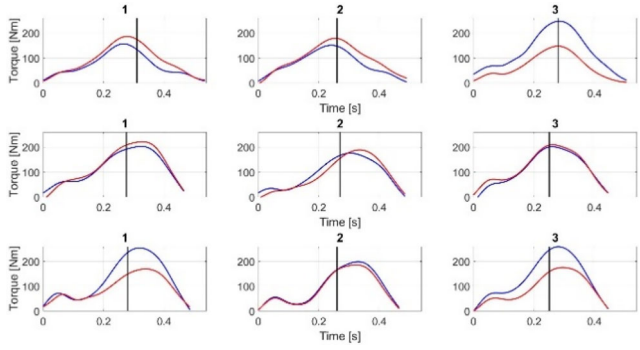


Figure 2. Evolution of the flexion-extension torques of the right (blue) and left (red) knees for 101 C (up), 105 C (middle) and 107 C (bottom) dives. For each line, each graph corresponds to a repeat. The vertical line corresponds to the maximal deflection moment.

3. Results and discussion

3.1. Knee flexion-extension angle

Right and left knees have a similar kinematic behaviour (Figure 1). Therefore, the hypothesis of a planar movement seems suitable for studying knee kinematics during a forward dive.

Diver's knees were in flexion at touchdown. Then, the diver started an extension which then remained nearly constant before the maximal deflection of the springboard. Finally, the diver was increasing extension until the take-off.

No tendency was observed regarding DF according to difficulty and quality of the studied dives. This observation may come from a similar DF for all the dives, which shows that the diver was repeatable considering his knee kinematics.

3.2. Knee flexion-extension torque

Regarding knee dynamics, the hypothesis of a planar movement seems not suitable (Figure 2). This asymmetry may also come from lateral dominance, anatomical asymmetry, posture, fatigue, traumas (Loffing et al. 2017) or an imbalance during the dive.

Torques were always positive even if flexion was observed at touchdown. This observation shows that the diver provides a resistive torque at touchdown to limit flexion increase due to contact with the springboard. During the constant extension phase observed in Figure 1, torques also remain constant, or even decrease. Maximal torques were then reached close to the maximal deflection. These maximal torques could be reached before (for 101 C 1 and 2) or after the maximal deflection (for all the other dives). Considering all the dives with a maximal torque after the maximal deflection, this duration increased as the dive difficulty increased. This phenomenon may come from a higher maximal torque for more difficult dives, which requires more time to be reached. No tendency was observed regarding DT according to dive quality.

4. Conclusions

This study enabled to study knee kinematics and dynamics from touchdown to take-off during forward dives. It was found that the hypothesis of a planar movement was suitable for studying knee kinematics but not dynamics.

No performance criteria were identified regarding the synchronization between knee behaviour and maximal springboard deflection. It was observed that the maximal knee torque increase with the difficulty of the dive.

A study involving more divers performing more dives could enable to validate the observed tendencies. Other type of dives may also be studied following the presented method.

Acknowledgements

The authors wish to thank Clémence Monnery for her help in preparing the experiment and identifying issues to study.

References

Demestre L, Grange S, Dubois C, Bideau N, Nicolas G, Pontonnier C, Dumont G. 2022. Characterization of the dynamic behavior of a diving board using motion capture data. Sports Eng. 25(1):21. doi:10.1007/s12283-022-00388-z.

FINA. 2017. Fina diving rules 2017–2021. Technical report.

Loffing F, Hagemann N, Strauss B, MacMahon C. 2017. Laterality in sports: theories and applications. New York: Academic Press.

Miller DI, Munro CF. 1985. Greg Louganis' springboard takeoff: I: temporal and joint position analysis. Int J of Sport Biomech. 1(3):209–220. doi:10.1123/ijsb.1.3.209.

Muller A, Pontonnier C, Puchaud P, Dumont G. 2019. CusToM: a Matlab toolbox for musculoskeletal simulation. J of Open Source Softw, Open J. 4(33):1–3.

Sinclair PJ, Walker CA, Rickards T. 2012. Kinematic determinants of dive height in springboard diving. Movement Sport Sci. n° 75(1):107–112. doi:10.3917/sm.075.0107.

KEYWORDS Human-structure interaction; synchronization; sport performance; knee flexion-extension

louise.demestre@invalides.fr

Computation of the wheelchair fencers reach space envelop – a preliminary study for assessing functional abilities

A. Raud[a], J. Loisel[b], M. Bourgain[a,c], C. Sauret[a,b] and H. Pillet[a]

[a]Institut de Biomécanique Humaine Georges Charpak (IBHGC), Arts et Métiers Institute of Technology, France; [b]Centre d'Etudes et de Recherche sur l'Appareillage des Handicapés, Institution Nationale des Invalides, Créteil, France; [c]EPF Graduate School of Engineering, Cachan, France

1. Introduction

During Paralympics events, wheelchair fencers compete under one of 2 categories depending on their classification of functional ability. According to Olympic rules, current classification is designed for assessing the trunk's functional ability in terms of the range, strength, and speed of trunk movement and balance. It consists of an evaluation of the extension and lateral inclination ability of the chest in different positions, with or without the use of a weapon. However, this classification is called into question, especially because it is performed without the supporting bar which athletes hold on to with their non-dominant arm. Indeed, a recent study observed that in competition conditions (i.e. with the supporting bar), athletes with different official classification displayed similar trunk ranges of motion (Fung et al. 2013). Furthermore, this method relies on qualitative criteria and remains rather subjective.

Hence, the objective of this study was to propose a new objective measurement method to assess the functional ability of the wheelchair fencers with or without trunk movement, based on reach space envelop (RSE).

2. Methods

2.1. Data collection

A control group, composed of ten right handed young healthy adults (5 females, 5 males) with no prior experience in fencing, was enrolled to participate in this study, as well as an additional international category B wheelchair fencer (study n° IRB00012476-2022-11-02-153). They were all equipped with markers aiming at measuring pelvis and upper limbs movement (Wu et al. 2005) placed on : manubrium, xyphoid process, the processes of the seventh cervical, acromion and on the middle of clavicles as well as second and fifth metacarpal heads. To complete, 4 markers were added on the anterior superior and inferior left and right iliac crests as well as two markers on the wheel centres of the wheelchair.

Volunteers were asked to perform one exploration of their maximum reach space envelop while sitting in a fencing wheelchair without a weapon. They were asked to hold the supporting bar, and no restriction on trunk movement were set. Both vertical and horizontal back and forth patterns were suggested.

Those movements were performed in a motion analysis room equipped with 10 cameras (Vicon, Vero 2.2) with a 100 Hz sampling rate.

2.2. Reach space envelop calculation

The RSE was computed with a custom frame for the pelvis. Custom frame origin was set in the middle between the anterior superior, left and right iliac crests. X-axis was defined as the axis passing through the centres of the wheelchair wheels from left to right, and Y-axis was set as the vertical axis. The end effector was set as the middle of the markers placed on the second and fifth metacarpal bones of the leading arm (Klopčar et al. 2007). The position of the end effector regarding the centre of the reference frame was described in spherical coordinates (displacement, azimuth, elevation).

2.3. Data treatment

The space was described as regular 5 degrees azimuthal and elevation sections. Only data with maximal distance to frame origin were kept for every portion of the segmented space. Raw distances to frame origin were processed through MATLAB software (R2022a) using a linear interpolation, thus provided a single value for each space section.

To examine results consistency, Pearson correlation coefficient between these values and maximum subject value of the whole space were computed. After distance values were normalised by subject maximum distance, a mean RSE was computed as the mean of all data of the control group. For the corresponding figure, values lay between 0 and 1 as percentages of the maximum distance to the origin. Whites areas correspond to space portions without data. For all figures, the results were plotted in a spherical mathematical projection on the azimuthal-elevation 2D plane.

Table 1. Statistical values for the Pearson correlation coefficients between mean value of each space portion and maximum subject envelop value computed for the whole space.

	Min	Max	Mean	Std
Normalized RSE	0.20	0.95	0.74	0.06

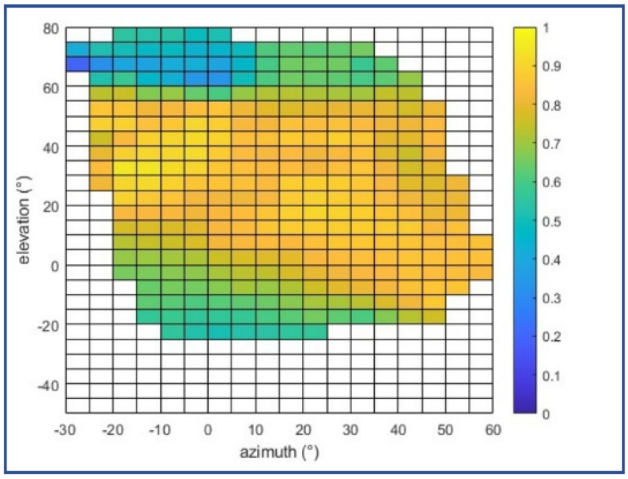


Figure 1. Colored map of the Pearson correlation coefficients between local value and maximum subject value for the control group.

3. Results and discussion

3.1. Consistency of the control group

Statistical values are reported in Table 1. Local results are reported in the coloured map of Figure 1. Except from extreme positions, data highly correlates.

It tends to indicate that subjects with no known pathology describe reach space envelops that are similar to each other.

However, results showed that extreme positions might be difficult to reach for some persons, even in the healthy population, which is visible through low correlation coefficient at these locations. However, this might also be due to an insufficient insistence during instructions or a too limited training period.

3.2. Reach space envelops

Mean normalized RSE of the control group is displayed in the colored map in Figure 2.

For the control group, maximum distance, corresponding to a value of 1, is obtained for azimuthal angles near 0° (arm is in the sagittal plane) and elevation angles around 40°. It decreases to 0.8 mainly when the elevation angle of the end effector decreases. Isovalue lines are mainly horizontal. Their local minimum is reached at around 20° of azimuthal angle.

This mean RSE was compared to a subject specific RSE obtained from an international category B wheelchair fencer to illustrate the method. Differences in term of localization of the 95% section (orange space portion) appear. Also, isovalue lines rise when the azimuthal angle rises, which can be explained by the lower trunk mobility of the wheelchair fencer. Yet, for azimuthal angles near to 0°, RSE of the wheelchair fencer

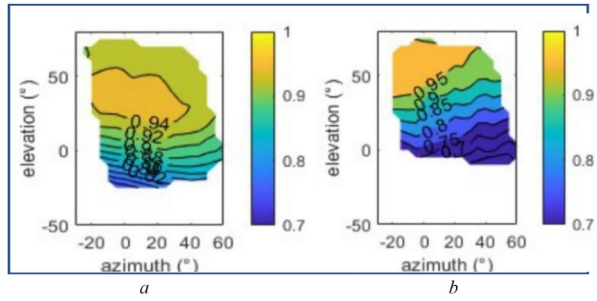


Figure 2. Mean normalized RSE of the control group (a). Subject specific normalized RSE (b).

reaches at least 95% of his maximum value for this area. It would indicate a higher shoulder mobility.

Moreover, lack of data for very low azimuthal angles can be considered as a consequence of a lower trunk mobility.

4. Conclusions

This study demonstrates the feasibility of this method to obtain and describe reach space envelop of wheelchair fencers. The same methodology can be used to describe other specific RSE: without trunk motion, with or without a foil and then provide quantitative data.

For a better understanding and use of this quantitative data, the graphical representation may be improved by adding a 3D description. Moreover, further developments are needed to determine uncertainties and to assess repeatability of such a method.

Although first results are promising, comparisons of RSE between category A and B wheelchair fencers are now needed to evaluate if this method could be used to establish more equitable categories.

References

Fung Y, Chan DKC, Caudwell K, Chow B. 2013. Is the wheelchair fencing classification fair enough? A kinematic analysis among world-class wheelchair fencers. EUJAPA. 6(1):17–29. doi:10.5507/euj.2013.002.

Klopčar N, Tomšič M, Lenarčič J. 2007. A kinematic model of the shoulder complex to evaluate the arm-reachable workspace. J Biomech. 40(1):86–91. doi:10.1016/j.jbiomech.2005.11.010.

Wu G, van der Helm FCT, Veeger HEJD, Makhsous M, Van Roy P, Anglin C, Nagels J, Karduna AR, McQuade K, Wang X, et al. 2005. ISB recommendation on definitions of joint coordinate systems of various joints for the reporting of human joint motion—part II: shoulder, elbow, wrist and hand. J Biomech. 38(5):981–992. doi:10.1016/j.jbiomech.2004.05.042.

KEYWORDS Wheelchair fencing; reach space; classification

antoine.raud@ensam.eu

Impact of holding a racket on upper limbs kinematics for para-badminton: a preliminary study

T. Marsan[a], I. Alberca[b], A. Faupin[b] and B. Watier[a,c]

[a]LAAS-CNRS, CNRS, UPS, Université de Toulouse, Toulouse, France; [b]Laboratoire IAPS, Université de Toulon, Toulon, France; [c]CNRS-AIST, JRL IRL, Tsukuba, Japan

1. Introduction

Wheelchair badminton was only introduced in the Paralympic scene during the Tokyo Games in 2021. Two classes are defined for this sport: WH1, who are athletes with little or no abdominal function, and WH2, who have abdominal function. The specificity of this sport, in term of movement, resides in the fact that athletes constantly performs back and forth motions with a racket in their hand.

The propulsion is then made difficult because of the contact with the handrim which is no longer made with the hand but through the racket. It has already been shown that holding the racket lowered propulsion effectiveness and increased the risk of injury by modifying the way the force is applied to the handrim (Alberca et al. 2022). In para-tennis, it has also been shown that holding a racket lowered the push time, and increased the power loss during propulsion (de Groot et al. 2017). The trunk flexion was also impacted by the racket grip (de Groot et al. 2017) which could lead to differences in upper limbs kinematics, and in temporal characteristics of propulsion, even without a racket (Sanderson and Sommer 1985). The impact of holding a racket on the upper limbs has not been studied for para-badminton, it could then be interesting to study the differences of the upper limbs kinematics of the para-badminton athletes when holding a racket.

Therefore, the aim of this study was to analyze the kinematics of the upper limbs during two types of propulsion: with and without the racket. It has been hypothesized that, since the trunk was impacted by the racket grip, the athlete belonging to the WH1 would compensate the lack of trunk mobility by increasing the range of motion of his upper limbs in comparison to the athlete belonging to WH2.

2. Methods

2.1. Participants

Two French elite para-badminton players volunteered for this study. One was competing in WH1 category (S_1), while the other one competed in WH2 category (S_2). The categories were defined according to the Badminton World Federation classification regulations. Their height and weight, (S_1 and S_2) were 1,68 m and 1,8 m, and 71 kg and 60 kg. Athletes used their own wheelchair designed for para-badminton, and their own racket. This research was authorized by EudraCT / IDRCB n° 2020-A02919-30.

2.2. Experimentation

Each athlete performed back and forth pushes over three meters during a minute under two conditions. The first one was without the racket (No Racket), and the second one with the racket in their hand (Racket).

A total of 15 markers were place on the scapula, forearm, arm, and hand on the side of the racket, according to (Wu and Cavanagh 1995) to perform a 3D-analysis of the kinematics of the upper limbs. Positions of the reflective markers were captured using a 22-cameras optoelectronic motion capture system (Vicon® System, ©Oxford Metrics Inc., UK) working at 200 Hz.

2.3. Data processing

The trajectories of the markers were smoothed using a sliding window average method over five frames. The OpenSim model with the scapulothoracic joint from Seth et al. (2016) was used. The joint angles were computed using the inverse kinematics tool of OpenSim 4.3 and filtered afterwards with a 2nd order Butterworth filter with a cutting frequency of 6 Hz.

The gleno-humeral elevation, elbow flexion, and wrist flexion have been computed for the different propulsions. The forward phase (FP) and backward phase (BP) have been manually identified when the athlete was changing direction. The range of motion of the elevation of the shoulder, the elbow flexion, and the wrist flexion was then reported for each phase. There was at least seven forward or backward phase for each acquisition, so the values were averaged over the seven first phases. The results of the upper limb on the side of the racket were reported. Given the low number of athletes, no statistical test was performed.

3. Results and discussion

The gleno-humeral elevation pattern did not differ between the Racket and No Racket trials (Figure 1), and so did the other coordinates. This might be due to the extensive training that both athletes had in

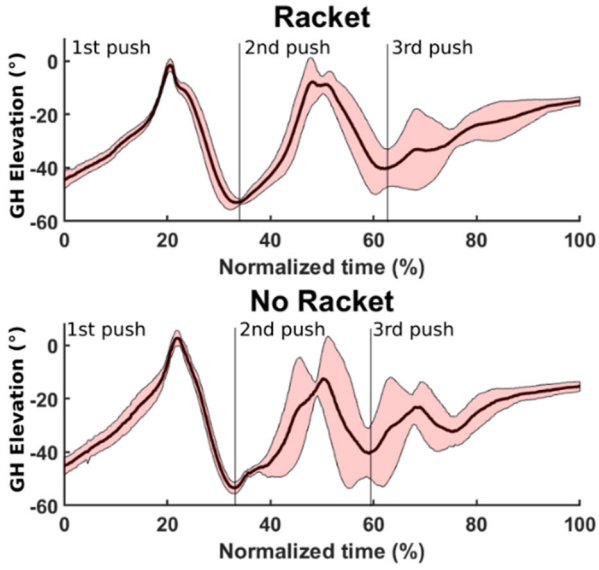


Figure 1. Mean (strong dark line) and standard deviation (red fill) of the evolution of the gleno-humeral elevation during the seven forward propulsions for S_1 with and without the racket.

Table 1. Amplitude (mean ± std) of the studied angles for both subjects with the two conditions.

Range of motion			GH elevation	Elbow flexion	Wrist flexion
S1	Racket	FP	50.9 ± 3.9	85.8 ± 8.0	61.8 ± 4.9
		BP	43.8 ± 2.8	72.3 ± 5.4	77.7 ± 2.0
	No racket	FP	55.4 ± 3.9	91.2 ± 6.9	62.9 ± 6.8
		BP	47.9 ± 1.9	65.4 ± 3.7	76.6 ± 3.1
S2	Racket	FP	57.5 ± 3.1	92.6 ± 6.2	76.6 ± 2.4
		BP	64.4 ± 2.8	81.2 ± 7.9	85.5 ± 5.8
	No racket	FP	59.9 ± 3.7	98.8 ± 5.5	72.8 ± 8.1
		BP	57.7 ± 2.1	87.8 ± 7.5	76.1 ± 18.3

FP is forward phase and BP is backward phase.

their wheelchair, and their ability to propel themselves even with a racket in their hand. However, it was observed that the range of motion of gleno-humeral elevation was higher, in average, over the second push while holding onto the racket for S_1 (Figure 1).

Overall, the range of motion of the upper limbs of S_2 were higher than the one of S_1 (Table 1) for both FP and BP. Nevertheless, athletes had a higher range of elbow flexion and gleno-humeral elevation (except S_2 without a racket) during FP than BP (Table 1). The differences observed between FP and BP here were mostly due to the different technique used by athletes to propel forward or backward.

However, there were differences between both activities. Indeed, for S_1, the range of motion of the gleno-humeral elevation was lower when holding a racket both for FP and BP. However, it was higher for S_2 for BP. The range of motion of the gleno-humeral elevation of S_1 was higher during the No Racket activity for both FP and BP but it was higher during BP and lower during FP during the No Racket activity for S_2.

The wrist of S_1 was the least impacted joint, with less than 1° in average of difference in range of motion between the two activities. S_2 had a higher wrist range of motion but a lower elbow range of motion during the Racket activity whereas S_1 had a higher elbow range of motion during BP and lower during FP.

The compensation in terms of range of motion of the upper limbs differed between both subjects. And the pattern of compensation was not the same during FP and BP, meaning that athletes had their own strategy to compensate the lack of grip on the handrim with their upper limbs.

4. Conclusions

This preliminary study was the first to investigate the impact of holding a racket on upper limbs kinematics during propulsion in para-badminton.

Differences have been found between the FP and BP which could be due to the different technique used to propel forward or backward. The differences due to holding the racket were however specific to each athlete.

Those results need to be confirmed on more athletes, to identify if the discrepancies come from the techniques used or from the differences in term of handicap, between athletes belonging to WH1 and WH2. Biomechanical analysis could then be useful to help classify athletes based on their mobilities.

References

Alberca I, Chénier F, Astier M, Combet M, Bakatchina S, Brassart F, Vallier J-M, Pradon D, Watier B, Faupin A. 2022. Impact of holding a badminton racket on spatio-temporal and kinetic parameters during manual wheelchair propulsion. Front Sport Act Living. 4:862760. doi: 10.3389/fspor.2022.862760.

de Groot S, Bos F, Koopman J, Hoekstra AE, Vegter RJK. 2017. Effect of holding a racket on propulsion technique of wheelchair tennis players. Scand J Med Sci Sports. 27(9):918–924. doi:10.1111/sms.12701.

Sanderson DJ, Sommer HJ. 1985. Kinematic features of wheelchair propulsion. J Biomech. 18(6):423–429. doi:10.1016/0021-9290(85)90277-5.

Seth A, Matias R, Veloso AP, Delp SL. 2016. A biomechanical model of the scapulothoracic joint to accurately capture scapular kinematics during shoulder movements. PLoS One. 11(1):e0141028. doi:10.1371/journal.pone.0141028.

Wu G, Cavanagh PR. 1995. ISB recommendations in the reporting for standardization of kinematic data. J Biomech. 28(10):1257–1261. doi:10.1016/0021-9290(95)00017-C.

KEYWORDS Motion capture; wheelchair badminton; upper limbs kinematics

tmarsan@laas.fr

Isokinetic assessment of glenohumeral rotator muscle strength endurance: influence of the number of contractions and computational method

E. Insalaco[a], Y. Blache[a], G. Vigne[a,b], S. Trama[a] and I. Rogowski[a]

[a]Laboratoire Interuniversitaire de Biologie de la Motricité – UR 7424, Université Lyon 1, Villeurbanne, France; [b]Centre Orthopédique Santy, FIFA Medical Center of Excellence, Lyon, France

1. Introduction

Shoulder injuries are common problems in athletes practicing sports involving upper extremities, such as rugby, tennis, handball or swimming. Such problems are due to the low congruence between the glenoid and humeral head, demanding high contribution of the rotator cuff (RC) muscle strength to stabilize the glenohumeral (GH) joint, while moving the arm (Gaudet et al. 2018). During sport practice, all the components of muscle strength ability are required (Schwank et al. 2022), and particularly the muscular endurance, defined as the ability to limit the strength decrement for an extended period. Isokinetic dynamometry is considered the 'gold standard' to assess strength objectively, as for maximal strength of RC muscles (Edouard et al. 2011). Currently, discrepancy in number of contractions (from 10 to until a decrement of 50% in maximal strength value), and in computational methods exists to characterize RC muscle endurance in GH internal (IR) and external (ER) rotation.

Therefore, this study aimed to explore the influence of the number of contractions and computational method on the reliability of muscle strength endurance measures assessed isokinetically.

2. Methods

2.1. Participants

Twenty healthy athletes (10 males, age: 23.5 ± 5.0 yrs; height: 173.3 ± 10.1 cm, mass: 67.6 ± 10.1 kg) performed two sessions, one week apart.

2.2. Experimental procedure

For each session, after a standardized warm-up, the participant was secured with two thorax belts in lying position on an isokinetic dynamometer (CON-TREX AG, Dübendorf, Switzerland). The arm assessed was abducted at 45° relative to the thorax in the scapular plane, i.e. 20° forward the frontal plane, and the elbow bent at 90°. From 0° position, i.e. forearm placed vertically, the participant performed bilaterally, series of reciprocal contractions in IR of 50°, and ER of 60° (total range of motion = 110°), with gravity correction: two submaximal and one maximal of five contractions in concentric mode at 120°/s, one submaximal and one maximal of three contractions in concentric then eccentric mode at 60°/s, and one submaximal of two contractions and one maximal of 50 contractions (Gaudet et al. 2018) in concentric mode at 120°/s (Guillemot et al. 2016). Sub-maximal and maximal series were interspersed by 30-s recovery, and maximal and submaximal series by 1-min. The dominant side was assessed first.

2.3. Data treatment and statistical analysis

After filtering (low-pass Butterworth order 4th; cutoff frequency =20 Hz) the signal of the 50-contractions series, muscle endurance was assessed by the decrement (Dec) in % in peak torque (PT) for IR and ER when considering only 10, 15, 20, 25, 30, 35, 40, 45 or 50 contractions (con) based on the following equations:

$$\mathrm{Dec1} = \frac{\text{maximal PT} - \text{minimal PT}}{\text{maximal PT}} * 100 \quad (1)$$

$$\mathrm{Dec2} = \frac{\text{mean PT of the 1st 4 con} - \text{mean PT of the last 4 con}}{\text{mean PT of the 1st 4 con}} * 100 \quad (2)$$

$$\mathrm{Dec3} = 100 - \frac{\text{mean PT of the last 3 con}}{\text{mean PT of the first 3 con}} * 100 \quad (3)$$

$$\mathrm{Dec4} = 100 - \frac{\text{Cumulated PT}}{\text{Maximal PT} * \text{total number of con}} * 100 \quad (4)$$

Analysis of variance for one intraindividual factor of 10 repeated measures were applied (JASP 0.17.1, University of Amsterdam, Netherlands) to assess the effect of number of contractions on the PT Dec for IR and ER. When $p \leq 0.05$, contrast analysis was performed to compare dec_i for a given number of contractions to 0%, meaning no PT Dec. Interclass coefficient of correlation ($ICC_{3,k}$) was computed using MATLAB (R2021b, The MathWorks Inc Natick, Massachusetts) to assess Dec_i intersession reliability, with $0.5 \leq$ ICC <0.7 for moderate, $0.7 \leq$ ICC <0.9 for high, and ICC ≥ 0.9 for very high reliability (Gautrey et al. 2013).

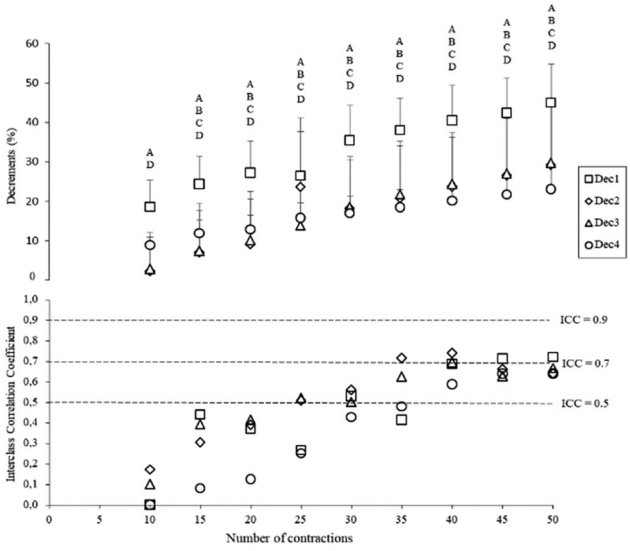


Figure 1. Mean (+ standard deviation) PT decrement for GH IR (top) and $ICC_{3,k}$ (bottom) according to the computational method (Dec_i) and number of contractions. Significantly different from 0% ($p < 0.001$) with A, B, C, D for Dec1, Dec2, Dec3, Dec4, respectively.

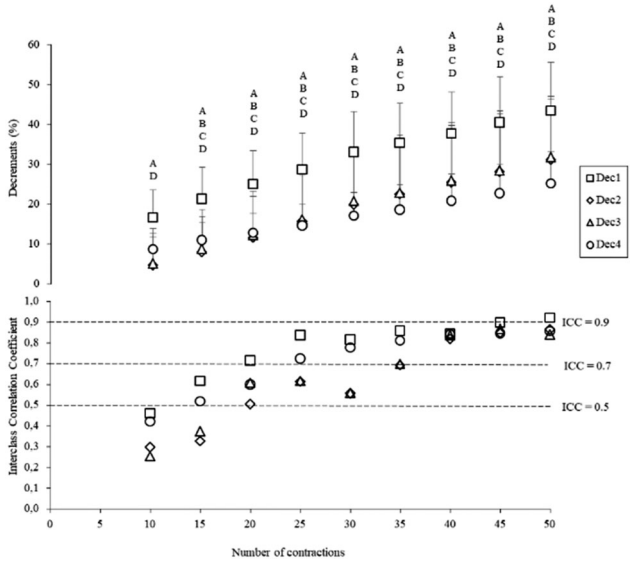


Figure 2. Mean (+ standard deviation) PT decrement for GH ER (top) and $ICC_{3,k}$ (bottom) according to the computational method (Dec_i) and number of contrac-tions. Significantly different from 0% ($p < 0.001$) with A, B, C, D for Dec1, Dec2, Dec3, Dec4 respectively.

3. Results and discussion

Based on the 80 series of 50 contractions (40 shoulders assessed twice), the required velocity of 120°/s was reached for all the contractions in IR and ER for 68 (85%) series. This rate was similar to the rates of 84.6% reported for 60°/s and 180°/s, and higher than 77% reported for 360°/s (Mueller et al. 2011).

Despite the number of contractions considered, Dec1 values were higher than values obtained for the three other computational methods for both IR and ER, that may be explained by the occurrence of maximal and minimal PT unrelated to a fixed number of contractions. The analysis of variance showed a significant effect of contraction number on PT Dec for IR and ER ($p < 0.001$). For both IR and ER, significant decrease was observed after 10 contractions for Dec1 and Dec4, and 15 contractions for Dec2 and Dec3 ($p < 0.001$; Figures 1 and 2). Our findings with equation Dec1 were similar to those reported by Gaudet et al. (2018).

Considering ICC values for IR Dec, moderate reliability was found after 35 contractions when using Dec1, Dec2 and Dec3, from 40 contractions with Dec4. High reliability was obtained with Dec2 for 35 and 40 contractions, and with Dec1 for 45 and 50 contractions (Figure 1). Regarding ICC values for ER Dec, moderate reliability was found after 15 contractions with dec1 and dec4, high reliability after 20 contractions with dec1. Regardless of the computational method, high reliability was obtained after 40 ER contractions. Regardless of the number of contractions and equations, the reliability of PT decrement seemed higher for ER than for IR. Despite the participant's upper body was secured with two thorax belts, more compensatory shoulder motions may occur during IR than ER. However, for both IR and ER, our values remained largely lower than 0.88 reported by Gautrey et al. (2013) and 0.98 by Maffiuletti et al. (2007). Such discrepancies may be explained by differences in movement studied: hip adduction and abduction in Gautrey et al. (2013), and knee flexion and extension in Maffiuletti et al. (2007). To the best of our knowledge, currently no study reported reliability in PT decrement for GH IR and ER.

4. Conclusions

The findings of this study revealed that, based on four computational methods involving peak torque values, a minimum of 15 contractions was required to observe significant decrement in peak torque values for glenohumeral internal and external rotator muscles. In addition, 40 contractions allowed muscle strength endurance outcome measure with high reliability to be found, while applying the same computational method for both the glenohumeral internal and external rotator muscles. Further studies may evaluate other computational methods, such as those involving work or those based on decay slope, to produce

outcome measures assessing muscular strength endurance of rotator cuff muscles.

References

Edouard P, Degache F, Beguin L, Samozino P, Gresta G, Fayolle-Minon I, Farizon F, Calmels P. 2011. Rotator cuff strength in recurrent anterior shoulder instability. J Bone Joint Surg Am. 93(8):759–765. doi:10.2106/JBJS.I.01791.

Gaudet S, Tremblay J, Dal Maso F. 2018. Evolution of muscular fatigue in periscapular and rotator cuff muscles during isokinetic shoulder rotations. J Sports Sci. 36(18):2121–2128. doi:10.1080/02640414.2018.1440513.

Gautrey CN, Watson T, Mitchell A. 2013. The effect of isokinetic testing speed on the reliability of muscle fatigue Indicators during a hip abductor-adductor fatigue protocol. Int J Sports Med. 34(7):646–653. doi:10.1055/s-0032-1321801.

Guillemot P, Jan J, Rochcongar P. 2016. Analysis of speed enforcement of 101 isokinetic tests performed on pathological shoulders. Sci Sports. 31(3):145–151. doi:10.1016/j.scispo.2016.03.001.

Maffiuletti NA, Bizzini M, Desbrosses K, Babault N, Munzinger U. 2007. Reliability of knee extension and flexion measurements using the Con-Trex isokinetic dynamometer. Clin Physiol Funct Imaging. 27(6):346–353. doi:10.1111/j.1475-097X.2007.00758.x.

Mueller S, Mayer P, Baur H, Mayer F. 2011. Higher velocities in isokinetic dynamometry: a pilot study of new test mode with active compensation of inertia. IES. 19(2):63–70. doi:10.3233/IES-2011-0398.

Schwank A, Blazey P, Asker M, Møller M, Hägglund M, Gard S, Skazalski C, Haugsbø Andersson S, Horsley I, Whiteley R, et al. 2022. Shoulder injury prevention, rehabilitation, and return to sport for athletes at all participation levels. J Orthop Sports Phys Ther. 52(1):11–28. doi:10.2519/jospt.2022.10952.

KEYWORDS Shoulder; internal rotation; external rotation; muscle fatigue

isabelle.rogowski@univ-lyon1.fr

Quantification of vibration exposure in horseback riders depending on the type of riding saddle: a preliminary study

J. Bonnigal[a], N. Forier-David[a], L. Laurent[a], C. Magnant[a], T. Provot[a,b] and A. Olivier[c]

[a]EPF – Graduate School of Engineering, Cachan, France; [b]Arts et Métiers Institute of Technology, Institut de Biomécanique Humaine Georges Charpak, IBHGC, UR 4494, F-75013, Paris, Université Sorbonne Paris Nord, Bobigny, France; [c]Institut Français du Cheval et de l'Équitation, IFCE, Saumur, France

1. Introduction

In horseback riding, the riding saddle plays a fundamental role in rider-horse interaction (Clayton et al. 2014). The main contact area between the horse and the rider is through the riding saddle. Professionals, who ride for several hours and different horses per day, are more exposed to mechanical stress on their spine, due to intensive and repeated practice. These riders revealed a prevalence of musculoskeletal disorders of the spine, particularly low back pain (Deckers et al. 2021). Considered as an aggravating factor in musculoskeletal disorders (Boshuizen et al. 1990), exposure to vibrations is regulated in the professional field. The quantification of vibrations is based on their frequency and amplitude, but also on the position and duration of exposure. Standards exist to limit this occupational exposure, and thus reduce its harmful effects on health (ISO 2631, 2002). To date, the exposure to vibrations of horseback riders has only been quantified in one study in the agriculture field (Zeng et al. 2017): their results suggest a moderate health risks for rider. However, no study has yet looked at this phenomenon in professional horseback riding. The aim of this pilot study is to quantify the human exposure to vibrations of professional horseback rider's lumbar spine area through the spectrum of the existing standards, depending on the riding saddle.

2. Materials and methods

One participant carried out the experimental protocol: a 37-year-old (1.74 m–85 kg) professional rider and instructor riding around 5–8 h per day. The participant was riding an 11-year-old horse. Two parameters were varied during data acquisition: the type of saddle and the paces of the horse. A jumping saddle (SJ) and a dressage saddle (DR) from the Devoucoux saddlery were used (Figure 1). Both are made of leather, with a wooden tree and a semi-curve seat for the SJ saddle and a carbon tree with a curve seat for the DR saddle. The protocol took place at three paces: walk, trot (rising trot and sitting trot) and canter. The participant performed several passages in a straight line: 2 passages at walk (one passage at the left hand then one passage at the right hand), 2 passages at rising trot, 2 passages at sitting trot, 2 passages at left canter and 2 passages at right canter. A Vicon Blue trident IMU was used to measure the high-frequency acceleration (sampling rate of 1600 Hz) and was placed at the level of the rider's lumbar spine (L5). The IMU was attached to the horseback rider (Figure 1) with double-sided tape, secured with an adhesive strip on top.



Figure 1. Rider posture on the SJ saddle (a) and on the DR saddle (b) and position of the IMU on the rider.

The raw vibration data were processed to extract three indicators from the standard (ISO 2631, 2002) and the directive (Directive-2002/44/EC, 2002) on human exposure to vibrations: the Total Vibration Value (TVV – [ms^{-2}]), representing the frequency-weighted vibration dose transmitted to the body in a seated position with a vibration input at the seat ; the Daily Exposure Action Value (DEA – [min]), representing the minimum duration of exposure to whole-body vibration to reach the action value (0.5 ms^{-2} according to the European directive) and the Daily Exposure Limit Value (DEL – [min]), representing the minimum duration of exposure to whole-body vibration to reach the limit value (1.15 ms^{-2} according to the European directive).

3. Results and discussion

The results regarding TVV at the lumbar spine are presented in the histogram in Figure 2. The results obtained are compared between paces and between saddles. Regarding the comparison between the saddles, the results obtained with the DR saddle are superior to those obtained with the SJ saddle (mean relative difference of 23%), especially in rising trot.

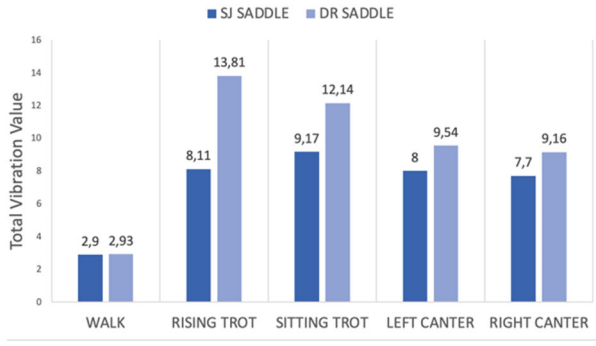


Figure 2. Histogram of total vibration value of the rider's lumbar spine area [m s^{-2}].

Table 1. Daily Exposure Action Value (DEA – [min]) and Daily Exposure limit value (DEL – [min]) at the three paces.

	DEA		DEL	
Paces	SJ Saddle	DR Saddle	SJ Saddle	DR Saddle
Walk	14 min	13 min	75 min	73 min
Rising trot	1 min 49s	1 min 25s	10 min	7 min 33s
Sitting trot	38s	49s	3 min 20s	6 min 48s
Canter	1 min 34s	1 min 43s	8 min 27s	9 min 08s

Nevertheless, the results at this pace must be nuanced because there is not a constant contact with the saddle. This implies regular impacts for the rider, adding a source of vibrations besides the horse motion.

Regarding the paces, the trot represents the most important pace in terms of vibration exposure, with a domination for the sitting trot in the SJ saddle, and for the rising trot in the DR saddle. The least restrictive pace is the walk. This finding is consistent with the type of pace: the walk is a walking pace and the slowest, while the others are jumping (trot) or tilted (canter) paces, which means repeated impacts every time the horse touches the ground after a flight time.

Regarding the Daily Exposure Action value (Table 1), there is a difference between the two saddles: the DR saddle has a higher time limit than the SJ saddle, except for rising trot. In terms of DEL, knowing that during a work session, a rider spends on average 10 min minimum at each pace, the values are low regarding trot and canter, considering only work at three paces, without jumping.

For comparison, the results of Zeng et al. (2017) for agricultural horseback riding, regarding daily vibration exposure, suggest moderate health risks. However, it should be noted that the experimental conditions are different with this pilot study for professional riding, on intensive practice of sport horseback riding. With respect to the time limit for exposure to vibrations considered, the value is less than an hour, considering that the participant only moved at walk mostly, and a little at trot.

The first limitation of this study lies in the population, which is made up of just one participant. Secondly, the participant performs daily 5–8 h of horseback riding. This intensive practice is completely out of line with the values obtained from the standard (ISO 2631, 2002). The rider is supposed to stop his activity after barely 10 min of trotting, knowing that a work session in horseback riding lasts on average one hour per horse. However, it is interesting to consider this indicator when planning the work sessions, to adapt work time to each pace depending on the defined target.

4. Conclusions

This pilot study on the quantification of human exposure to vibrations of riders' spine-lumbar suggests that horseback riding could lead to health risk for professional riders following the European Directive. The type of riding saddle plays a major role in the transmission of vibrations, particularly by modifying the rider's posture (different rotation of the pelvis, modification of the leg position).

These standards do not seem really suitable for the world of horseback riding. It would be judicious to adapt the vibration exposure indicators to the specific characteristics of equestrian practice, in particular by taking into account the horse's and rider's motion, as well as optimising the placement of the sensors at the saddle. They could be used optimally to adapt training sessions and as another evaluation indices of the riders' musculoskeletal disorders of the lumbar spine. These indicators could also be used in the process of validating equipment with saddle manufacturers to improve their design.

References

Boshuizen HC, Bongers PM, Hulshof ECT. 1990. Back disorders and occupational exposure to whole-body vibration. Int J Ind Ergon. 6(1):55–59. juillet doi:10.1016/0169-8141(90)90050-C.

Clayton HM, O'Connor KA, Kaiser LJ. 2014. Force and pressure distribution beneath a conventional dressage saddle and a treeless dressage saddle with panels. Vet J. 199(1):44–48. doi:10.1016/j.tvjl.2013.09.066.

Deckers I, De Bruyne C, Roussel NA, Truijen S, Minguet P, Lewis V, Wilkins C, Van Breda E. 2021. Assessing the sport-specific and functional characteristics of back pain in horse riders. Comp Exercise Physiol. 17(1):7–15. doi:10.3920/CEP190075.

Directive 2002/44/EC of the European parliament and of the Council of 25 June 2002 on the minimum health and

safety requirements regarding the exposure of workers to the risks arising from physical agents (vibration).

ISO 2631-1: mechanical vibration and shock – assessment of whole-body vibration exposure of individuals. 2002.

Zeng X, Trask C, Kociolek A. 2017. Whole-body vibration exposure of occupational horseback riding in agriculture: a ranching example. Am J Ind Med. 60(2):215–220. doi: 10.1002/ajim.22683.

KEYWORDS Horseback rider; Whole-Body vibration; lumbar spine; ISO 2631; experimental measurement

juliette.bonnigal-riondel@epfedu.fr

Trunk kinematics in wheelchair badminton: preliminary results

I. Alberca[a], T. Marsan[b], Félix Chénier[c], B. Watier[b,d] and A. Faupin[a]

[a]Laboratoire IAPS, Université de Toulon, Toulon, France; [b]LAAS- CNRS, CNRS, UPS, Université de Toulouse, Toulouse, France; [c]Mobility and Adaptive Sports Research Lab, Université du Québec à Montréal, Centre for Interdisciplinary Research in Rehabilitation of Greater Montreal, Montreal, Canada; [d]CNRS-AIST, JRL IRL, Tsukuba, Japan

1. Introduction

Wheelchair badminton is a relatively new sport that was officially integrated into the international Paralympic scene at the Tokyo Games in 2021. This wheelchair sport presents several peculiarities in terms of movement, which is solely done through forward (FP) and backward propulsion (BP). Due to this specificity of movement and the internal logic of badminton, players must perform significant forward and backward trunk tilts to retrieve net shots or clearances. Trunk postural control is crucial for stabilizing the entire body and generating muscular force during physical activity. When the trunk is stable, it is easier and safer to transfer the forces applied along the body to perform any motor task, improving muscular action, and reducing joint load (Kibler et al. 2006). In addition, studies have identified important differences in upper limb kinematics, temporal characteristics of propulsion (Sanderson and Sommer 1985), and energy expenditure (Vanlandewijck et al. 1994) depending on the degree of trunk flexion. Therefore, studying trunk kinematics is a key element to consider in wheelchair badminton. There are two classes of athletes in this sport: WH1, who are athletes with little or no abdominal function, and WH2, who have abdominal function. These differences in abdominal function notably affect postural stability and propulsion capacity (Gagnon et al. 2009).

The aim of this case study is to compare the trunk kinematics of two wheelchair badminton players, one belonging to the WH1 class and the other to the WH2 class. This analysis will allow for a better understanding of the impact of abdominal function on postural stability and performance in this wheelchair sport.

2. Methods

2.1. Participants

Our study involved the participation of two French elite para-badminton players of classes WH1 and WH2, who reported no injury or pain that could impede their wheelchair propulsion. The categories were defined according to the BWF classification regulations. Their height and weight were 1.68 m and 1.8 m, and 71 kg and 60 kg. They used their own wheelchair designed for para-badminton, and their own racket. This research was authorized by EudraCT/IDRCB n° 2020-A02919-30.

2.2. Experimentation

The two athletes were asked to perform consecutive sprints in FP and BP for one minute on a straight line of 3 meters. They started from a standing start in FP and then, once the big wheels of the wheelchair crossed the three-meter line, they started again in BP and so on for one minute. The tests were conducted in a laboratory on a wooden parquet surface. Kinematics were recorded using an optoelectronic system composed of 22 cameras (Vicon® System, ©Oxford Metrics Inc., UK) arranged in a circular manner. The following markers were recorded at a frequency of 200 Hz: right and left occipital and temporal bones, manubrium, C7, T8, xiphoid process, 6th right and left ribs, high, low, right and left scapular spines, acromion, center of the clavicle, medial and lateral epicondyles of the right and left elbows, right and left radial and ulnar styloid processes, rigid body of 4 markers on the right and left arm, right and left radius (technical markers), and 2nd and 5th right and left metacarpal heads.

2.3. Data processing

Data were processed using Python 3.11 and the Kinetics Toolkit library (Chénier 2021). A trunk segment was created from the middle point of T8 and xiphoid process to the middle point of C7 and manubrium. The trunk angle was calculated by projecting this segment in the sagittal plane. The phases of FP and BP as well as the transition from FP to BP (TBP) and the transition from BP to FP (TFP) phases were manually identified by video analysis and marked using events. Peak angles were calculated for each phase and each transition. Given the nature of our case study, no statistical test was performed.

3. Results and discussion

The test results of the study are presented in Table 1.

According to Table 1, both athletes performed consecutive forward trunk inclinations during the FP and BP. This allowed them to achieve synchronous

Table 1. Peak trunk inclination angles. +forward, −backward.

	Peak angle FP (°)	Peak angle BP (°)
WH1	60.36 (5.66)	24.55 (6.04)
WH2	76.63 (2.99)	49.06 (6.22)
WH2-WH1	+16.27	+24.51
	Peak angle TFP (°)	Peak angle TBP (°)
WH1	33.23 (8.12)	−27.93 (3.28)
WH2	75.91 (4.73)	−14.51 (3.57)
WH2-WH1	+42.68	−13.42

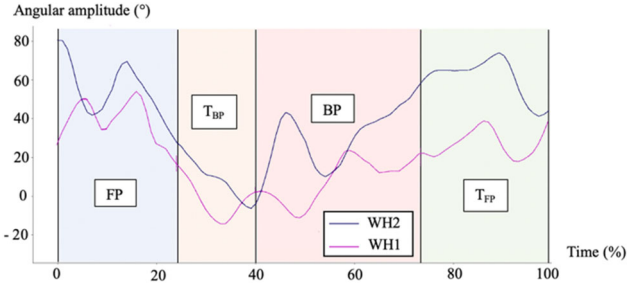


Figure 1. Example of a complete cycle of FP-TBP-BP- TFP for each athlete.

propulsion. Figure 1 illustrates this and the transition phases.

During TFP, the athletes positioned their trunk in a forward inclination to brake efficiently and be able to restart in FP. Conversely, they positioned their trunk in a backward inclination during TBP. This position allows them to brake more quickly by placing their center of gravity behind the wheelchair.

Comparing the results of the two athletes, it appears that WH2 exhibited greater forward trunk inclinations during both FP and BP as well as during TFP, compared to WH1. These differences can be explained by differences in the athletes' abilities. Indeed, WH2 has abdominal strength that allows him to perform significant forward trunk inclinations during propulsion and braking without falling. Conversely, WH1, who lacks abdominal strength, will fall if he inclines his trunk too far forward. He will then have to use his arms to lift his upper body, which could slow him down.

Regarding TFP, it is WH1 who performs the greatest trunk inclinations backward. Here also, the results can be explained by abdominal strength. Indeed, WH1, not having abdominal strength, will not be able to control his backward trunk inclination. Furthermore, WH2 does not have a backrest which may limit his backward trunk inclinations to avoid any falls.

4. Conclusions

The preliminary results of this case study reveal differences between the two classes of athletes regarding trunk inclination. Athlete WH2 seems to perform more significant forward inclinations than athlete WH1, while the latter performs more pronounced backward trunk inclinations. These preliminary results of this case study are a step towards a better understanding of the kinetics of wheelchair badminton, but this requires further in-depth studies on the subject. It would also be interesting to examine the risks of injury associated with joint amplitudes, especially at the shoulders and wrists, to better prevent injuries. Therefore, further research is necessary by studying other joints. Additionally, the results obtained could help athletes and coaches identify strategic positioning on the court based on athletes' abilities. Finally, if differences in trunk inclinations exist between the WH1 and WH2 classes in our case study, it would be interesting to see if this is also the case for a larger cohort of athletes. These identified differences could contribute to the athlete classification process based on functional classification.

Acknowledgements

The authors thank the various participants in the study as well as the laboratory of the LAAS-CNRS.

References

Chénier F. 2021. Kinetics toolkit: an open- source python package to facilitate research in biomechanics. JOSS. 6(66):3714. doi:10.21105/joss.03714.

Gagnon D, Verrier M, Masani K, Nadeau S, Aissaoui R, Popovic M. 2009. Effects of trunk impairments on manual wheelchair propulsion among individuals with a spinal cord injury: a brief overview and future challenges. Topics in Spinal Cord Inj Rehabil. 15(2):59–70. doi:10.1310/sci1502-59.

Kibler WB, Press J, Sciascia A. 2006. The role of core stability in athletic function. Sports Med. 36(3):189–198. doi:10.2165/00007256-200636030-00001.

Sanderson DJ, Sommer HJ. 1985. Kinematic features of wheelchair propulsion. J Biomech. 18(6):423–429. doi:10.1016/0021-9290(85)90277-5.

Vanlandewijck YC, Spaepen AJ, Lysens RJ. 1994. Wheelchair propulsion efficiency: movement pattern adaptations to speed changes. Med Sci Sports Exerc. 26(11):1373–1381.

KEYWORDS Wheelchair badminton; trunk kinetics; forward propulsion; backward propulsion

ilona.alberca@univ-tln.fr

Validation of walking events detecting algorithm during Nordic walking of healthy subjects

M. Blandeau, R. Lesaffre and L. Wallard

LAMIH, CNRS, UMR 8201, Univ. Polytechnique Hauts-de-France, Valenciennes, France

1. Introduction

Nordic walking popularity as a physical activity has increased in last 15 years due to its playfulness and easy accessibility. Nordic walking is more and more considered as a physical practice during rehabilitation to improve gait patterns or counteract the deterioration of walking quality (e.g. Ben Mansour et al. 2018). Moreover, Nordic walking is known for its social and psychological benefits (Zurawik 2020) and differs to normal walking both in kinematics and tool usage (poles). Nevertheless, because of its practice in ecological situations, carrying out a classical analysis of Nordic walking through the detection of walking events is a challenge.

Detection of walking events is at the core of gait analysis. Gait can be broken down into cycles defined by walking events, Heel Strike (HS) and Toe Off (TO) (Perry 2010). They are usually detected in biomechanics studies using forces platform or through the use of algorithms based on kinematics data from optoelectronic systems (Fonseca et al. 2022). Despite a very large number of articles dedicated to estimating walking events through kinematics, no articles were found on the specific practice of Nordic walking.

Hence, the purpose of this study is to test the ability of three classical algorithms for detecting walking events on a practice of walking as well as Nordic walking.

2. Methods

2.1. Participants

Seventeen subjects without known osteoarticular pathologies and engaged in regular physical activity gave their voluntarily consent to participate in this study (age: 26.4 ± 5.9 years; height: 172.18 ± 7.2 cm; mass: 74.47 ± 15.2 kg).

2.2. Protocol

A total of 49 reflective markers were placed on each subjects following the recommendation of the IOR Full Body Model. Markers' 3D trajectories were recorded with a 12 cameras motion capture system (VICON) with a framerate of 200 Hz.

Each participant was asked to walk over a 10-m corridor on which were placed 4 Kistler forces platform Type 9286 A. In order to prevent subjects from targeting their gait at the force platform, subjects walked as many times as required to step 10 times exactly on at least one platform. To do this, one of the experimenters took care of observing the walking of subjects on the force platforms in contact with feet.

The first passage was done in normal walking, the second in fast walking and the third in Nordic walking with poles (all conditions were at self-selected speed). Concerning the passage in Nordic walking, the participants had a period of familiarization with walking in sticks of about 5 min in order not to distort the results of participants not initiated to the practice.

2.3. Data analysis

Two different datasets were used to compute the walking events. Reference events were computed with the force platform data. Reference HS and TO were defined when the vertical force reached a value respectively above or below 20 N (Fonseca et al. 2022). Kinematics based events were computed *via* the 3D trajectories of marker which were processed according to the event detection algorithms proposed in (Zeni et al. 2008) [Zeni 1] and [Zeni 2], and (Hreljac and Marshall 2000) [HMA]. The [Zeni 1], [Zeni 2] and [HMA] algorithms are respectively based on positions, velocities and accelerations of foot and sacrum markers.

Reference timing was subtracted to the three other algorithms to obtain the average time difference in HS and TO detection between algorithms and forces platforms according to the 3 walking conditions. After verification of the normality, repeated measures two-ways ANOVA were performed on both HS and TO errors depending on the 3 algorithms and walking conditions. A Post Hoc test was carried out in order to verify these significant differences by pairing *T*-test with Bonferroni corrections.

Data processing and statistical computation were carried out on Matlab software. Statistical tests were performed using the 0D SPM toolbox to investigate potential effect of walking condition on the mean detection error of HS and TO events.

3. Results and discussion

Fifty-one acquisitions were collected for all subjects who walked between 3 and 10 times over the corridor

Table 1. Mean error and standard deviation (in sec) of HS and to detection between algorithms and forces platform for each gait condition.

	HS			TO		
	HMA	Zeni 1	Zeni 2	HMA	Zeni 1	Zeni 2
Normal	−0.08	−0.04	−0.04	0.03	0.01	0.01
	± 0.08	± 0.02	± 0.02	± 0.03	± 0.03	± 0.04
Fast	−0.05	−0.03	−0.03	0.03	0.01	0.01
	± 0.07	± 0.01	± 0.01	± 0.01	± 0.01	± 0.01
Nordic	−0.02	−0.03	−0.03	0.02	0.01	0.01
	± 0.07	± 0.01	± 0.01	± 0.02	± 0.03	± 0.03

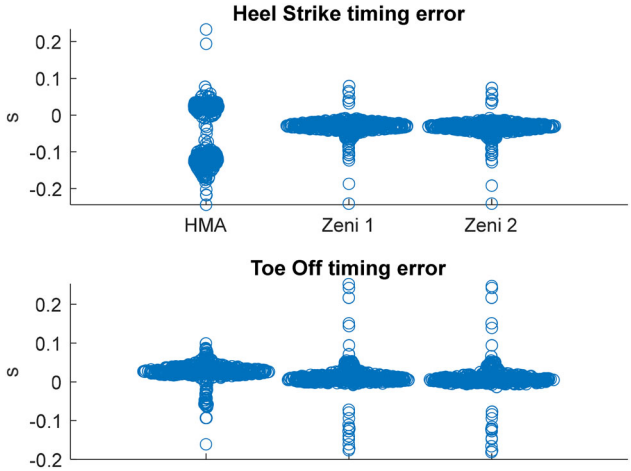


Figure 1. Timing error for HS and to depending on the three algorithms for all conditions.

for each condition. A total of 223 walking events were identified for normal walking, 153 for Fast walking and 183 for Nordic walking. Mean error and standard deviation between the force platform data and the [Zeni 1], [Zeni 2] and [HMA] algorithms according to the gait conditions for HS and TO detection has been carried out (cf. Table 1).

The [HMA] algorithm presents an average error between 0.08 s and 0.02 s depending on the gait conditions. On the other hand, the [Zeni 1] and [Zeni 2] algorithms show an error between 0.04 and 0.01 s. Moreover, for each algorithm, the Nordic walking condition represents the lowest average error. Finally, for the 3 algorithms, the lowest average error was in the detection of TO compared to HS, and that whatever the gait condition.

The 2-ways RM ANOVA yielded significant results for both HS and TO detection according to gait condition.

For HS detection event (cf. Figure 1), the results showed a significant difference both on the algorithm and walking condition ($p = 0.002$). Significant differences were found between [HMA] and [Zeni 1] and between [HMA] and [Zeni 2] ($p < 0.001$) but not between [Zeni 1] and [Zeni 2] on all walking conditions. Similarly, all algorithms result significantly changed their timing error depending on the walking condition ($p < 0.001$).

For TO detection event (cf. Figure 1), the results showed a significant difference only on the algorithm choice ($p = 0.002$). Post-hoc analysis yieled a significant difference between [HMA] and [Zeni 1] and between [HMA] and [Zeni 2] ($p < 0.001$) but not between [Zeni 1] and [Zeni 2] on all walking conditions

Interestingly, the [HMA] HS estimation precision improves with gait speed increase whereas [Zeni 1] and [Zeni 2] stay constant. It might be due to the content of the [HMA] algorithm based on acceleration and jerk; quicker kinematics could improve the precision of event detection. Theses results shows that both Zeni algorithm seem more appropriate for the study of nordic walking.

4. Conclusion

The aim of this study was to test the ability of three classical algorithms for detecting walking events on 3 gait conditions (normal walking, fast walking and Nordic walking). All algorithms were successful in detecting walking events (HS and TO), with better results for [Zeni 1] and [Zeni 2] especially for HS. Moreover, [Zeni 1] and [Zeni 2] appears to be more robust related to walking speed.

Despite the presence of significant differences between the algorithms for each condition, all three algorithms obtained accurate average errors in the Nordic walking condition compared to other conditions for either HS or TO. These results encourage the feasibility of detecting walking events on a Nordic walking practice with embedded motion capture systems.

References

Ben Mansour K, Gorce P, Rezzoug N. 2018. The impact of Nordic walking training on the gait of the elderly. J Sports Sci. 36(20):2368–2374. doi:10.1080/02640414.2018.1458396.

Fonseca M, Dumas R, Armand S. 2022. Automatic gait event detection in pathologic gait using an auto-selection approach among concurrent methods. Gait Posture. 96:271–274. doi:10.1016/j.gaitpost.2022.06.001.

Hreljac A, Marshall RN. 2000. Algorithms to determine event timing during normal walking using kinematic data. J Biomech. 33(6):783–786. Jun. doi:10.1016/s0021-9290(00)00014-2.

Perry J. 2010. Gait analysis: normal and pathological function. J Sports Sci Med. 9(2):353.

Zeni JA, Jr, Richards JG, Higginson JS. 2008. Two simple methods for determining gait events during treadmill and overground walking using kinematic data. Gait Posture. 27(4):710–714. doi:10.1016/j.gaitpost.2007.07.007.

Zurawik MA. 2020. Socio-environmental influences on Nordic walking participation and their implications for well-being. J Outdoor Recreat Tourism. 29:100285.

KEYWORDS Nordic walking; gait; events; kinematics; algorithm

mathias.blandeau@uphf.fr

Wheelchair caster power losses due to rolling resistance

Z. Pomarat[a], T. Marsan[b], A. Faupin[a], Y. Landon[c] and B. Watier[b,d]

[a]Laboratoire IAPS, Université de Toulon, Toulon, France; [b]LAAS-CNRS, CNRS, UPS, Université de Toulouse, Toulouse, France; [c]ICA, Université de Toulouse, Toulouse, France; [d]CNRS-AIST, JRL IRL, Tsukuba, Japan

1. Introduction

The gross mechanical efficiency of the manual wheelchair (MWC) propulsion movement is defined as the ratio between power applied to the hand rim and energy expenditure associated. The values reported in the literature for wheelchair propulsion are particularly low (between 2.0 and 10.5%) compared to other movements (between 18 and 23% for cycling and between 20 and 40% for walking (Zepeda et al. 2016)). Thus, the MWC propulsion movement is a major issue in sports performance.

The energy losses during the MWC propulsion were mainly due to rolling resistance (RR) (Bascou 2012). Testing methods evaluating the RR of a MWC were mostly focused on the evaluation of the RR of the entire wheelchair, without isolating the front caster.

However, caster wheels are responsible for the rotation around the vertical axis and the stability of the wheelchair. As such their study must not be neglected for both daily and sports applications.

Many authors agreed that the geometry and the material of the casters, the surface, the mass distribution between rear wheels and front casters (Sauret et al. 2012) and the load applied on the front casters (Ott et al. 2022) had a significant impact on the RR force acting on the system. However, until now, no study has evaluated the power dissipated due to RR.

Hence, the purpose of this study was to evaluate the power losses due to RR in front casters during wheelchair propulsion. Four casters with different geometries and materials were used. The tests were conducted on two surfaces with different deformation properties, at a specific speed and under several loadings. It was expected that the casters with the smallest diameters would generate the most power losses. It was also hypothesized that the lowest power would be dissipated on the less deformable floor, regardless of the caster or the loading.

2. Methods

2.1. Experimentation

Four casters (1Spherical, Ø50,8 mm; 2Omniwheel, Ø127 mm; 3Skate, Ø52 mm; 4Roller, Ø80 mm) were tested on two surfaces representative of indoor sports surfaces (parquet floor and Taraflex-type PVC floor). A specific test bench adapted from a cutting bench was used. It was composed of a horizontal plane moving back and forth and a 6-axis force sensor (3-D dynamometer type 9257B, Kistler). The force sensor measured the efforts applied by the surface to the caster when the horizontal plane was translating back and forth at 1.1 m/s. The speed was chosen to correspond to a daily normal displacement speed (Chan et al. 2018). Tests were conducted under four compressive loads (50 N, 100 N, 150 N, 200 N). These loading conditions were based on the literature with a total mass system (subject and wheelchair) of 100 kg with a loading on each caster of 5%, 10%, 15%, and 20% of this total mass (Chan et al. 2018). Speed data were measured at 200 Hz. Forces were measured at 1000 Hz. Each caster was tested once under the surface and load conditions described above, for a total of 32 tests.

2.2. Data processing

Load data were resampled at 200 Hz and filtered with a 2nd order Butterworth low-pass filter (4 Hz-cut-off frequency). Loading data were synchronized with the speed data. Power (P) dissipated by the caster was calculated as the product of the horizontal force (F_h) and the linear speed (v) of the plane:

$$P = F_h.v$$

The whole roundtrips were identified and data were processed only on forward phases (between 2 and 11 depending on the trial). The mean and standard deviation (SD) of the power dissipated was calculated for each trial. To evaluate the impact of the different parameters (loading, surface and caster type), the mean and the standard deviation of the mean powers was calculated for the trials implying the parameter. The mean power over all the trials was also calculated as a reference.

3. Results and discussion

The power dissipated on the Taraflex was more than four times higher than on the parquet and was higher than the average power over all the trials (Figure 1). This result could be explained by the deformable

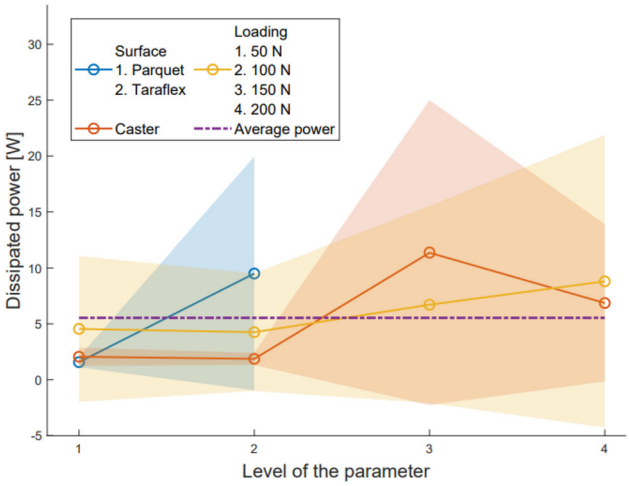


Figure 1. Impact of the parameters on the dissipated power for the trials. The colored areas reprensent the standard deviation.

Table 1. Mean and standard deviations of the power dissipated [W] during the trials for the different casters.

		1	2	3	4
50 N	P	1.4 ± 0.4	1.4 ± 0.4	1.4 ± 0.7	0.8 ± 0.4
	T	1.9 ± 1.0	1.8 ± 0.8	5.6 ± 2.9	4.7 ± 2.3
100 N	P	1.5 ± 0.5	1.4 ± 0.5	1.3 ± 0.6	0.9 ± 0.6
	T	1.9 ± 1.1	2.1 ± 1.1	15.0 ± 7.8	9.9 ± 2.1
150 N	P	1.5 ± 0.5	1.5 ± 0.5	2.5 ± 1.0	2.1 ± 0.8
	T	2.9 ± 1.6	2.6 ± 1.4	25.2 ± 12.7	15.4 ± 1.1
200 N	P	1.6 ± 0.5	1.4 ± 0.5	2.2 ± 1.0	2.3 ± 1.1
	T	3.7 ± 1.8	2.7 ± 1.4	37.8 ± 19.1	18.8 ± 9.4

nature of the Taraflex, which corroborates with a result stated by Chan et al. (2018).

At loadings of 50 N and 100 N, the power dissipated was roughly equivalent and lower than the average power. From 100 N, the power dissipated varied linearly with the loading. Beyond 150 N, the loading had a critical effect on the power dissipated since it was much higher than the average power (Figure 1). The fact that a loading of 50 N implies more dissipated power than a loading of 100 N was surprising. This could be explained by the relation between the impact of the loading and the diameter of the caster (Zepeda et al. 2016). The interaction between combined factors could surestimate the effect of each individual factor (Ott et al. 2022).

The power dissipated by the spherical and the Omniwheel casters were equivalent and more than two times lower than the average power. The skate caster dissipated almost four times more power than the spherical and Omniwheel casters (Figure 1). Several authors have shown that casters with a lower diameter dissipated more power (Sauret et al. 2012). However, the smallest caster in this study (spherical) dissipated the less power. This could be explained by the geometry and the material of the spherical caster which implied a contact surface between the caster and the surface much lower than the one for skate and roller casters. In assessing the impact of the parameters on the dissipated power, some SD values were higher than the mean values, leading to the negative values shown in Figure 1. These SD values reflect a large variability of results between conditions, which can be explained by a possible variability between measurements due to surface irregularities, for example, or by parameter interdependance.

On the parquet, the lowest power was 0.8 ± 0.4 W (50 N, roller). On the Taraflex, the lowest power dissipated was 1.8 ± 0.8 W (50 N, Omniwheel). The highest power dissipated was 37.8 ± 19.1 W (200 N, Taraflex, skate) (Table 1).

The SD values were particularly high on the Taraflex. Once again, this could be explained by the deformation of the surface during the trial which involved a larger contact surface between the Taraflex and the caster.

4. Conclusions

This study was the first one evaluating the power dissipated due to RR in front casters during wheelchair propulsion. Thus, the results of this study cannot be compared to literature.

This study was also the first one investigating the effect of a floor representative of sports applications as a Taraflex-type PVC floor and a spherical caster. This study has shown that the Taraflex floor considerably increases the dissipated power, regardless the other parameters. Then, it would not be recommended to use this type of floor for sports performance. This study also revealed that spherical and Omniwheel casters seem to be interesting candidates for use on wheelchairs. A future study will investigate the impact on the speed and the direction of translation (front or back) on the dissipated power. In the field, tests must also validate the present results by mounting the casters on the wheelchairs.

References

Bascou J. 2012. Analyse biomécanique pour la compréhension et l'amélioration du fauteuil roulant dans son application au tennis de haut niveau. Available from: https://pastel.hal.science/pastel-00831253/document

Chan FHN, Eshraghi M, Alhazmi MA, Sawatzky BJ. 2018. The effect of caster types on global rolling resistance in manual wheelchairs on indoor and outdoor surfaces.

Assistive Technol. 30(4):176–182. doi:10.1080/10400435.2017.1307880.

Ott J, Wilson-Jene H, Koontz A, Pearlman J. 2022. Evaluation of rolling resistance in manual wheelchair wheels and casters using drum-based testing. Disabil Rehabil Assistive Technol. 17(6):719–730.

Sauret C, Bascou J, Rmy N de S, Pillet H, Vaslin P, Lavaste F. 2012. Assessment of field rolling resistance of manual wheelchairs. JRRD. 49(1):63. doi:10.1682/JRRD.2011.03.0050.

Zepeda R, Chan F, Sawatzky B. 2016. The effect of caster wheel diameter and mass distribution on drag forces in manual wheelchairs. J Rehabil Res Dev. 53(6):893–900. doi:10.1682/JRRD.2015.05.0074.

KEYWORDS Casters; manual wheelchair; power losses; rolling resistance

zpomarat@laas.fr

Wrist extensor tendon forces during tennis forehand might be modulated by player-specific technique

B. Goislard de Monsaberta, T. Cartier[a], A. Herbaut[b] and L. Vigouroux[a]

[a]Aix-Marseille University, CNRS, ISM, Marseille, France; [b]Human Factors & Ergonomics Department, Decathlon SportsLab Research and Development, Lille, France

1. Introduction

Lateral epicondylitis, also known as tennis elbow, is a major health issue among tennis players as well as in other part of the population, e.g. assembly line workers or musicians (Lenoir et al. 2019). This musculoskeletal disorder affects hand extensor tendons, results in substantial pain and impairments for sporting and everyday activities and can require more than 12 months for full recovery (Lenoir et al. 2019). Unfortunately, prevention remains limited by the lack of data regarding biomechanical risk factors, especially because *in vivo* evaluation of hand tendon forces remains challenging. Musculoskeletal modeling is a non-invasive method to estimate muscle and joint loading from motion capture data and has already provided insights in biomechanical loadings during tennis playing (Martin et al. 2014). Nonetheless, such modeling approach was never applied to study hand mechanical loading during tennis playing. The objective of this study was thus to develop a musculoskeletal model to provide new insight into hand tendon loading in tennis players.

2. Methods

2.1. Participants and protocol

An Advanced player (ITN 3; 19 y; 185 cm; 64 kg; grip strength: 653 N; eastern grip position) and an Intermediate player (ITN 7; 19 y; 183 cm; 73 kg; grip strength: 1195 N; semi-western grip) participated in a two-step protocol. The first step consisted in a series of grip force tasks to establish a relationship between electromyographic (EMG, Trigno, Delsys, MA, 2000 Hz) activities and grip force (3.3-cm diameter cylindrical handle, Sixaxes, FR). The second step consisted in performing forehand drives to hit a target with a ball being sent by a ball machine. The forehand drives were performed at two different shot speeds (Slow and Fast) and with three different rackets (R1, R2 and R2w) with different mass (270–320 g) and transverse moment of inertia (125–162 kg cm^2).

2.2. Motion capture data acquisition

Upper limb and hand three-dimensional kinematics were tracked using reflective markers (Figure 1) and a seven-camera motion capture system (MX T40, Vicon, Oxford, UK). EMG activities were synchronously recorded for four forearm muscles (FCR: flexor carpi radialis, ECR: extensor carpi radialis, FDS: flexor digitorum superficialis, and EDC: extensor digitorum communis, see Figure 1).

2.3. Muscle force estimation

An electromyography-informed musculoskeletal model was developed to estimate the tendon forces of 42 hand muscles, including both finger intrinsic and extrinsic as well as wrist prime movers. The model relied on an inverse-dynamics approach (Goislard de Monsabert et al. 2012) with three main inputs: grip force estimated from FDS EMG activity (step 1), wrist net moments deduced from marker displacement data and EMG-informed muscle force estimation using FCR, ECR and EDC force-length-activation relationships (Goislard de Monsabert et al. 2020). The model was run for five specific time points (Figure 2) from beginning of forward acceleration to end of follow-through phases (vertical dashed bars on Figure 1). From the 42 tendon forces estimated by the model, muscle group forces of finger (ΣF^{F-ext}) and wrist (ΣF^{W-ext}) extensors were calculated by summing the forces of the four EDC and the three wrist extensors, respectively.

2.4. Data analysis

For comparison between players, muscle group forces at pre-impact were first normalized and expressed as percentage of maximal grip force (MGF) and then

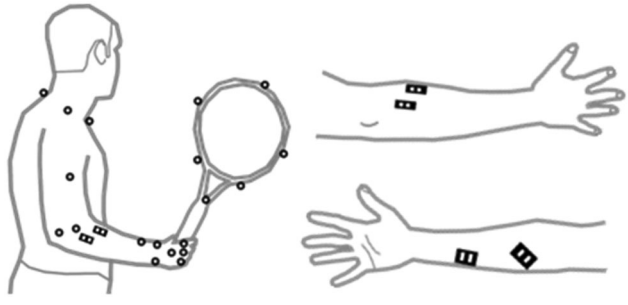


Figure 1. Illustrations of the positions of the motion capture markers (left panel) and surface EMG electrodes (right panels).

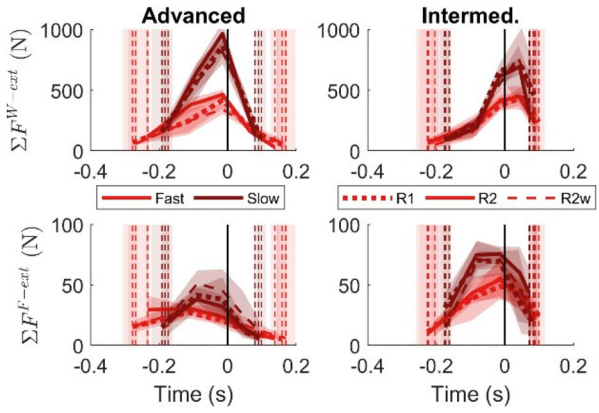


Figure 2. Mean and standard deviation ($n = 5$ shots) of muscle group forces of the wrist extensors (W-ext) and finger extensors (F-ext) for the two players (Advanced and Intermediate). Slow shots are represented in lighter red while Fast ones are darker. Line styles correspond to different rackets. Vertical solid line at 0s represents ball-racket impact.

Table 1. Mean ± one standard deviation values ($n = 5$ shots) of wrist extensor group force efficiency (ΣF^{W-ext}) at Pre-Impact for both players (Advanced and Intermediate) for each of the shot speeds (Slow and Fast) performed with the three rackets (R1, R2, R2w).

	Efficiency index (%MGF/V_{ball})	
ΣF^{W-ext} at Pre-Impact	Slow	Fast
Advanced		
R1	4.3 ± 0.5	5.3 ± 0.4
R2	4.7 ± 0.4	5.6 ± 0.6
R2w	4.8 ± 0.7	5.1 ± 0.3
Intermediate		
R1	1.7 ± 0.2	1.6 ± 0.1
R2	1.7 ± 0.2	1.6 ± 0.2
R2w	1.7 ± 0.3	1.8 ± 0.2

divided by the ball velocity after impact (V_{ball}) in ms^{-1} to express the muscle efficiency (Martin et al. 2014). A low value corresponds to a greater efficiency.

3. Results and discussion

Wrist extensor forces were 10 times higher than finger extensor ones (Figure 2). This low implication of finger extensor is in contradiction to previous EMG recordings (Morris et al. 1989) but for which no information was provided regarding shot speed or player-specific technique. Wrist extensor tendon forces increased with shot speed but were moderately affected by racket properties. When comparing players based on efficiency index (Table 1), the results suggest that the loadings in wrist extensors of the Advanced player were up to three times higher than for the Intermediate one. This inefficient coordination of the Advanced player does not result from the grip force level, which were comparable between players but from the wrist flexion-extension moment which was 3.5 times higher compared to the Intermediate player.

These higher joint moments and tendon loadings for the Advanced player were linked to the dynamics of the racket and upper limb joints. Compared to the Intermediate player, this player's technique involved less smooth racket trajectories at the transition between preparation and forward acceleration with a greater elbow movement amplitude. The two players also used different a grip positions which influences joint coordination (Elliott et al. 1997). The use of an eastern grip position might have participated in the increased elbow extension, leading to a greater racket-shoulder distance and in a different hand orientation, influencing the sharing between the wrist moment components, i.e. flexion-extension and radial-ulnar deviation. These results suggest that player-specific technique, such as racket trajectories, joint coordination and grip position, might modulate importantly wrist extensor tendon loading, potentially leading to a higher risk of LE.

4. Conclusions

The results of this study confirmed wrist extensors are exposed to high mechanical loadings and that player-specific characteristics might modulate this loading. Further studies are required to clarify the factors influencing finger and wrist biomechanical loadings during tennis gesture.

Acknowledgements

Part of the study was funded through a research collaboration between the Decathlon company and the Aix-Marseille university. The authors will not receive any financial benefits from the results of this study and declare no competing interest. The authors would like to thank the participants for their patience and Dr Hugo Hauraix for his assistance during the data acquisition.

References

Elliott B, Takahashi K, Noffal G. 1997. The influence of grip position on upper limb contributions to racket head velocity in a tennis forehand. Journal of Applied Biomechanics. 13(2):182–196. doi:10.1123/jab.13.2.182.

Goislard de Monsabert B, Hauraix H, Caumes M, Herbaut A, Berton E, Vigouroux L. 2020. Modelling force-length-activation relationships of wrist and finger extensor muscles. Med Biol Eng Comput. 58(10):2531–2549. doi:10.1007/s11517-020-02239-0.

Goislard de Monsabert B, Rossi J, Berton E, Vigouroux L. 2012. Quantification of hand and forearm muscle forces during a maximal power grip task. Med Sci Sports Exerc. 44(10):1906–1916. doi:10.1249/MSS.0b013e31825d9612.

Lenoir H, Mares O, Carlier Y. 2019. Management of lateral epicondylitis. Orthop Traumatol Surg Res. 105(8S):S241–S246. doi:10.1016/j.otsr.2019.09.004.

Martin C, Bideau B, Ropars M, Delamarche P, Kulpa R. 2014. Upper limb joint kinetic analysis during tennis serve: assessment of competitive level on efficiency and injury risks: upper limb joint kinetics during tennis serve. Scand J Med Sci Sports. 24(4):700–707. doi:10.1111/sms.12043.

Morris M, Jobe FW, Perry J, Pink M, Healy BS. 1989. Electromyographic analysis of elbow function in tennis players. Am J Sports Med. 17(2):241–247. doi:10.1177/036354658901700215.

KEYWORDS Tennis; muscle force; musculoskeletal model; motion capture; electromyography

Benjamin.goislard-de-monsabert@univ-amu.fr

Musculoskeletal biomechanics

Analysis of paediatric vertebral growth of the lumbar spine through a statistical shape model, page S285.
ArUco-based stylus reliability for 3D digitalisation of glenohumeral cartilage contour, page S288.
Characterizing posture and scapulothoracic joint using biplanar radiography: an *in vitro* evaluation, page S291.
Evaluating the effect of drumstick length on hand muscle activation: a preliminary study, page S294.
From synovial joint morphogenesis to design of contact interfaces, page S297.
Opto-mechanical characterisation of intervertebral disc mimicking phantoms, page S300.
Retention loss and wear of attachment systems for implant retained mandibular overdentures, page S303.
Using EMG to solve the muscle redundancy problem in musculoskeletal models, page S306.

Analysis of paediatric vertebral growth of the lumbar spine through a statistical shape model

N. M. Castoldi[a,b], D. O'Rourke[b], M. Antico[b], L. Gregory[c], V. Sansalone[a] and P. Pivonka[b]

[a]Univ Gustave Eiffel, CNRS, UMR 8208, MSME, Univ Paris Est Creteil, Créteil, France; [b]School of Mechanical, Medical and Process Engineering, Queensland University of Technology, Brisbane, Australia; [c]Clinical Anatomy and Paediatric Imaging Laboratory, Queensland University of Technology, Brisbane, Australia

1. Introduction

Among vertebrates, humans are unique concerning their fully upright posture allowing bipedal locomotion. However, human bipedalism has created a 'terrific mechanical imbalance', and the upright spine was recently considered a 'Scar of Evolution' due to spinal diseases exclusive to humans, such as adolescent idiopathic scoliosis (Smit 2020), which can be associated with disabling conditions, leading to a high mortality rate (Wong and Tan 2010). The relevance of growth-related pathologies highlights the need for a good understanding of the respective changes in the spinal shape, which are poorly understood in the paediatric population. However, while there is ample research on vertebral geometry in adults, not enough clinical and experimental data is available on the paediatric population, since it is hard to justify clinical imaging of children and teenagers. Therefore, the goal of this study is to fill this gap by analysing the main shape and size variations of the fourth lumbar vertebra (L4) in a healthy paediatric population aged 9–19 years old (y/o) through the development of a statistical shape model (SSM), as proposed by Cootes et al. (1995). This model uses clinical images from an available database and analyses the L4 shape and geometry evolution given its similarity in shape with most vertebrae and its position in a highly mechanically loaded environment (Bruno et al. 2017).

2. Material and Methods

2.1. Materials

Abdominopelvic multi-slice computed tomography (MSCT) scans of 66 healthy Australian individuals (36 males and 30 females) were selected from the 'Skeletal Biology and Forensic Anthropology Virtual Osteological Research Database'. The sample database is comprised of de-identified retrospective DICOM from different hospitals (Philips Brilliance 64 CT; and Toshiba Aquilion TSX-101A CT). MSCT scans were obtained with patients lying in an extended supine position (legs straight). The selected scans consist of 6 MSCT per age group, which vary from 9 to 19 y/o. Every age group presents the same number of male and female patients, except from the 10 y/o group, which has 5 male and 1 female MSCT, and the 11 y/o group, that presents 4 male and 2 female MSCT. No differentiation regarding sex were made in the construction of the SSM.

2.2. Methods

Three-dimensional surface meshes of the L4 were created for every MSCT through manual segmentation using the 3D Medical Image Processing Software Materialise MIMICS (Figure 1A). Thereafter, all analysis were performed using MATLAB R2022a. The correspondence of meshes was achieved using a volume-to-volume approach. Therefore, the average shape $-s$ from all vertebrae (Figure 2 left) was used as the baseline mesh (BSL), and all the remaining meshes were applied to the target set (Ti), where i varies from 1 to the total number of patients. The BSL was then deformed to match all targets in two stages: a rigid registration to correct rotation, translation, and scaling of BSL; and a non-rigid registration that deforms the BSL using an iteratively optimised locally weighted rigid deformation (Figure 1B, top). The registration process ensures that all studied samples are constituted by the same number of points (n_p) in corresponding positions. The shape and size variation throughout the dataset was examined by a principal component analysis (PCA). For every subject, its shape s_i was described by the vertex coordinates of every node. Since our work aims to study the shape and size variance related to age, we included the patient age as the last component of our shape vector, as such

$$s_i = \left(x_1,\ y_1,\ z_1, \ldots, x_{n_p},\ y_{n_p},\ z_{n_p},\ \text{age}_i\right)^T \quad (1)$$

Subsequently, $-s$ and the average age (14.41 y/o) were subtracted from all s_i to form the data matrix D (Figure 1B, bottom). Singular value decomposition then computes the eigenvectors of the covariance matrix D, which describes the modes of variation of the shape and age, called the principal components (PC). For every PC, new vertebral shapes s_t can be expressed by $\bar{s}$ and a linear combination of the eigenvectors, as

$$s_t = \bar{s} + \sum_{t=1}^{PC} \boldsymbol{p}_t \lambda_t \quad (2)$$

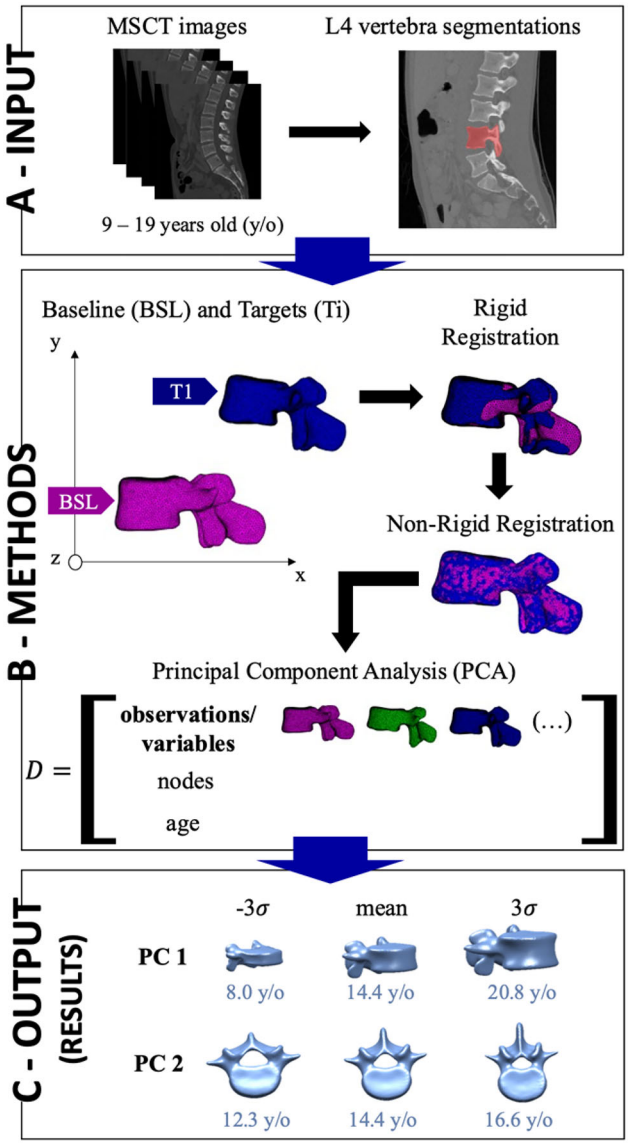


Figure 1. SSM algorithm scheme: from input dataset to output (results).

where $\boldsymbol{p}_t$ represents the eigenvectors for every PC, and λ_t is the coefficients associated with the corresponding eigenvectors. Variations in shape and age can be seen when analysing different standard deviations (σ).

3. Results and discussion

Based on our SSM results, we found that the first seven PCs can explain up to 85% of shape and size variability (Figure 2 right). We evaluated the quality of our model using the root mean square error, which was calculated by recreating the total dataset with the SSM for every PC as described in Equation 2 and comparing it to the original data.

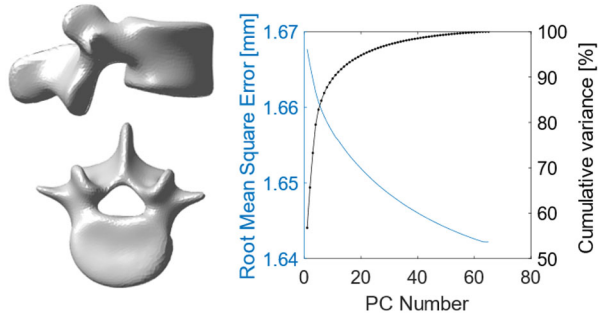


Figure 2. Mean L4 shape (left). cumulative variance of PCA and root mean square error (right).

Our analysis revealed a maximum error of 1.67 mm, which indicates a reasonable level of accuracy giving the vertebral dimensions. Finally, results show that 56.8% of shape and size variation with age is represented by an isotropic volumetric growth of the vertebra (PC 1 – Figure 1C, top), and around 10% of variation is represented by the variation in size of the spinal canal (PC 2 – Figure 1C, bottom). Further PCs also highlight the elongation of the spinal processes with age, and specially the increase in vertebral height.

4. Conclusions

To the best of the authors' knowledge, this study represents the first SSM of a paediatric lumbar vertebra. Our findings demonstrate significant growth in all dimensions, which slightly deviates from the typical expectation that vertebral bodies grow mainly in height at the growth plates, due to their endochondral ossification. Moreover, our SSM analysis revealed insights into specific growth patterns, including variations in the shape of the spinal canal, which have not been previously explored. Similar results were obtained using a reduced dataset of 44 vertebrae, supporting the relevance of these findings. Overall, our results provide valuable information regarding the shape and size variability of vertebrae during the growth process in paediatric populations. Better understanding these growth patterns can aid in the development of more accurate and effective models of vertebral growth and development and help improve decision-making in paediatric spinal surgeries. Future work will investigate the evolution of bone microstructure and the potential influence of sex on growth patterns.

Acknowledgements

We thank the CNRS IRP Coss&Vita, and the International French Society of Biomechanics.

References

Bruno AG, Burkhart K, Allaire B, Anderson DE, Bouxsein ML. 2017. Spinal loading patterns from biomechanical modeling explain the high incidence of vertebral fractures in the thoracolumbar region. J Bone Miner Res. 32(6):1282–1290. doi:10.1002/jbmr.3113.

Cootes TF, Taylor CJ, Cooper DH, Graham J. 1995. Active shape models-their training and application. Comput Vision Image Understanding. 61(1):38–59. doi:10.1006/cviu.1995.1004.

Smit TH. 2020. Adolescent idiopathic scoliosis: the mechanobiology of differential growth. JOR Spine. 3(4):e1115. doi:10.1002/jsp2.1115.

Wong HK, Tan KJ. 2010. The natural history of adolescent idiopathic scoliosis. Indian J Orthop. 44(1):9–13. doi:10.4103/0019-5413.58601.

KEYWORDS Vertebral growth; statistical shape model; lumbar spine; L4

natalia.muhl-castoldi@u-pec.fr

ArUco-based stylus reliability for 3D digitalisation of glenohumeral cartilage contour

F. Moissenet[a,b], C. Elmo Kulanesan[c], K. Co[d], P. Rodriguez[e], P. Vacher[c], J.-Y. Beaulieu[f] and N. Holzer[a,e]

[a]Biomechanics Laboratory, Geneva University Hospitals and University of Geneva, Geneva, Switzerland; [b]Kinesiology Laboratory, Geneva University Hospitals and University of Geneva, Geneva, Switzerland; [c]Laboratoire SYMME, Université Savoie Mont Blanc, Annecy-le-Vieux, France; [d]Laboratory of Simulation and Movement Modeling, School of Kinesiology and Exercise Sciences, Université de Montréal, Montreal, Canada; [e]Department of Surgery, Geneva University Hospitals, Geneva, Switzerland; [f]Department of Anatomy, Faculty of Medicine, University of Geneva, Geneva, Switzerland

1. Introduction

Developments in vision introduced new approaches for optical tracking based on binary square fiducial markers. Garrido-Jurado et al. (Garrido-Jurado et al. 2014) suggested highly reliable fiducial markers called ArUco markers. On this basis, several authors proposed to combine multiple ArUco markers to define a hand-held stylus (Le et al. 2022). Their studies demonstrated that this approach can led to a sub-millimetric accuracy tracking with a low-cost system based on a simple 2D camera. Still, the reliability of such a stylus remains unknown. The aim of this study was to assess the inter and intra-observer reproducibility of an ArUco-based localisation stylus. This was tested during the 3D digitalisation of the glenoid cartilage related to the glenohumeral joint.

2. Methods

2.1. Specimen preparation

Ten fresh-frozen, unembalmed adult arms (5 right / 5 left sides) were used. None of the limbs had an advanced degenerative joint disease confirmed by direct inspection and radiographs before experiments. The Cantonal Commission for Research Ethics approved this study (2020-00598). Dissection of the pieces consisted in resecting all the soft parts to preserve only bones and cartilages.

2.2. Cartilage contour digitalisation

Cartilage contours were digitalised using an ArUco-based localisation stylus (Figure 1). The 3D localisation of the stylus tip (1-mm radius spherical contact probe) was made available using a set of planar

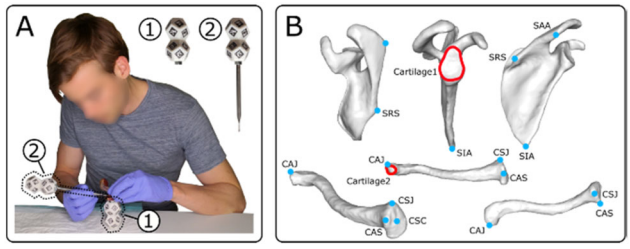


Figure 1. Cartilage contours digitalisation procedure.

ArUco markers (Garrido-Jurado et al. 2014) glued on the surface of a double dodecahedron secured at the other extremity of the stylus. The position of ArUco markers was recorded by a 3.1-Mpx monocular camera (EXO252 MU3, SVS-Vistek, Germany) equipped with a 12-mm focus camera zoom length (PENTAX TV, PENTAX, Japan) at each motion frame (3 Hz). The digitalisation process was performed sequentially. First, a set of anatomical landmarks (Figure 1) were pointed by one examiner (PR) to define bone coordinate systems. Second, the contour of the glenoid cartilage related to the glenohumeral joint was digitalised. To assess the inter and intra-observer reliability of this digitalisation procedure, 3 examiners (PR, CE, FM) performed 3 consecutive digitalisations of each cartilage contour.

2.3. Bone coordinate systems

To allow comparison between digitalisations, the 3D point clouds defining each cartilage contour were expressed in a bone coordinate system. This coordinate system was defined using the previously defined anatomical landmarks following the recommendations of the International Society of Biomechanics (ISB) (Wu et al. 2005). To record the position and orientation of the bone coordinate system, the bone was also instrumented with a double dodecahedron made of ArUco markers (Figure 1).

2.4. Position, orientation, and shape of the cartilage contour

Firstly, the cartilage contour 3D point cloud was projected orthogonally on its least-squares plane. The resulting 2D point cloud was fitted with an ellipse using a least-squares approach based on orthogonal distance. An ellipse coordinate system, centred on the resulting ellipse centre, was defined using 3 unit vectors: along the ellipse major axis, along the ellipse minor axis, and along the least-squares plane normal vector pointing laterally. Secondly, the cartilage 3D point cloud contour was projected orthogonally on a plane having as normal vector the previously defined

Table 1. Intra-class correlation and standard error of measurement observed for the glenoid cartilage related to the glenohumeral joint.

	Intra-observer		Inter-observer	
	ICC	SEM (%)	ICC	SEM (%)
X_{cart}	0.89‡	1.1 (3.6) †	0.85‡	1.3 (4.1) †
Y_{cart}	0.95†	1.0 (5.7) †	0.71*	2.3 (13.6) ‡
Z_{cart}	1.00†	0.4 (2.4) †	0.99†	0.6 (3.3) †
α_{cart}	0.98†	0.9 (4.4) †	0.97†	1.1 (5.3) †
β_{cart}	0.92†	1.1 (10.2) ‡	0.91†	1.2 (11.0) ‡
γ_{cart}	0.95†	1.7 (1.8) †	0.93†	1.9 (2.1) †
L_1	0.92†	0.2 (1.1) †	0.77‡	0.3 (1.9) †
L_2	0.96†	0.1 (1.1) †	0.89‡	0.2 (1.8) †
r	0.68*	3.0 (7.9) †	0.64*	3.2 (8.4) †

Classification: † excellent; ‡ good; * moderate.

unit vector along the ellipse minor axis. The resulting 2D point cloud was fitted with a least-squares circle. A cartilage contour was thus defined by 9 parameters. Six parameters describe its 3D position (X_{cart}, Y_{cart}, Z_{cart}) and orientation (α_{cart}, β_{cart}, γ_{cart}) in the bone coordinate system. Three other parameters describe its shape: ellipse major and minor axes length (L_1 and L_2), and the least-squares circle radius (r).

2.5. Statistical analysis

Intra-observer repeatability and inter-observer reproducibility were computed using an intra-class correlation (ICC), respectively ICC_{intra} and ICC_{inter} following the methodology proposed by Chia and Sangeux (Chia and Sangeux 2017). ICC estimates were completed with the standard error of measurement (SEM).

3. Results and discussion

Statistical analysis results are reported in Table 1. Overall, 35.2 ± 2.4 s were required by each examiner to digitalise the contour of a glenoid cartilage. Intra-observer reproducibility demonstrated good to excellent agreement with an ICC ranging between 0.89 and 1.00, with excellent SEM values, except for the radius of the least-squares circle. Inter-observer reproducibility demonstrated good to excellent agreement with an ICC ranging between 0.77 and 0.99, with excellent SEM values. Only the cartilage position along the inferior-superior $\mathbf{Y_b}$ axis and the least-squares circle radius demonstrated poorer results.

The proposed approach allows for cartilage shape analysis. Concerning the glenoid cartilage, its mean length and width were respectively 28.8 ± 1.2 mm and 20.4 ± 1.2 mm and are consistent with previous studies (Hata et al. 1992). The 3D radius of curvature was 38.1 ± 5.5 mm which is also consistent with previous measurements (McPherson et al. 1997).

This study has some limitations. First, due to the mean age of the specimens (77.4 ± 9.99 years), cartilage morphologic changes may have appeared due to various progression of osteoarthritis making arduous cartilage surface identification. Still, good to excellent agreements were obtained in such conditions. Second, this approach being guided by the operator's vision, it can lead to several discrepancies when the targeted structure is not well recognisable. Hence, it appeared that the inferior-superior limits of the glenoid cartilage were more difficult to identify in a reliable way, which corresponds to the fibrocartilaginous transition area between the glenoid cartilage and the labrum fibrous tissue in the superior and inferior parts of the glenoid. Third, the parameter set used to describe the cartilage position, orientation, and shape might not be adaptable to every cartilage type. In particular, some cartilages are flatter than others, leading to discrepancies when trying to fit a sphere to estimate their curvature. Fourth, the study could have been performed on phantom pieces (e.g. sawbones) to allow both accuracy and reliability assessment. Still, this study is part of a wider project being performed on anatomical pieces.

4. Conclusions

The use of an ArUco-based localisation stylus can thus be a low-cost, reliable, and accurate (Le et al. 2022), approach to digitalise anatomical structures such as shoulder cartilage contours in cadaveric studies.

References

Chia K, Sangeux M. 2017. Quantifying sources of variability in gait analysis. Gait Posture. 56:68–75. doi:10.1016/j.gaitpost.2017.04.040.

Garrido-Jurado S, Muñoz-Salinas R, Madrid-Cuevas FJ, Marín-Jiménez MJ. 2014. Automatic generation and detection of highly reliable fiducial markers under occlusion. Pattern Recognit. 47(6):2280–2292. doi:10.1016/j.patcog.2014.01.005.

Hata Y, Nakatsuchi Y, Saitoh S, Hosaka M, Uchiyama S. 1992. Anatomic study of the glenoid labrum. J Shoulder Elbow Surg. 1(4):207–214. doi:10.1016/1058-2746(92)90015-U.

Le T-S, Tran Q-V, Nguyen X-L, Lin C-Y. 2022. Solpen: an accurate 6-DOF positioning tool for vision-guided robotics. Electronics. 11(4):618. doi:10.3390/electronics11040618.

McPherson EJ, Friedman RJ, An YH, Chokesi R, Dooley RL. 1997. Anthropometric study of normal glenohumeral

relationships. J Shoulder Elbow Surg. 6(2):105–112. doi: 10.1016/s1058-2746(97)90030-6.

Wu G, van der Helm FCT, Veeger HEJ, Makhsous M, Van Roy P, Anglin C, Nagels J, Karduna AR, McQuade K, Wang X, et al. 2005. ISB recommendation on definitions of joint coordinate systems of various joints for the reporting of human joint motion—part II: shoulder, elbow, wrist and hand. J Biomech. 38(5):981–992. doi:10.1016/j.jbiomech.2004.05.042.

KEYWORDS Surface digitalisation; hand-held stylus; ArUco markers; cartilage; shoulder

florent.moissenet@unige.ch

Characterizing posture and scapulothoracic joint using biplanar radiography: an in vitro evaluation

S. Bousigues[a], L. Gajny[a], W. Skalli[a], X. Ohl[b] and N. Hagemeister[c]

[a]Arts et Métiers Institute of Technology, Institut de Biomécanique Humaine Georges Charpak, Paris, France; [b]Maison Blanche, CHU Reims, France; [c]Ecole de Technologie Supérieure, Montréal, Canada

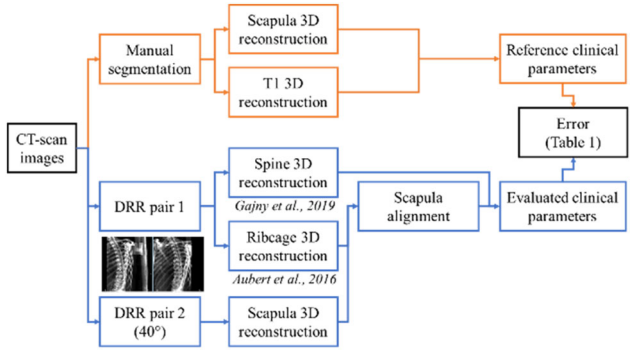


Figure 1. Evaluation process carried out on each CT-scan.

1. Introduction

Scapula position and patient posture have been shown to be interesting in clinical research. For example, the authors (Yamamoto et al. 2015) investigated the relationship between posture and rotator cuff tears, and the authors (Moroder et al. 2020) showed the interest of considering the patient's posture for prosthesis planning. Therefore, the use of biplanar radiography in a standing position seemed interesting to investigate the relationship between posture and shoulder disorders. Methods exist to reconstruct the spine (Gajny et al. 2019), the ribcage (Aubert et al. 2016) and the scapula, but the 3D reconstruction of the scapula is performed on images taken in different planes (with a 40° axial rotation (Bousigues et al. 2023)) from those of the spine and the rib cage. Recently, an interactive method has been proposed to obtain all the bone segments in the same reconstruction in two steps. The first step was a registration based on annotated landmarks on the X-rays. Then, manual adjustments were made using a collision detection algorithm (Gilbert et al. 1988) to avoid interpenetration with the ribcage. This method has been previously evaluated *in vivo* with a reproducibility study (Bousigues et al. 2023). The 95% confidence interval was less than 3° for protraction, and less than 5° for the other parameters. Although the reproducibility was assessed in this previous study, the trueness of these measurements was not evaluated. We propose here an *in vitro* evaluation of the accuracy of the presented method.

2. Methods

Four cadaver CT-scans from previous studies were used. Each scan was used both to create a reference and to generate two pairs of Digitally Reconstructed Radiographs (DRRs). The first pair was designed to reproduce biplanar radiographs in the frontal and lateral planes. The second pair was acquired with an axial rotation of 40° (Figure 1).

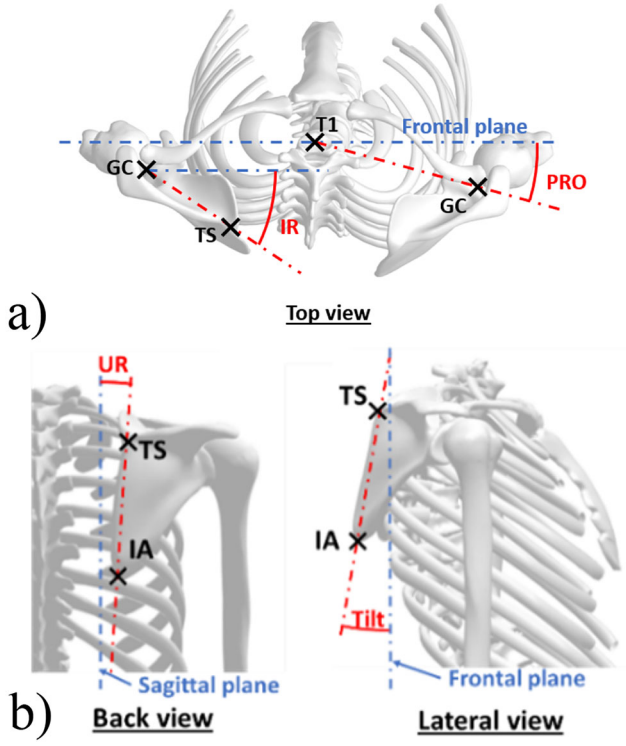


Figure 2. (a) Illustration of protraction and internal rotation (with GC: Glenoid Centre; TS: Trigonum spinae; and T1: Centre of the T1 vertebra body). (b) Illustration of the upward rotation and the tilt (TS: Trigonum spinae, IA: Inferior angle).

2.1. Creation of a reference

The T1 vertebra, the pelvic bone, and the scapulae were manually segmented using MITK-GEM (Pauchard et al. 2016). The mesh elements belonging to regions of interest were manually identified using a in-house software. Clinical parameters were then calculated as references.

Table 1. Mean values obtained on the clinical parameters and difference obtained between the reference and the evaluated method.

	Errors Scan 1	Errors Scan 2	Errors Scan 3	Errors Scan 4
PRO [°]	0.5	−2.3	−2.9	−1.7
IR [°]	−0.6	−4.6	−1.1	1.7
UR [°]	2.3	2.3	1.1	−2.1
Tilt [°]	−2.9	0.3	1.6	−1.1

2.2. Evaluated method

The scapula was reconstructed on the 40° DRR images, while the spine (Gajny et al. 2019) and the ribcage were reconstructed on the frontal and lateral DRR images by a trained operator.

The scapula was then registered on the frontal and lateral X-rays in two steps. First, both pairs of radiographs were annotated, and the scapula was roughly registered. For *in vivo* subjects, when they change position in the cabin, there is also a noticeable movement at the scapula that does not occur when DRRs are performed as both pairs are done on the same CT-scan. This would obviously introduce a bias, with the coarse alignment. Therefore, prior to registration, and to trigger this coarse alignment step, a position/-orientation uncertainty was added to this coarse registration before it was projected onto the X-rays. This was done by applying a random number derived from a normal distribution with a standard deviation of ten (degrees and millimetres) around and along the different rotation axes of the scapula coordinate system from (Kolz et al. 2020). A trained user was then asked to manually adjust the position of the scapula so that its contours matched the radiographic contours of the images, using a collision algorithm (Gilbert et al. 1988) to alert the user of interpenetrations between the scapula and the ribcage. Clinical parameters were calculated on the 3D registered reconstructions. The clinical parameters were then computed twice: first, using the manual segmentation on the CT-scan images as reference, and second using the above-mentioned registration method on the DRR. The calculated clinical parameters are the protraction (PRO), internal rotation (IR), tilt and upward rotation (UR). Their definitions were adapted from the article by (Moroder et al. 2020) (Figure 2). Errors reported in Table 1 are the difference between clinical parameters obtained with each process.

3. Results and discussion

The results obtained are synthesized in Table 1. The mean error for the protraction is −1.6° (PRO). It is −1.1° for the internal rotation (IR), 0.9 for the upward rotation (UR) and −0.5 for the tilt. The maximum error is 4.6° for the internal rotation. The mean values (and standard deviation) observed by (Moroder et al. 2020) on the 200 shoulders were 88.4 (4.7) for PRO, 41.4 (5.2) for IR, 13.3 (5.1) for UR, and 19.4 (8.6) for the tilt. In regards to these values, the method presented seems sufficiently precise to express differences in the measurements of these angles, but it seems that we need to remain cautious concerning the UR.

The sample size is small, but the results seem promising, especially considering the small number of alternatives to perform similar measurements in functional position. One limitation would be the similarity between EOS and DRR images. A user would not confuse images from these 2 systems, but there are difficulties specific to each type of image. A second limitation of this study is related to the fact that the cadaver is not in the position in which the images are usually taken. This position affects the absolute values of the angles that are obtained, but it should not have a major impact on the accuracy results.

4. Conclusions

The presented accuracy study confirms that the method allows to quantify the position and orientation of the scapula with the possibility to assess the global spinal alignment. The accuracy should be further evaluated in additional subjects, but the proposed method shows promising results.

References

Aubert B, Vergari C, Ilharreborde B, Courvoisier A, Skalli W. 2016. 3D reconstruction of rib cage geometry from biplanar radiographs using a statistical parametric model approach. Comput Methods Biomech Biomed Eng Imaging Visualization. 4(5):281–295. doi:10.1080/21681163.2014.913990.

Bousigues S, Gajny L, Skalli W, Aloui S, Ohl X, Tétreault P, Hagemeister N. 2023. A method to characterize posture and the scapulothoracic joint using biplanar radiography. CMBBE Oral Presentation in Paris, France.

Gajny L, Ebrahimi S, Vergari C, Angelini E, Skalli W. 2019. Quasi-automatic 3D reconstruction of the full spine from low-dose biplanar X-rays based on statistical inferences and image analysis. Eur Spine J. 28(4):658–664. doi:10.1007/s00586-018-5807-6.

Gilbert EG, Johnson DW, Keerthi SS. 1988. A fast procedure for computing the distance between complex objects in three-dimensional space. IEEE J Rob Autom. 4:193–203.

Kolz CW, Sulkar HJ, Aliaj K, Tashjian RZ, Chalmers PN, Qiu Y, Zhang Y, Foreman KB, Anderson AE, Henninger HB. 2020. Reliable interpretation of scapular kinematics

depends on coordinate system definition. Gait Posture. 81:183–190. doi:10.1016/j.gaitpost.2020.07.020.

Moroder P, Akgün D, Plachel F, Baur ADJ, Siegert P. 2020. The influence of posture and scapulothoracic orientation on the choice of humeral component retrotorsion in reverse total shoulder arthroplasty. J Shoulder Elbow Surg. 29(10):1992–2001. doi:10.1016/j.jse.2020.01.089.

Pauchard Y, Fitze T, Browarnik D, Eskandari A, Pauchard I, Enns-Bray W, Pálsson H, Sigurdsson S, Ferguson SJ, Harris TB, et al. 2016. Interactive graph-cut segmentation for fast creation of finite element models from clinical ct data for hip fracture prediction. CMBBE.

Yamamoto A, Takagishi K, Kobayashi T, Shitara H, Ichinose T, Takasawa E, Shimoyama D, Osawa T. 2015. The impact of faulty posture on rotator cuff tears with and without symptoms. J Shoulder Elbow Surg. 24(3):446–452. doi:10.1016/j.jse.2014.07.012.

KEYWORDS Scapula; biplanar radiography; posture

sandrine.bousigues@ensam.eu

Evaluating the effect of drumstick length on hand muscle activation: a preliminary study

B. Goislard de Monsabert[a], T. Corriol[a], R. Raspail[a,b] and J.-N. Theron[b]

[a]CNRS, Aix-Marseille University, Marseille, France; [b]Hand Rehabilitation Centre, Marseille, France

1. Introduction

Percussionists and drummers are particularly exposed to musculoskeletal disorders (MSD) due to the physical demands of the constraints associated to their musical gesture. A recent study concluded that 70% of drummers experienced playing-related MSD and that the majority of them are tendinopathies at the hand and wrist levels (Azar 2020). This high prevalence is due to the physical demands and the associated mechanical loadings withstood by their musculoskeletal tissues. The drummer must indeed hit different elements, including cymbals made of metals, with wooden drumsticks to produce a sound. This gesture involves a multi-segment coordination of the upper limb (Altenmüller et al. 2020) ending with the drumstick impact, thus implying complex muscle coordination to control the sound and rhythm and manage shock absorption. Unfortunately, MSD prevention remains insufficiently provided during musical education and is limited by the lack of data quantifying the loadings on the musculoskeletal system of drummers. Previous works have studied the muscular co-activation at the wrist during different types of drumming exercises using electromyography (Fujii et al. 2009; Beveridge et al. 2020). Investigating electromyographic activity is relevant to determine the relative implication of agonists and antagonists and identify excessive or abnormal muscle solicitations. Nevertheless, most of these studies investigated the influence of expertise on the muscle activation whereas prevention requires to quantify how musculoskeletal loading are influenced by ergonomic parameters including drumsticks characteristics and drummer-specific technique, such as posture. The objective of this study was to propose a protocol to investigate the influence of drumstick length on activation of hand muscles during drumkit playing and present preliminary results on a drummer.



Figure 1. Illustration of the video plane Recording motion of markers placed on the forearm and hand.

2. Methods

2.1. Participant and protocol

Three drummers were tested but the results of only one participant will be presented here: a non-professional but experienced male drummer (Age: 45; Height: 168 cm; Hand length: 19.5 cm; Experience: 30 yrs; Weekly practice: 25 hrs).

2.2. Task

The drummer was instructed to perform sixteenth notes, alternating left and right hands, in *forte* (loudly) while maintaining the sound level as constant as possible and respecting as accurately as possible the tempo given by a metronome.

2.3. Material

Participants performed the task on a practice pad (EVANS 'RealFeel' RF-12 G). The pad height and orientation was fixed but the participant could adjust the height of his drum seat (Gibraltar) once, at the beginning of the protocol.

Three different models of VicFirth 5 A Hickory drumstick pairs were presented to the drummer only varying in length: Classic ($L = 406$ mm), Extreme ($L = 419$ m), Freestyle ($L = 432$ mm). The types of the drumsticks were hidden by black marker.

A smartphone microphone app (Redmi note 8 pro, Xiaomi) was used to record the sound produced while performing the task in each trial. A smartphone video app (iPhone 11, Apple) with the flash activated was used to film the motion of three reflective markers placed on the lateral epicondyle, the ulnar styloid and the fourth metacarpal head (Figure 1). A wireless surface EMG system (Trigno, Delsys, Natick, MA, 2000 Hz) was used to record the electrical activity of two muscles, i.e. *flexor digitorum supeficialis* (FDS) and *extensor carpi radialis brevis* (ECRB). Electrode placement was determined by skin palpation during

Table 1. Variability in tapping loudness σ_s and in inter-tapping time σ_t, amplitude of wrist movement Θ_{wrist}, and hand-dumstick tip distance $d_{hand\text{-}tip}$ for each drumstick model.

	Classic409 mm	Extreme419 mm	Freestyle432 mm
σ_t (ms)	5	3	4
σ_s (du)	0.83	0.94	0.52
Θ_{wrist} (°)	34	33	31
$d_{hand\text{-}tip}$ (%)	68	70	73

muscle contraction and by visual observation during functional motions.

2.4. Protocol

The participant was first equipped with EMG sensors. Then, he performed a guided warm-up including dynamic and static stretching of the shoulder, the elbow, the wrist, and fingers. Two types of maximal voluntary contraction were then performed: a maximal grip force exertion and a maximal wrist extension against manual resistance. Each MVC was performed while the drummer held his personal drumstick, with the shoulder in neutral position, the elbow flexed at 90° and the wrist at 0° of flexion and deviation and was repeated twice. Reflective markers were then posittioned. The participants then performed the drumming task for the three drumstick models (Classic, Extreme, Freestyle) at three tempi (40, 120 and 200bpm) specified by an electronic metronome. Each drumstick/tempi condition was repeated twice, separated by at least 1 min rest, and only the data from second trial was used.

2.5. Data analysis

The variability in inter-tapping time (σ_t) was determined by calculating the standard deviation of the time separating two drumstick impact from video files. The variability in tapping loudness (σ_s) was determined by calculating the standard deviation of the peaks in the normalized data from the audio file. The maximal wrist amplitude (Θ_{wrist}) was determined by subtracting the highest and lowest wrist angle value obtained by tracking the marker positions in the video files using Kinovea. The relative distance between the the hand and the drumstick tip ($d_{hand\text{-}tip}$) was calculated once per drumstick model on the first frame of the trial and expressed as percentage of drumstick length.

EMG signals were first bandpass filter (butterworth 2nd order, zero lag, 20–400 Hz), rectified and an envelope was determined using a lowpass filter (butterworth 2nd order, zero-lag, 3 Hz). For each trial, a mean peak activation was calculated for each muscle by averaging peak envelope values by the maximal envelope value in the MVC trial of that muscle.

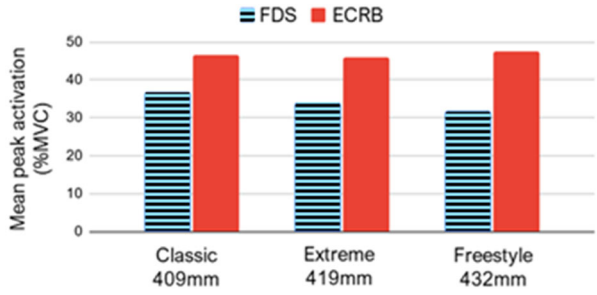


Figure 2. Mean peak activation of FDS and ECRB for each drumstick model.

3. Results and discussion

Only the data related to the 200bpm tempo will be presented and no statistical analysis was run such that only trends are discussed.

In terms of performance, drumstick length did not seem to impact the regularity in terms of timing, i.e. no variation of σ_t but the longer sticks (Freestyle) might have resulted in more regular sound power, i.e. lower σ_s, (Table 1). The kinematic analysis did not reveal a major effect of drumstick length, but the use of the longer drumstick could have resulted in smaller wrist movement amplitude (Θ_{wrist}) and a hand positioning ($d_{hand\text{-}tip}$) further away from the stick tip.

The results of peak EMG activation suggests that drumstick length could influence hand muscle activation (Figure 2). While wrist extensor (ECRB) peak activation seemed to remain constant, finger and wrist flexor (FDS) peak activation could have decreased by about 5% with the longer drumstick. This suggests that the ECRB acts as stabilizer of wrist joint motion and its activation is not related to drumstick characteristics. Considering that the hand placement relative to the drumstick could have increased with drumstick length, the drummer had to move more mass when performing his tapping gesture. The reduction in FDS peak activation with the longer drumstick could then suggest that the drummer used this added inertia to reduce muscle implications and maintain temporal and sound level regularity.

4. Conclusions

Only one participant was studied so no strong conclusion can be drawn but the study suggests that hand biomechanics during drumkit playing require more interest. Beyond testing a larger population

sample, further studies should investigate the influence of other ergonomic parameters, such as seat height, on wrist and finger muscle implications.

Acknowledgements

No external funding was received for this study.

References

Altenmüller E, Trappe W, Jabusch H-C. 2020. Expertise-related differences in cyclic motion patterns in drummers: a kinematic analysis. Front Psychol. 11: 538958. doi:10.3389/fpsyg.2020.538958.

Azar NR. 2020. Rates and patterns of playing-related musculoskeletal disorders in drummers. Med Probl Perform Art. 35(3):153–161. doi:10.21091/mppa.2020.3020.

Beveridge S, Herff SA, Buck B, Madden GB, Jabusch H-C. 2020. Expertise-related differences in wrist muscle co-contraction in drummers. Front Psychol. 11:1360. doi:10.3389/fpsyg.2020.01360.

Fujii S, Kudo K, Ohtsuki T, Oda S. 2009. Tapping performance and underlying wrist muscle activity of non-drummers, drummers, and the world's fastest drummer. Neurosci Lett. 459(2):69–73. doi:10.1016/j.neulet.2009.04.055.

KEYWORDS Musical gesture; biomechanics; kinematics; electromyography; musculoskeletal disorders

benjamin.goislard-de-monsabert@univ-amu.fr

From synovial joint morphogenesis to design of contact interfaces

D. Hernández–Aristizábal, S. Arroyave–Tobón and J. M. Linares

Aix–Marseille Univ, CNRS, ISM, Marseille, France

1. Introduction

During synovial joint morphogenesis (SJM), articular cartilage growth not only depends on biochemical cues but also on the loading conditions (Galea et al. 2021). In general, cyclic hydrostatic compressive stress promotes chondrocyte proliferation, while high shear stress promotes cartilage ossification (Palmoski and Brandt 1984; Sah et al. 1989). This process of shaping, along with a complex lubrication system provided by the synovial fluid, generates joints with remarkable wear resistance (Neville et al. 2007).

In mechanical engineering joints are also common. They are used as transfer load mechanisms, and failure usually is driven by wear—material lost on the surface. In addition, when the contact pressure is not uniform along the contact surface, failure by wear occurs even faster (Kato 2002).

As the improvement of wear resistance of engineering joints is still a current problem, the development of design strategies inspired by SJM results attractive.

In this study, we present an SJM–inspired generative design strategy that leads to two–dimensional contact profiles with uniform contact pressure.

2. Methods

2.1. Bio–inspired growth rules

As mentioned above, in synovial joint morphogenesis, hydrostatic compressive stress promotes chondrocyte proliferation and, in consequence, cartilage growth. In contrast, high shear stress triggers cartilage ossification and in consequence cartilage becomes bone and it does not grow anymore. Regarding the process of shaping, these two rules can be translated into: compressive stress promotes growth while high shear stress inhibits it.

2.2. Adaptation of the growth rules

Synovial joints are enclosed in the synovial capsule. This capsule prevents the synovial fluid from leaking. In addition, the load transfer from one bone to another is mediated by the fluid. In consequence, the stress distribution within the bones is different from the one resulting if such a transfer is mediated by direct contact (also called dry contact).

Human-made joints are usually lubricated as well. However, in many cases the lubrication film is very small, and load transfer stops being mediated by lubrication and starts being mediated by direct contact. As these cases are more prone to failure, we shall focus on them.

As we mentioned above, the morphogenesis depends on the state of stress of cells. Nonetheless, the stress distribution changes from capsule-mediated to direct-contact-mediated load transfer. Thus, it is necessary to adapt the growth rules. For that, we propose a second inhibition of growth by high compressive stress. In biological terms, it would mean that ossification would not only be promoted at cells under high shear but also at cells under high compressive stress.

2.3. Isotropic growth

So far, the proposed rules lead to unbounded growth. Nonetheless, both in nature and in engineering, it would be unrealistic. Therefore, we include an additional growth rule to restrict the process: given a maximum reference stress, the domain should be expanded if the maximum stress is higher and contracted otherwise.

The equilibrium equation for the growth is then given by:

$$\nabla \cdot (\boldsymbol{\sigma} + \sigma_g \boldsymbol{I}) = 0,$$

$$\sigma_g = \alpha \sigma_h^* H(\tau^* - 0.5) H\left(\sigma_h^* - 0.5\right) + \frac{\tau^{\text{ref}} - \tau^{\max}}{\tau^{\text{ref}} + \tau^{\max}},$$

$$H(\gamma) = \frac{1}{1 + \exp(\beta\gamma)}.$$

Where $\boldsymbol{\sigma}$ and $\boldsymbol{I}$ are respectively the Cauchy stress and the identity tensors; σ_g reproduces the growth rules; σ_h^* and τ^* are respectively the normalised hydrostatic compressive and shear stresses; τ^{ref} and τ^{max} are respectively the reference and maximum shear stresses; α is a positive parameter that indicates the strength of the growth force; and $H(\cdot)$ is a smooth version of the Heaviside function, namely the Sigmoid function, that reproduces the inhibition when the stresses are too high.

2.4. Case of study

For this exposition, let us consider an elastic cylinder in contact with an elastic plane, both with a Young modulus of 210 GPa and a Poisson coefficient of 0.3,

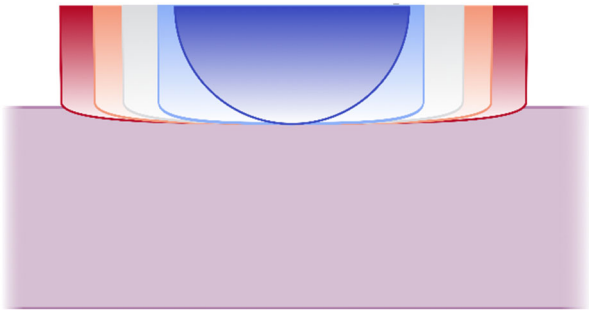


Figure 1. Schematic evolution (from blue to red lines) of the evolving geometry.

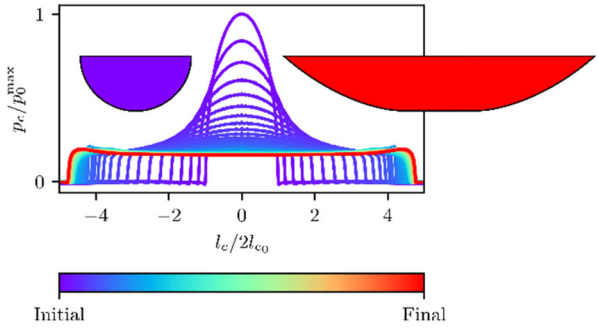


Figure 2. Evolution (from purple to red lines) of the contact pressure along the contact line. l_c refers to arc length from the centre of the contact zone.

and a load of 10 kN. For the growth function we consider $\alpha = 1$GPa and $\beta = 10$.

2.5. Algorithm

To test the proposed model, we developed a finite element algorithm based on Code_Aster. It is an iterative procedure divided in three steps: (i) the stresses due to the external load are computed, (ii) the growth forces following the adapted rules are applied and (iii) the geometry is updated. The implementation can be found in: https://github.com/sarroyavet/BioDesign_ANR/tree/main/StressAdaptiveDesignOf2D

3. Results and discussion

The bio–inspired process of adaptation was first tested without considering the growth restriction. Figure 1 shows a schematic representation of the evolution of the geometry. In this case, the contact area enlarges and the contact pressure becomes uniform. These results show that the proposed adaptive growth rules lead to an adaptation of the shape in order to obtain a uniform contact pressure. Nonetheless, as a secondary effect, the contact area is also affected.

To handle it, we added an additional growth rule: isotropic expansion/contraction to regulate the size of the contact region. Figure 2 shows the results obtained when a maximum shear stress restriction of 1 GPa is added. As we can see, the contact pressure becomes uniform and the contact length augments until the maximum shear stress restriction is satisfied. Therefore, the proposed methodology is able to provide contact interfaces with uniform pressure that also satisfy other design requirements—in this case, a specific maximum shear stress.

Nonetheless, the growth restriction has also an impact on the distribution of the pressure distribution. In particular it promotes the appearance of a slight edge effect. Therefore, both the adapted rules and the isotropic growth have an impact on the pressure distribution and on size of the contact zone. Future work could address this issue and separate the treatment of each aspect determining a term to exclusively modify the pressure distribution and another for the size of the contact region.

4. Conclusions

In this work, we tested a bio–inspired growth process to produce contact interfaces able to provide a uniform distribution of contact pressure. We used the stress–adaptive rule present in synovial joint morphogenesis: growth is proportional to hydrostatic compressive stress and inhibited by high shear stress, and we added an additional inhibition by high compressive stress. This growth rule allowed us to obtained contact interfaces with uniform pressure but whose size we could not controlled. To handle this, we included an additional rule that promotes global expansion (contraction) when the maximum shear stress is higher (lower) than a given requirement. As a result, the present methodology can make uniform the contact pressure and establish the size of the contact region. Nonetheless, both rules affected both the pressure distribution and the size. Therefore, we consider that future work should focus on separating these two aspects in independent terms.

References

Galea GL, Zein MR, Allen S, Francis-West P. 2021. Making and shaping endochondral and intramembranous bones. Dev Dyn. 250(3):414–449. doi:10.1002/dvdy.278.

Kato K. 2002. Classification of wear mechanisms/models. Proc Inst Mech Eng J J Eng Tribolo. 216(6):349–355.

Neville A, Morina A, Liskiewicz T, Yan Y. 2007. Synovial joint lubrication—does nature teach more effective engineering lubrication strategies? Proce Inst Mech Eng C J Mech Eng Sci. 221(10):1223–1230.

Palmoski MJ, Brandt KD. 1984. Effects of static and cyclic compressive loading on articular cartilage plugs in vitro. Arthritis Rheum. 27(6):675–681. doi:10.1002/art.1780270611.

Sah RL, Kim YJ, Doong JY, Grodzinsky AJ, Plaas AH, Sandy JD. 1989. Biosynthetic response of cartilage explants to dynamic compression. J Orthop Res. 7(5):619–636. doi:10.1002/jor.1100070502.

KEYWORDS Bio-inspiration; generative design; morphogenesis; contact interface; stress adaptation

david.HERNANDEZ-ARISTIZABAL@univ-amu.fr

Opto-mechanical characterisation of intervertebral disc phantoms

R. Allais[a], A. Capart[b], A. Da Silva[b] and O. Boiron[a]

[a]CNRS, Centrale Marseille, IRPHE, Aix Marseille University, Marseille, France; [b]CNRS, Centrale Marseille, Institut Fresnel, Aix Marseille University, Marseille, France

1. Introduction

Degeneration of the intervertebral discs (IVD) is a natural process that appears as early as twenty years of age and does not present any particular clinical symptoms. It is only after a period of several years to several decades, when pain appears, that a diagnosis can be made using usually magnetic resonance imaging. The severity of the disease is commonly assessed by grading schemes relying on contrast imaging analysis and one of the clinical goals in recent years is to better objectify the diagnosis through quantitative imaging. In this context, photoacoustics (PA) is a promising approach as it allows a non invasive spectroscopic probing of soft tissues to retrieve physiological markers of degeneration such as porosity or collagen concentration. A previous work by Metwally (2019) on lumbar porcine discs showed the potential of PA for such a goal. Hence, in this preliminary study we aim to create and characterise hydrogels which mimic the optical, mechanical and acoustic properties of an IVD to assess the possibility to use photoacoustics for disc degeneration estimation.

Briefly, photoacoustics can be seen as a two-step process. First, a medium is hit by a laser pulse and then an acoustic wave is created as a result of the optical energy absorbed. From the measured acoustic signal which probed the medium, the goal is first to retrieve the initial acoustic pressure and subsequently the optical parameters through inverse problems resolutions. Finally, the chromophores concentrations of the medium that we target, water and collagen, can be deduced from the optical properties. The optical part is governed by the radiative transfer equation (Equation 1) which models the light propagation in the medium. This equation on the specific intensity (L in W m^{-2} sr^{-1}) is parametrised by the light speed c, a phase function p describing the optical scattering anisotropy of the medium and two coefficients μ_a and μ_s defining respectively the optical absorption and scattering of the medium. For soft tissues, this rather computationally expensive equation is often reduced to a diffusion equation (Equation 2) under the 'light diffusion approximation', which holds for IVD. This equation on the fluence (ϕ in W m^{-2}) is parametrised by μ_a and $\mu_s' \approx 0.1\mu_s$. A thorough derivation of these equations and their assumptions can be found in Arridge (1999). Hence, knowing the values of these two parameters is required to optically characterise a medium.

$$\frac{1}{c}\frac{\partial L}{\partial t} + \nabla L.s = -(\mu_a + \mu_s)L + \mu_s \int_{4\pi} p(s,s')L(r,s',t)ds' + S \tag{1}$$

$$\frac{1}{c}\frac{\partial \phi(r,t)}{\partial t} - \nabla.(D(r)\nabla\phi(r,t)) + \mu_a(r)\phi(r,t) = S(r)$$
$$With\ D(r) = \frac{1}{3(\mu_a(r) + \mu_s'(r))} \tag{2}$$

2. Methods

2.1. Phantoms preparation

With the end goal of mimicking an IVD, we used agarose hydrogels with TiO_2 powder. We hypothesised that the mechanical response of our samples would be driven by the agarose concentration while the optical response would be mostly tuned by the TiO_2 concentration. The agarose concentration ranges from 0.25 to 2% w/w and the TiO_2 ranges from 0.1 to 0.5 mg/mL. Briefly, a mix of agarose and TiO_2 was mixed in ddH_20 and heated under magnetic stirring. Finally, the solution was poured in cylindrical moulds and stored at 4 °C for gelation. As for now, only one sample was made for each combination of agarose and TiO_2 concentration, resulting in 12 hydrogels to characterise.

2.2. Optical characterisation

Under the light diffusion approximation, the optical coefficients μ_a and μ_s' can be experimentally estimated using the integral reflectance and an empirical model as defined by Gobin et al. (1999). Thus, with this approach we could find the relationships between the optical properties of our samples and the components' concentrations and, on the other hand, by varying the wavelength of the light source from 590 to 815 nm by step of 25 nm, characterize the absorption spectrum of our samples.

2.3. Mechanical characterisation

The hydrogels were punched to create 32 mm-large and 20 mm-tall cylindrical samples on which we performed an unconfined stress relaxation compression at the room temperature using a custom-built test

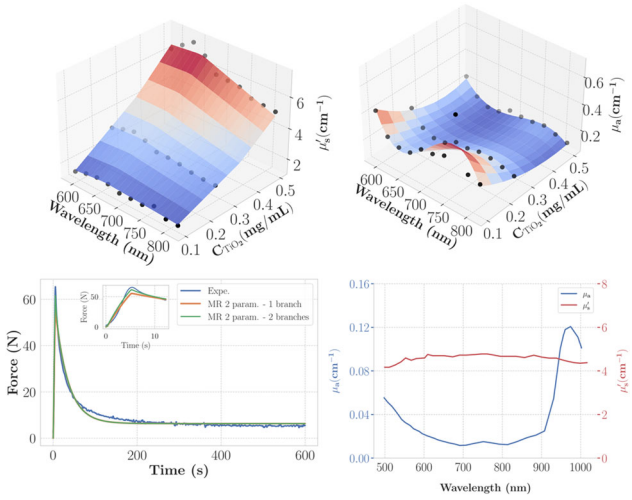


Figure 1. (A) μ_s' and μ_a (B) as a function of λ and C_{TiO2} for a 1% agarose Hydrogel. The black dots display the experimental data. (C) Example of model fitting to the stress relaxation data. (D) Typical IVD μ_a and μ_s' values based on the water and collagen measurements of Sekar et al. (2017).

bench. Then, we modelled the hydrogels by a Mooney–Rivlin law with two parameters (C_{10} and C_{01}) and two viscoelastic branches following a Maxwell-generalised model. The inverse problem was solved using Levenberg-Marquardt algorithm and the built-in optimisation module of *COMSOL Multiphysics 5.5*. To ease the optimisation, the problem was solved in two steps: we first found the best values of the Mooney–Rivlin parameters and one viscoelastic branch and then we ran a second optimisation using these values to find the best parameters for the second viscoelastic branch.

3. Results and discussion

Our first results suggest that optical scattering is mostly driven by the TiO_2 concentration (C_{TiO2}): μ_s' increases linearly with C_{TiO2} and decreases with the wavelength (λ) between 590 and 815 nm (Figure 1A). Moreover, for C_{TiO2} above 0.5 mg/mL, TiO_2 appears to marginally impact the absorption spectrum (Figure 1B); hence, the optical absorption can be tuned with the agarose concentration while the scattering is driven by the TiO_2. Assuming the IVD as a biphasic medium made up of water and collagen and knowing the porosity, one can compute typical values of μ_a and μ_s' for IVD at different levels of degeneration. Using the reference values of Sekar et al. (2017), our hydrogels show optical scattering similar to IVD but the optical absorption appears too strong (Figure 1A,B,D). This could be due to experimental limitations: the approach relying on the integral reflectance could be inaccurate for weakly absorbing samples; a validation experiment using integrating-spheres is planned.

Table 1. Values of the Mooney–Rivlin and first viscoelastic branch parameters (mean ± std).

	C_{10} (kPa)	C_{01} (kPa)	β (-)	τ (s)
Agar. 0.5%	3.9 ± 0.4	−2.8 ± 0.4	2.7 ± 0.7	121.7 ± 31.5
Agar. 1%	13.7 ± 3.4	−9.5 ± 2.4	3.0 ± 0.9	123.6 ± 16.7
Agar. 2%	11.8 ± 1.6	−6.1 ± 1.3	10.3 ± 2.2	29.3 ± 3.5

As for the mechanical problem, our models fit well the experimental relaxation curves (average RMSE <0.65N). Adding a second viscoelastic branch considerably improves the short-term fit (Figure 1C). Notably, it decreases the maximal error by up to 50%.

The average values of the Mooney–Rivlin and first viscoelastic branch parameters are reported in Table 1. Our results are in good agreement with the literature; similar trend are reported for hydrogels whose agarose concentration ranges from 3 to 5% (Wang et al. 2021). In their hydrogels, Wang and colleagues reported values of 28.4 kPa for C_{10} and −20.8 kPa for C_{01} with a trend to increase with agarose concentration. However, these values fall short when compared to the one taken by Schmidt et al. (2007) in their numerical model of an IVD in which they use C_{10} = 180 kPa and C_{01} = 45 kPa for the annulus fibrosus.

4. Conclusions

Our first results are promising as we now have baseline values for both mechanical and optical parameters. Acquisition and numerical simulations of photoacoustic signals are ongoing. Meanwhile, future work will consist in adapting the components to better model an IVD. To improve the optical absorption we plan to add collagen while we project to use chondroitin sulfate or crosslinking to better tune the mechanical response of our hydrogels.

References

Arridge S. 1999. Optical tomography in medical imaging. Inverse Prob. 15(2):R41–R93. doi:10.1088/0266-5611/15/2/022.

Gobin L, Blanchot L, Saint-Jalmes H. 1999. Integrating the digitized backscattered image to measure absorption and reduced-scattering coefficients in vivo. Appl Opt. 38(19): 4217–4227. doi:10.1364/ao.38.004217.

Metwally K. 2019. Probing intervertebral discs with photoacoustics. European Conference on Biomedical Optics. Washington (DC): Optica Publishing Group.

Schmidt H, Kettler A, Heuer F, Simon U, Claes L, Wilke H-J. 2007. Intradiscal pressure, shear strain, and fiber

strain in the intervertebral disc under combined loading. Spine. 32(7):748–755. doi:10.1097/01.brs.0000259059.90430.c2.

Sekar SKV, Bargigia I, Mora AD, Taroni P, Ruggeri A, Tosi A, Pifferi A, Farina A. 2017. Diffuse optical characterization of collagen absorption from 500 to 1700 nm. J Biomed Opt. 22(1):15006. doi:10.1117/1.JBO.22.1.015006.

Wang X, June RK, Pierce DM. 2021. A 3-D constitutive model for finite element analyses of agarose with a range of gel concentrations. J Mech Behav Biomed Mater. 114:104150. doi:10.1016/j.jmbbm.2020.104150.

KEYWORDS Intervertebral disc; photoacoustics; soft tissue; hydrogel; characterisation

roman.allais@centrale-marseille.fr

Retention loss and wear of attachment systems for implant retained mandibular overdentures

R. Wakam[a], S. Ramalingam[a], K. B. Mawussi[a], C. Gorin[b] and A. Benoit[a]

[a]URB2i, Montrouge, France; [b]URP2496, Montrouge, France

1. Introduction

The implant-retained mandibular overdenture stabilized on 1 or mainly 2 implants provides numerous benefits at the functional, structural, and psychosocial levels when compared to the conventional mandibular overdentures (Thomason et al. 2009). The choice of the attachment system is crucial, as it has a direct impact on the ability of patients to manage their prosthesis, the amount of aftercare and cost, the overall patient satisfaction, and the clinical success, that depends mainly on the retention force of the attachment system (Maniewicz et al. 2020). The most common complications are the wear, the retention loss over time, and the consequent need of maintenance to regularly activate or replace the retention device. There is little evidence for a preferable indication of any type of unsplinted attachment system and our recent systematic review (Wakam et al. 2022) highlighted the need for more standardization of the protocols measuring their retention, especially regarding implant angulation, in order to facilitate comparison between studies. The purpose of the present study was to evaluate and compare the retention loss and the wear of three resilient unsplinted attachment systems: a well-established ball attachment system, the Ball System (Nobel) with three positions of its retention device (maximum, medium and low retention) and two new cylindrical attachment systems, Locator R-Tx® with white (LW), pink (LP) and blue (LB) retention devices, and Novaloc® with black (NK), green (NG) and white (NW) retention devices. The central hypothesis is that retention behavior and wear differ between attachment systems, implying different maintenance needs.

2. Methods

The implant ($n = 4$), its corresponding abutment ($n = 4$), the color-coded or position-coded retention devices ($n = 8$ for each) and the matrix metal housing of the three unsplinted attachment systems are incorporated within pre-drilled resin blocks simulating mandibular bone and the removable prosthesis (Figure 1). The assemblies are subjected to 10,000 insertion-removal cycles with a vertical loading of 19.6 N and a crosshead speed of 60 mm/min, using a chewing simulator. At cycles 10, 100, 1000, 5000, and 10,000, samples are removed from the chewing simulator to measure the retention force on a universal testing machine as the average of the maximal dislodgement force to separate the male and female parts during 10 consecutive insertion-removal cycles.

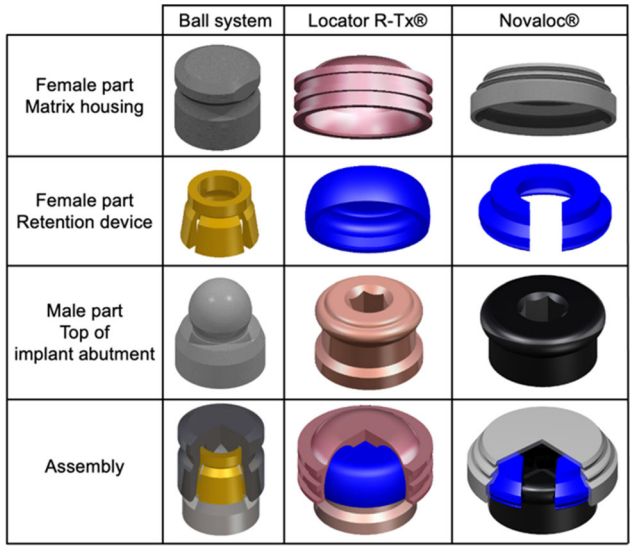


Figure 1. Diagram of the studied attachment systems.

Micro-computed tomography of cylindrical attachment systems' female parts is performed before each retention measurement using X-ray Quantum FX μCT (voxel size 40 μm) to control their angulation in relation to the insertion axis and to characterize wear of the retention device. For ball attachment systems, a binocular magnifier Leica MC170 HD is used to measure the width of retention devices' principal slit related to their calibration and wear.

Statistical analysis is performed using Graphpad Prism software, considering one retention device as the statistical unit. A two-way Anova test is applied, followed by post-hoc tests. Differences are considered significant at $p < 0.05$.

3. Results and discussion

For cylindrical attachment systems, angulations lower than clinical significance (3°) were reached between the matrix housing and the insertion axis thanks to the blocks' machining and the operator's meticulousness. For ball attachment systems, the variability

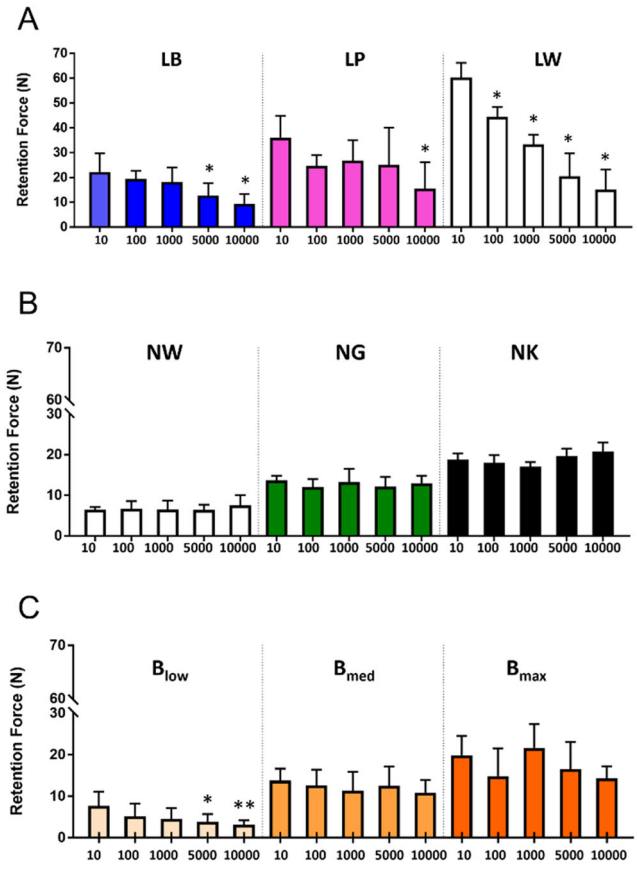


Figure 2. Evolution of the retention force of (A) Locator R-Tx®, (B) Novaloc® and (C) the ball system as a function of the number of cycles. *, the difference is significant compared to the initial retention force of the considered retention device.

observed in their calibration reflects the inaccuracies due to the manual adjustment of their position.

The initial retention range is similar between the Ball System and the Novaloc® and broader for the Locator R-Tx®. Retention is stable over time for the Novaloc® and for the medium and maximum retention positions of the Ball System. The Locator R-Tx® shows a significant retention loss, observed as early as cycle 100 for the white retention device. Thus, the higher retention provided by the Locator R-Tx® on the first day of oral use decreases progressively to reach levels of retention similar to the Novaloc® or the Ball System, in accordance with the literature (Friedrichsen et al. 2023).

Male parts of cylindrical attachment systems do not show any signs of wear whereas scratches are visible at the equator of ball abutments. Wear measurements on female parts are in progress. First results show an increase of the smallest diameter of the retention device of Locator R-Tx® whereas no change is observed for the Novaloc®. For ball attachment systems, the slit width slightly increases with the number of cycles and abrasions are observed at the top of the retention device's inner surface.

The observed differences in retention loss and wear can be explained by the different materials (gold, PEEK, Nylon) and designs of the studied AS.

This *in vitro* study enables a fair comparison between the three studied attachment systems. However, the results cannot be directly transposed to a clinical situation where a removable overdenture stabilized on 2 implants is generally recommended and where parameter related to the patient (bruxism, lingual parafunction …) or to the prosthesis (implant number, orientation …) can affect retention.

4. Conclusions

This study proposes a standardized material and method allowing intra- and inter-attachment system comparison simulating an implant-retained mandibular overdenture stabilized on 1 implant aligned with the insertion axis. After 10,000 insertion-removal cycles, all attachment systems still provide a satisfactory retention force, above 5 N considered as a threshold for patient satisfaction. Within the highlighted limitations, the retention loss is significantly higher for the Locator R-Tx® followed by the Ball System. The Novaloc® provides a stable retention overtime. Retention loss seems correlated to the first observations of wear regarding the progressive opening of Locator R-Tx® retention device and of the principal slit of the Ball System retention device. The damage observed in this *in vitro* study reflects the regular clinical maintenance needs to replace or activate the retention device. Further studies are needed to analyze the impact of the number of attachment systems retaining the prosthesis or their angulation to the insertion axis, that will affect their retentive behavior.

References

Friedrichsen M, Dirksen D, Runte C. 2023. In vitro measurement of the retention force of two stud attachment systems during cyclic load. J Prosthodont. doi:10.1111/jopr.13665.

Maniewicz S, Badoud I, Herrmann FR, Chebib N, Ammann P, Schimmel M, Müller F, Srinivasan M. 2020. In vitro retention force changes during cyclic dislodging of three novel attachment systems for implant overdentures with different implant angulations. Clin Oral Implants Res. 31(4):315–327. doi:10.1111/clr.13567.

Thomason JM, Feine J, Exley C, Moynihan P, Müller F, Naert I, Ellis JS, Barclay C, Butterworth C, Scott B, et al.

2009. Mandibular two implant-supported overdentures as the first choice standard of care for edentulous patients – the York Consensus Statement. Br Dent J. 207(4):185–186. doi:10.1038/sj.bdj.2009.728.

Wakam R, Benoit A, Mawussi KB, Gorin C. 2022. Evaluation of retention, wear and maintenance of attachment systems for single or two-implant-retained mandibular overdentures: a systematic review. Materials. 15(5):1933. doi:10.3390/ma15051933.

KEYWORDS Mandibular overdenture; removable prosthesis; attachment system; retention force; cyclic loading

aurelie.benoit@u-paris.fr

Using EMG to solve the muscle redundancy problem in musculoskeletal models

S. Hinnekens[a], P. Mahaudens[b], C. Detrembleur[b] and P. Fisette[a]

[a]iMMC-MEED, Université catholique de Louvain, Louvain-la-Neuve, Belgium; [b]IREC-NMSK, Université catholique de Louvain, Bruxelles, Belgium

1. Introduction

Computing muscle forces *via* a musculoskeletal model with a purely mathematical approach such as optimisation usually copes with the problem of muscle redundancy, i.e. infinity of solutions for a given configuration. One way to solve this problem is to use cost functions and optimisation methods which reflect actual muscle strategies the best. It often requires an experimental validation realised afterwards. Alternatively, experimental input such as electromyography (EMG), measured during an upfront experiment, can be used to feed the model and to guide the solving towards muscle forces physiologically more correct. For the trunk, if this approach is not new (Granata and Marras 1995), it is still underused (Gould et al. 2021). Therefore, in this study, EMG was used as input of a model of the trunk to compute muscle forces and resulting intervertebral efforts – forces and torques – in the lumbar spine for a static configuration in the Sorensen test posture. To illustrate the necessity of EMG as input, a single participant was asked to produce three muscle strategies for the same position. Whereas the mathematical optimisation cannot see any difference in muscle forces, it is expected that the EMG-based solutions reflect the strategies better.

2. Methods

2.1. Experiment

One 28-year-old male subject (175 cm, 90 kg) participated voluntarily in the experiment. He produced three different muscle strategies in the Sorensen test posture. Lying on a table in a prone position with the trunk unsupported, he had to maintain the trunk aligned with the lower limbs while being (i) the most relaxed as possible (relaxed configuration), (ii) the most stressed as possible (stressed configuration) and (iii) in an intermediate level between relaxed and stressed (mid configuration).

EMG signals of back – lumbar (LP) and thoracic paravertebral (TP) muscles, quadratus lumborum (QL), latissimus dorsi (LD) – and abdominal – rectus abdominis, externus obliquus – muscles were recorded during the experiment. Each configuration was performed twice: unloaded and loaded with an external mass equal to 20% of the body mass. Maximal voluntary contractions (MVC) were recorded prior to the exercises for EMG normalisation.

2.2. Model

A multibody model representing the experiment was developed but it included only muscles actually activated during the experiment: LP, TP, QL and LD.

Muscle forces were quantified *via* two methods: an EMG-based deterministic distribution of a global equivalent force between all muscles (Hinnekens et al. 2021) and one based on optimisation. For the latter, a trust-region algorithm for constrained optimisation was used to implement two cost functions: minimising the sum of cubed muscle stresses (s^3) and minimising the largest relative muscle force (mM) $s^3: \ min \sum_i \left(\frac{F_i}{PCSA_i}\right)^3$ & $mM: \ minmax\left(\frac{F_i}{F_{max,i}}\right)$ with F_i the force in the ith muscle fascicle, $PCSA_i$ its physiological cross-sectional area and $F_{max,i}$ its maximum isometric force.

We made the hypothesis that the spine and its surrounding intrinsic muscles were assimilated to a beam whose intervertebral efforts – compression and shear forces and bending torque – are computed according to the beam theory through multibody constrained forces and torques. Intervertebral efforts were consequently overestimated with respect to the reality. Finally, they were translated into equivalent stresses considering an intervertebral disc with a cross-section area of 18 cm^2. This was done for both computation methods.

3. Results and discussion

EMG amplitudes of back muscles recorded during the experiment (Figure 1) showed varied muscle strategies as expected. Loaded cases produced obviously highest EMG amplitudes. For the relaxed and mid configurations, TP were the most activated for both unloaded and loaded cases. For the stressed configuration, LP were the most activated for the unloaded case.

LD was not expected to be as active, particularly for the loaded cases. LD produced the highest EMG amplitude among all EMG amplitudes for the loaded stressed configuration. This high activation of LD in

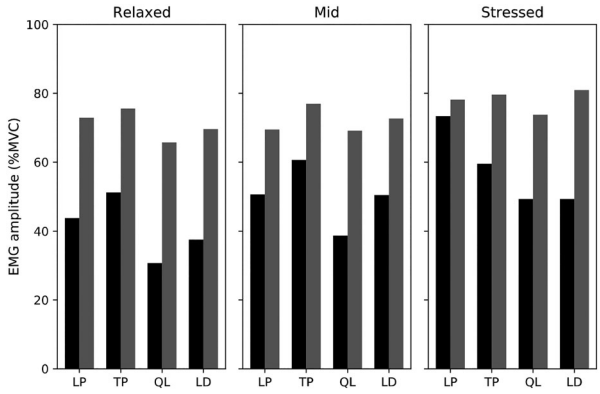


Figure 1. EMG amplitudes (%MVC) of LP, TP, QL and LD for the three configurations and for both unloaded (in black) and loaded (in grey) cases.

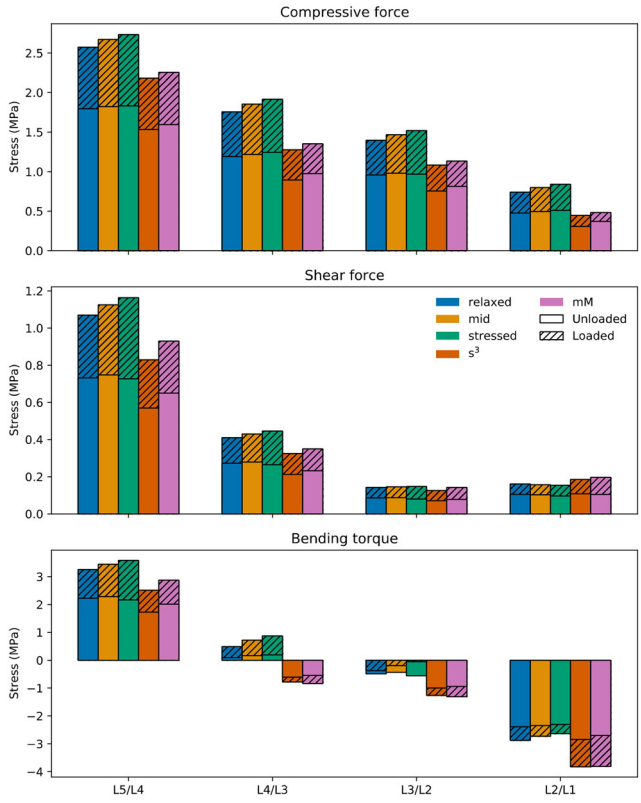


Figure 2. Stresses in the four superior lumbar discs corresponding to (top) compressive and (middle) shear forces and (bottom) bending torque. Non-hatched and hatched bars represented unloaded and loaded cases respectively.

this study may come from the bilateral role of this muscle in helping for hyperextension of the trunk (Kendall et al. 2005).

The varied muscle strategies recorded led to varied distributions of muscle forces for the EMG-based approach whereas the optimisation-based approach could not see any differences between the three configurations (not shown).

Figure 2 showed the equivalent stresses associated to compressive and shear forces and bending torque for the four upper lumbar discs computed with the EMG-based approach (relaxed, mid and stressed) and by the optimisation (s^3 and mM). First, the optimisation could not distinguish between the three configurations while the EMG-based approach could. Second, the optimisation produced relatively intense stresses associated to the bending torque at L3/L2 and L2/L1 levels, particularly for the loaded case but also produced lower or relatively similar stresses for other lumbar levels and efforts.

The greatest stresses were associated to the bending torque. Positive values indicate intervertebral discs in which posterior internal fibres are in compression while anterior internal fibres are in traction; negative values indicate the opposite. At L3/L2 level, there were smaller stresses for loaded cases (relaxed, mid and stressed) than for unloaded cases probably due to the zero-point crossing of the bending torque around L3/L2 level for the loaded cases.

For the unloaded case (non-hatched bars in Figure 2), the mid configuration produced the greatest stresses in shear force and bending torque. It might be due to the EMG-based approach which evenly distributed muscle forces between LP and LD (see Figure 1) while for the stressed configuration, LP were favoured. Given the geometry of LD fascicles, it resulted in greater stresses in shear force and bending torque.

4. Conclusions

This study aimed at highlighting how relevant EMG can be as input for musculoskeletal models, especially when solving the muscle redundancy problem for varied muscle strategies achieved by the same subject.

The EMG-based approach had some limitations, showed by highest stresses of the mid configuration for the unloaded case. Besides, the deterministic muscle force distribution was based on a non-negative linear regression computed on two masses only, resulting in a small increase for LP when adding the load.

Future work will focus on embedding EMG input in the optimisation process itself (Granata and Marras 1995) to make it more physiologically relevant, by modulating its cost functions and/or constraints so as to discern clearly different muscle strategies.

References

Gould SL, Cristofolini L, Davico G, Viceconti M. 2021. Computational modelling of the scoliotic spine: a literature review. Numer Methods Biomed Eng. 37(10):3503. doi:10.1002/cnm.3503.

Granata KP, Marras WS. 1995. An EMG-assisted model of trunk loading during free-dynamic lifting. J Biomech. 28(11):1309–1317. doi:10.1016/0021-9290(95)00003-z.

Hinnekens S, Mahaudens P, Detrembleur C, Fisette P. 2021. Quantifying back muscle forces in the Sorensen test: influence of individual strategies on intervertebral efforts. Comput Methods in Biomech Biomed Eng. 24(S1):S163–S164.

Kendall FP, McCreary EK, Provance PG, Rodgers MM, Romani WA. 2005. Muscle: testing and function with posture and pain. Baltimore (MD): lippincott Williams & Wilkins.

KEYWORDS Electromyography; muscle redundancy; musculoskeletal model; optimisation; back muscles

simon.hinnekens@uclouvain.be

Injury biomechanics and traumatology

Biomechanical analysis of arthroplasty and arthrodesis of lumbar spine: Experimental validation of a patient-specific finite element model, page S310.
Development of a statistical model of the full skeleton combining shape and a rib quality indicator to assess the risk of rib fracture, page S313.
Development of a surrogate model to represent drones in head impacts, page S315.
Linear viscoelastic material calibration method for judo impact simulation, page S318.
Mechanical behavior of a healthy premolar assessed by digital color holograph and finite element method, page S320.
Simplified abdomen model to evaluate the intra-abdominal pressure variation after hernia repair, page S322.
What is the impact of the surgical approach on functional recovery after total hip arthroplasty? a narrative review, page S325.

Biomechanical analysis of arthroplasty and arthrodesis of lumbar spine: evaluation of a patient-specific finite element model

F. Zot[a], E. Ben Brahim[a,c], Y. Ledoux[b], M. Mesnard[b], M. Severyns[a,d], J. Sandoval[a], M. A. Laribi[a], T. Vendeuvre[a,c] and A. Germaneau[a]

[a]Institut Pprime, UPR 3346 CNRS, Université de Poitiers – ISAE ENSMA, Poitiers, France; [b]Institut de Mécanique et d'Ingénierie, UMR 5295 CNRS, Université de Bordeaux, Bordeaux, France; [c]Department of Orthopaedic Surgery and Traumatology, University Hospital, Poitiers, France; [d]Orthopaedic and Traumatology Department, Clinique Porte Océane, Les Sables d'Olonne, France

1. Introduction

Lumbar Degenerative Disc Disease (DDD) can be treated with different surgical approaches, such as arthrodesis and arthroplasty. Only the latter technique is able to preserve some of the natural mobilities of the spine, by replacing the affected disc with a mobile prosthesis. Several implant technologies fall under the term of Total Disc Replacement (TDR): ball-and-socket, mobile core and viscoelastic prostheses (Abi-Hanna et al. 2018). It is still unclear whether the different prostheses result in the same mechanical response to physiological loadings, which could affect the surgical outcome. It has been reported that 34% of patients develop facet arthrosis within 2 years after surgery (Furunes et al. 2020). To prevent the development of facet arthrosis after lumbar TDR, it is necessary to identify its causes. The objective of this work is to perform a mechanical stress analysis on the facet joints involved by TDR solution from a patient-specific finite element approach coupled with an experimental validation.

2. Methods

2.1. Finite element model

To develop the intact FE models (Figure 1), CT-scans of fresh-frozen anatomical specimens of lumbar spines (L4-S1; 3Males; 63.7 ± 12.6 years) provided by the anatomy laboratory of the University of Poitiers (ABS Lab) were used. The three-dimensional geometries of the vertebrae and intervertebral discs were extracted using image segmentation of CT scans (3D Slicer software, voxel size $= 0.689 \times 0.689 \times 0.250\,\text{mm}^3$) and were imported to Ansys Mechanical (Version 2022R1, Ansys Inc., USA) for FE modelling (Figure 1).

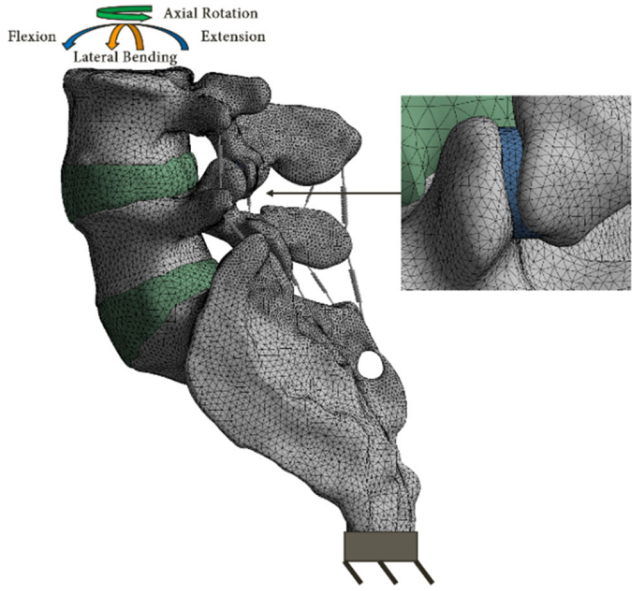


Figure 1. Patient specific FE model.

Table 1. Mechanical properties used in the FE model.

Component	Elastic modulus (MPa)	Poisson ratio	Reference
Bone	12,000	0.3	(Park et al. 2013)
Cartilage endplate	23.8	0.42	(Finley et al. 2018)
Articular cartilage	11	0.4	(Park et al. 2013)
Annulus fibrosus	8.4	0.45	(Shin et al. 2007)
Nucleus pulposus	1	0.49	(Shin et al. 2007)

Properties of materials are given in Table 1. Homogeneous bone material was considered for the vertebrae. The discs consisted of an annulus fibrosus and a central nucleus pulposus. To model the facet joints, a cartilaginous body was positioned between the superior and inferior articular processes. The ligaments of the lumbar spine were modelled with uniaxial springs assuming non-linear behaviour (Shin et al. 2007).

To develop the operated models, the L4-L5 disc of the intact models was removed, as well as the anterior and posterior longitudinal ligaments of this level, and replaced by an implant (3 different types of TDR prostheses and an arthrodesis fusion cage). The implants were fixed to the vertebrae to simulate the stability after bone remodelling.

2.2. Experimental analysis

A 7-DoF robotic arm (i.e. Franka Emika) was used to perform the mechanical tests. As the robot is torque-controlled, a compliant control strategy was implemented to apply a 6-DoF desired load to the spinal

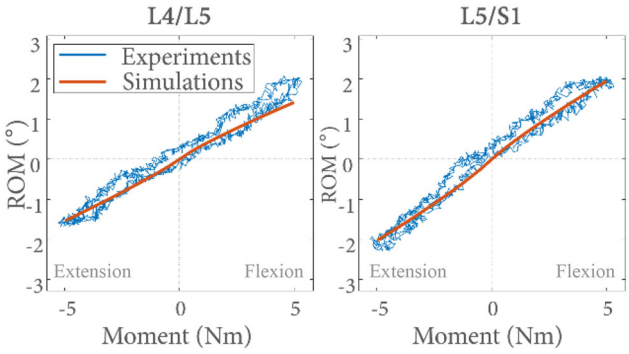


Figure 2. Experimental and numerical ROM during application of a moment reproducing flexion/extension.

segments, based on a desired motion imposed on the robot's end-effector.

Forces and moments were measured using a 6-axis load sensor positioned on the fixed extremity of the spine segment. The position of each vertebra was tracked using Qualisys Motion Capture, which consists of 8 high-resolution infrared cameras allowing to perform mark tracking. Three marks were positioned on each vertebra to measure motions of each spine level during loading.

For both the FE model and the experiments, loadings consisted of pure moments (±5 Nm) applied to the upper vertebra to reproduce physiological movements of flexion, extension, lateral bending and axial rotation. The lower part of the sacrum was fixed.

3. Results and discussion

3.1. Validation of the FE models

The validity of the models was assessed by comparing the computed ROM of the intact models and the measured ROM of the spinal segments at each level (Figure 2).

Differences on ROM values were lower than 20% between the numerical and the experimental results during flexion/extension (Figure 2), as well as for lateral bending and axial rotation. This validated that our models were representative of the behaviour of the spinal specimens used in this study. However, the stiffness of the spines was higher than that reported in the literature (Yamamoto et al. 1989). This may be due to the age of the donors and the fact that they were subject to DDD which is associated with hypomobility of the lumbar spine (Yao et al. 2013).

3.2. Mechanical effects of the implants on the facet joints

The models implanted with ball-and-socket and mobile core prostheses showed an increase in both ROM (×2) and dissipated friction energy in the facet joints at the surgical level (around ×10), whereas a decrease was observed at the adjacent level. This may show that there was a transfer of loads between the two levels, these two implants behaving as a ball joint. The models with viscoelastic models presented similar results to intact models, which may mean that this implant's stiffness is higher than that of a healthy disc. Arthrodesis models seem to show an increase in loads in the facet joints at the adjacent level. In a future work, it would be interesting to define a threshold of stress that increases the risk of facet joint arthrosis, which could help guide the surgeons during the surgical planning.

4. Conclusions

This study presented first results towards the validation of the lumbar spine that allowed the comparison of the mechanical behaviour of different surgical approaches to treat DDD. Arthrodesis models showed a transfer of the loads to the adjacent level while the surgical level remained fixed. In the arthroplasty models, although all prostheses fell under the same TDR name, their mechanical behaviour varied significantly. These results highlight the potential benefits of using patient-specific surgical implants with FE analysis to assist surgeons in selecting the most appropriate implant for each patient.

Acknowledgements

The authors thank the anatomy laboratory of the University of Poitiers (ABS Lab) for the spine segments, and the Nouvelle-Aquitaine for its financial support. Also, we thank the companies Centinel Spine and Spine Innovation for providing their prostheses.

References

Abi-Hanna D, Kerferd J, Phan K, Rao P, Mobbs R. 2018. Lumbar disk arthroplasty for degenerative disk disease: literature review. World Neurosurgery. 109:188–196. doi: 10.1016/j.wneu.2017.09.153.

Finley SM, Brodke DS, Spina NT, DeDen CA, Ellis BJ. 2018. FEBio finite element models of the human lumbar spine. Comput Methods Biomech Biomed Eng. 21(6): 444–452. doi:10.1080/10255842.2018.1478967.

Furunes H, Berg L, Espeland A, Thoresen H, Neckelmann G, Brøgger HM, Småstuen MC, Brox JI, Storheim K, Hellum C. 2020. Facet arthropathy following disc replacement versus rehabilitation: a prospective study with 8-year follow-up. Spine. 45(21):1467–1475. doi:10.1097/BRS.0000000000003600.

Park WM, Kim K, Kim YH. 2013. Effects of degenerated intervertebral discs on intersegmental rotations, intradiscal pressures, and facet joint forces of the whole lumbar

spine. Comput Biol Med. 43(9):1234–1240. doi:10.1016/j.compbiomed.2013.06.011.

Shin DS, Lee K, Kim D. 2007. Biomechanical study of lumbar spine with dynamic stabilization device using finite element method. Comput-Aided Des. 39(7):559–567. doi:10.1016/j.cad.2007.03.005.

Yamamoto I, Panjabi MM, Crisco T, Oxland T. 1989. Three-dimensional movements of the whole lumbar spine and lumbosacral joint. Spine. 14(11):1256–1260. doi:10.1097/00007632-198911000-00020.

Yao Q, Wang S, Shin J-H, Li G, Wood K. 2013. Motion characteristics of the lumbar spinous processes with degenerative disc disease and degenerative spondylolisthesis. Eur Spine J. 22(12):2702–2709. doi:10.1007/s00586-013-2918-y.

KEYWORDS Lumbar spine; biomechanical analysis; finite element model; experimental validation

francois.zot@univ-poitiers.fr

Development of a statistical model of the full skeleton combining shape and a rib quality indicator to assess the risk of rib fracture

M. Hoffmann[a], M.-C. Chevalier[a], Y. Lafon[a], B. Gilles[b], P. Petit[c], P. Baudrit[d] and P. Beillas[a]

[a]Univ Eiffel, Univ Lyon 1, LBMC UMR_T 9406, Univ Lyon, Lyon, France; [b]Anatoscope, Montpellier, France; [c]LAB PSA Renault, Nanterre, France; [d]CEESAR, Nanterre, France

1. Introduction

Elderly road users are particularly prone to rib fractures, which can be affected by changes in the mechanical and geometrical properties of the ribs. Geometrical characteristics of the ribcage, including size and shape, were shown to affect the risk of rib fracture. Statistical shape models (SSM) of the thorax were developed to describe these geometrical variations but the effect of age does not seem so large compared to other factors (Shi et al. 2014) that it could explain the increasing risk with age. Shi and other thorax SSM do not include other variables that could be relevant for injury prediction such as bone quality indicators. This may be an important limitation when trying to predict the effect of age on the injury risk.

Also, for safety, a full body SSM would be useful as injuries result from the interaction of the full body (stature, mass, etc.) with the restraint system. However, due to sparse clinical imaging data and the complexity of the building process, SSM typically describe a single bone or region. A full body SSM would currently require assembling several models (as in the UMTRI Humanshape), which may preclude the study of relationships between body regions. Finally, SSM are also typically not publicly available, limiting their use and possibilities of refinement.

The Thorax-DSR project aims to study the effect of age on rib fractures using a new, open-source full skeleton statistical model combining shape and rib quality indicators. The project focused first on the formulation of a rib quality indicator that could be measured on CT-scans at clinical resolutions. A first indicator was validated using Post-Mortem Human Surrogate (PMHS) data previously collected at CEESAR for which fracture status, CT-scans and average mineral density of a segment of the 4th rib are available. A midsize male full body finite element model (Global Human Body Model Consortium GHBMC M50 v6) was subjected to the same test conditions as 54 PMHS. Combined with rib strains predicted by the model, the mineralization was found to be a predictor of the number of rib fractures. In parallel, the mineralization was correlated to a CT-based measurement, namely the mean Hounsfield value measured on the same rib segment used to measure the mineralization (RibHU). As the CEESAR dataset mostly includes older PMHS, RibHU was also computed on 68 CT-scans from the New Mexico Decedent Image Database (NMDID). This demonstrated the large effect of age on RibHU, its large variance (Figure 1), and the possibility to measure a rib quality indicator on a clinical quality CT-scan.

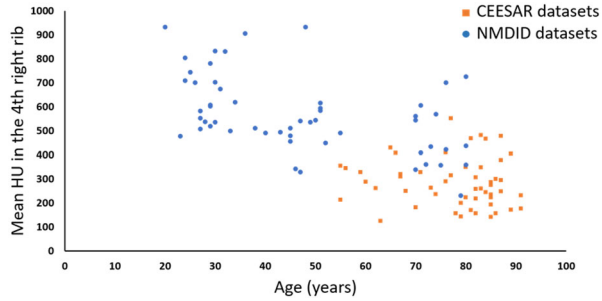


Figure 1. Relationship between RibHU and age.

Based on these encouraging results, the development of a full skeleton statistical model combining shape (segmented from full body CT-scans from the CEESAR and NMDID databases) and the rib quality indicator was initiated. This abstract aims to present the methods, solutions and resulting workflow implemented for the model development.

2. Methods

For their SSM development, Shi et al. used data from 89 CT-scans and observed that over 90% of the variance could be captured with less than 10 modes. Other studies used sample numbers between 80 and 160. For the current work, the 54 PMHS from CEESAR already used for the simulation work (16 females and 38 males) were selected. As their ages range from 55 to 91, the selection was completed by 68 PMHS from NMDID that were pre-selected (34 females, 34 males, ages from 20 to 80). PMHS with prostheses were excluded and, when present, small imaging artefacts (e.g. teeth implants) were mitigated using wxDicom (Treece 2017).

Both imaging datasets include full body CT-scans in supine position performed in three sessions focused on the head, trunk and lower extremities. While the CEESAR scans were performed on frozen PMHS, some postural changes are present between

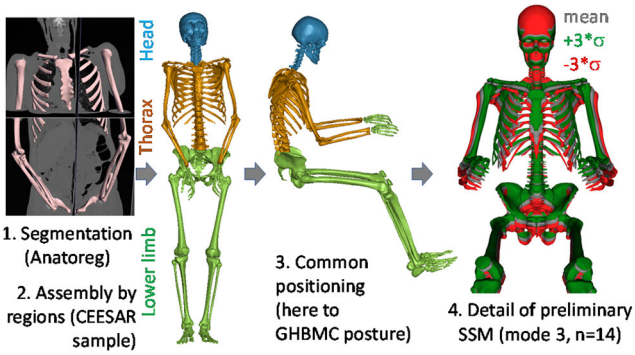


Figure 2. Overview of the process implemented to develop the statistical model.

scans in NMDID. Therefore, it was decided to segment each scan separately and to assemble them based on their overlapping regions. Rather than using a landmark based method for the SSM development as in Shi et al. (2014), a process combining the segmentation and correspondence steps was selected as in Moreau (2018). The CT-scan was segmented by registering a deformable and articulated reference mesh using a dedicated interactive positioning and deformation process allowing to use various types of targets for the registration (landmarks, mesh or image, Anatoreg software, Anatoscope). The reference mesh was based on a manual segmentation (PMHS 635, www.piper-project.org). First, a landmark to landmark registration was performed, followed by a mesh to mesh registration and image to image when needed. Landmarks were defined on the image and a rough segmentation of the CT-scan in 3D Slicer (www.slicer.org).

After segmentation, the registered mesh was downsampled, symmetrized and its posture changed to a reference posture. For now, that posture is defined using the GHBMC onto which the reference mesh was registered. The posture change was done using a bone by bone orientation by least squares and adjustments to maintain the contact areas between adjacent bones. The process is automated (ongoing final tuning) and other postures will be defined (e.g. standing). This approach is expected to facilitate subsequent morphing of the GHBMC for simulations. The statistical model is finally computed on the mesh coordinates (about 71,000 points) and RibHU using the PCA function of the Scikit-Learn library.

3. Results and discussion

An overview of the process is shown Figure 2. To illustrate the feasibility of the workflow, a first statistical model was computed using partial segmentations from previous efforts (www.piper-project.org, Moreau 2018) that were for now completed at the full skeleton by morphing based on the subject size. The replacement of missing regions and the addition of data based on the NMDID CT-scans is ongoing.

Beyond RibHU, age and weight, other discrete parameters will be added including anthropometric parameters measured on the skin surface (e.g. circumferences) and measurements made directly on the model (stature). These will be useful to develop regressions between shape and parameters available in large anthropometric databases (e.g. NHANES).

4. Conclusions

A new, scalable process was implemented to generate full skeletal models and rib quality indicators from full body CT-scans and to prepare them for statistical modelling. The process was verified on a preliminary dataset and the data processing is ongoing. To facilitate reuse, completion or refinement, the statistical model will be released under a Creative Commons Attribution license at www.piper-project.org.

In parallel, segmentations on PMHS for which test data are available will be used to personalize the GHBMC and to refine the relationship between RibHU and fracture by jointly accounting for size and shape. Then, the statistical model will be used to morph the GHBMC and develop simulation-based risk curves for rib fractures as a function of age, sex, size, and bone indicator. Beyond this work, the statistical model could be used to generate plausible full body models for impact and RibHU, that can be measured in a clinical context, may be useful to inform patients on their risk of rib fracture.

References

Moreau B. 2018. Modélisation statistique de la géométrie 3D de la cage thoracique à partir d'images médicales en vue de personnaliser un modèle numérique de corps humain pour la biomécanique du choc automobile [PhD thesis. Univ Montpellier].

Shi X, Cao L, Reed PM, Rupp JD, Hoff C, Hu J. 2014. A statistical human rib cage geometry model accounting for variations by age, sex, stature and body mass index. J Biomech. 47(10):2277–2285. doi:10.1016/j.jbiomech.2014.04.045.

Treece GM. 2017. Refinement of clinical X-ray computed tomography (CT) scans containing metal implants. Comput Med Imaging Graph. 56:11–23. doi:10.1016/j.compmedimag.2017.01.005.

KEYWORDS Statistical model; full body; rib cage; bone indicator; CT-scan

philippe.beillas@univ-eiffel.fr

Development of a surrogate model to represent drones in head impacts

C. Pozzi[a], F. Bermond[a], M. Ragonet[b], F. Coussa[b] and P. Beillas[a]

[a]LBMC UMR_T9406, Univ Lyon, Univ Lyon 1, Univ Eiffel, Lyon, France; [b]ONERA – DMAS – Centre de Lille, LILLE CEDEX

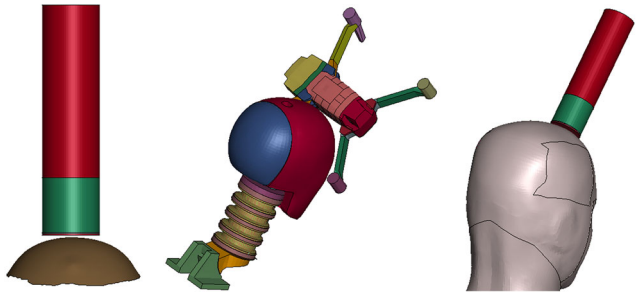


Figure 1. Rigid surface (left), Hybrid III (centre) or GHBMC (right) were simulated against both simplified (centre) and surrogate models (left, right).

1. Introduction

The increasing use of professional and personal Unmanned Aircraft Systems (UAS), or drones, raises the issue of injuries such as skull fractures in case of impact with humans, triggering regulatory responses. Due to speed and energy differences, injury criteria developed for automotive safety may have important limitations. Stark et al. (2019) used Post-Mortem Human Surrogates (PMHS) to study drone impacts with real drones. They observed a fracture and measured injury criteria that are inconsistent with values typically encountered in automotive safety. However, these tests are challenging to reproduce numerically in the absence of publicly available model of the test drones. Complementary tests that could be easily reproduced could be useful to understand the loading mechanisms and validate numerical models or procedures, especially at high speeds for which numerical models or dummies were not validated. Rather than using actual drones in these tests, it would seem desirable to use drone surrogates representing their key characteristics while being simple enough to implement in physical tests and in simulations.

The objectives of this study are to (1) design and validate numerically a concept of drone surrogate in preparation of future tests (2) test a drone model to use to simulate the tests from Stark et al. For this, the responses of models representing either a drone structure (simplified model) or a model with a rigid mass covered by honeycomb (surrogate model candidate) will be compared against various test conditions. The drone test case is the DJI Mavic 2.

2. Methods

2.1. Drone models development

Two finite element models were developed in LS-DYNA (Figure 1): (1) a simplified model based on a surface scan of the drone components (plastic shell, reinforcements, electronic cards, battery cells, arms, etc.) and (2) a surrogate model with a rigid mass covered by honeycomb aiming to represent the effective drone mass and its energy absorption capability, respectively. The honeycomb is composed of several layers to allow progressive compression and energy absorption. Such model could be implemented physically and used in testing.

2.2. Test conditions and simulation process

First, to help adjust both components of the simplified model and characteristics of the surrogate model, three reference physical tests with an actual drone were performed at Onera against a rigid surface similar to a skull shape (22 m/s, just over the highest speed in Stark's study). Then, to see if further adjustments were needed, the models were used against a Hybrid III dummy as in tests with actual drones performed in the past at Univ. Eiffel (15 m/s) (Berthe et al.). The models were finally used against a head model (Global Human Body Model Consortium, GHBMC M50-O v6.0) in conditions similar to Stark et al. (18.5 and 21.5 m/s). The impact condition between the side of the drone body and the forehead was selected for all simulations.

3. Results and discussion

3.1. Impacts on rigid surface

Different combinations of surrogate mass and honeycomb layers as well as properties of the simplified model were simulated to try to match the experimental reaction force-time curve (Figure 2, top). The selected drone surrogate (Figure 2, top) has a mass of 300 g (actual drone: 730 g) and three honeycomb layers, with thicknesses of 42.5, 1, and 1.5 mm and pressures of 7.0, 3.0 and 1.3 MPa, respectively. Both models were able to approximate the experimental response during the loading phase (0–0.3 ms). Then, both approached the magnitude of the experimental force plateau (0.3–0.6 ms) although a short peak force is present for the simplified model. However, both models had a quicker rebound and their unloading

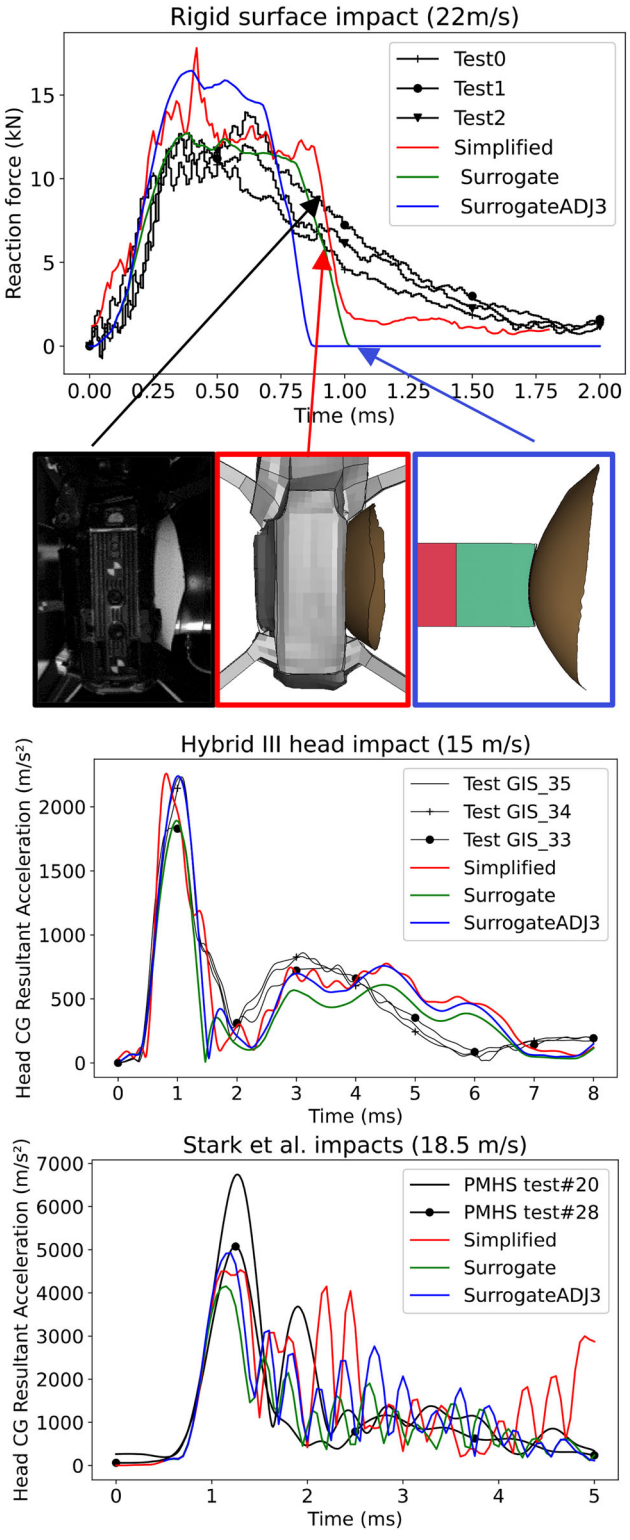


Figure 2. Responses in the three load cases. Accelerations are filtered with a SAE CFC1000 filter. Only 18.5 m/s results are shown for Stark. Images at 1 ms. Physical tests in black.

phase (from 0.6 ms) did not match the experimental curve. This was attributed to the extensive damage on the physical drone decoupling some of the mass from the bulk of the drone.

3.2. Impacts on the Hybrid III head

The drone surrogate rebound occurred much earlier than for the simplified model and physical drone. As defined for the rigid impact, the drone surrogate led to a lower head acceleration (peak and duration) compared to the simplified model and two of the three physical tests (Figure 2, center). Increasing the mass by 75 g and honeycomb pressure by 20% was required to align its response with the others. The new surrogate was labelled surrogateADJ3. Such properties would have led to an overestimation of the force in the rigid shape simulation (Figure 2, top).

3.3. Impacts on GHBMC human model

As for the Hybrid III, the drone surrogate rebound was too early. The accelerations measured at Stark's location varied substantially between the different models and the two tests (Figure 2, bottom). The adjusted surrogate and simplified model approximated the first peak of test #28, hence underestimating the one of test #20. After that, large vibrations were visible in Stark's test #20 and simplified model while these were less marked on other curves. Similar trends were observed at 21.5 m/s. These may result from the deformability of the skull and seem difficult to predict.

Finally, none of the simulations (18.5 and 21.5 m/s as in Stark) resulted in GHBMC skull fractures. This is coherent with Stark et al. (2019) tests and previous simulations underlining the absence of fracture in the GHBMC for honeycomb pressures below 10 MPa (Pozzi et al. 2022).

3.4. Effective mass

When analyzing the response of the simplified model, it was observed that a large proportion of the drone was still moving forwards after the head peak acceleration was reached. This could explain the low value of the effective mass of the drone surrogate (compared to the physical one) and the early rebound. The effective mass to consider was affected by the boundary condition (fixed vs. interaction with a moving head), suggesting impacts on a fixed surface are not sufficient to determine drone surrogate properties although they are useful to identify initial parameters.

4. Conclusions

Both simplified and adjusted surrogate models were able to load the head in a way that is close to the physical test (first acceleration phase). Larger differences were visible later (rebound). Considering the large

differences between actual physical drones (Stark et al. 2019), this confirms the interest of using drone surrogates in future tests to load the head in a plausible manner while helping with the reproducibility (numerically or by other teams). However, due to limitations related to the effective mass and rebound, the simplified model approach should be favored if trying to validate a human head model against the tests from Stark et al. Future work will include the application of the same method to another drone tested by Stark et al. and testing on dummy and PMHS using a physical implementation of the drone surrogate.

Acknowledgements

This work is part of the Ground Impact Study II project funded by the French Directorate General for Civil Aviation (DGAC). The findings and conclusions do not necessarily represent the views of the funding organization. We thank John Bolte (Ohio State Univ.) for providing details about the Stark et al.'s study.

References

Berthe J, Coussa F, Beillas, P, Bermond F. 2019. Drone impact on human beings: experimental investigation with sUAS. Conference ASIDIC, Jun 2019, MADRID, Spain.

Pozzi C, Paccard B, Bermond F, Beillas P. 2022. Fracture sensitivityof a human head model in surrogate drone impacts. IRCOBI 2022 Conference.

Stark DB, Willis AK, Eshelman Z, Kang YS, Ramachandra R, Bolte JH 4th, McCrink M. 2019. Human response and injury resulting from head impacts with unmanned aircraft systems. Stapp Car Crash J. 63:29–64.

KEYWORDS Drone impact; drone surrogate; head injury; finite element models

philippe.beillas@univ-eiffel.fr

Linear viscoelastic material calibration method for judo impact simulation

F. Jonca[a], M. Faillot[b,c], P. Decq[a,b,c], S. Laporte[a] and B. Sandoz[a]

[a]Arts et Métiers Institute of Technology, Université Sorbonne Paris Nord, IBHGC – Institut de Biomécanique Humaine Georges Charpak, HESAM Université, Paris, France; [b]Neurosurgery, Assistance Publique Hôpitaux de Paris Beaujon, Clichy, France; [c]Université Paris Cité, Paris, France

1. Introduction

Mild traumatic brain injuries (mTBI) are present in many contact sports such as judo where brain concussions were observed during training (Yokota and Ida 2016). A way to understand and reduce mTBI is to simulate injurious cases using finite-element head models. However, it is necessary to know impacted surface properties and few resources are available for judo mats. In existing models for mats, elastic behaviour is well-handled but viscoelastic one is difficult to tune.

This abstract presents a viscoelastic model tuning to model a judo mat according to the EU standard used by the International Judo Federation (IJF), and to asses injury risk by using the Head Injury Criterion (HIC) (Versace 1971).

2. Methods

2.1. Viscoelastic model

A generalized Kelvin–Voigt model was used to consider judo mat viscoelastic behaviour (Figure 1). Judo mats for IJF competition are certified using EU standard EN-12503 using falling-mass tests heights and impactor cross-sections variations to investigate its dynamic response. Standard cases are presented in Table 1.

To characterise mat properties, these cases were numerically simulated. Mat was assumed to not be fully compressed during trials. Judo mats are made of foam, where a decoupled behaviour could be assumed between compression direction and transverse ones if not fully compressed. A truss model was then assumed with properties computed by multiplying local ones with a cross-section S. This leads to stiffnesses k_0, k_1 and a damping c. Cross-section was assumed circular with a diameter $d = 20\ mm$. Length was set as $L = 50\ mm$, like the actual commercialised judo mats.

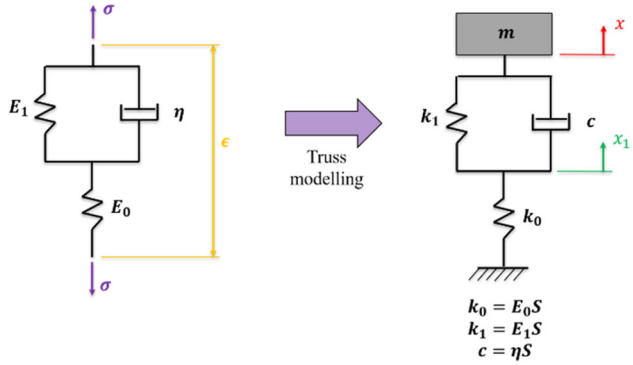


Figure 1. Left: generalized Kelvin–Voigt viscoelastic model. σ is stress applied and ϵ is the strain observed. Right: resultant truss model to simulate trials.

Impactor was modelled as a mass $m = 8$ kg with an impact speed of $v_0 = -\sqrt{2gh}$ where gravity $g = 9.81\ ms^{-2}$ and h the drop height. Then, mat response was described using Equation 1.

$$M\ddot{X} + C\dot{X} + KX = F^{ext} \tag{1}$$

Where

$$X = \begin{bmatrix} x \\ x_1 \end{bmatrix},\ M = \begin{bmatrix} m & 0 \\ 0 & 0 \end{bmatrix},\ C = \begin{bmatrix} c & -c \\ -c & c \end{bmatrix},$$
$$K = \begin{bmatrix} k_1 & -k_1 \\ -k_1 & k_0 + k_1 \end{bmatrix} \text{ and } F^{ext} = \begin{bmatrix} -mg \\ 0 \end{bmatrix}.$$

Initial conditions for this problem are a mass with a speed v_0 and a null position for x and x_1.

2.2 Inverse solving

According to EN-12503 standard, 2 parameters are used to describe dynamic behaviour. The first parameter is the maximal deceleration a during impact. The second parameter is resilience r : the ratio between output and input impactor kinetic energy. The task is to identify the $(k_0,\ k_1,\ c)$ of a mat, from the simulation of each impact case of the EN 12503 standard.

Long-term stiffness $k_T = 54.6\ N.mm^{-1}$ was fixed according to EN 12503 standard. Hence, k_1 was constrained relative to k_0 using Equation Equation 2.

$$k_1 = \frac{k_0 k_T}{k_0 - k_T} \tag{2}$$

Then initial problem was to find $(k_0,\ c)$ solving Equation 3.

$$f(k_0, c) = (a, r) - (a_0, r_0) = 0 \tag{3}$$

A Newton-Raphson algorithm was used with initial conditions $(k_0, c)_1 = \left(2k_T,\ 2\sqrt{k_1 m}\right)$. At each iteration i, Equation 1 was solved using an implicit Newmark scheme with a timestep of $10^{-4}\ ms$. Couple $(a, r)_i$

Table 1. Reference for maximal deceleration and resilience for each case in standard EN 12503-3.

Case	1	2	3	4
Impactor diameter d (mm)	43		116	
Height h (cm)	20	60	20	60
Maximal deceleration a_0 (g)	30	90	40	85
Resilience r_0 (%)	30	28	32	28

were then deduced. Corresponding Jacobian matrix J_i was computed using finite differences. Then, $(k_0, c)_{i+1}$ was computed using Equation 4.

$$(k_0, c)_{i+1} = (k_0, c)_i - J_i^{-1} f(k_0, c)_i \quad (4)$$

Algorithm was iterated until a least-square criterion based on a and r was below a defined tolerance of 10^{-6}. Optimizations were performed on a computation cluster (Intel Xeon Gold 5220 R 2.2 GHz, 35.75Mo memory cache).

2.3. Material identification and injury risk assessment

Local material properties (E_0, E_1, η) were deduced by dividing global ones to cross-section S. Median properties were computed. For each property computed and median, Equation 1 was solved on all cases. Resulting a and r were then compared to reference ones in Table 1. Material chosen were the one which fitted the best an interval of [−10%, 10%].

Injury risk was then evaluated using HIC for both drop heights in Table 1. Values were compared to the threshold 240, corresponding to a probability of 50% to have a mTBI (Newman and Shewchenko 2000).

3. Results and discussion

All cases converged properly. Median properties were $(E_0 = 2.2MPa; E_1 = 189.5kPa; \eta = 18.9MPa.s)$ and gave results which fitted in the defined interval. These properties were then considered. Computation of long-term Young's modulus E_T gave values around $173.4kPa$. This is consistent with the literature (Tomin and Kmetty 2022). This was expected, as equivalent stiffness was imposed by the EN 12503 standard.

Figure 2 presents HIC values for both drop heights, which were lower than injury threshold. Hence, for the cases defined by EN 12503 standard, the proposed model predicts no mTBI. It is then hypothesized that the proposed model is relevant, as standard is likely to try to ensure non-concussive sport mats.

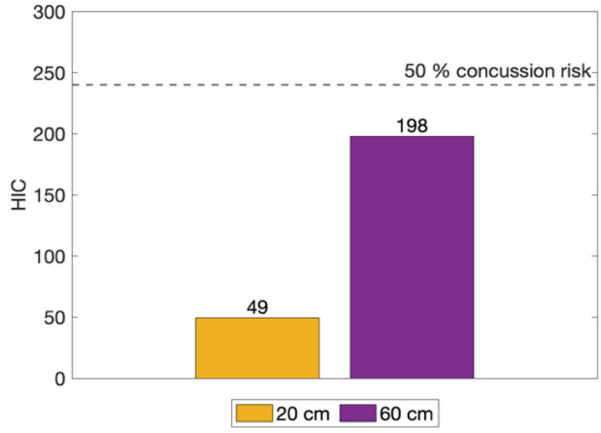


Figure 2. HIC values computed for both drop heights.

The proposed model is simpler than non-linear ones but has 2 main limitations. First, it did not consider non-linear elasticity observed in foams. However, this is not an issue for impact cases because wave propagation induces small perturbations. Second, truss model was chosen for numerical considerations (more stable). A finite-element model would be better to consider impactor diameter and optimize directly on local properties.

4. Conclusion

This study proposes a dynamic viscoelastic model for judo mats according to IJF standards. Model proposed has the advantage to be easy-to-tune with 3 parameters and to be representative on wave propagation. Therefore, the proposed material model could be used for modelling head/mat interface in mTBI simulations for judo.

References

Newman JA, Shewchenko N. 2000. A proposed new biomechanical head injury assessment function – the maximum power index. Stapp Car Crash Conference.

Tomin M, Kmetty A. 2022. Polymer foams as advanced energy absorbing materials for sports applications—A review. J Appl Polym Sci. 139(9):51714. doi:10.1002/app.51714.

Versace J. 1971. A review of the severity index. SAE Technical Paper 710881.

Yokota H, Ida Y. 2016. Acute subdural hematoma in a judo player with repeated head injuries. World Neurosurg. 91: 671.e1–671.e3. doi:10.1016/j.wneu.2016.03.101.

KEYWORDS Judo; mild TBI; viscoelastic model; inverse solving

francoisjonca@ensam.eu

Mechanical behavior of a healthy premolar assessed by digital color holograph and finite element method

P. Picart[a], M. Secail[a], S. Montresor[a], S. Valette[b], M. Fages[c], M. Ducret[d] and R. Richert[e]

[a]Laboratoire d'Acoustique de l'Université du Mans, CNRS 6613, Institut d'Acoustique – Graduate School (IA-GS), Le Mans Université, Av. O. Messiaen, Le Mans, France; [b]Centre de Recherche en Acquisition et Traitement de l'Image pour la Santé, UMR 5220 CNRS/INSA, Villeurbanne, France; [c]Laboratoire Bioingénierie et Nanosciences, Université de Montpellier, Montpellier, France; [d]Laboratoire de Biologie tissulaire et Ingénierie thérapeutique, UMR5305 CNRS/UCBL, Université de Lyon, Lyon, France; [e]Laboratoire de Mécanique des Contacts et Structures, UMR 5259 CNRS/INSA, Université de Lyon, Villeurbanne, France

1. Introduction

Understanding the biomechanical behaviour of the tooth appears decisive to prevent root fractures, improve restorative techniques and *in fine* promote long-term strategies. Traditionally, our comprehension of this behaviour is based on analysis of finite element models validated using a strain gauge (Richert et al. 2020). Yet, relying solely on a strain gauge to measure tooth strain has limitations because it can only record data from one location, and it is challenging to attach the gauge securely to the tooth, leading to potential inaccuracies. Conversely, interferometry makes it possible to obtain information on the surface deformation field of the tooth and its restoration according to different methods of generating amplitude interference from two separate beams of light waves (Xia et al. 2018). From interferograms or holograms, the deformation from the relative phase of the two waves can be calculated. This technique has a very high sensitivity evaluated at about 10 nm and has led to a better understanding of dental behaviour evaluating the mechanical role of major parts of the dental structure such as enamel *in vitro* and *in silico* (Barak et al. 2009). However, the biomechanical role of finer histological structures of the tooth such as dentin-enamel junction remains poorly understood (Desoutter et al. 2023).

The goal of this paper is to evaluate the displacement of a healthy premolar prepared axially and submitted under axial loading under interferometry and to compare it with the predictions of its finite element model.

2. Methods

2.1. Finite element modelling

A healthy first maxillary premolar extracted for orthodontic reasons was prepared following previous protocols (Xia et al. 2018), embedded in a dental acrylic resin, and was scanned using a cone beam computed tomography (Planmeca ProMax 3D, Helsinki, Finland) operating at 120 kV, 100 mAs, with a slice thickness of 0.75 mm and the volume was recorded in DICOM format. The different anatomical structures of the tooth (dentin, enamel, pulp) and its resin support were segmented based on a semi-automatic procedure. The segmented 3D image was then meshed using 202,636 quadratic tetrahedral elements after a convergence test (Valette et al. 2008). All dental materials were supposed homogeneous and linearly elastic. The attributed material properties were referenced from the literature (Richert et al. 2020). There was a perfect bonding between each component of the tooth and its support, and a static vertical load was applied to the top of the vestibular cuspid of the crown to simulate a compression test. The nodes of the lateral and lower faces of the resin support were constrained to prevent any displacement. The FEA was conducted on the Abaqus software 6.14 (Dassault Systèmes, Vélizy-Villacoublay, France) to calculate *in silico* the displacements and strains of the loaded tooth.

2.2. Digital holography

Four flat steel compression rods were used, and the force sensor has been calibrated with its module (printed circuit with 6.5 V mains supply, INA118P amplifier, regulator, resistor). The compression was carried out using the Labview software (National Instruments, Austin, USA – TX) to control the position of the motor during the test. At the same time, the surface of the tooth was illuminated by a 50 mW YAG laser with a green wavelength of 532 nm to create digital holographic fringes following published protocols (Xia et al. 2018). The tooth images were recorded using an ORCA (Hamamatsu, Tokyo, Japan) Charge-Coupled Device (CCD) sensor and HCImage internal camera software and the force was applied with a motor step of 5 μm from 0 N to 250 N.

The recorded digital holograms are obtained from the interferences between the reference wave and the object wave diffracted by the surface of the sample. The *in vitro* displacement at each point of the sample can therefore be expressed as a function of the phase difference $\Delta\phi(x,y)$ between two holograms. This displacement U_c can be expressed as a linear function between U_x, U_y and U_z for each node of the mesh. The digital holograms were

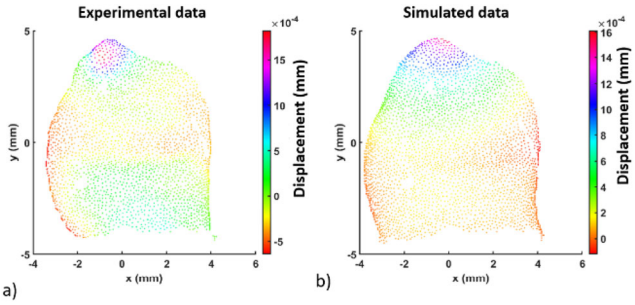


Figure 1. Biomechanical behaviour of the premolar loaded with the displacement U_c evaluated *in vitro* by holography (a), the displacement calculated *in silico* by finite element method (b) for $F = 42.87$ N.

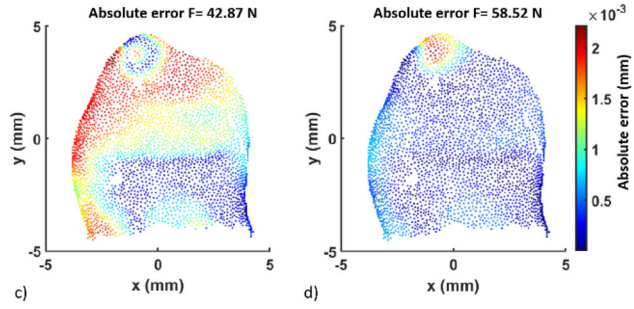


Figure 2. Absolute error between experimental and simulated U_c for $F = 42.87$ N (c) and $F = 58.52$ N (d).

analyzed using Matlab software (MathWorks, Natick, USA, MA). A mask based on binary grayscale contrasts is applied to restrict the analysis to the shape of the tooth only. The tooth being more rigid than the tooth holder, a rigid body movement exists and was considered when post-processing data. For each load of the experiment, the error map was calculated by comparing experimental to the simulated displacement.

3. Results and discussion

The order of magnitude of U_c (10^{-4} mm) and its distribution are close between *in vitro* and *in silico* experiments: there are strong displacements on the vestibular cusp of the tooth and these decrease in the cervical areas. Locally, the error is very variable from one point to another, but this could be explained by the fact that the meshes are not the same *in silico* and *in vitro* (Figure 1).

The error also varied greatly depending on the force, notably before 50 N, but was restricted only to the vestibular cusp over 50 N (Figure 2). Within the limits of the restricted sample size, the current finite element model might appear poorly adapted to simulate the premolar over 50 N. This could be of particular importance as masticatory forces could exceed 100 N depending on cranio-facial morphology or age.

Large strains were present in the dentin areas compared to the enamel ones on the finite element model. Stress distribution patterns revealed flexion in the cervical areas where dentin is mostly present. These results are in accordance previous studies that emphasize the decisive role of the enamel cup, and the necessity to preserve it in clinic (Barak et al. 2009).

However, it's of particular importance to note that different anatomical features present at the dentin-enamel junction such as were not considered in the finite element model whereas this component greatly influenced the biomechanical behavior of the tooth, notably by preventing crack propagation from enamel into dentin (Xia et al. 2018). The current study constitutes a first proof of concept on a unique tooth but experiments on a larger sample size are now required to validate material laws for the dentin-enamel junction notably over 50 N.

4. Conclusions

The method of digital holography appears to be a promising tool for assessing the biomechanical behavior of the premolar and validating material laws. Future works are now required to explore the effectiveness of this method on a larger sample size and investigate the role of the dentin-enamel junction.

References

Barak M, Geiger S, Chattah N, Shahar R, Weiner S. 2009. Enamel dictates whole tooth deformation: a finite element model study validated by a metrology method. J Struct Biol. 168(3):511–520. doi:10.1016/j.jsb.2009.07.019.

Desoutter A, Felbacq D, Gergely C, Varga B, Bonnet L, Etienne P, Vialla R, Cuisinier F, Salehi H, Rousseau E, et al. 2023. Properties of dentin, enamel and their junction, studied with Brillouin scattering and compared to Raman microscopy. Arch Oral Biol. 152:105733. 152 doi: 10.1016/j.archoralbio.2023.105733.

Richert R, Farges JC, Tamimi F, Naouar N, Boisse P, Ducret M. 2020. Validated finite element models of premolars: a scoping review. Materials. 13(15):8:3280–3289. doi:10.3390/ma13153280.

Valette S, Chassery D, Prost R. 2008. Generic remeshing of 3D triangular meshes with metric-dependent discrete voronoi diagrams. IEEE Trans Visual Comput Graphics. 14(2):369–381. doi:10.1109/TVCG.2007.70430.

Xia R, Picart P, Montresor S, Guo R, Li JC, Yusuf Solieman O, Durand JC, Fages M. 2018. Mechanical behavior of CAD/CAM occlusal ceramic reconstruction assessed by digital color holography. Dent Mater. 34(8):1222–1234. doi:10.1016/j.dental.2018.05.007.

KEYWORDS Holography; finite element analysis; premolars; mechanical behavior; validation

raphael.richert@univ-lyon1.fr

Simplified abdomen model to evaluate the intra-abdominal pressure variation after hernia repair

Y. Wen[a], P. Rousset[b], G. Passot[c] and A. Bel-Brunon[a]

[a]INSA Lyon, CNRS, LaMCoS, UMR5259, Univ Lyon, Villeurbanne, France; [b]HCL, Lyon Sud University Hospital, Lyon 1 Claude Bernard University, CICLY – EA3738, Pierre Bénite, France; [c]HCL, Lyon Sud University Hospital, Lyon 1 Claude Bernard University – EMR, Pierre Bénite, France

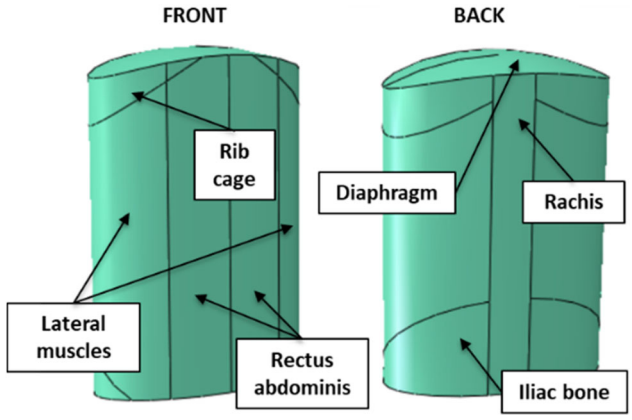


Figure 1. Geometry of the abdomen model.

1. Introduction

Ventral hernia is a defect in the abdominal wall leading to the externalization of abdominal organs outside the abdominal wall, under the skin. This pathology cannot heal by itself. Ventral hernia repair consists in reintegrating the content of a hernial sac within the abdomen and close the hole, possibly with a synthetic reinforcement. Numerical studies have been performed to investigate the abdominal wall response to daily life activities (Pachera et al. 2016) or to hernia repair (Guérin and Turquier 2013). Abdominal wall heterogeneity, non-linearity and anisotropy, as well as muscle contraction, have been included to provide a deep understanding of the wall components interactions and evaluate the mechanical loadings on the tissues; validation is however still needed for this application.

In the present work, we focus on hernia repair intra-operatively: when the contents of the hernial sac is reintegrated in the abdomen, the intra-abdominal pressure (IAP) increases and the tension applied to the hole edges to close it increases. Increased IAP is a quantity of interest as a large IAP could lead to breathing issues for the patient, while tension on the hole edges could lead the surgeons to perform an additional and invasive act, namely separate the abdominal wall muscles to manage suturing the hole. We aim to develop a simple model of the abdomen mechanical response to a variation of its internal volume to generate a database that would provide the surgeon with an estimation of IAP and tension for a given patient, based on his/her anatomy.

2. Methods

2.1. Abdomen modeling

The abdomen is modeled in a simplified and parametric way. It consists of a pseudo-elliptic cylinder, close by a dome at its top, corresponding to the diaphragm, and a plane at the bottom, corresponding to the pelvic floor (Figure 1). The cylinder is partitioned to delineate deformable and rigid parts. Namely, the rib cage and rachis are considered rigid while the abdominal wall, the diaphragm and the pelvis floor are deformable. The abdomen is meshed with linear triangular shell elements.

Table 1. Patients categories.

Stature (cm)	Age	BMI
<150	18–30	15–20
150–160	30–45	20–25
160–170	45–60	25–30
170–180	> 60	30–35
180–190		35–40
>190		> 40

In this study, deformable tissues are modeled as linear elastic. Based on the in-vivo data acquired by Song et al. (Song et al. 2006), two Young moduli are considered for the abdominal wall: 27.7 kPa for men and 21.0 kPa for women. The diaphragm and pelvic floor Young moduli are 11.5 MPa and 0.65 MPa respectively and their thickness is 1.9–1.4 mm (men/-women) and 7.15 mm respectively.

Patient categories were modeled based on their sex, age, Body Mass Index (BMI) and stature (Table 1), by adapting the model geometry (ellipse axes and height) and the abdominal wall thickness. Preliminary measurements showed that the abdominal cavity height is linearly related to the patient height. A linear relationship between BMI and the ellipse minor and major axes was postulated, and another linear relationship between the BMI and age on the one hand and the muscle groups thickness one the other hand was determined based on the morphometric work of Jourdan et al. (2020).

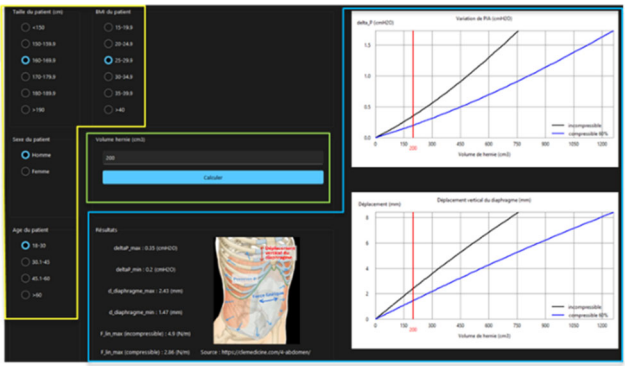


Figure 2. Screenshot of the estimation software: yellow box: patient data; green box: hernial sac volume; blue box: results.

The elliptic cavity was considered as a fluid cavity and inflated to 5 cmH_2O using Abaqus/Static (Smith 2009). The quantities of interest, namely the pressure and volume evolution, the diaphragm apex vertical displacement, as well as the force per unit length along the abdominal wall central line (between the two Rectus Abdominis) were stored for each simulation to build a database.

2.2. Graphical interface

A graphical interface dedicated to the surgeons was coded in Python. The surgeon enters the patient's age, sex, stature and BMI categories, and the software displays the corresponding simulation results found in the database, that is the evolution of the quantities of interest with respect to the cavity added volume (due to pressure increase in the simulation). The idea here is to use the simulation results in the opposite way as they were generated: for a given hernial sac volume (measured pre-operatively on the patient CT-scan) aiming to re-enter the abdomen, corresponding to a volume increase in the simulated abdomen, the software can provide the corresponding increase in pressure, force per unit length and diaphragm apex displacement. As some abdominal organs are hollow, the abdominal content is compressible, so we chose to provide a range for the results, representing a variation of the abdominal volume of 100% and 60% of the hernial sac volume respectively.

3. Results and discussion

Patient BMI and stature (modeled by the height and ellipse size) are the most influential factors on the variation of IAP, while age and sex are less prevalent. The quantities of interest exhibit a non-linear response. Figure 2 shows the graphical interface displaying the simulation results for a given patient category. In the blue box (results), the red line defines the intercept between the pressure (top) and diaphragm apex displacement (bottom) curves for the specific hernial volume. The black and blue curves correspond to 100% and 60% of the hernial sac volume respectively. These preliminary results illustrate a workflow to provide a real-time answer to a practical question raised by surgeons. However, it has not been yet validated. Preliminary validation based on pre- and post-operative CT images as well as intra-operative intravesical pressure measurements on a few patients seem to show that, as expected, the simulated pressure increase is too small, so a hyperelastic stiffening constitutive law for the abdominal would probably be more appropriate. Muscle activation should not be necessary as what is modeled here occurs while the patient is anesthetized. The patient variability as seen on CT images also seems to show that the linear correlations postulated in this work between BMI and the elliptic axes cannot accurately enough represent the patients' anatomy; measuring the actual patient geometrical features required for the model directly on the pre-operative images is a way to gain accuracy, despite increasing the processing time required prior to simulation. Finally, the assumption that the abdominal content is compressible, while realistic, requires further quantification based on the segmentation of the hernial sac and the abdominal cavity before and after surgery.

4. Conclusions

This work is a first step towards a more comprehensive inclusion of the abdomen complexity in our model. Once validated, the Finite Element simulation could be used to update the database and help surgeons anticipating intra-operative complications and adapting their practice as a consequence, thanks to a real-time estimation of the mechanical quantities at stake in their procedure.

References

Guérin G, Turquier F. 2013. Impact of the defect size, the mesh overlap and the fixation depth on ventral hernia repairs: a combined experimental and numerical approach. Hernia. 17(5):647–655. doi:10.1007/s10029-013-1050-6.

Jourdan A, Soucasse A, Scemama U, Gillion JF, Chaumoitre K, Masson C, Bege T. 2020. Abdominal wall morphometric variability based on computed tomography: influence of age, gender, and body mass index. Clin Anat. 33(8):1110–1119. doi:10.1002/ca.23548.

Pachera P, Pavan PG, Todros S, Cavinato C, Fontanella CG, Natali AN. 2016. A numerical investigation of the healthy abdominal wall structures. J Biomech. 49(9):1818–1823. doi:10.1016/j.jbiomech.2016.04.019.

Smith M. 2009. ABAQUS/standard user's manual. United States: Dassault Systèmes Simulia Corp.

Song C, Alijani A, Frank T, Hanna G, Cuschieri A. 2006. Elasticity of the living abdominal wall in laparoscopic surgery. J Biomech. 39(3):587–591. doi:10.1016/j.jbiomech.2004.12.019.

KEYWORDS Abdominal wall; ventral hernia repair; finite element simulation; real-time

aline.bel-brunon@insa-lyon.fr

What is the impact of the surgical approach on functional recovery after total hip arthroplasty? a narrative review

P. Henry[a,b], M. Blandeau[a], P. Pudlo and L. Wallard[a]

[a]Univ. Polytechnique Hauts-de-France, LAMIH, CNRS, UMR 8201, Valenciennes, France; [b]Kinik Inc, Boucherville, Canada

1. Introduction

Osteoarthritis (OA) is the most common degenerative joint disease in the elderly, becoming a major public health problem. Osteoarthritis affects approximately 240 million people worldwide, including more than 10 million in France (Katz et al. 2021). Hip OA is characterized by severe musculoskeletal pain and limitation of joint movements that progressively decrease the autonomy and quality of life of these patients. For example, gait is exemplified by abnormal gait patterns associated with reduced walking speed, reduced hip muscle strength, and higher energy costs compared to asymptomatic adults (Wallard et al. 2017). Given all of these considerations, direct surgical treatment is advocated for hip OA. The surgeon approaching a hip faces a dilemma: expose himself extensively to implant a biarticular prosthesis and preserve the gluteal musculature to avoid instability of his arthroplasty. In order to do so, surgeons have devised three major technical approaches that combine ease of surgery with postoperative risks and recovery (Petis et al. 2015). The surgical approach for total hip replacement can be performed using three main methods: the anterior approach, the posterior approach and the lateral approach. The objective of this narrative study is therefore to quantify the different consequences of these approaches on the functional and motor capacities of patients. We hypothesize that the anterior approach allowed a better recovery of functional ability, in particular thanks to a better preservation of muscles and surrounding tissues during the operation.

2. Methods

This narrative review was conducted in these two databases: PubMed, ScienceDirect. The inclusion criteria were: articles written in English, articles published between 2010 and 2023. To collect the different studies, we used the following term selections: (‘total hip arthroplasty’ OR ‘total hip replacement’ OR ‘Primary hip replacement’) AND ('gait’ OR 'locomotion’ OR ‘walk’ OR 'functional recovery’ OR 'functional capacity’) AND ('approach’ OR 'surgery approach’) NOT (‘fracture’). 94 articles were retrieved from the databases. Only articles on primary hip arthroplasty were selected. By cross-referencing, four relevant studies were also included.

All selected articles can be found on the corresponding author ResearchGate account.

3. Results and discussion

A total of 98 potentially relevant articles were identified, of which 72 met the inclusion criteria. We can note that the evidence for successful arthroplasty is based on the goals of pain alleviation, improved quality of life and restoration of function. (Learmonth et al. 2007). These assessments were are often carried out through the use of questionnaires (e.g. HOOS, OHS, SF-36).

In this narrative review 30 articles compared the effects of the anterior versus posterior approach, 11 compared the anterior versus lateral approach and 1 compared the lateral versus posterior approach. 8 studied all 3 approaches. The remaining articles studied different techniques within a single approach.

The posterior approach involves an incision at the back of the hip, allowing the surgeon to access the joint by cutting through certain muscles. The advantages of this approach are easier visibility of the hip joint and better stability of the prosthesis. However, the posterior approach may result in more post-operative pain and an increased risk of hip dislocation due to greater post-operative muscle weakness. Indeed, abductor insufficiency is a common comparison between the posterior and lateral approaches. A 2018 systematic review suggested that the lateral approach has an increased incidence of abductor insufficiency after Total Hip Arthroplasty (THA) (Petis et al. 2018).

The lateral approach is a third option. This technique involves an incision on the side of the hip, allowing the surgeon to access the joint by moving certain muscles. The advantages of this approach are direct visibility of the hip joint and faster recovery than the posterior approach. However, the lateral approach can result in more postoperative pain, and abductor weakness (Waddell et al. 2010).

The most common approach and preferred by surgeons for hip replacement surgery is the anterior approach (Chechik et al. 2013). This technique involves an incision at the front of the hip, allowing the surgeon to access the joint while sparing the

musculature. This approach requires more experience on the part of the surgeon to be performed correctly (Ramadanov et al. 2021; Zhang et al. 2022). However, the benefits of this approach include reduced hospital stay, decreased postoperative pain, decreased risk of hip dislocation, and faster recovery. Patients who have undergone total hip replacement *via* the anterior approach tend to have a faster recovery of their ability to stand, walk and climb stairs than patients operated on *via* the posterior approach. Patients operated on with an anterior approach may have a faster, more energy-efficient gait, which can improve their quality of life in a very short time. They may also have more hip flexion, which may facilitate activities such as climbing stairs or playing certain sports (Kohnen et al. 2017).

In this sense, this narrative review notes that, for the anterior approach, some articles found a significant temporal effect for maximum hip extension between 3 days and 3 months postoperatively as well as on stride length (Böhm et al. 2016). Beyond 3 months, this difference disappears with the lateral approach (Reichert et al. 2018).

4. Conclusions

Most studies suggest that the direct anterior approach may be associated with greater early postoperative improvements than lateral and posterior approaches. The choice of approach will depend on the surgeon's preference and experience, as well as the specific needs of the patient. All three approaches are widely used and all have their advantages and disadvantages. However, the differences dissipated to give similar results one year after surgery. These results confirm that the direct anterior approach allows for more rapid restoration of function after arthroplasty. Post-surgery, patients present better motor and functional capacities, allowing them to practice physical activities quicker, safer and without presenting proven pain. Patients should discuss their options with their surgeon and ask all necessary questions before making an informed decision. Future works would be dedicated to the evaluation of rehabilitation efficiency depending on the surgical approach.

References

Böhm H, Hagemeyer D, Thummerer Y, Kipping R, Stöckle U, Scheuerer K. 2016. Rehabilitation of gait in patients after total hip arthroplasty: comparison of the minimal invasive Yale 2-incision technique and the conventional lateral approach. Gait Posture. 44:110–115. doi:10.1016/j.gaitpost.2015.10.019.

Chechik O, Khashan M, Lador R, Salai M, Amar E. 2013. Surgical approach and prosthesis fixation in hip arthroplasty worldwide. Arch Orthop Trauma Surg. 133(11):1595–1600. doi:10.1007/s00402-013-1828-0.

Katz JN, Arant KR, Loeser RF. 2021. Diagnosis and treatment of hip and knee osteoarthritis: a review. JAMA. 325(6):568–578. doi:10.1001/jama.2020.22171.

Kohnen C, Vancauter M, M'Bra I, Feyder C, Wallard L, Detrembleur C, Mahaudens P, Postlethwaite D, Dubuc J-E, Cornu O. 2017. Minimal-invasive posterior, anterior and anterolateral approach in hip replacement: is there a difference in functional outcome and restoration of hip biomechanics? SM Orthopedics Muscular Syst. 1(1):1001–1006.

Learmonth ID, Young C, Rorabeck C. 2007. The operation of the century: total hip replacement. Lancet. 370(9597):1508–1519. doi:10.1016/S0140-6736(07)60457-7.

Petis S, Howard JL, Lanting BL, Vasarhelyi EM. 2015. Surgical approach in primary total hip arthroplasty: anatomy, technique and clinical outcomes. Can J Surg. 58(2):128–139. doi:10.1503/cjs.007214.

Petis SM, Vasarhelyi EM, Howard JL, Lanting BA. 2018. Gait analysis following release of the short external rotators during an anterior approach for total hip arthroplasty. Hip Int. 28(6):584–590. doi:10.1177/1120700017752514.

Ramadanov N, Bueschges S, Liu K, Lazaru P, Marintschev I. 2021. Comparison of short-term outcomes between direct anterior approach (DAA) and SuperPATH in total hip replacement: a systematic review and network meta-analysis of randomized controlled trials. J Orthop Surg Res. 16(1):324. doi:10.1186/s13018-021-02315-7.

Reichert JC, von Rottkay E, Roth F, Renz T, Hausmann J, Kranz J, Rackwitz L, Nöth U, Rudert M. 2018. A prospective randomized comparison of the minimally invasive direct anterior and the transgluteal approach for primary total hip arthroplasty. BMC Musculoskelet Disord. 19(1):241. doi:10.1186/s12891-018-2133-4.

Waddell J, Johnson K, Hein W. 2010. Orthopedic practice in total hip arthroplasty and total knee arthroplasty: results from the Global Orthopaedic Registry (GLORY). Am J Orthop. 39(9 Suppl):5.

Wallard L, Cornu O, Dubuc JE, Mahaudens P, M'bra KI, Postlethwaite D, Van Cauter M, Detrembleur C. 2017. Does the quantitative functional assessment allow to better guide the treatment of the patient with severe hip osteoarthritis? Comput Methods Biomech Biomed Eng. 20(sup1):S207–S208. doi:10.1080/10255842.2017.1382935.

Zhang B, Liu S, Liu Z, Liu B, Huo J, Li M, Han Y. 2022. Clinical and radiologic outcomes in patients undergoing primary total hip arthroplasty with Collum Femoris Preserving stems: a comparison between the direct anterior approach and the posterior approach. BMC Musculoskelet Disord. 23(1):77. doi:10.1186/s12891-022-05040-2.

KEYWORDS Total hip arthroplasty; surgical approach; functional recovery; locomotion; gait analysis

philippe.henry@uphf.fr

Tissue engineering and material by design

3D printed TPU tensile biaxial characterization, page S328.
Interest of porous materials for a mandibular rehabilitation with an implant-supported fixed prosthesis: a numerical study, page S331.
Modelling the mechanical behavior of the spinal cord and epidurally implanted surgical lead for Spinal Cord Stimulation (SCS) using the Finite Element Method (FEM), page S333.
Numerical scheme for dynamic elastographic measurements in the cornea, page S335.
Numerical study of flow rate variations in microfluidic dynamic cell culture, page S337.

3D printed TPU tensile biaxial characterization

M. Evin[a], M. Py[a], Y. Godio-Raboutet[a], Y Park[b] and L. Kadem[b]

[a]Aix-Marseille Univ., Univ. Gustave Eiffel, LBA, Marseille, France; [b]Concordia University, Montréal, Canada

1. Introduction

The use of 3D-printed material for a realistic and biomimetic experimental modelling has been increasing for educational purpose in the field of clinical use in surgery (Pugliese et al. 2018). Such techniques have improved morphological bio-realism of developed synthetic phantoms as well as reproducible process creation compared to silicone molding. However, the mechanical behaviour of the 3D-printed material might be affected by the printing process, the printing parameters and the pattern selected.

While the mechanical characterization of 3D materials is standardized and described by shore durometer testing (ASTM D2240-00), the relations between shore description and mechanical tensile tests remain limited in the literature when dealing with 3D-printed materials.

This preliminary work aims at evaluating the mechanical properties of 3D-printed Thermoplastic polyurethane (TPU) material for different the pattern and 3D printing parameters for two different TPUs and on two different 3D printers.

2. Methods

2.1. Samples preparation

Two different TPUs were used for printing the specimens: TPU 85 A Natural (Ultrafuse, BASF, 2.85 mm) and Ninja Flex TPU 85 A.

3D printing parameters for all print were: plate temperature of 50 °C and 40 °C, printing temperature of 235 °C for both with first layer printing temperature of 245 °C and 235 °C on a Ultimaker S5 (Ultimaker, Utrecht, Netherlands) for respectively the TPU 85 A and Lulzbot TAZ6 with a flexystruder V2 nozzle for the NinjaTek 85 A (NinjaTek, Lititz, USA).

The samples were designed as parallelepiped squares with the following dimensions:11 mm by 11 mm by 1.5 mm. For the 3 Ultimaker specimens, 5 inferior layers were printed with an infill density of 100%, layer height of 0.1 mm (TPU85A) and 0.3 mm (NinjaTek85A). Three different printing patterns were used for each material (grid, concentric and line for TPU85A and line, concentric and zigzag for NinjaTek85A).

Table 1. Tested 3D printed specimens.

Pattern	Nb	3D Printer	Infill	Material
Grid	5	Ultimaker	100	TPU
Concentric	5	Ultimaker	100	TPU
Line	5	Ultimaker	100	TPU
Zig-zag	4	LulzbotTAZ6	0–100	Ninja, Flex TPU
Concentric	4	LulzbotTAZ6	0–100	Ninja Flex TPU
Line	4	LulzbotTAZ6	0–100	Ninja Flex TPU

The number of tested samples could be found in Table 1. An additional dog-bone specimen was also printed for uniaxial test with a size of 150 mm by 20 mm by 4 mm, and a gauge section of 60 mm by 10 mm by 4 mm, in TPU85A. Printing parameters were 7 inferior and superior layers, 100% infill, temperature fixed as previously described for the TPU85A.

2.2. Uniaxial and biaxial tensile tests

The uniaxial tests were performed on ACUMEN 3 axial/torsion electrodynamic device (MTS System corporation, Eden Prairie, Minnesota, USA) with an embedded load cell of 3 kN and an external load cell of 2 kN (9317 C, Kistler, Les Utilis, France) located above the specimen. The jaws enable fixation without slipping. The test protocol consisted in a simple ramp with a 1% strain rate.

The biaxial tensile test system description can be found in (Laville et al. 2020) and is a custom-made system with four step motors (Zaber, Vancouver, Canada) and four load cells (50 N, sensitivity 0.001 N) controlled by a HBM PMX system (HBM). Four rakes are used and a specific guide for positioning the sample was created to insure reproducibility of the positioning

Two Phantom Miro C110 cameras (12-bits 1.3 MPixel CMOS sensor, at 915 fps and 1280 px by 1024 px image definition, Vision Research Phantom, Wayne, New Jersey, USA) were used to monitor the tests.

2.3. Data analysis

Strain and stress were computed as engineering strain (load on the axis divided by the initial cross-section area) and stress (displacement of the axis divided by the initial length of the specimen in the given axis).

Bi-linear piecewise fit was performed optimising r^2 for the whole fit and for each direction of the material. Uniaxial TPU test was used to identify an 3rd

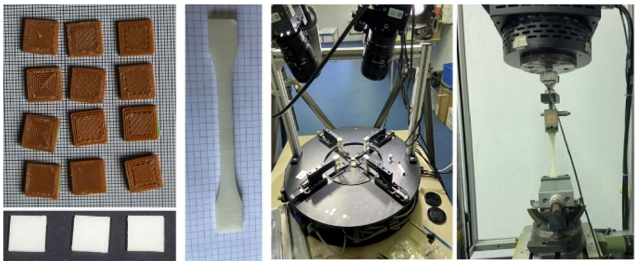


Figure 1. Tested specimens NinjaTek85A (top left) and TPU85A specimen (bottom left); biaxial tensile test (centre); uniaxial tensile test (right).

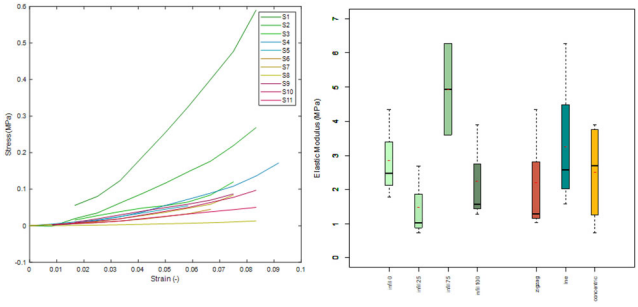


Figure 2. Strain stress curves (left) and boxplot (infill 0, 25, 75 and 100% and the 3 patterns-right) for Ninja Flex samples.

order Ogden model as follow s (Ogden et al. 2004):

$$\sigma = \sum_{p=1}^{N} \mu_p \left(\lambda^{\alpha_p} - \lambda^{\frac{1}{2}\alpha_p}\right)$$

with λ, the stretch, σ the Cauchy stress, $N = 3$ the order of the model and (μ_p, α_p) the identified coefficients using lsqcurve fit function in Matlab (Mathworks, Natick, USA). Wilcox test was used to assed differences between pattern and infill parameters (R Core Team 2020).

3. Results and discussion

Uniaxial test of the TPU dog-bone specimen resulted in an elastic modulus of 24.88 MPa (r^2 of 0.99).

For the TPU85A samples, line pattern resulted in elastic modulus in one axis of 2.03 ± 0.61 MPa and 3.24 ± 0.19 MPa in the other axis; grid pattern elastic moduli were found to be 1.91 ± 0.54 MPa and 3.75 ± 2.38 MPa and concentric pattern elastic moduli were 2.04 ± 0.49 MPa 4.85 ± 3.4 MPa (r^2 ranging between 0.98 and 0.99).

For NinjaTek85A, one sample (infill 75%, zigzag) was excluded from the analysis. Results are presented in Figure 2 as strain stress curves as well as boxplots for infill impact and pattern impact depiction. Elastic modulus ranged from 0.72 to 6.27 MPa. Line pattern elastic moduli averaged for the two axes were 3.25 ± 2.1 MPa, 2.5 ± 1.51 MPa for concentric pattern and 1.97 ± 1.57 MPa for zigzag pattern.

When compared to reported manufacturer values for TPU85 material Young's modulus (20 MPa after ISO 527), this result could be considered acceptable. When comparing uniaxial and biaxial tests however, the effect of the printing pattern could not be ignored.

For the NinjaTek 85 A, the tensile modulus (ASTM D638) is reported to be 12.41 MPa which is within the values found depending on the pattern and infill condition.

Several limitations could be noted as the lack of uniaxial testing for Ninja Flex TPU 85 A, as well as the limited number of samples, and the equi-axial biaxial testing only. Additionally, a constitutive model such as Mooney Rivlin (5 parameters) could have been tested as in compression tests for auxetic structures (Shepherd et al. 2020). This identification of parameters for the constitutive model will then require a large amount of test, an optimized variability of parameters with lower increment between infill values.

4. Conclusions

The characterization of developed 3D printing materials could be a good alternative to the actual use of silicone materials for which reproducibility of the mold creation could be challenging and could complete the synthetic material testing standardization mostly developed for polymers. Further studies could include numerical simulations and sensitivity analysis to address the impact of different patterns and predict the resulting mechanical behavior. Biaxial tensile tests on synthetic material enable a complete testing and validation of material characterization, a necessary step before any further use of the material.

Acknowledgements

The authors thank Cyril Grébonval from Glad Medical for his help and advice on dog-bone specimen uniaxial testing as well as Christophe Pradille and Yannick Tillier for the biaxial test system development.

References

Laville C, Pradille C, Tillier Y. 2020. Mechanical characterization and identification of material parameters of porcine aortic valve leaflets. J Mech Behav Biomed Mater. 112:104036. doi:10.1016/j.jmbbm.2020.104036.

Ogden RW, Saccomandi G, Sgura I. 2004. Fitting hyperelastic models to experimental data. Comput Mech 34(6): 484–502. doi:10.1007/s00466-004-0593-y.

Pugliese L, Marconi S, Negrello E, Mauri V, Peri A, Gallo V, Auricchio F, Pietrabissa A. 2018. The clinical use of 3D printing in surgery. Updates Surg. 70(3):381–388. doi:10.1007/s13304-018-0586-5.

R Core Team. 2020. R: a language and environment for statistical computing. Vienna (Austria): R Foundation for Statistical Computing.

Shepherd T, Winwood K, Venkatraman P, Alderson A, Allen T. 2020. Validation of a finite element modeling process for auxetic structures under impact. Phys Status Solidi B. 257(10):1900197. doi:10.1002/pssb.201900197.

KEYWORDS Synthetic material; 3D printing; biaxial tensile tests

morgane.evin@univ-eiffel.fr

Interest of porous materials for a mandibular rehabilitation with an implant-supported fixed prosthesis: a numerical study

S. Lemaire, V. Berry-Kromer, F. Thiebaud and C. Bouby

CNRS, Arts et Métiers ParisTech, LEM3, F-54000, Université de Lorraine, Nancy, France

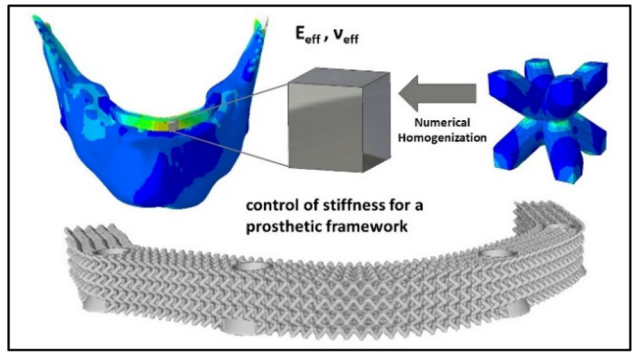


Figure 1. General procedure for the numerical simulation and unit cell of the lattice structure.

1. Introduction

Several possibilities are available for the restoration of a fully edentulous mandible using implant-supported prostheses. A solution using only four implants, with two straight anterior and two tilted posteriors, was originally proposed by Maló in Portugal named 'All-On-Four' concept. This type of prosthesis is based on an attractive principle combining aesthetic, economic and medical considerations. However, it shows several cases of early failures such as loosening of implants and sometimes fracture of the prosthetic framework. Some biological complications can also arise at the bone-implant interface for example. To prevent these complications, the study is focused on the improvement of the prosthetic concept in the direction of a better biomimicry, by analyzing the effects on the mandibular body. Bulk material results in prosthetic framework with a fairly high rigidity that can be deleterious to the mandible. The idea is to lower the rigidity of the prosthetic framework, by introducing porosities in the material. To achieve this goal, focus is laid on the possible use of lattice structures.

2. Method

2.1. Optimisation of the prosthetic framework

In order to control the stiffness and according to this study, the framework was optimized using properties of a lattice structure: the body-centered cubic (BCC) structure. This structure was chosen for its ease of meshing compared to other lattice structures, but also for its good mechanical properties and quasi-isotropic behavior at high relative densities (Mehboob et al. 2020). The idea was to topologically optimize the homogeneous framework using this lattice structure (Figure 1). For this purpose, it was necessary to determine the equivalent homogeneous medium through the determination of a representative volume element (RVE). This homogenization allowed the identification of an effective Young's modulus (E_{eff}) and Poisson's ratio (ν_{eff}). This study was conducted with Abaqus finite element software and will be combined with experimental testing. The lattice structure was numerically tested in compression, by applying a displacement on the top. The determination of E_{eff} was performed by using the reaction force and also the strain energy to validate the results. For ν_{eff} the ratio between the transverse and longitudinal strain was used.

2.2. Finite element modelling

To perform this study, a physiological finite element model was developed. It allows the simulation of different masticatory cycles through the use of isolated forces associated with different masticatory muscles and the application of a coefficient corresponding to the muscle activation (Favot et al. 2014). The masticatory phases studied are the maximum Intercuspal Clenching Position (ICP), the Incisive Clenching (INC) and the Right unilateral Molar clenching (RMOL). The model is composed of cortical and trabecular bones and the prosthesis. The prosthesis is an assembly of four structures: the prosthetic framework, the four implants, the screws and the multibases. The false gum and the teeth were not considered. All contacts are considered as 'Tie'. The effect of the anatomical structures between the two condyles that limit mandibular displacement was controlled by the use of elastic springs. The natural medial temporo-mandibular convergence of the non-prosthetic mandible was respected. This convergence is between 0 and 2.4 mm according to Chen et al. (2013). The numerical model includes the non-prosthetic mandible (Ref) and the restored mandible with bulk titanium framework (Ti) or composed of the previously described lattice structure (LS).

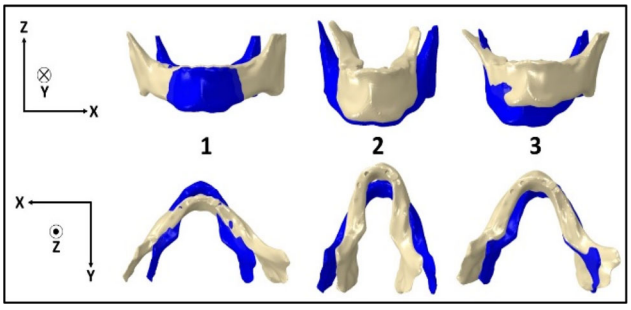


Figure 2. Deformed configuration in beige (magnification-scale factor of 40) of the non-prosthetic mandible during the different masticatory phases (1: ICP, 2: INC, 3: RMOL).

3. Results and discussion

The study of the BCC- unit cell was conducted on a 3D model. Regardless the size of the unit cell, the struts diameter and the type of boundary condition, the convergence of E_{eff} and ν_{eff} was achieved for a repetition of 4 unit cells in each direction of the space. The choice of unit cell size was therefore made based on this RVE, and also the limit thickness of the prosthetic framework to avoid disturbing the dental occlusion. The struts diameter was adjusted to approach the elastic modulus of the cortical bone. Moreover, it was necessary to consider the decrease in stiffness of the numerical model compared to the experimental (Wang et al. 2017). Finally, the unit cell selected has a dimension of 1x1x1 mm^3 with a strut diameter of 0.4 mm. The RVE results to an $E_{eff} = 21.5$ GPa and $\nu_{eff} = 0.385$. The associated relative density is $\rho_{rel} = 0.56$.

Figure 2 shows that for the ICP and INC phases, the transformation is mainly in the xy-horizontal plane. The intercondylar distance (x-direction) has a maximum amplitude during ICP phase with 1.36 mm. For INC phase, the amplitude is 1.23 mm. The RMOL phase has a lower amplitude but more complex motions. It leads to a transformation of the mandible in the 3 planes of space, but especially along x and z. These natural transformations were compared numerically with prosthetic reconstruction for LS and Ti framework.

Regarding results in Table 1, it can be noted that the vertical displacements during ICP and INC phases are negligible. Furthermore, the motion is more complex during RMOL, generating a torsion of the right ramus. Nevertheless, the horizontal displacements of RMOL phase are negligible compared to the other two phases. For the rehabilitated mandible, whether for the Ti or LS framework, the vertical displacements are very small for all phases. The horizontal displacements with the LS framework are the closest to those of the non-prosthetic mandible.

Table 1. Maximum horizontal (U_H) and vertical (U_V) displacements in the non-prosthetic mandible (Ref) with bulk titanium (Ti) and lattice structure (LS) framework reconstruction as a function of ICP, INC and RMOL phases.

	U_H (mm)			U_V (mm)		
	Ti	LS	Ref	Ti	LS	Ref
ICP	1.17	1.27	1.36	0.08	0.08	0.11
INC	1.02	1.09	1.23	0.07	0.07	0.09
RMOL	0.36	0.39	0.42	0.08	0.08	0.10

These results support the idea of reducing the stiffness of the prosthetic framework to ensure that the natural kinematic of the mandible is respected. The stresses generated within the bar will be lower for the LS than the Ti one, and therefore the physiology of the mandibular movement will be preserved.

4. Conclusions

This numerical study was focused on the prosthetic framework constituting the fixed implant-supported prosthesis. For this purpose, the behaviour of the restored mandible with two types of framework was compared to the natural mandible. The use of a lattice structure enables better preservation of the mandible's natural movements. This type of framework would also allow a better adhesion of the acrylic resin for the addition of the false gum and the teeth. Further research are in progress to investigate the influence of this acrylic resin on the mechanical behavior of the prosthesis, depending on its distribution throughout it.

References

Chen C-C, Lin C-C, Lu T-W, Chiang H, Chen Y-J. 2013. Feasibility of differential quantification of 3D temporomandibular kinematics during various oral activities using a cone-beam computed tomography-based 3D fluoroscopic method. J Dent Sci. 8(2):151–159. doi:10.1016/j.jds.2012.09.025.

Favot L-M, Berry-Kromer V, Haboussi M, Thiebaud F, Ben Zineb T. 2014. Numerical study of the influence of material parameters on the mechanical behaviour of a rehabilitated edentulous mandible. J Dent. 42(3):287–297. doi:10.1016/j.jdent.2013.11.027.

Mehboob H, Tarlochan F, Mehboob A, Chang S-H, Ramesh S, Harun WSW, Kadirgama K. 2020. A novel design, analysis and 3D printing of Ti-6Al-4V alloy bio-inspired porous femoral stem. J Mater Sci Mater Med. 31(9):78. doi:10.1007/s10856-020-06420-7.

Wang L, Kang J, Sun C, Li D, Cao Y, Jin Z. 2017. Mapping porous microstructures to yield desired mechanical properties for application in 3D printed bone scaffolds and orthopaedic implants. Mater Des. 133:62–68. doi:10.1016/j.matdes.2017.07.021.

KEYWORDS Dental prosthesis; lattice structure; finite element modeling

samuel.lemaire@univ-lorraine.fr

Modelling the mechanical behavior of the spinal cord and epidurally implanted surgical lead for spinal cord stimulation (SCS) using the finite element method (FEM)

T. Le Tutour[a,b,c], T. Ferrand[a,c], G. Pons[c], K. El Houari[b], S. Collin[b], L. Caillé[c], J. Dany[a], M. Billot[a], M. Roulaud[a], R. Guillevin[d], M. Rochette[b], P. Rigoard[a,c] and A. Germaneau[c]

[a]PRISMATICS Lab (Predictive Research in Spine/Neuromodulation Management and Thoracic Innovation/Cardiac Surgery), Poitiers University Hospital, Poitiers, France; [b]Ansys France, Villeurbanne, France; [c]Institut Pprime, UPR 3346, CNRS – Université de Poitiers – ISAE-ENSMA, Poitiers, France; [d]DACTIM, UMR CNRS 7348, Université de Poitiers et CHU de Poitiers, Poitiers, France

1. Introduction

Patients (10–50%) experience persistent leg or back pain after spine surgery (Chan and Peng 2011) which can be treated with Spinal Cord Stimulation (SCS). SCS is an effective procedure for the treatment of neuropathic extremity pain, it consists in implanting a lead array in the epidural space, targeting nerve fibers of the spinal cord to activate the inhibitory circuitry of pain (Melzack and Wall 1965). Mechanical effects linked to lead implantation on the surrounded tissues are not really studied. Furthermore, mechanical failures of implant, including breakage and migration, can probably and significantly limit the effectiveness of SCS. Finite Element (FE) simulations from patient specific modelling can offer solutions to predict electrical and mechanical behavior of implant in order to avoid any mechanical damage. The objective of this work was to study the mechanical behavior of the spine and spinal cord during SCS considering patient daily movements.

2. Methods

2.1. Geometry

To build a patient specific simulation, a geometrical model of a T8-T10 spine section (Figure 1a) was derived from MRI data of the Cerebro-Spinal Fluid (CSF) and spine. Spinal Cord Toolbox (De Leener et al. 2017) was used to register the PAM50 template (De Leener et al. 2018) (Polytechnique Aix-Marseille Université/ Montreal Neurological Institute) to subject space. Dura-mater, epidural space and inter-vertebral disks were extrapolated.

Table 1. Material properties (Scifert et al. 2002).

Materials	Young modulus (MPa)	Poisson's ratio
White mater	0.0667	0.499
Dura mater	31.5	0.45
CSF	0.001	0.499
Vertebra (bone)	10000	0.3
Annulus fibrosus	4.2	0.45
Nucleus pulposus	1	0.499
Extradural tissue	0.0016	0.495
Lead	0.141	0.41

2.2. Study design

Material properties allocated for each component of the model are given in Table 1 (Scifert et al. 2002).

Concerning loading conditions, a moment of 1 N m was applied on the top surface of the T8 vertebra. The loading axis was varied to mimic the movements of flexion/extension (x) and axial rotation (z). T10 vertebra bottom surface was fixed.

FEM was performed (Ansys 2023R1) to compute displacement, strain and stress fields on tissues (spinal cord, CSF, dura mater and epidural space).

The simulations for each movement were run without and with electrode, by completing with material properties the zone corresponding to the electrode. Contact type of this zone and epidural space was also changed between these two setups. All contacts were assumed to be bonded except for the spinal cord / CSF contacts and lead array / epidural space (for the simulations with a lead array).

3. Results and discussion

Using this model, we were able to observe mechanical fields on an implanted surgical electrode and on the tissues, and how it changes local strain on tissues (Figure 1).

The average displacement of the lead array was found to be of 2.65 mm and 2.91 mm with and without electrode respectively (Table 2) during flexion highlighting a stiffening effect of the implanted device.

Presence of electrode involves local concentration of high strain values in particular around the extremities. This preliminary study has to be completed with a stress analysis to identify levels of interface contact pressures involved by the presence of the SCS device. A specific analysis has also to be led on the device to determine stress levels and to study risks of mechanical failure according to physiological loadings with higher values of imposed moments. A validation of this approach could be envisaged by performing biomechanical tests on anatomical spine segments.

Then a multi-physical approach will be envisaged coupling electrical and mechanical simulation to analyse effectiveness of SCS during posture variations and movements

Table 2. Displacement values during flexion-extension movements.

	Maximal lead array zone displacement (mm)		Average lead array zone displacement (mm)		Maximal spinal cord displacement (mm)		Average spinal cord displacement (mm)	
Movement/lead array presence	Yes	No	Yes	No	Yes	No	Yes	No
Flexion/extension	4.73	5.31	2.65	2.97	5.40	5.43	2.42	2.46
Axial rotation	7.81	7.43	4.00	3.93	6.39	6.38	2.62	2.61

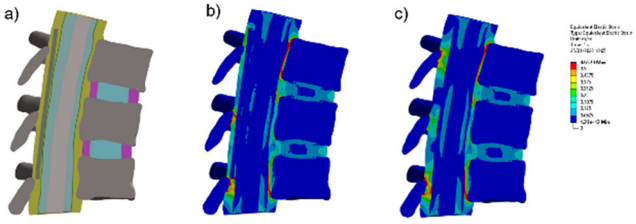


Figure 1. (a) Sagittal cross section of the model after flexion. (b) Equivalent strain with implanted lead array. (c) Equivalent strain without lead array.

4. Conclusions

This model could enhance our understanding of spinal cord biomechanics under the influence of SCS and help to refine electrical models by considering patient postural changes.

References

Chan C, Peng P. 2011. Failed back surgery syndrome. Pain Med. 12(4):577–606. doi:10.1111/j.1526-4637.2011.01089.x.

De Leener B, Fonov VS, Collins DL, Callot V, Stikov N, Cohen-Adad J. 2018. PAM50: unbiased multimodal template of the brainstem and spinal cord aligned with the ICBM152 space. NeuroImage. 165:170–179. doi:10.1016/j.neuroimage.2017.10.041.

De Leener B, Lévy S, Dupont SM, Fonov VS, Stikov N, Louis Collins D, Callot V, Cohen-Adad J. 2017. SCT: spinal Cord Toolbox, an open-source software for processing spinal cord MRI data. NeuroImage. 145:24–43. doi:10.1016/j.neuroimage.2016.10.009.

Melzack R, Wall PD. 1965. Pain mechanisms: a new theory: a gate control system modulates sensory input from the skin before it evokes pain perception and response. Science. 150(3699):971–979. doi:10.1126/science.150.3699.971.

Scifert J, Totoribe K, Goel V, Huntzinger J. 2002. Spinal cord mechanics during flexion and extension of the cervical spine: a finite element study. Pain Physician. 5(4):394–400.

KEYWORDS Spinal cord stimulation; finite element method; mechanical and electrical simulations; patient specific modeling

tom.le.tutour@univ-poitiers.fr

Numerical scheme for dynamic elastographic measurements in the cornea

G. Merlinia[b], S. Imperiale[b] and J.-M. Allain[a,b]

[a]LMS, Ecole Polytechnique, CNRS—Université Paris-Saclay, France; [b]Inria – Palaiseau, France

1. Introduction

The cornea is the outer transparent lens of the eye provides two thirds of the refractive power. The shape, similar to a dome, is given by a balance between the intraocular pressure applied by inner fluids and the mechanical properties related to a complex microstructure. Indeed, mechanical properties are fundamental indicators in clinics. For example, the keratoconus is a progressive deformation of the cornea into a cone, due to a weakening of the tissue. An early detection of the pathology could prevent the degeneration of the tissue and loss of vision. Among the different methods to study the mechanical response of the cornea, dynamic optical coherence elastography (dOCE) is a promising technique, as it gives access to localized information in a clinical environment. It is based on in-vivo tracking of shear waves propagation as a result of a transient stimulation. A Finite Element modelling reproducing the experimental results could allow to study the mechanical properties and have a diagnosis of the tissue. In nearly incompressible materials, such as the cornea, the excited elastic wave is decoupled in shear waves that are 150 times slower than the compressional waves. The double-scale of the phenomena has a major effect on the stability of the scheme for the approximation of the wave propagation, resulting in very long computations. In addition, the enforcement of incompressibility is a well-known problem in FE modelling, which causes an over constraint of the solution and incorrect computation of pressure. The objective of this study is to propose an efficient scheme to obtain a reliable modelling of transient elastography measurements applied to the cornea and to improve tissue characterization techniques.

2. Methods

2.1. Space discretization strategy

The acoustic micro-Tapping is a recent excitation technique developed by Ambroziński et al. (2016) that generates a low-frequency shear waves with a short pressure pulse on the cornea surface. In order to model the resulting shear-wave propagation phenomenon, we propose a FE approximation with high-order Spectral elements together with a Mass Lumping approach (Cohen 2002). This method allows to strongly reduce the computational cost for Mass matrix inversion, by computing the mass matrix integrals with the Gauss-Lobatto rule and finally obtaining a diagonalisation of the Mass matrix.

Incompressibility is a well-known problem in FE approximation with pure displacement method, due to locking, ill-conditioning of the stiffness matrix and incorrect pressures approximations. To overcome these limitations, we use a mixed formulation with the introduction of the pressure as a variable defined in a FE space with lower order. In particular, we choose ℚ!-ℚ#$%& elements (Bernardi and Maday 1999) for the approximation of the displacement and pressure field, as a good compromise between accuracy of the solution and efficiency. In addition, we propose a new definition of the divergence operator to efficiently compute the volumetric contribution of the solution, by strongly reducing the number of computations to obtain the pressure solution.

2.2. Time discretization strategy

Given the large-scale problem and the complex geometry of the cornea, we need a fully explicit scheme. The explicit leapfrog scheme would be a natural choice as it shows high efficiency and second order accuracy. However, the stability is guaranteed if the scheme is at least fast as the fastest oscillating phenomena. As a consequence, the time-step is strongly decreased by the velocity of compressional waves and the number of iterations to complete the simulation are proportionally increased. In this study, we propose a strategy inspired by local time-stepping method and based on the use of Chebyshev Polynomials in the form proposed by Grote et al. (2022). With the modified scheme, the contribution of the pressure wave is computed explicitly in an inner loop and the 'new' stability condition is less restrictive on the largest time-step that ensures stability. The application of the Chebyshev polynomials is fundamental to obtain the optimal number of iterations to compute the volumetric component of the solution. While maintaining stability and accuracy, we obtain a fully explicit algorithm that is more efficient in terms of CPU time compared to the standard LF scheme.

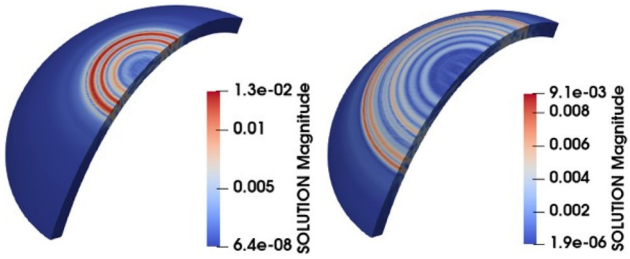


Figure 1. Simulation of shear wave propagation in nearly-incompressible isotropic cornea at $t = 2$ ms (on the right) and $t = 4$ ms (on the left).

3. Results and discussion

We have performed simulations of elastic wave propagation in homogeneous isotropic cornea. Comparing the classic LF scheme to our modified scheme, we obtain simulations that in the latter case are almost three times faster. In particular, with 2.5 million of DoFs and the ratio between the Lamé parameters $\lambda/\mu = 500$ (Poisson ratio $\nu = 0.499$), we measure with classic LF scheme a computational time of 615 *s*, while with the modified scheme the simulation was completed after 260 s with a $L(L^{"}(\Omega))$ error of 2%. In order to clarify this result, we underline that the new stability condition with a larger time-step comes at a price: at each step we have to apply the pressure operator for each iteration of the inner loop. The efficiency of the scheme relies on the fact that the computational cost to apply the pressure operator is significantly smaller with respect to the cost for the shear operator, also due to the optimizing choices adopted for the space discretization strategy.

In particular, we measure an average computational time for the shear operator that is around 0.034s and for pressure operator that is 0.016s. This difference will be larger when we will consider a more complex description of the cornea behavior and loading condition. In fact, the cornea has a non-linear anisotropic behavior due to the presence of collagen fibrils and it is subjected to the posterior pressure applied by inner fluids. As a consequence, the shear operator will be enriched by the anisotropic component and the prestress effect.

References

Ambroziński Ł, Song S, Yoon SJ, Pelivanov I, Li D, Gao L, Shen TT, Wang RK, O'Donnell M. 2016. Acoustic micro-tapping for non-contact 4D imaging of tissue elasticity. Sci Rep. 6(1):38967. doi:10.1038/srep38967.

Bernardi C, Maday Y. 1999. Uniform inf–sup conditions for the spectral discretization of the stokes problem. Math Models Methods Appl Sci. 09(03):395–414. doi:10.1142/S0218202599000208.

Cohen GC. 2002. Higher-order numerical methods for transient wave equations [Internet]. Berlin, Heidelberg: Springer Berlin Heidelberg. [accessed 2022 Aug 1]. doi:10.1007/978-3-662-04823-8.

Grote MJ, Michel S, Sauter S. 2022. Stabilized leapfrog based local time-stepping method for the wave equation [Internet]. [accessed 2022 Aug 1]. http://arxiv.org/abs/2005.13350.

KEYWORDS Dynamic elastography; incompressibility; numerical scheme; cornea

giulia.merlini@polytechnique.edu

Numerical study of flow rate variations in microfluidic dynamic cell culture

I. Zarpellon Nascimento[a], T. Messelmani[a], C. Legallais[a], E. Leclerc[a,b], R. Jellali[a] and A. Le Goff[a]

[a]BMBI UMR 7338 CNRS UTC; [b]LIMMS IRL 2820 CNRS – IIS, University of Tokyo

1. Introduction

Microfluidic chambers are commonly used to culture cells and expose them to a well-defined wall shear stress, that depends on the fluid flow rate and on the microfluidic chamber dimensions (Mehling and Tay 2014). In microfluidic organ-on-chip devices, culture medium usually flows in closed loop in order to mimic blood circulation in the human body. Closed loop microfluidic circulation can be achieved by different means, including centrifugation (Garcia-Cordero 2010), valve-including pressure-driven circuits (de Graaf 2022). Here, we study the flow of culture medium though a biochip installed in a parallel culture platform connected with a peristaltic pump (Baudoin 2012). The goal is to provide guidelines for experimental design based on microscale flow engineering (Stone 2004).

2. Methods

To achieve closed loop circulation of culture medium through a cell-seeded biochip, we use a peristaltic pump as illustrated in Figure 1. Ideally, the flow rate Q' entering the biochip should match exactly the flow rate Q imposed by the pump (Figure 1a). In some experiments however, the medium accumulates in the inlet well. In this case Q' is smaller than Q and may become insufficient to feed and oxygenate cells (Figure 2b). In order to design culture chambers and define suitable culture conditions, we model the flow through the biochip in order to identify the range of parameters where biochips can be safely operated with peristaltic pumps.

The pressure drop between the inlet and outlet wells depends on the biochip hydraulic resistance R, which increases as cells proliferate in the chamber (Messelmani 2022): $\Delta P = RQ'$. If $Q = Q'$, the fluid index in inlet and outlet wells remains stable, else the time evolution of fluid index in the inlet well H is governed by the difference between the two flow rates. We consider three different expressions for ΔP, in the case of (1) a tight system (2) a system with air leaking from the seal between the well and the lid (3) a system with fluid leaking at the well/biochip junction.

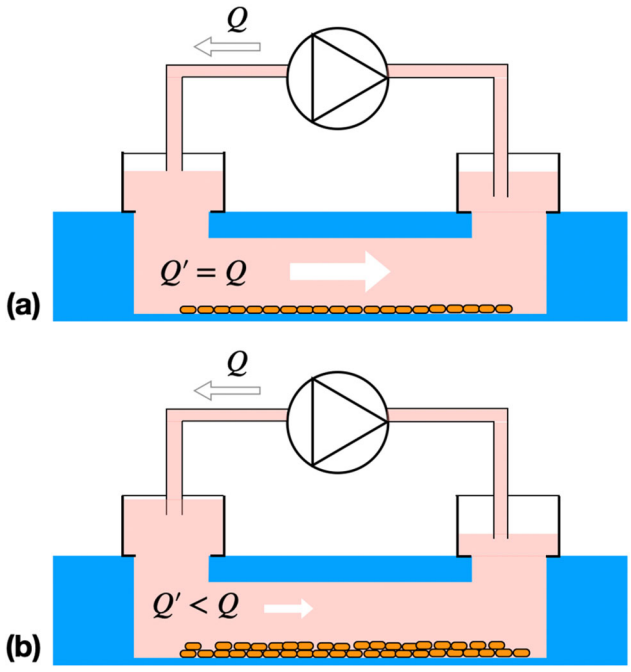


Figure 1. (a) Perfect and (b) imperfect balance between pump and biochip flow rates.

We get three different systems of first-order differential equations. Numerical integration of these equations is performed in Python using scipy.integrate subpackage. A fifth-order implicit Runge-Kutta method was chosen in order to avoid non-physical oscillations.

3. Results and discussion

3.1. Tight circuit

In a tight circuit, the total volume of liquid and the amount of air above the free surfaces are both conserved. We compute the pressures in inlet and outlet well assuming mass conservation. Since air is compressed in the inlet well, even a moderate increase in fluid index is sufficient to reach the target flow rate (Figure 2a) after about half an hour.

3.2. Air leak

We model an air leak by introducing a threshold pressure for the air in the inlet well. Beyond this threshold, air leaks through the seal and the pressure no longer increases, even if the volume of air above the fluid keeps decreasing. An equilibrium can be reached in this situation if the threshold P_m is sufficiently large. The limit value depends on R and Q. When an equilibrium is found, the fluid index in the

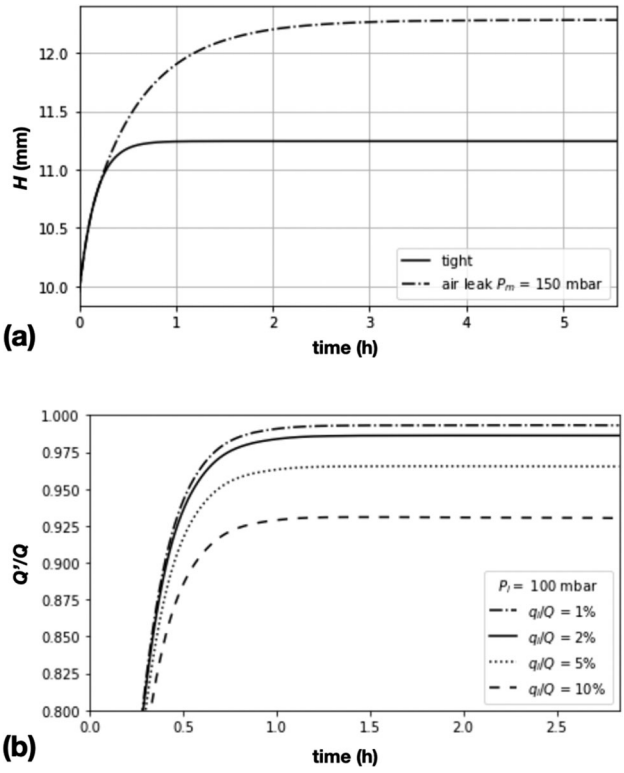


Figure 2. Simulation of the time evolution of (a) the fluid index in the inlet well and (b) the flow rate through the biochip.

inlet well is larger than in a tight circuit and the response time is also increased, as illustrated in Figure 2a.

3.3. Liquid leak

We model a liquid leak by allowing fluid to leave the inlet well with a flow rate q_l when the pressure in the liquid at the bottom of the inlet well reached a threshold P_l. Figure 2b shows that for $P_l = 100$ mbar, an equilibrium situation is reached within one hour, where Q' is very close to Q. For this value of P_l, leaks occur only for the circuits containing the most resistive biochips. When P_l decreases, culture medium is more likely to leak at the connector, even for moderate values of biochip resistance. If P_l is too low for the pressure difference between the two wells to match the pressure drop corresponding to Q, the system cannot function in appropriate conditions and the cells cultured in the biochip are at risk. The dimensions of the biochips and of the wells should therefore be chosen so that the pressure drop in the biochip does not exceed the limit pressure the device can withstand.

4. Conclusions

We demonstrate that in most situations an equilibrium situation is reached, in which culture medium flows through the biochip at the desired flow rate. The characteristic time to reach this equilibrium ranges from a few minutes to an hour, which remains short in comparison with the doubling time of most cell types. The system can operate even when it is not perfectly tight, unless the resistance is too large.

References

Baudoin R, Alberto G, Paullier P, Legallais C, Leclerc E. 2012. Parallelized microfluidic biochips in multi well plate applied to liver tissue engineering. Sens Actuators B Chem. 173:919–926. doi:10.1016/j.snb.2012.06.050.

de Graaf MNS, Vivas A, van der Meer AD, Mummery CL, Orlova VV. 2022. Pressure-driven perfusion system to control, multiplex and recirculate cell culture medium for organs-on-chips. Micromachines. 13:1359. doi:10.3390/mi13081359.

Garcia-Cordero JL, Basabe-Desmonts L, Ducrée J, Ricco AJ. 2010. Liquid recirculation in microfluidic channels by the interplay of capillary and centrifugal forces. Microfluid Nanofluid. 9(4–5):695–703. doi:10.1007/s10404-010-0585-4.

Mehling M, Tay S. 2014. Microfluidic cell culture. Curr Opin Biotechnol. 25:95–102. doi:10.1016/j.copbio.2013.10.005.

Messelmani T, Le Goff A, Souguir Z, Maes V, Roudaut M, Vandenhaute E, Maubon N, Legallais C, Leclerc E, Jellali R. 2022. Development of liver-on-chip integrating a hydroscaffold mimicking the liver's extracellular matrix. Bioengineering. 9(9):443. doi:10.3390/bioengineering9090443.

Stone HA, Stroock AD, Ajdari A. 2004. Engineering flows in small devices. Annu Rev Fluid Mech. 36(1):381–411. doi:10.1146/annurev.fluid.36.050802.122124.

KEYWORDS Microfluidics; cell culture; biochip

anne.le-goff@utc.fr